Fluxional Carbon Cages and their 'Shapeshifting' Properties

BISMILLAH, AISHA,NAZIRAN

Durham University
Department of Chemistry

Fluxional Carbon Cages and their ‘Shapeshifting’ Properties

Aisha Naziran Bismillah

A Thesis Submitted for the Degree of Doctor of Philosophy

June 2019

Dedicated to my loving parents

– Haji Mohammed Bismullah

– Hajjan Nasim Bismillah

Table of Contents

Abstract

Fluxional carbon cages[1] such as bullvalene, the barbaralyl cation and barbaralane are molecules which possess 'shapeshifting' properties. These shapeshifting properties arise through rapid and reversible Cope rearrangements, which allow for every carbon atom to exchange with every other carbon atom giving rise to thousands of degenerate valence isomers. This rare phenomenon is crucial in the study of the fundamental concept of valence isomerisation and can manifest as a dynamic structural library arising from a single, rigid molecule.[2]

The possibility of accessing a large number of nondegenerate isomers from functionalised bullvalene derivatives has been utilised to design shapeshifting sensors,[3] where the equilibrium distribution is shifted through specific noncovalent bonding interactions or dynamic covalent bonds when interacting with different guests. Applications of these molecules, however, are restricted by their lengthy and low-yielding syntheses as well as their structural complexity, which hinders a full understanding over equilibria and rearrangements.

This Thesis will discuss investigations into barbaralane structures – an attractive alternative fluxional scaffold which can be readily synthesised and exists as just two isomers in rapid flux at room temperature. New classes of tractable fluxional carbon cages have been explored with their rearrangements and equilibria being fully understood and controlled, in both the solution and solid state. These bistable nondegenerate systems are later elaborated into highly fluxional cations – the stability of which is tuned by substituent effects.

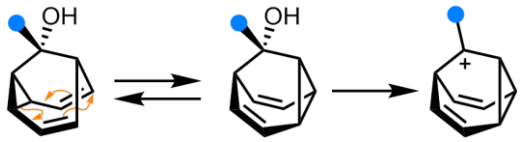

Figure 1. Nondegenerate interconverting barbaralanes which form cationic fluxional carbon cages. Functional groups are represented by coloured circles.

1. (a) W. von E. Doering and W. R. Roth, *Tetrahedron*, 1963, **19**, 175; (b) P. Alhberg, D. L. Harris and S. Winstein, *J. Am. Chem. Soc.* 1993, **115**, 7445; (c) J. G. Henkel and J. T. Hane, *J. Org. Chem.* 1983, **48**, 3858.
2. P. R. McGonigal, C. de León, Y. H. Wang, A. Homs, C. R. Solorio-Alvardo and A. M. Echavarren, *Angew. Chem. Int. Ed.* 2012, **51**, 13093.
3. (a) K. K. Larson, M. He, J. F. Teichert, A. Naganawana and J. W. Bode, *Chem. Sci.* 2012, **3**, 1825; (b) J. F. Teichert, D. Mazunin and J. W. Bode, *J. Am. Chem. Soc.* 2013, **135**, 1134.

Declaration

The scientific work described in this Thesis was carried out in the Chemistry Department at Durham University between October 2015 and June 2019. Unless otherwise stated, it is the work of the author and has not been submitted in whole or in support of an application for another degree or qualification at this or any other University or institute of learning.

Signed:

Date: 21st June 2019

Conferences Attended and Presentations Given

1. RSC Macrocyclic and Supramolecular Chemistry Meeting, University of Durham, UK, December 2015.
Poster presentation: *The Dynamic Covalent Rearrangements of the Barbaralyl Cation*

2. Durham University Researchers' Poster Competition, University of Durham, UK, April 2016.
Poster presentation: *Shapeshifting Molecules as Chemical Sensors*

3. RSC North Eastern Organic Division Regional Meeting, University of Newcastle, UK, April 2016.
Poster presentation: *The Dynamic Covalent Rearrangements of the Barbaralyl Cation*

4. RSC North Western Organic Division Regional Meeting, University of Central Lancashire, UK, May 2016.
Poster presentation: *The Dynamic Covalent Rearrangements of the Barbaralyl Cation*

5. Durham University Chemistry Postgraduate Gala, University of Durham, UK, June 2016.
Poster presentation: *The Dynamic Covalent Rearrangements of the Barbaralyl Cation*

6. RSC Macrocyclic and Supramolecular Chemistry Meeting, University of Edinburgh, UK, December 2016.
Poster presentation: *The Dynamic Covalent Rearrangements of the Barbaralyl Cation*

7. RSC North Eastern Organic Division Regional Meeting, University of Durham, UK, March 2017.

8. Durham University Chemistry Postgraduate Gala, University of Durham, UK, June 2017.
Oral presentation: *Shapeshifting Barbaralols and Barbaralyl Cations*

9. 12th International Symposium on Macrocyclic & Supramolecular Chemistry, University of Cambridge, UK, July 2017.

10. 16th European Symposium on Organic Reactivity, University of Durham, UK, September 2017.
Poster presentation: *The Dynamic Covalent Rearrangements of the Barbaralyl Cation*

11. 46th John Stauffer Distinguished Lecture in the Sciences, University of Southern California, USA, April 2018.

12. 2nd Early Career Researchers Macrocyclic and Supramolecular Chemsitry Meeting, University of Manchester, UK, July 2018.
Oral presentation: *Shape-Selective Crystallisation of Fluxional Carbon Cages*

13. Supramolecular Chemistry at Work (SupraLyom), University of Lyon, France, December 2018.
Poster presentation: *Shape-Selective Crystallisation of Fluxional Carbon Cages*

14. STEM for Britain, Houses of Parliament, UK, March 2019.
Poster presentation: *Shapeshifting Molecules as Chemical Sensors*

Awards, Grants and Scholarships

1. Ustinov Travel Grant, December 2015 | Individual award of £100 to present research at the 2015 Macrocyclic and Supramolecular Chemistry Meeting.

2. Royal Society of Chemistry Travel Bursary, December 2015 | Grant of £100 to disseminate research on 'The Dynamic Covalent Rearrangements of the Barbaralyl Cation'.

3. Durham University Researchers' Poster Competition – Best Faculty of Science Poster Prize, April 2016 | 'Shapeshifting Molecules as Chemical Sensors', acknowledgement of the effective communication of research to individuals with diverse backgrounds.

4. RSC North Western Organic Division Regional Meeting – Poster Prize, May 2016 | 'The Dynamic Covalent Rearrangements of the Barbaralyl Cation', poster prize winner for original research in the area of organic chemistry.

5. RSC Macrocyclic and Supramolecular Chemistry Meeting – Poster Prize, December 2016 | 'The Dynamic Covalent Rearrangements of the Barbaralyl Cation', poster prize winner for innovative research in the area of supramolecular chemistry.

6. Durham University Science Faculty Researchers' 3 Minute Thesis Competition – Best Faculty of Science, March 2017 | 'The Synthesis and Study of Shapeshifting Molecules', acknowledgement of the effective communication to a non-specialist audience in 3 minutes.

7. Royal Society of Chemistry Travel Grant, April 2017 | Grant of £130 to travel to the 12th International Symposium on Macrocyclic & Supramolecular Chemistry.

8. Durham University Science Faculty Researchers' 3 Minute Thesis Competition – Audience Favourite Award, May 2017 | Acknowledgement by the audience of the effective communication to a non-specialist audience in 3 minutes.

9. Ustinov Travel Grant, May 2017 | Individual grant of £100 to travel to the 12th International Symposium on Macrocyclic & Supramolecular Chemistry.

10. Regional 3 Minute Thesis Competition – Best Presentation of 2017 Award, June 2017 | 'The Synthesis and Study of Shapeshifting Molecules', acknowledgement of the effective communication to a non-specialist audience in 3 minutes.

11. British Women of Federation Graduates – Marjorie Shaw Scholarship, June 2017 | Competitive grant of £1000 awarded in recognition of academic excellence.

12. 16th European Symposium on Organic Reactivity – 2nd Place Poster Prize, September 2017 | 'The Dynamic Covalent Rearrangements of the Barbaralyl Cation', poster prize winner for original research in the area of organic reactivity.

13. RSC Researcher Mobility Grant, January 2018 | Competitive Grant of £3024 to travel overseas (University of Southern California to work with Professor G. K. Surya Prakash) to undertake a short scientific visit for research purposes.

14. *Chem. Soc. Rev.* Oral Presentation Prize, July 2018 | 'Shape-Selective Crystallisation of Fluxional Carbon Cages', oral presentation prize awarded at the RSC's 2018 Early Career Researchers Macrocyclic and Supramolecular Chemistry meeting for innovative research and excellent presenting skills in the area of supramolecular chemistry.

15. US–UK Fulbright All Disciplines Scholar Award, February 2019 | Principle candidate awarded $60000 for a Postdoctoral position at Dartmouth College under the supervision of Professor Ivan Aprahamian.

16. STEM for Britain, March 2019 | Invited to present ground-breaking research to members of parliament at the national science, technology, engineering and maths (STEM) competition for early-career researchers.

17. SciFinder Future Leaders Participant, May 2019 | Selected to participate in the international CAS Future Leaders programme for early-career scientists.

Acknowledgements

786

[Bismi'llāhi 'r-Rahmāni 'r-Rahīm]

"Verily, with every hardship there is ease" **(إِنَّ مَعَ الْعُسْرِ يُسْرًا)** [Surah Inshirah 94: 6]

Paul McGonigal. Without you I wouldn't be the chemist or person I am today. Thank you for allowing me to work on an incredible and challenging project, in an amazingly skilled research group under the guidance of an invaluable, exceptionally gifted supervisor. Your sage advice and insightful criticism has shaped my career journey in such a way that I will be eternally indebted. I am extremely grateful for your admiration of my strengths, pursuance of my weaknesses and patient encouragement which has allowed me to become the best researcher I can possibly be. Thank you will never be enough. What I am even more appreciative for though, is being pushed to my limits every now and then so that my research is as close to perfection as it can be, you not answering my every question so that I can arrive at my own answers while creating my own theories and being taught the difference between an em and en dash in hope that everything I write will be grammatically correct. It is an absolute honour to have completed my PhD under your mentorship.

Durham University and Funding Agencies. I am grateful to Durham University for providing me endless resources and to all the funding agencies (EPSRC, RSC, BFWG and FFWG) which have supported me financially.

Collaborators. G. K. Surya Prakash, Archith Nirmachander, Vicente Galvan and Alain Goeppert – thank you for my unforgettable time at USC and contributing to my project invaluably. Marc Etherington and Andrew Danos – thanks for allowing me to aid your projects with my skills while becoming a team and good friends.

Alyssa Avestro. Thank you for getting me through the hardest year of my PhD and providing me with endless advice and encouragement throughout all my years. You are an absolute inspiration and I am always in awe of you. I want you to know that I wouldn't have got to the end without you by my side as my friend and role model.

James Walton. A huge thanks for guidance and support throughout my years at Durham. I hope you continue to roll down the hill without me and miss our card-signing conversations. I know I will.

Academic Staff. Certain staff members deserve a mention for their input towards my PhD and they include: Mark Wilson, Matt Kitching, David Hodgson, and Paul Hodgkinson. Ann-Marie O'Donoghue must have a special mention for her kindness.

Andrew Tropylium Turley. I couldn't have asked for a better brother in the McG group. Thank you for picking me up and pushing me along every time I fall, heart-to-heart every so often, instilling your immense knowledge into me and challenging me when it comes to glassware and solvents (don't deny it). Post Malone till we die!

Phil Hope. I have never met someone who brings me so much joy on a daily basis. Thank you for lighting up every dull day in Durham, lunch breaks with scientific discussions and genuine care for my day-to-day activities while making sure I live my best life in and out of the lab. Tell me Ma I won't be coming home for tea!

Alice Harnden. My housemate, my NMR buddy and my best friend. I thank you for sharing this journey with me from start to end and teaching me how to bake as a pro.

Gemma Parker. Thanks for being my bestie, phone calls, trips every so often and making sure that our friendship is only filled with true support, love and barbaralols.

Jack Fradgley. Thank you for brunch on the weekend, overcoming your hatred of buses for me and testing my patience every day. I know I tested you tenfold. 3 6 9 11.

Postdoc Crew. Jiri Sturala, thank you looking out for me since day one and providing me with endless knowledge that I should already know. Brette Chapin, thank you for our coffee dates with heartfelt chats, proof-reading everything I write and never judging me. Abhijit Mallick, thank you for making all the late nights and weekends much easier, bestowing me with your expertise and eventually becoming my friend.

CG235. The submission of this Thesis would not have been possible without the continued support of the past and present members in the McGonigal, Avestro and Walton groups. I am grateful for the scientific puzzles we have solved together and the continuous banter which my PhD would not be complete without. Thank you to everyone for also listening to my music choice every day without complaining. Names that must be mentioned are: Chris Jennings, Jasmine Cross, Kas Khan, Ismay Fox, Robert O'Niell, Tom Thorogood, Aina Rebesa, TJ Mitchell, Pavan Kumar, David Bradley and Ketaki Samanta. Burhan Hussein, Luke Williams and Atreyee Mishra – I have no doubt that CG235 will be left in the best of hands (with snacks).

Juan Aguilar. My PhD has relied very heavily on NMR and I am certain I would not have got any of my spectra without you letting me loose on the spectrometers. Thank you for dealing with my princess tantrums, tolerating me pushing the spectrometer to its limits and allowing NMR to become a home filled with spectra and friendship.

Dimitry Yufit. Your expertise has been utterly invaluable. A huge thank you conducting X-ray analyses on everything I give you, theorising how my crystals should be grown and what I should be attempting while always being so friendly.

Analytical Services, Administrative and Technical Staff. I would like to thank all the members of the analytical services, administrative and technical staff for their cooperative assistance throughout my PhD. Special mentions go to: Raquel Belda-Vidal, Jean Eccleston, Catherine Hefferrnan, Annettte Passmore and David Apperely. Alice Smith and Ivan Smith – my mornings wouldn't be complete without you both.

Dr Ian Pomery and Dr Anthony Parkins. Thank you for providing me with the best healthcare and making sure that my MS never limits me in any way. My nurses also deserve a special mention, thank you for being so comforting and friendly.

The Girls. Charlotte, Jenny, Emily, Halima, Atikah, Najma and Sabrina – thank you for reminding me of the world outside of my lab and office. You girls are amazing!

James Ashcroft. Thank you for always being there, no matter what, no matter when, no matter where. I owe you a lot more than you will ever take credit for.

My family at Five Oaks. I love all of you endlessly. Abba – your prayers are everything to me. A huge thank you to Chacha and Kani for being my go-to parents whenever I have needed extra support, courage and love. Kashif, Aftab and Bilal – thank you for being the best brothers a sister could ask for, always wanting what is best for me no matter what and spoiling me endlessly. Fiazia, you are the reason I got into research so thank you for providing me with endless inspiration. Then there's Ashia, Zuhaib and Adeela whom this journey wouldn't be complete without. Lastly, Ibrahim and Inayah, thank you providing me with immense cuteness and making my time away from the lab 100% worth it! I am thankful for the joy you both bring me.

My loving parents. I am nothing without you. Thank you for celebrating every success with me, constantly being proud of me and never allowing me to give up. Your endless prayers, immeasurable support and pure love have got me through the worst and best days of my PhD. This Thesis is for both of you.

Abbreviations

Ac	Acetyl
AIBN	Azobisisobutyronitrile
ASAP	Atmospheric solids analysis probe
BDSB	Bromodiethylsulphonium bromopentachloroantimonate(V)
br	Broad
Bu	Butyl
CD	Cyclodextrin
COSY	Correlation spectroscopy
d	Doublet
DCE	1,2-Dichloroethane
DFT	Density functional theory
DIPEA	*N*,*N*-Diisopropylethylamine
DMAP	4-(Dimethylamino)pyridine
DMF	Dimethylformamide
DMSO	Dimethyl sulphoxide
dvcpc–dvcpc	Divinylcyclopropylcarbinyl–divinylcyclopropyl
equiv.	Equivalents
EXSY	Exchange spectroscopy
ESI	Electrospray ionisation
Et	Ethyl
HMBC	Heteronuclear multiple-bond correlation spectroscopy
HPLC	High-performance liquid chromatography
HR	High resolution
HSQC	Heteronuclear single-quantum correlation spectroscopy
IPr	1,3-Bis(2,6-diisopropylphenyl)imidazol-2-ylidene
JohnPhos	(2-Biphenyl)di-*tert*-butylphosphine.
LDA	Lithium Diisoproylamide
m	Multiplet
Me	Methyl
Mosher's Acid	α-Methoxy-α-trifluoromethylphenyl acetic acid

M.P.	Melting point
MS	Mass spectrometry
NBS	*N*-bromosuccinimide
NMO	*N*-methylmorpoline *N*-oxide
NMR	Nuclear magnetic resonance
NOESY	Nuclear overhauser effect spectroscopy
NVOC	*o*-Nitroveratryloxycarbonate
Ph	Phenyl
q	Quartet
ROESY	Rotating frame nuclear overhauser effect spectroscopy
rt	Room temperature
s	Singlet
ssNMR	Solid-state nuclear magnetic resonance
t	Triplet
TFA	Trifluoroacetic acid
THF	Tetrahydrofuran
TLC	Thin-layer chromatography
UV	Ultraviolet
VT	Variable-temperature
VT NMR	Variable-temperature nuclear magnetic resonance
VT-XRD	Variable-temperature X-ray diffraction
XRD	X-ray diffraction

Note: conventional abbreviations for units, physical quantities and stereochemical terms are not included here.

General Experimental Methods

Materials: All reagents were purchased from commercial suppliers (Sigma-Aldrich, Acros Organics, Fluorochem or Alfa Aesar) and used without further purification.

Instrumentation and Analytical Techniques: Analytical thin-layer chromatography (TLC) was performed on neutral aluminium sheet silica gel plates (Fluka, 60778-25EA) and visualised under UV irradiation (254 nm). Nuclear magnetic resonance (NMR) spectra were recorded using a Bruker Advance (III)-400 (^{1}H 400.130 MHz and ^{13}C 100.613 MHz), Varian Inova-500 (^{1}H 500.130 MHz and ^{13}C 125.758 MHz), Varian VNMRS-600 (^{1}H 600.130 MHz and ^{13}C 150.903 MHz) or a Varian VNMRS-700 (^{1}H 700.130 MHz and ^{13}C 176.048 MHz) spectrometer, at a constant temperature of 298 K unless otherwise stated. For variable-temperature (VT) measurements, operating temperatures were calibrated using an internal calibration solution of MeOH and glycerol. Chemical shifts (δ) are reported in parts per million (ppm) relative to the signals corresponding to residual non-deuterated solvents [$CDCl_3$: δ = 7.26 or 77.16, CD_2Cl_2: δ = 5.32 or 54.00, CD_3CN = δ = 1.94, 1.32 or 118.26, $(CD_3)_2CO$ = δ = 2.50 or 39.5, C_4D_8O = δ = 1.73, 3.58 or 25.5, D_2O δ = 4.79]. Coupling constants (J) are reported in Hertz (Hz). ^{13}C NMR Experiments were proton-decoupled, whereas ^{19}F NMR experiments are coupled and referenced to an internal standard, hexafluorobenzene (HFB, δ = 164.99 ppm), unless otherwise stated. Assignments of ^{1}H and ^{13}C NMR signals were accomplished by two-dimensional NMR spectroscopy (COSY, NOESY, HSQC, HMBC). NMR spectra were processed using MestReNova version 11. Data are reported as follows: chemical shift; multiplicity; coupling constants; integral and assignment. Low-resolution atmospheric solids analysis probe (ASAP)-MS were performed using a Waters Xevo QTOF equipped with an ASAP. High-resolution electrospray (HR-ESI) and ASAP (HR-ASAP) mass spectra were measured using a Waters LCT Premier XE high resolution, accurate mass UPLC ES MS (also with ASAP ion source). Melting points (M.P.) were recorded using a Gallenkamp (Sanyo) apparatus and are uncorrected.

Thesis Layout

Chapter 1 provides an introduction to fluxional carbon cages, discussing their properties, initial synthetic efforts and the modern-day approaches by which they can be accessed. The applications of fluxional carbon cages (in particular bullvalene) are also discussed where analyte binding can occur through covalent bonding and noncovalent bonding interactions. Chapter 2 focuses on a series of barbaralanes that interconvert between two nondegenerate isomers in solution, but resolve to single isomers in the solid state. Chapter 2 is presented in the form of an article which has recently been published in a peer-reviewed journal. No attempts have been made to rewrite this work out of context; however minor asthetic alterations have been made in the interest of consistency throughout the Thesis. The original paper is reproduced in its original format at the end of this Thesis. Chapter 3 discusses the covalent and noncovalent control over a fluxional sp^3–carbon stereocentre in solution and in the solid state. Finally, Chapter 4 describes several novel synthetic pathways towards generating a barbaralane bearing several substituents which can be utilised to generate stable cationic fluxional carbon cages. Chapters 3 and 4 have been formulated in a style suitable for publication at a later date, including a focussed discussion of the key data followed by a more comprehensive account of the data in Experimental Sections and Appendices. Chapter 5 summarises the advances made within the area of fluxional carbon cages during the duration of this Thesis.

CHAPTER 1

FLUXIONAL CARBON CAGES: SYNTHESIS, PROPERTIES AND APPLICATIONS

Synopsis

This introductory Chapter focuses first on the concept of fluxional carbon cages, describing how their 'shapeshifting' properties arise while explaining how slight structural alterations in the core of the fluxional carbon cage can generate different numbers of degenerate and nondegenerate isomers. This explanation is followed by discourse on the primary fluxional molecules: bullvalene, barbaralane and the barbaralyl cation. Early investigations into bullvalene synthesis are explored, followed by the shift to more streamlined syntheses with the use of computational methods which help to elucidate structures within an isomeric mixture. The classic and modern syntheses of barbaralane and its substituted derivatives are also addressed. Seminal studies into the barbaralyl cation are presented containing explanations into important intermediates, rearrangements, reaction mechanisms and energy barriers where ^{13}C labelling is considered to provide vital information. Finally, applications of fluxional carbon cages (in particular bullvalene) such as investigations into analyte binding through noncovalent bonding interactions and covalent bonding are evaluated.

1.1 Fluxional Carbon Cages

Fluxional carbon cages such as bullvalene[1] (**1**), the barbaralyl cation[2] (**2**), barbaralane[3] (**3**) and semi-bullvalene[4] (**4**) (Figure 1.1) are dynamic structures that undergo rapid and reversible Cope rearrangements (the rupture and formation of a single and/or double bonds without the migration of atoms or groups), allowing their atomic skeletons to reconfigure dynamically without breaking apart. These rearrangements cause the relative positions and orientations of any appended functional groups to switch back and forth between thousands of distinct molecular shapes.

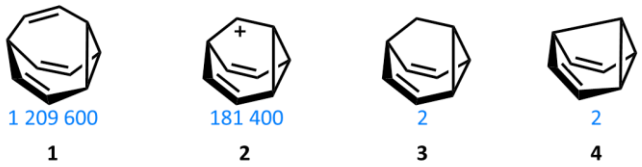

Figure 1.1. Structural formulas of bullvalene (**1**), the barbaralyl cation (**2**), barbaralane (**3**) and semi-bullvalene (**4**) with their respective number of degenerate isomers (blue text).

This unique occurrence is intriguing to chemists as these carbon cages exemplify that a dynamic structural library can exist from a single rigid molecule. At the same time, fluxional molecules have proven to be crucial in the study of the fundamental concept of valence isomerisation, while demonstrating that they have the potential to adapt their chemical structures in response to their environment.[5] Since Doering and Roth[1a] first predicted the properties and structure of bullvalene (**1**), fluxional carbon cages have attracted the curiosity of the chemistry community and have been investigated in solution and in the solid state while being exploited as chemical sensors for biologically active compounds.[5b,6] However, systems utilising a bullvalene core have, until recently, only been accessible through difficult syntheses with low yields. These systems have proven challenging to understand due to the vast number of isomers which are in equilibria, with rearrangements that are continually occurring at ambient temperatures. Recent advances within the field of synthetic organic chemistry[7] combined with resourceful computational calculations[8] have facilitated the preparation of several substituted derivatives, as well as investigations into their

intricate systems and interesting applications, while also allowing for more tractable systems to be synthesised, examined and fully understood.

1.2 Dynamic Cope Rearrangements

Fluxional carbon cages are molecules that can rapidly pass back and forth between a large number of constitutional isomers, imparting 'shapeshifting' properties. These isomers can interconvert through low-energy [3,3]-sigmatropic rearrangements where a σ-bonded atom or group, flanked by one or more π-electron systems, shifts to a new location with a corresponding redistribution of the C–C bonds. In principle, each dynamic isomer can have a distinct structure with a different bonding connectivity, lie in equilibrium and be interconverted by a series of reversible rearrangements giving rise to dynamic constitutional isomerism (Scheme 1.1).

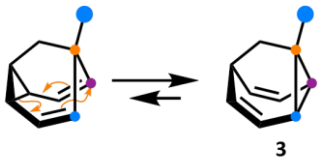

Scheme 1.1. A substituted barbaralane with its Cope rearrangement demonstrating dynamic constitutional isomerism. Coloured circles exhibit carbon atoms remaining in the same relative positions. The larger blue circle represent a functional group.

Due to this fluxionality, bullvalene (**1**) and the barbaralyl cation (**2**) can exist as a mixture of thousands of degenerate isomers which can interconvert rapidly, resulting in all carbon and hydrogen signals appearing equivalent on the nuclear magnetic resonance (NMR) timescale at ambient temperature. For example, the ^{1}H NMR spectrum for bullvalene (**1**) at room temperature consists of a single broad peak however, at temperatures around –60 °C, the four aliphatic and six olefinic protons of the molecule give rise to distinct signals.[9] Bullvalene (**1**) – a cyclopropane connected with three vinyl arms connected at a methine group – can interconvert between 1 209 600 degenerate valence isomers by strain-assisted Cope rearrangements, whereas barbaralane (**3**) – a rigid tricyclic diene with a methylene bridge – interconverts between two degenerate isomers. Barbaralane (**3**) is only able to interconvert between two isomers due to the olefins only residing on two arms of the cage; therefore when the Cope rearrangement takes place and the π-bonds are

reorganised, every methine group remains in an essentially unchanged position (relative to the others as only the bonding is altered). However, bullvalene (**1**) contains an additional olefin opening up the third arm of the carbon cage to sigmatropic rearrangements. This additional pathway allows every carbon to change its relative position with every other carbon, through a series of sequential sigmatropic rearrangements giving rise to thousands of degenerate isomers (Scheme 1.2).

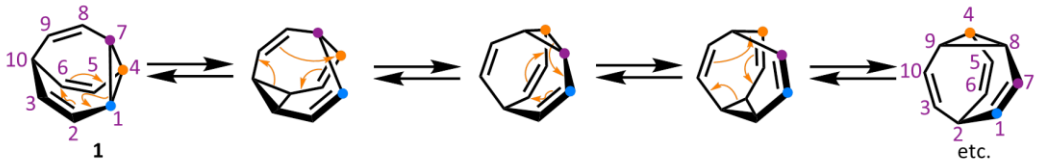

Scheme 1.2. Bullvalene (**1**) with five of its valence isomers demonstrated through Cope rearrangements; coloured circles and numbers demonstrate the movement of the cyclopropane carbon atoms.

The case for the barbaralyl cation (**2**) is slightly different as even though there are only two participating olefins, the positive charge produces a vacant p-orbital into which electron density can be shifted facilitating the participation of the third arm in the rearrangements. Analogous fluxional carbon cages also exist (*i.e.*, azabullvalene[10] and semi-bullvalene (**4**) (Figure 1.1)); however, the number of accessible isomers remains dependent on the number of participating olefins and vacant p-orbitals within the skeletal framework. Functionalised derivatives (Figure 1.2) provide nondegenerate valence isomers with inequivalent constitutions; therefore, when their C–C bonds trade places with one another, the positions and relative orientations of their substituents are altered, endowing them with dynamic shapes and making them ideal building blocks for adaptive chemistry.

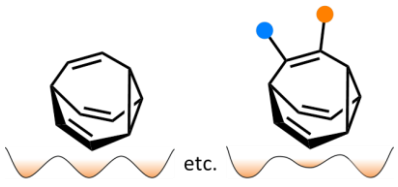

Figure 1.2. An unfunctionalised degenerate bullvalene *vs* functionalised nondegenerate bullvalene. A schematic representation illustrates the changes in degeneracy when functionalisation occurs. Blue and orange circles represent different functional groups.

1.3 Bullvalene

Bullvalene (**1**) is a structurally unique, small hydrocarbon molecule consisting of ten carbon atoms and ten hydrogen atoms allowing for ten distinguishable positions with three symmetry axes – that exists as a mixture of degenerate isomers that rapidly interconvert through a series of rearrangement reactions. Anecdotally, the name bullvalene was derived from the nickname of Doering, known by his students as the 'bull'. Owing to the usually tough research group seminars, bullvalene (**1**) was chosen to rhyme with fullvalene – combining Doering's nickname with another molecule of great interest for the research group at the time. At the same time, the suffix 'valene' is also used to name compounds that undergo valence isomerisation.[1d] Early investigations of bullvalene chemistry focused on improving the synthetic methodology used to prepare compound **1**. The initial methodology utilised ultraviolet (UV) irradiation[11] as a key step towards the synthesis of bullvalene (**1**) and was followed by bromination to form another important intermediate, bromobullvalene.[12] Bromobullvalene helped to form the basis of rational synthetic strategies into a wide range of substituted bullvalenes where investigations remained reliant upon temperature-dependent NMR studies.[13] Recent advances within the field of organic chemistry – where functionalised bullvalones[14] have proven to be important intermediates and organometallic chemistry has served as a crucial synthetic step – combined with quantum computational methods[8] have led to more streamlined syntheses of bullvalene derivatives while also allowing for the prediction of isomer networks.

1.3.1 Classical Syntheses of Bullvalenes

The properties and structure of bullvalene (**1**) were first postulated in 1963 by Doering and Roth as part of a study on thermal rearrangements.[1a] Within the same year Schröder serendipitously encountered the structure by investigating the dimerisation of cyclooctatetraene (**5**) and subsequently exploring its photolysis (Scheme 1.3).[1b] Although the overall yield is rather low at 6%, this two-step synthesis is still one of the shortest preparations of bullvalene (**1**) to date.[1b,15,16] The synthesis proceeds by the dimerisation of cyclooctatetraene occurring at 100 °C forming **6**

which is then photochemically opened in diethyl ether to form **1** and benzene as a by-product.

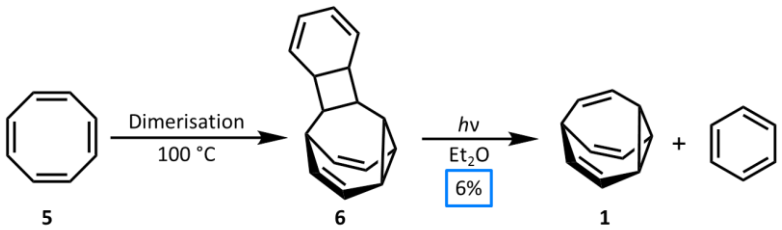

Scheme 1.3. The first synthesis of bullvalane (**1**) with a yield of 6% as demonstrated by Schröder.[1a]

Inspired by this first synthetic procedure, the research groups of Doering and Scott utilsied photolysis of other unsaturated alicyclic systems as precursors to access bullvalene (**1**) with higher yields (Scheme 1.4).[11] Doering and co-workers prepared bullvalene (**1**) by irradiating 4a,8a-dihydronaphthalene (**7**) in *n*-pentane at 0 °C, with compound **7** made by partial thermal decomposition of hydrocarbon **8**. Although this synthetic pathway is short, it was deemed impractical[16] due to the formation of naphthalene and other unwanted products which proved difficult to separate from compound **1**. The synthetic procedure that Scott and co-workers designed was based on irradiating bicyclo[4.2.2]deca-2,4,7,9-tetraene (**9**) to afford bullvalene (**1**) cleanly in a yield of 64%. The main drawback of this procedure was the low-yielding and tedious synthesis of compound **9** from **10**. Simultaneously, the thermal decomposition of the tosylhydrazone sodium salt (**10**) led to a complex mixture of $C_{10}H_{10}$ products including compounds **9** and **7** with yields of 38% and 12%, respectively.

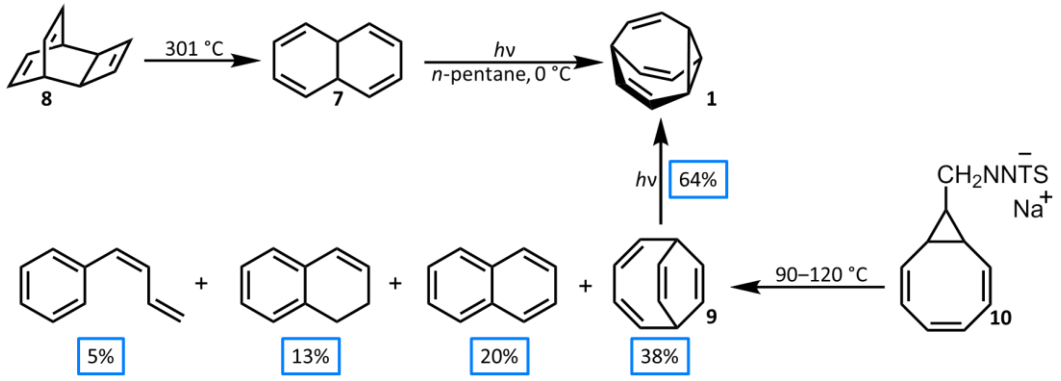

Scheme 1.4. Two synthetic procedures towards bullvalane (**1**) produced by Doering and Scott.[17,18]

Serrotosa[17] and Doering[18] developed synthetically different and lengthy pathways to first form barbaralone (**11**) followed by different synthetic conversions to bullvalene (**1**) (Scheme 1.5). Doering and co-workers first treated barbaralone (**11**) with diazomethane in a one-carbon homologation to produce bullvalone (**13**) with a yield of 24% along with its isomeric aldehyde (**12**) in a yield of 24%. Reduction of compound **13** with sodium borohydride produced the corresponding alcohol (**14**) which was acetylated with acetic anhydride in pyridine at 130 °C to form compound **15** in a yield of 40% over two steps. The final step involved pyrolysis of **15** at a very high temperature of 345 °C to produce the desired into bullvalene (**1**).

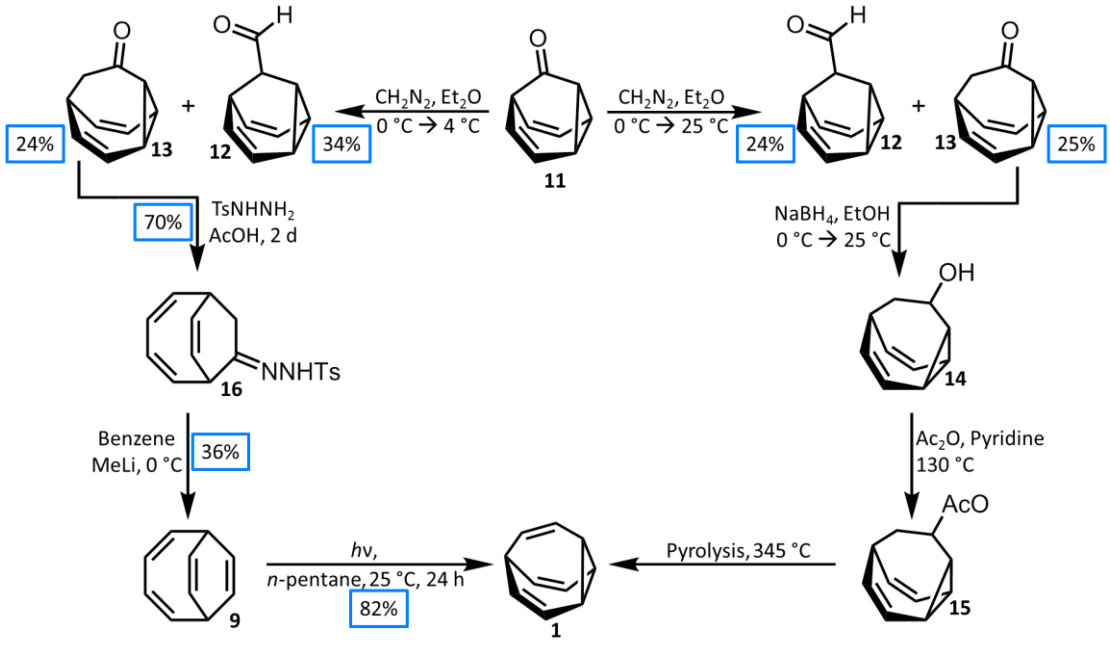

Scheme 1.5. Two different synthetic pathways towards bullvalane (**1**) produced by Doering and Serratosa.[17,18]

Encouraged by this procedure, the Serrotosa group treated barbaralone (**11**) in a similar manner to also produce bullvalone (**13**) and compound **12** in yields of 24% and 34%, respectively. From here, compound **13** was treated with *p*-toluenesulphonyl hydrazine in acetic acid to produce the tosylhydrazone (**16**) in a yield of 70%. Anionic fragmentation of compound **16** with excess methyllithium in benzene at 0 °C gave compound **9** which was then converted to bullvalene (**1**) through UV irradiation. The desired compound (**1**) was produced in a yield of 82%.

Progress into the preparation of various mono- and poly-substituted bullvalene derivatives was pioneered by Schröder, Oth and co-workers, who generally used bullvalene to form the common intermediates bromobullvalane[19] (**17**) and dibromobullvalene[20] (**18**) (Scheme 1.6). Bromobullvalene (**17**) is prepared in two steps by dibromination of compound **1** with bromine, followed by a dehydrobromination step with potassium *tert*-butoxide. Dibromobullvalene (**18**), is prepared by repeating the sequence of dibromination and dehydrobromination on compound **17**. These intermediates allowed for several bullvalene derivatives to be synthesised[20a,21] through subsequent synthetic steps[16] such as the reaction of bromobullvalene (**17**) with magnesium to form a bullvalene Grignard derivative[22] (**19**), or by treating dibromobullvalene (**18**) with Gilman's reagent (*i.e.*, Me_2CuLi or Ph_2CuLi) to form dimethylbullvalene (**20**) and diphenylbullvalene (**21**) respectively as mixtures of nondegenerate valence isomers.[23] Dimethylbullvalene (**20**) formed the 5,2-, 6,2- and 6,3-disubstituted isomers in a ratio of 1:3.2:2.3 whereas diphenylbullvalene (**21**) formed the same isomers in a different ratio of 1:5.7:7.6.[23]

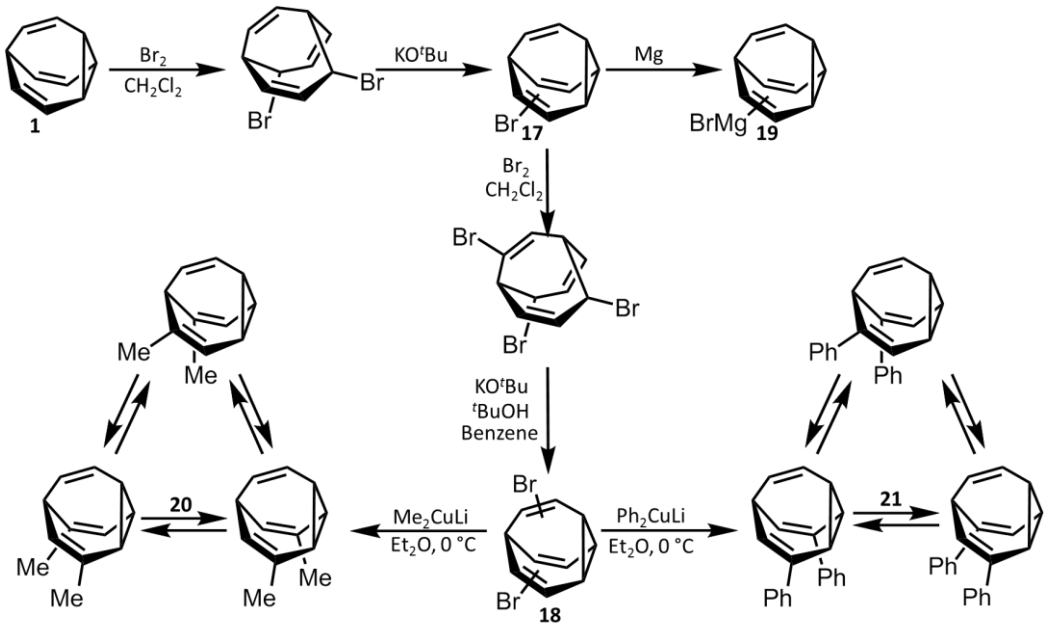

Scheme 1.6. Preparation of bromobullvalene (**17**) and dibromobullvalene (**18**). Compound **17** reacts with magnesium to form a bullvalene Grignard compound (**19**). Compound **11** is added to Me_2CuLi to form three valence isomers of dimethylbullvalene (**20**) whereas the addition of Ph_2CuLi forms the same three diphenylbullvalene (**21**) valence isomers but in a different isomeric ratio.

1.3.2 Advances within the Syntheses of Bullvalenes

In 2006, Bode and co-workers developed a concise and scalable synthesis of a tetra-substituted functionalised bullvalene[14] (**22**) (Scheme 1.7), which has subsequently been used as an essential building block for the synthesis of other, further elaborately-substituted bullvalenes. The study of these tetra-substituted bullvalanes allow for insights and fundamental knowledge into their rearrangements, equilibria, isomeric composition and most interestingly, their supramolecular interactions which permit the sensing and binding of several guest molecules.[5b,24]

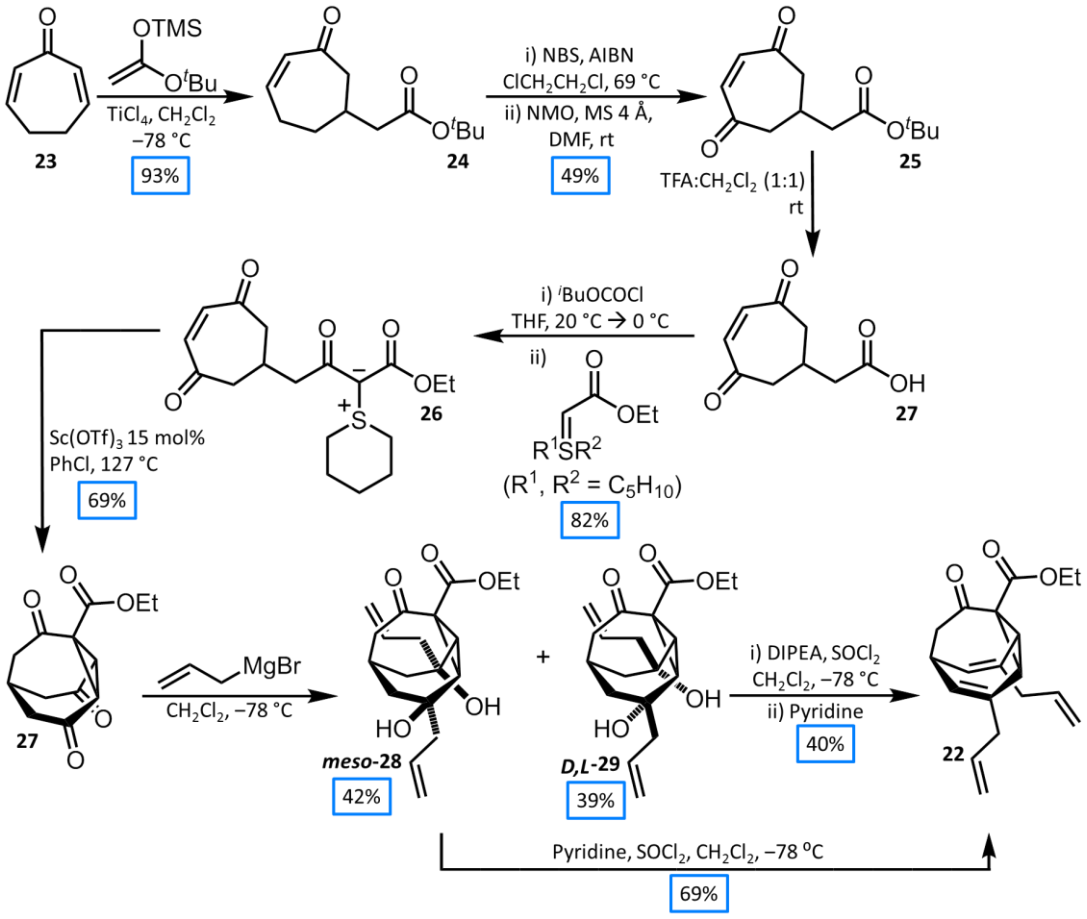

Scheme 1.7. Multi-step synthesis of the tetra-substituted functionalised bullvalene **22** produced by Bode and co-workers.

The synthesis of **22** begins with cycloheptadienone (**23**), which is subjected to a titanium tetrachloride Mukaiyama–Michael addition[25] to provide the enone (**24**) with a yield of 93%. Radical bromination of compound **24** followed by oxidation with *N*-methylmorpholine-*N*-oxide (NMO) affords **25** which is then subsequently

deprotected with a 1:1 mixture of trifluoroacetic acid and dichloromethane. The formation of the stabilised ylide (**26**), proceeds through activation of the acid (**27**) with *iso*-butyl chloroformate followed by coupling with the sulphur ylide.[26,27] A novel Lewis acid catalysed intramolecular cyclopropanation permits the smooth conversion of **26** into the important triketone (**27**) with a yield of 69%. Compound **27** undergoes a highly regioselective addition of allylmagnesium bromide to two of the ketones (not adjacent to the ester functional group) producing a 3:2 mixture of ***meso*-20** in a 42% yield and ***D,L*-21** in a 39% yield. Both ***meso*-28** and ***D,L*-29** were successfully converted into bullvalane (**22**) using similar methods.[28] Premixing thionyl chloride and pyridine in dichloromethane before adding ***meso*-28** afforded **22** in a yield of 69%, whereas ***D,L*-29** was first treated with a solution of Hünig's base (DIPEA) and thionyl chloride followed by the addition of pyridine to yield **22** in a lower yield of 40%. Although **22** is an important precursor towards tetra-substituted bullvalenes, further synthetic steps are required to form other tetra-substituted bullvalenes with different functional groups. These functional groups are required for different applications and overall this equates to a longer synthetic procedure in which overall yields are relatively low.[29]

The most concise and efficient synthesis of bullvalene (**1**), as well as a range of mono- and di-substituted analogues, is a simple two-step procedure with yields ranging 40–81% that was reported by Fallon and co-workers[8] (Scheme 1.8). Inspired by Buono's work in 2006,[30] reporting that cyclooctatetraene (**5**) undergoes a [6+2] cycloaddition reaction with alkynes in the presence of a CoI_2(dppe)/ZnI_2/Zn catalyst system to give bicyclo[4.2.2]deca-2,4,7,9-tetraene (**9**), combined with Scott's discovery of compound **9** photoisomering through a di-π-methane rearrangement back to bullvalane (**1**),[11b] Fallon foresaw a shorter synthetic pathway to substituted bullvalenes. Employing this reaction pathway, several bicyclo[4.2.2]deca-2,4,7,9-tetraene precursors (**23**) were synthesised featuring alcohols, benzyl and silyl groups with good yields ranging 61–91%. UV irradiation of these precursors in acetone provides the corresponding substituted bullvalenes (**24**) with a 71% yield of bullvalene (**1**) itself. This procedure however, doesn't tolerate electron-withdrawing groups or demonstrate the formation of aryl-substituted bullvalenes.

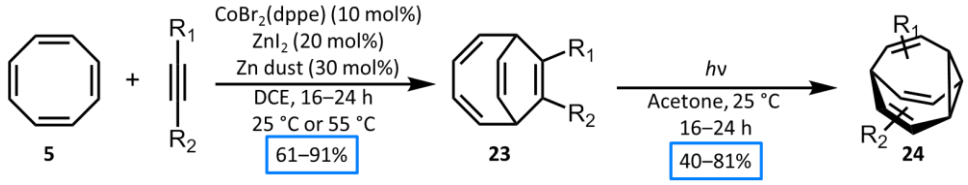

Scheme 1.8. Most practical and concise synthesis of bullvalene (**1**) and a variety of mono- and di-substituted analogues (**24**) as reported by Fallon and co-workers.

Interestingly, when phenyl-substituted bicyclo[4.2.2]deca-2,4,7,9-tetraene (**25**) was irradiated under the same conditions as compounds **23**, another product, lumibullvalene (**27**), was isolated with a yield of 63% (Scheme 1.9). The desired bullvalene product was not detected in the reaction mixture, as it was not formed seemingly due to the di-π-methane rearrangement proceeding through an alternative pathway and forming isolumibullvalane (**26**). Compound **26** presumably undergoes a cyclopropane-accelerated Cope rearrangement. Although, the switch in reactivity is not fully understood, access to lumibullvalene frameworks may prove useful in other aspects of chemistry.[11b]

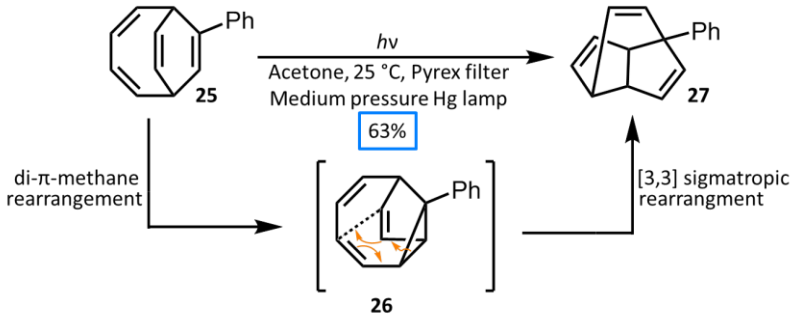

Scheme 1.9. Synthesis of phenyl-substituted lumibullvalene (**27**) forming from isolumibullvalene (**26**).

In parallel to publishing improved synthetic routes, Fallon built upon Bode's convenient isomer coding system[29c] to develop a programme which can enumerate any possible substituted bullvalene network to assist in understanding the challenging ensemble of exchanging bullvalene isomers (Figure 1.3). This computational toolbox evaluates the full rearrangement network and generates corresponding isomer codes – a system used to help show which positions are substituted and their corresponding isomers all as different codes – and interconnecting transition states while identifying enantiomeric pairs. Comparing experimental isomer ratios for mono- and di-

substituted bullvalenes (determined by low-temperature NMR) against the computationally predicted ratios does show consistency; however, di-substituted bullvalanes also require two-dimensional (2D) experiments due to their complex mixtures and signal overlap. This computational technique not only addresses the issue of understanding complex mixtures but will also prove to be a valuable system when analysing bullvalene mixtures.

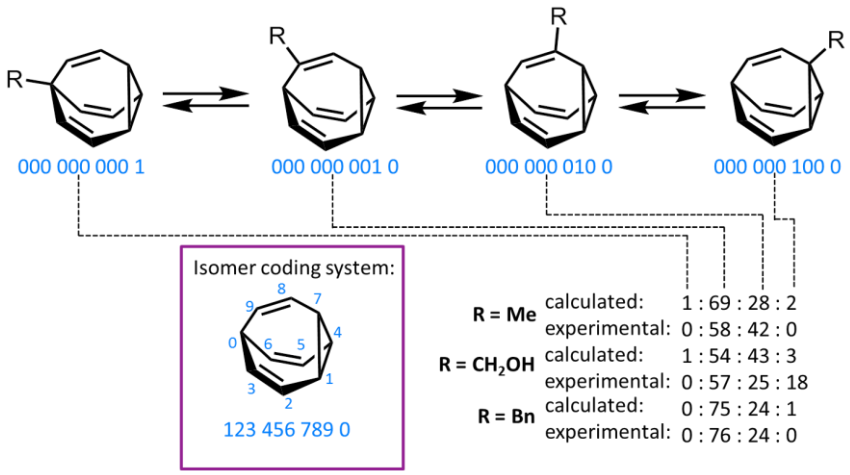

Figure 1.3. Isomer coding system relating to the mono-substituted bullvalene network analysis, including experimental and computationally predicted isomer ratios.

1.4 Barbaralane

Barbaralanes are rigid tricyclic dienes with a C_9H_{10} skeleton and have been reported in the literature as early as the 1960s.[1a] Although the structure of barbaralane (**3**) ring system differs slightly from bullvalene (**1**) as an ethylene arm is replaced by a methylene bridge, the main difference between the molecules remains the number of degenerate valence isomers. Neutral barbaralane (**3**) is a system with fluxional character at ambient temperatures which interconverts between only two isomers due to strain-assisted Cope rearrangements. The first report of a barbaralane was a derivative containing a carbonyl group (*i.e.*, barbaralone (**11**)) which was prepared as an intermediate[31] for the synthesis of bullvalene (**1**). The chemical properties and characteristics of the barbaralane (tricyclo[3.3.1.$0^{2,8}$-nona-3,6,-diene) system and its derivatives have been of substantial interest sparking a wealth of new synthetic procedures[32] while also demonstrating intriguing rearrangements which have been investigated by a combination of analyses including computational calculations.[32c,33]

As barbaralane (**3**) only fluctuates between two degenerate isomers unlike other shapeshifting molecules, the isomeric mixtures have proven easier to understand. Therefore, synthetic evolution has focused on creating concise methods towards structurally simple barbaralanes in tractable systems to allow for investigations into their shapeshifting dynamics and equilibria.[7,8]

1.4.1 Traditional Syntheses of Barbaralanes

The first synthesis of a barbaralane derivative, barbaralone (**11**), was reported in 1963[31] and was built upon in 1967[18] by Doering and co-workers in their attempt to improve the synthesis of bullvalene (**1**) (Scheme 1.10). The key step of the synthetic route involves an intramolecular carbene insertion into the central double bond of the cycloheptatriene ring system resulting in the formation of the carbonyl-containing derivative (**11**). The synthesis starts with a Buchner reaction of ethyl diazoacetate and benzene which proceeds under harsh conditions and long reaction times to yield cycloheptatriene[16] **28**. Hydrolysis of the ester[16] (**28**) to the carboxylic acid (**29**) is followed by a conversion into an acyl chloride (**30**) using thionyl chloride. The synthetic pathway proceeds through the use of diazomethane with **30** to afford the diazomethyl ketone (**31**). Compound **31** is subsequently treated with copper(II) sulphate in a mixture of benzene and hexanes under reflux to yield the ketocarbene so that the carbonyl containing derivative, barbaralone (**11**) can be formed in an intramolecular cyclopropanation reaction. Surprisingly, barbaralone (**11**) rearranges at a faster rate than bullvalene (**1**) which may be a result of an inductive effect from the carbonyl group or perhaps from the larger angle strain, which is relieved slightly within the transition state.[34]

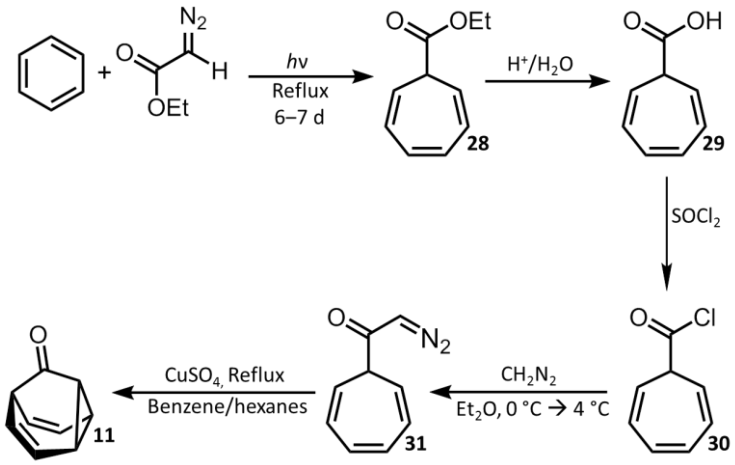

Scheme 1.10. Synthesis of barbaralone (**32**) by Doering and Roth.

Subsequently, barbaralone (**11**) has been produced by a range of different synthetic pathways[13,17,18,35] – acting as a key intermediate in the synthesis of bullvalene (**1**). Most methods utilise diazomethane as an important reagent to form a key diazomethyl ketone intermediate (**31**), which upon heating at reflux with a source of copper (*i.e.*, Cu(II) acetylacetonate) would afford the desired barbaralone (**11**). Due to barbaralane's fluxional character at ambient temperatures, other research groups such as the Paquette[36] group pursued functionalised barbaralane systems. The synthetic methods include homologating barbaralone (**11**) with a Wittig reagent, methylenetriphenyl-phosphorane, to form a methylene derivative or by treating cyclooctatetraene (**5**) with antimony pentafluoride in liquid sulphur dioxide to form a sulphone barbaralane derivative by a 1,5-cycloaddition.

It was Henkel in 1983[3a] who reported the first efficient synthesis of barbaralane (**3**) in five steps starting from 2-adamantanone (**32**) with an overall yield of 59% (Scheme 1.11). The synthesis proceeds under mild conditions and takes a completely different route from previous approaches (*i.e.*, the carbene insertion method) that had suffered from one or more low-yielding steps. The procedure to synthesise barbaralane (**3**) starts with the treatment of 2-adamantanone (**32**) and sodium azide in methanesulphonic acid to give the carboxylic acid (**33**) with a yield of 80%. Oxidative decarboxylation of compound **33** was accomplished by treatment with lithium diisopropylamide followed by oxygenation and an acidic workup to give compound **34**. Allylic bromination of **34** with *N*-bromosuccinimide (NBS) gave the

bromo ketone (**35**) which participated in a base-catalysed ring closure to afford barbaralone (**11**) with a high yield of 95%. Barbaralone (**11**) is then transformed to a tosylhydrazone which forms barbaralane (**3**) by treatment with *n*-butyllithium in tetrahydrofuran causing a Bamford-Stevens type elimination.[37]

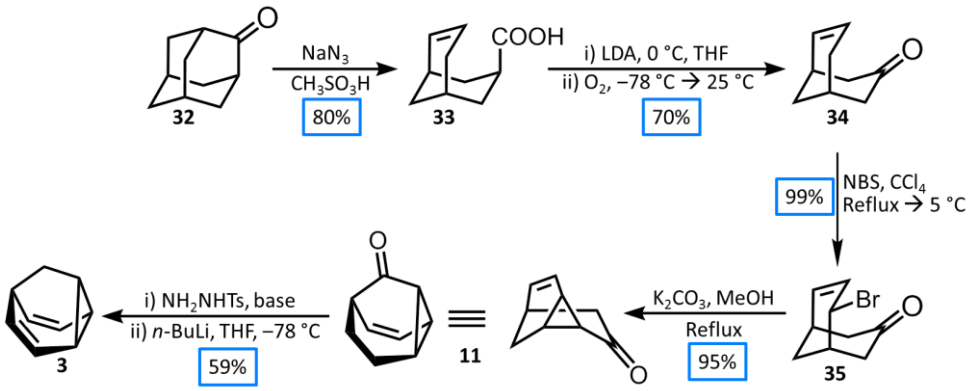

Scheme 1.11. Stepwise procedure to synthesise barbaralane (**3**) from 2-adamantanone (**32**) as demonstrated by Henkel and co-workers.

In 1995, Quast and co-workers developed a synthetic procedure towards a series of 3,7-substituted barbaralanes with varying functionality including cyano and phenyl groups[38] (Scheme 1.12). The synthesis starts with 3,7-bicyclo[3.3.1]nonanedione (**36**) which, when treated with phenyllithium, affords phenyl-1-oxaadmantanol (**37**). Compound **37** is then subjected to a mixture of boron triflouride and diethyl ether with a slight excess of acetic anhydride to afford compound **38**. The reaction which produces compound **38** also generates other uncharacterised products, but hydrolysis with aqueous sodium hydroxide allowed these unknown products to form compound **38**, leading to a high overall yield of 84%. Subsequently, cerium(III) chloride and phenylithium was treated readily with compound **38** to afford the single tertiary alcohol (**39**). A solution of sulphuric acid in acetic acid was used to dehydrate alcohol **39** quantitatively to yield diphenyldiene (**40**). The formation of diphenyldiene (**40**) was followed by allylic bromination with NBS to form compound **41** which was confirmed by X-ray crystallography. The final step involves the reductive cyclisation of compound **41** with a zinc-copper couple under irradiation to yield the desired 3,7-phenylbarbaralane (**42**). The overall yield for this synthesis is 50%, which compares

favorably with another procedure reported by Kessler and Ott who also utilsied compound **36** as a key precursor but only achieved an overall yield of 10%.[39]

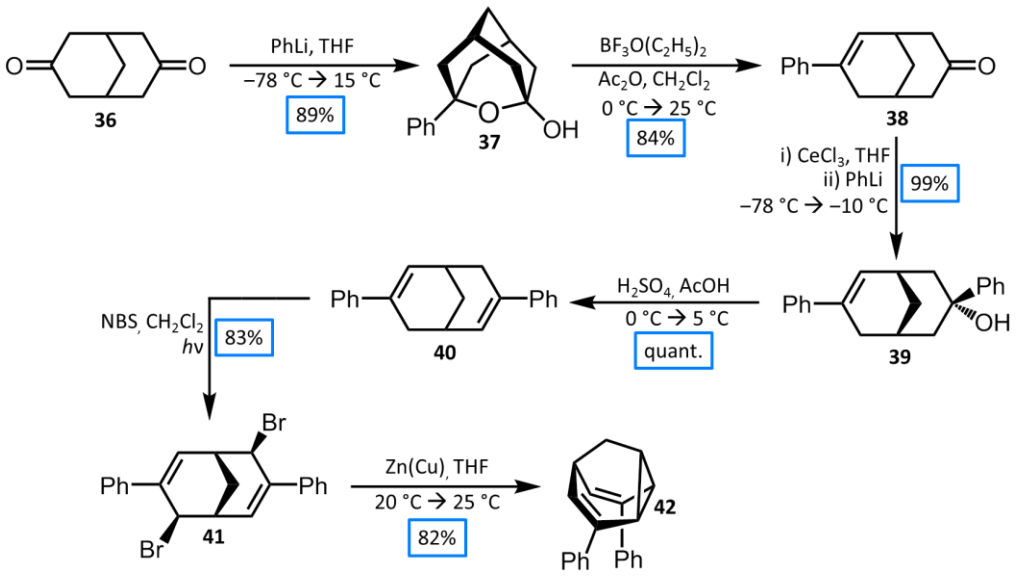

Scheme 1.12. Stepwise procedure to synthesise 3,7-phenylbarbaralane (**42**) as reported by Quast and co-workers.

The following year, Quast built upon his previous research and produced a pathway towards 2,6-substituted barbaralanes with a variety of different functional groups (Scheme 1.13).[40] An example which follows a similar method for the synthesis of 3,7-substituted barbaralanes is 2,6-bis(phenylethynyl)barbaralane (**43**). The synthesis starts with an analogous derivative of 3,7-bicyclo[3.3.1]nonanedione (**32**) in which the difference is the position of the carbonyl groups. Meerwein's diketone **44** is first treated with cerium(III) chloride[41] following the addition of phenyllithium which affords the *endo,endo*-2,6,-diol **45** in a high yield of 94%. Dehydration of compound **45** with sulphuric acid in acetic acid gives rise to compound **42** in the same manner as demonstrated in Scheme 1.11. Radical bromination with NBS formed compound **47**, which was then subjected to a reductive cyclisation to form 2,6-bis(phenylethynyl)barbaralane (**43**) in a yield of 82%. The synthetic procedures that Quast and co-workers have developed allow for the synthesis of a range of substituted barbaralanes in different positions with varying functionality. This method produces high yields for individual synthetic steps with a drastic improvement for overall yields in comparison to other reported procedures.[39]

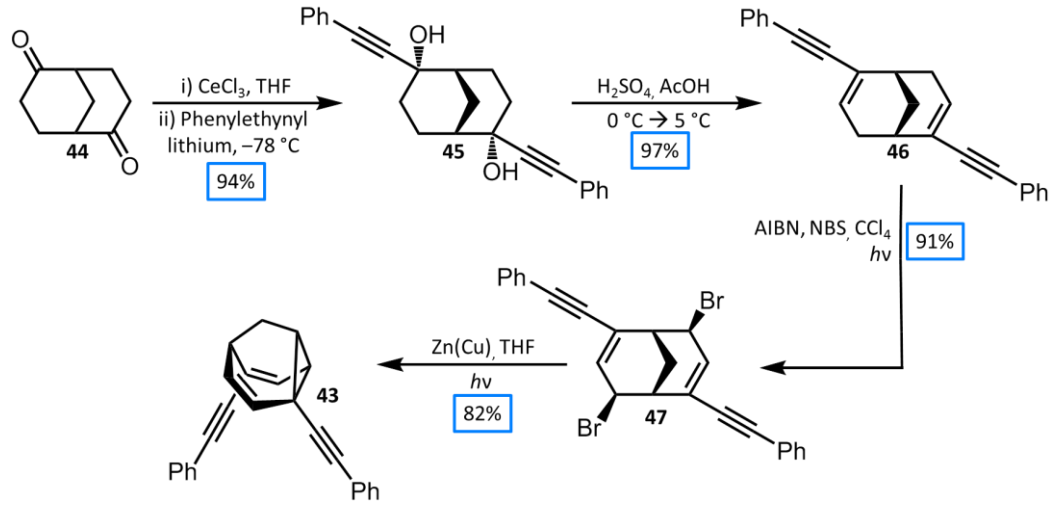

Scheme 1.13. Synthesis of 2,6-bis(phenylethynyl)barbaralane (**43**) as developed by Quast and co-workers.

1.4.2 Recent Developments in the Synthesis of Barbaralanes

Cationic gold complexes have the ability to promote a wide variety of cyclisations while exerting exquisite control over competitive reaction pathways (by the stabilisation of intermediates with carbenic character). These advantageous properties have allowed Echavarren and co-workers[7a] to investigate the gold-catalysed cycloisomerisations of alkynyl cycloheptatrienes in addition to examining the mechanism of the resulting indene formation (Scheme 1.14).

Investigations into the reaction of several alkynyl cycloheptatrienes (**48**) in the presence of different gold salts and π-Lewis acids demonstrate a rapid isomerisation to indene products with a varying ratio of regioisomers. It was established that catalyst **49** exhibited excellent bias towards regioisomer **50**, whereas the use of a highly electrophilic phopshite-gold(I) complex **51** exclusively led to regioisomer **52**. Investigating this mechanism through isotopic ^{13}C labelling experiments proved the presence of an intermediate barbaralyl species – a fluxional barbaralyl cation (**53**) – after treatment with gold(I) catalyst **54**. Entrapment with an external nucleophile, such as methanol, allowed the isolation of barbaralane methyl ethers **55** in addition to minor amounts of indene. The barbaralane methyl ether with a naphthalene functional group was produced in 40% yield with its structure was confirmed by X-ray crystallographic analysis. This evidence provides for a new method towards functionalised barbaralanes from easily-prepared alkynyl cycloheptatrienes under

mild conditions and in promising yields. The generation of gold-stabilised barbaralyl intermediates (**53**) has led to a simple two-step synthesis of barbaralanes (**55**) in which functionalisation can be modified through substituents on the alkynyl cycloheptatriene or the interception of the barbaralyl intermediate with alternative nucleophiles.

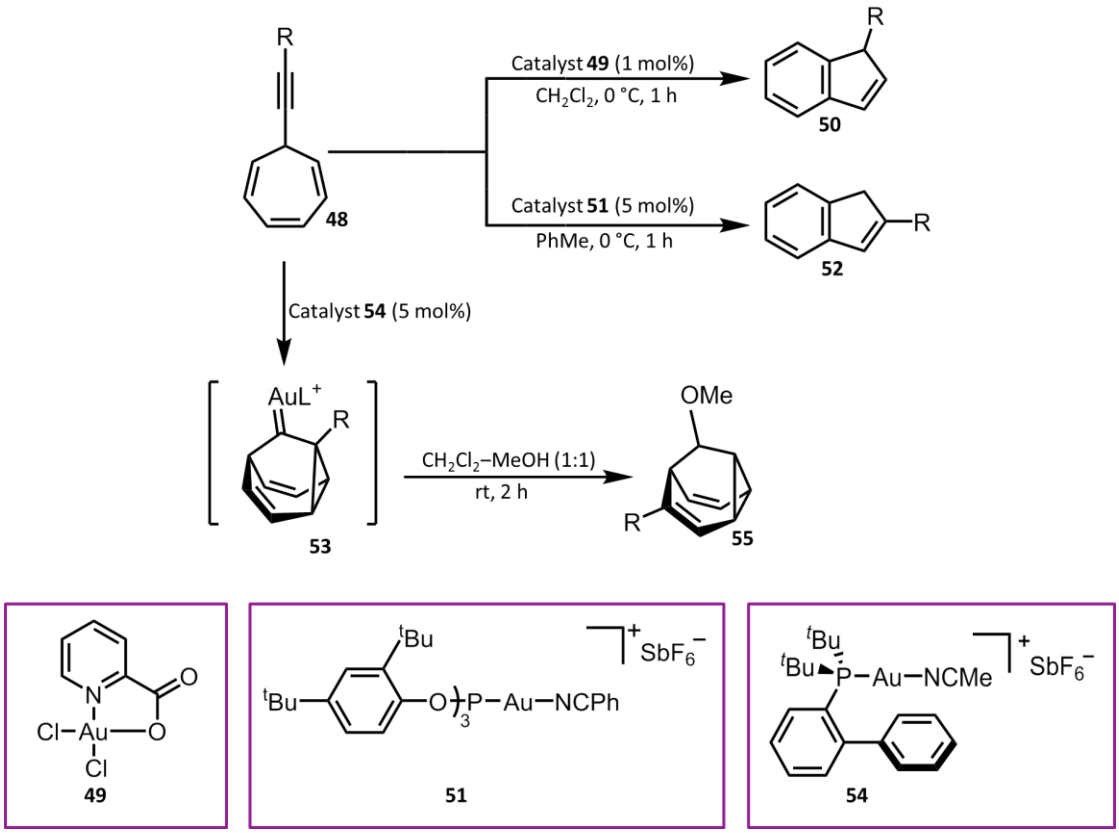

Scheme 1.14. General procedure used to synthesise substituted barbaralane methyl ethers (**55**) from alkynyl cycloheptatrienes (**48**) which, when subjected to different conditions, can also lead to indenes **50** and **52**.

Pursuing these gold-catalysed 1,6-enyne cyclisations, Echavarren reported a general and straightforwards synthesis of barbaralone (**11**) and 1-substituted barbaralones (**56**) from commercially available reagents in just two steps (Scheme 1.15) in 2016.[7b] Due to gold-catalysed oxidations of alkynes being shown to take place readily with oxidants such as sulphoxides or amine *N*-oxides forming α-oxo gold(I) carbenes,[42,43] Echavarren envisioned that the oxidation of the previously encountered intermediate barbaralyl species (**53**) could lead to substituted barbaralones (**56**).

Initial studies by Echavarren and co-workers tested a phenyl-substituted alkynyl cycloheptatriene with various gold(I) catalysts in the presence of different oxidants. It was determined (through comparing the yields of the different reactions) that the optimised strategy utilised the oxidant diphenyl sulphoxide as well as the gold(I) catalyst (acetonitrile)[(2-biphenyl)di-*tert*-butylphosphine]gold(I) hexafluoroantimonate (**57**). The use of these reagents effectively promotes the cyclisation (Scheme 1.15) by first activating and coordinating to the alkyne triple bond, before attack of the external oxidant to afford an α-oxo gold(I) carbene which is then oxidised *in situ* undergoing intramolecular cyclopropanation to produce the desired barbaralone (**56**). To assess the generality of this oxidative cyclisation, various alkynyl cycloheptatrienes were successfully prepared in yields ranging from 34% to 94%. The reaction pathway produced several substituted barbaralones (**56**) featuring electron-donating and -withdrawing, *ortho*-, *meta*-, and *para*-substituents on a phenyl ring as well as alkyl groups, all in good to excellent yields ranging from 45% to 95%, with barbaralone (**11**) itself accessed in a high yield of 97%.

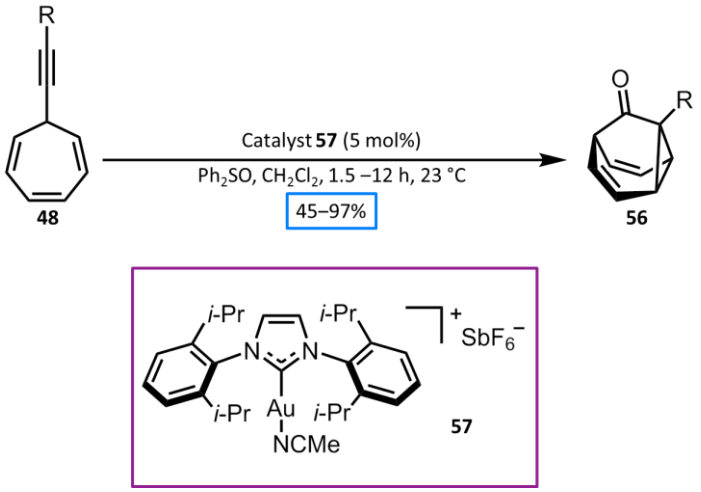

Scheme 1.15. General procedure used to synthesise barbaralone (**11**) and substituted barbaralones (**56**) from substituted alkynyl cycloheptatrienes (**48**) as developed by Echavarren and co-workers.

The 1,6-enyne cyclisation of **48** is promoted with a Lewis-acidic gold(I) catalyst *via* the formation of the fluxional barbaralyl cation intermediate (**53**). It is assumed that the oxidising agent acts on the barbaralyl cation intermediate (**53**) rather than on the alkyne, otherwise two products would be expected due to the two regioisomeric α-oxo gold(I) carbenes (**54**) and (**55**) (Scheme 1.16). Whereas **55** could lead to barbaralones (**56**) through intramolecular cyclopropanation, intermediate **54** would be

undesirable giving rise to benzylic oxidation products which Echavarren and co-workers did not observe. This indicates that **54** and **55** are not likely to be intermediates. Overall, this barbaralone (**56**) synthesis is the shortest to date and enables the simple and easy access to substituted fluxional carbon cages.

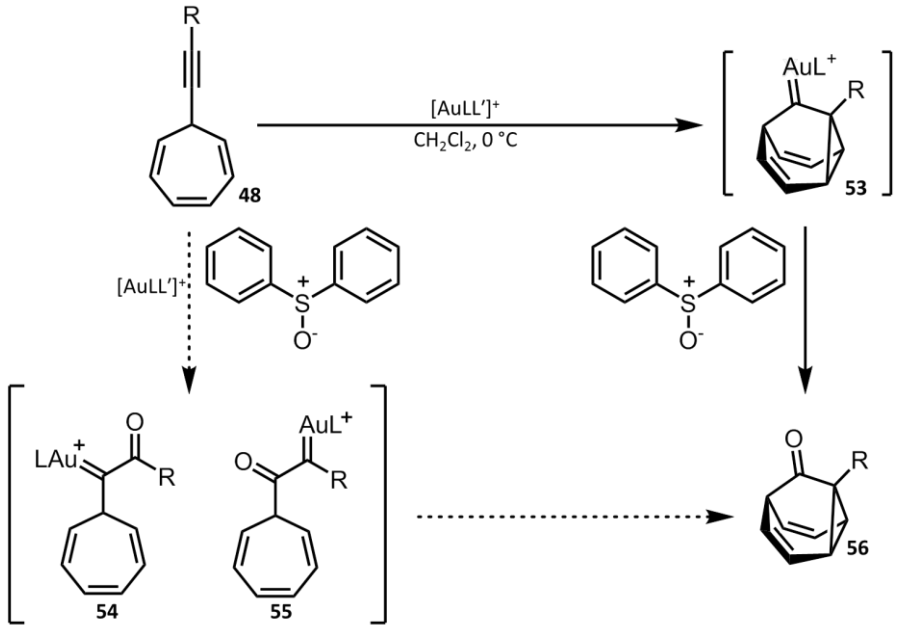

Scheme 1.16. Two different mechanistic pathways for the formation of barbaralones (**56**) by gold(I)-catalysed oxidative cyclisation of alkynyl cycloheptatrienes (**48**).

1.5 The Barbaralyl Cation

The barbaralyl cation[2] (**2**) is a hugely fluxional $C_9H_9^+$ cationic hydrocarbon which undergoes sequential low-energy pericyclic rearrangements through divinylcyclopropylcarbinyl–divinylcyclopropylcarbinyl (dvcpc–dvcpc) rearrangements (Scheme 1.17). These dvcpc–dvcpc rearrangements proceed through the opening of the three-membered cyclopropyl ring, which allows for the formation of another cyclopropyl ring at the same time. This dvcpc–dvcpc rearrangement has a measured energy barrier ($\Delta G^{\neq}$) of <16 kJ·mol^{-1}, where each methine is only able to exchange with every other methine allowing for interconversion between a set number of isomers. At a slightly higher energy barrier ($\Delta G^{\neq}$) of 21.5 kJ·mol^{-1}, the rearrangement can proceed *via* a bicyclo[2.3.3]nonatrienyl transition state (**57**) which, in combination with the dvcpc–dvcpc pathway, allows for every carbon to exchange with every other carbon and gives rise to degenerate isomers. Due to the barbaralyl

cation (**2**) having a unique stereoelectronic configuration which allows it to be highly reactive (in both degenerate and nondegenerate rearrangements), an even higher energy barrier ($\Delta G^{\neq}$) of 43.5 kJ·mol^{-1} an irreversible rearrangement takes place to form a 1,4-bishomotropylium cation (**58**).[44-47]

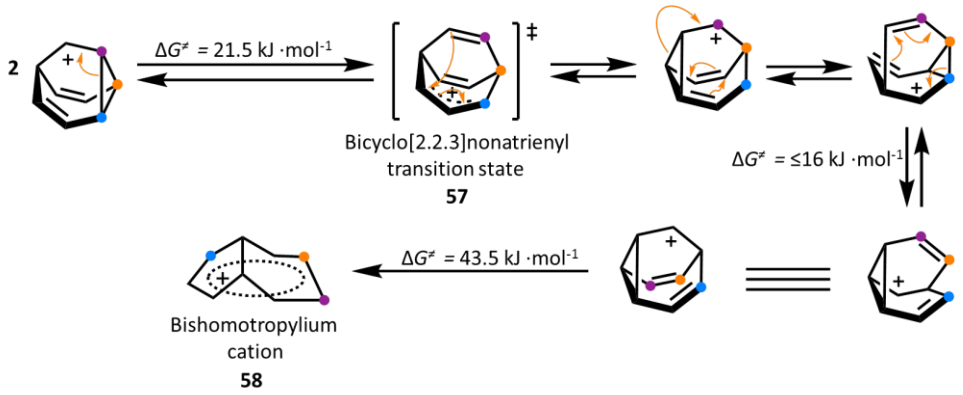

Scheme 1.17. Barbaralyl cation (**2**) dvcpc–dvcpc rearrangements occurring through a bicyclo[2.3.3]nonatrienyl transition state (**57**) and rearranging to a 1,4-bishomotropylium cation (**58**). Coloured circles demonstrate the movement of the cyclopropane carbon atoms.

Barbaralyl cations were first postulated to be intermediates during solvolysis of their corresponding alcohol precursors in acetic acid[47] however they were later prepared by Winstein and Alhberg as long-lived fluxional species.[2a,2c,2e] As fluxional barbaralyl cations demonstrate interesting rearrangements with intriguing intermediates – such as 1,4-bishomotropyliums[4] ions – the 1980s saw several NMR[48] and computational studies[49] on the parent molecule (**2**) as well as substituted derivatives. However, the difficulty in handling these compounds, combined with the low-yielding, multistep synthesis[18] and harsh reaction conditions (entailing the use of superacidic media), limits the extent to which the chemistry of this dynamic carbon skeleton can be explored. Although, recent studies utilising gold catalysis have led to the direct generation of fluxional cations avoiding the use of dangerous and dangerous conditions.[7a]

1.5.1 Initial Barbaralyl Cation Studies

The first barbaralyl cation to be directly observed in superacid by ^{1}H NMR spectroscopy was the 9-methyl-9-barbaralyl cation (**59**)[2a,2c,2e] in 1970. The 9-methyl-9-barbaralyl cation (**59**) can be prepared from three different alcohol precursors[3b] (**60**,

61 and **62**) in a mixture of various superacids at temperatures ranging from –135 °C to –115 °C (Scheme 1.18).

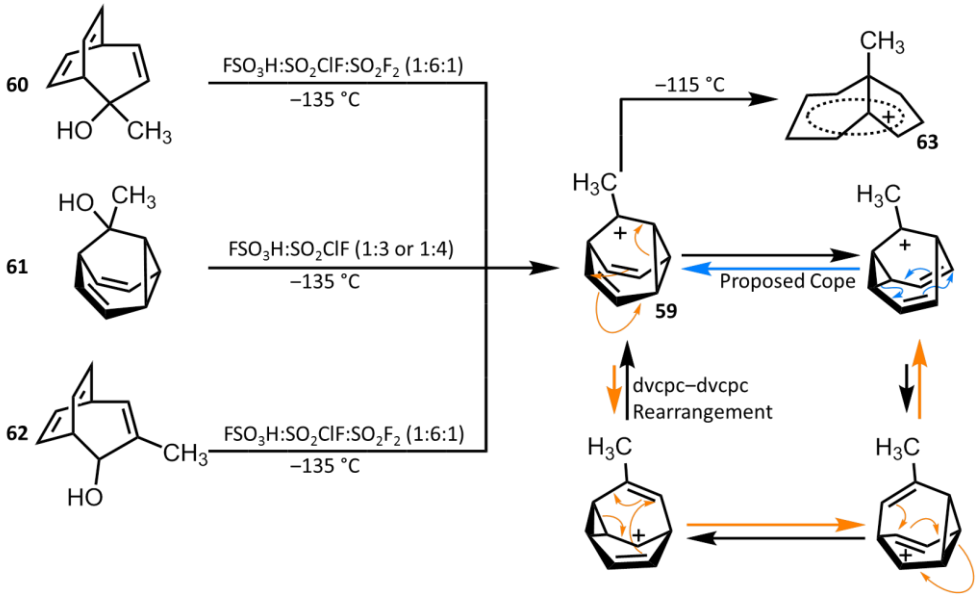

Scheme 1.18. Formation of the 9-methyl-9-barbaralyl cation (**59**) from three alcohol precursors (**60**, **61**, and **62**) which proceed through a dvcpc–dvcpc mechanism before irreversibly forming a 1,4-bishomotropylium cation (**63**).

The structure of cation **59** has been determined by ^{1}H and ^{13}C NMR, including ^{13}C spin-saturation experiments, which have helped to elucidate reaction mechanisms between the degenerate rearrangements.[46] Interestingly, the temperature dependence of the ^{1}H NMR spectrum of the 9-methyl-9-barbaralyl cation (**59**) in the temperature range of –135 °C to –115 °C showed that cation **59** undergoes a partially degenerate rearrangement with the same effect as a Cope rearrangement, *i.e.*, giving rise to many degenerate isomers. The rearrangement barrier ($\Delta G^{\neq}$) was calculated to be 30.5 kJ·mol^{-1} at –129 °C.[46] Comparing this value against barbaralanes rearrangement barrier ($\Delta G^{\neq}$) (**11**) (42.7 kJ·mol^{-1} at –93 °C)[46] indicated that the positive charge might have an accelerating effect on the proposed Cope rearrangement and therefore providing an alternative route to **59** for rearrangements. This alternative rearrangement was revealed through ^{13}C spin-saturation experiments to be a dvcpc-dvcpc rearrangement (Scheme 1.18). Increasing the temperature to –115 °C demonstrated the corresponding 1,4-bishomotropylium cation (**63**) (also confirmed by ^{1}H NMR spectroscopy) which was stable up to –80 °C allowing for several NMR

studies into charge delocalisation before rearrangements occurred at higher temperatures into a mixture of several products which were unidentified.[2]

Investigations by Ahlberg and co-workers into the degenerate and nondegenerate rearrangements from several cations to their corresponding 1,4-bishomotropylium ions revealed that substitution increases the activation energy barrier to both types of rearrangements, presumably increasing the stability of the cation (Scheme 1.19).[2,3b] Research conducted on the parent barbaralyl cation (**2**) estimated a barrier ($\Delta G^{\neq}$) to total degenerate rearrangements of 21.5 kJ·mol^{-1} and a barrier to the irreversible rearrangement ($\Delta G^{\neq}$) to the bishomotropylium (**58**) of 43.5 kJ·mol^{-1}.[3b] On the other hand, the methyl barbaralyl cation (**59**) showed the irreversible rearrangement to the bishomotropylium cation (**63**) to be 46.0 kJ·mol^{-1} whereas the barrier of total degenerate rearrangements ($\Delta G^{\neq}$) was measured to be 30.5 kJ·mol^{-1}.[2c] Lastly, the barrier ($\Delta G^{\neq}$) for the reversible rearrangement of a dimethyl barbaralyl cation (**64**) was measured to be 31.7 kJ·mol^{-1} (resembling the value obtained for the rearrangement of **59**),[3b] suggesting a connection between their rearrangement mechanisms. This data suggests that the introduction of an electron donating substituent stabilises that barbaralyl cation, and subsequently increasing the activation energy barriers associated with its rearrangement. It is still not known what the effect of substitution with several electron-donating and resonance-stabilising groups would have on the different rearrangement processes. It may be possible to choose substituents that allow for relatively low energy reversible rearrangements while disfavouring the irreversible rearrangement to the 1,4-bishomotropylium cation.

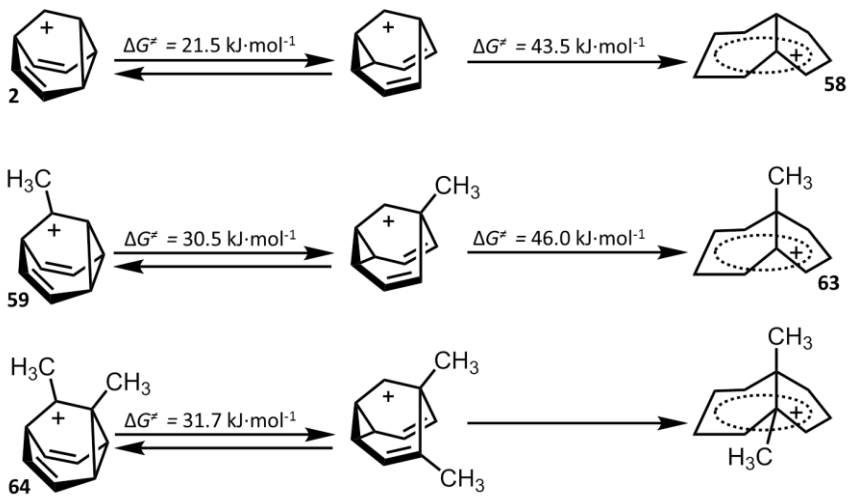

Scheme 1.19. Barbaralyl cations (**2**, **59** and **64**) experiencing dvcpc–dvcpc rearrangements before undergoing irreversible isomerisation to their corresponding bishomotropylium ions.

Due to controversy regarding the structures of the barbarlyl cation (**2**), in 1983 Ahlberg and co-workers conducted several ^{13}C NMR investigations into two different ^{13}C labelled precursors (**65** and **66**) in hope that they would be able to confirm the structure of the parent barbaralyl cation (**2**) (Schemes 1.20 and 1.21).[46,48] Compound **65** was synthesised first and then treated with several superacids to form the $(CH)_8{}^{13}CH^+$ cation (Scheme 1.20). The ^{13}C NMR spectrum at –135 °C showed a broad band at 118.5 ppm, confirming the fast scrambling of all nine carbon atoms. Upon lowering the temperature to –150 °C, the single signal broadened and split into two new signals residing at 101 and 152 ppm with an area ratio as 6:3. Lowering the temperature further did not produce any new peaks and only sharpened the current signals. As the expected signals resembling the structure of cation **67** did not appear, therefore cation **67** cannot be a possible structure for the totally degenerate ion. However, this result does not allow for the discrimination between structures **68** and **69**.

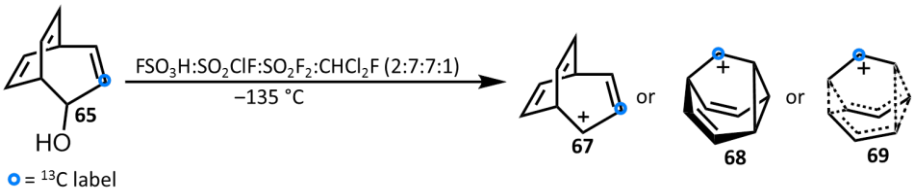

Scheme 1.20. Treatment of the ^{13}C-labelled alcohol **65** with superacid in order to clarify the structure of the barbaralyl cation.

Simultaneously, Ahlberg and co-workers also synthesised a specific octa-deuterated and ^{13}C-labelled precursor (**66**) which was also treated in the same superacid mixture at –135 °C (Scheme 1.21).[48] The ^{13}C NMR spectrum of the $(CD)_8{}^{13}CH^+$ cation was similar to that of the $(CH)_8{}^{13}CH^+$ cation but the broad singlet from the $(CD)_8{}^{13}CH^+$ cation was shifted to a higher frequency by 4.5 ppm[46,48] relative to the $(CH)_8{}^{13}CH^+$ cation. At the same time, upon lowering the temperature to –151 °C, the two signals that formed were also shifted. Interestingly, out of the two peaks, the higher frequency peak had shifted to a lower frequency by 1 ppm whereas the lower frequency peak had shifted to a higher frequency by 6 ppm, showing a decrease in shielding around the cationic carbon centre. These changes – caused by the isotopic perturbation – confirm the structure of the cation to be **70** and not **71**. Since the equilibrium of **71** most likely has an equilibrium constant smaller than one (due to the difference in zero-point energy between a cyclopropane and olefinic carbon-hydrogen bond), a downfield shift of the singlet at –135 °C might be observed. However, the two signals at –151 °C are not expected to shift relative to those of the $(CD)_8{}^{13}CH^+$ cation, since the six cyclopropane carbon-hydrogen bonds and the three olefinic carbon-hydrogen bonds are equivalent.

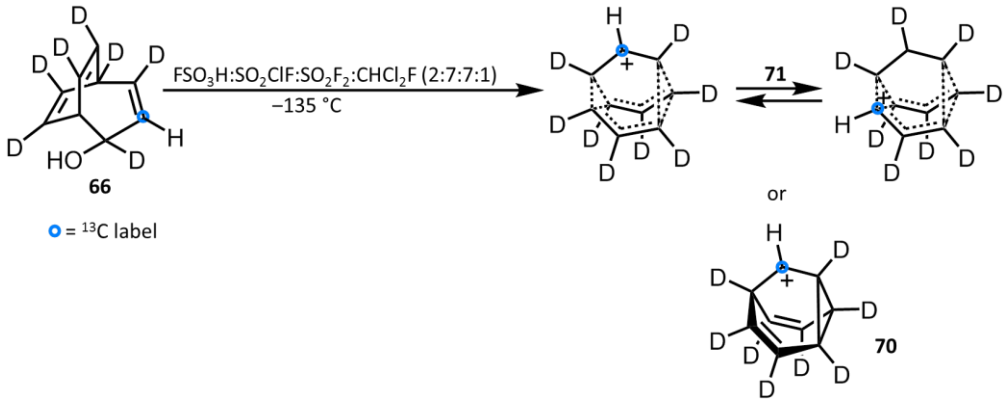

Scheme 1.21. Treatment of the ^{13}C-labelled octa-deuterated alcohol **66** with superacid to confirm the structure of the barbaralyl cation as **70**.

1.5.2 Modern Barbaralyl Cation Investigations

In 2012, Echavarren and co-workers reported the generation of a fluxional barbaralyl intermediate generated from alkynyl cycloheptatrienes under very mild conditions.[7a] Depending on the gold(I) catalyst, the gold-stabilised barbaralyl intermediates evolve to generate either 1- or 2-substituted indenes.

In order to gather evidence for the intermediacy of the barbaralyl species which would initially be generated by a 1,6-enyne cyclisation, the authors carried out experiments with the gold(I)-catalyst **72** on two alkynyl cycloheptatrienes (**73** and **74**) bearing pendant olefins (Scheme 1.22). Substrate **73** underwent a cycloisomerisation to generate the barbaralanes **75** and **75′**, whereas compound **74** formed the tautomers **76** and **76′**. The tautomeric barbaralanes **75** and **75′** were found to interconvert rapidly on the NMR timescale at room temperature in $CDCl_3$ and were also detected as a disordered 1:1 mixture *via* X-Ray crystallographic analysis – presumably due to fluxionality in the solid state. Compound **76** however was observed as a single tautomer in the solid state. The formation of barbaralane compounds confirmed the presence of a short-lived cationic barbaralyl species.

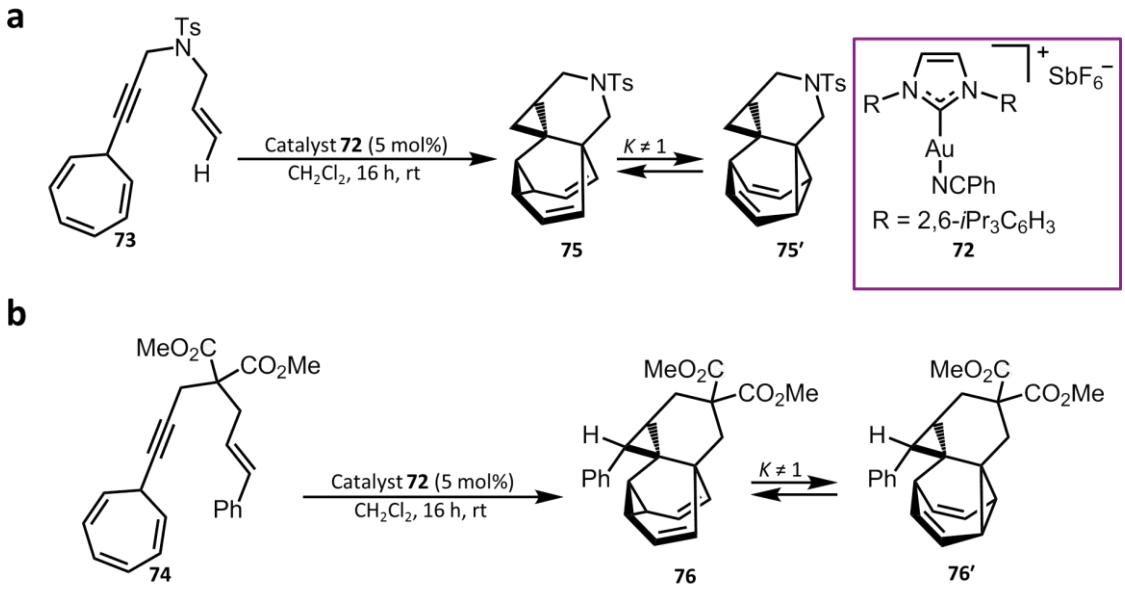

Scheme 1.22. Trapping experiments for the elucidation of the intermediate barbaralyl species in the gold-catalysed isomerisation of alkynyl cycloheptatrienes.

To determine whether the short-lived cationic barbaralyl species (**53**) formed through a series of short steps or through numerous rearrangements, alkynyl cycloheptatrienes (**77**) were prepared containing a ^{13}C label. If the barbaralyl intermediate could undergo manifold pericyclic rearrangements, the ^{13}C label would disperse throughout the barbaralane skeleton. The ^{13}C labels were placed on each of the carbons within the alkyne by using differently labelled synthetic precursors (Scheme 1.23). The

results demonstrated that for the 1-substituted indene (**78**) and the barbaralane (**79**) there was only one location for the label. However, the 2-substituted indene presented two locations (**80** and **81**) as a result of resonance in the proposed intermediate. These findings established that the mechanism proceeds through a small number of steps, rather than undergoing multiple rearrangements before forming the indene products. The mechanism was deemed to be a degenerate dvcpc-dvcpc rearrangement with the number of energetically accessible nondegenerate isomers – hence the number of possible rearrangements – being reduced in comparison to the parent barbaralyl cation (**2**) due to the substitution on the alkynyl cycloheptatriene.[48c]

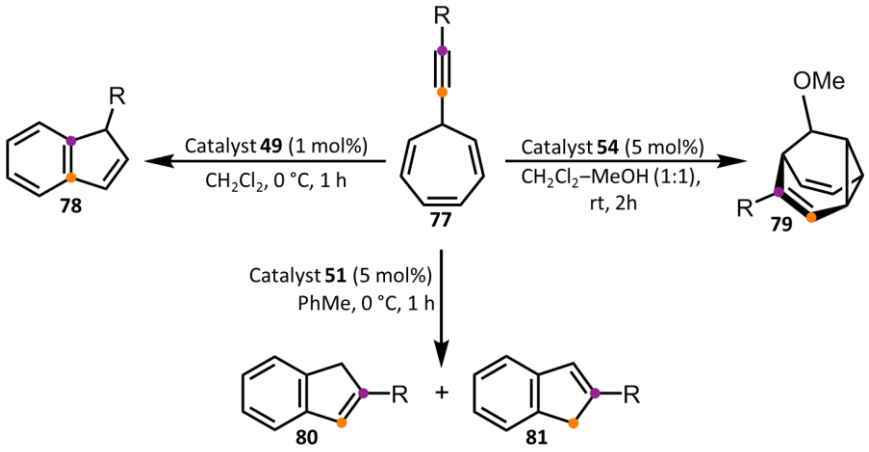

Scheme 1.23. Determination of cationic barbaralyl species (**53**) undergoing degenerate dvcpc-dvcpc rearrangements through isotopic labelling experiments. Orange and purple coloured circles demonstrate the ^{13}C labels.

1.6 Applications of Fluxional Carbon Cages

At the molecular level, select organic molecules are known to possess 'shapeshifting' properties (*i.e.*, rapid and reversible constitutional isomerism),[50] however this fluxionality usually occurs between a few distinct states or configurations. Examples include alkene isomerisation which can be used as the basis for vision,[51] or ring-chain tautomerisation which can be common in carbohydrate monomers.[52] These fluxional properties arise from intramolecular isomerisation processes, which is a characteristic shared with bullvalene (**1**). Fluxional carbon cages such as bullvalene (**1**) differ in a sense because they have the ability to transform their shape and properties on a large scale in response to their environments.[5,6] Owing to their 'shapeshifting' properties,

fluxional carbon cages, such as bullvalene (**1**) have found use as adaptable molecules in binding interactions, chemical sensing and the development of materials with unique properties.[53] Applications utilising bullvalenes as sensors date back to the 1970s, when Schöder and co-workers reported the selective binding of metal ions exploiting a crown ether-functionalised bullvalene.[54] Investigations pioneered by Bode[14,24,29] have provided the basis for the synthesis of a range of elaborately functionalised bullvalenes while also delivering extensive insight into their rearrangements and behaviour through high-performance liquid chromatography (HPLC) isolation, circular dichroism and NMR spectroscopies and computational studies combined with network construction and analysis. Most recently, Bode has demonstrated that tetra-substituted bullvalenes can respond to their environment and adopt structures with favourable supramolecular interactions leading to applications such as the chemical sensing and molecular guest binding.[5b,6]

1.6.1 Proof of Concept

As mentioned in 1979, Schöder and co-workers described the synthesis of two crown ether-functionalised bullvalenes (**82**) with varying ring size.[54a] In 1983,[54b] Schöder reported the application of these crown ether-functionalised bullvalenes (**82**) in the selective binding of metal ions such as ammonium and potassium[54a] (Scheme 1.14). This approach relied on their shapeshifting properties combined with the low preference of the crown ether substituent for a specific site on the bullvalene core. It was anticipated that the crown ether group – attached to the bullvalene – would adopt different ring sizes as the bullvalene core interconverts between isomers through low-energy [3,3]-sigmatropic rearrangements, leading to the selective binding of several metal ions depending on their size. Although only weak host–guest interactions were observed, providing low selectivities in the accommodation of different alkali and ammonium cations of differeing size, Schöder's study provided an initial proof of concept for the use of shapeshifting molecules as chemical sensors.

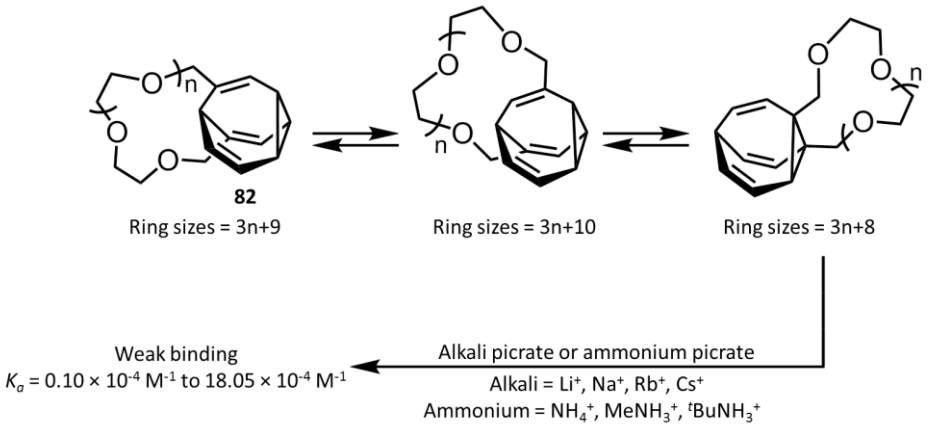

Scheme 1.24. Application of a crown-ether substituted bullvalene (**82**) towards the binding of metal cations.

1.6.2 Developing Bullvalanes as Chemical Sensors

From Bode's preliminary reports demonstrating bullvalene molecules interacting and responding to analytes through appended recognition elements,[5a] he anticipated that the isomer distribution of an oligo-substituted bullvalene could change when interacting with fullerene analytes and shift the equilibrium distribution to a population which is characteristic to a specific fullerene analyte (Scheme 1.25).

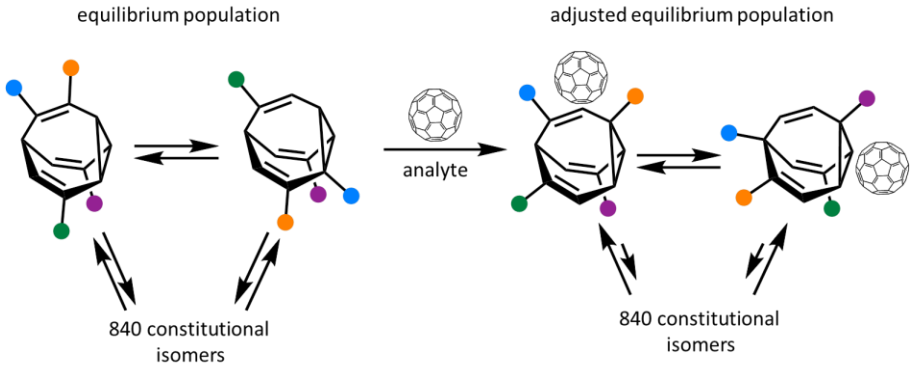

Scheme 1.25. Oligo-substituted bullvalene altering its isomer distribution and equilibrium population upon the addition of a fullerene analyte. Coloured circles represent functional groups.

In 2012, Bode and co-workers synthesised a dynamic ^{13}C-labelled bisporphyrin-bullvalene (**83**) (the ^{13}C label was either placed on an olefin, cyclopropane ring or bridgeheaded methinyl group), and studied its application to the chemical sensing of fullerene derivatives.[5b] To test the ability of **83** and its capability to report interactions with a fullerene analyte, a ^{13}C NMR of **83** was run in the absence of an analyte so the

peak patterns generated could be observed. The resulting ^{13}C NMR spectrum was depicted in a simplified manner by plotting the chemical shift of each peak against its intensity. The ^{13}C-labelled bisporphyrin-bullvalene (**83**) was then treated with fullerene C_{70} and the resulting ^{13}C NMR spectrum, altered to the simplified manner, provided a distinguishable change in the corresponding peaks. Investigations with other fullerene analytes (C_{60} and a pyrrolidine derivative (derC_{60})) also demonstrated altered spectra proving that the dynamic bullvalene core could readily distinguish closely related analytes with only minor structural variations (Figure 1.4).

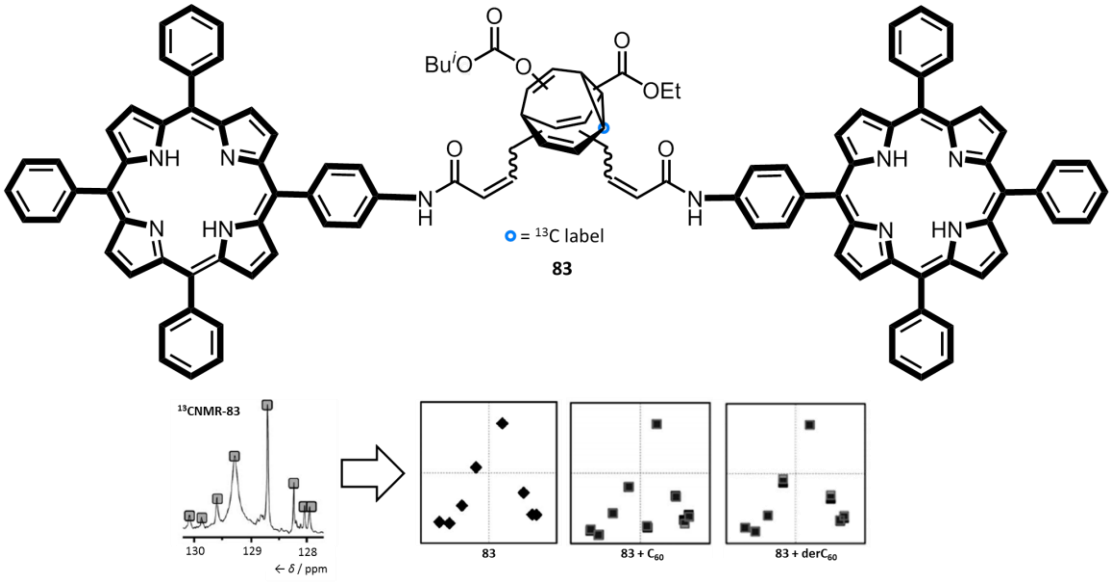

Figure 1.4. ^{13}C-labelled bisporphyrin-bullvalene (**83**) and a graphical representation of its ^{13}C NMR spectrum converted to its corresponding peak pattern showing the equilibrium population. Upon the addition of various fullerene analytes the equilibrium population has shifted. **83**: 2.8 mM of **83** in CS_2 with 3% CD_2Cl_2 observed at 150 MHz. **83 + C_{60}**: 2.8 mM **65** and 2 equiv. of C_{60} in CS_2 with 3% CD_2Cl_2 observed at 150 MHz. **83 + derC_{60}**: 2.8 mM **65** and 2 equiv. of derC_{60} in CS_2 with 3% CD_2Cl_2 observed at 150 MHz. All graphical representations are two trials overlaid.

The use of **83** to detect and differentiate fullerene analytes is straightforward, as only a ^{13}C NMR experiment and minimal data processing is required to generate reproducible, analyte-specific peak patterns. The ability to differentiate between fullerenes arises from a 'key recognition event' in which the porphyrin recognition motifs interact with the fullerenes analytes through noncovalent bonding interactions. Due to the porphyrin groups interacting with the fullerene analytes, there is a large possibility that other recognition domains added to the bullvalene core would allow for the sensing of several classes of analytes, however a benchmark of analytes under

controlled conditions must be established. The ability to change the recognition motifs highlights the usefulness and advantages of the shapeshifting nature of the sensor which may even allow for molecular sensing in applications ranging from disease detection to the analysis of new materials.[5b]

The following year Bode and co-workers challenged themselves to achieve analyte binding through covalent bonding in hope that a more distinct bullvalene isomer distribution would lead to a more pronounced change in the ^{13}C NMR spectrum. In 2013, Bode reported the development of a dynamic bis-boronic acid-based sensor array for the diverse detection of polyols, such as flavanols and carbohydrates, which allowed for distinct and reproducible signals by a single ^{13}C NMR measurement.[6] Conversion of the ^{13}C NMR to an easy-to-read barcode provided an effective and convenient method to catalogue polyol analytes.

A ^{13}C-labelled bis-boronic acid bullvalene (**84**) was synthesised. Compound **84**'s ^{13}C NMR spectrum was compared against a mixture of **84** with a chlorogenic acid analyte (**85**) in a dimethyl sulphoxide (DMSO)/phosphate buffer solution (pH = 7.2), acquiring the spectra under otherwise identical conditions. The results demonstrated an adapted equilibrium population (a shift in the equilibrium when an analyte is present) of **84** in the presence of analyte **85** (Figure 1.5). For ease of recognition and comparison, the ^{13}C NMR signals were converted to barcodes through binning – a technique used for pattern recognition when studying metabolites in body fluids by NMR.[55]

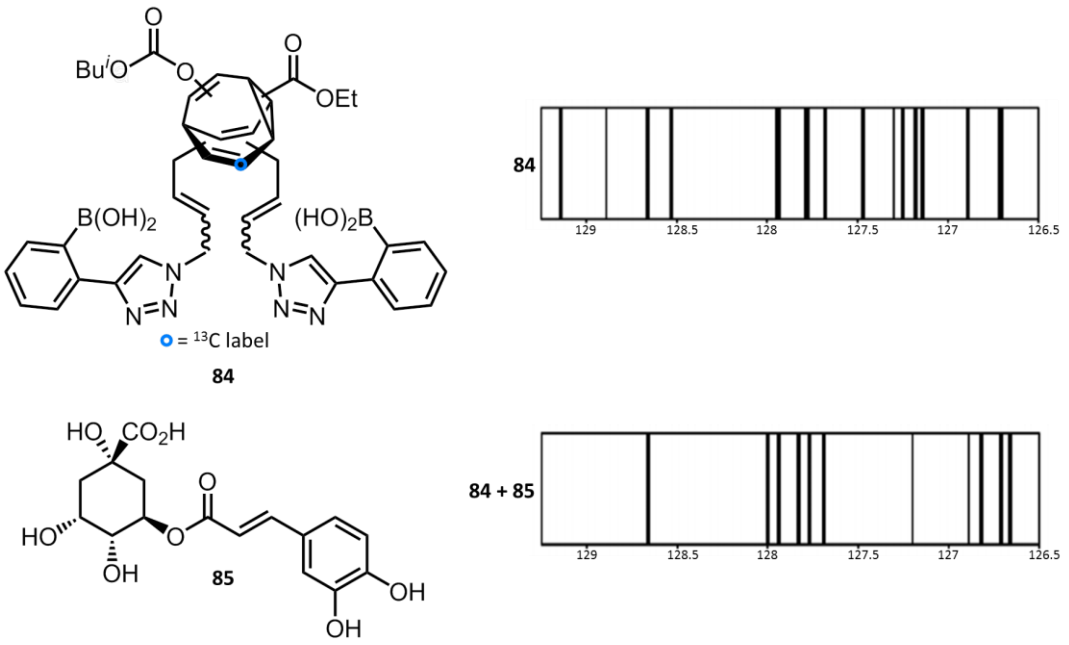

Figure 1.5. ^{13}C-labelled bis-boronic acid bullvalene (**84**) and its corresponding barcode compared to a barcode corresponding to a mixture of **84** and **85** (1:2 mixture) in 0.6 mL of a 9:1 mixture of DMSO-d_6/phosphate buffer.

The performance of dynamic sensor **84** was then assessed in the presence of a variety of naturally occurring/biologically relevant polyols, with NMR analysis confirming an adapted equilibrium population for all analytes in comparison to just the distribution of the bis-boronic acid bullvalene (**84**). The barcode patterns generated are distinct from the reference barcode of the bullvalene sensor (**84**) itself with changes occurring through the number of lines present as well as their thickness (intensity) and chemical shift. Comparing structurally similar analytes, such as epicatechin gallate (**86**) and epigallocatechin gallate (**87**), also provided different barcodes, showing that the bullvalene (**84**) is readily able to distinguish between various polyols with similar structural features (Figure 1.6). The ability of bullvalene (**66**) to differentiate similar molecules demonstrates that the sensing of various analytes is feasible, owing to the adaptable nature of the dynamic bullvalene backbone of the sensor. However, sensing structurally similar analytes produces very small differences in the barcodes. As a result of only minor differences when reading out the barcode or detecting a significant signal to generate a barcode, problems are likely to arise. Also, too many sensor signals are concealed by the signals of the analyte, meaning no clear distinction can be made.

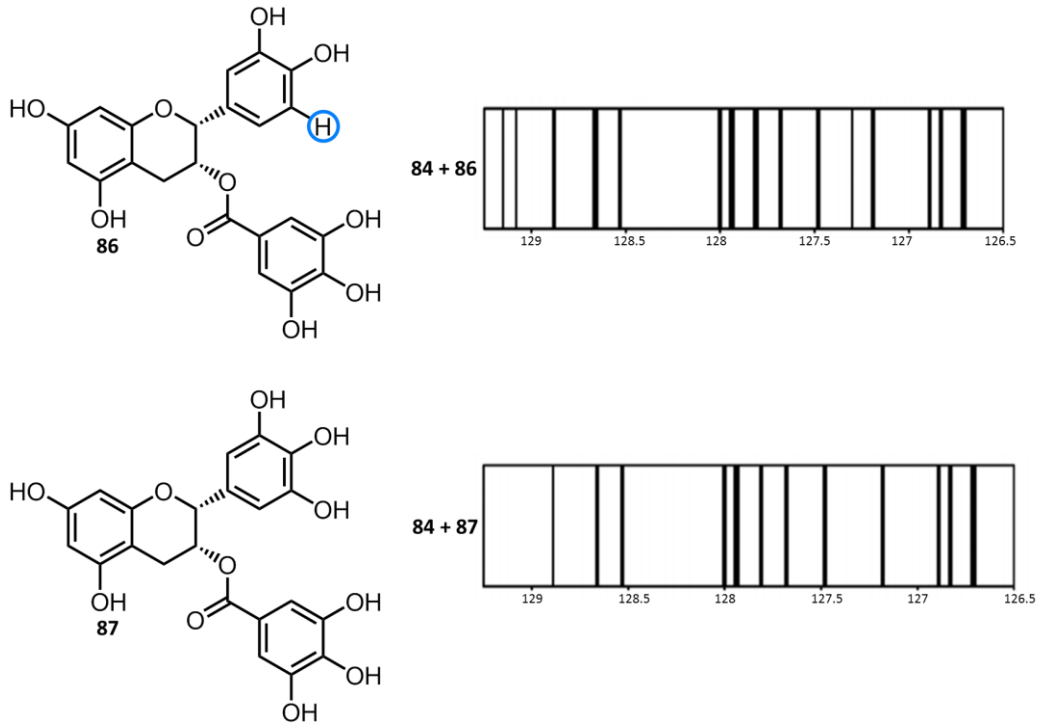

Figure 1.6. Barcodes of a 1:2 mixture of **84** with either analyte **86** or **87** in a 9:1 mixture of DMSO-d_6/phosphate buffer. Blue circles demonstrate the difference between the analytes.

In addition the barcodes also revealed that sensing a mixture of analytes is possible; however the strongest binding analyte will dominate the corresponding barcode. In classic sensor arrays, if selective recognition is required for a specific analyte the scope is generally reduced[56-58] and optimisation is required for each different analyte.[59] However, bullvalene sensor (**84**) constitutes a potential advantage over classic sensor arrays as optimisation is not required and the selectivity is not reduced. As a negative control, a structurally similar static bis-boronic acid bullvalene was synthesised and tested as a sensor, but due to the fixed backbone (preventing the sensor adapting and shapeshifting), no significant changes in the ^{13}C NMR were observed

The chemical robustness of the oligo-substituted bullvalene core opens up the possibility of extending its reporting capabilities to *in vivo* applications using *in vivo* NMR spectroscopy by designing sensors with targeting and solubilising groups.[60,61] To further improve the sensitivity of the ^{13}C NMR experiment and reading, incorporating a ^{13}C atom into a position on the bullvalene core that bears a proton would allow for the indirect detection using a HSQC experiment. Nevertheless, these

shapeshifting sensors provide a convenient method to catalogue various analytes using only a single ^{13}C NMR measurement.[6]

A crucial component of utilising fluxional carbon cages in applications, such as the binding and sensing of analytes, is the ability to halt the reversibility of the equilibrium (*i.e.*, the fluxional behaviour) while analysing the adapted product.[29a] Bode prepared a bullvalene derivative with a photolabile carbonate substitutent (**88**) (Scheme 1.25) by trapping the lithium enolate of bullvalone (**89**). The HPLC trace of the *o*-nitroveratryloxycarbonate (NVOC) bisallyl bullvalene (**89**) demonstrated several peaks. Upon irradiation at 365 nm for 20 hours, peaks corresponding to the starting material (**88**) as well as bullvalene **89** disappeared, leaving the adapted bullvalene **90** behind. These results prove that the fluxional behaviour can be terminated by the addition of an appropriate photocleavable group, and that isolation of an adapted product can take place if required. Furthermore, the formation of the bullvalene as an enol carbonate of the static bullvalone presents an ideal platform to which a number of chemical mechanisms can be introduced to modulate the dynamic nature of the system.[29a]

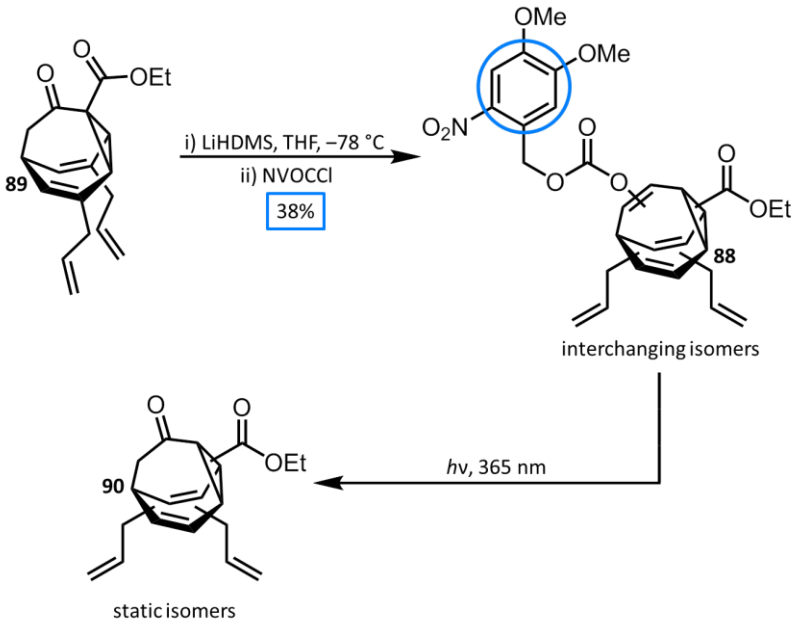

Scheme 1.25. Synthesis and photolysis of (NVOC) bisallyl bullvalene (**89**). Blue circles show the photocleavable group.

1.7 Overview

Fluxional carbon cages are unique molecules possessing 'shapeshifting' properties which arise through rapid and reversible Cope rearrangements. This rare phenomenon has proven to be fundamental to the concept of valence isomerisation, demonstrates that a dynamic structural library can exist from a single rigid molecule and has applications which show that the equilibrium population and isomer distribution can be altered through specific noncovalent bonding interactions or dynamic covalent bonds upon interactions with different guests. Since the prediction of the first fluxional carbon cage, over fifty years ago, these molecules still remain of great interest as they are relatively unexplored and have the potential to create promising artificial scaffolds from which to explore complex biological systems and create new functional materials.

As shown in this Introduction, initial research into fluxional carbon cages first focused on improving the synthetic techniques used to create these molecules, where investigations remained reliant upon temperature-dependent NMR studies. Recent advances in the field of organic chemistry combined with quantum computational methods, have allowed for a more streamlined synthesis of fluxional carbon cages, specifically bullvalene, while also allowing for the predication of isomer networks. Although the efficient preparation of these fluxional carbon cages – where organometallic chemistry has proven to be a crucial step contributing considerably to the synthetic advances – have recently been reported, the dynamics, equilibria and rearrangements of these intriguing cages have not yet been explored. It is only tetra-substituted bullvalenes (which rely on long and low-yielding synthetic methods) that have been exploited in the binding and sensing of a variety of guest molecules prompting minor investigations in their equilibria and isomeric composition.

Based on recent synthetic developments we explore substituted nondegenerate barbaralanes – a fluxional scaffold which can readily be synthesised and just exists as two isomers in rapid flux (removing complex fluxional mixtures) – and show that their equilibria and rearrangements, in both solution and solid state can be fully understood and controlled. Essential knowledge into dynamics and equilibria of

barbaralane molecules will pave the way for the precise determination of complex mixtures which has the potential of unveiling new and innovative applications within the area of systems chemistry.

1.8 References

1. (a) W. von E. Doering and W. R. Roth, *Tetrahedron*. 1963, **19**, 175; (b) G. Schröder, *Angew. Chem.* 1963, **75**, 722; *Angew. Chem. Int. Ed. Eng.* 1963, **2**, 481; (c) A. Adult, *J. Chem. Educ.* 2001, **78**, 924; (d) H. G. Viehe, *Angew. Chem. Int. Ed. Eng.* 1965, **4**, 746.

2. (a) P. Ahlberg, D. L. Harris and S. Winstein, *J. Am. Chem. Soc.* 1970, **92**, 5545; (b) D. Cremer, P. Svensson, E. Kraka and P. Ahlberg, *J. Am. Chem. Soc.* 1993, **115**, 7445; (c) P. Ahlberg, J. B. Grutzner, D. L. Harris and S. Winstein, *J. Am. Chem. Soc.* 1970, **92**, 3478; (d) B. Grutzner and S. Winstein, *J. Am. Chem. Soc.* 1970, **92**, 3186; (e) P. Ahlberg, D. L. Harris and S. Winstein, *J. Am. Chem. Soc.* 1970, **92**, 2146.

3. (a) J. G. Henkel and J. T. Hane, *J. Org. Chem.* 1983, **48**, 3858; (b) C. Engdahl and P. Ahlberg, *J. Am. Chem. Soc.* 1979, **101**, 3940; (c) L. G. Greifenstein, J. B. Lambert, M. J. Broadhurst, L. A. Paquette, *J. Org. Chem.* 1973, **38**, 1210; (d) G. G. Cristoph, S. Hardwick, U. Jacobsson Y.-B. Koh, R. Moerck and L. A. Paquette, *Tetrahedron. Lett.* 1977, **14**, 1249.

4. H. E. Zimmerman and G. L. Grunwald, *J. Am. Chem. Soc.* 1996, **88**, 183.

5. (a) A. R. Lippert, V. L. Keleshian and J. W. Bode, *Org. Biomol. Chem.* 2009, **7**, 1529; (b) K. K. Larson, M. He, J. F. Teichert, A. Naganawa and J. W. Bode, *Chem. Sci.* 2012, **3**, 1825.

6. J. F. Teichert, D. Mazunin and J. W. Bode, *J. Am. Chem. Soc.* 2013, **135**, 11314.7.

7. (a) P. R. McGonigal, C. de León, Y. H. Wang, A. Homs, C. R. Solorio-Alvarado and A. M. Echavarren, *Angew. Chem. Int. Ed*. 2012, **51**, 13093; (b) S. Ferrer and A. M. Echavarren, *Angew. Chem. Int. Ed*. 2016, **55**, 11178.

8. O. Yahiaoui, L. F. Pašteka, B. Judeel and T. Fallon, *Angew. Chem. Int. Ed.* 2018, **57**, 2570.

9. J. F. M. Oth, K. Müllen, J. –M. Gilles and G. Schröder, *Helv. Chim. Acta*. 1974, **57**, 1415.

10. G. A. Molander, L. N. Cavalcanti, B. Canturk, P. S. Pan and L. E. Kennedy, *J. Org. Chem.* 2009, **74**, 7364.

11. (a) W. von E. Doering and J. W. Rosenthal, *J. Am. Chem. Soc.* 1966, **88**, 2078; (b) M. Jones and L. T. Scott, *J. Am. Chem. Soc.* 1967, **89**, 150.

12. J. F. M. Oth, R. Merényi, J. Nielsen and G. Schröder, *Chem. Ber.* 1965, **98**, 3358.

13. J. Casas and F. Serratosa, *An. Quim.* 1977, **73**, 300.

14. A. R. Lippert. J. Kawobamrung and J. W. Bode, *J. Am. Chem. Soc.* 2006, **128**, 14738.

15. (a) G. Schröder, *Chem. Ber.* 1964, **97**, 3140; (b) R. Merényi, J. F. M. Oth and G. Schröder, *Chem. Ber.* 1964, **97**, 3150.

16. S. Ferrer and A. M. Echavarren, *Synthesis.* 2019, **51**, 1037.

17. J. Font, F. Löpez and F. Serratosa, *Tetrahedron. Lett.* 1972, **13**, 2589.

18. W. von E. Doering, B. M. Ferrer, E. T. Fossel, J. H. Hatenstein, M. Jr. Jones, G. Klumpp, R. M. Rubin and M. Saunders, *Tetrahedron.* 1967, **23**, 3943.

19. J. F. M. Oth, R. Merényi, J. Nielsen and G. Schröder, *Chem. Ber.* 1965, **98**, 3358.

20. (a) G. Schröder and J. F. M. Oth, *Angew. Chem. Int. Ed. Engl.* 1967, **6**, 414; (b) J. F. M. Oth, R. Merényi, G. Engel and G. Schröder, *Tetrahedron. Lett.* 1966, **7**, 3377.

21. (a) C. Hoogzand, J. Nielsen and J. F. M. Oth, *Tetrahedron. Lett.* 1970, **11**, 2287; (b) K. Sarma, W. Witt and G. Schröder, *Chem. Ber.* 1986, **119**, 2339.

22. J. F. M. Oth, E. Machens, H. Röttele and G. Schröder, *Justus. Liebigs. Ann. Chem.* 1971, **745**, 112.

23. (a) K. Rebsamen, H. Röttele and G. Schröder, *Chem. Ber.* 1993, **126**, 1429; (b) K. Rebsamen, H. Röttele and G. Schröder, *Chem. Ber.* 1993, **126**, 1419.

24. J. F. Teichert, D. Mazunin and J. W. Bode, *J. Am. Chem. Soc.* 2013, **135**, 11314.

25. T. Mukaiyama, *Angew. Chem. Int. Ed. Engl.* 1977, **16**, 817.

26. V. K. Aggarwal, H. W. Smith, G. Hynd, R. V. H. Jones, R. Fieldhouse, and S. E. Spey, *J. Chem. Soc., Perkin Trans.* 2000, **1**, 3267.

27. For examples of acylation of sulphonium ylides see: (a) K. W. Ratts and A. N. Yao, *J. Org. Chem.* 1966, **31**, 1689; (b) E. Zielger, H. Wittmann and H. Sterk, *Monatsh. Chem.* 1987, **118**, 115.

28. A. E. Greene and M. T. Edgar, *J. Org. Chem.* 1989, **54**, 1468.

29. (a) A. R. Lippert, A. Naganawa, V. L. Keleshian and J. W. Bode, *J. Am. Chem. Soc.* 2010, **132**, 15790; (b) M. He, J. W. Bode, *Proc. Natl. Acad. Sci. USA.* 2011, **108**, 14752; (c) M. He, J. W. Bode, *Org. Biomol. Chem.* 2013, **11**, 1306.

30. M. Achard, M. Mosrin, A. Tenagli and G. Buono, *J. Org. Chem.* 2006, **71**, 2907.

31. W. von E. Doering and W. R. Roth, *Angew. Chem. Int. Ed. Engl.* 1963, **2**, 115.

32. (a) C. W. Jefford, J. –C. Rossier and J. A. Zuber, *Angew. Chem. Int. Ed. Engl.* 1982, **21**, 549; (b) R. Trinks and K. Müllen, *Chem. Ber.* 1987, **120**, 1481; (c) J. M. Mellor, B. S. Pons and J. H. A. Stibbard, *J. C. S. Chem. Comm.* 1979, 759.

33. L. M. Jackmann, E. Fernandes, M. Heubes and H. Quast, *Eur. J. Org. Chem.* 1998, 2209.

34. J. B. Lambet, *Tetrahedron. Lett.* 1963, **4**, 1901.

35. (a) H. Stetter and H. Stark, *Chem. Ber.* 1959, **92**, 732; (b) R. H. Shapiro and M. J. Heath, *J. Am. Chem. Soc.* 1967, **89**, 5743.

36. (a) L. A. Paquette, U. Jacobsson and M. Oku, *J. C. S. Chem. Comm.* 1975, 115; (b) L. G. Griefenstein, J. B. Lambert, M. J. Broadhurst and . L. A. Paquette, *J. Org. Chem.* 1973, **38**, 1211.

37. R. H. Shapiro, *Org. React.* 1976, **23**, 405.

38. H. Quast, M. Witzel, E. –M. Peters, K. Peters and H. G. von Schnering, *Leibigs. Ann.* 1995, 725.

39. (a) H. Kessler and W. Ott, *J. Am. Chem. Soc.* 176, **98**, 5014; (b) A. McKillop and J. A. Tarbin, *Tetrahedron. Lett.* 1983, **24**, 1505.

40. H. Quast, C. Becker, M. Witzel, E. –M. Peters, K. Peters and H. G. von Schnering, *Leibigs. Ann.* 1996, 985.

41. H. Quats, J. Carlsen, H. Roschert, E. –M. Peters, K. peters, H. G. Von Schnering, *Chem. Ber.* 1992, **125**, 2591.

42. (a) L. Zhang, *Acc. Chem. Res.* 2014, **47**, 877; (b) Z. Zheng, Z. Wang, Y. Wang, L. Zhang, *Chem. Soc. Rev.* 2016, **45**, 4448.

43. (a) D. Vasu, H. –H. Hung, S. Bhunia, S. A. Gawade, A. Das, R. –S. Liu, *Angew. Chem. Int. Ed.* 2011, **50**, 6911; *Angew. Chem.* 2011, **123**, 7043; (b) D. B. Huple, S. Ghorpade, R. –S. Liu, *Adv. Synth. Catal.* 2016, **358**, 1348; (c) J. Schulz, J. Jasik, A. Gray, J. Roithová, *Chem. Eur. J.* 2016, **22**, 9827.

44. G. Olah and G. K. Surya Prakash, *Carbocation Chemistry*, A John Wiley and Sons, 1st edition, 2004.

45. G. Olah. G. K. Surya Prakash, Árpád Molnár and Jean Sommer, *Superacid Chemistry*, A John Wiley and Sons, 2nd edition, 2009.

46. P. Ahlberg, G. Jonsäll and C. Engdahl *Advances in Physical Organic Chemistry*, Elsevier, 1st edition, 2008.

47. J. C. Barborak, J. Daub, D. M. Follweiler and P. v. R. Schleyer, *J. Am. Chem. Soc.* 1969, **91**, 7760.

48. (a) P. Ahlberg, C. Engdalh, G. Jonsäll, *J. Am. Chem. Soc.* 1981, **103**, 1583; (b) C. Engdalh, G. Jonsäll and P. Ahlberg, *J. Am. Chem. Soc.* 1983, **105**, 891; (c) C. Engdalh, G. Jonsäll and P. Ahlberg, *J. C. S. Chem. Comm.* 1979, 626; (d) C. Engdalh and P. Ahlberg, *J. Phys. Org. Chem.*1990, **3**, 349.

49. P. Ahlberg, D. L. Harris, M. Roberts, P. Warner, P. Seidel, M. Sakai, D. Cook, A. Diaz, J. P. Dirlam, H. Hamberger and S. Winstein, *J. Am. Chem. Soc.* 1972, **94**, 7063.

50. (a) J. W. Bode and K. Suzuki, *Tetrahedron. Lett.* 2003, **44**, 3559; (b) K. C. Nicolaou, T. Montagnon, G. Vassilikogiannakis and C. J. Mathison, *J. Am. Chem. Soc.* 2005, **127**, 8872; (c) D. J. Thoburn, W. Luttke, C. Benedict and H. H. Limach, *J. Am. Chem. Soc.* 1966, **118**, 12459; (d) S. Warren, A. Chow, G. Fraenkel and T. V. Ragababu, *J. Am. Chem. Soc.* 2003, **125**, 15402.

51. R. W. Schoenlein, L. A. Mathies and C. V. Shank, *Science.* 1991, **254**, 412.

52. T. C. Crawford, G. C. Andrews, H. Fabul and G. N. Chmurny, *J. Am. Chem. Soc.* 1980, **102**, 2220.

53. (a) S. Otto and K. Severin, *Top. Curr. Chem.* 2007, **277**, 267; (b) S. J. Rowan, S. J. Cantrill, G. R. L. Cousins, J. K. M. Sanders and J. F. Stoddart, *Angew. Chem. Int. Ed.* 2002, **41**, 989; (c) J. M. Lehn, *Chem. Eur. J.* 1999, **5**, 2455.

54. (a) G. Schröder and W. Witt, *Angew. Chem. Int. Ed.* 1979, **18**, 311; (b) K. Sarama, W. Witt and G. Schröder, *Chem. Ber.* 1983, **116**, 3800.

55. A. Craig, O. Cloaero, E. Holmes, K. J. Nicholoson and J. C. Lindon, *Anal. Chem.* 2006, **78**, 2262.

56. (a) T. D. James, K. Sandanayke and S. Shinkai, *Angew. Chem. Int. Ed.* 1996, **35**, 1910; (b) S. Jin, Y. Cheng, S. Reid, M. Li, and B. Wang, *Med. Res. Rev.* 2010, **30**, 171; (c) W. Wang, X. M. Gao and B. H. Wang, *Curr. Org. Chem.* 2002, **6**, 1285; (d) S. Hagihara, H. Tanaka and S. Matile. *J. Am. Chem. Soc.* 2008, **130**, 5656.

57. T. D. James, M. D. Phillips and S. Shinkai, *Boronic acids in saccharide recognition*, RSC publishing Cambridge, 1st edition, 2006.

58. W. Yang, X. Gao, and B. Wang, *Biological and Medicinal Applications of Boronic Acids*. Wiley-VCH, Weinheim, 1st edition, 2005.

59. (a) P. D. Beer and P. A. Gale, *Angew. Chem. Int. Ed.* 2001, **40**, 486; (b) A. Ikeda and S. Shinkai, *Chem. Rev.* 1997, **97**, 1713; (c) R. Martinez-Manez and F. Sancenon, *Chem. Rev.* 2003, **103**, 4419; (d) E. A. Mayer, R. K. Castellano and F. Diedrich, *Angew. Chem. Int. Ed.* 2003, **42**, 1210.

60. B. M. Goodson, *J. Magn. Reson.* 2002, **155**, 157.

61. J. C. Lindon, E. Holmes and J. K. Nicholoson, *Prog. Nuc. Mag. Reson. Spectrosc.* 2001, **39**, 1.

CHAPTER 2

SHAPE-SELECTIVE CRYSTALLISATION OF FLUXIONAL CARBON CAGES

Published as *'Shape-Selective Crystallisation of Fluxional Carbon Cages*' – A. N. Bismillah, J. Sturala, B. M. Chapin, D. S. Yufit, P. Hodgkinson and P. R. McGonigal, *Chem. Sci.* 2018, **9**, 8631.

Featured in *'2018 Chemical Science HOT Article Collection'*

Chosen as *'2018 ChemSci Pick of the Week Collection'*

Featured on the cover of *Chem. Sci.* 2018, **9**, Issue 46.

Synopsis

This Chapter discusses the novel synthesis of a series of five barbaralanes which each interconvert dynamically between two constitutional isomers in solution, but resolve to single isomers upon crystallisation. Unexpectedly, the minor solution-phase isomers are resolved in two cases. Through, dynamic NMR, crystallographic and DFT analyses, we show that the isomer observed in the solid state is not a direct consequence of the equilibrium distribution in solution or any specific noncovalent interactions. Rather, the dynamic preferential crystallisation is directed by differences in molecular size and shape.

Acknowledgements

The following people are gratefully acknowledged for their contribution to this chapter: Dr Jiri Sturala carried out the *in silico* modelling – in particular the calculations of the solution-phase equilibria and chemical shifts. Dr Brette M. Chapin helped with the synthesis of compound **1b**/**1b′**. Dr Dimitry S. Yufit solved all the X-ray crystal structures and performed the variable-temperature X-ray crystallography measurements. Dr Paul Hodgkinson carried out the *in silico* modelling for the ^{13}C NMR solid-state chemical shifts. Lastly, Dr Paul R. McGonigal calculated the intermolecular interaction energies, the electrostatic potential maps and Hirshfeld surfaces of the solid-state structures. We thank Dr Mark Miller and Professor Jon Steed for useful discussions. We are grateful to Dr David Apperley and Dr Raquel Belda-Vidal for assistance with NMR measurements.

2.1 Introduction

Fluxional carbon cages, such as bullvalene[1] and the barbaralyl cation[2] (Figure 2.1a), undergo reversible pericyclic rearrangements on a grand scale.[3] Sequential, low-energy steps interconvert large numbers of degenerate isomers. For example, bullvalene passes back and forth between 1.2 million degenerate valence isomers[1] by strain-assisted Cope rearrangements. Functionalised derivatives, on the other hand, give rise (Figure 2.1b) to nondegenerate valence isomers with distinct constitutions.[4] When their C-C bonds trade places with one another, the positions and relative orientations of their substituents are altered, endowing them with dynamic shapes (Figure 2.1c) and making them ideal building blocks for adaptive chemistry.[5] Bode *et al.*[6] have taken advantage of these phenomena to design shapeshifting bullvalene sensors – the equilibrium distribution of tetra-substituted bullvalene isomers is shifted in a manner when interacting with different guests, either by specific noncovalent interactions[6b] or dynamic covalent bonds.[6c]

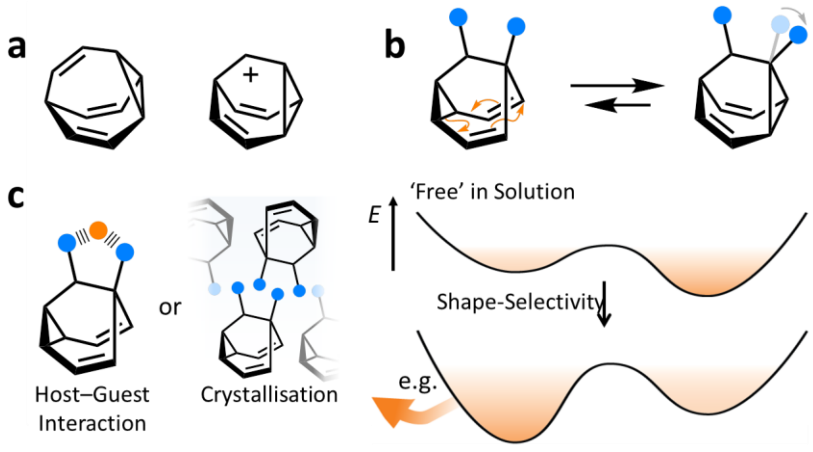

Figure 2.1. Structural formulas of (a) bullvalene, the barbaralyl cation and (b) a di-substituted barbaralane, showing its isomerisation. The relative orientations of the substituents, which are represented by blue circles, are altered by the isomerisation. (c) A schematic representation illustrates changes in relative energies of isomers in panel b as a result of a shape-selective intermolecular contact, *e.g.*, through noncovalent bonding with a guest, represented as an orange circle, or by crystal packing.

Here we report on the influence of shape over the crystallisation of fluxional carbon cages. Neutral barbaralanes, which equilibrate (Figure 2.1b) between sets of two non-equivalent valence isomers[7] in solution, are resolved to single valence isomers upon crystallisation. By analysing NMR spectra of solutions and powdered samples, X-ray

crystal structures and DFT models, we observe that (i) the dynamic isomerisation is 'frozen' in the solid state and (ii) relatively small differences in the substituents dictate which constitutional isomer is found upon crystallisation. Three of the compounds crystallise as the major solution-phase valence isomers, *i.e.*, their molecular structures in the solid state match those of the thermodynamically favoured species in solution. However, two compounds crystallise (Figure 2.1c) as the minor solution-phase valence isomers, achieving more densely packed crystals by adopting molecular structures that fit together more effectively. Size- and shape-matching of these fluxional molecules to their surroundings outweigh the inherent energetic preference of the shapeshifting equilibrium.

2.2 Results and Discussion

We synthesised (Scheme 2.1) fluxional mixtures of nondegenerate barbaralanes **1**/**1′** in two steps from alkynyl cycloheptatriene precursors **2**. Gold-catalysed cycloisomerisation of **2** proceeds[2c] through barbaralyl cation intermediates, which are oxidised[2d] *in situ* by diphenyl sulphoxide to afford barbaralanes **3** in 58–75% yields. Subsequent addition of arylmagnesium bromide reagents to **3** gives barbaralanes **1**/**1′**, each bearing a tertiary alcohol[8] and two aromatic rings. The aromatic ring at the 1/5′-position of each barbaralane breaks the symmetry of the Cope rearrangements, giving rise to the pairs of valence isomers **1** and **1′**. We reasoned that these pairs of nondegenerate valence isomers would be useful compounds for probing the shapeshifting properties of fluxional carbon cages. Compared to the huge numbers of valence isomers accessible to other systems, analysis of the double-well-type potential energy surface (Scheme 2.1) of **1**/**1′** is more tractable. At the same time, the rearrangement still modulates the molecular shape to some extent – the strain present in the tricyclic cores of **1** and **1′** is slightly different, regulating the relative orientations of the two aromatic rings. Five sets of barbaralanes (**1a**–**e**/**1a′**–**e′**) were prepared in which the groups at the *p*-positions of the aromatic rings (R^1 and R^2) are varied between OMe, F, and H.

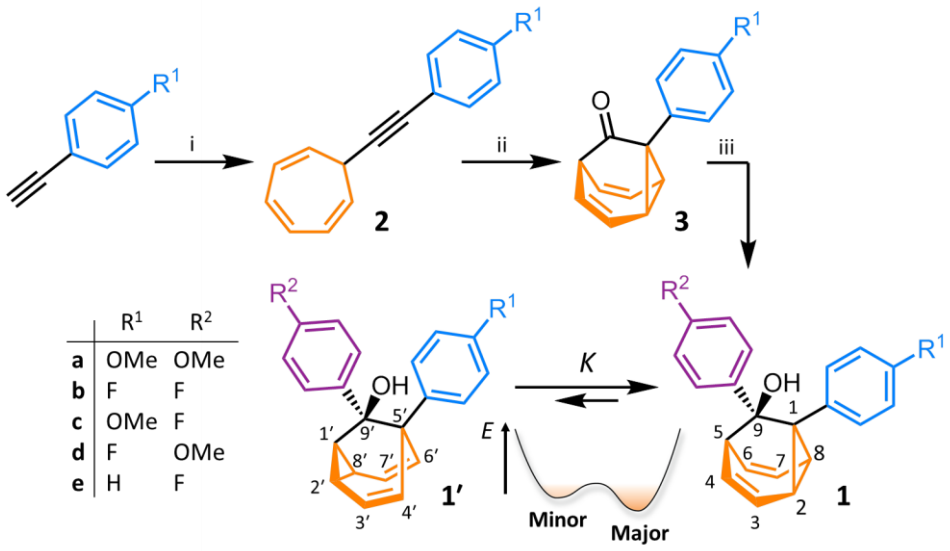

	R^1	R^2
a	OMe	OMe
b	F	F
c	OMe	F
d	F	OMe
e	H	F

Scheme 2.1. Synthesis of fluxional carbon cages **1**/**1′**. Reagents and conditions: (i) *n*-Buli, THF, –78 °C, 40 min then tropylium tetrafluoroborate, rt, 16 h, (ii) IPrAu(MeCN)BF_4 (5 mol%), Ph_2SO (2 equiv.), CH_2Cl_2, rt, 16 h, 58–75%; (iii) *p*-$R^2C_6H_4MgBr$, THF, 0 °C to rt, 16 h, 43–96%. A schematic potential energy diagram illustrates the equilibrium, *K*, between **1′** and **1**. IPr = 1,3-bis(2,6-diisopropylphenyl)imidazol-2-ylidene.

Isomers **1** and **1′** are in fast exchange when observed by solution-phase NMR spectroscopy. Consequently, each pair of exchangeable sites gives rise to one peak. The chemical shift of each peak represents an average of the two discrete chemical environments, weighted by the position of the equilibrium, which enables us to identify the major isomer (Appendix, Section 2.5.1). For example, the ^{13}C peak associated with position 2 of **1a** and position 4′ of **1a′** appears (Figure 2.2) at 49.6 ppm in $CDCl_3$ at 298 K, which is closer to the resonance of an divinyl cyclopropane group[9] (~25 ppm) than that of a *cis*-dialkylolefin group[10] (~135 ppm). This observation allows us to assign **1a** as the major isomer[11] and to estimate an equilibrium constant of ~3.5 ppm (Appendix, Section 2.5.2), as well as a Gibbs free energy difference, ΔG, of ~3 kJ·mol^{-1}. These conclusions are supported by DFT modelling (Table 2.1) (Appendix, Section 2.5.3), which predicts that **1a** is lower in energy than **1a′** by a margin of ~5 kJ·mol^{-1}. Further NMR and DFT analyses reveal that *K* is only minimally affected by varying the R^1 and R^2 groups at the *p*-positions of the aromatic rings. The substituents are sufficiently remote from the barbaralane core that their electronic and steric differences have little impact–structure **1** remains

the thermodynamically favoured solution-phase valence isomer for all derivatives (**1a**–**e**).

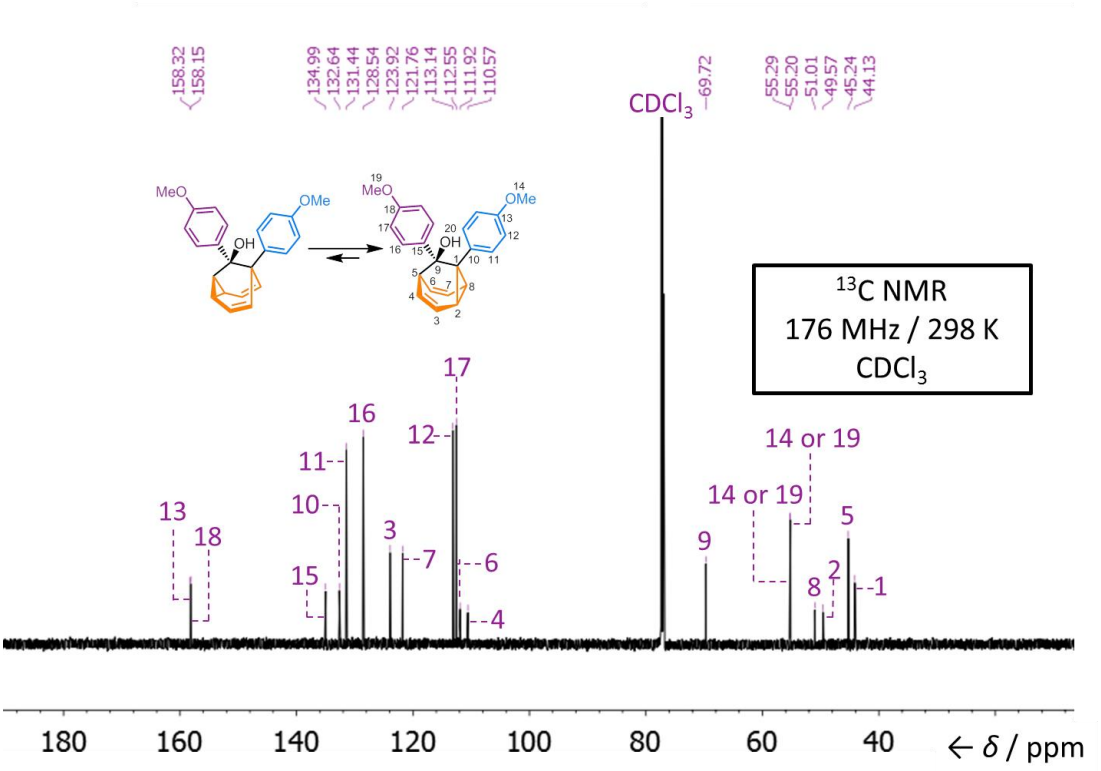

Figure 2.2. Assigned ^{13}C NMR spectrum of **1a**/**1a′**.

Table 2.1. Calculated energies and Gibbs free energies (ΔG) in kJ·mol^{-1} compared to the transition state (taken as a reference) (Appendix, Section 2.5.1).

DFT Functional	1a/1a′			1b/1b′		
	$\Delta G_1^{\dagger}$ ($\Delta E_1^{\dagger}$)[a]	$\Delta G_2^{\dagger}$ ($\Delta E_2^{\dagger}$)[b]	ΔG (ΔE)[c]	$\Delta G_1^{\dagger}$ ($\Delta E_1^{\dagger}$)[a]	$\Delta G_2^{\dagger}$ ($\Delta E_2^{\dagger}$)[b]	ΔG (ΔE)[c]
B3LYP – GD3	20.1 (25.4)	14.9 (21.0)	-5.2 (-4.4)	20.5 (25.0)	15.2 (20.9)	-5.3 (-4.1)
M06-2X – GD3	32.3 (37.6)	31.3 (38.1)	-1.0 (-0.5)	32.7 (37.0)	31.5 (37.8)	-1.2 (0.8)
CAM-B3LYP – GD3	36.5 (42.6)	31.1 (38.1)	-5.4 (-4.5)	35.9 (42.2)	30.6 (38.0)	-5.3 (-4.2)
B3LYP	24.5 (29.0)	15.2 (20.4)	-9.3 (-8.6)	24.8 (28.9)	15.0 (20.3)	-9.8 (-8.6)
ωB97X-D	33.2 (37.8)	38.7 (34.9)	-4.5 (-2.9)	33.1 (37.3)	29.6 (34.7)	-3.5 (-2.6)

[a] calculated as $E_{TS} - E_1$; [b] calculated as $E_{TS} - E_1'$; [c] calculated as $\Delta G_2^{\dagger} - \Delta G_1^{\dagger}$.

In order to probe the equilibria further, we also recorded solution-phase ^{1}H NMR spectra of bis(4-anisyl)barbaralane **1a**/**1a′** (Appendix, Section 2.5.4) and bis(4-fluorophenyl)barbaralane **1b**/**1b′** (Figure 2.3) at low temperatures. The temperature-dependent spectroscopic changes are consistent with the behaviour of two

nondegenerate valence isomers interconverting rapidly through a low-lying transition state. For example, the signal for the 8/6′ positions of **1b**/**1b′** shifts (Figure 2.3) from 3.55 ppm at 292 K to 3.31 ppm at 165 K, moving further towards the chemical shift expected for a cyclopropyl resonance, while the signal associated with 6/8′ moves towards the olefinic region, shifting from 5.50 ppm at 292 K to 5.60 ppm at 149 K. Therefore, the equilibrium shifts further in favour of the thermodynamically favoured isomer **1b** at lower temperatures, which would be expected for a Boltzmann distribution of nondegenerate isomers.

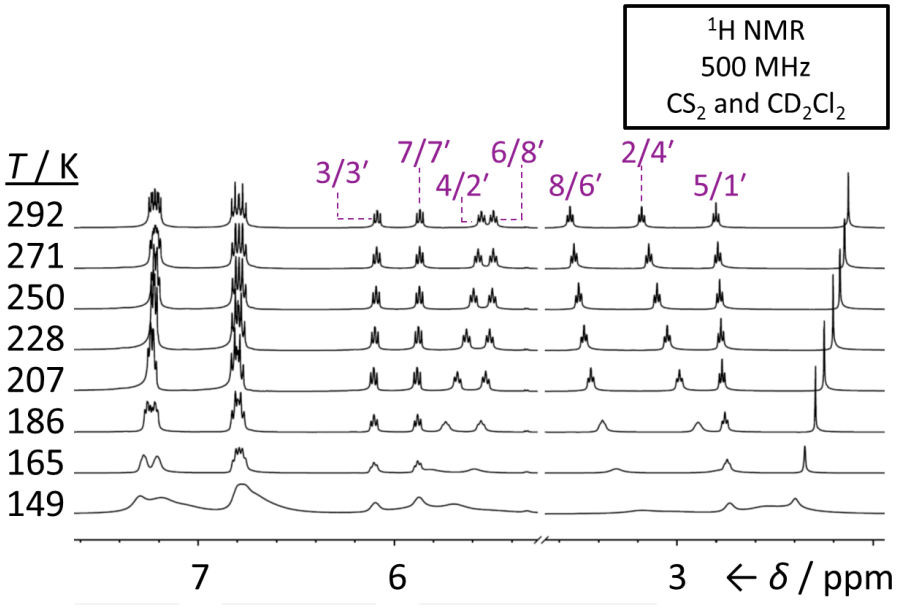

Figure 2.3. Partial ^{1}H NMR spectra of **1b**/**1b′**. As the temperature is decreased, the equilibrium shifts towards the lower-energy isomer **1b**. At temperatures below 186 K, the broadening of peaks indicates the reversible Cope rearrangement is entering the slow-exchange regime. Selected resonances are labelled according to the numbering in Scheme 2.1.

All five **1**/**1′** derivatives form crystalline solids, allowing us to analyse (Figure 2.4) their solid-state structures by single-crystal X-ray diffraction (Appendix, Section 2.5.5).[12] The fluxional mixtures of **1**/**1′** undergo dynamic preferential crystallisation,[13] *i.e.*, just one valence isomer from each pair of fluxional carbon cages crystallises from the mixture.[14,15] The bis(4-anisyl)barbaralane crystallises (Figure 2.4) as the major solution-phase valence isomer **1a**. Similarly, the barbaralanes bearing one 4-fluorophenyl group and one 4-anisyl group each adopt the major solution-phase structures **1c** and **1d** upon crystallisation. Surprisingly, however, we observed the more strained molecular structures in crystals of the bis(4-fluorophenyl)barbaralane

1b′ and its phenyl analogue **1e′**. While the *p*-substituents have little influence over the solution-state valence isomerism of the five **1**/**1′** derivatives, it appears that a subtle change at a position distant from the barbaralane core, such as switching out the OMe group of **1c**/**1c′** for a F atom (*i.e.*, giving **1b**/**1b′**), is sufficient to bias crystallisation in favour of another valence isomer.[16]

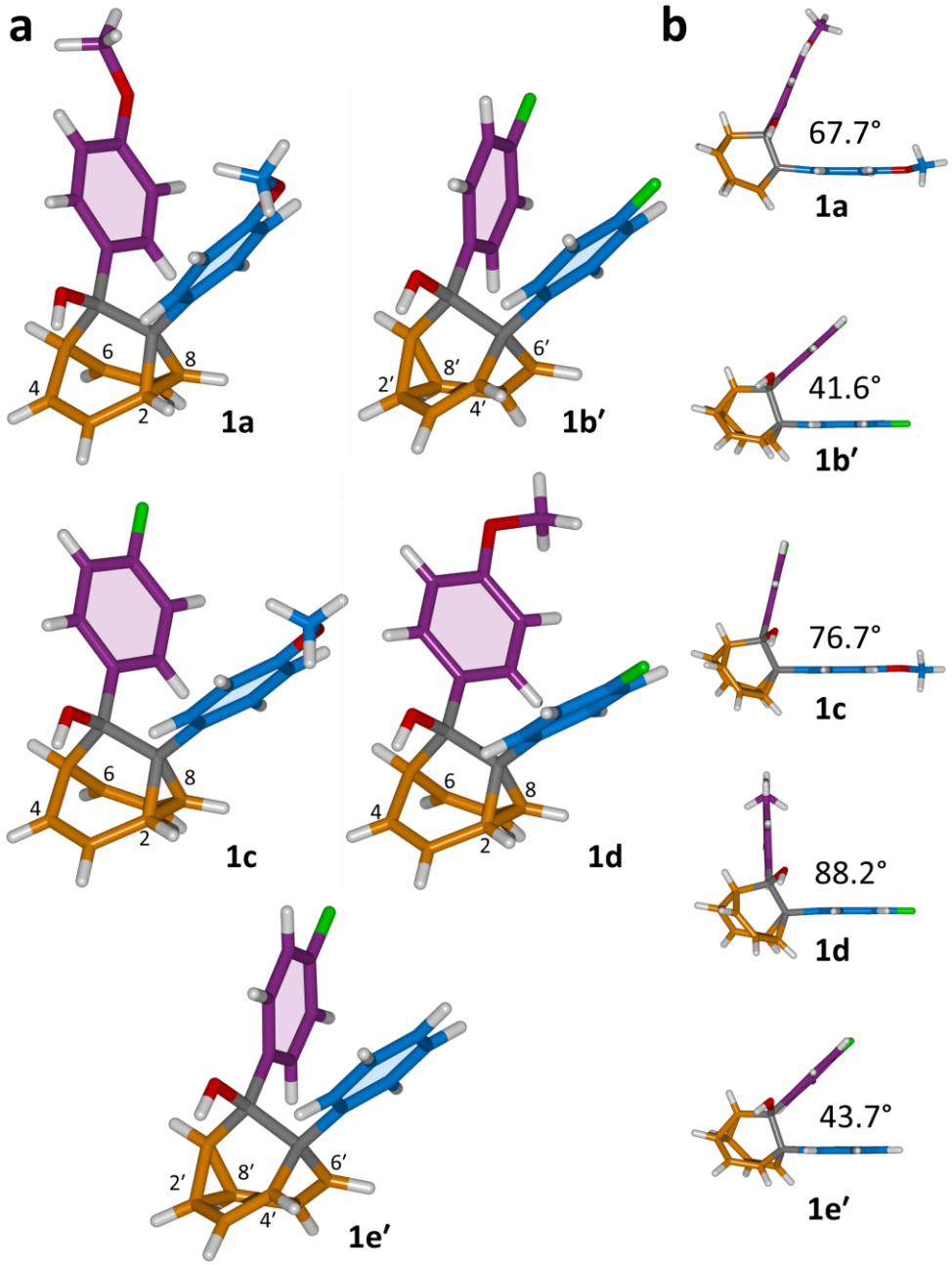

Figure 2.4. X-ray crystal structures of **1**/**1′** shown in stick representations.[12] (a) Whereas the major solution-phase valence isomers are obtained in some cases (**1a**, **1c** and **1d**), the minor solution-phase isomers crystallise preferentially in others (**1b′** and **1e′**). (b) Side-on views show the variation in

dihedral angles between the planes of the aromatic rings. Selected interatomic distances at 120 K (Å): **1a**, C2–C8 1.592(2), C4···C6 2.359(2); **1b′**, C2–C8′ 1.592(3), C4′···C6′ 2.353(2); **1c**, C2–C8 1.582(2), C4···C6 2.364(2); **1d**, C2–C8 1.586(2), C4···C6 2.367(2); **1e′**, C2′–C8′ 1.591(2), C4′···C6′ 2.345(2). Oxygen atoms are shown in red, fluorine atoms are green, hydrogen atoms are white, and carbon atoms are blue, purple, orange or grey.

Although some fluxional carbon cages[17] are known to become 'fixed' structures upon crystallisation, others[18] remain fluxional. Variable-temperature X-ray diffraction (VT-XRD) measurements performed on single crystals of **1a** and **1b′** show negligible changes in C–C distances of bonds involved in Cope rearrangement (Appendix, Section 2.5.6). For example, the C2–C8 bond length of **1a** only changes from 1.592 Å at 120 K to 1.604 Å at 370 K. The identities of **1** and **1′** isomers in the solid state can also be distinguished by comparing (Figure 2.5) their low-temperature solution and ambient-temperature solid-state ^{13}C NMR spectra (Appendix, Section 2.5.7). At 149 K, the solution-phase equilibria are biased heavily towards **1a** and **1b**, so both solution-phase spectra show (Figure. 2.5a,d) similar patterns of peaks in their alkyl regions. Unlike the solid-state NMR (ssNMR) spectrum of the bis(4-anisyl)barbaralane (Figure. 2.5b), which matches closely with its solution spectra (in keeping with its assignment by X-ray diffraction as structure **1a**), the ssNMR spectrum (Figure. 2.5c) of the bis(4-fluorophenyl)barbaralane is markedly different (Appendix, Section 2.5.8). The ssNMR spectrum indicates structure **1b′** is favoured over **1b**. Hence, the ssNMR and VT-XRD data are both consistent with the barbaralanes **1**/**1′** having fixed constitutions in the solid state.

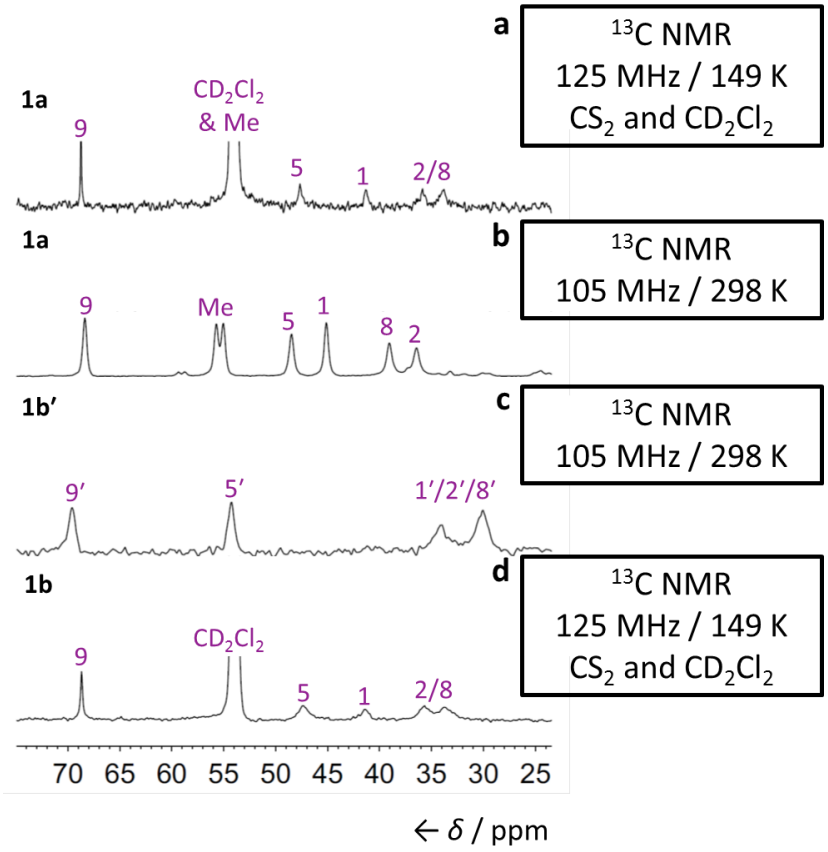

Figure 2.5. Comparison of partial ^{13}C NMR spectra of **1a**/**1a′** and **1b**/**1b′** acquired (a,d) at low temperatures and (b,c) as powders at ambient temperature. Peaks are labelled according to the numbering in Scheme 2.1.

The barbaralane cage acts as a hinge between its two aromatic substituents, giving (Figure 2.4b) the molecules V-shaped structures. Notably, the dihedral angles between the planes of these aromatic rings in the solid state vary substantially between the different derivatives. Compounds **1a**, **1c**, and **1d** have relatively wide dihedral angles >67°, whereas the dihedral angles of **1b′** and **1e′** are both <44°.[19] Inspection (Figure. 2.6 and Appendix, Section 2.5.5) of the solid-state superstructures reveals that these changes in dihedral angles are linked to differences in the crystal packing. Indeed, the packing is dominated by the way in which the V-shaped units fit together, rather than any specific noncovalent interactions. Compounds **1a**, **1c**, and **1d** pack with a preference to arrange their V-shaped structures head-to-tail, while **1b′** and **1e′** are arranged head-to-head, allowing their aromatic groups to interdigitate. We attribute changes between these two modes of packing primarily to differences in the sizes of the R^1 and R^2 groups. A 4-anisyl group is too large to allow efficient

interdigitation, so the head-to-tail arrangement is favoured in which the aromatic rings are splayed around a neighbouring barbaralane. This geometry is most easily accommodated by the **1**-isomer form. Conversely, **1b′** and **1e′** lack 4-anisyl groups, so they are able to achieve more densely packed lattices than the other derivatives (1.39–1.44 *vs* 1.33–1.35 g·cm^{-3}) by adopting head-to-head arrangements. The 4-fluorophenyl and phenyl groups are small enough for the aromatic rings to pack together efficiently, favouring smaller dihedral angles that are more accessible when the barbaralane adapts to the slightly higher energy **1′**-isomer. Although there is more strain in the molecular structure, the relatively small (~5 kJ·mol^{-1}) energy penalty to adopt the structure of the minor solution-state isomer must be overridden by a more favourable lattice energy, making the **1′**-isomer favoured in the solid state.[20]

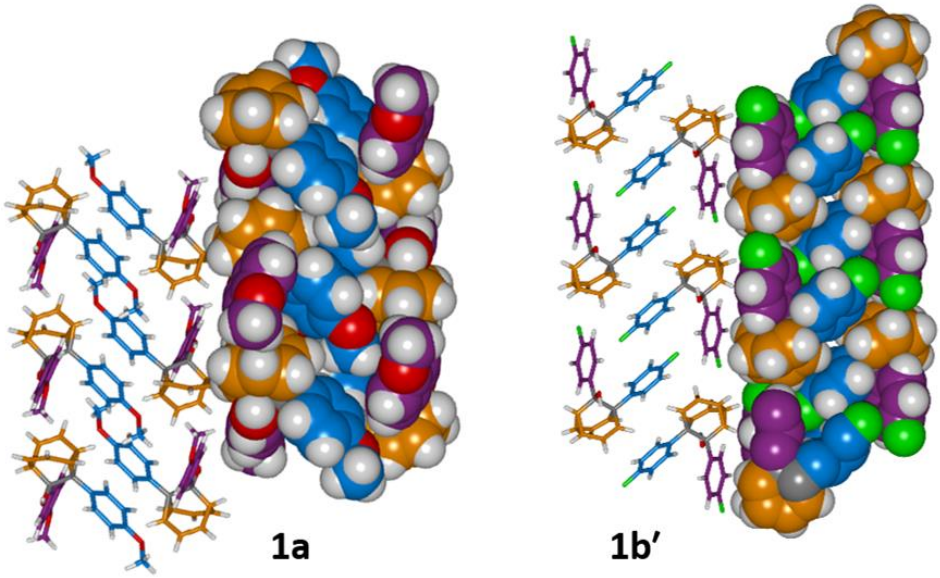

Figure 2.6. Solid-state superstructures of **1a** and **1b′** shown in partial stick and space-filling representations and viewed along the crystallographic *b*-axes. The superstructures of **1c** and **1d** are similar to **1a**, whereas the superstructure of **1e′** (Appendix, Section 2.5.5) is isostructural with **1b′**. Calculated densities (g·cm^{-3}): **1a**, 1.33; **1b′**, 1.44; **1c**, 1.35; **1d**, 1.35; **1e′**, 1.39.

The alcohol function (which might normally be expected to dictate[17] the packing) is overcrowded and electrostatic potential maps show (Appendix, Section 2.5.9) that the aromatic rings are only mildly polarised. In order to search for noncovalent bonding interactions, we calculated the Hirshfeld surfaces[18] of each crystal structure. The Hirshfeld surfaces show (Appendix, Section 2.5.10) that no interatomic distances are significantly closer than the sum of the respective van der Waals radii. For example,

the most prominent close contacts present (Figure. 2.7) in **1d** and **1e′** are weak O–H···C and C–H···C interactions, which each remain within ~0.2 Å of the sum of the van der Waals radii.[23]

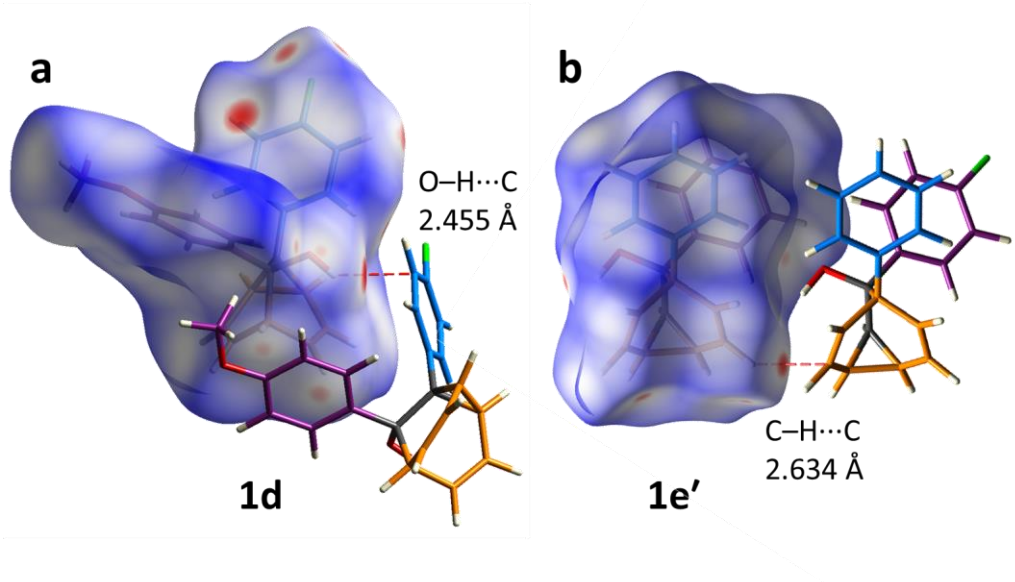

Figure 2.7. Calculated Hirshfeld surfaces for the X-ray crystal structures of (a) **1d** and (b) **1e′**, showing the most significant close contacts with neighbouring molecules, which do not correspond to appreciable noncovalent bonding interactions.

We confirmed this lack of significant, specific noncovalent bonding interactions by performing DFT modelling (CE-B3LYP[24]) of all the intermolecular interactions in the solid state (Appendix, Section 2.5.11). These calculations allow us to elucidate the total interaction energies (E_{tot}) between neighbouring molecules based on the individual energetic components of electrostatics (E_{ele}), polarisation (E_{pol}), dispersion forces (E_{dis}) and repulsion (E_{rep}).[25] For example, we examined (Figure. 2.8) a cluster of fourteen neighbouring molecules surrounding a central molecule in the structure of **1e′**. The fourteen neighbours account for all of the molecules that come within 3.8 Å of the central molecule. As would be expected, the pairs of **1e′** molecules that are closest, having the smallest centroid-to-centroid distances (R), generally interact most strongly with one another. Molecules in position D and F are separated (Table 2.2) from the central molecule by R <7 Å and have interaction energies of E_{tot} = –31.1 and –43.5 kJ·mol^{-1}, respectively, which are the strongest pairings present in the structure. Dispersion forces account for the majority of their attractive intermolecular

interactions, contributing energies of E_{dis} = –46.8 for D and E_{dis} = –51.4 kJ·mol^{-1} for F. Overall, the modelling for the full series of five **1**/**1′** derivatives shows (Appendix, Section 2.5.11) that dispersion forces[26] (which are influenced by the shape of the molecules and their packing) make up the major component of the interactions between molecules in all of the packing motifs, dominating the overall lattice energies in each case. This observation is consistent with our description of these molecules packing in the solid state in a manner that is influenced more by molecular shape than by any specific noncovalent bonding interactions.

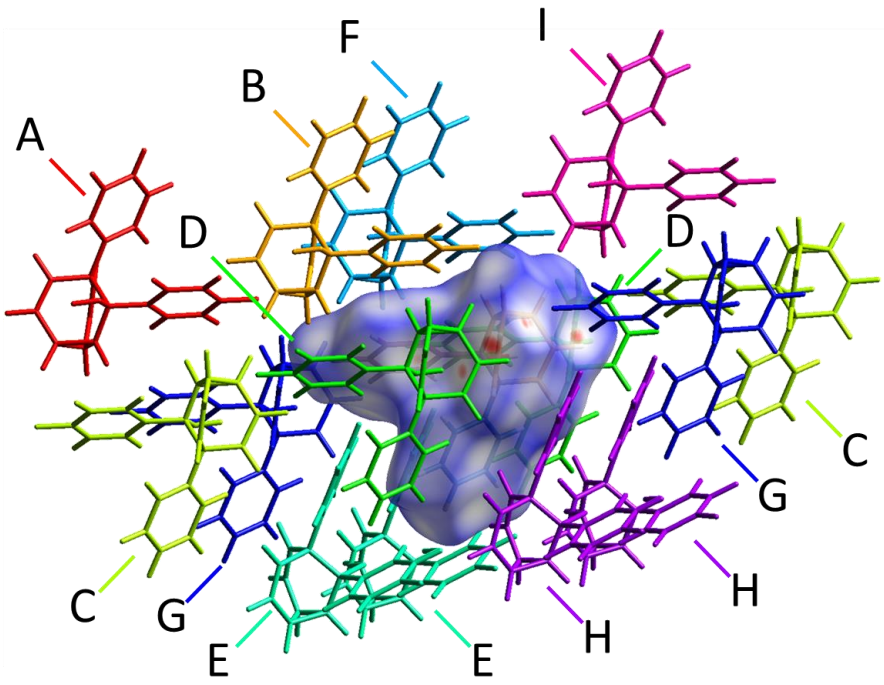

Figure 2.8. A section of the solid-state superstructure of **1e′** in which a central molecule (overlaid with its modelled Hirshfeld surface) is surrounded by its 14 nearest neighbours (labelled A–I). Molecules A–I are shown in stick representation. Labels are duplicated for molecules that reside at symmetry-related coordinates relative to the central molecule.

Table 2.2. Calculated intermolecular interaction energies (kJ·mol^{-1}) for pair of molecules in the solid-state structure of **1e′**.

Neighbouring Molecule[a]	Interaction Energies / kJ·mol^{-1}					
	R / Å[b]	E_{ele}	E_{pol}	E_{dis}	E_{rep}	E_{tot}[c]
A	13.29	2.1	-0.2	-1.3	0.0	1.0
B	7.94	-10.1	-1.4	-31.2	20.3	-26.3
C	11.59	-2.3	-0.4	-3.8	0.6	-5.6
D	6.20	-8.4	-2.4	-46.8	32.8	-31.1
E	8.26	-5.0	-0.9	-30.3	18.7	-20.8
F	6.63	-14.8	-2.8	-51.4	30.9	-43.5
G	9.79	-5.0	-0.8	-16.1	11.7	-12.7
H	7.90	-6.3	-1.1	-31.5	17.9	-23.8
I	11.04	1.1	-0.4	-8.1	1.8	-5.1

[a]The labels A–I correspond to those shown in Figure 2.8 and refer to the nearby molecules in the solid state. [b]R is the centroid-to-centroid distance between the labelled molecule and the central molecule. Centroids are based on the coordinates of all atoms in each molecule and are not weighted by mass. [c]E_{tot} is the sum of the individual interaction energy components E_{ele}, E_{pol}, E_{dis} and E_{rep}.

2.3 Conclusions

In summary, by investigating the dynamic isomerisation of nondegenerate barbaralanes, we have found that their crystallisation is directed by the shapes of their fluxional isomers. Either the major or the minor solution-phase isomer may be resolved as a result of their assembly in crystal lattices, becoming kinetically trapped in the solid state. At present, it has not been possible to discern precisely the shapes available to the most advanced shapeshifting sensors,[6] which encompass hundreds of constitutional isomers and conformationally flexible substituents. Our observations, based on a bistable fluxional carbon cage with rigid substituents, illustrate that shape-selective interactions can override the inherent thermodynamic differences between even closely related valence isomers. Understanding the relationship between shape-selectivity and the energetics of fluxional carbon cages will aid the development of shapeshifting sensors and other applications of adaptive molecules.

2.4 Experimental Details

2.4.1 Specific Experimental Methods

For general experimental details see page *xix*. Solid-State NMR spectra were recorded on a V-NMRS-400 (^{1}H 399.88 MHz and ^{13}C 105.56 MHz). The spectra were acquired using cross-polarisation with a 90-s recycle delay and 5-ms contact time for **1b′** ms and 30-s recycle delay and a 7-ms contact time for **1a**. All spectra were recorded at ambient probe temperature (approximately 25 °C) and at a spin rate of 10 kHz. Spectra are reported relative to an external sample of neat tetramethylsilane (referencing was carried out by setting the high- frequency signal from adamantane to 38.5 ppm). The X-ray single-crystal diffraction data for 1-(4-fluorophenyl)tricyclo[3.3.1.02,8]nona-3,6-dien-9- one, **1a**, **1c**, **1d**, and **1e′** were collected at 120.0(2) K using λMoKα radiation (λ = 0.71073 Å) on a Bruker D8Venture (Photon100 CMOS detector, IμS-microsource, focusing mirrors) diffractometer and for compound **1b′** on an Agilent XCalibur (Sapphire-3 CCD detector, fine-focus sealed tube, graphite monochromator) diffractometer, both equipped with Cryostream (Oxford Cryosystems) open-flow nitrogen cryostats. Multi-temperature measurements for compounds **1a** and **1b′** were performed on the latter instrument. The heating rate was 120°/h in both cases. All structures were solved by direct method and refined by full-matrix least squares on F 2 for all data using Olex2[27] and SHELXT[28] software. All non-disordered non-hydrogen atoms were refined anisotropically, hydrogen atoms were located in the difference Fourier maps and refined isotropically. The hydrogen atoms in high-temperature structures **1a** and **1b′** were placed into calculated positions and refined in riding mode.

2.4.2 Synthesis of Di-Substituted Barbaralanes

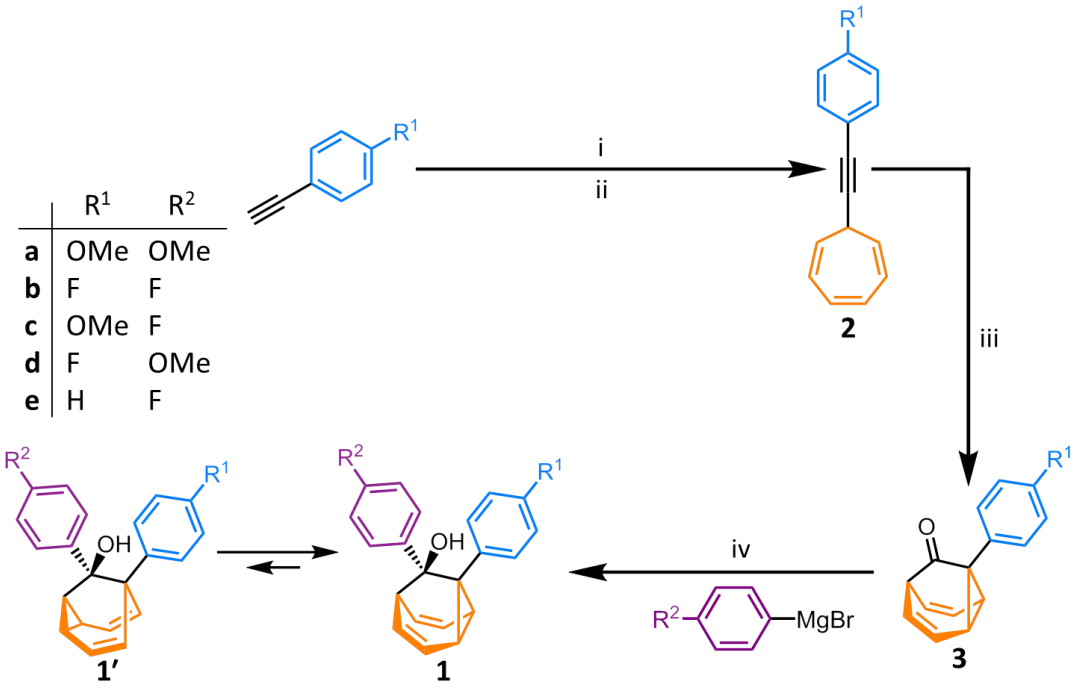

Scheme 2.2. General synthesis of substituted alkynyl cycloheptatrienes, barbaralanes and di-substituted barbaralanes according to modified literature[2c,2d] procedures. Reagents and conditions: (i) *n*-BuLi / THF / –78 °C / 40 min, (ii) tropylium tetrafluoroborate / rt / 16 h, (iii) IPrAu(MeCN)BF_4 (5 mol%) / Ph_2SO / CH_2Cl_2 / rt / 16 h, (iv) either (a) THF / 0 °C to rt / 16 h or (b) diglyme / Bu_4NI / THF / 0 °C to rt / 16 h. IPr = 1,3-bis(2,6-diisopropylphenyl)imidazol-2-ylidene.

7-[2-(4-Anisyl)ethynyl]cyclohepta-1,3,5-triene (2a)

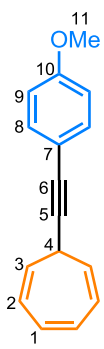

4-Ethynylanisole (330 mg, 2.5 mmol) was placed into an oven-dried round-bottomed flask fitted with a septum under a N_2 atmosphere. Anhydrous THF (15 mL) was added and the resulting solution was cooled to –78 °C before adding *n*-BuLi (1.0 mL, 2.6 mmol, 2.5 M in hexanes) and stirring for 40 min at this temperature. Tropylium tetrafluoroborate (455 mg, 2.5 mmol) was added, and the mixture was allowed to reach rt and stirred for 16 h. The reaction was quenched with a saturated aqueous solution of NH_4Cl (30 mL), then extracted with EtOAc (3 × 20 mL). The combined organic extracts were dried over $MgSO_4$, filtered and the solvent removed under reduced pressure. The crude residue was purified by column chromatography (Teledyne Isco CombiFlash Rf+ system, 24 g SiO_2, hexanes−EtOAc, gradient elution) to yield the title compound as a pale yellow solid (470 mg, 2.11 mmol, 85%). **M.P.** 70 – 72 °C (lit.[3] 69 – 71 °C). **^{1}H NMR** (400 MHz, $CDCl_3$) δ 7.40 (d, *J* = 8.7 Hz, 2H, H_8), 6.84 (d,

J = 8.7 Hz, 2H, H_9), 6.78 – 6.53 (m, 2H, H_1), 6.28 – 6.09 (m, 2H, H_2), 5.51 – 5.31 (m, 2H, H_3), 3.81 (s, 3H, H_{11}), 2.69 (tt, *J* = 5.6, 1.5 Hz, 1H, H_4). **^{13}C NMR** (151 MHz, $CDCl_3$) δ 159.5 (C_{10}), 133.2 (C_8), 131.2 (C_1), 124.8 (C_2), 123.6 (C_3), 115.7 (C_7), 114.0 (C_9), 89.7 (C_5), 80.5 (C_6), 55.4 (C_{11}), 32.4 (C_4). **HR-ASAP-MS** *m/z* = 223.1123 $[M+H]^+$ (calculated for $C_{16}H_{15}O^+$ = 223.1117).

Spectroscopic data were consistent with those published previously.[2c,2d]

7-[2-(4-Fluorophenyl)ethynyl]cyclohepta-1,3,5-triene (2b)

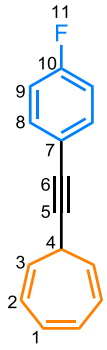

1-Ethynyl-4-fluorobenzene (600 mg, 5.0 mmol) was placed into an oven-dried round-bottomed flask fitted with a septum under a N_2 atmosphere. Anhydrous THF (15 mL) was added and the resulting solution was cooled to –78 °C before adding *n*-BuLi (2.0 mL, 5.1 mmol, 2.5 M in hexanes) and stirring for 40 min at this temperature. Tropylium tetrafluoroborate (910 mg, 5.0 mmol) was added, and the mixture was allowed to reach rt and stirred for 16 h. The reaction was quenched with a saturated aqueous solution of NH_4Cl (30 mL), then extracted with EtOAc (3 × 20 mL). The combined organic extracts were dried over $MgSO_4$, filtered and the solvent removed under reduced pressure. The crude residue was purified by column chromatography (Teledyne Isco CombiFlash Rf+ system, 24 g SiO_2, hexanes−EtOAc, gradient elution) to yield the title compound as a yellow oil (852 mg, 3.88 mmol, 81%). **^{1}H NMR** (400 MHz, $CDCl_3$) δ 7.53 – 7.34 (m, 2H, H_8), 7.08 – 6.93 (m, 2H, H_9), 6.77 – 6.63 (m, 2H, H_1), 6.29 – 6.18 (m, 2H, H_2), 5.42 (dd, *J* = 9.1, 5.5 Hz, 2H, H_3), 2.71 (t, *J* = 5.5, 1.5 Hz, 1H, H_4). **^{13}C NMR** (151 MHz, $CDCl_3$) δ 162.4 (d, J_{CF} = 248.8 Hz, C_{10}), 133.7 (d, J_{CF} = 8.3 Hz, C_8), 132.0 (C_1), 125.0 (C_2), 123.0 (C_3), 120.0 (C_7), 115.6 (d, J_{CF} = 22.0 Hz, C_9), 90.8 (C_5), 79.7 (C_6), 32.3 (C_4). **^{19}F NMR** (376 MHz, $CDCl_3$) δ –114.9 (m, F_{11}). **HR-ASAP-MS** *m/z* = 209.0768 $[M-H]^+$ (calculated for $C_{15}H_{10}F^+$ = 209.0761).

Spectroscopic data were consistent with those published previously.[2c,2d]

7-[2-Phenylethynyl)cyclohepta-1,3,5-triene (2e)

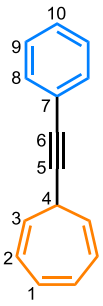

Phenylacetylene (255 mg, 2.5 mmol) was placed into an oven-dried round-bottomed flask fitted with a septum under a N_2 atmosphere. Anhydrous THF (15 mL) was added and the resulting solution was cooled to –78 °C before adding *n*-BuLi (1.0 mL, 2.6 mmol, 2.5 M in hexanes) and stirring for 40 min at this temperature. Tropylium tetrafluoroborate (455 mg, 2.5 mmol) was added, and the mixture was allowed to reach rt and stirred for 16 h. The reaction was quenched with a saturated aqueous solution of NH_4Cl (30 mL), then extracted with EtOAc (3 × 20 mL). The combined organic extracts were dried over $MgSO_4$, filtered and the solvent removed under reduced pressure. The crude residue was purified by column chromatography (Teledyne Isco CombiFlash Rf+ system, 24 g SiO_2, hexanes−EtOAc, gradient elution) to yield the title compound as a yellow oil (281 mg, 1.46 mmol, 58%). **^{1}H NMR** (700 MHz, $CDCl_3$) δ 7.50 – 7.47 (m, 2H, H_8), 7.34 – 7.321 (m, 3H, H_9 and H_{10}), 6.73 – 6.68 (m, 2H, H_1), 6.26 – 6.21 (m, 2H, H_2), 5.45 (dd, J = 8.7, 5.5 Hz, 2H, H_3), 2.73 (tt, J = 5.6, 1.5 Hz, 1H, H_4). **^{13}C NMR** (176 MHz, $CDCl_3$) 131.9 (C_8), 131.2 (C_1), 128.4 (C_9), 128.0 (C_{10}), 124.9 (C_2), 123.6 (C_7), 123.3 (C_3), 91.2 (C_5), 80.7 (C_6), 32.4 (C_4). **HR-ASAP-MS** *m/z* = 191.0857 $[M-H]^+$ (calculated for $C_{15}H_{11}^+$ = 191.0855).

Spectroscopic data were consistent with those published previously.[2c,2d]

In room temperature solutions, each of the barbaralones[27] and barbaralanes below exist as mixtures of two rapidly interconverting valence isomers. Based on our experimental observations, the structures bearing an aryl group at position 1 are the major species present in solution for all of the compounds investigated. The NMR spectroscopic assignments below, which have been made with the aid of two-dimensional NMR techniques, are labelled according to numbering of the major species. However, the species are in fast exchange on account of rapid strain-assisted Cope rearrangement. The chemical shifts of each nucleus are representative of the time-averaged chemical environment they experience as part of the two isomers.

(±)-1-(4-Anisyl)tricyclo[3.3.1.0^{2,8}]nona-3,6-dien-9-one (3a)

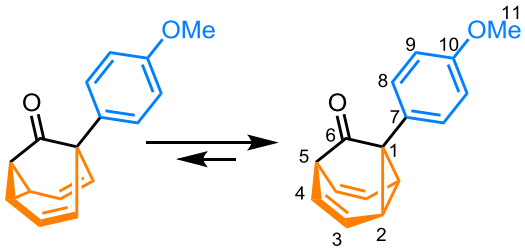

7-[2-(4-Anisyl)ethynyl]cyclohepta-1,3,5-triene (1.0 g, 4.5 mmol) and diphenyl sulfoxide (1.8 g, 9.0 mmol) were charged in a flask and dissolved in anhydrous CH_2Cl_2 (15 mL) at rt, with no particular precautions to exclude air. (Acetonitrile)[1,3-bis(2,6-diisopropylphenyl)imidazol-2-ylidene]gold(I) tetrafluoroborate (160 mg, 0.2 mmol, 5 mol%) was added in one portion at the same temperature and the reaction mixture was stirred for 16 h. The reaction was quenched with Et_3N (10 drops) and the solvent was removed under reduced pressure. The crude residue was purified by column chromatography (Teledyne Isco CombiFlash Rf+ system, 24 g SiO_2, hexanes−EtOAc, gradient elution) to yield the title compound as a cream-coloured solid (0.81 g, 3.39 mmol, 75%). **M.P.** 78 – 80 °C (lit.[2d] 79 – 81 °C). **^{1}H NMR** (600 MHz, $CDCl_3$) δ 7.16 (d, *J* = 8.8 Hz, 2H, H_8), 6.90 (d, *J* = 8.7 Hz, 2H, H_9), 5.93 – 5.89 (m, 2H, H_4), 5.88 – 5.84 (m, 2H, H_3), 3.80 (s, 3H, H_{11}), 3.34 – 3.17 (m, 2H, H_5), 3.10 – 2.98 (m, 2H, H_2). **^{13}C NMR** (151 MHz, $CDCl_3$) δ 208.5 (C_6), 159.2 (C_{10}), 130.8 (C_8), 128.9 (C_7), 125.0 (C_4), 121.5 (C_3), 114.2 (C_9), 55.4 (C_{11}), 49.1 (C_5), 42.2 (C_2), 39.1 (C_1). **HR-ASAP-MS** *m/z* = 239.1075 $[M+H]^+$ (calculated for $C_{16}H_{15}O_2^+$ = 239.1067).

Spectroscopic data were consistent with those published previously.[2d]

(±)-1-(4-Fluorophenyl)tricyclo[3.3.1.0^{2,8}]nona-3,6-dien-9-one (3b)

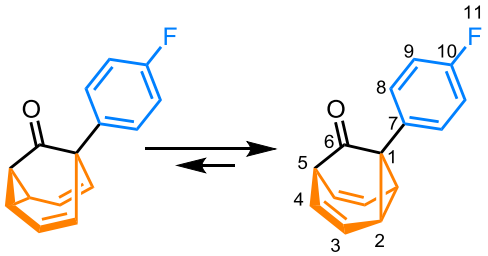

7-[2-(4-Fluorophenyl)ethynyl]cyclohep-ta-1,3,5-triene (374 mg, 1.8 mmol) and diphenyl sulfoxide (720 mg, 3.6 mmol) were charged in a flask and dissolved in anhydrous CH_2Cl_2 (15 mL) at rt, with no particular precautions to exclude air. (Acetonitrile)[1,3-bis(2,6-diisopropylphenyl)-imidazol-2-ylidene]gold(I) tetrafluoroborate (63.5 mg, 0.1 mmol, 5 mol%) was added in one portion at the same temperature and the reaction mixture was stirred for 16 h. The reaction was quenched with Et_3N (4 drops) and the solvent was removed under

reduced pressure. The crude residue was purified by column chromatography (Teledyne Isco CombiFlash Rf+ system, 24 g SiO_2, hexanes−EtOAc, gradient elution) to yield the title compound as a pale yellow crystalline solid (262 mg, 1.24 mmol, 65%). **M.P.** 111 – 113 °C (lit.[2d] 112 – 115 °C). **^{1}H NMR** (600 MHz, $CDCl_3$) δ 7.24 – 7.19 (m, 2H, H_8), 7.04 (dd, J = 8.7, J_{HF} = 8.7 Hz, 2H, H_9), 5.96 – 5.88 (m, 2H, H_4), 5.88 – 5.84 (m, 2H, H_3), 3.23 (tt, J = 6.3, 1.2 Hz, 1H, H_5), 3.10 – 3.05 (m, 2H, H_2). **^{13}C NMR** (151 MHz, $CDCl_3$) δ 207.8 (C_6), 162.2 (d, J_{CF} = 246.3 Hz, C_{10}), 132.7 – 132.4 (m, C_7), 132.10 (d, J_{CF} = 8.2 Hz, C_8), 124.4 (C_4), 121.2 (C_3), 115.4 (d, J_{CF} = 21.5 Hz, C_9), 48.7 (C_5), 42.4 (C_2), 39.0 (C_1). **^{19}F NMR** (376 MHz, $CDCl_3$) δ -117.7 (tt, J_{FH} = 8.7, 5.3 Hz, F_{11}). **HR-ASAP-MS** m/z = 227.0876 $[M+H]^+$ (calculated for $C_{15}H_{12}OF^+$ = 227.0867).

Spectroscopic data were consistent with those published previously.[2d]

(±)-1-Phenyltricyclo[3.3.1.0.^{2,8}]nona-3,6-dien-9-one (3e)

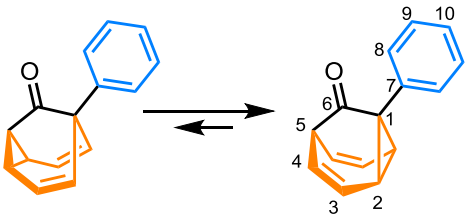

7-[2-Phenylethynyl)cyclohepta-1,3,5-triene (475 mg, 2.47 mmol) and diphenyl sulfoxide (1.0 g, 4.94 mmol) were charged in a flask and dissolved in anhydrous CH_2Cl_2 (15 mL) at rt, with no particular precautions to exclude air. (Acetonitrile)[1,3-bis(2,6-diisopropylphenyl)imidazol-2-ylidene]gold(I) tetrafluoroborate (88 mg, 0.1 mmol, 5 mol%) was added in one portion at the same temperature and the reaction mixture was stirred for 16 h. The reaction was quenched with Et_3N (5 drops) and the solvent was removed under reduced pressure. The crude residue was purified by column chromatography (Teledyne Isco CombiFlash Rf+ system, 24 g SiO_2, hexanes−EtOAc, gradient elution) to yield the title compound as a cream-coloured solid (297 mg, 1.43 mmol, 58%). **M.P.** 104 – 105 °C (lit.[2d] 104 – 105 °C). **^{1}H NMR** (700 MHz, $CDCl_3$) δ 7.35 (dd, J = 8.2, 6.9 Hz, 2H, H_9), 7.31 – 7.27 (m, 1H, H_{10}), 7.24 (dd, J = 8.1, 1.4 Hz, 2H, H_8), 5.94 – 5.90 (m, 2H, H_4), 5.89 – 5.83 (m, 2H, H_3), 3.30 – 3.17 (m, 1H, H_5), 3.15 – 2.96 (m, 2H, H_2). **^{13}C NMR** (176 MHz, $CDCl_3$) δ 208.2 (C_6), 136.9 (C_7), 129.7 (C_8),

128.7 (C_9), 127.9 (C_{10}), 125.0 (C_4), 121.5 (C_3), 49.2 (C_5), 42.0 (C_2), 39.7 (C_1). **HR-ASAP-MS** *m/z* = 209.0952 $[M+H]^+$ (calculated for $C_{15}H_{13}O^+$ = 209.0961).

Spectroscopic data were consistent with those published previously.[2d]

(±)-1,9-Bis(4-anisyl)tricyclo-[3.3.1.0^{2,8}]nona-3,6-dien-9-ol (1a)

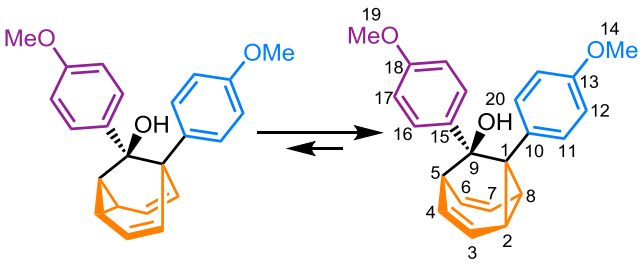

Magnesium turnings (115 mg, 4.78 mmol) and I_2 (59 mg, 0.2 mmol, 5 mol%) were placed in an oven-dried two-necked round-bottomed flask fitted with a condenser and a septum under a N_2 atmosphere. The flask was gently heated with a heat gun until the I_2 started to sublime. The flask was cooled down to rt. A quarter of a solution of 4-bromoanisole (980 mg, 4.6 mmol) in anhydrous THF (10 mL) was added to the reaction mixture, which was heated until it reached reflux. Upon gentle reflux, the remaining solution of 4-bromoanisole in anhydrous THF was added dropwise over 30 min. The reaction mixture was heated at reflux for 30 min before cooling to rt. In an oven-dried round-bottomed flask, under an atmosphere of N_2, was added Bu_4NI (36.0 mg, 0.1 mmol), anhydrous diglyme (0.21 mL, 201 mg, 1.5 mmol), and the Grignard solution (prepared above).[6] Anhydrous THF (15 mL) was added and the solution was cooled to 0 °C for 30 min with stirring. 1-(4-Anisyl)tricyclo[3.3.1.0^{2,8}]nona-3,6-dien-9-one (225 mg, 0.9 mmol) was added dropwise over 30 min at the same temperature. The reaction mixture was stirred for 16 h, where the temperature was raised from 0 °C to rt, following removal of the ice bath. The reaction was quenched with a saturated aqueous solution of NH_4Cl (10 mL), then extracted with EtOAc (3 × 20 mL). The combined organic extracts were dried over $MgSO_4$, filtered and the solvent removed under reduced pressure. The crude residue was purified by column chromatography (Teledyne Isco CombiFlash Rf+ system, 24 g Al_2O_3, hexanes−CH_2Cl_2, gradient elution) to yield **1a** as a white solid (158 mg, 0.46 mmol, 43%). **M.P.** 128 – 130 °C. **^{1}H NMR** (700 MHz, $CDCl_3$) δ 7.20 (d, *J* = 9.0 Hz, 2H, H_{16}), 7.18 (d, *J* = 9.5 Hz, 2H, H_{11}), 6.70 (d, *J* = 8.7 Hz, 2H, H_{12}), 6.68 (d, *J* = 8.9 Hz, 2H, H_{17}), 6.07 – 6.00 (m, 1H,

H_3), 5.84 – 5.79 (m, 1H, H_7), 5.59 – 5.53 (m, 1H, H_4), 5.50 – 5.46 (m, 1H, H_6), 3.73 (s, 6H, H_{19} and H_{14}), 3.50 – 3.45 (m, 1H, H_8), 3.17 – 3.10 (m, 1H, H_2), 2.80 (t, J = 6.8 Hz, 1H, H_5), 2.14 (s, 1H, H_{20}). **^{13}C NMR** (176 MHz, $CDCl_3$) δ 158.3 (C_{13}), 158.2 (C_{18}), 135.0 (C_{15}), 132.6 (C_{10}), 131.4 (C_{11}), 128.5 (C_{16}), 123.9 (C_3), 121.8 (C_7), 113.1 (C_{12}), 112.6 (C_{17}), 111.9 (C_6), 110.6 (C_4), 69.7 (C_9), 55.3 (C_{14} or C_{19}), 55.2 (C_{14} or C_{19}), 51.0 (C_8), 49.6 (C_2), 45.2 (C_5), 44.1 (C_1). **HR-ASAP-MS** *m/z* = 346.1568 $[M]^+$ (calculated for $C_{23}H_{22}O_3^+$ = 346.1564).

(±)-1,9-Bis(4-fluorophenyl)tricyclo-[3.3.1.0^{2,8}]nona-3,6-dien-9-ol (1b)

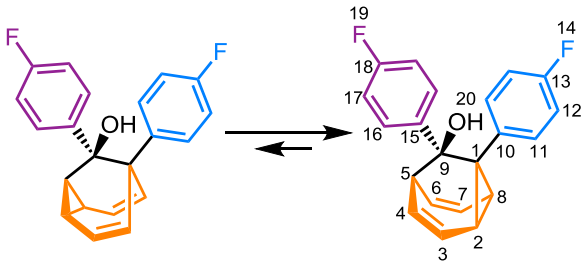

Magnesium turnings (118 mg, 4.9 mmol) and I_2 (62 mg, 0.2 mmol, 5 mol%) were placed in an oven-dried two-necked round-bottomed flask fitted with a condenser and a septum under a N_2 atmosphere. The flask was gently heated with a heat gun until the I_2 started to sublime. The flask was cooled down to rt. A quarter of a solution of 1-bromo-4-fluorobenzene (0.5 mL, 823 mg, 4.7 mmol) in anhydrous THF (10 mL) was added to the reaction mixture, which was heated until it reached reflux. Upon gentle reflux, the remaining solution of 1-bromo-4-fluorobenzene in anhydrous THF was added dropwise over 30 min. The reaction mixture was heated at reflux for 30 min before cooling to rt. 1-(4-Fluorophenyl)tricyclo[3.3.1.0^{2,8}]nona-3,6-dien-9-one (162 mg, 0.7 mmol) was transferred to an oven-dried round-bottomed flask, and the flask was purged with N_2. Anhydrous THF (10 mL) was added and the solution was cooled to 0 °C. The Grignard solution (prepared above) was added dropwise over 30 min to the barbaralone. The reaction mixture was stirred for 16 h, and the temperature was raised from 0 °C to rt, following removal of the ice bath. The reaction was quenched with a saturated aqueous solution of NH_4Cl (10 mL), then extracted with EtOAc (3 × 20 mL). The combined organic extracts were dried over $MgSO_4$, filtered and the solvent removed under reduced pressure. The crude residue was purified by column chromatography (Teledyne Isco CombiFlash Rf+ system, 24 g SiO_2, hexanes−CH_2Cl_2, gradient elution) to yield **1b** as an off-white powder (215 mg, 0.67

mmol, 93%). **M.P.** 116 – 118 °C. **^{1}H NMR (**700 MHz, $CDCl_3$) δ 7.28 (ddd, *J* = 8.6, 5.4, 2.7 Hz, 2H, H_{16}), 7.23 (ddd, *J* = 8.5, 5.4, 2.6 Hz, 2H, H_{11}), 6.90 – 6.84 (m, 4H, H_{12} and H_{17}), 6.07 (ddd, *J* = 8.7, 7.0, 0.8 Hz, 1H, H_3), 5.87 (dd, *J* = 8.6, 7.0 Hz, 1H, H_7), 5.46 (dddd, *J* = 8.2, 7.0, 1.3, 1.5 Hz, 1H, H_4), 5.43 (dddd, *J* = 8.5, 6.9, 1.5, 1.5 Hz, 1H, H_6), 3.63 (ddd, *J* = 6.7, 6.7, 1.5 Hz, 1H, H_8), 3.31 (ddd, *J* = 7.1, 7.1, 1.4 Hz, 1H, H_2), 2.84 (t, *J* = 6.8 Hz, 1H, H_5), 2.28 (s, 1H, H_{20}). **^{13}C NMR** (176 MHz, $CDCl_3$) δ 161.7 (d, J_{CF} = 245.5 Hz, C_{13}), 160.6 (d, J_{CF} = 245.0 Hz, C_{18}), 138.2 (d, J_{CF} = 3.1 Hz, C_{15}), 136.0 (d, J_{CF} = 3.2 Hz, C_{10}), 131.8 (d, J_{CF} = 7.9 Hz, C_{11}), 128.9 (d, J_{CF} = 7.8 Hz, C_{16}), 123.9 (C_3), 121.7 (C_7), 114.4 (d, J_{CF} = 21.1 Hz, C_{12}), 113.9 (d, J_{CF} = 20.9 Hz, C_{17}), 108.3 (C_6), 106.7 (C_4), 69.5 (C_9), 54.3 (C_8), 53.1 (C_2), 44.7 (C_1), 44.3 (C_5). **^{19}F NMR** (376 MHz, $CDCl_3$) δ –119.3 (tt, J_{FH} = 8.6, 5.5 Hz, F_{14} or F_{19}), –120.0 (tt, J_{FH} = 8.6, 5.5 Hz, F_{14} or F_{19}). **HR-ASAP-MS** *m/z* = 322.1176 $[M]^+$ (calculated for $C_{21}H_{16}OF_2^+$ = 322.1168).

(±)-9-(4-Fluorophenyl)-1-(4-anisyl)tricyclo[3.3.1.0^{2,8}]nona-3,6-dien-9-ol (1c)

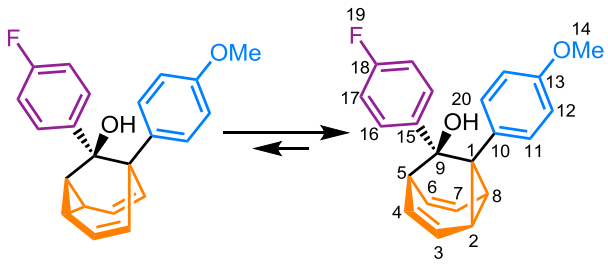

Magnesium turnings (57 mg, 2.4 mg) and I_2 (30 mg, 0.12 mmol, 5 mol%) were placed in an oven-dried two-necked round-bottomed flask fitted with a condenser and a septum under a N_2 atmosphere. The flask was gently heated with a heat gun until the I_2 started to sublime. The flask was cooled down to rt. A quarter of a solution of 1-bromo-4-fluorobenzene (410 mg, 2.4 mmol) in anhydrous THF (10 mL) was added to the reaction mixture, which was heated until it reached reflux. Upon gentle reflux, the remaining solution of 1-bromo-4-fluorobenzene in anhydrous THF was added dropwise over 30 min. The reaction mixture was heated at reflux for 30 min before cooling to rt. 1-(4-Anisyl)tricyclo[3.3.1.0^{2,8}]nona-3,6-dien-9-one (94 mg, 0.40 mmol) was transferred to an oven-dried round-bottomed flask, and the flask was purged with N_2. Anhydrous THF (10 mL) was added and the solution was cooled to 0 °C. The Grignard solution (prepared above) was added dropwise over 30 min to the barbaralone. The reaction mixture was stirred for 16 h, and the temperature was raised from 0 °C to rt,

following removal of the ice bath. The reaction was quenched with a saturated aqueous solution of NH_4Cl (10 mL), then extracted with EtOAc (3 × 20 mL). The combined organic extracts were dried over $MgSO_4$, filtered and the solvent removed under reduced pressure. The crude residue was purified by column chromatography (Teledyne Isco CombiFlash Rf+ system, 24 g SiO_2, hexanes−CH_2Cl_2, gradient elution including 0.5% Et_3N in the elution) to yield **1c** as a light yellow solid (73 mg, 0.23 mmol, 59%). **M.P.** 122 – 124 °C. **^{1}H NMR** (700 MHz, $CDCl_3$) δ 7.25 – 7.23 (m, 2H, H_{16}), 7.19 – 7.09 (m, 2H, H_{11}), 6.81 (d, *J* = 8.8 Hz, 2H, H_{17}), 6.70 (d, *J* = 8.8 Hz, 2H, H_{12}), 6.05 (ddd, *J* = 8.6, 6.9, 0.8 Hz, 1H, H_3), 5.83 (ddd, *J* = 8.8, 6.9, 0.6 Hz, 1H, H_7), 5.51 (ddd, *J* = 8.2, 6.7, 1.4 Hz, 1H, H_4), 5.45 (ddd, *J* = 8.4, 6.8, 1.4 Hz, 1H, H_6), 3.73 (s, 3H, H_{14}), 3.53 (dd, *J* = 6.7, 1.5 Hz, 1H, H_8), 3.19 (dd, *J* = 6.7, 1.4 Hz, 1H, H_2), 2.79 (ddd, *J* = 6.7, 1.4 Hz, 1H, H_5), 2.19 (s, 1H, H_{20}). **^{13}C NMR** (176 MHz, $CDCl_3$) δ 161.6 (d, J_{CF} = 244.6 Hz, C_{18}), 158.4 (C_{13}), 138.5 (d, J_{CF} = 3.2 Hz, C_{15}), 132.2 (C_{10}), 131.4 (C_{11}), 129.1 (d, J_{CF} = 7.8 Hz, C_{16}), 124.1 (C_3), 121.9 (C_7), 113.9 (d, J_{CF} = 21.0 Hz, C_{17}), 113.2 (C_{12}), 110.4 (C_6), 109.0 (C_4), 69.7 (C_9), 55.3 (C_{14}), 52.4 (C_8), 51.1 (C_2), 44.9 (C_5), 44.5 (C_1). **^{19}F NMR** (376 MHz, $CDCl_3$) δ –120.2 – 120.4 (m, F_{19}). **HR-ASAP-MS** *m/z* = 317.1330 $[M\text{-}OH]^+$ (calculated for $C_{22}H_{18}OF^+$ = 317.1336).

(±)-9-(4-Anisyl)-1-(4-fluoro-phenyltricyclo[3.3.1.0^{2,8}]nona-3,6-dien-9-ol (1d)

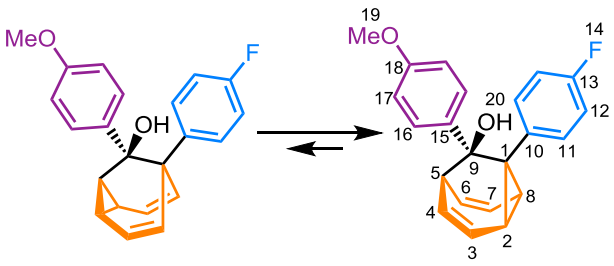

Magnesium turnings (120 mg, 5.30 mg) and I_2 (67 mg, 0.3 mmol, 5 mol%) were placed in an oven-dried two-necked round-bottomed flask fitted with a condenser and a septum under a N_2 atmosphere. The flask was gently heated with a heat gun until the I_2 started to sublime. The flask was cooled down to rt. A quarter of a solution of 4-bromoanisole (980 mg, 5.3 mmol) in anhydrous THF (10 mL) was added to the reaction mixture, which was heated until it reached reflux. Upon gentle reflux, the remaining solution of 4-bromoanisole in anhydrous THF was added dropwise over 30 min. The reaction mixture was heated at reflux for 30 min before cooling to rt. 1-(4-Fluorophenyl)tricyclo[3.3.1.0^{2,8}]nona-3,6-

dien-9-one (200 mg, 0.9 mmol) was transferred to an oven-dried round-bottomed flask, and the flask was purged with N_2. Anhydrous THF (10 mL) was added and the solution was cooled to 0 °C. The Grignard solution (prepared above) was added dropwise over 30 min to the barbaralone. The reaction mixture was stirred for 16 h, and the temperature was raised from 0 °C to rt, following removal of the ice bath. The reaction was quenched with a saturated aqueous solution of NH_4Cl (10 mL), then extracted with EtOAc (3 × 20 mL). The combined organic extracts were dried over $MgSO_4$, filtered and the solvent removed under reduced pressure. The crude residue was purified by column chromatography (Teledyne Isco CombiFlash Rf+ system, 24 g SiO_2, hexanes−CH_2Cl_2, gradient elution including 0.5% Et_3N in the elution) to yield **1d** as a colourless sticky residue (284 mg, 0.85 mmol, 96%). **^{1}H NMR** (700 MHz, $CDCl_3$) δ 7.24 – 7.18 (m, 2H, H_{11}), 7.19 – 7.10 (m, 2H, H_{16}), 6.91 – 6.78 (m, 2H, H_{12}), 6.75 – 6.57 (m, 2H, H_{17}), 6.04 (ddd, *J* = 8.7, 6.9, 0.8 Hz, 1H, H_3), 5.83 (ddd, *J* = 8.6, 6.9, 0.6 Hz, 1H, H_7), 5.54 – 5.46 (m, 1H, H_4), 5.43 (ddd, *J* = 8.4, 6.9, 1.5 Hz, 1H, H_6), 3.73 (s, 3H, H_{19}), 3.63 – 3.46 (m, 1H, H_8), 3.36 – 3.10 (m, 1H, H_2), 2.81 (tt, *J* = 6.8, 0.7 Hz, 1H, H_5), 2.15 (s, 1H, H_{20}). **^{13}C NMR** (176 MHz, $CDCl_3$) δ 161.7 (d, J_{CF} = 245.3 Hz, C_{13}), 158.2 (C_{18}), 136.4 (d, J_{CF} = 3.1 Hz, C_{10}), 134.6 (C_{15}), 131.9 (d, J_{CF} = 7.9 Hz, C_{11}), 128.4 (C_{16}), 123.9 (C_3), 121.6 (C_7), 114.4 (d, J_{CF} = 21.1 Hz, C_{12}), 112.6 (C_{17}), 109.7 (C_6), 108.2 (C_4), 69.6 (C_9), 55.2 (C_{19}), 53.2 (C_8), 51.9 (C_2), 44.8 (C_5), 44.5 (C_1). **^{19}F NMR** (376 MHz, $CDCl_3$) δ –119.5 – 119.7 (m, F_{14}). **HR-ASAP-MS** *m/z* = 317.1346 $[M\text{-}OH]^+$ (calculated for $C_{22}H_{18}FO^+$ = 317.1336).

(±)-9-(4-Fluorophenyl)-1-phenyl-tricyclo[3.3.1.0^{2,8}]nona-3,6-dien-9-ol (1e)

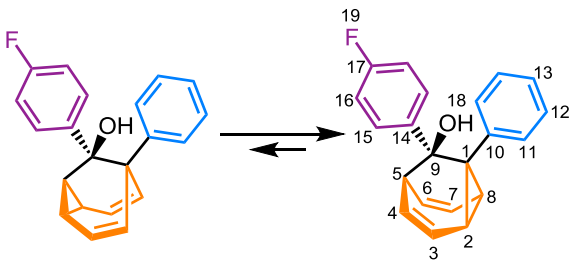

Magnesium turnings (203 mg, 8.4 mmol) and I_2 (9 mg, 0.07 mmol, 5 mol%) were placed in an oven-dried two-necked round-bottomed flask fitted with a condenser and a septum under a N_2 atmosphere. The flask was gently heated with a heat gun until the I_2 started to sublime. The flask was cooled down to rt. A quarter of a solution of 1-bromo-4-fluorobenzene (1.5 g, 8.4 mmol) in

anhydrous THF (10 mL) was added to the reaction mixture, which was heated until it reached reflux. Upon gentle reflux, the remaining solution of 1-bromo-4-fluorobenzene in anhydrous THF was added dropwise over 30 min. The reaction mixture was heated at reflux for 30 min before cooling to rt. 1-Phenyltricyclo-[3.3.1.0.^{2,8}]nona-3,6-dien-9-one (293 mg, 1.4 mmol) was transferred to an oven-dried round-bottomed flask, and the flask was purged with N_2. Anhydrous THF (5 mL) was added and the solution was cooled to 0 °C. The Grignard solution (prepared above) was added dropwise over 30 min to the barbaralone. The reaction mixture was stirred for 16 h, and the temperature was raised from 0 °C to rt, following removal of the ice bath. The reaction was quenched with a saturated aqueous solution of NH_4Cl (10 mL), then extracted with EtOAc (3 × 20 mL). The combined organic extracts were dried over $MgSO_4$, filtered and the solvent removed under reduced pressure. The crude residue was purified by column chromatography (Teledyne Isco CombiFlash Rf+ system, 24 g SiO_2, hexanes−CH_2Cl_2, gradient elution including 0.5% Et_3N in the elution) to yield **1e** as a white solid (315 mg, 1.04 mmol, 74%). **M.P.** 122 – 123 °C. **^{1}H NMR** (600 MHz, $CDCl_3$) δ 7.27 – 7.22 (m, 4H, H_{11} and H_{15}), 7.19 – 7.12 (m, 3H, H_{12} and H_{13}), 6.84 – 6.77 (m, 2H, H_{16}), 6.09 – 6.03 (m, 1H, H_3), 5.88 – 5.82 (m, 1H, H_7), 5.55 – 5.49 (m, 1H, H_4), 5.48 – 5.42 (m, 1H, H_6), 3.59 (dd, *J* = 6.8 Hz, 1H, H_8), 3.25 (dd, *J* = 6.8 Hz, 1H, H_2), 2.81 (dd, *J* = 6.8 Hz, 1H, H_5), 2.23 (s, 1H, H_{18}). **^{13}C NMR** (151 MHz, $CDCl_3$) δ 161.7 (d, J = 244.8 Hz, C_{17}), 140.3 (C_{10}), 138.4 (d, J = 3.2 Hz, C_{14}), 130.3 (C_{11}), 129.0 (d, J = 7.8 Hz, C_{15}), 127.7 (C_{12}), 126.8 (C_{13}), 124.0 (C_3), 121.8 (C_7), 113.9 (d, J = 20.9 Hz, C_{16}), 110.3 (C_6), 108.9 (C_4), 69.8 (C_9), 52.5 (C_8), 51.3 (C_2), 44.9 (C_1), 44.9 (C_5). **^{19}F NMR** (376 MHz, $CDCl_3$) δ -120.23 (tt, J_{FH} = 8.7, 5.5 Hz, F_{19}). **HR-ESI-MS** *m/z* = 287.1246 $[M–OH]^+$ (calculated for $C_{21}H_{16}F^+$ = 287.1231).

2.5 Appendix of Supplementary Data and Discussion

2.5.1 Structural Assignment by 2D NMR

In order to determine which structure, **1** or **1′**, is the major species present in solution, we used 2D NMR spectroscopy. Briefly, we are able to differentiate the signals arising from the two barbaralane positions next to the tertiary alcohol based on the fact that one is a quaternary centre (position 1/5′), which gives rise to a lower

intensity ^{13}C signal on account of its long relaxation time, and the other is a tertiary centre (position 5/1′). Position 5/1′ is easily distinguishable from the other tertiary alkyl ^{13}C signals as the protons at positions 2/4′ and 8/6′ (linked to the ^{13}C by HSQC) show a COSY correlation (e.g., Figure 2.9, blue dashed line). From here, we are then able to assign the structure as either **1** instead of **1′** because we observe that 5/1′ bridges the *cis*-dialkylolefins as it correlates *via* COSY (e.g., Figure 2.9, purple dashed line) to the olefins at positions 4 and 6 (in structure **1**) but not the cyclopropyl ring at positions 2′ and 8′ (in structure **1′**).

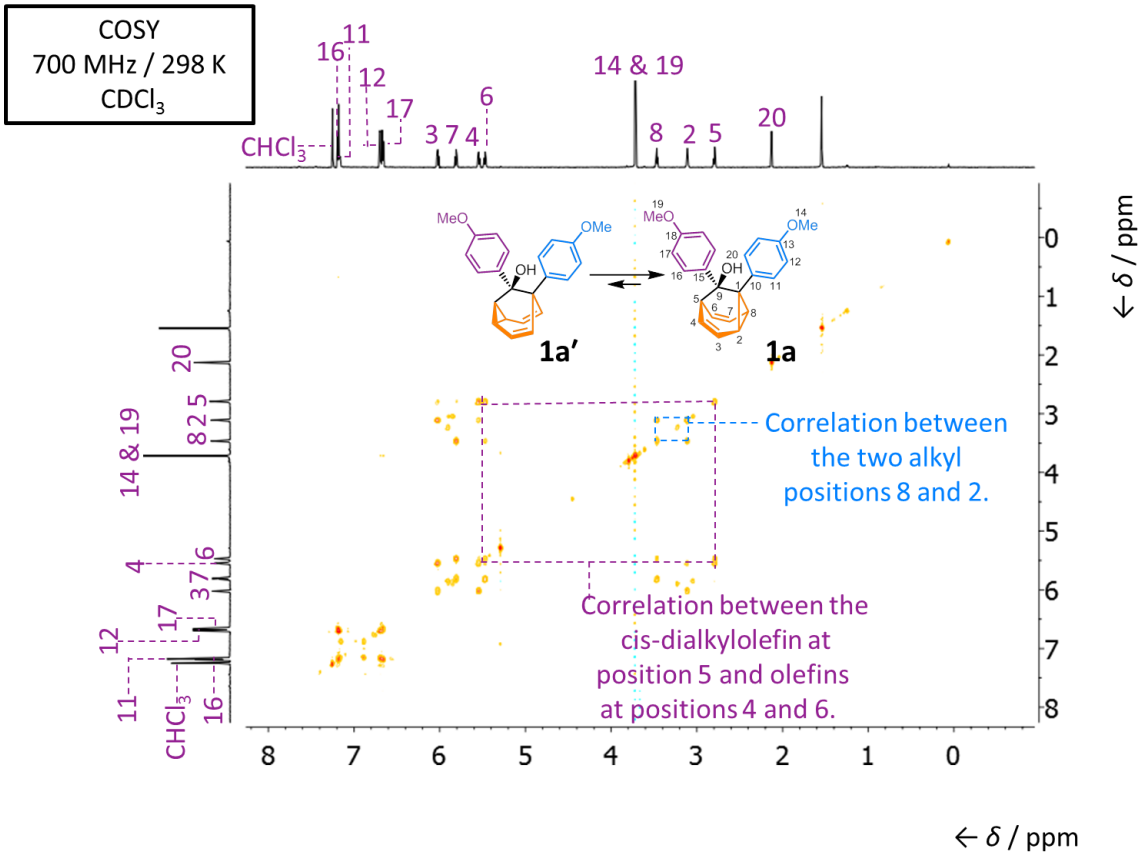

Figure 2.9. COSY spectrum of **1a**/**1a′**.

2.5.2 Estimation of Equilibrium Constants based on Chemical Shifts

In solution, **1** and **1′** are present in unequal proportions (p_1 and $p_{1'}$). In the fast exchange regime, p_1 and $p_{1'}$ can be estimated by treating the experimentally observed chemical shift (δ_{obs}) as a weighted average of the chemical shifts of the individual components, δ_1 and $\delta_{1'}$:

$$\delta_{obs} = p_1\delta_1 + p_{1'}\delta_{1'}$$

Equation 2.1. Equation to determine δ_{obs}.

We estimated equilibrium constants for **1**/**1′** in solution by comparing the δ_{obs} values measured from ^{13}C NMR spectra to those typical for the functional groups present in the molecule, allowing us to approximate δ_1 and $\delta_{1'}$. A divinyl cyclopropane group has a ^{13}C chemical shift of ~25 ppm (see reference 10), while a *cis*-dialkylolefin group has a ^{13}C chemical shift of ~135 ppm (see reference 11) in $CDCl_3$ at 298 K. The equilibrium constant K relates to p_1 and $p_{1'}$, as well as the free energy difference ΔG.

$$K = \frac{p_1}{p_{1'}} = e^{-\frac{\Delta G}{RT}}$$

Equation 2.2. A variation of the equilibrium constant.

2.5.3 Calculation of Solution-Phase Equilibria

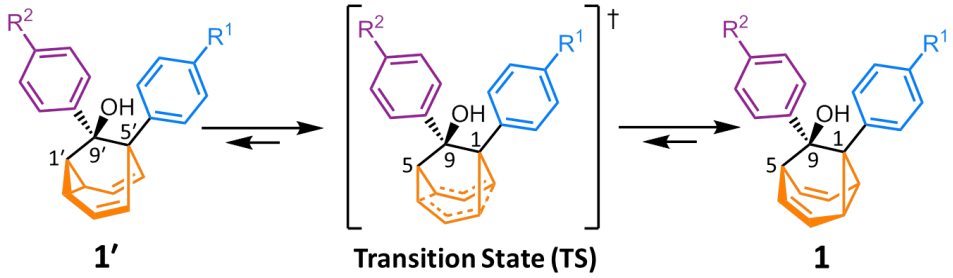

Scheme 2.3. The ground- and transition-state species modelled by DFT calculations.

1 and **1′** interconvert *via* a [3,3]-sigmatropic Cope rearrangement. If one only one substituent is present on the barbaralane (*i.e.*, on position 9), the isomers are energetically indistinguishable, *i.e.*, degenerate. However, in the case of two substituents, the isomers are nondegenerate and the equilibrium is shifted towards one isomer. To determine the more stable isomer, *in silico* methods were used to gain better insight into the processes. Both isomers were optimised in Gaussian 16, rev A.03[28] to minima (confirmed by frequency calculations on the same level of theory having no imaginary frequency) by DFT functionals (B3LYP,[29] CAM-B3LYP,[30] M06-2X[31]) using Def2-TZVP basis set and GD3 empirical dispersion[32] to take into

account weak long-range interactions. C-PCM solvent model[33] was used to describe CS_2 as a solvent (as this solvent was used in NMR studies). For comparison, the calculations were also performed without GD3 dispersion using DFT functionals (B3LYP, ωB97X-D[34]), Def2-TZVP basis set and C-PCM model for CS_2. In all cases, isomer **1** was deemed to be more stable. In addition, the transition state was also found, and the barrier connecting these two minima was estimated. The transition state was confirmed by frequency calculations to have one imaginary frequency, which corresponds to the displacement of atoms forming either **1** or **1′**. All Gibbs free energies were calculated at 298 K, including ZPE corrections, and gas phase thermochemistry was not scaled. The ultrafine grid option was used in all calculations. The results are summarised in Table 2.1 (Results and Discussion). Calculated energies are very similar to each other; except for the B3LYP DFT functional, which is known to underestimate reaction barriers more than the other DFT functionals.[35] The energy difference between **1** and **1′** is quite small and sometimes **1′** is even energetically favoured, although Gibbs free energy favours **1**. This suggests that the enthalpy and entropy factors are dominant in the equilibrium formation.

Based on the results in Table 2.1 (Results and Discussion), the ^{13}C NMR chemical shifts were calculated using GIAO method implemented in Gaussian 16 for both structures to assist with the assignment of the measured data using B3LYP DFT functional, De2-TZVP basis set, GD3 empirical dispersion model, C-PCM solvent model for CS_2 and geometry from the previous optimisation at the same level of theory. The chemical shifts are referenced to tetramethylsilane optimised at the same level of theory. The ^{13}C NMR chemical shifts are summarised in Table 2.3 and 2.4, comparing against the experimental shifts observed at ambient temperatures for $CDCl_3$ solutions. There is much better agreement between the experimental values and the shifts calculated for the **1** isomer than those calculated for the **1′** isomer. This corroborates our assignment of **1** as the major isomer in solution.

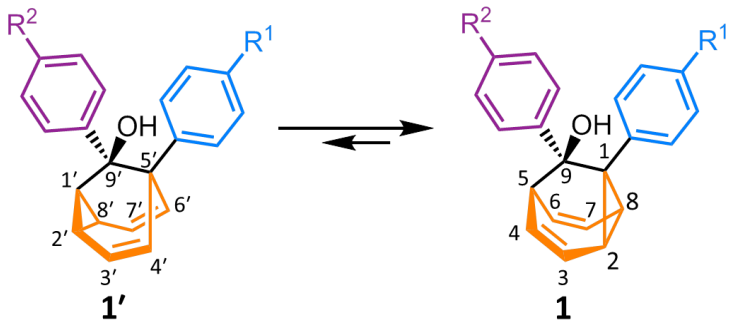

Scheme 2.4. Equilibrium between **1** and **1′** in the solution state at room temperature. Atomic positions labelled for Tables 2.3 and 2.4.

Table 2.3. ^{13}C chemical shifts (ppm) observed at ambient temperature and calculated by DFT for **1**.

Atom	Observed ^{13}C NMR Chemical Shift (δ)		Calculated ^{13}C NMR Chemical Shift (δ) for 1	
	1a/1a′	1b/1b′	1a	1b
1	44.1	44.7	51.3	51.5
2	49.6	53.1	42.3	44.3
3	123.9	123.9	133.4	131.4
4	110.6	106.7	132.5	134.0
5	45.2	44.3	56.6	56.2
6	111.9	108.3	133.9	132.6
7	121.8	121.7	131.4	133.5
8	51.0	54.3	44.4	42.1
9	69.7	69.5	77.0	77.2

Table 2.4. ^{13}C chemical shifts (ppm) observed at ambient temperature and calculated by DFT for **1′**.

Atom	Observed ^{13}C NMR Chemical Shift (δ)		Calculated ^{13}C NMR Chemical Shift (δ) for 1	
	1a/1a′	1b/1b′	1a′	1b′
1	44.1	44.7	63.0	63.1
2	49.6	53.1	137.4	136.9
3	123.9	123.9	130.5	129.0
4	110.6	106.7	33.9	39.0
5	45.2	44.3	36.7	36.8
6	111.9	108.3	38.9	34.2
7	121.8	121.7	128.5	130.8
8	51.0	54.3	137.8	136.8
9	69.7	69.5	78.5	78.6

2.5.4 Variable-Temperature NMR Spectroscopy

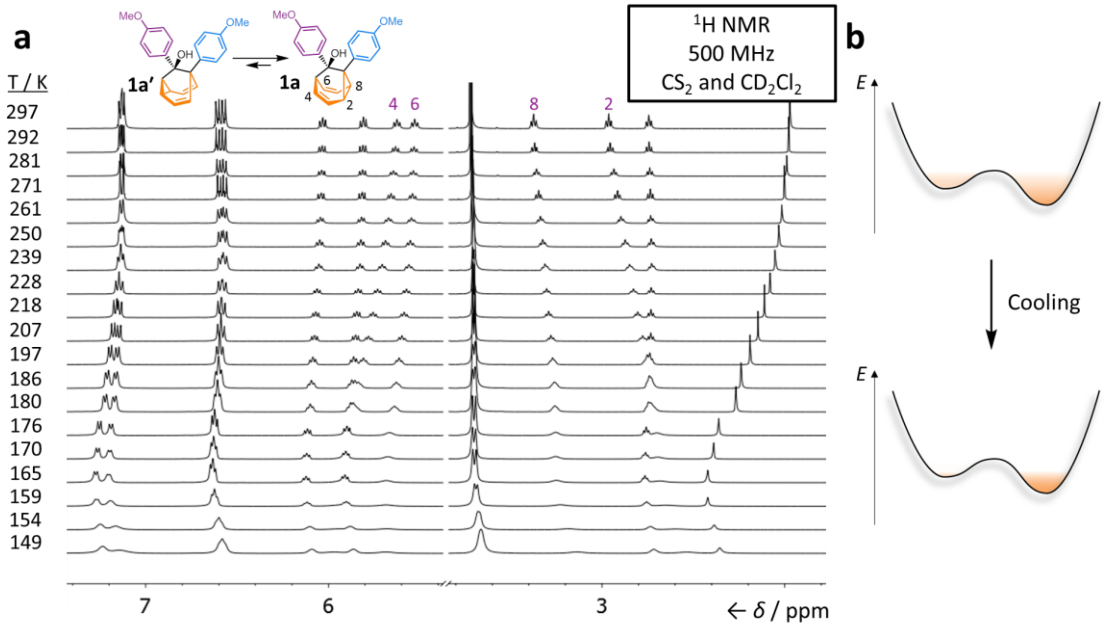

Figure 2.10. (a) Partial ^{1}H NMR spectra of **1a**/**1a′**, recorded from 297 K to 149 K and (b) schematic illustration of the change in equilibrium population on a simplified potential energy surface as temperature decreases.

The barbaralanes undergo a rapid and reversible Cope rearrangement in solution. Isomer **1a** is in fast exchange with isomer **1a′**, giving rise to a single set of resonances in the ^{1}H NMR spectrum recorded (Figure 2.10) at ambient temperature. The chemical shift of each nucleus is indicative of its time-averaged chemical environment. For example, the proton labelled as position 2 in Figure 2.10 has character arising from being part of both a divinyl cyclopropane (**1a**) and a *cis*-dialkyl olefin (**1a′**) environment. Its chemical shift of 2.9 ppm falls between the limits of ~1.8 ppm (typical[9] for a divinyl cyclopropane) and ~5.4 ppm (typical[10] for a *cis*-dialkylolefin) that would be expected if the structure was fixed in either state. It is, however, closer to the limit expected for a divinyl cyclopropane; therefore, **1a** appears to be the major isomer in solution. Similarly, position 8 has mostly cyclopropane character, while position 4 and 6 have a majority of olefin character, confirming this conclusion. Upon reducing the temperature, the signals relating to these nuclei undergo marked changes in their chemical shifts. The signals arising from protons 2 and 8 shift to a lower frequency, becoming more cyclopropane-like, while the resonances of protons 4 and 6 shift downfied, becoming more olefin-like.

These changes arise (Figure 2.10b) from perturbation of the equilibrium position upon cooling. At lower temperatures, there is less of the minor isomer present, so the NMR resonances shift towards the limits expected if the major isomer was the sole species. The signals appear to remain in fast exchange, even at very low temperatures. Below 154 K, the signals begin to broaden into the baseline, suggesting that the coalescence temperature may be in that region.

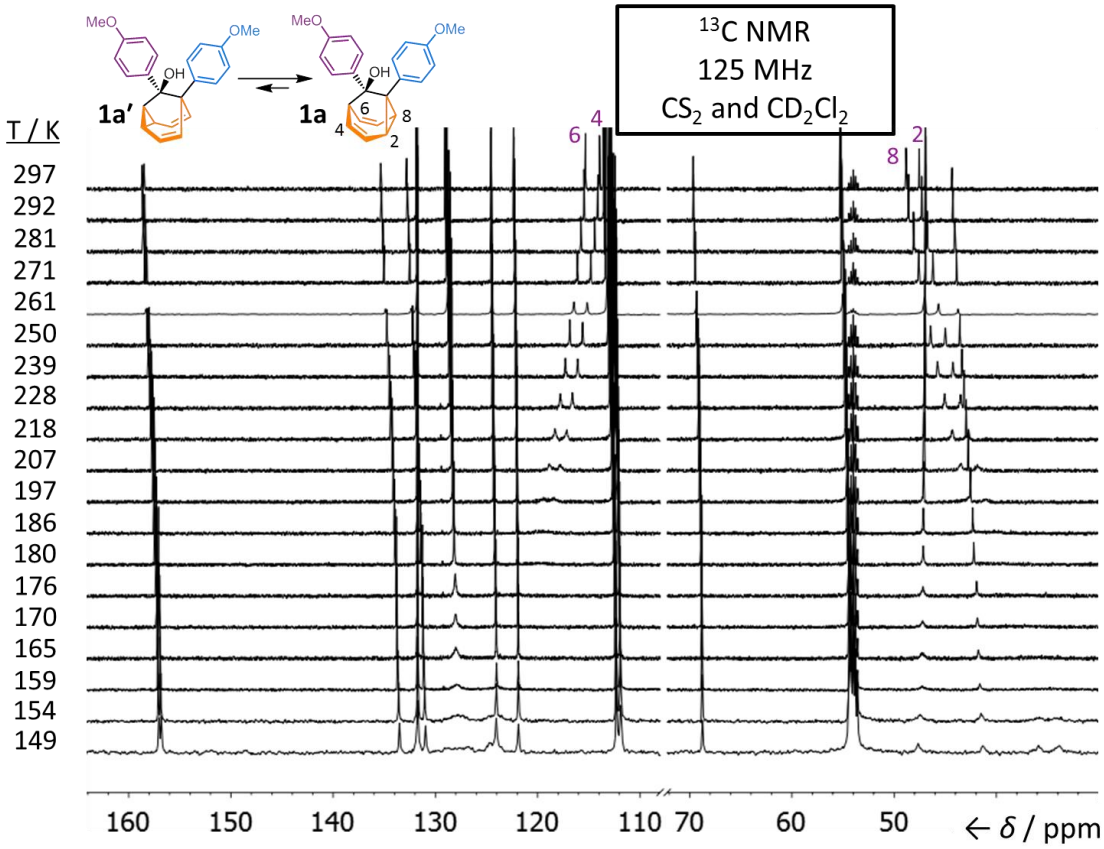

Figure 2.11. ^{13}C NMR spectra of **1a/1a′**, recorded from 297 K to 149 K.

The VT ^{13}C NMR spectra for **1a/1a′** also helps to confirm that the chemical shifts are a weighted average of both the isomers and that the equilibrium shifts in favour of the major isomer as the temperature is decreased. This is demonstrated in the ^{13}C NMR spectra (Figure 2.11) because the positions marked as 6 and 4 shift downfield, becoming more olefin-like, whereas the positions marked as 8 and 2 shift further towards a lower frequency, becoming more cyclopropane-like.

Compound **1b**/**1b′** is also a fluxional mixture (where the major isomer in solution is **1b**), which interconverts between two nondegenerate isomers. As with compound, **1a**/**1a′**, the ^{1}H NMR spectrum at ambient temperature only demonstrates a single set of resonances where the chemical shifts represent an average of both the chemical environments within the different valence isomers. As the temperature is reduced for **1b**/**1b′**, the resonances of the protons 4 and 6 shift to a higher frequency, whereas the resonances of the protons 8 and 2 shift towards a lower frequency. The changes observed in the nuclei are identical to that of **1a**/**1a′**. This data from this compound corroborates that **1b** is the major isomer at lower temperatures and that although the resonances shift the equilibrium towards the major isomer; the signals are still interconverting even at very low temperatures. The rearrangement only becomes slow relative to the chemical shift differences of exchanging sites at the lowest accessible[36] temperatures – the lineshapes of peaks such as 6/8′ and 8/6′ broaden (Figure 2.11) below 186 K and merge with the baseline at 149 K. This observation is consistent with a low energy barrier, ΔG, similar to those reported previously[37] for barbaralane Cope rearrangements, *i.e.*, 30–40 kJ·mol^{-1}.[38]

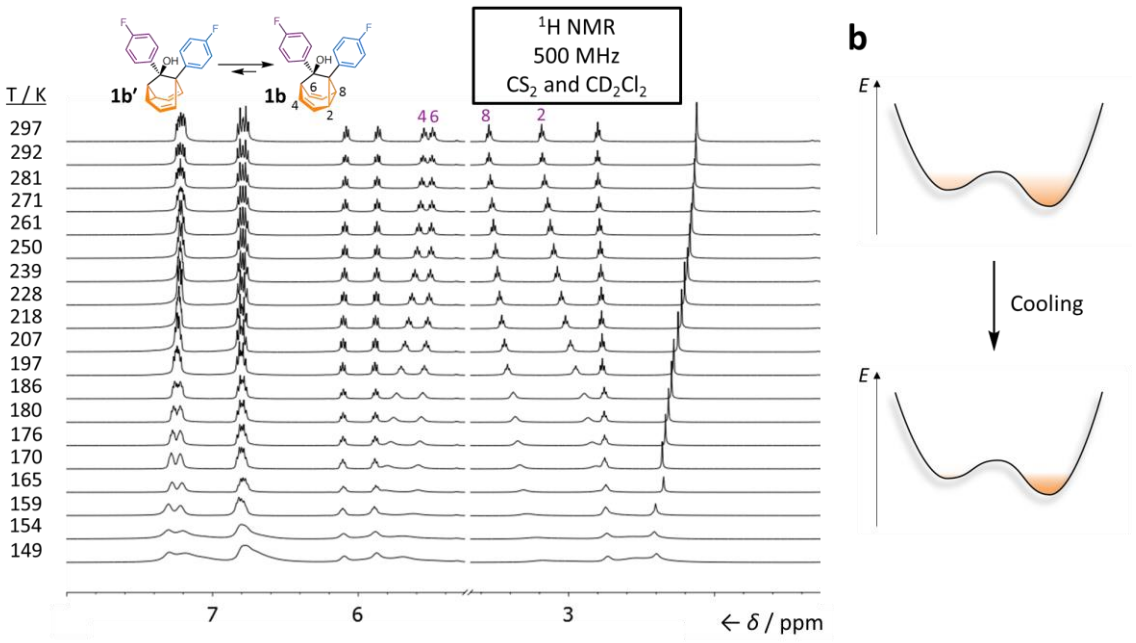

Figure 2.12. (a) Partial ^{1}H NMR spectra of **1b**/**1b′**, recorded from 297 K to 149 K and (b) schematic illustration of the change in equilibrium population on a simplified potential energy surface as temperature decreases.

The VT ^{13}C NMR spectra of **1b**/**1b′** (Figure 2.12) are near-identical to the VT ^{13}C NMR spectra of **1a**/**1a′**. As in Figure 2.12, the positions marked as 6 and 4 shift downfield, becoming more olefin-like, whereas the positions marked as 8 and 2 shift further towards a lower frequency, becoming more cyclopropane-like. The data from the VT ^{13}C NMR for **1b**/**1b′** validates that the equilibrium shifts in favour of the major isomer as the temperature is lowered.

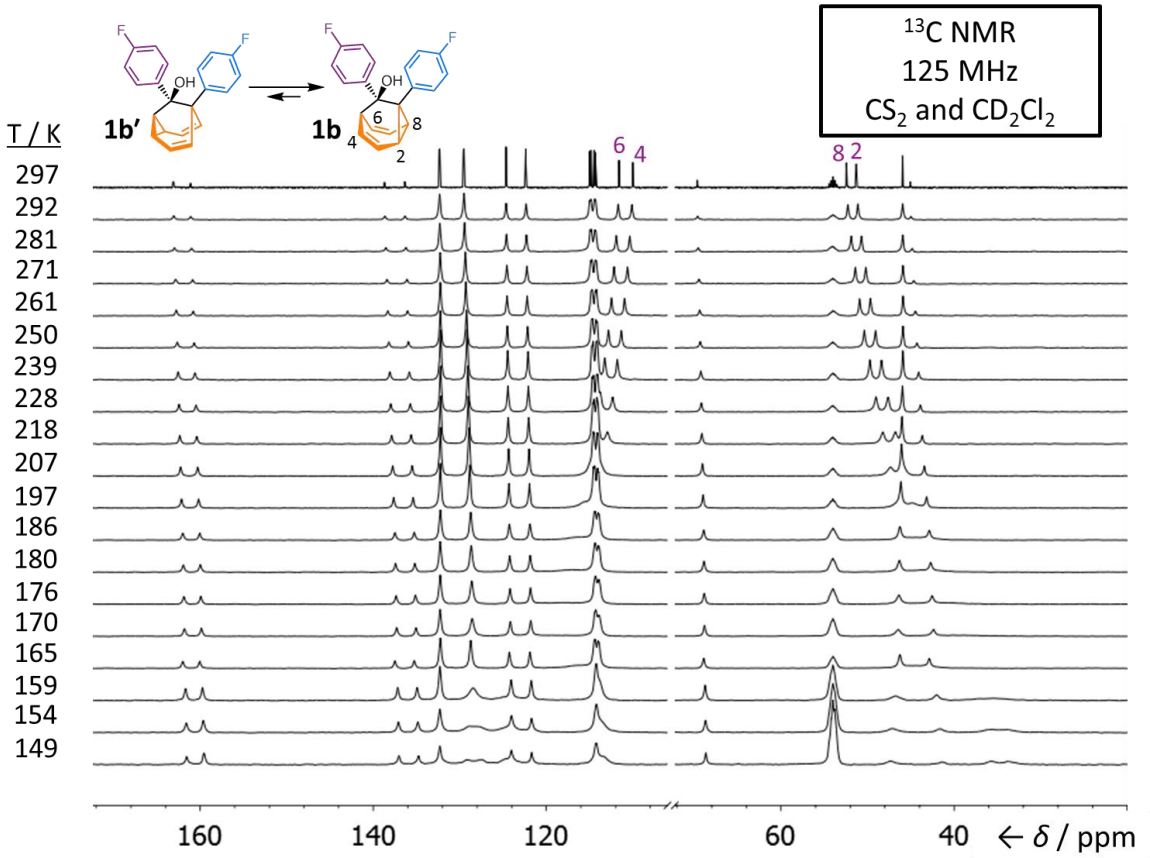

Figure 2.13. Partial ^{13}C NMR spectra of **1b**/**1b′**, recorded from 297 K to 149 K.

2.5.5 X-ray Crystallographic Analysis

(±)-1-(4-Fluorophenyl)tricyclo[3.3.1.0^{2,8}]nona-3,6-dien-9-one

Crystals of 1-(4-fluorophenyl)tricyclo[3.3.1.^{2,8}]nona-3,6-dien-9-one suitable for X-ray diffraction were grown by slow evaporation of a hexanes–CH_2Cl_2 solution at 5 °C.

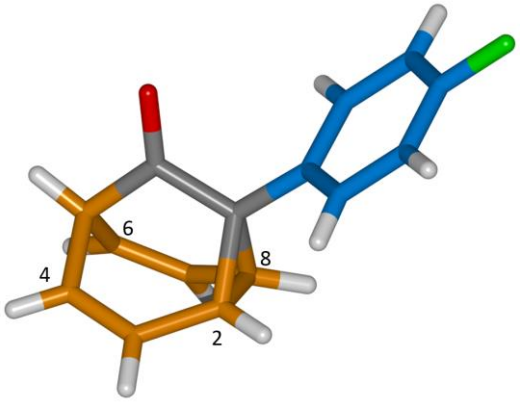

Figure 2.14. Solid-state structure of 1-(4-fluorophenyl)tricyclo[3.3.1.^{2,8}]nona-3,6-dien-9-one.

Crystal System: Orthohombic

Space group: $P2_12_12_1$

Unit Cell Parameters: a = 9.9209(4) Å, b = 9.9803(4) Å, c = 11.1024(4) Å, α = 90 °, β = 90 °, γ = 90 °, V = 1099.29(7) Å^3, Z = 4

Interatomic Distances / Å: C2–C8 = 1.54, C4···C6 = 2.41.

Calculated density: 1.36691 g·cm^{-3}

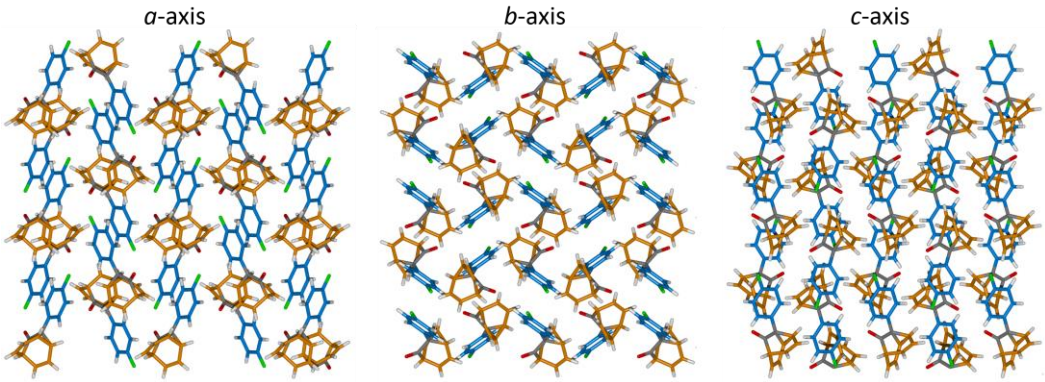

Figure 2.15. Solid-state superstructure of 1-(4-fluorophenyl)tricyclo[3.3.1.^{2,8}]nona-3,6-dien-9-one viewed along the three unit cell axes.

(±)-1,9-Bis(4-anisyl)tricyclo-[3.3.1.0^{2,8}]nona-3,6-dien-9-ol (1a)

Crystals of **1a** suitable for X-ray diffraction were formed through spontaneous crystallisation of a saturated CH_2Cl_2 solution upon standing. See Figure 2.4 in the Results and Discussion.

Crystal System: Monoclinic

Space group: $P2_1/c$

Unit Cell Parameters: a = 13.5882(7) Å, b = 9.2068(5) Å, c = 14.8687(8) Å, α = 90 °, β = 111.2938(18) °, γ = 90 °, V = 1733.14(16) Å^3, Z = 4

Calculated density: 1.32748 g·cm^{-3}

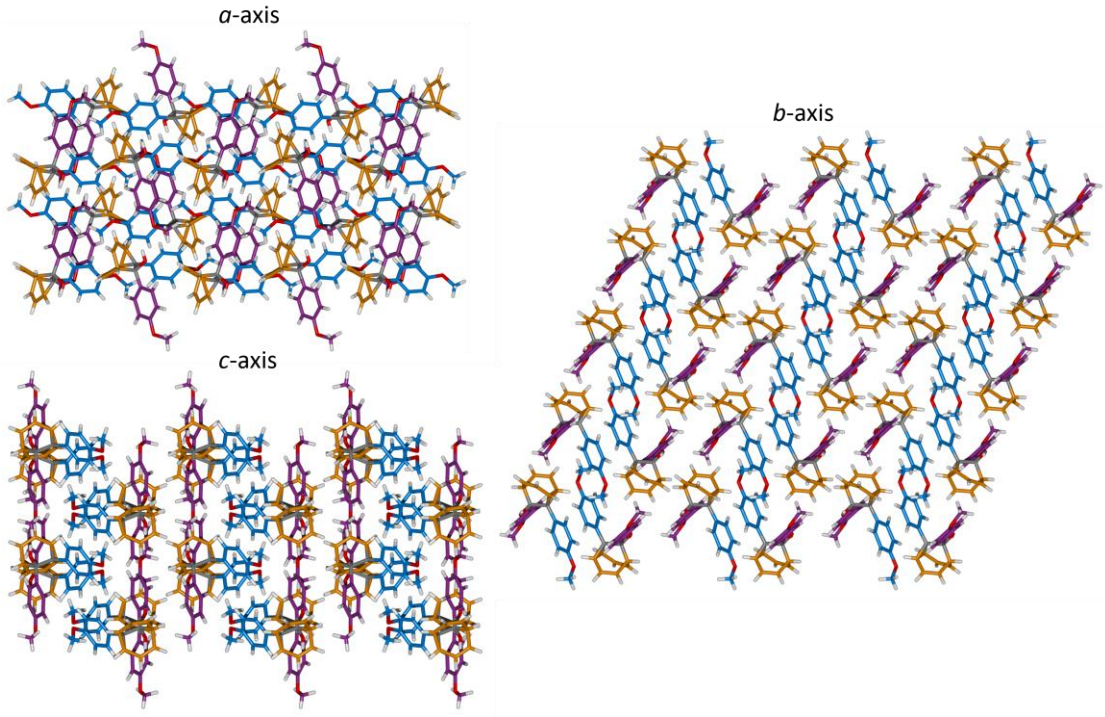

Figure 2.16. Solid-state superstructure of **1a** viewed along the three unit cell axes.

(±)-1,9-Bis(4-fluorophenyl)tricyclo-[3.3.1.0^{2,8}]nona-3,6-dien-9-ol (1b′)

Crystals of **1b′** suitable for X-ray diffraction were grown by slow cooling of a hot and saturated MeCN solution. See Figure 2.4 in the Results and Discussion.

Crystal System: Monoclinic

Space group: $P2_1/n$

Unit Cell Parameters: a = 9.7695(8) Å, b = 6.1770(5) Å, c = 24.650(2) Å, α = 90 °, β = 90.360(7) °, γ = 90 °, V = 1487.5(2) Å^3, Z = 4

Calculated density: 1.43926 g·cm^{-3}

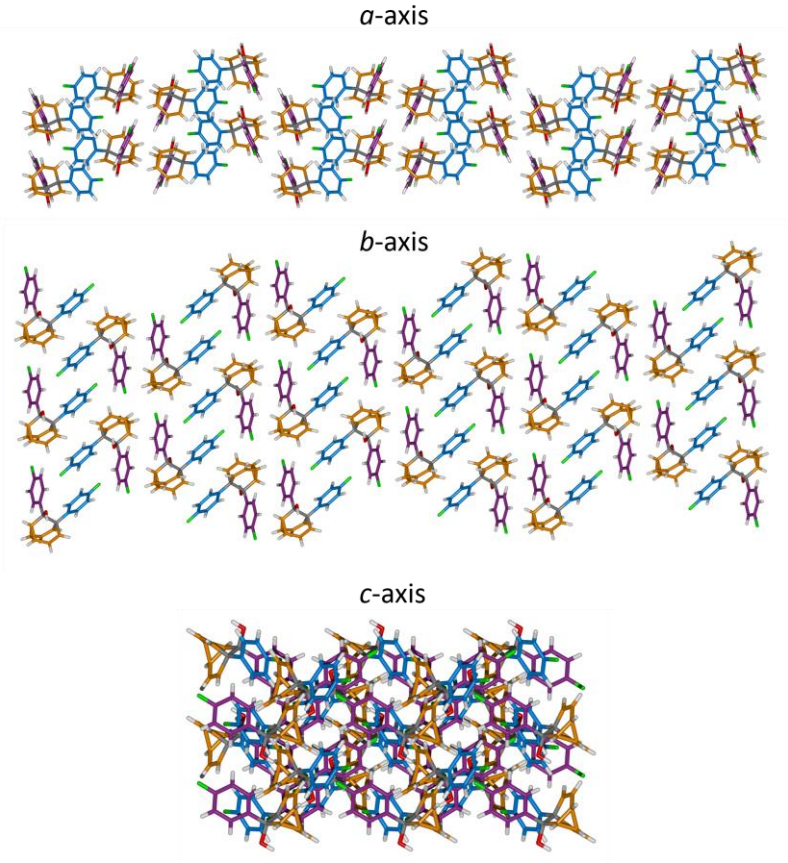

Figure 2.17. Solid-state superstructure of **1b′** viewed along the three unit cell axes.

(±)-1,9-(4-Fluorophenyl)-1-(4-anisyl)tricyclo[3.3.1.0^{2,8}]nona-3,6-dien-9-ol (1c)

Crystals of **1c** suitable for X-ray diffraction were grown by slow cooling of a hot and saturated MeCN solution. See Figure 2.4 in the Results and Discussion.

Crystal System: Monoclinic

Space group: $P2_1/c$

Unit Cell Parameters: a = 16.0612(11) Å, b = 7.1500(5) Å, c = 14.5266(10) Å, α = 90 °, β = 98.455(3)°, γ = 90 °, V = 1650.1(2) Å^3, Z = 4

Calculated density: 1.34589 g·cm^{-3}

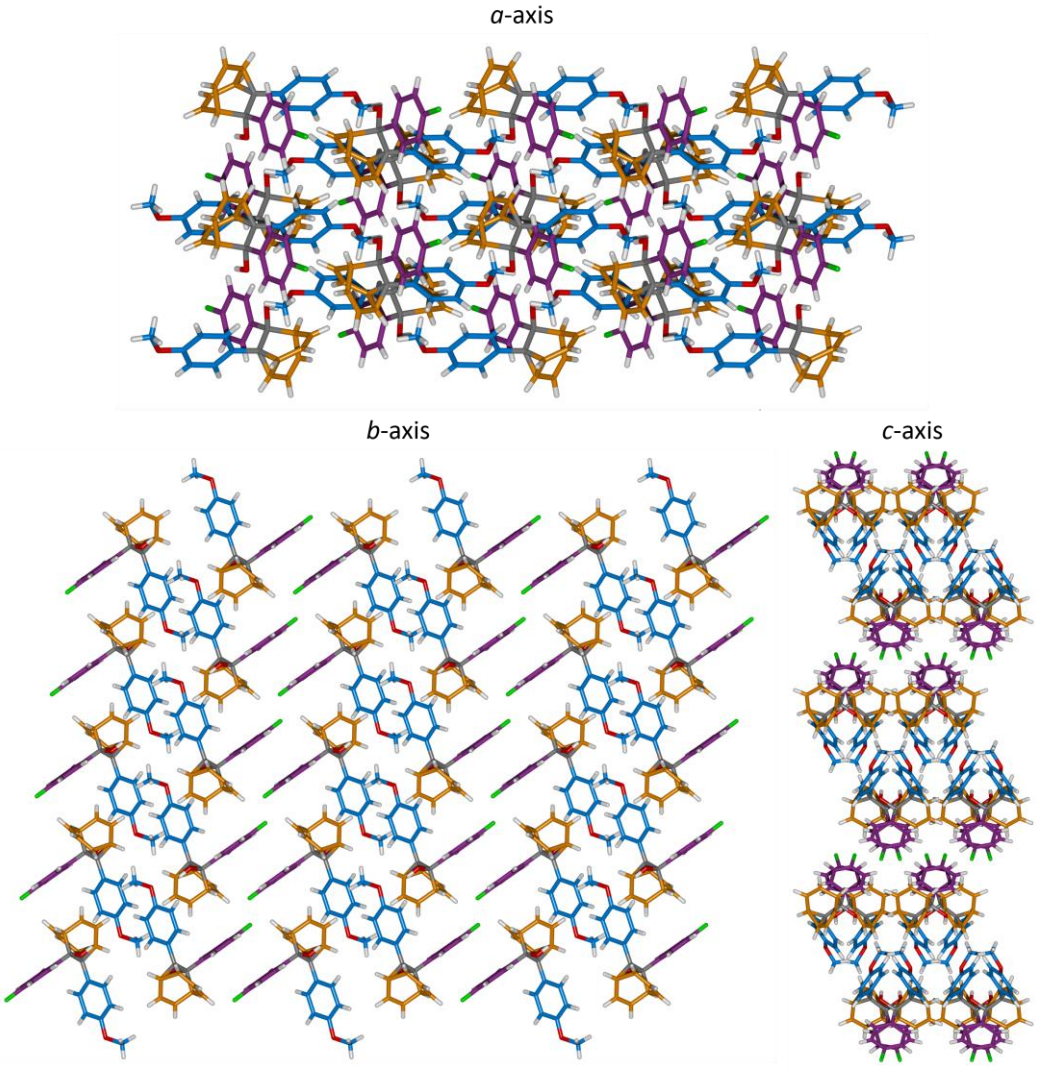

Figure 2.18. Solid-state superstructure of **1c** viewed along the three unit cell axes.

(±)-1,9-(4-Anisyl)-1-(4-fluoro-phenyltricyclo[3.3.1.0^{2,8}]nona-3,6-dien-9-ol (1d)

Crystals of **1d** suitable for X-ray diffraction were grown by diffusion of H_2O vapour into a saturated MeOH solution. See Figure 2.4 in the Results and Discussion.

Crystal System: Monoclinic

Space group: $P2_1/c$

Unit Cell Parameters: a = 18.8480(7) Å, b = 7.4991(3) Å, c = 12.2152(5) Å, α = 90 °, β = 107.6909(15)°, γ = 90 °, V = 1644.88(11) Å^3, Z = 4

Calculated density: 1.35013 g·cm^{-3}

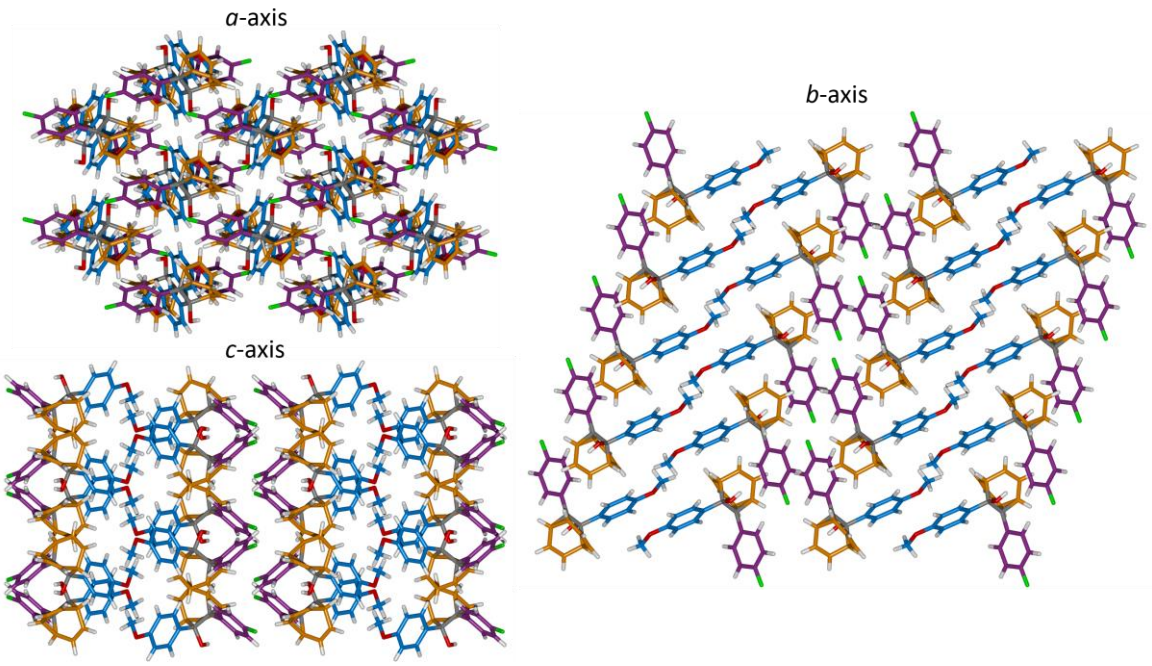

Figure 2.19. Solid-state superstructure of **1d** viewed along the three unit cell axes.

(±)-1,9-(4-Fluorophenyl)-1-phenyl-tricyclo[3.3.1.0^{2,8}]nona-3,6-dien-9-ol (1e′)

Crystals of **1e′** suitable for X-ray diffraction were grown by diffusion of H_2O vapour into a saturated MeOH solution. See Figure 2.4 in the Results and Discussion.

Crystal System: Monoclinic

Space group: $P2_1/n$

Unit Cell Parameters: a = 9.7901(6) Å, b = 6.2016(4) Å, c = 24.0401(14) Å, α = 90 °, β = 92.931(2)°, γ = 90 °, V = 1457.67(16) Å^3, Z = 4

Calculated density: 1.38675 g·cm^{-3}

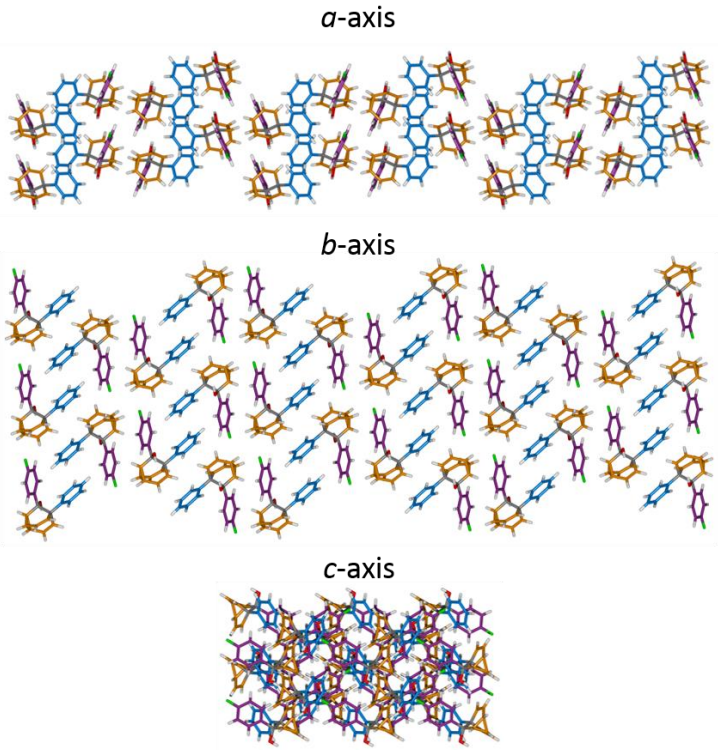

Figure 2.20. Solid-state superstructure of **1e′** viewed along the three unit cell axes.

2.5.6 Variable-Temperature X-ray Crystallographic Analysis

As the barbaralanes undergo a rapid and reversible Cope rearrangement in solution, we also investigated whether this rearrangement occurs within the solid state (Schemes 2.5 and 2.6). X-ray crystallography data for **1a** and **1b′** was acquired at four different temperatures: 120 K, 270 K, 320 K and 370 K. At each temperature, the interatomic distances between specific nuclei were measured (Tables 2.5 and 2.7) and the distances were converted to percentages relative to the distances measured at 120 K (Tables 2.4 and 2.6).

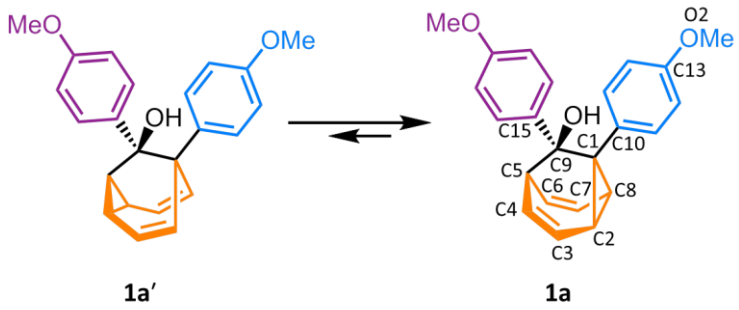

1a′ **1a**

Scheme 2.5. Potential solid-state equilibrium between **1a** and **1a′**. Atomic positions labelled here also apply to Tables 2.5 and 2.6 and Figure 2.23.

Table 2.5. Interatomic distances for specific nuclei of **1a** measured at various temperatures.

Nuclei	Interatomic Distance / Å			
	120 K	**270 K**	**320 K**	**120 K**
C9-C1	1.533(2)	1.533(2)	1.533(2)	1.536(2)
C1-C8	1.514(2)	1.507(2)	1.507(2)	1.505(2)
C1-C2	1.509(2)	1.511(2)	1.513(2)	1.511(2)
C8-C2	1.592(2)	1.590(2)	1.599(2)	1.604(2)
C2-C3	1.465(1)	1.460(2)	1.456(2)	1.452(2)
C6-C7	1.334(2)	1.325(3)	1.327(2)	1.332(3)
C7-C8	1.467(1)	1.436(2)	1.461(2)	1.454(2)
C3-C4	1.338(2)	1.331(2)	1,322(3)	1.325(3)
C5-C6	1.512(2)	1.504(2)	1.506(3)	1.502(2)
C4-C5	1.509(2)	1.506(2)	1.510(2)	1.505(3)
C9-C5	1.556(1)	1.557(2)	1.555(1)	1.556(2)
C9-C15	1.523(1)	1.523(2)	1.527(2)	1.525(2)
C1-C10	1.498(1)	1.503(2)	1.504(2)	1.501(2)
C13-O2	1.371(1)	1.376(2)	1.376(2)	1.375(2)
C4···C6	2.359(2)	2.345(2)	2.347(2)	2.335(3)
C3···C7	3.015(2)	3.004(2)	3.004(2)	3.001(3)
C2···C7	2.630(2)	2.627(2)	2.629(2)	2.628(2)
C8···C3	2.642(2)	2.632(2)	2.636(2)	2.635(3)

Table 2.6. Interatomic distances converted of **1a** to percentages relative to 120 K for specific nuclei measured at various temperatures.

Nuclei	Interatomic Distance / Å			
	120 K	**270 K**	**320 K**	**120 K**
C9-C1	100.0	100.0	100.0	100.2
C1-C8	100.0	99.5	99.5	99.4
C1-C2	100.0	100.1	100.3	100.1
C8-C2	100.0	99.9	100.4	99.3
C2-C3	100.0	99.7	99.4	99.1
C6-C7	100.0	99.3	99.5	99.9
C7-C8	100.0	99.7	99.6	99.1
C3-C4	100.0	99.5	98.8	99.0
C5-C6	100.0	99.5	99.6	99.3
C4-C5	100.0	99.8	100.1	99.7
C9-C5	100.0	100.1	99.9	100.0
C9-C15	100.0	100.0	100.3	100.1
C1-C10	100.0	100.3	100.4	100.2
C13-O2	100.0	100.4	100.4	100.3
C4···C6	100.0)	99.4	99.5	99.0
C3···C7	100.0	99.6	99.6	99.5
C2···C7	100.0	99.9	100.0	99.9
C8···C3	100.0	99.6	99.8	99.7

The variable-temperature X-ray crystallography data for **1a** reveals (Figure 2.21) that only minor changes occur between the specific nuclei measured as the temperature is raised. If the Cope rearrangement occurs within the solid state, we would expect there to be large changes in the distances between the nuclei. In particular, we would expect there to be significant changes between **C8-C2** and **C4···C6** – the positions where the Cope rearrangement occurs, *i.e.*, a cyclopropyl ring is broken between **C8-C2** and forms between **C4···C6**. As the variation in the bond length is negligible (< 1%) for these nuclei, this indicates that the structures are fixed within the solid state, and therefore, no Cope rearrangement is occurring

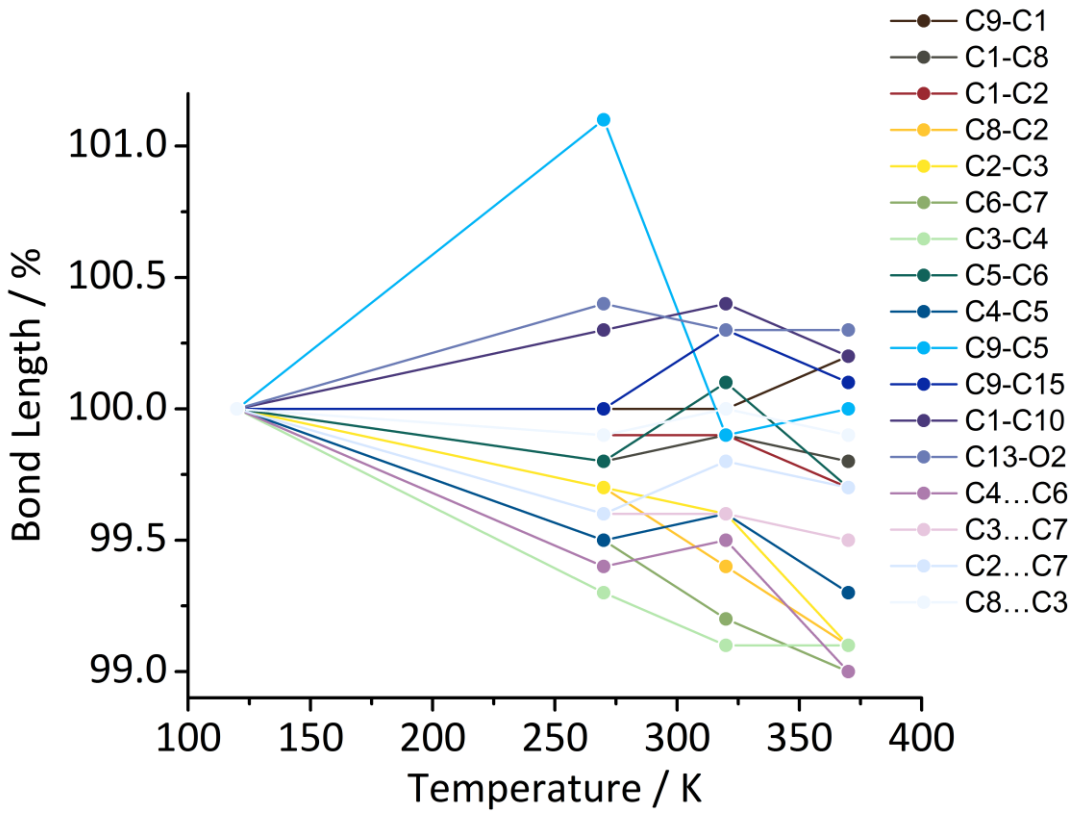

Figure 2.21. The bond lengths present in **1a** (as a percentage relative to the bond length at 120 K) plotted versus temperature.

The variable-temperature X-ray crystallography data for **1b′** also confirms there is no Cope rearrangement occurring in the solid state. For **1b′**, we would expect there to be large changes in the distances between the nuclei **C1′-C2′** and **C4′···C6′**, as this is where a cyclopropyl ring is broken/formed. Figure 2.22 shows that the variation in the bond lengths for these nuclei is again minimal (< 1%).

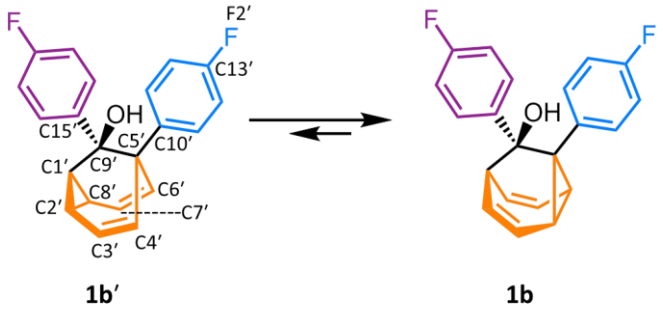

Scheme 2.6. Potential solid-state equilibrium between **1b** and **1b′**. Atomic positions labelled here also apply to Tables 2.7 and 2.8 and Figure 2.22.

Table 2.7. Interatomic distances for specific nuclei of **1b′** measured at various temperatures.

Nuclei	Interatomic Distance / Å			
	120 K	**270 K**	**320 K**	**120 K**
C9′-C1′	1.518(3)	1.509(2)	1.508(2)	1.508(2)
C1′ -C8′	1.497(3)	1.496(2)	1.495(2)	1.494(3)
C1′ -C2′	1.508(3)	1.503(2)	1.503(2)	1.500(3)
C8′ -C2′	1.592(3)	1.591(2)	1.595(2)	1.610(3)
C8′ -C7′	1.461(3)	1.455(2)	1.450(2)	1.430(3)
C2′ -C3′	1.461(3)	1.462(2)	1.456(2)	1.446(3)
C6′ -C7′	1.332(3)	1.328(2)	1.327(2)	1.325(3)
C3′ -C4′	1.337(3)	1.333(2)	1.3282)	1.331(3)
C5′ -C6′	1.518(3)	1.519(2)	1.516(2)	1.517(2)
C4′ -C5′	1.524(3)	1.520(2)	1.520(2)	1.521(2)
C9′ -C5′	1.587(3)	1.593(2)	1.592(2)	1.590(2)
C5′ -C10′	1.522(3)	1.517(2)	1.516(2)	1.514(2)
C9′ -C15′	1.518(3)	1.521(2)	1.519(2)	1.520(2)
C13′ -F2′	1.367(3)	1.363(2)	1.360(2)	1.358(3)
C4′ ⋯C6′	2.353(3)	2.342(2)	2.336(2)	2.328(3)
C3′ ⋯C7′	2.990(3)	2.989(2)	2.928(2)	2.976(3)
C2′ ⋯C7′	2.626(3)	2.622(2)	2.619(2)	2.622(3)
C8′ ⋯C3′	2.626(3)	2.626(2)	2.622(2)	2.621(3)

Table 2.8. Interatomic distances converted of **1b′** to percentages relative to 120 K for specific nuclei measured at various temperatures

Nuclei	**Interatomic Distance / Å**			
	120 K	**270 K**	**320 K**	**120 K**
C9′-C1′	100.0	99.4	99.3	99.3
C1′ -C8′	100.0	99.9	99.9	99.8
C1′ -C2′	100.0	99.7	99.7	99.5
C8′ -C2′	100.0	99.9	100.2	101.1
C8′ -C7′	100.0	99.6	99.2	98.6
C2′ -C3′	100.0	100.1	99.7	99.0
C6′ -C7′	100.0	99.7	99.6	99.5
C3′ -C4′	100.0	99.7	99.3	99.6
C5′ -C6′	100.0	100.1	99.9	99.9
C4′ -C5′	100.0	99.7	99.7	100.1
C9′ -C5′	100.0	100.4	100.3	100.2
C5′ -C10′	100.0	99.7	99.6	99.5
C9′ -C15′	100.0	100.2	100.1	100.1
C13′ -F2′	100.0	99.7	99.5	99.3
C4′ ⋯C6′	100.0	99.5	99.3	98.9
C3′ ⋯C7′	100.0	100.0	99.7	99.2
C2′ ⋯C7′	100.0	99.8	99.9	99.8
C8′ ⋯C3′	100.0	100.0	99.8	99.8

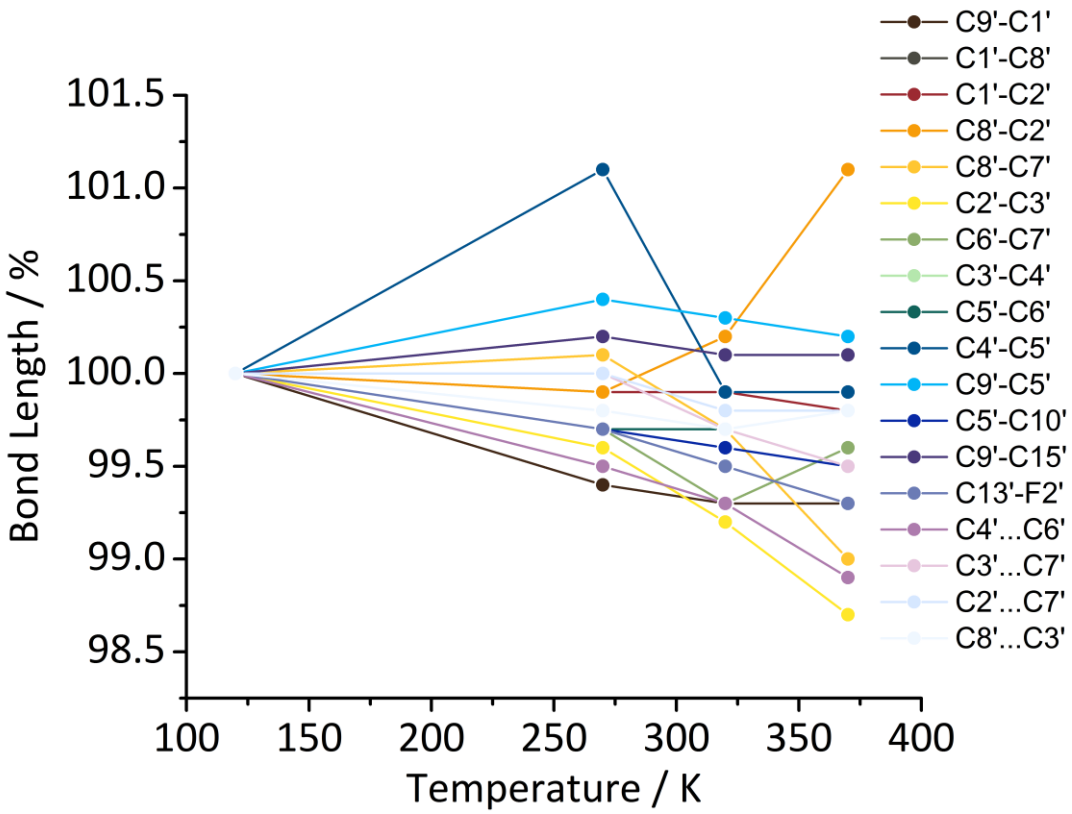

Figure 2.22. The bond lengths present in **1b′** (as a percentage relative to the bond length at 120 K) plotted versus temperature.

2.5.7 Solid-State NMR Spectroscopy

Solid-state NMR (ssNMR) spectroscopy for **1a** was acquired and then compared against the ^{13}C NMR spectra acquired at the temperature of 149 K in the solution state. An interrupted decoupling solid-state experiment was also acquired so that quaternary and primary carbons could be determined and then assigned correctly. The comparison between the spectra helps to corroborate our hypothesis that as we go lower in temperature in the solution state, the equilibrium shifts towards the major isomer (**1a**) and that less of the minor isomer (**1a′**) is present. We also observe that the solution-state spectrum acquired at 149 K is very similar to the solid-state spectrum (especially in the lower frequency section of Figure 2.23). As the spectra are alike, this helps us to confirm that the assignment within the solution state is correct (at 298 K and at 149 K) and at the same time, the interrupted decoupling experiment and CASTEP calculations (*vide infra*), have allowed us to assign the majority of the peaks in the solid-state spectrum.

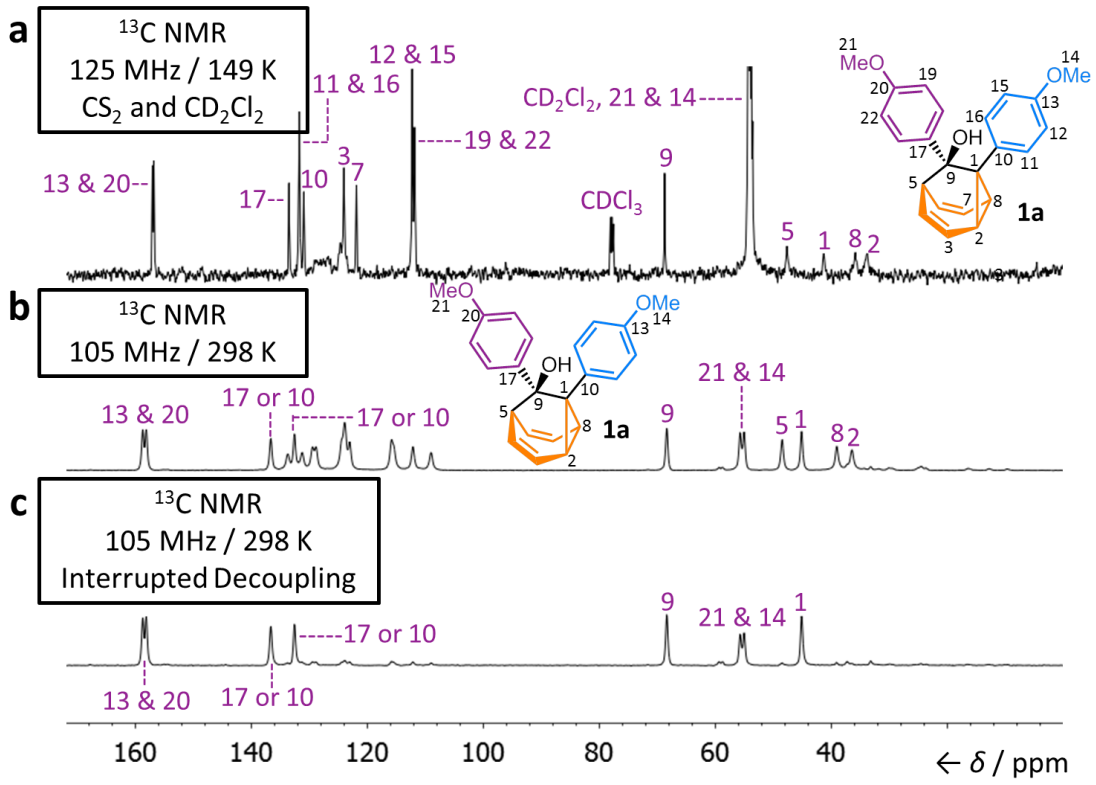

Figure 2.23. Comparison of ^{13}C NMR spectra of **1a** under different conditions: (**a**) in a CS_2–CD_2Cl_2 solution at 149 K, (**b**) in the solid state, and (**c**) in the solid state using an interrupted decoupling pulse sequence to determine quaternary and primary carbons.

ssNMR experiments for **1b′** were performed, including an interrupted decoupling experiment, and these were compared against the solution-state ^{13}C NMR spectrum for **1b**/**1b′** acquired at the temperature of 149 K. Comparing the solid-state NMR spectrum and the solution-state spectrum, there are clear differences. The solid-state NMR signals do not match up with the solution-state NMR signals, as would be expected if the structures are not the same. At 149 K, the solution-phase equilibria is biased towards **1b**, whereas isomer **1b′** is present as the sole isomer in the solid state. The dissimilarity between the spectra confirms that the species in the solution and solid states are different. At the same time, the ssNMR spectrum helps to confirm the structure of **1b′**, as the interrupted decoupling experiment shows that the position marked as 5′ is a quaternary carbon (Figure 2.24c), whereas in the solid-state NMR spectrum of **1a**, the quaternary carbon is labelled as 1 (Figures 2.24b and 2.24c) and this peak lines up in a near-identical manner to the low-temperature solution state NMR spectrum. In Figure 2.24, the lower frequency peaks representing the tricyclic

barbaralane framework in the solution state spectrum, do not line up with the peaks in the solid-state spectrum. Again, these observations show that different isomers are adopted in the solution and solid state.

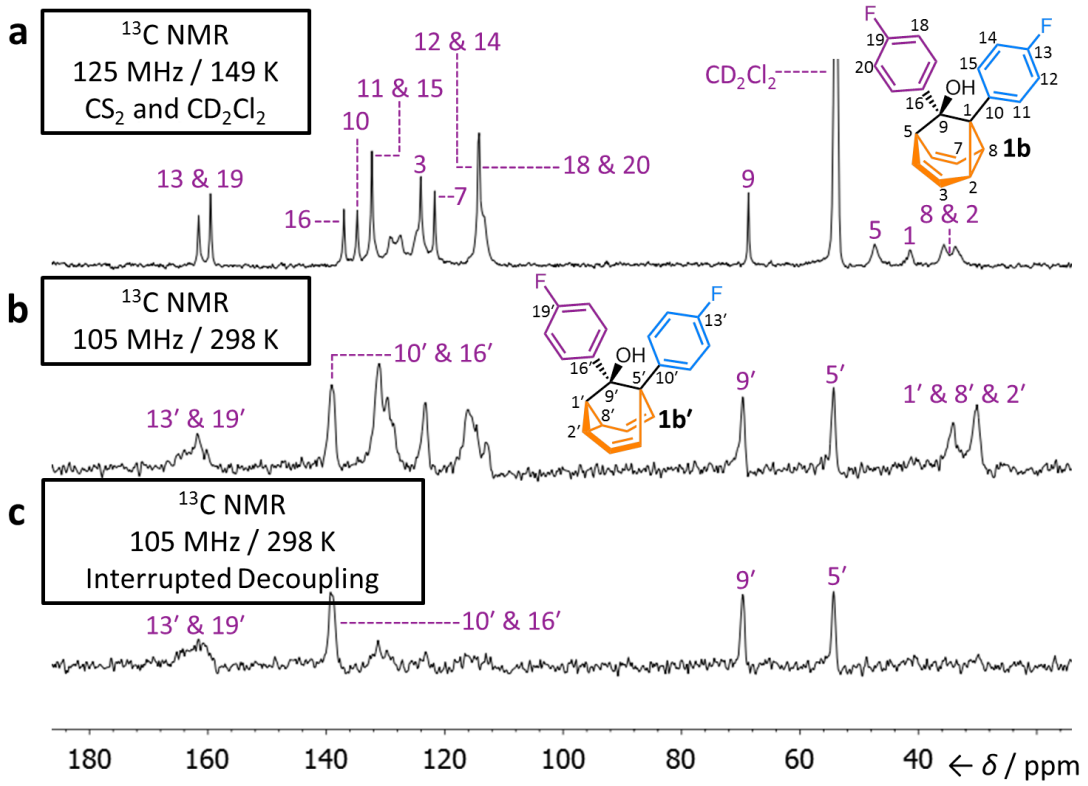

Figure 2.24. Comparison of ^{13}C NMR spectra of **1b**/**1b′** under different conditions: (**a**) in a CS_2–CD_2Cl_2 solution at 149 K, (**b**) in the solid state, and (**c**) in the solid state using an interrupted decoupling pulse sequence to determine quaternary carbons.

2.5.8 Calculation of ^{13}C Solid-State NMR Chemical Shifts

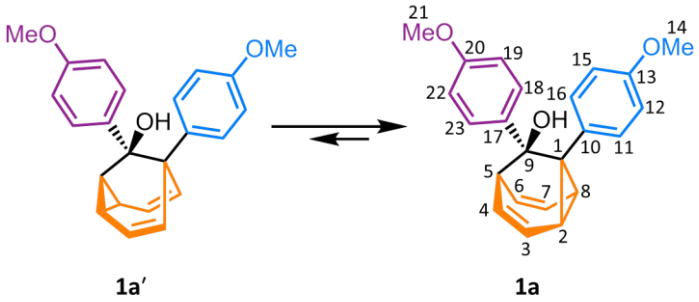

1a′ **1a**

Scheme 2.7. Equilibrium between **1a** and **1a′** in the solution state at room temperature. Atomic positions labelled for Table 2.9.

Table 2.9. Comparison of experimental ^{13}C NMR chemical shifts (solid and solution state at 149 K) against calculated solid-state ^{13}C chemical shifts (ppm).

Atom	Solid-State Calculated ^{13}C NMR Chemical Shift (δ)[d]	Solid-State Experimental ^{13}C NMR Chemical Shift (δ)	Solution-State Experimental Low-Temperature ^{13}C NMR Chemical Shift (δ)
1	51.3	45.1	41.3
2	41.3	36.5 or 39.1	33.8
3	130.3	[c]	124.0
4	131.2	[c]	[a]
5	52.1	48.5	47.6
6	130.7	[c]	[a]
7	132.2	[c]	121.9
8	44.8	39.1 or 36.5	35.9
9	72.8	68.4	68.7
10	137.1	136.7 or 132. 6	131.0
11 or 16	137.1	[c]	131.7
12 or 15	119.6	[c]	112.3
13	166.0	158.7 or 158.1	157.0
14 or 21	57.6	55.7 or 55.1	[b]
15 or 12	111.6	[c]	112.3
16 or 11	139.5	[c]	131.7
17	141.7	136.7 or 132.6	133.5
18 or 22	134.6	[c]	[a]
19 or 22	115.6	[c]	111.9
20	164.8	158.7 or 158.1	156.8
21 or 14	55.9	55.7 or 55.1	[b]
22 or 19	119.4	[c]	111.9
23 or 18	133.5	[c]	[a]

[a] peaks have broadened into baseline; [b] peaks are overlapping with the solvent (CD_2Cl_2); [c] unable to assign unambiguously; [d] ^{13}C shielding of 170 ppm used.

First principles calculations of NMR shifts in crystalline forms were carried out using the GIPAW method implemented in CASTEP v17.2.[39] All calculations were performed using the PBE functional[40] and on-the-fly generated ultrasoft pseudopotentials with a cut-off energy of 600 eV. Geometry optimisation of all atomic positions was carried out with the centre of mass and unit cell parameters fixed at the values determined by single-crystal X-ray diffraction. Integrals were taken over the Brillouin zone using a Monkhorst-Pack grid with a maximum *k*-point sample spacing of 0.1 $Å^{-1}$, corresponding to 1 × 2 × 1 and 2 × 2 × 1 grids for **1a** and **1b′**, respectively. ^{13}C isotropic shifts were obtained from calculations of NMR parameters from the optimised structures using tools

relying on the magres file format and MagresPython library.[41]

Calculations of the ^{13}C NMR chemical shifts in the solid state are based on the X-ray crystallographic data, and as both **1a** and **1b′** demonstrate different structures in the solid state, calculations of ^{13}C NMR chemical shifts in the solid state bear significant importance. The solid-state samples were prepared as powders (which were obtained by evaporating a solution of the barbaralane), and although the ^{13}C NMR chemical shifts in the solid state can be measured experimentally (Figures 2.23 and 2.24), precise values were desired (Figures 2.25 and 2.26).

Firstly, looking at the data for **1a** and comparing the calculated ^{13}C NMR chemical shifts in the solid state against the experimental chemical shifts, all the values are relatively similar. At the same time, from the ^{13}C and ^{1}H VT NMR for **1a**/**1a′** (Figure 2.10 and Figure 2.11) we have shown that as the temperature is lowered, the equilibrium shifts further towards **1a**. This means that as we reach the lowest temperature attainable (149 K), there is less of the minor isomer and the spectrum acquired will resemble a spectrum showing the major isomer as the sole species. The solution-state experimental ^{13}C NMR chemical shifts are also similar to both the experimental and calculated solid-state ^{13}C NMR chemical shifts, and this observation reinforces the conclusion that the structure of the major isomer in the solid state is the same as that in the solution state at low temperature, due to a shift in the equilibrium.

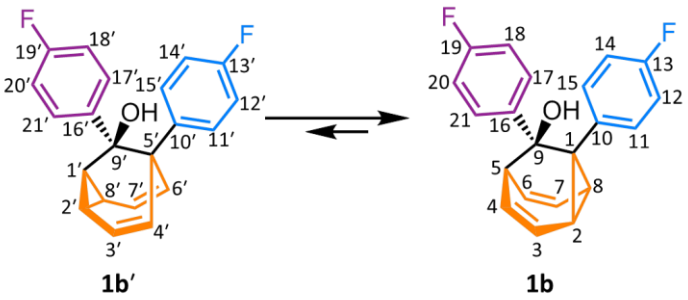

Scheme 2.8. Equilibrium between **1b** and **1b′** in the solution state at room temperature. Atomic positions labelled for Table 2.10.

Table 2.10. Comparison of experimental ^{13}C NMR chemical shifts (solid and solution state at 149 K) against calculated solid-state ^{13}C chemical shifts (ppm).

Atom	Solid-State Calculated ^{13}C NMR Chemical Shift (δ)[d]	Solid-State Experimental ^{13}C NMR Chemical Shift (δ)	Solution-State Experimental Low-Temperature ^{13}C NMR Chemical Shift (δ)
1′/5	41.3	34.1 or 30.1[b]	41.4
2′/4	35.8	34.1 or 30.1[b]	[a]
3′/3	130.0	[c]	124.0
4′/2	135.0	[c]	33.8 or 35.7
5′/1	59.6	54.3	47.4
6′/8	137.1	[c]	35.7 or 33.8
7′/7	130.9	[c]	121.7
8′/6	33.2	34.1 or 30.1[b]	[a]
9′/9	75.8	69.7	68.7
10′/10	145.6	139.1[b]	134.8
11′ or 15′/11 or 15	137.7	[c]	132.3
12′ or 14′/12 or 14	120.9	[c]	114.3
13′ or 19′/13 or 19	172.3	161.8[b]	161.6
14′or 12′/14 or 12	119.3	[c]	114.3
15′ or 11′/15 or 11	137.5	[c]	132.3
16′/16	145.8	139.1[b]	137.0
17′ or 21′/17 or 21	137.1	[c]	[a]
18′ or 20′/18 or 20	123.0	[c]	114.2
19′ or 13′/19 or 13	173.7	161.8[b]	159.6
20′ or 18′/20 or 18	116.6	[c]	114.2
21′ or 17′/21 or 17	135.5	[c]	[a]

[a] peaks have broadened into baseline; [b] peaks are overlapping with the solvent (CD_2Cl_2); [c] unable to assign unambiguously; [d] ^{13}C shielding of 170 ppm used.

As mentioned previously, the ^{13}C and ^{1}H VT NMR spectra acquired for **1b**/**1b′** show that as the temperature is decreased, the resonances shift in a manner so that the spectrum at the lowest temperature (149 K) shows mainly the structure for **1b** and only a minimal amount of **1b′**. Following from this observation, the solution-state experimental chemical shifts should differ from both the solid-state calculated and experimental ^{13}C NMR chemical shifts. This is indeed what is apparent in the comparison. The differences in the chemical shifts corroborate that the structure in the solid state is the minor isomer **1b′** and that the structure in the solution state at low temperature is mainly **1b**. Upon further inspection, the solid-state calculated chemical shifts for the atoms 4′/2 and 6′/8, in comparison to the solution-state low-temperature experimental chemical shifts are

completely different, and this is due to the dissimilar structures in the solid and solution states. As the structures are different, in the solid state (**1b′**) the protons labelled as 4′ and 6′ will resemble a *cis*-dialkyl olefin whereas in the solution state (**1b**) the protons labelled as 2 and 8 will resemble a divinyl cyclopropane. As the chemical environments are different in the adopted structures, there will be large differences in the chemical shifts, and this is what we observe.

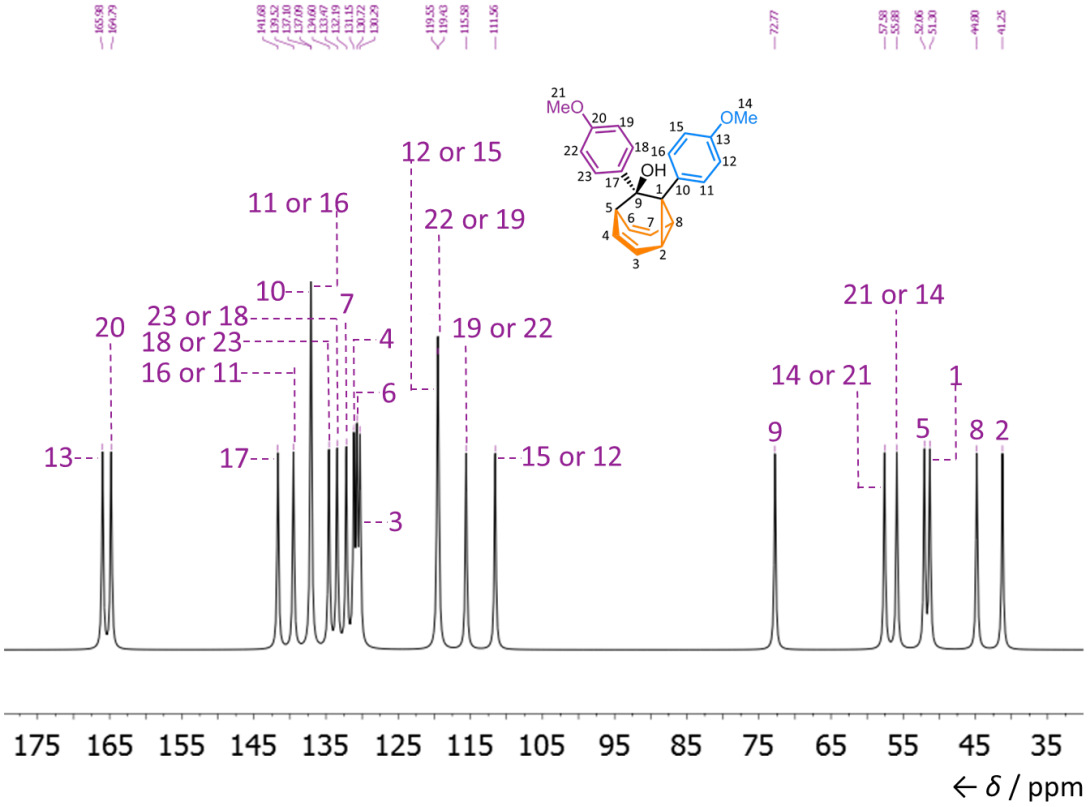

Figure 2.25. Calculated solid state ^{13}C NMR spectrum of **1a**.

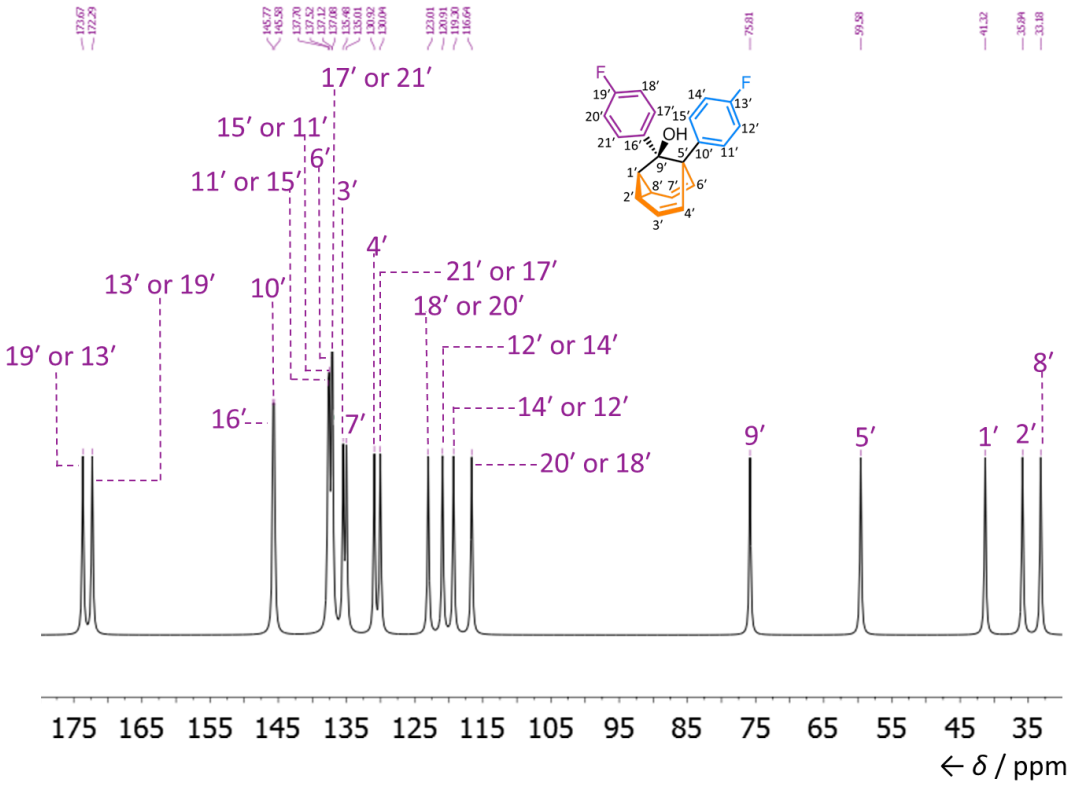

Figure 2.26. Calculated solid state ^{13}C NMR spectrum of **1b′**.

2.5.9 Electrostatic Potential Maps of Solid-State Structures

Electrostatic potential maps (Figure 2.27) were calculated using Gaussian 09, starting from the atomic coordinates obtained by X-ray crystallography and using the B3LYP functional and 3-21G basis set. Isovalues of 0.01 are used for mapped surface and the colour scale displays electrostatic potentials of –0.135 (red) to +0.135 (blue). It is clear from inspecting the maps that the heteroatoms are the most polarised areas of the structures, as would be expected, and that the aromatic surfaces are only mildly polarised. There is no indication that this mild polarisation gives rise to any aromatic interactions in the solid state, as the partially polarised regions do not match up with one another in the crystal lattice.

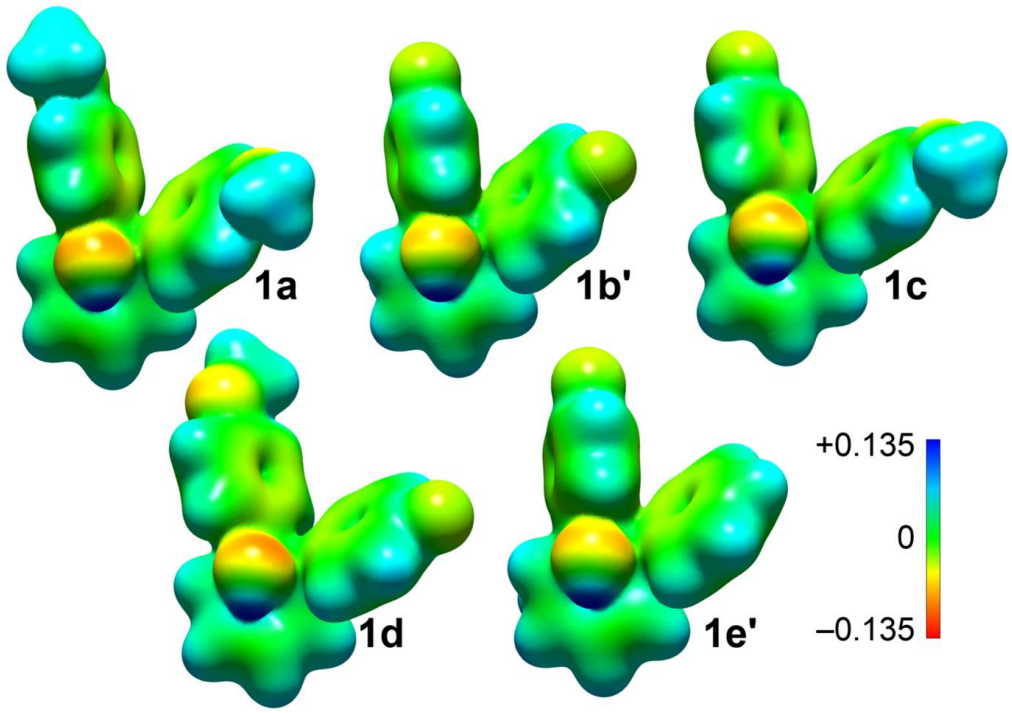

Figure 2.27. Calculated (B3LYP/3-21G) electrostatic potential maps for the solid-state geometries of the barbaralanes **1**/**1′**.

2.5.10 Hirshfeld Surfaces of Solid-State Structures

Hirshfeld surfaces[42] give insight into the interactions between molecules in the crystal lattices. We calculated Hirshfeld surfaces for the crystal packing structures of **1**/**1′** in CrystalExplorer17[43] using an isovalue of 0.5 and mapping the normalised contact distance, d_{norm}. The surfaces highlight (Figures 2.28–2.44) in red any regions in which the molecular surfaces meet at distances shorter than the sum of van der Waals radii, while white and blue illustrate regions where they meet at distances that are the sum of the van der Waals radii or longer, respectively. Overall, the Hirshfeld surfaces of **1**/**1′** reveal there are only a few contacts that are slightly shorter than the sum of van der Waals radii–there are only a small number of red patches, which are faint in colour and small in size. This data suggests that there are no strong and specific noncovalent interactions in the solid state that direct the crystal packing. In two cases, **1a** and **1c**, the tertiary alcohol appears to be involved in a O–H···O contact with a neighbouring OMe group. However, the H···O distances are much longer (by ~0.3 Å) than the mean distance[44] of 1.974 Å expected for a O–H···O hydrogen bond in the solid state, so these can only be considered very weak interactions, at most. The other contacts that appear

shorter than the sum of van der Waals radii, e.g., some C–H···F and C–H···C contacts, are also rather weak and would not be expected to dictate the crystal packing.

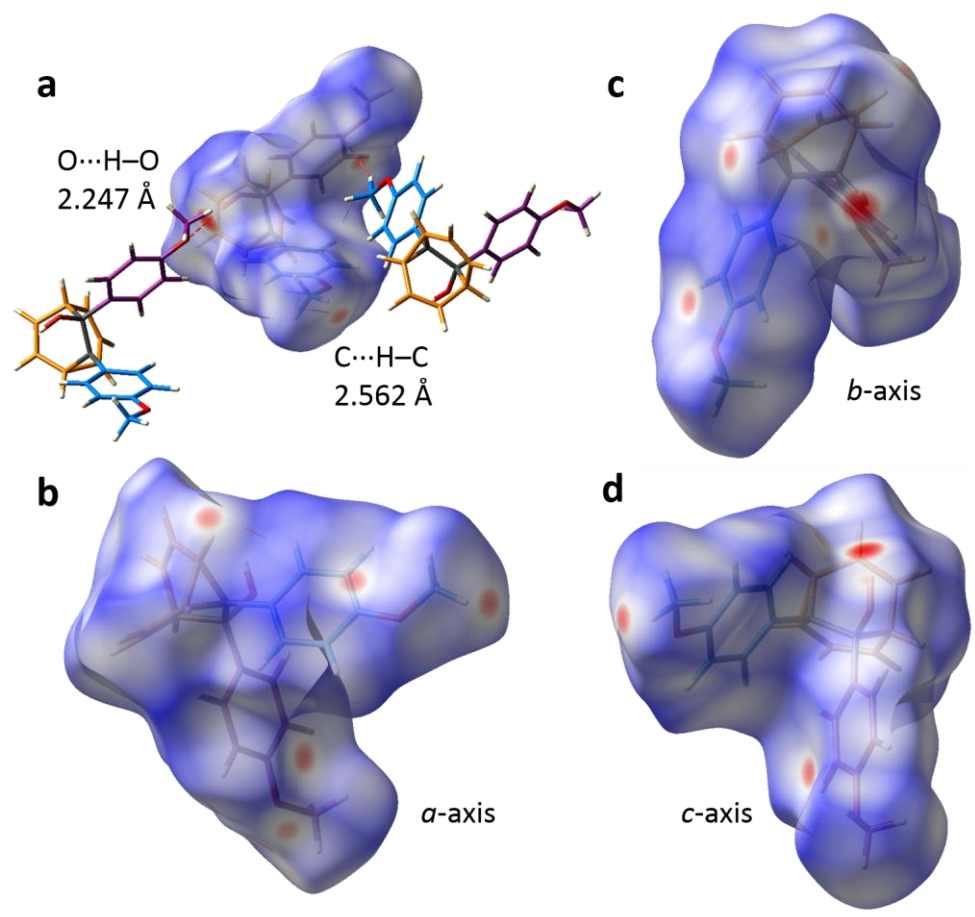

Figure 2.28. Hirshfeld surface of **1a**, showing (a) the most significant close contacts, as well as views of the surface along the crystallographic (b) *a*-axis, (c) *b*-axis, and (d) *c*-axis.

Crystals of **1a** exhibit (Figure 2.28) a few contacts that are slightly closer than the sum of van der Waals radii. Most are C–H···C contacts, but there is also a weak O–H···O interaction that measures 2.247 Å – significantly longer than the 1.974 Å expected for a O–H···O hydrogen bond.

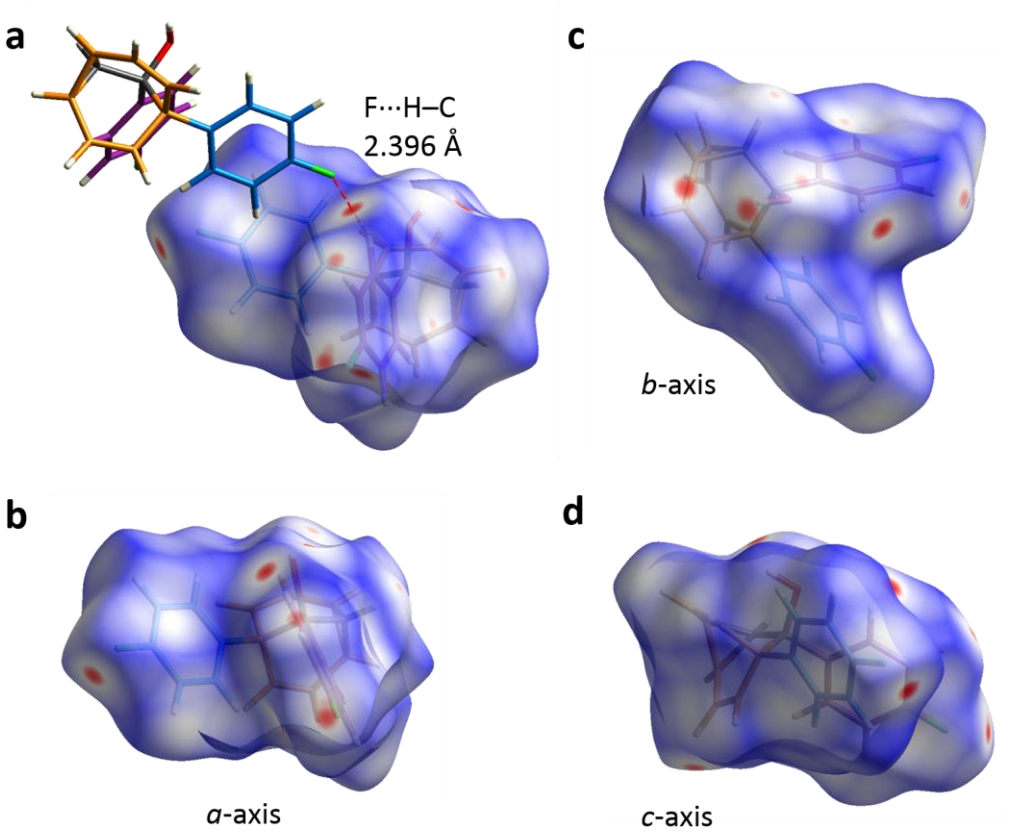

Figure 2.29. Hirshfeld surface of **1b′**, showing (a) the most significant close contact, as well as views of the surface along the crystallographic (b) *a*-axis, (c) *b*-axis, and (d) *c*-axis.

Crystals of **1b′** also exhibit (Figure 2.29) a few contacts that are slightly closer than the sum of van der Waals radii. Again, most of them are C–H···C contacts, but there is also a C–H···F contact involving a sp^2 C–H of one of the 4-fluorophenyl rings. None of the contacts correlate with a strong noncovalent bonding interaction.

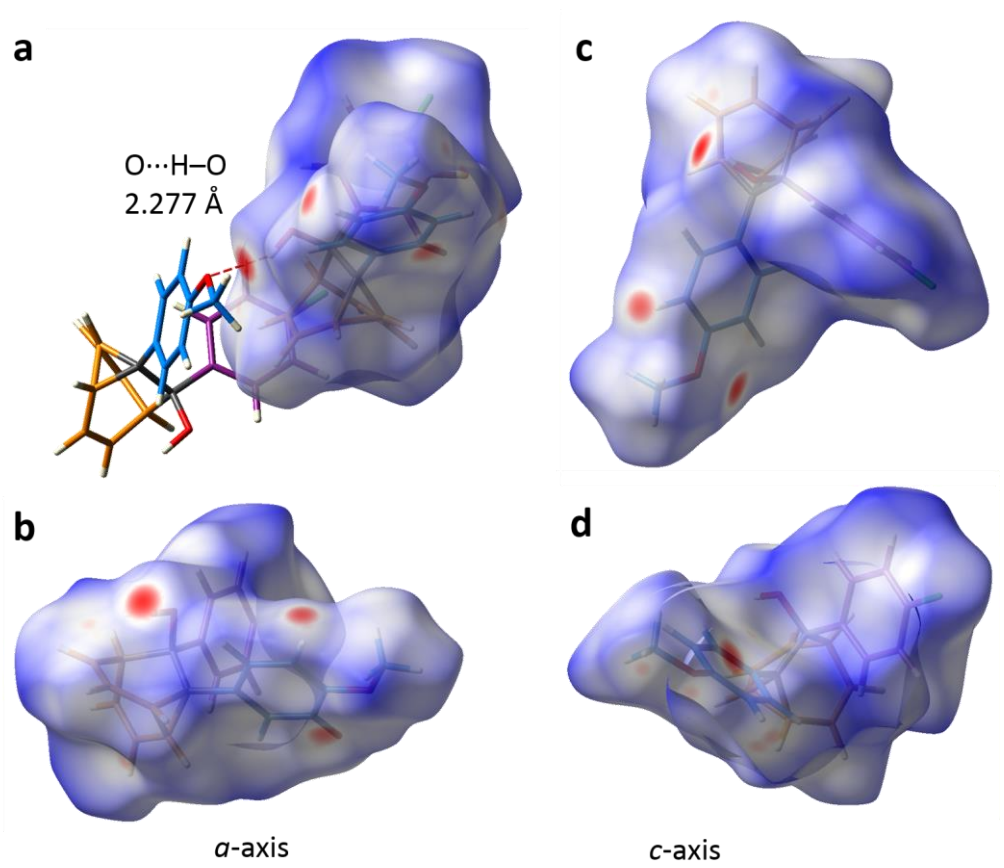

Figure 2.30. Hirshfeld surface of **1c**, showing (a) the most significant close contact, as well as views of the surface along the crystallographic (b) *a*-axis, (c) *b*-axis, and (d) *c*-axis.

Crystals of **1c** pack in a manner that is similar to **1a** and close contacts present (Figure 2.30) are very similar. As for **1a**, there is a weak O–H···O interaction that measures 2.277 Å – significantly longer than the 1.974 Å expected for a O–H···O hydrogen bond.

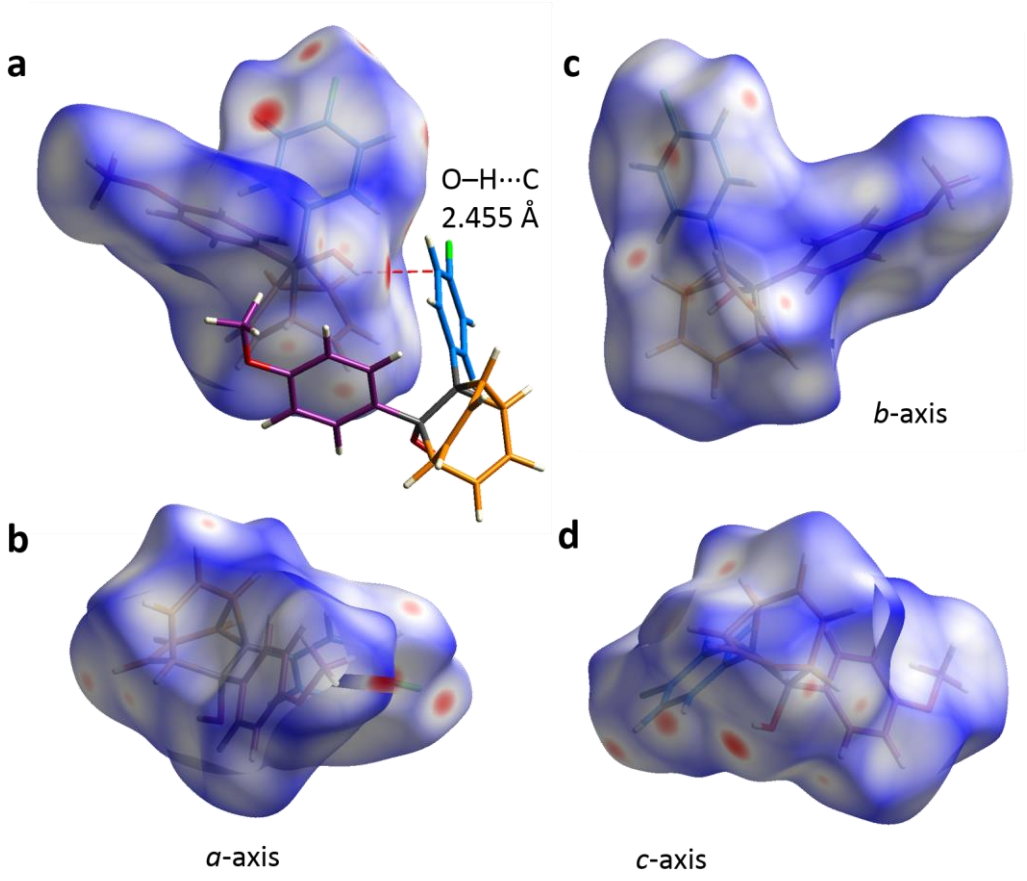

Figure 2.31. Hirshfeld surface of **1d**, showing (a) the most significant close contact, as well as views of the surface along the crystallographic (b) *a*-axis, (c) *b*-axis, and (d) *c*-axis.

Crystals of **1d** are also similar to **1a** (and, therefore, to **1c**). Unlike **1a** and **1c**, however, there are no O–H···O close contacts (Figure 2.31). As the packing is essentially unchanged in the absence of these contacts, this observation confirms our assertion that any O–H···O hydrogen bonds present in the solid-state structures of **1a** or **1c** are weak and do not dictate the packing.

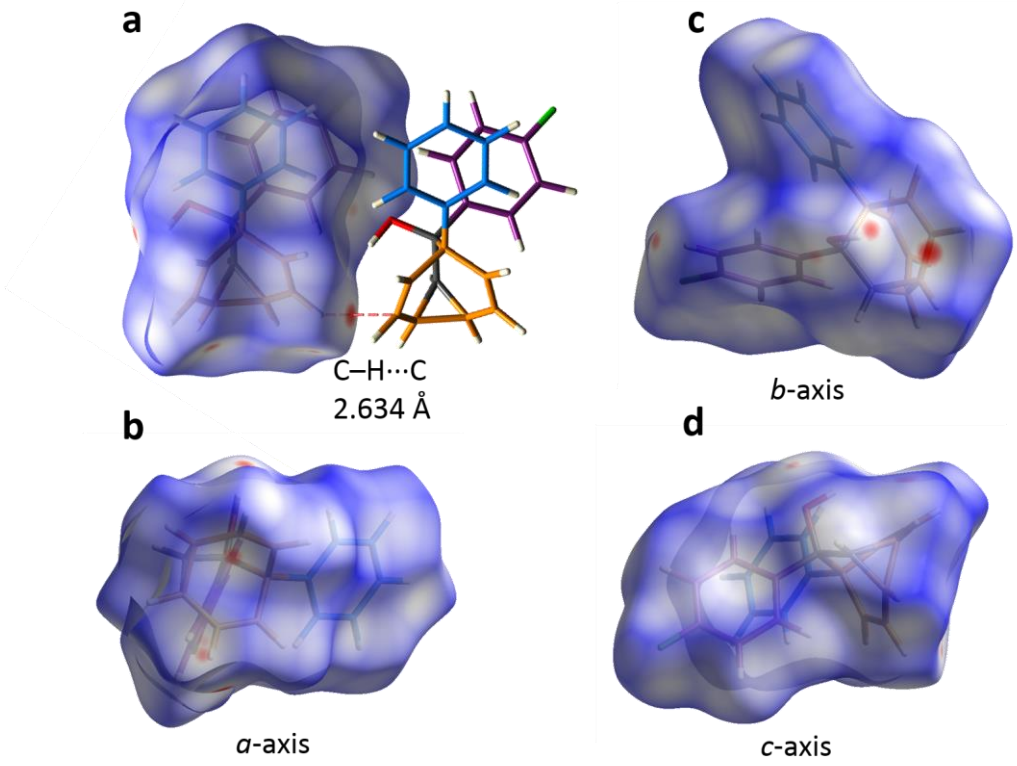

Figure 2.32. Hirshfeld surface of **1e′**, showing (a) the most significant close contact, as well as views of the surface along the crystallographic (b) *a*-axis, (c) *b*-axis, and (d) *c*-axis.

The packing structure of **1e′** is isostructural with **1b′**. As expected, the Hirshfeld surface (Figure 2.32) shows that there are only very few contacts closer than the sum of van der Waals radii. Those that are present do not correlate with any strong noncovalent bonding interactions.

Hirshfeld fingerprint diagrams show (Figure 2.33) similarities between **1a**, **1c**, and **1d** in one grouping and between **1b′** and **1e′** in another grouping. This observation confirms our categorisation of the packing structures into two groups and matches well with our hypothesis that it is the packing that causes the switch in preference for valence isomer **1** or **1′**.

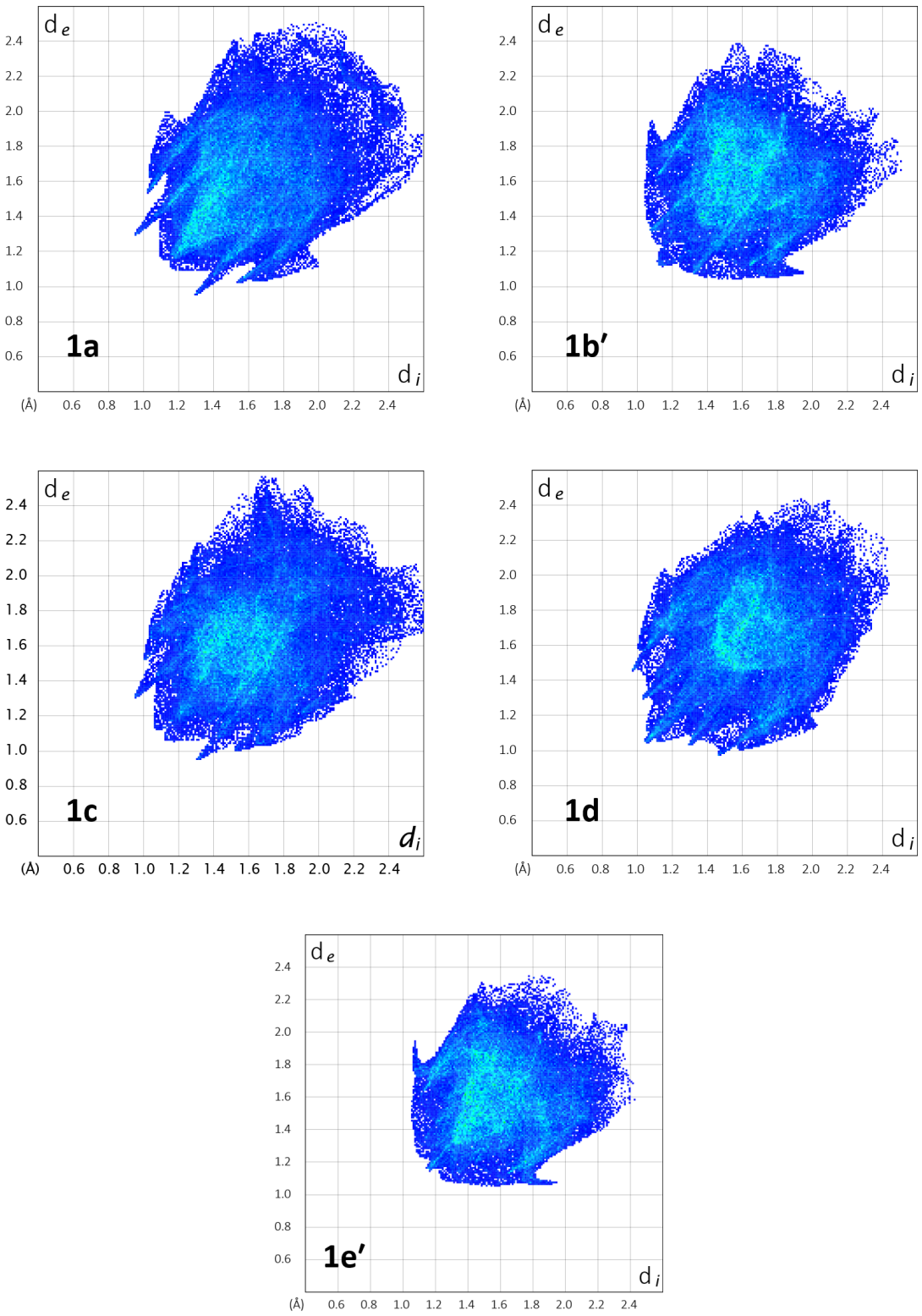

Figure 2.33. Calculated Hirshfeld fingerprints for the X-ray crystal structures of the barbaralanes **1**/**1′**.

2.5.11 Calculation of Intermolecular Energies in the Solid State

We performed DFT calculations to quantify the interaction energies between neighbouring molecules in the solid state using the CE-B3LYP [B3LYP/6-31G(d,p)] energy model[42] in CrystalExplorer17.[43] Based on the X-ray crystal structure coordinates, a cluster was generated around a central molecule, extending to molecules that come within 3.8 Å of the central molecule at any point. As each of the crystal structures of **1**/**1′** have only one unique molecule in the unit cell ($Z' = 1$), all of the surrounding molecules are related to the central molecule by a symmetry operation (labelled 'Symmetry Op.' in Tables 2.11–2.15). These energy calculations allow us to elucidate the total interaction energies (E_{tot}, in $kJ \cdot mol^{-1}$) between neighbouring molecules, based on the individual components for electrostatic (E_{ele}), polarization (E_{pol}), dispersion (E_{dis}), and repulsion (E_{rep}) energies. In each of the Tables below, *N* indicates the number of molecules of a particular symmetry operation included in the cluster. *R* is the distance between the molecular centroids (mean atomic position) of the central molecule and the molecule generated by the given symmetry operation. A colour code is given for each table entry, which matches the colouring of the relevant molecules in the corresponding cluster diagrams, Figures 2.34–2.38.

For all of the structures we modelled, not only is the overall lattice energy dominated (Tables 2.11–2.15) by the dispersion energy term, E_{dis}, but dispersion also makes the largest contribution to the total intermolecular interaction energy between each pair of neighbouring molecules. This observation is consistent with our description of these molecules packing in the solid state in a manner that is influenced more by molecular shape than by any specific noncovalent bonding interactions.

Table 2.11. Calculated intermolecular interaction energies (in kJ·mol^{-1}) for the solid-state structure of **1a**.

N	Symmetry Op.	*R* / Å	E_{ele}	E_{pol}	E_{dis}	E_{rep}	E_{tot}
1	-x, -y, -z	8.65	-10.3	-2.4	-30.8	24.0	-24.6
2	-x, y+1/2, -z+1/2	8.98	-6.7	-1.5	-33.3	20.8	-24.4
1	-x, -y, -z	14.98	-1.1	-0.1	-2.5	0.2	-3.2
2	x, -y+1/2, z+1/2	7.51	-8.0	-2.5	-43.5	27.5	-31.3
2	x, y, z	9.21	-19.8	-3.5	-29.9	30.6	-30.7
1	-x, -y, -z	6.86	-2.2	-0.7	-29.5	13.8	-20.0
2	-x, y+1/2, -z+1/2	9.79	-10.9	-2.1	-29.9	21.5	-25.8
2	x, -y+1/2, z+1/2	11.01	-1.9	-0.4	-10.1	6.0	-7.3
1	-x, -y, -z	8.18	-10.2	-1.7	-48.3	29.2	-36.1

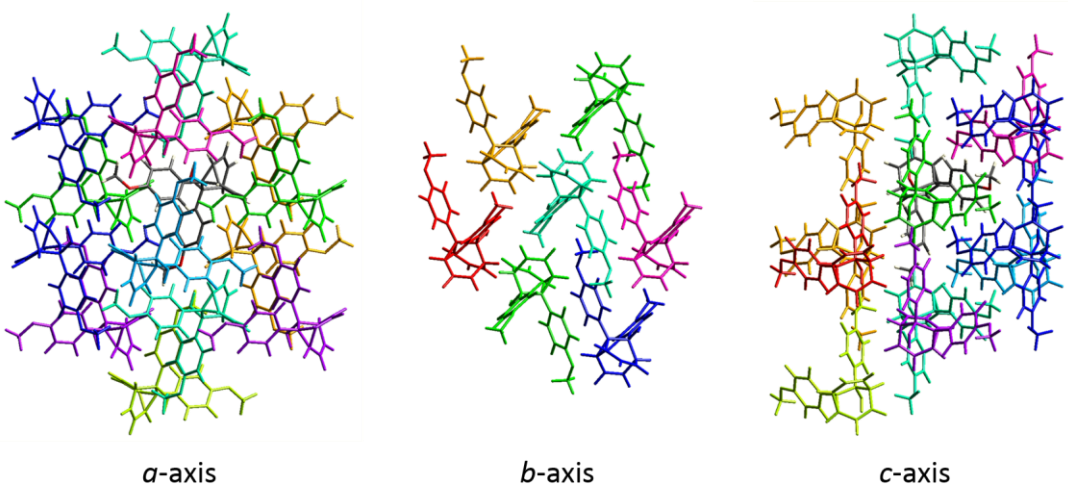

Figure 2.34. The cluster of molecules used to model intermolecular interaction energies listed in Table 2.11. The central molecule is coloured according to atom type (C, grey; H, white; O, red) and surrounding molecules are coloured to match the colour code in Table 2.11.

Table 2.12. Calculated intermolecular interaction energies (in kJ·mol^{-1}) for the solid-state structure of **1 b′**.

	N	Symmetry Op.	*R* / Å	E_{ele}	E_{pol}	E_{dis}	E_{rep}	E_{tot}
	1	-x, -y, -z	11.65	1.8	-0.5	-7.5	1.5	-4.1
	2	-x+1/2, y+1/2, -z+1/2	7.64	-7.7	-0.9	-33.5	18.8	-26.4
	2	x, y, z	9.77	-5.5	-0.7	-16.6	12.6	-13.0
	2	x, y, z	11.56	-2.3	-0.4	-3.9	0.6	-5.8
	1	-x, -y, -z	8.30	-11.0	-1.4	-32.7	23.8	-26.5
	2	-x+1/2, y+1/2, -z+1/2	8.20	-2.3	-1.4	-27.2	14.5	-18.2
	2	x, y, z	6.18	-8.3	-2.5	-47.4	33.3	-31.4
	1	-x, -y, -z	7.12	-14.9	-2.7	-50.6	30.1	-43.2
	1	-x, -y, -z	13.22	1.7	-0.2	-1.4	0.0	0.5

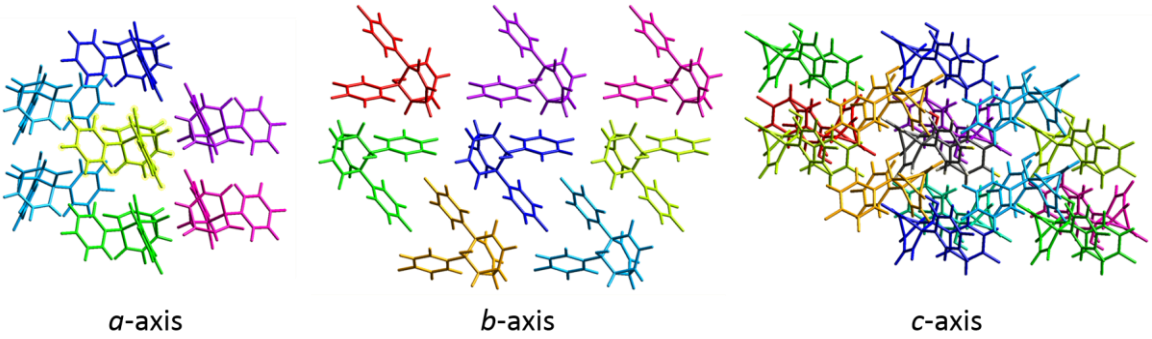

Figure 2.35. The cluster of molecules used to model intermolecular interaction energies listed in Table 2.12. The central molecule is coloured according to atom type (C, grey; H, white; O, red) and surrounding molecules are coloured to match the colour code in Table 2.12.

Table 2.13. Calculated intermolecular interaction energies (in kJ·mol^{-1}) for the solid-state structure of **1 c**.

	N	Symmetry Op.	*R* / Å	E_{ele}	E_{pol}	E_{dis}	E_{rep}	E_{tot}
	2	x, -y+1/2, z+1/2	7.49	-17.5	-3.1	-57.6	44.8	-43.3
	1	-x, -y, -z	8.42	-8.0	-1.8	-31.9	20.8	-24.7
	1	-x, -y, -z	9.86	-0.9	-0.7	-13.3	2.3	-11.6
	2	-x, y+1/2, -z+1/2	11.13	-0.0	-0.4	-3.9	0.6	-3.4
	2	x, y, z	7.15	-4.9	-1.0	-25.1	14.0	-19.1
	2	x, -y+1/2, z+1/2	9.00	-6.1	-0.5	-21.7	13.8	-17.3
	1	-x, -y, -z	8.42	-4.2	-0.8	-26.8	15.0	-19.1
	2	-x, y+1/2, -z+1/2	9.48	-12.6	-2.5	-39.3	31.0	-30.3
	1	-x, -y, -z	13.95	-9.0	-1.3	-9.4	9.8	-12.6

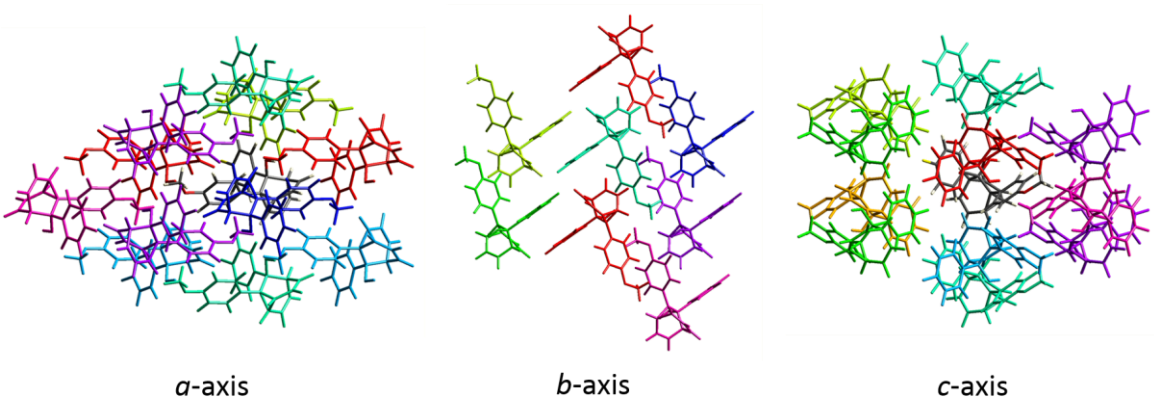

Figure 2.36. The cluster of molecules used to model intermolecular interaction energies listed in Table 2.13. The central molecule is coloured according to atom type (C, grey; H, white; O, red) and surrounding molecules are coloured to match the colour code in Table 2.13.

Table 2.14. Calculated intermolecular interaction energies (in kJ·mol^{-1}) for the solid-state structure of **1 d**.

	N	Symmetry Op.	*R* / Å	E_{ele}	E_{pol}	E_{dis}	E_{rep}	E_{tot}
	2	-x, y+1/2, -z+1/2	9.58	-8.5	-1.3	-23.3	19.4	-18.3
	2	x, -y+1/2, z+1/2	6.63	-21.4	-3.7	-63.5	52.9	-48.0
	1	-x, -y, -z	11.99	-2.4	-0.9	-9.6	6.3	-7.6
	1	-x, -y, -z	9.42	-2.3	-0.6	-16.6	5.0	-14.3
	2	x, y, z	7.50	-6.6	-1.4	-15.8	10.2	-15.5
	2	-x, y+1/2, -z+1/2	12.92	-1.3	-0.6	-6.4	1.3	-6.5
	1	-x, -y, -z	9.69	-11.6	-2.7	-43.7	35.1	-30.6
	2	x, -y+1/2, z+1/2	7.84	-7.6	-0.9	-37.6	24.2	-26.4
	1	-x, -y, -z	11.52	-1.2	-0.4	-7.3	2.7	-6.2

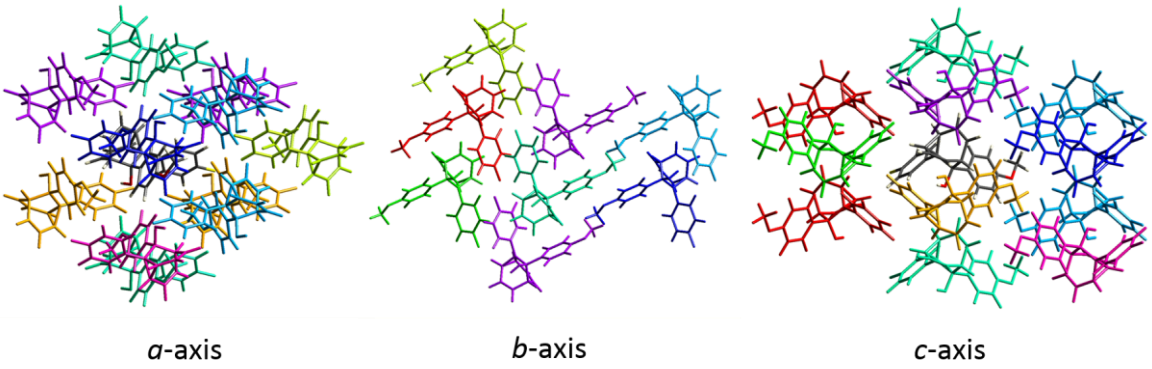

Figure 2.37. The cluster of molecules used to model intermolecular interaction energies listed in Table 2.13. The central molecule is coloured according to atom type (C, grey; H, white; O, red) and surrounding molecules are coloured to match the colour code in Table 2.13.

Table 2.15. Calculated intermolecular interaction energies (in kJ·mol^{-1}) for the solid-state structure of **1 e′**.

	N	Symmetry Op.	*R* / Å	E_{ele}	E_{pol}	E_{dis}	E_{rep}	E_{tot}
	1	-x, -y, -z	13.29	2.1	-0.2	-1.3	0.0	1.0
	1	-x, -y, -z	7.94	-10.1	-1.4	-31.2	20.3	-26.3
	2	x, y, z	11.59	-2.3	-0.4	-3.8	0.6	-5.6
	2	x, y, z	6.20	-8.4	-2.4	-46.8	32.8	-31.1
	2	-x+1/2, y+1/2, -z+1/2	8.26	-5.0	-0.9	-30.3	18.7	-20.8
	1	-x, -y, -z	6.63	-14.8	-2.8	-51.4	30.9	-43.5
	2	x, y, z	9.79	-5.0	-0.8	-16.1	11.7	-12.7
	2	-x+1/2, y+1/2, -z+1/2	7.90	-6.3	-1.1	-31.5	17.9	-23.8
	1	-x, -y, -z	11.04	1.1	-0.4	-8.1	1.8	-5.1

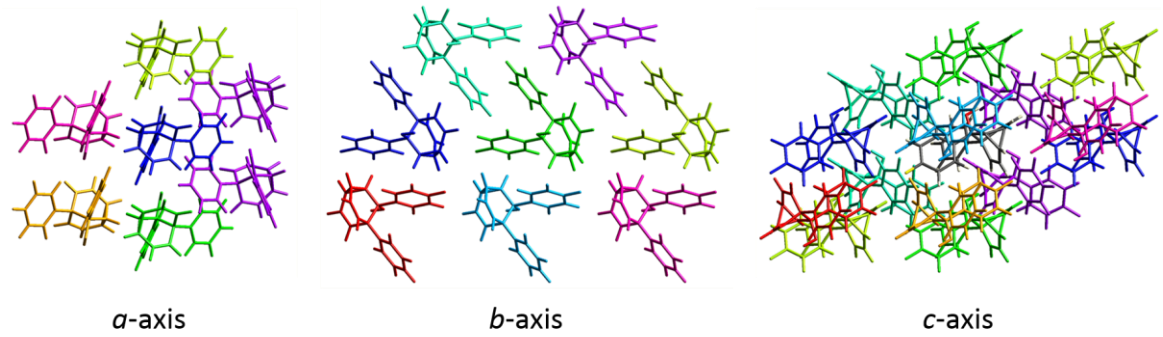

Figure 2.38. The cluster of molecules used to model intermolecular interaction energies listed in Table 2.13. The central molecule is coloured according to atom type (C, grey; H, white; O, red) and surrounding molecules are coloured to match the colour code in Table 2.13.

2.6 References

1. (a) W. von E. Doering and W. R. Roth, *Tetrahedron* 1963, **19**, 715; (b) G. Schröder, *Angew. Chem.* 1963, **75**, 722; (c) A. Ault, *J. Chem. Educ.* 2001, **78**, 924; (d) O. Yahiaoui, L. F. Pašteka, B. Judeel and T. Fallon, *Angew. Chem. Int. Ed.* 2018, **57**, 2570.

2. (a) P. Ahlberg, D. L. Harris and S. Winstein, *J. Am. Chem. Soc.* 1970, **92**, 4454; (b) D. Cremer, P. Svensson, E. Kraka and P. Ahlberg, *J. Am. Chem. Soc.* 1993, **115**, 7445; (c) P. R. McGonigal, C. de León, Y. H. Wang, A. Homs, C. R. Solorio-Alvarado and A. M. Echavarren, *Angew. Chem. Int. Ed.* 2012, **51**, 13093; (d) S. Ferrer, A. M. Echavarren, *Angew. Chem. Int. Ed.* 2016, **55**, 11178.

3. S. Jalife, J. I. M.-G. Wu, G., P. von Ragué Schleyer, M. A. Fernández-Herrera and G. Merino, *Chem. Commun.* 2015, **51**, 5391.

4. (a) D. J. Tantillo and R. Hoffmann, *Acc. Chem. Res.* 2006, **39**, 477; (b) J.-M. Lehn, *Top. Curr. Chem.* 2012, **322**, 1.

5. J. -M. Lehn, *Angew. Chem. Int. Ed*. 2015, **54**, 3276.

6. (a) A. R. Lippert, A. Naganawa, V. L. Keleshian and J. W. Bode, *J. Am. Chem. Soc.* 2010, **132**, 15790; (b) K. K. Larson, M. He, J. F. Teichert, A. Naganawa and J. W. Bode, *Chem. Sci.* 2012, **3**, 1825; (c) J. F. Teichert, D. Mazunin and J. W. Bode, *J. Am. Chem. Soc.* 2013, **135**, 11314.

7. C. W. Jefford, J. C. Rossier and J. A. Zuber, *Angew. Chem. Int. Ed. Engl.* 1982, **21**, 549.

8. Barbaralanes **1**/**1′** were prepared and isolated as racemic mixtures. For simplicity, only one enantiomer of each compound is shown.

9. R. E. Moore, J. A. Pettus and J. Mistysyn, *J. Org. Chem.* 1974, **39**, 2201.

10. E. Pretsch, P. Bühlmann and M. Badertscher, *Structure Determination of Organic Compounds*, Springer-Verlag, Berlin Heidelberg, 4th edn, 2009, pp. 91

11. Previous investigations have shown the preference of alkyl and aryl substituents to occupy a barbaralane 1-position over a 5-position. J. C. Barborak, S. Chari and P. von Ragué Schleyer, *J. Am. Chem. Soc.* 1971, **93**, 5275. See also reference 2d.

12. For crystal data, see the ESI and The Cambridge Crystallographic Data Centre (CCDC) 1857573-1857583, 1857874. These data can be obtained from www.ccdc.cam.ac.uk/data_request/cif.

13. (a) R. O. Gould, C. L. Jones, T. A. Stephenson and D. A. Tocher, *J. Organomet. Chem.* 1984, **264**, 365; (b) J. L. Davidson, W. F. Wilson, L. Manojlović-Muir and K. W. Muir *J. Organomet. Chem.* 1983, **254**, C6-C10; (c) K. M. J. Brands and A. J. Davies *Chem. Rev.* 2006, **106**, 2711; (d) Y. Kitamoto, K. Suzuki, N. Morohashi, K. Sakai and T. Hattori *J. Org. Chem.* 2013, **78**, 597; (e) M. Sakamoto and T. Mino, in *Advances in Organic Crystal Chemistry: Comprehensive Reviews*, ed. R. Tamura and M. Miyata, Springer, Tokyo, 1st edition, 2015.

14. Some monosubstituted bullvalenes resolve to single isomers upon crystallisation. (a) K. Müller, H. Zimmermann, C. Krieger, R. Poupko and Z. Luz, *J. Am. Chem. Soc.* 1996, **118**, 8006; (b) R. Poupko, K. Müller, C. Krieger, H. Zimmermann and Z. Luz, *J. Am. Chem. Soc.* 1996, **118**, 8015; (c) Z. Luz, L. Olivier, R. Poupko, K. Müller, C. Krieger and H. Zimmermann, *J. Am. Chem. Soc.* 1998, **120**, 5526.

15. There has been one report of a minor valence isomer crystalising from a solution of a bullvalene derivative. However, the assignment of the major species in the solution-phase equilibrium is somewhat ambiguous and it has not been possible to discern what forces control the crystallisation. P. Luger and K. Roth, *J. Chem. Soc., Perkin Trans. 2* 1989, 649.

16. During our experiments, we did not observe any crystals of solvates or conformational polymorphs. The limited conformational freedom of **1**/**1′** and limited potential for hydrogen bonding suggest they are unlikely to be highly polymorphic.

17. (a) R. D. Miller and C. S. Yannoni, *J. Am. Chem. Soc.* 1980, **102**, 7396; (b) W. W. Win, K. G. Grohmann and L. Todaro, *J. Org. Chem.* 1994, **59**, 2803; (c) J. Siegwarth, J. Bornhöft, C. Näther and R. Herges, *Org. Lett.* 2009, **11**, 3450. See also articles cited in references 2d, 12 and 13.

18. (a) V. Macho, R. D. Miller and C. S. Yannoni, *J. Am. Chem. Soc.* 1983, **105**, 3735; (b) I. Sellner, H. Schuster, H. Sichert, J. Sauer and H. Nöth, *Chem. Ber.* 1983, **116**, 3751; (c) L. M. Jackman, A. Benesi, A. Mayer, H. Quast, E. M. Peters, K. Peters and H. G. von Schnering, *J. Am. Chem. Soc.* 1989, **111**, 1512; (d) S. Schlick, Z. Luz, R. Poupko and H. Zimmermann, *J. Am. Chem. Soc.* 1992, **114**, 4315; (e) R. V. Williams, V. R. Gadgil, P. Luger, T. Koritsanszky and M. Weber, *J. Org. Chem.* 1999, **64**, 1180; (f) A. Benesi, R. Bertermann, H. Förster, M. Heubes, L. M. Jackman, T. Koritsanszky, P. Luger, A. Mayer, H. Quast, M. Seefelder and D. Zobel, *J. Am. Chem. Soc.* 2000, **122**, 4455.

19. The differences in dihedral angles coincide with changes to the C1–C9/C5′–C9′ distances in the barbaralane core. The averaged C1–C9 distance for **1a**, **1c**, and **1d** is 1.534 Å, whereas the averaged C5′–C9′ distance for **1b′** and **1e′** is 1.586 Å, showing that the movement of the divinylcyclopropane motif influences the geometries near the aromatic rings.

20. Differences in lattice energies of ~5 kJ·mol^{-1} between conformational polymorphs are relatively common. See (a) P. G. Thompson and G. M. Day, *Chem. Sci.* 2014, **5**, 3173; (b) J. Nyman, G. M. Day, *CrystEngComm* 2015, **17**, 5154. Even though the isomerisation of the barbaralanes described here causes changes in constitution, rather than just conformation, the energetic differences are of similar magnitude to some conformational changes. It is reasonable, therefore, that the small energetic preference of the fluxional Cope rearrangements can be outweighed upon crystallisation.

21. E. N. Baker and R. E. Hubbard, *Prog. Biophys. Mol. Bio.* 1984, **44**, 97.

22. M. A. Spackman and D. Jayatilaka, *CrystEngComm*, 2009, **11**, 19.

23. R. S. Rowland and R. Taylor, *J. Phys. Chem.* 1996, **100**, 7384.

24. The CE-B3LYP functional was used instead of other DFT functionals, e.g., CAM-B3LYP or MN15-L, because its implementation in CrystalExplorer allows calculation of the individual interaction energy terms in addition to the total energy. It should be noted that CE-B3LYP is different to the original B3LYP functional, which is not suitable for calculation of weak interactions. It reproduces counterpoise-corrected B3LYP-D2/6-31G(d,p) energies with mean absolute deviation about 1 kJ·mol^{-1} and gives a mean absolute deviation of just 2.5 kJ·mol^{-1} compared to CCSD(T)/CBS while using much less computational time. See reference 20.

25. M. J. Turner, S. Grabowsky, D. Jayatilaka and M. A. Spackman *J. Phys. Chem. Lett.* 2014, **5**, 4249.

26. J. P. Wagner and P. R. Schreiner, *Angew. Chem. Int. Ed.* 2015, **54**, 12274.

27. O. V. Dolomanov, L. J. Bourhis, R. J. Gildea, J. A. K. Howard, H. J. Puschmann, *Appl. Crystallogr.* 2009, **42**, 339.

28. G. M. Sheldrick. *Acta. Crystallogr. Sect. A Found. Crystallogr.* 2008, **64**, 112.

29. E. R. Johnston, S. J. Barber, M. Jacormet and J. C. Barborak, *J. Am. Chem. Soc.* 1998, **120**, 1489.

30. Guassian 16, Revision A.03, M. J. Frisch, G. W. Trucks, H. B. Schlegel, G. E. Scuseria, M. A. Robb, J. R. Cheeseman, G. Scalmani, V. Barone, G. A. Petersson, H. Nakatsuji, X. Li, M. Caricato, A. V. Marenich, J. Bloino, B. G. Janesko, R. Gomperts, B. Mennucci, H. P. Hratchian, J. V. Ortiz, A. F. Izmaylov, J. L. Sonnenberg, D. Williams-Young, F. Ding, F. Lipparini, F. Egidi, J. Goings, B. Peng, A. Petrone, T. Henderson, D. Ranasinghe, V. G. Zakrzewski, J. Gao, N. Rega, G. Zheng, W. Liang, M. Hada, M. Ehara, K. Toyota, R. Fukuda, J. Hasegawa, M. Ishida, T. Nakajima, Y. Honda, O. Kitao, H. Nakai, T. Vreven, K. Throssell, J. A. Jr. Montgomery, J. E. Peralta, F. Ogliaro, M. J. Bearpark, J. J. Heyd, E. N. Brothers, K. N. Kudin, V. N. Staroverov, T. A. Keith, R. Kobayashi, J. Normand, K. Raghavachari, A. P. Rendell, J. C. Burant, S. S. Iyengar, J. Tomasi, M. Cossi, J. M. Millam, M. Klene, C. Adamo, R. Cammi, J. W. Ochterski, R. L. Martin, K. Morokuma, O. Farkas, J. B. Foresman, D. J. Fox, Gaussian, Inc., Wallingford CT, 2016.

31. A. D. Becke, *J. Phys. Chem.* 1993, **98**, 5648.

32. T. Yanai, D. P. Tew, N. C. Handy, *Chem. Phys. Lett.* 2004, **393**, 51.

33. Y. Zhao, D. Truhlar, *Theor. Chem. Acc.* 2008, **120**, 215.

34. S. Grimme, J. Antony, S. Ehrlich, H. Krieg, H. *J. Chem. Phys.* 2010, **132**, 154104.

35. M. Cossi, N. Rega, G. Scalmani, V. J. Barone, *Comput. Chem.* 2003, **24**, 669.

36. J.-D Chai, M. Head-Gordon, *Phys. Chem. Chem. Phys.* 2008, **10**, 6615.

37. M. Lingwood, J. R. Hammond, D. A. Hrovat, J. M. Mayer, W.T Borden, *J. Chem. Theory Comput.* 2006, **2**, 740.

38. A CH_2Cl_2-CS_2 solvent mixture gave the best compromise of solubility and low freezing point, but freezes below 149 K.

39. H. Günther, J. Runsink, H. Schmickler, P. Schmitt, *J. Org. Chem.* 1985, **50**, 289.

40. A metastable bullvalene isomer has been isolated by chromatography. a) M. He, J. W. Bode, *Proc. Natl Acad. Sci. USA* 2011, **108**, 14752; b) M. He, J. W. Bode, *Org. Biomol. Chem.* 2013, **11**, 1306

41. S. J. Clark, M. D. Segall, C. J. Pickard, P. J. Hasnip, M. J. Probert, K. Refson, M. C. Z. Payne, *Kristallogr.* 2005, **220**, 567.

42. J. P. Perdew, K. Burke, M. Ernzerhof, *Phys. Rev. Lett.* 1996, **77**, 3865.

43. S. Sturniolo, T. F. G. Green, R. M. Hanson, M. Zilka, K. Refson, P. Hodgkinson, S. P. Brown, S. J. R. Yates, *Solid State Nucl. Magn. Reson.* 2016, **78**, 64.

44. M. J. Turner, J. J. McKinnon, S. K. Wolff, D. J. Grimwood, P. R. Spackman, D. Jayatilaka, M. A. Spackman, CrystalExplorer17 (2017). University of Western Australia.

45. M. A. Spackman, Jayatilaka, D. *CrystEngComm*, 2009, **11**, 19-31.

46. T. Steiner, G. R. Desiraju, *Chem. Commun.* 1998, 891.

CHAPTER 3

COVALENT AND NONCOVALENT CONTROL OVER A FLUXIONAL sp^3–CARBON STEREOCENTRE

Synopsis

This Chapter discusses the unique synthesis of nine novel barbaralanes which interconvert between stereoisomers in the solution state through dynamic chirality. In the solid state we show that this dynamic chirality can be switched off allowing for the full control over a fluxional sp^3–carbon stereocentre. Through solution and solid-state NMR, crystallographic and DFT analyses, we show that covalently linking a chiral motif to a barbaralane and encapsulating the barbaralane inside a chiral β-CD host biases the stereochemistry of the fluxional sp^3–carbon stereocentre in solution and in the solid state.

Acknowledgements

The following people are gratefully acknowledged for their contribution to this chapter: MChem student Toby G. Johnson helped to synthesise some barbaralane derivatives (**1**/**1′**, **2**/**2′**, **3**/**3′** and **4**/**4′**), grew crystal structures of **1′**, **2** and **5**/**5′** and ran CD measurements. Dr Dimitry S. Yufit solved all the X-ray crystal structures and grew the crystal structure of **3**. Lastly, Dr Paul R. McGonigal carried out all the *in silico* modelling. We are grateful to Dr Juan A. Aguilar and Dr David Apperley for assistance with NMR measurements.

3.1 Introduction

Chirality[1] is a common fundamental symmetry property of elemental particles, molecules or even macroscopic objects such as human hands. Objects are defined as chiral if they exist as a pair of 'left-handed' and 'right-handed' mirror images that cannot be superimposed; these are known as enantiomers.[2] Chirality has been a fundamental area of research in chemistry since its discovery by Pasteur[3] and has proven to be vital in chemistry and biology[4] with exploitations ranging from drug design[5] and molecular machines[6] to materials science.[7] Dynamic chirality, on the other hand is a much rarer phenomenon and occurs through a low-energy barrier to racemisation, allowing for the interconversion of enantiomers.[6a] Currently, dynamic chirality at stereogenic centres is dominated by nitrogen[8] and phosphorous[9] species which are capable of rapid pyramidal inversion. However, even though carbon centres containing different substituents are generally configurationally stable (unless bonds at the stereogenic carbon centre are broken and reformed), there are examples of enantiomerisation at a carbon atom where constituent bonds are not broken, such as the migration of labile functional groups that are remote from a stereogenic centre.[10] The most recent example of a dynamic stereogenic carbon centre belongs to Miller and co-workers,[11] who have demonstrated (Figure 3.1a) a molecular system exhibiting stereodynamic behaviour without the cleavage of a constituent bond or through the remote migration of functional groups, but *via* a redox interconversion phenomenon. While the redox interconversion results in dynamic chirality of a stereogenic carbon centre, it cannot be entirely switched off (*i.e.*, the fluxional behaviour continues in the solid state) and redox-active groups must be present within the structure which may limit the functionality and applications in biological systems.[12]

Fluxional molecules, such as bullvalene[13] and the barbaralyl cation,[14] can undergo rapid strain-assisted Cope rearrangements. Their C–C bonds are able to trade places with one another constantly, encompassing large numbers of permutations while altering the positions and relative orientations of their substituents. In principle, this phenomenon allows for enormous numbers of distinct molecules with distinguishable

shapes to exist in self-contained equilibria. Bullvalene's ability to access a large number of isomers has been utilised by the Bode research group (Figure 3.1b) who have investigated tetra-substituted bullvalenes as adaptive sensors – their isomer distribution and equilibrium population is altered upon the addition of an analyte and this can be monitored by NMR spectroscopy.[15] The equilibrium distribution is shifted through specific noncovalent bonding interactions or dynamic covalent bonds. However, the vast complexity of potentially thousands of isomers in equilibrium hinders the molecules specificity.

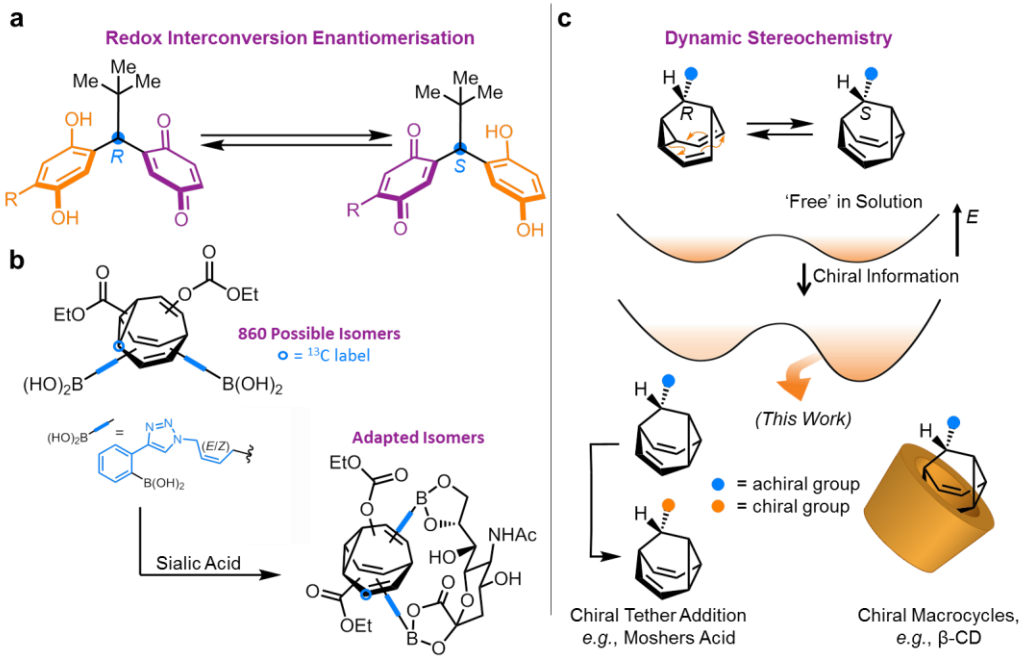

Figure 3.1. (a) Stereodynamic behaviour through redox interconversion as demonstrated by Miller and coworkers and (b) a tetra-substituted bullvalene showing a shift in equilibrium and isomer distribution upon binding with sialic acid. (c) A schematic representation illustrates changes in relative energies of isomers and stereochemistry as a result of either the addition of a chiral tether or noncovalent bonding interactions produced by chiral macrocycles.

Barbaralane[16] offers an attractive alternative fluxional scaffold in which the molecule exists as just two valence isomers in rapid flux at room temperature (due to a low energy strain-assisted Cope rearrangement). 9-Substituted barbaralanes also possess a dynamic sp^3-carbon stereocentre which exhibit dynamics more akin to those of a rapidly inverting nitrogen centre than a conventional tetravalent carbon centre. Through covalent modification (*i.e.*, attaching an appropriately selected chiral tether) and using molecular recognition properties of macrocyclic hosts such as chiral

cyclodextrins to create noncovalent bonding interactions, we expect to control the equilibrium distribution of the barbaralanes stereoisomers in favour of one of the two configurations in solution and in the solid state (Figure 3.1c).

Here we report on the influence of covalent modifications and noncovalent bonding interactions over a fluxional sp^3–carbon stereocentre which allows for equilibrium between two sets of enantiomers or diastereoisomers in solution. These fluxional carbon cages impart dynamic chirality in solution state, but in the solid state this dynamic chirality can be switched off allowing for full analysis of the fluxional sp^3–carbon stereocentres. By analysing NMR spectra of solution and powdered samples, X-ray crystal structures, DFT models and calculating association constants, we observe that (i) covalently attaching a chiral tether allows for the equilibrium to be pushed towards the thermodynamically favoured diastereoisomer in solution state which also dynamically preferentially crystallises in the solid state, and (ii) noncovalent bonding interactions in solution and in the solid state show that a host–guest complex is formed (with a one-to-one binding stoichiometry) and that in the solid state there is full control over the fluxional sp^3–carbon stereocentre (with presumed control in the solution state).

3.2 Results and Discussion

3.2.1 Covalent Control over a Fluxional sp^3–carbon Stereocentre

We synthesised (Scheme 3.1) four barbaralanes (**1**/**1′**, **2**/**2′**, **3**/**3′** and **4**/**4′**) covalently modified with chiral tethers. The first barbaralanes (**1**/**1′** and **2**/**2′**) have been covalently modified using the two enantiomers (*R* and *S*, respectively) of α-methoxy-α-trifluoromethylphenylacetic acid (Mosher's acid).[17] In the presence of oxalyl chloride and catalytic DMF the Mosher's acids are converted to their corresponding acid chlorides *in situ*, undergoing an esterification reaction when treated with barbaralol (**5**/**5′**). This esterification affords barbaralanes **1**/**1′** and **2**/**2′** in yields of 79% and 58%, respectively. The second sets of barbaralanes (**3**/**3′** and **4**/**4′**) are instead formed with barbaralone (**6**) through a Borch reductive amination[18] with the readily available and relatively cheap enantiomers of 1-phenylethylamine. Employing

sodium cyanoborohydride and mildly acidic conditions allows for the selective reduction of the protonated imine, generated *in situ* from the condensation of the barbaralone (**6**) and amine, rather than the carbonyl of barbaralone (**6**). Barbaralanes **3**/**3′** and **4**/**4′** are produced in yields of 49% and 78%, respectively. Intermediate **6** is formed through a gold-catalysed cycloisomerisation reaction of **7** which proceeds through a barbaralyl cation intermediate.[19a] This fluxional intermediate is oxidised *in situ* by diphenyl sulphoxide to afford **6**, which can be readily reduced to **5**/**5′** using lithium aluminum hydride under inert conditions.[19b]

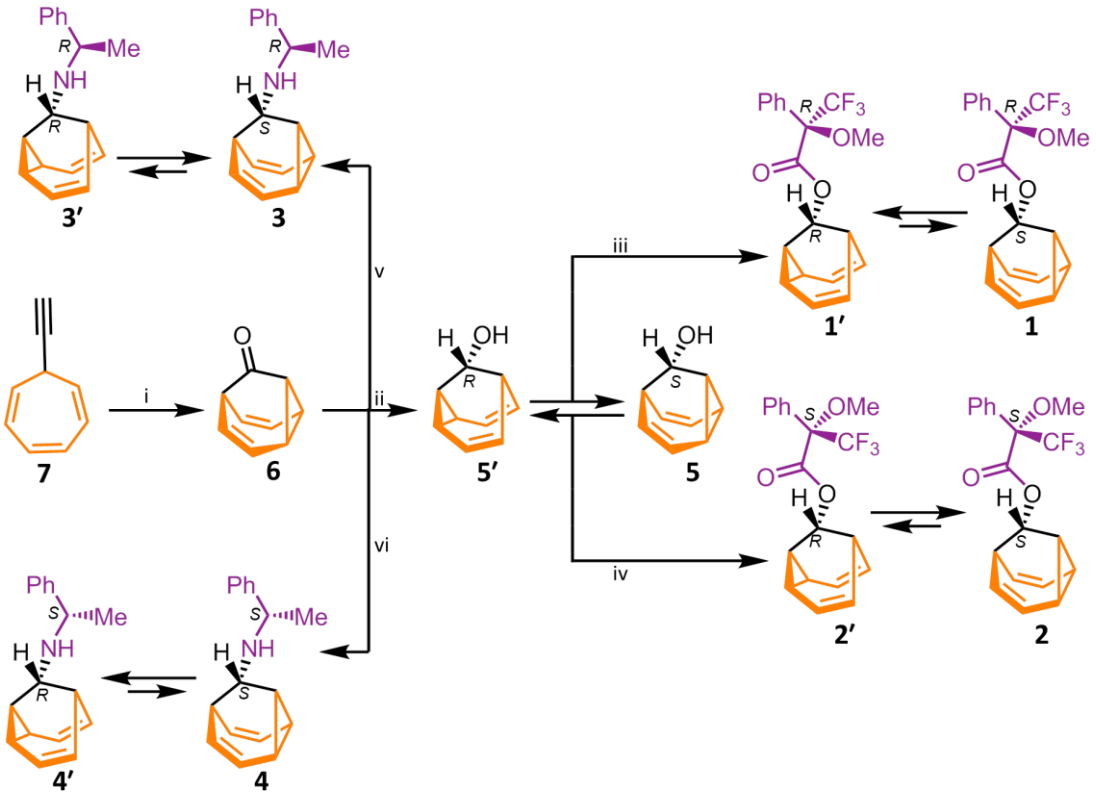

Scheme 3.1. Synthesis of barbarlanes **1**/**1′**, **2**/**2′**, **3**/**3′** and **4**/**4′**. Reagents and conditions: (i) IPrAu(MeCN)BF_4 (5 mol%), Ph_2SO (2 equiv.), CH_2Cl_2, rt, 16 h, 60%; (ii) $LiAlH_4$, Et_2O, 0 °C, 3 h, 78%; (iii) $(COCl)_2$, (*R*)-(+)-Mosher's acid, hexanes, DMF, 90 min, rt then DMAP, $CHCl_3$, Et_3N, rt, 5d, 79%; (iv) $(COCl)_2$, (*S*)-(–)-Mosher's acid, hexanes, DMF, 7 h, rt then DMAP, $CHCl_3$, Et_3N, rt, 3d, 58%; (v) (*R*)-(+)-1-phenylethylamine, CH_3COOH, 30 min then $NaBH_3CN$, 13 d, rt; 49% (vi) (*S*)-(–)-1-phenylethylamine, CH_3COOH, 30 min then $NaBH_3CN$, 13 d, rt, 78%. IPr = 1,3-bis(2,6-diisopropylphenyl)imidazol-2-ylidene.

The addition of a chiral motif to the barbaralane core gives rise to diastereoisomers which can rapidly interconvert through a simple Cope rearrangement. Solution-phase NMR spectroscopy provides conclusive evidence that the Cope rearrangement (and

therefore the interconversion between the diastereoisomers) is occurring at room temperature. Each pair of exchangeable sites gives rise to one peak; therefore, the chemical shift of each peak represents an average of the two discrete chemical environments weighted by the position of the equilibrium. For example, the proton labelled as position either 2/4′ and 4/2′ or 6/8′ and 8/6′ in Figure 3.2 has character arising from being part of both a divinylcyclopropane (**1**) and a cis-dialkyl olefin (**1′**) environment. Its chemical shift of 4.0 ppm falls between the limits of ~1.8 ppm (typical for a divinyl cyclopropane)[20] and ~5.4 ppm (typical for a *cis*-dialkylolefin)[21] that would be expected if the structure was fixed in either state.

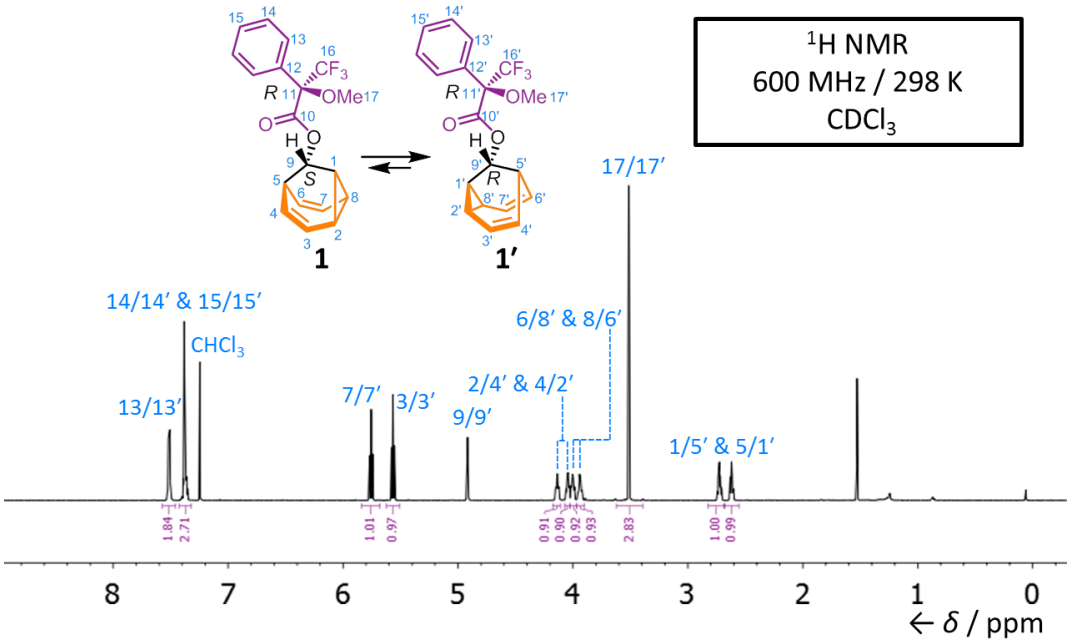

Figure 3.2. Partial ^{1}H NMR spectrum of barbarlane **1**/**1′** demonstrating the presence of two interconverting diastereoisomers.

Barbaralone (**6**) is an achiral molecule as a result of an internal mirror plane (in the plane of the carbonyl bridge), but another orthogonal mirror plane can be imagined as being induced by the rapid dynamics of the barbaralane core. Due to this induced mirror plane, the exchange of cyclopropane and olefinic environments appear as a broad singlet. Upon the generation of a stereogenic centre at the position nine of the barbaralane (as observed with **5**/**5′**), two valence enantiomers are formed and the internal mirror plane is removed. The removal of this mirror plane results in the

desymmetrisation of the molecule and subsequently the cyclopropane and olefinic environments split into two inequivalent peaks remaining in the fast-exchange regime (Figure 3.3). Covalently linking a chiral tether to the barbaralane core (as observed with **1**/**1′**) removes the remaining mirror plane and entirely desymmetrises the core so that every proton on the barbaralane core has its own unique chemical environment. For example, the broad singlet present in Figure 3.3a labelled as position 2, 4, 6 and 8 has changed into four distinctly split peaks in Figures 3.3c and 3.3d ,

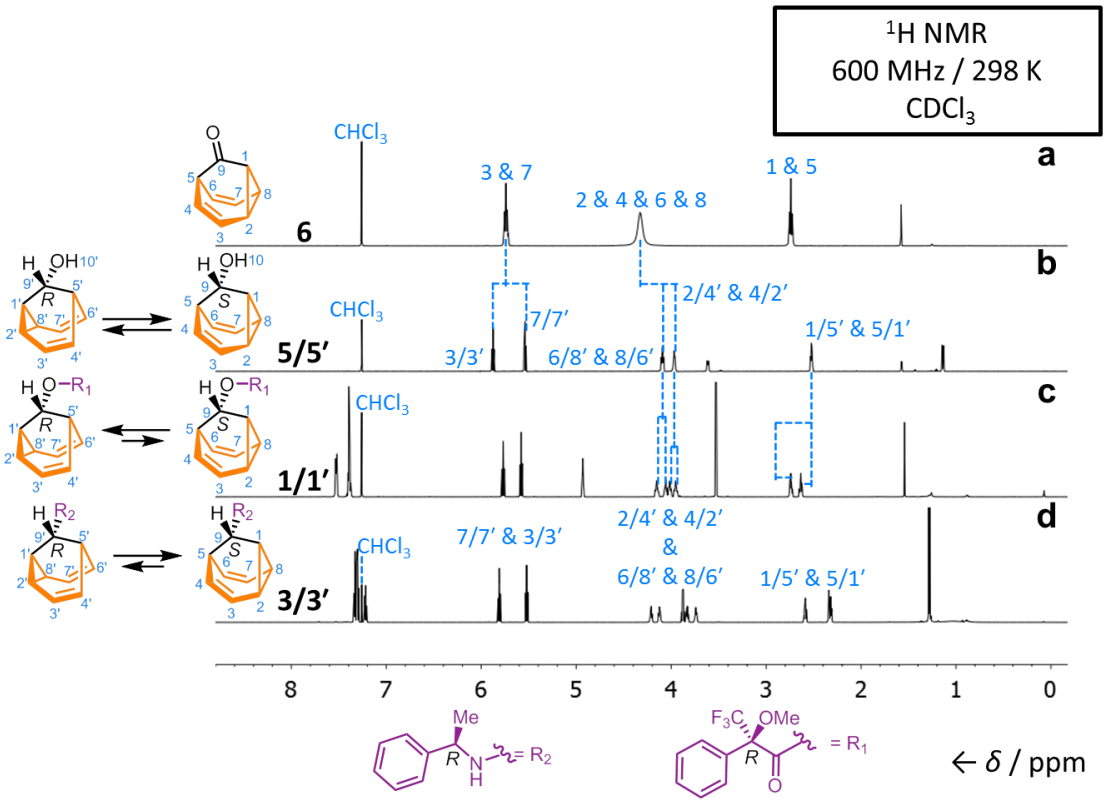

Figure 3.3. Partial ^{1}H NMR spectra of (a) barbaralone (**6**), (b) barbaralol (**5**/**5′**), (c) barbaralane (Mosher's ester) **1**/**1′** and (d) barbaralane (chiral amine) **3**/**3′**. The spectra show the sequential desymmetrisation of the barbaralyl core with environments splitting as they become chemically inequivalent.

Although, desymmetrisation takes place, the chiral tether molecules still exist in solution as a mixture of interconverting nondegenerate diastereoisomers. Since barbaralol **5**/**5′** in the solution state interconverts between two degenerate isomers, the equilibrium constant, *K*, is 1.0 and therefore the averaged peaks are exactly half way between the two individual structures in exchange.[19] For example, the proton signal corresponding to position 2/4′ is exactly halfway between the signals for 2 and 4′ if

two structures were fixed in either state. The positions of the four peaks of barbaralane **1**/**1′** (Figure 3.3c) are comparable to the position of the same peaks in barbaralol **5**/**5′** suggesting that the energy difference between the diastereomeric states is small. Comparing the position of the four central peaks of barbaralane **1**/**1′** (Figure 3.3c) against those of barbaralane **3**/**3′** (Figure 3.3d) shows a greater separation, which also suggests that the energy difference for barbaralane **3**/**3′** is larger than for barbaralane **1**/**1′** (Figure 3.3d). The position of the four central peaks also suggests that the equilibrium constant (*K*) between the two diastereoisomers is not equal to one.

The dynamics of the barbaralyl core cannot be determined through circular dichroism spectroscopic analysis, since a racemic mixture of chiral molecules of a fixed or dynamic configuration would provide no discernible difference. As the barbaralanes only interconvert between two diastereoisomers (and not enantiomers), the chirotopical response is not cancelled out. Analysis of **5**/**5′** and **6** was not conducted as a nil circular dichroism response would be expected for a racemate (**5**/**5′**) or achiral species (**6**). Analysis of the barbaralane derivatives (**1**/**1′**, **2**/**2′**, **3**/**3′** and **4**/**4′**) (Figure 3.4) with a covalently affixed chiral tether (which dominates and produces the absorption), was conducted as these species contain a chirotopic chromophore allowing for a positive Cotton effect for one enantiomer and an equal and opposite Cotton effect for the other enantiomer, confirming the presence of the two different enantiomers.[1a] Indeed, clear mirror image traces for each pair of chiral tether derivatives confirmed that the synthesised species were enantiomeric (Figure 3.4). The equilibrium distribution of the epimers formed from each unique chiral tether cannot be determined without further analysis, nor can the dynamic nature of the barbaralyl core be discerned. The Cotton effect due to the barbaralyl core likely resides outside the range of spectroscopic analysis, with a band predicted in the range just below 190 nm, due to the π-π* transition of conjugated carbon double bonds.[22]

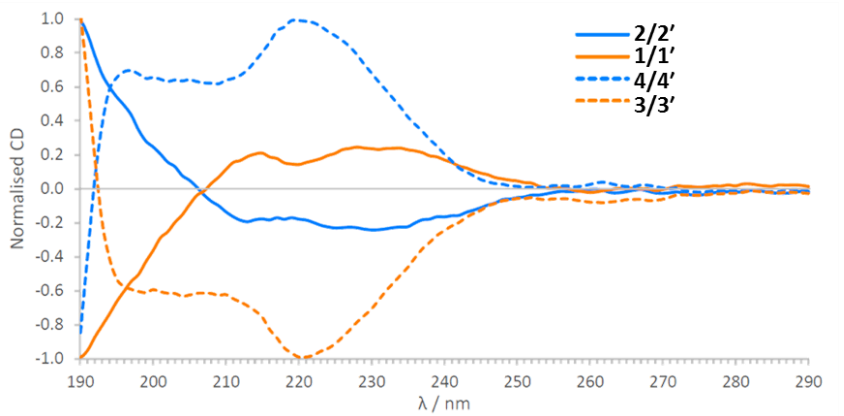

Figure 3.4. Normalised circular dichromism spectra of barbarlanes **1**/**1′** (0.040 mg mL^{-1}), **2**/**2′** (0.040 mg mL^{-1}), **3**/**3′** (0.045 mg mL^{-1}) and **4**/**4′** (0.050 mg mL^{-1}). Spectra are measured at 298 K in MeCN.

In order to probe the equilibrium further, we also recorded solution-phase ^{1}H and ^{13}C NMR spectra of covalently modified barbaralane **2**/**2′** at low temperatures ranging from 296 K to 194 K (Figure 3.5b) (Appendix, Section 3.6.1.3).[23] At room temperature, the diastereomers appear to exist in a ratio which is almost 1:1 of interconverting configurations, owing to the close proximity of the olefinic and cyclopropane chemical shifts (H_2, H_4, H_6 and H_8). Cooling below the coalescence temperature acted to separate these environments into the slow-exchange regime, so that chemical shifts are closer to those expected for a divinyl cyclopropane and for a *cis*-dialkylolefin. Analysis of the chemical shift variation as a function of temperature should have allowed quantitative evaluation of the kinetic and thermodynamic parameters determining the dynamic chirality of the carbon stereogenic centre of **2**/**2′**, but in the slow-exchange regime the equilibrium was deemed to shift explicitly in preference of the thermodynamically favoured diastereoisomer **2′** (Figure 3.5a) on account of the shift in the Boltzmann distribution at low temperature. This result was confirmed by *in silico* modelling in which conformer states and the associated energy differences between conformers were generated for barbaralanes **1**/**1′** and **3**/**3′** (Appendix, Section 3.6.1.2). Although these calculations only enable the determination of relative energies (ΔE) and not absolute Gibbs free energies (ΔG) (entropy was not taken into account), they are able to determine the thermodynamically favoured diastereoisomer in the solution state. Diastereoisomers **1**/**1′** were determined to have a ground state energy difference of ~7 $kJ{\cdot}mol^{-1}$ with the

lower energy isomer **1′** being thermodynamically favoured. On the other hand, diastereoisomers **3**/**3′** were determined to have a lower ground-state energy difference of ~3 kJ·mol^{-1}, with the lower energy isomer **3** being thermodynamically favoured. Overall, introduction of a covalently bound chiral tether of fixed absolute configuration allows the solution-state equilibrium to shift slightly in favour of the thermodynamically favoured configuration at room temperature. Upon cooling the solution-state equilibrium is shown to be dominated by the thermodynamically preferred diastereoisomer.

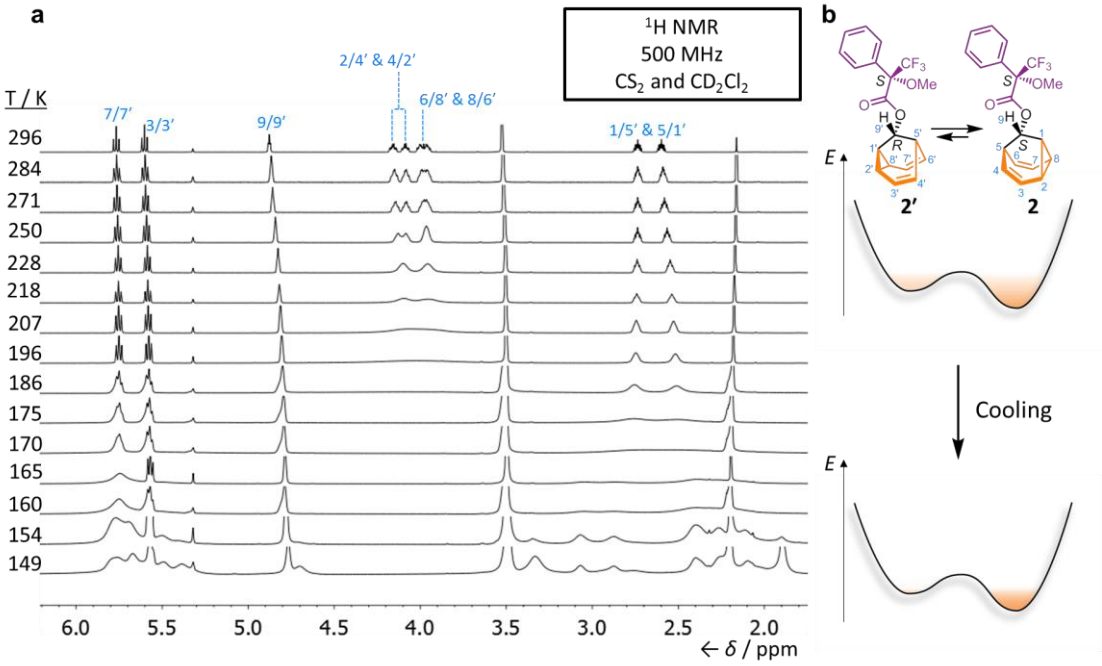

Figure 3.5. (a) Partial ^{1}H VT NMR spectra of **2**/**2′** and (b) a schematic illustration of the change in equilibrium population on a simplified potential energy surface as temperature decreases.

Barbaralanes **1**/**1′** and **2**/**2′** form crystalline solids, allowing analysis of their solid-state structures and absolute configuration by single-crystal X-ray diffraction. The fluxional mixtures, which rapidly epimerise through a strain-assisted Cope rearrangement were found to undergo dynamic preferential crystallisation,[24] *i.e.*, just one diastereoisomer from each pair of fluxional carbon cages crystallises from the mixture (Figure 3.6) (Appendix, Section 3.6.1.4).[25] Barbaralane **1**/**1′** dynamically preferentially crystallised as the thermodynamically favoured diastereoisomer (**1′**) with calculations also showing that **1′** was ~7 kJ·mol^{-1} lower in energy compared to

1. Barbaralane **2**/**2′** also crystallised as its thermodynamically favoured diastereoisomer (**2**). This thermodynamic preference biases the equilibrium distribution in solution in favour of the preferred diastereoisomer and results in its selective crystallisation in the solid state. The absolute configuration of the solution-phase dynamically chiral barbaralyl stereocentre can be controlled through covalent attachment of a Mosher's acid chiral tether allowing for its subsequent dynamic preferential crystallisation. Linking an enantiopure motif with fixed chirality to the barbaralane core has biased the solution-phase equilibrium in favour of the preferred diastereomer and crystallisation has fixed it in an enantiopure solid-state structure.

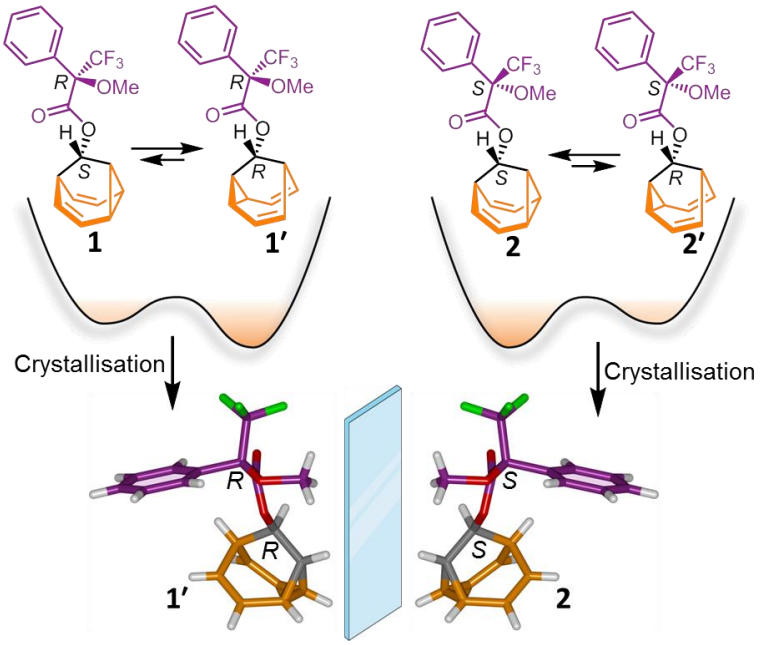

Figure 3.6. Barbaralanes **1**/**1′** and **2**/**2′** showing their solution-phase diastereoisomers interconverting at room temperature with a schematic illustration showing the relative stereochemistry. Through dynamic preferential crystallisation a single enantiomer was resolved in the solid state as confirmed by X-ray crystallography.

Interconverting diastereoisomeric mixtures of barbaralanes **3**/**3′** and **4**/**4′** formed oils at room temperature but changed to solids in cooler temperatures. Barbaralanes **3**/**3′** dynamically preferentially crystallised as diastereoisomer **3** which was predicted to be the thermodynamically favoured diastereomer by ~3 $kJ \cdot mol^{-1}$. The X-ray diffraction-quality crystal obtained gave a weak data set (with a Flack parameter of 5.6)[26] which allowed for elucidation of the molecular structure and relative stereochemistry, but not absolute assignment of configuration (Appendix, Section 3.6.1.4). Since the

absolute configuration of the 1-phenylethylamine was known and its retention in the barbaralane confirmed by circular dichroism spectroscopy, the absolute configuration of the sp^3–carbon stereocentre could be determined. While the 1-phenylethylamine chiral tether displays the same potential for control as the Mosher's acid tether – instead favouring the stereocentre opposite to the chiral tether – the difficulty in obtaining a crystalline material only allows for control in solution and partial control in the solid state.

Having determined that barbaralanes **1**/**1′** and **2**/**2′** preferentially crystallise as the thermodynamically favoured diastereoisomer, their solid-state structures were probed further through ^{13}C solid-state NMR (ssNMR) spectroscopy. ssNMR experiments were performed for barbaralane **1′** (Appendix, Section 3.6.1.5). Comparison to the low-temperature solution-phase ^{13}C NMR spectrum of **2** (Figure 3.7) supports the hypothesis that the diastereoisomer with the same sp^3–carbon stereocentre and chiral tether (*i.e.*, *R* and *R*) is the thermodynamically favoured diastereisomer and that the equilibrium is slightly shifted in solution at room temperate but is dominant at low temperatures. While direct comparison of the same derivative analysed by both solid-state NMR and VT NMR spectroscopy would have been more desirable, the two derivatives are enantiomers of the same favoured diastereomer and thus their ^{13}C NMR spectra will be identical allowing for analysis. Although, the higher frequency resonances of the ^{13}C ssNMR spectrum are poorly separated, they match well with the experimental solution and simulated solid-state spectra (Figure 3.7), allowing for the reliable assignment of the lower frequency section of the NMR in all three spectra.

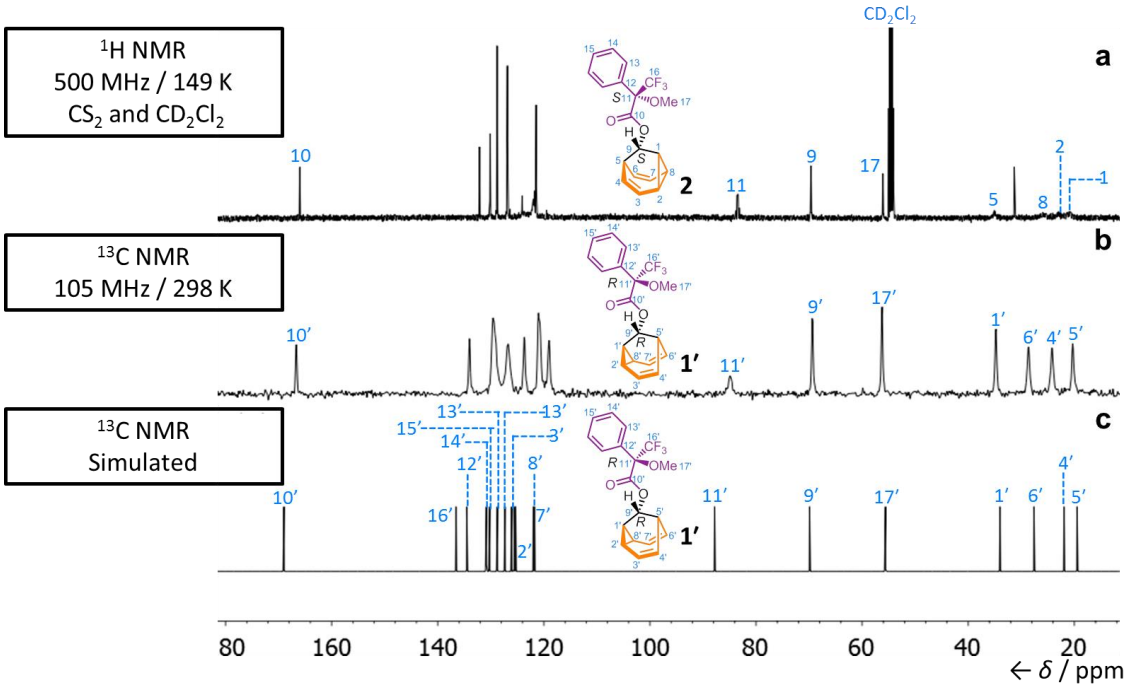

Figure 3.7. Comparison of ^{13}C NMR spectra of **1′** and **2** under different conditions: (a) barbaralane **2** in a CS_2–CD_2Cl_2 solution at 149 K, (b) barbaralane **1′** in the solid state, and (c) the calculated solid-state spectrum of **1′**.

3.2.2 Noncovalent Control over a Fluxional sp^3–carbon Stereocentre

Investigations so far feature a covalently bound chiral tether to a barbaralane core, creating a set of diastereoisomers, which in turn allows for the covalent control of the barbaralanes' fluxional sp^3–carbon stereocentre in solution and in the solid state. We were interested to see whether we could control the fluxionality of the sp^3–carbon stereocentre (in solution and in the solid state) without using an affixed chiral tether, but instead utilising chiral macrocycles such as cyclodextrins to induce the control through noncovalent bonding interactions.

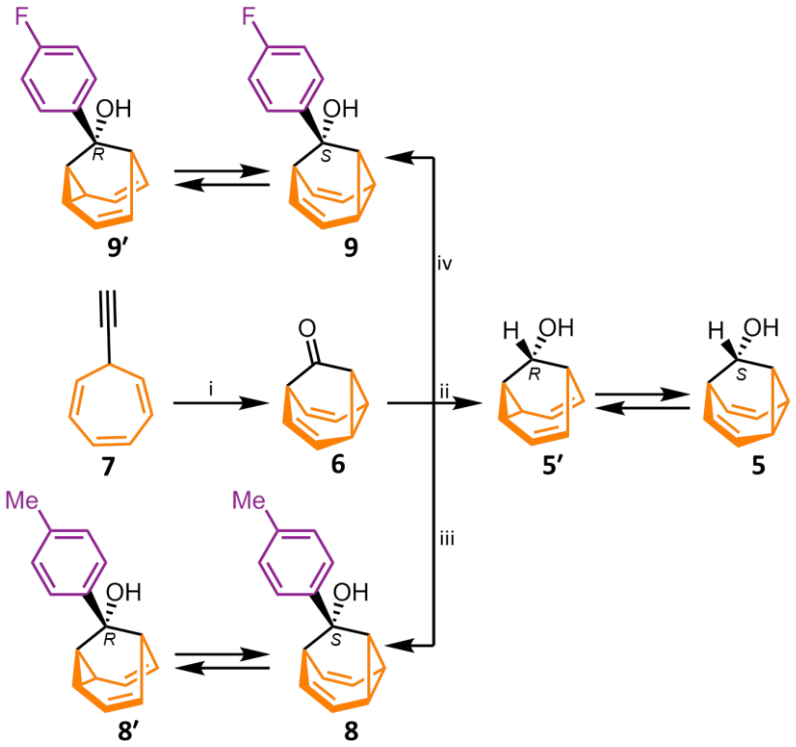

Scheme 3.2. Synthesis of barbarlanes **8**/**8′** and **9**/**9′**. Reagents and conditions: (i) IPrAu(MeCN)BF_4 (5 mol%), Ph_2SO (2 equiv.), CH_2Cl_2, rt, 16 h, 60%; (ii) $LiAlH_4$, Et_2O, 0 °C, 3 h, 78%; (iii) magnesium turnings, THF, 4-bromotoluene, reflux to rt then **6**, 0 °C to rt, 80%; (iv) magnesium turnings, THF, 1-bromo-4-fluorobenzene, reflux to rt then **6**, 0 °C to rt, 67%. IPr = 1,3-bis(2,6-diisopropylphenyl)imidazol-2-ylidene.

We synthesised two sets of nondegenerate fluxional barbaralanes (**8**/**8′** is one set of nondegenerate fluxional barbaralanes and **9**/**9′** is another set of nondegenerate fluxional barbaralanes) in two steps from alkynyl cycloheptatriene precursor **7**. Gold-catalysed cycloisomerisation of **7** proceeds through a fleeting barbaralyl cation intermediate which is oxidised by diphenyl sulphoxide to afford barabarlone (**8**). Subsequent addition of arylmagnesium bromides to **6** generates the barbaralanes bearing a tertiary alcohol and one aromatic ring. Structural assignment of barbaralanes **8**/**8′** and **9**/**9′** has been completed using two-dimensional NMR techniques (Appendix, Section 3.6.2.1). Barbaralanes **8**/**8′** are enantiomers of one another and when observed by solution-phase NMR spectroscopy, the chemical shifts prove to represent an average of two different chemical environments (a divinylcyclopropane and a *cis*-dialkylolefin), providing conclusive evidence for the

interconversion between the enantiomers (Figure 3.8). Barbaralanes **9**/**9′** are also a set of enantiomers also showing the same interconversion.

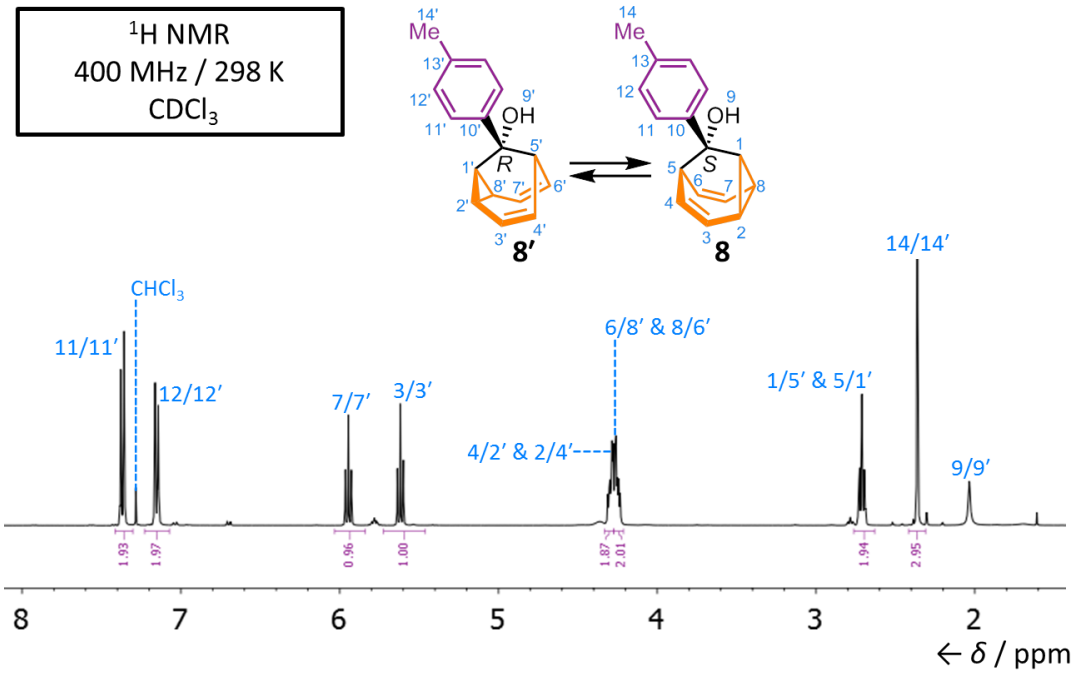

Figure 3.8. Partial ^{1}H NMR spectrum of barbaralane **8**/**8′** demonstrating the presence of two interconverting enantiomers.

At room temperature barbaralone's (**6**) ^{1}H NMR spectrum contains a broad singlet consisting of the cyclopropane and olefinic environments (Figure 3.9a). Upon the addition of a stereogenic centre (as observed with **8**/**8′**), two enantiomers are formed (removing an internal mirror plane) resulting in the cyclopropane and olefinic environments splitting into two inequivalent peaks (Figure 3.9b) – similar to that of barbaralol **5**/**5′**. Upon encapsulation within a chiral cyclodextrin (CD) host, such as β-CD, the remaining mirror plane is removed, allowing the barbaralane to become desymmetrised entirely (Figure 3.9c). Therefore, the two cyclopropane and olefinic environments split even further into four distinct peaks. Although desymmetrisation takes place, **8**/**8′** still exists as enantiomers in solution and although it is unknown as to which enantiomer is favored in the solution state, there is substantial evidence that the barbaralane molecules 'feel the presence' of the chiral environment provided by the CD. Upon comparing the chemical shift of the four distinct peaks (~4.4 ppm) (Figure 3.9c) against those of barbaralol (**5**/**5′**) in Figure 3.3, the energy difference

between the two enantiomers in the presence of CD is suggested to be small (due to the close proximity of the peaks). However, since the absolute chemical shifts of the pure static enantiomers in the presence of β-CD cannot be determined, the energy difference cannot be calculated and neither can the determination of which enantiomer is thermodynamically favoured.

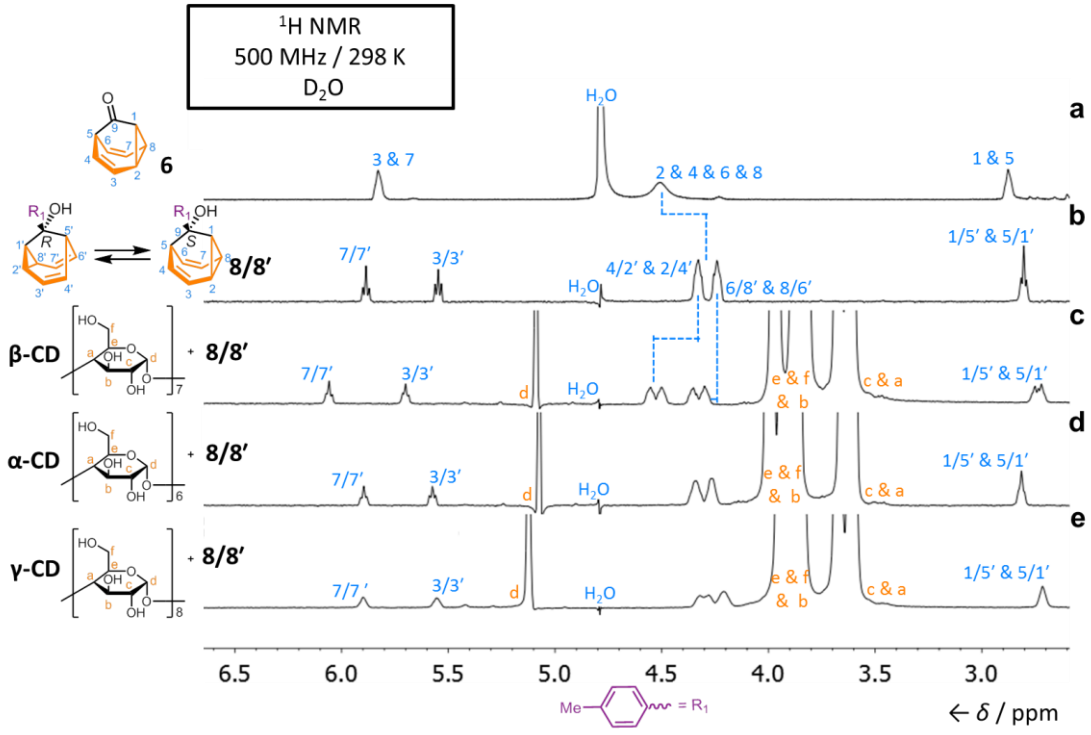

Figure 3.9. Partial ^{1}H NMR spectra of (a) barbaralone (**6**) (13.5 mM) (**6**), (b) barbaralane **8**/**8′** (4.0 mM), (c) barbaralane **8**/**8′** (4.0 mM) and β-CD (8.0 mM), (d) barbaralane **8**/**8′** (4.0 mM) and α-CD (8.0 mM) and (e) barbaralane **8**/**8′** (4.0 mM) and γ-CD (8.0 mM). Spectra shown in panels b-e have been acquired using presaturation with Robust-5 and PROJECT pulse sequences to suppress the water signal.

Initial solution-phase ^{1}H NMR studies of barbaralane **8**/**8′** with either α-, β- or γ-cyclodextrin (CD) demonstrate that β-CD binds more strongly than α-CD or γ-CD (Figure 3.9). The stronger binding is evident as upon the addition of β-CD to **8**/**8′**, the cyclopropane and olefinic environments split into four distinct peaks, whereas upon the addition of γ-CD only a small splitting in the peaks is observed. A larger change in the chemical shift is also observed with β-CD. α-CD does not demonstrate any splitting or shifting in the cyclopropane and olefinic environments. Studies into determining which CD binds more strongly with **5**/**5′** and **6** were also conducted

however; all CDs demonstrated a similar change in the chemical shift (Appendix, Section 3.6.2.2). Due to barbaralane **8**/**8′** showing a stronger interaction with β-CD and solubilising in D_2O much better than barbaralane **9**/**9′**, all binding studies have been conducted with **8**/**8′**.

In order to determine the strength of the binding event between barbaralane **8**/**8′** and β-CD as well as the stoichiometry, binding constants were calculated through ^{1}H NMR titrations (Appendix, Section 3.6.2.3). Conducting an NMR titration at different concentrations (for the same host–guest complex) and observing similar binding constants within the same stoichiometry model allows for the determination of the stoichiometry of interactions (*i.e.*, one-to-one or two-to-one) as well as the association constant (K_a).[27] A titration of β-CD (12.33 mM) into **8**/**8′** (1.23 mM) was carried out in D_2O such that a ^{1}H NMR spectrum was acquired after each addition of β-CD (Figure 3.10). The spectra show that as more of the chiral macrocycle is added to a solution of **8**/**8′**, the two equivalent positions representing the cyclopropane and olefinic environments (2/4′, 4/2′, 6/8′ and 8/6′) split into four inequivalent chemical environments. Positions 1/5′ and 5/1′ also demonstrate a change in multiplicity. Without any β-CD, the signal is a clear triplet, but upon the addition of β-CD the signal changes to a multiplet representing two overlapping, inequivalent resonances. The ^{1}H NMR titration was repeated at a different concentration (β-CD at 6.16 mM and **8**/**8′** at 0.62 mM) and the same results were observed. The stoichiometry was determined[27] and the data was fit using BindFit[28] (the chemical shifts of positions 11/11′, 12/12′, 3/3′ and 7/7′ were plotted) and two optimisation algorithims (Nelder-Mead[29] and L-BFGS-B[30]) for comparative reasons (Figure 3.11). The data fit a one-to-one binding isotherm with an average association constant of 5.5×10^3 M^{-1} ± 2.81%. The same experiments were conducted for **5**/**5′** (plotting the chemical shifts for positions 3/3′, 7/7′, 1/5′ and 5/1′) and **6** (plotting the chemical shifts for positions 3, 7, 1 and 5). Barbaralol (**5**/**5′**) and barbaralone (**6**) both also fit a one-to-one binding isotherm with smaller average association constants of 7.8×10^2 M^{-1} ± 3.10% and 9.0×10^2 M^{-1} ± 2.87%, respectively (Appendix, Section 3.6.2.3).

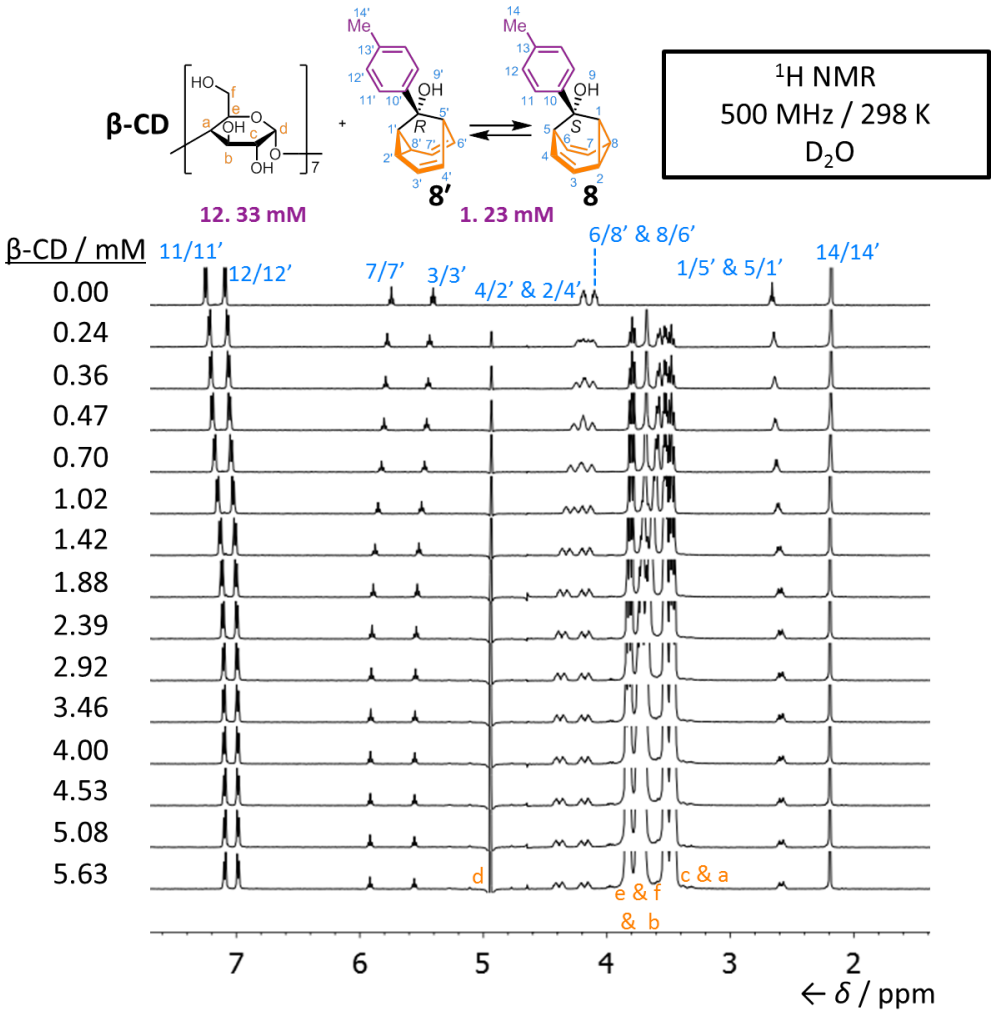

Figure 3.10. Partial ^{1}H NMR spectra of barbarlane **8**/**8′** (1.23 mM) solutions containing different concentrations of β-CD. All spectra have been acquired using presaturation with Robust-5 and PROJECT pulse sequences to suppress the water signal.

Given that the literature shows adamantane and its derivatives (which are structurally similar to barbaralone (**6**)) forming a one-to-one inclusion complex with β-CD[31] where association constants typically in the range of 10^3–10^4,[32] our results agree rather well, and confirm that **8**/**8′**, **5**/**5′** and **6** form one-to-one inclusion complexes with characteristic association constants for small organic molecules. These results demonstrate that **8**/**8′** has a stronger association constant (six-fold enhancement) to β-CD in comparison to **5**/**5′** and **6**. The stronger association constant suggests that the presence of an aromatic group contributes positively in the binding event with the chiral CD. The results also suggest that the size of the molecule may allow for

enhanced binding interactions (*i.e.*, barbaralane **8**/**8′** is larger in size compared to **5**/**5′** and **6**).

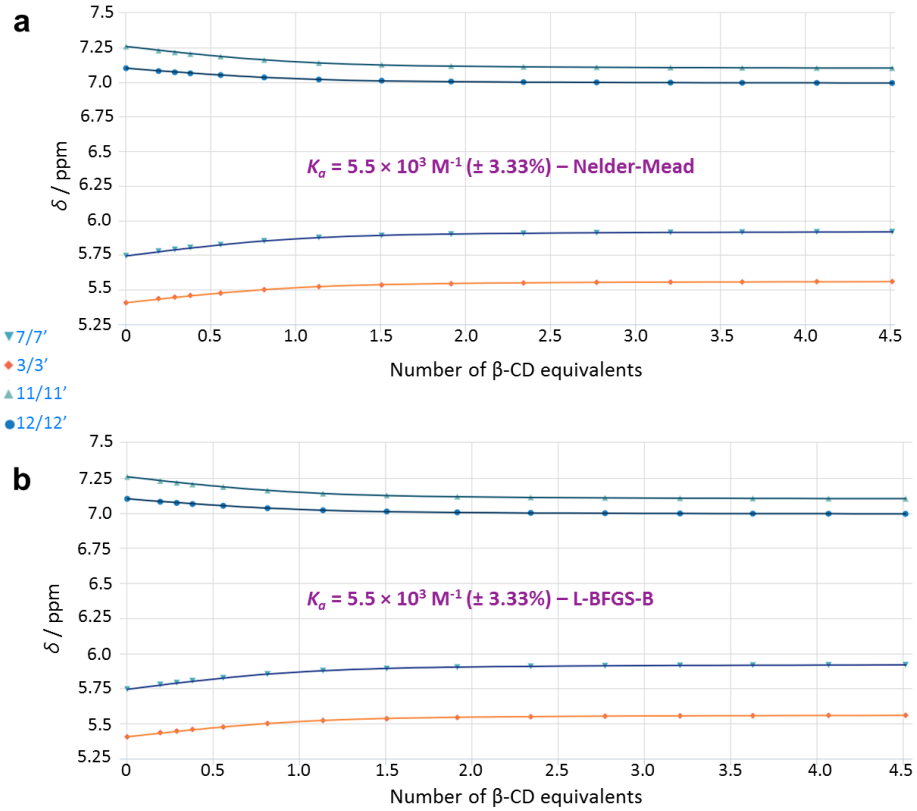

Figure 3.11. Chemical shifts (ppm) plotted against number of β-CD equivalents and fit to a one-to-one binding curve using the (a) Nelder-Mead algorithm or the (b) L-BFGS-B algorithm. Association constants are given with their respective errors. Proton labels correspond to those shown in Figure 3.10.

Binding constants between small organic molecules – such as 1-carboxylic acid substituted adamantanes – and β-CD are known to be weakened in the presence of solvents other than water.[33] Even small amounts (5%) of DMSO are known to reduce the affinity significantly.[33a] As our desired control over a fluxional sp^3–carbon stereocentre relies on the noncovalent bonding interactions between the barbaralane molecules and the β-CD to control the fluxional sp^3–carbon stereocentre, our investigations must be completed in water. Therefore, we are unable to complete low-temperature NMR measurements (below 0 °C) to determine which enantiomer in the presence of β-CD is favoured. Due to our inability to determine which enantiomer is favoured in the solution state, our efforts moved towards the solid state.

We primarily observed dynamic disorder within single crystal X-ray diffraction analysis, therefore in order to halt the dynamic disorder, we synthesised two new barbaralane molecules (**10**/**10′** and **11**/**11′**) while unexpectedly generating a third (**12**/**12′**/**12″**). Barbaralane **10**/**10′** was chosen in hope that a bulkier group would fit in a better manner inside the β-CD, whereas **11**/**11′** was chosen to form strong hydrogen bonds with the outside hydrophilic ring of the β-CD, allowing for the dynamic disorder observed in the solid state to be diminished.

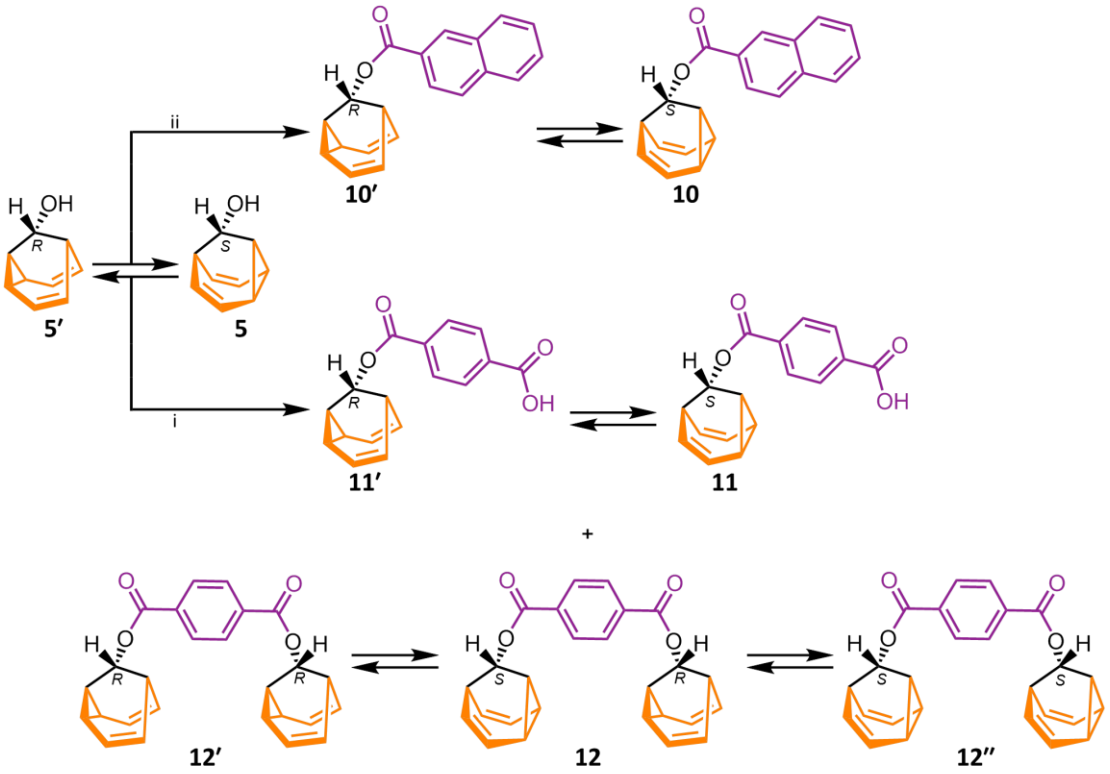

Scheme 3.3. Synthesis of barbaralanes **10**/**10′**, **11**/**11′** and **12**/**12′**/**12″**. Reagents and conditions: (i) terephthaloyl chloride, $CHCl_3$, DMAP, Et_3N, 25% (**11**/**11′**) and 27% (**12**/**12′**/**12″**); 2-naphthoyl chloride, $CHCl_3$, barbaralol, DMAP, Et_3N, 80%.

The barbaralanes are synthesised using the same esterification methodology as previously described (Scheme 3.1) in 25–80% yields. Interestingly, the reaction of terephthaloyl chloride with barbaralol (**5**/**5′**) also resulted in a dimeric barbaralane species which was found to interconvert between three stereoisomers at room temperature through Cope rearrangements. The interconversion was evidenced by averaged ^1H and ^{13}C NMR spectra. A crystal of the dimeric barbaralane species

suitable for X-ray diffraction was grown and the structure preferentially crystallised as the *meso*-diastereoisomer (**12**) (*i.e.*, *R* and *S*) (Appendix, Section 3.6.2.4). The dimeric barbaralane represents one of the first molecular structures capable of accessing three stereoisomers due to the dynamic chirality of the fluxional sp^3–carbon stereocentre.

During our time synthesising the newer barbaralane series, we were able to obtain a single crystal suitable for X-ray diffraction of barbaralol **5**/**5′** and β-CD which did not display dynamic disorder (Figure 3.12). The single crystals were grown by the slow cooling of an aqueous solution of the two compounds in a 1:1 ratio from 100 °C to room temperature over the course of two weeks which was followed by slow evapouration of the solution.

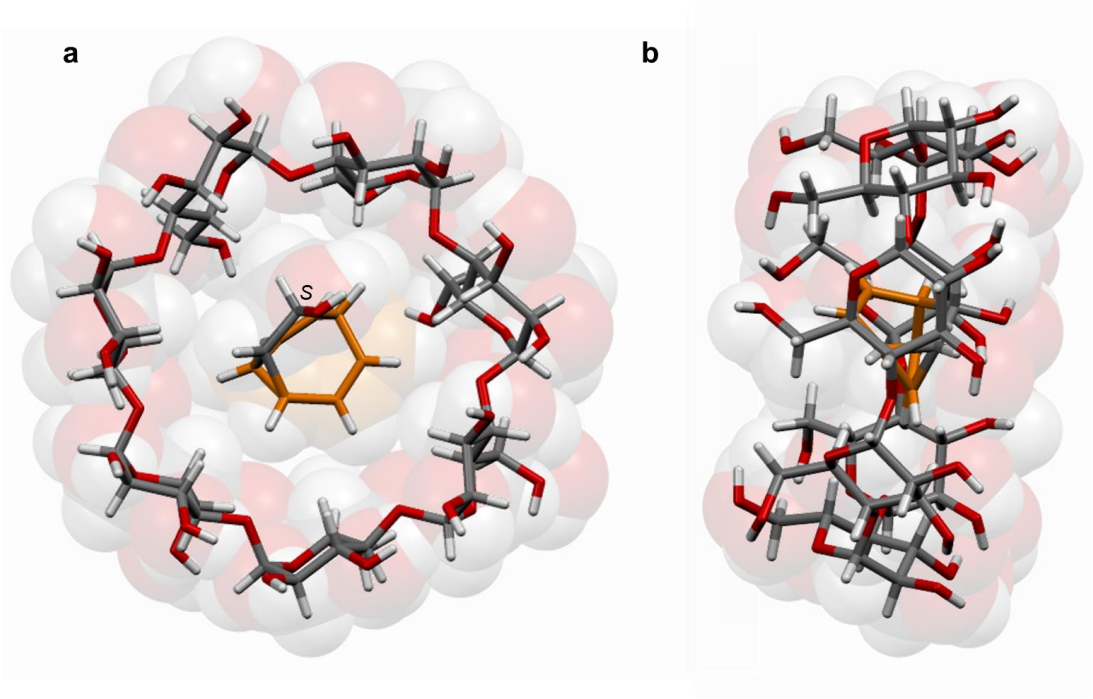

Figure 3.12. Solid-state superstructure of the host–guest complex, β-CD and barbaralol **5** as viewed (a) from above and (b) from the side.

The crystal structure confirms that a host–guest complex is formed with a one-to-one binding stoichiometry authenticating our results derived from the ^{1}H NMR titrations. The guest was observed to preferentially crystallise as the *S*-enantiomer demonstrating that the chiral CD allows for noncovalent control over the fluxional

sp^3–carbon stereocentre in the solid state (barbaralol **5**/**5′** itself crystallises as a racemate (Appendix, 3.6.2.4)). The dynamic chirality is observed to be halted in the solid state and pushed completely towards the *S*-enantiomer showing that the dynamic chirality properties are dependent on the noncovalent bonding interactions with the chiral CD.

3.3 Conclusions

In summary, by investigating the dynamic chirality of barbaralane molecules which contain a fluxional sp^3–carbon stereocentre, we have found that by covalently linking a chiral tether we can slightly skew the solution-state equilibrium at room temperature towards a thermodynamically favoured diastereoisomer. At low temperatures, the Boltzmann distribution shifts almost entirely towards this thermodynamically preferred diastereoisomer. The dynamic chirality is arrested in the solid state, forming only the thermodynamically favoured diastereoisomer and demonstrating that the dynamic chirality properties are dependent on the barbaralane's environment (*i.e.*, the addition of an affixed chiral tether). Controlling the same fluxional sp^3–carbon stereocentre through noncovalent bonding interactions with β-CD is currently ongoing. At present, the solution-state equilibrium (with the chiral CD) cannot be determined, but association constants are similar to those of small organic molecules, confirming that a binding event is taking place through noncovalent bonding interactions. Solid-state analysis confirms that a host–guest complex is formed with a one-to-one binding stoichiometry validating our solution-state experiments. Through noncovalent bonding interactions we see that the dynamic chirality of the sp^3–carbon stereocentre is halted in the solid state, showing that the *S*-enantiomer for barbaralol **5**/**5′** preferentially crystallises in the presence of a chiral β-CD. The chiral CD is imperative in controlling the sp^3–carbon stereocentre through noncovalent bonding interactions. Although this work is currently ongoing, these results represent an unprecedented example of dynamic chirality and can disclose innovative approaches to enantioselective sensing. Considering the central role of chirality in chemistry, and the fact that dynamic chirality is often overlooked, studies of this kind have not only

exciting implications for basic science but also open new avenues for the development of molecular devices and materials for practical applications.

3.4 Future Work

Future experiments will continue to be directed towards noncovalent control of a fluxional sp^3–carbon stereocentre using the chiral macrocycle β-CD. *In silico* calculations will be performed to help identify the thermodynamically preferred enantiomer (in the solution state) for both barbaralanes (**8**/**8′** and **9**/**9′**) and barbaralol (**5**/**5′**) when in the presence of β-CD. *In silico* calculations will also determine the preferred enantiomer in the solid state for the two barbaralanes **8**/**8′** and **9**/**9′**. In parallel, the solid-state ^{13}C NMR shifts of both enantiomers of barbaralanes (**8**/**8′** and **9**/**9′**) and barbaralol (**5**/**5′**) in the presence of β-CD will also be calculated. The crystalline solids of β-CD and barbaralol **5**/**5′** will undergo solid-state ^{13}C NMR experiments and be compared against the calculated solid-state ^{13}C NMR shifts for further corroboration. Through these experiments we will be able to determine the thermodynamically favoured enantiomer for all compounds in solution and in the solid state, proving that full control of the fluxional sp^3–carbon stereocentre through noncovalent bonding interactions is possible.

3.5 Experimental Details

3.5.1 Specific Experimental Methods

For general experimental details see page *xix*. Solution-state ^{1}H NMR spectra for barbaralone (**6**), barbaralol (**5**/**5′**) and barbaralane (**8**/**8′**) with either α-CD, β-CD or γ-CD were acquired on a Varian Inova-500 (^{1}H 500.130 MHz and ^{13}C 125.758) MHz spectrometer with either presaturation or a pulse sequence combining Robust-5 and PROJECT pulse sequences.[34] Solid-state ^{13}C NMR spectra were obtained at 100.63 MHz using a Bruker Avance III HD spectrometer and a 3.2 mm (rotor outside diameter) magic-angle spinning probe. Spectra were recorded using cross polarisation with TOSS spinning sideband suppression with a 120 s recycle delay, 1 ms contact time, at a spin-rate of 10 kHz at 20 °C. Spectral referencing was with respect to external, neat tetramethylsilane (referencing was carried out by setting the high-frequency signal from adamantane to 38.5 ppm). The X-ray single-crystal diffraction data were collected at 120.0(2) K using λMoKα radiation (λ = 0.71073 Å) on either a Bruker D8Venture (Photon100 CMOS detector, IμS-microsource, focusing mirrors) diffractometer for barbaralanes **3** and **8**/**8′**, barbaralol **5**/**5′**and the host–gust complex of β-CD and barbaralol **5** or an Agilent XCalibur (Sapphire-3 CCD detector, fine-focus sealed tube, graphite monochromator) diffractometer for barbaralanes **1′**, **2**, **11**/**11′** and **12**. Both diffractometers were equipped with Cryostream (Oxford Cryosystems) open-flow nitrogen cryostats. All structures were solved by direct method and refined by full-matrix least squares on F2 for all data using Olex2[35] and SHELXT[36] software. All non-hydrogen atoms were refined anisotropically and hydrogen atoms were placed in the calculated positions and refined in riding mode. Circular dichroism spectroscopy was carried out at 20 °C in a Jasco J-1500 spectrometer, provided with a MCB-100 mini circulation bath from the same brand. All samples were recorded as the average of 6 scans (1.00 nm data pitch, continuous scanning mode, 50 nm min, 1 scanning speed, 3 nm bandwidth) using a QS high-precision cell with 0.1 cm of path length from Hellma Analytics.

3.5.2 Synthesis of Chiral Tethers

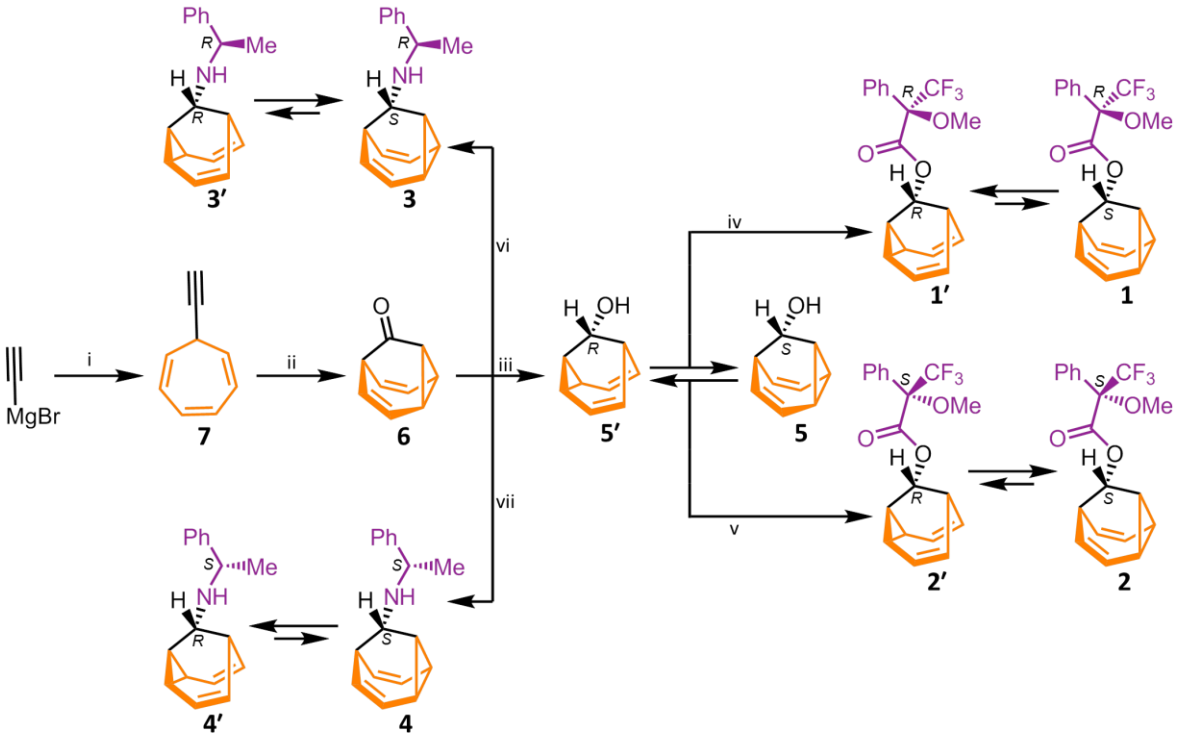

Scheme 3.4. Synthesis of compounds **7**, barbaralone (**6**), barbaralol (**5**/**5′**), (*R*)- and (*S*)-Moshers ester (**1**/**1′** and **2**/**2′**) and (*R*)- and (*S*)-phenylamine (**3**/**3′** and **4**/**4′**). Reagents and conditions: (i) LiCl / THF / tropylium tetrafluoroborate / –78 °C to rt, (ii)IPrAu(MeCN)BF_4 (5 mol%) / Ph_2SO (2 equiv.) / CH_2Cl_2 / rt / 16 h, (iii) $LiAlH_4$ / Et_2O / 0 °C / 3 h, (iv) $(COCl)_2$ / (*R*)-(+)-Mosher's acid / hexanes / DMF / 90 min / rt then DMAP / $CHCl_3$ / Et_3N / rt / 5 d, (v) $(COCl)_2$ / (*S*)-(–)-Mosher's acid / hexanes / DMF / 7 h, / rt then DMAP / $CHCl_3$ / Et_3N / rt / 3 d, (vi) (*R*)-(+)-1-phenylethylamine / CH_3COOH / 30 min / $NaBH_3CN$ / rt / 13 d, (vii) (*S*)-(–)-1-phenylethylamine / CH_3COOH / 30 min / $NaBH_3CN$ / rt / 13 d. IPr = 1,3-bis(2,6-diisopropylphenyl)imidazol-2-ylidene.

7-Ethynylcyclohepta-1,3,5-triene (7)

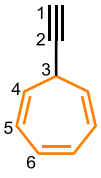

Anhydrous LiCl (0.524 g, 12.40 mmol) was placed in an oven-dried round-bottomed flask fitted with a septum under an N_2 atmosphere. Anhydrous THF was added (38 mL) and the resulting solution was cooled to –78 °C before adding a solution of ethynyl magnesium bromide (22.5 mL, 12.2 mmol, 0.5 M in THF) and stirring for 10 min at this temperature. Tropylium tetrafluoroborate (1.00 g, 5.62 mmol) was added to the reaction mixture and the reaction mixture was stirred for 16 h, where the temperature was raised to rt, following removal of the ice bath. The reaction was quenched with a saturated

aqueous solution of NH_4Cl (20 mL), then extracted with Et_2O (3 × 30 mL). The combined organic extracts were then dried over $MgSO_4$, filtered and the solvent removed under reduced pressure (rotary evaporator bath at 16 °C, ≥ 100 mbar). The crude residue was purified by column chromatography (Teledyne Isco CombiFlash Rf+ system, 24 g SiO_2, *n*-pentane) to give the title compound as a colouress oil (539 mg, 4.6 mmol, 83%). **^{1}H NMR** (600 MHz, $CDCl_3$) δ 6.66 (dd, *J* = 3.7, 2.7 Hz, 2H, H_6), 6.33 – 6.07 (m, 2H, H_5), 5.40 – 5.16 (m, 2H, H_4), 2.73 – 2.43 (m, 1H, H_3), 2.17 (d, *J* = 2.6 Hz, 1H, H_1). **^{13}C NMR** (151 MHz, $CDCl_3$) δ 131.2 (C_6), 125.1 (C_5), 123.0 (C_4), 85.8 (C_2), 68.5 (C_1), 31.5 (C_3). **HRMS-ASAP** *m/z* = 117.0701 $[M+H]^+$ (calculated for C_9H_9 = 117.0704).

Spectroscopic data were consistent with those published previously.[19b]

Tricyclo[3.3.1.0^{2,8}]nona-3,6-dien-9-one (6)

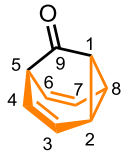

7-Ethynylcyclohepta-1,3,5-triene (1.0 g, 8.68 mmol) and diphenyl sulphoxide (3.51 g, 17.0 mmol) were charged in a flask and dissolved in anhydrous CH_2Cl_2 (15 mL) at 25 °C, with no particular precautions taken to exclude air. (Acetonitrile)[1,3-bis(2,6-diisopropylphenyl)-imidazol-2-ylidene]gold(I) tetrafluoroborate (309 mg, 0.43 mmol, 5 mol%) was added in one portion at the same temperature and the reaction mixture was stirred for 16 h. The reaction was quenched with 10 drops of Et_3N and the solvent was removed under reduced pressure. The crude residue was purified by column chromatography (Teledyne Isco CombiFlash Rf+ system, 24 g SiO_2, hexanes−EtOAc, gradient elution) to give the title compound as a light yellow solid (685 mg, 5.18 mmol, 60%). **M.P.** 55 – 57 °C (lit.[19b] 50 – 51 °C). **^{1}H NMR** (700 MHz, $CDCl_3$) δ 5.97 – 5.51 (m, 2H, H_1 and H_5), 4.32 (br s, 4H, H_2 and H_4 and H_6 and H_8), 2.90 – 2.55 (m, 2H, H_3 and H_7). **^{13}C NMR** (176 MHz, $CDCl_3$) δ 211.0 (C_9), 121.7 (C_3 and C_7 or C_2, C_4, C_6 and C_8), 121.5 (C_3 and C_7 or C_2, C_4, C_6 and C_8), 38.3 (C_1 and C_5). **HRMS-ASAP** *m/z* = 133.0648 $[M-H]^+$ (calculated for C_9H_9O = 133.0653).

Spectroscopic data were consistent with those published previously.[19b]

In room temperature solutions, barbaralol (**5**/**5′**) and each of the barbaralanes (**1**/**1′**, **2**/**2′**, **3**/**3′** and **4**/**4′**) exist as mixtures of two rapidly interconverting stereoisomers. Based on our experimental observations the labelled structures for the barbaralanes (**1**/**1′**, **2**/**2′**, **3**/**3′** and **4**/**4′**) are the thermodynamically favoured species in the solution state. The NMR spectroscopic assignments below, which have been made with the aid of two-dimensional NMR techniques, are labelled according to numbering of the favoured species. However, the species are in fast exchange on account of rapid strain-assisted Cope rearrangements and the chemical shifts of each nucleus are representative of the time-averaged chemical environments they experience as part of the two diastereoisomers.

(±)-Tricyclo[3.3.1.0^{2,8}]nona-3,6-dien-9-ol (5/5′)

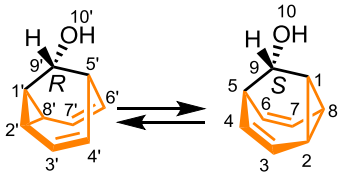

$LiAlH_4$ (120 mg, 3.16 mmol) in anhydrous Et_2O (5 mL) was placed and suspended in an oven-dried round-bottomed flask fitted with a septum under a N_2 atmosphere. The solution was cooled to 0 °C and then a solution of tricyclo[3.3.1.0^{2,8}]nona-3,6-dien-9-one (200 mg, 1.51 mmol) in anhydrous Et_2O (5 mL) was added dropwise. The reaction mixture was stirred at this temperature for 3 h. The reaction was quenched with saturated potassium sodium tartrate solution (25 mL) and allowed to warm to rt before being extracted with Et_2O (3 × 30 mL). The combined organic extracts were dried over $MgSO_4$ and the solvent was removed under reduced pressure (rotary evaporator bath at 16 °C, ≥ 100 mbar). The crude residue was purified by column chromatography (Teledyne Isco CombiFlash Rf+ system, 24 g SiO_2, *n*-pentane−Et_2O, gradient elution) to give the title compound as a white solid (159 mg, 1.18 mmol, 78%). **M. P.** 82 – 84 °C (lit.[19b] 86 – 88 °C). **^{1}H NMR** (400 MHz, $CDCl_3$) δ 5.88 (t, *J* = 7.9 Hz, 1H, H_3), 5.54 (t, *J* = 7.6 Hz, 1H, H_7), 4.16 – 4.04 (m, 2H, H_6 and H_8), 4.02 – 3.92 (m, 2H, H_2 and H_4), 3.61 (d, *J* = 3.3 Hz, 1H, H_9), 2.59 – 2.47 (m, 2H, H_5 and H_1), 1.14 (s, 1H, H_{10}). **^{13}C NMR** (151 MHz, $CDCl_3$) δ 123.3 (C_3), 120.9 (C_7), 76.5 (C_6 and C_8), 72.3 (C_2 and C_4), 62.5 (C_9), 31.8 (C_5 and C_1). **HRMS-ASAP** *m/z* = 117.0699 $[M\text{-}OH]^+$, calculated for C_9H_9: 117.0704.

Spectroscopic data were consistent with those published previously.[19b]

Tricyclo[3.3.1.0^{2,8}]nona-3,6-dien-9-yl (*R*)-3,3,3-trifluoro-2-methoxy-2-phenylproponate (1/1′)

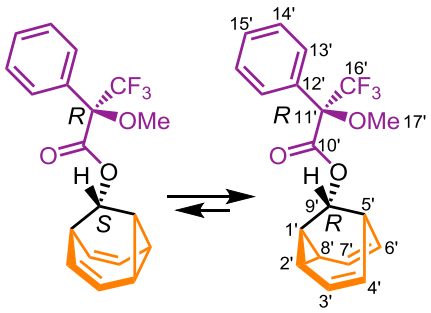

In an oven-dried round-bottomed flask fitted with a septum under a N_2 atmosphere, oxalyl chloride (100 µL, 1.18 mmol) was added to a stirred solution of (*R*)-(+)-Mosher's acid (56 mg, 0.24 mmol) in anhydrous hexanes (8 mL) and anhydrous DMF (4.8 µL, 0.06 mmol). The reaction mixture was left to stir for 7 h at rt before being left in the freezer overnight. The reaction mixture was filtered and the filtrate was removed under reduced pressure. This residue, tricyclo[3.3.1.0^{2,8}]nona-3,6-dien-9-ol (40 mg, 0.30 mmol) and DMAP (26 mg, 0.21 mmol) were dissolved in anhydrous $CHCl_3$(3 mL) before Et_3N (120 µL, 0.86 mmol) was added dropwise to the stirred reaction mixture at rt under an N_2 atmosphere. The reaction was left to stir for 3 d, after which it was quenched with a saturated solution of NH_4Cl (50 mL) and extracted with $CHCl_3$ (3 × 50 mL). The combined organic extracts were washed with H_2O (1 × 100 mL), dried over $MgSO_4$, filtered and the solvent was removed under reduced pressure. The crude residue was purified by column chromatography on SiO_2 in a pasteur pipette eluted with hexanes, to give the title compound as a white solid (66 mg, 0.19 mmol, 79%). **M.P.** 79 – 81°C. **^{1}H NMR** (700 MHz, $CDCl_3$) δ 7.60 – 7.50 (m, 2H, $H_{13'}$), 7.43 – 7.35 (m, 3H, $H_{14'}$ and $H_{15'}$), 5.77 (t, *J* = 7.9 Hz, 1H, $H_{7'}$), 5.58 (t, *J* = 7.6 Hz, 1H, $H_{3'}$), 4.94 (t, *J* = 3.2 Hz, 1H, $H_{9'}$), 4.17 – 4.14 (m, 1H, $H_{2'}$ or $H_{4'}$), 4.08 – 4.04 (m, 1H, $H_{4'}$ or $H_{2'}$) 4.03 – 4.00 (m, 1H, $H_{6'}$ or $H_{8'}$), 3.97 – 3.94 (m, 1H, $H_{8'}$ or $H_{6'}$), 3.53 (s, 3H, $H_{17'}$), 2.76 – 2.73 (m, 1H, $H_{5'}$ or $H_{1'}$), 2.65 – 2.62 (m, 1H, $H_{5'}$ or $H_{1'}$). **^{13}C NMR** (176 MHz, $CDCl_3$) δ 166.3 ($C_{10'}$), 132.3 ($C_{12'}$), 129.5 ($C_{15'}$), 128.3 ($C_{14'}$), 127.4 ($C_{13'}$), 123.3 (q, J_{CF} = 288 Hz, $C_{16'}$), 121.7 ($C_{7'}$), 121.2 ($C_{3'}$), 84.5 (d, J_{CF} = 27 Hz, $C_{11'}$), 76.1 ($C_{2'}$ or $C_{4'}$), 74.2 (C $C_{8'}$ or $C_{6'}$), 73.2 ($C_{2'}$ or $C_{4'}$), 70.7 ($C_{8'}$ or $C_{6'}$), 69.6 ($C_{9'}$), 55.4 ($C_{17'}$), 28.2 ($C_{1'}$ or $C_{5'}$), 27.7 ($C_{5'}$ or $C_{1'}$). **^{19}F NMR** (376 MHz,

$CDCl_3$) δ –75.09 (s, $F_{16'}$). **HRMS-ASAP** *m/z* = 351.1203 $[M+H]^+$, calculated for $C_{19}H_{18}O_3F_3$: 351.1208.

Tricyclo[3.3.1.$0^{2,8}$]nona-3,6-dien-9-yl (*S*)-3,3,3-trifluoro-2-methoxy-2-phenylproponate (2/2′)

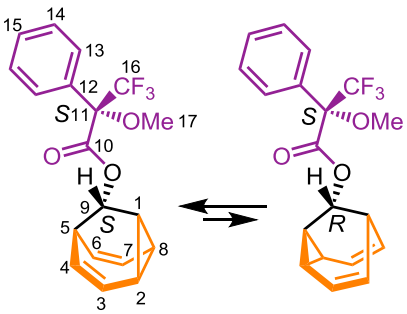

In an oven-dried round-bottomed flask fitted with a septum under a N_2 atmosphere, oxalyl chloride (50 µL, 0.58 mmol) was added to a stirred solution of (*S*)-(–)-Mosher's acid (28 mg, 0.12 mmol) in anhydrous hexanes (5 mL) and anhydrous DMF (10 µL, 0.13 mmol). The reaction mixture was left to stir for 90 min at rt before being left in the freezer for 60 h. The reaction mixture was filtered and the filtrate was removed under reduced pressure. This residue, tricyclo[3.3.1.$0^{2,8}$]nona-3,6-dien-9-ol (18 mg, 0.13 mmol) and DMAP (13 mg, 0.11 mmol) were dissolved in anhydrous $CHCl_3$ (1.5 mL) before Et_3N (55 µL, 0.39 mmol) was added dropwise to the stirred reaction mixture at rt under an N_2 atmosphere. The reaction was left to stir for 5 d, after which it was quenched with a saturated solution of NH_4Cl (25 mL) and extracted with $CHCl_3$ (3 × 25 mL). The combined organic extracts were washed with H_2O (1 × 50 mL), dried over $MgSO_4$, filtered and the solvent was removed under reduced pressure. The crude residue was purified by column chromatography on SiO_2 in a pasteur pipette eluted with hexanes, to give the title compound as a white solid (25 mg, 0.07 mmol, 58%). **M.P.** 79 – 81°C. **^{1}H NMR** (600 MHz, $CDCl_3$) δ 7.56 – 7.50 (m, 2H, H_{13}), 7.42 – 7.35 (m, 3H, H_{14} and H_{15}), 5.77 (t, *J* = 7.9 Hz, 1H, H_7), 5.58 (t, *J* = 7.6 Hz, 1H, H_3), 4.93 (t, *J* = 3.1 Hz, 1H, H_9), 4.19 – 4.12 (m, 1H, H_2 or H_4), 4.10 – 4.04 (m, 1H, H_2 or H_4), 4.04 – 3.99 (m, 1H, H_6 or H_8), 3.97 – 3.93 (m, 1H, H_8 or H_6), 3.53 (s, 3H, H_{17}), 2.77 – 2.71 (m, 1H, H_5 or H_1), 2.67 – 2.61 (m, 1H, H_1 or H_5). **^{13}C NMR** (151 MHz, $CDCl_3$) δ 166.5 (C_{10}), 132.4 (C_{12}), 129.6 (C_{15}), 128.4 (C_{14}), 127.6 (C_{13}), 123.4 (q, J_{CF} = 288 Hz, C_{16}), 121.8 (C_7), 121.3 (C_3), 84.6 (q, J_{CF} = 27 Hz, C_{11}), 76.3 (C_2 or C_4), 74.4 (C_6 or C_8), 73.4 (C_2 or C_4), 70.9 (C_6 or C_8), 69.8 (C_9), 55. 6 (C_{17}), 28.3 (C_1 or C_5), 27.8 (C_5 or C_1). **^{19}F NMR**

(376 MHz, $CDCl_3$) δ –75.09 (s, F_{16}). **HRMS-ASAP** *m/z* = 351.1213 $[M+H]^+$, calculated for $C_{19}H_{18}O_3F_3$: 351.1208.

N-(*R*)-1-(Phenylethynyl)-tricyclo[3.3.1.$0^{2,8}$]-nona-3,6-dien-9-amine (3/3′)

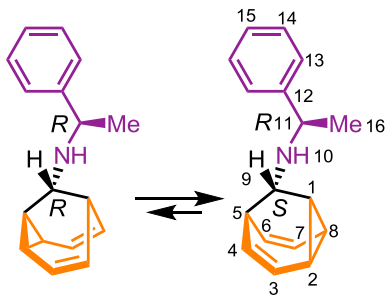

In an oven-dried round-bottomed flask fitted with a septum under a N_2 atmosphere, tricyclo[3.3.1.$0^{2,8}$]nona-3,6-dien-9-one (80 mg, 0.61 mmol) and (*R*)-(+)-1-phenylethylamine (250 µL, 1.96 mmol) were dissolved in anhydrous MeOH (0.80 mL). Glacial acetic acid (25 µL) was added dropwise to the stirred reaction mixture and left for 30 min. Sodium cyanoborohydride (50 mg, 0.80 mmol, 1.2 equiv.) was then added to the reaction mixture, which was left to stir for 13 d at rt. The mixture was quenched with 5 drops of Et_3N and the solvent was removed under reduced pressure. This material was dissolved in an aqueous solution of $NaHCO_3$ (50 mL) and extracted with CH_2Cl_2 (5 × 25 mL). The combined organic extracts were washed with brine (1 × 50 mL), H_2O (1 × 50 mL), dried over $MgSO_4$, filtered and the solvent was removed under reduced pressure. The crude residue was purified by column chromatography (Teledyne Isco CombiFlash Rf+ system, 4 g SiO_2, hexanes-EtOAc, gradient including 1% Et_3N in the elution) to give the title compound as a colourless oil (112 mg, 0.47 mmol, 78%). **^{1}H NMR** (600 MHz, $CDCl_3$) δ 7.37 – 7.28 (m, 4H, H_{13} and H_{14}), 7.22 (tt, *J* = 7.1, 1.6 Hz, 1H, H_{15}), 5.81 (t, *J* = 7.8 Hz, 1H, H_7), 5.52 (t, *J* = 7.7 Hz, 1H, H_3), 4.23 – 4.20 (m, 1H, H_2 or H_4), 4.14 – 4.11 (m, 1H, H_2 or H_4), 3.88 (q, *J* = 6.5 Hz, 1H, H_{11}), 3.85 – 3.82 (m, 1H, H_6 or H_8), 3.76 – 3.72 (m, 1H, H_6 or H_8), 2.60 – 2.57 (m, 1H, H_5 or H_1), 2.36 – 2.33 (m, 1H, H_9), 2.33 – 2.30 (m, 1H, H_1 or H_1), 1.28 (d, *J* = 6.5 Hz, 3H, H_{16}), 1.03 (br. s, 1H, H_{10}). **^{13}C NMR** (151 MHz, $CDCl_3$) δ 146.1 (C_{12}), 128.5 (C_{13}), 126.9 (C_{15}), 126.8 (C_{14}), 123.1 (C_7), 121.3 (C_3), 81.4 (C_2 or C_4), 77.5 (C_6 or C_8), 71.2 (C_2 or C_4), 67.4 (C_6 or C_8), 54.9 (C_{11}), 44.6 (C_9), 29.7 (C_1 or C_5), 29.1 (C_5 or C_1), 25.3 (C_{16}). **HRMS-ASAP** *m/z* = 238.1592 $[M+H]^+$, calculated for $C_{17}H_{20}N$: 238.1596.

_N_-(_S_)-1-(Phenylethynyl)-tricyclo[3.3.1.$0^{2,8}$]-nona-3,6-dien-9-amine (4/4′)

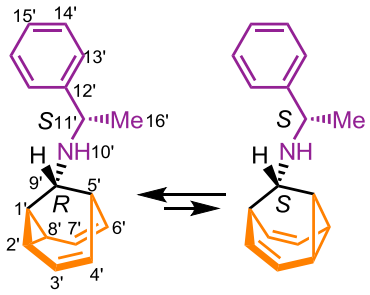

In an oven-dried round-bottomed flask fitted with a septum under a N_2 atmosphere, tricyclo[3.3.1.$0^{2,8}$]nona-3,6-dien-9-one (80 mg, 0.61 mmol) and (*S*)-(–)-1-phenylethylamine (250 µL, 1.96 mmol) were dissolved in anhydrous MeOH (0.80 mL). Glacial acetic acid (25 µL) was added dropwise to the stirred reaction mixture and left for 30 min. Sodium cyanoborohydride (50 mg, 0.80 mmol, 1.2 equiv.) was then added to the reaction mixture, which was left to stir for 13 d at rt. The mixture was quenched with 5 drops of Et_3N and the solvent was removed under reduced pressure. This material was dissolved in an aqueous solution of $NaHCO_3$ (50 mL) and extracted with CH_2Cl_2 (5 × 25 mL). The combined organic extracts were washed with brine (1 × 50 mL), H_2O (1 × 50 mL), dried over $MgSO_4$, filtered and the solvent was removed under reduced pressure. The crude residue was purified by column chromatography (Teledyne Isco CombiFlash Rf+ system, 4 g SiO_2, hexanes-EtOAc, gradient including 1% Et_3N in the elution) to give the title compound as a colourless oil (71 mg, 0.30 mmol, 49%). **^{1}H NMR** (700 MHz, $CDCl_3$) δ 7.36 – 7.28 (m, 4H, $H_{13'}$ and $H_{14'}$), 7.22 (tt, *J* = 7.2, 1.5 Hz, 1H, $H_{15'}$), 5.81 (t, *J* = 7.8 Hz, 1H, $H_{7'}$), 5.52 (t, *J* = 7.7 Hz, 1H, $H_{3'}$), 4.23 – 4.20 (m, 1H, $H_{2'}$ or $H_{4'}$), 4.14 – 4.11 (m, 1H, $H_{2'}$ or $H_{4'}$), 3.88 (q, *J* = 6.5 Hz, 1H, $H_{11'}$), 3.85 – 3.82 (m, 1H, $H_{8'}$ or $H_{6'}$), 3.76 – 3.72 (m, 1H, $H_{8'}$ or $H_{6'}$), 2.60 – 2.57 (m, 1H, $H_{5'}$ or $H_{1'}$), 2.35 – 2.33 (m, 1H, $H_{9'}$), 2.33 – 2.30 (m, 1H, $H_{5'}$ or $H_{1'}$), 1.28 (d, *J* = 6.5 Hz, 3H, $H_{16'}$), 1.03 (br. s, 1H, $H_{10'}$). **^{13}C NMR** (176 MHz, $CDCl_3$) δ 146.1 ($C_{12'}$), 128.5 ($C_{13'}$), 126.9 ($C_{15'}$), 126.8 ($C_{14'}$), 123.1 ($C_{7'}$), 121.3 ($C_{3'}$), 81.4 ($C_{2'}$ or $C_{4'}$), 77.4 ($C_{8'}$ or $C_{6'}$), 71.2 ($C_{2'}$ or $C_{4'}$), 67.4 ($C_{8'}$ or $C_{6'}$), 54.9 ($C_{11'}$), 44.6 ($C_{9'}$), 29.7 ($C_{1'}$ or $C_{5'}$), 29.1 ($C_{5'}$ or $C_{5'}$), 25.3 ($C_{16'}$). **HRMS-ASAP** *m/z* = 238.1592 [M+H]+, calculated for $C_{17}H_{20}N$: 238.1596.

3.5.3 Synthesis of Mono-Substituted Barbaralanes

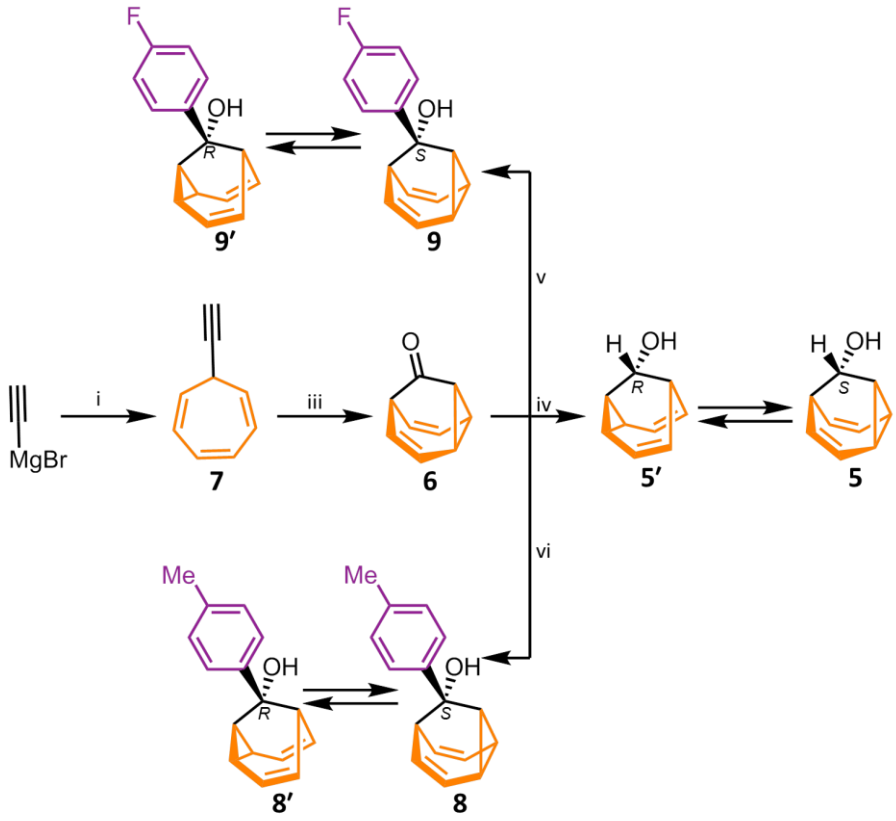

Scheme 3.5. Synthesis of compounds **7**, barbaralone (**6**), barbaralol (**5**/**5′**), tolyl barbaralane (**9**/**9′**) and fluorophenyl barbaralane (**8**/**8′**). Reagents and conditions: (i) LiCl / THF / –78 °C, (ii) tropylium tetrafluoroborate / rt, (iii) IPrAu(MeCN)BF_4 (5 mol%) / Ph_2SO (2 equiv.) / CH_2Cl_2 / rt / 16 h, (iv) $LiAlH_4$ / Et_2O / 0 °C / 3 h, (v) magnesium turnings / THF / 4-bromotoluene / reflux to rt then barbaralone / 0 °C to rt , (vi) magnesium turnings / THF / 1-bromo-4-fluorobenzene / reflux to rt then barbaralone / 0 °C to rt. IPr = 1,3-bis(2,6-diisopropylphenyl)imidazol-2-ylidene.

In room temperature solutions, each of the barbaralanes (**8**/**8′** and **9**/**9′**) exist as mixtures of two rapidly interconverting stereoisomers. For clarity, we have only labelled one of the enantiomers, but all enantiomers are in fast exchange on account of rapid strain-assisted Cope rearrangement. The chemical shifts of each nucleus are representative of the time-averaged chemical environments they experience as part of the two enantiomers.

(±)-6-(4-Tolyl)bicyclo[3.2.2]nona-3,8-dien-6-ol (8/8′)

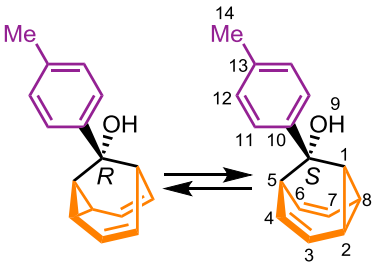

Magnesium turnings (100 mg, 4.54 mmol) and I_2 (57 mg, 0.23 mmol, 5 mol%) were placed in an oven-dried two-necked round-bottomed flask fitted with a condenser and a septum under a N_2 atmosphere. The flask was gently heated with a heat gun until the I_2 started to sublime. The flask was cooled down to rt. A quarter of a solution of 4-bromotoluene (760 mg, 4.5 mmol) in anhydrous THF (10 mL) was added to the reaction mixture, which was heated until it reached reflux. Upon gentle reflux, the remaining solution of 1-bromo-4-fluorobenzene in anhydrous THF was added dropwise over 30 min. The reaction mixture was heated at reflux for 30 min before cooling to rt. Tricyclo[3.3.1.$0^{2,8}$]nona-3,6-dien-9-one (111 mg, 0.84 mmol) was transferred to an oven-dried round-bottomed flask, and the flask was purged with N_2. Anhydrous THF (10 mL) was added and the solution was cooled to 0 °C. The Grignard solution (prepared above) was added dropwise over 30 min to the tricyclo[3.3.1.$0^{2,8}$]nona-3,6-dien-9-one solution. The reaction mixture was stirred for 16 h, and the temperature was raised from 0 °C to rt, following removal of the ice bath. The reaction was quenched with a saturated aqueous solution of NH_4Cl (10 mL), then extracted with EtOAc (3 × 20 mL). The combined organic extracts were dried over $MgSO_4$, filtered and the solvent removed under reduced pressure. The crude residue was purified by column chromatography (Teledyne Isco CombiFlash Rf+ system, 24 g SiO_2, hexanes−CH_2Cl_2, gradient elution including 0.5% Et_3N in the elution) to yield the title compound as a cream-coloured solid (136 mg, 0.61 mmol, 80%). **M.P.** 59 – 61°C. **^{1}H NMR** (700 MHz, $CDCl_3$) δ 7.33 (d, *J* = 8.2 Hz, 2H, H_{11}), 7.12 (d, *J* = 7.9 Hz, 2H, H_{12}), 5.91 (t, *J* = 7.7 Hz, 1H, H_7), 5.58 (t, *J* = 7.6 Hz, 1H, H_3), 4.28 – 4.24 (m, 2H, H_8 and H_6), 4.24 – 4.21 (m, 2H, H_4 and H_2), 2.83 – 2.57 (m, 2H, H_5 and H_1), 2.33 (d, *J* = 0.7 Hz, 3H, H_{14}), 1.98 (s, 1H, H_9). **^{13}C NMR** (176 MHz, $CDCl_3$) δ 140.4 (C_{10}), 136.8 (C_{13}), 128.6 (C_{12}), 126.4 (C_{11}), 123.2 (C_7), 120.9 (C_3), 77.8 (C_4 and C_2), 75.5 (C_8 and C_6), 68.6 (C_9), 38.2 (C_5 and C_1), 21.2 (C_{14}). **HRMS-ASAP** *m/z* = 207.1154 $[M\text{-}OH]^+$, calculated for $C_{16}H_{15}$: 207.1174.

(±)-6-(4-Fluorophenyl)bicyclo[3.2.2]nona-3,8-dien-6-ol (9/9′)

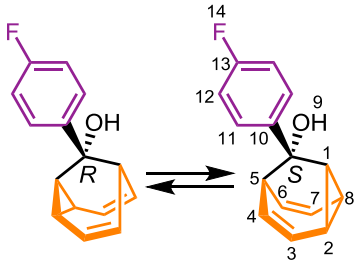

Magnesium turnings (120 mg, 5.04 mmol) and I_2 (64 mg, 0.25 mmol, 5 mol%) were placed in an oven-dried two-necked round-bottomed flask fitted with a condenser and a septum under a N_2 atmosphere. The flask was gently heated with a heat gun until the I_2 started to sublime. The flask was cooled down to rt. A quarter of a solution of 1-bromo-4-fluorobenzene (875 mg, 5.00 mmol) in anhydrous THF (10 mL) was added to the reaction mixture, which was heated until it reached reflux. Upon gentle reflux, the remaining solution of 1-bromo-4-fluorobenzene in anhydrous THF was added dropwise over 30 min. The reaction mixture was heated at reflux for 30 min before cooling to rt. Tricyclo[3.3.1.$0^{2,8}$]nona-3,6-dien-9-one (111 mg, 0.84 mmol) was transferred to an oven-dried round-bottomed flask, and the flask was purged with N_2. Anhydrous THF (10 mL) was added and the solution was cooled to 0 °C. The Grignard solution (prepared above) was added dropwise over 30 min to the tricyclo[3.3.1.$0^{2,8}$]nona-3,6-dien-9-one solution. The reaction mixture was stirred for 16 h, and the temperature was raised from 0 °C to rt, following removal of the ice bath. The reaction was quenched with a saturated aqueous solution of NH_4Cl (10 mL), then extracted with EtOAc (3 × 20 mL). The combined organic extracts were dried over $MgSO_4$, filtered and the solvent removed under reduced pressure. The crude residue was purified by column chromatography (Teledyne Isco CombiFlash Rf+ system, 24 g SiO_2, hexanes−CH_2Cl_2, gradient elution including 0.5% Et_3N in the elution) to yield the title compound as a white solid (129 mg, 0.84 mmol, 67%). **M.P.** 60 – 62°C. **^{1}H NMR** (700 MHz, $CDCl_3$) δ 7.48 – 7.19 (m, 2H, H_{11}), 7.07 – 6.75 (m, 2H, H_{12}), 5.92 (t, J = 7.7 Hz, 1H, H_7), 5.59 (t, J = 7.7 Hz, 1H, H_3), 4.29 – 4.24 (m, 2H, H_6 and H_8), 4.24 – 4.17 (m, 2H, H_2 and H_4), 2.68 – 2.61 (m, 1H, H_5 and H_1), 2.04 (s, 1H, H_9). **^{13}C NMR** (176 MHz, $CDCl_3$) δ 162.7 (d, J_{CF} = 245.2, C_{13}), 139.20 (C_{10}), 128.20 (d, J_{CF} = 8.0, C_{11}) 123.3 (C_7), 121.0 (C_3), 114.67 (d, J_{CF} = 21.1, C_{12}), 77.8 (C_4 and C_2), 75.4 (C_8 and C_6), 68.5 (C_9), 38.3 (C_1 and C_5). **^{19}F NMR** (376 MHz, CDC_{l3}) δ –119.30 (m, F_{14}). **HRMS-ASAP** *m/z* = 211.0923 [M-OH]$^+$, calculated for $C_{15}H_{12}F$: 211.0911.

3.5.3 Synthesis of Improved Mono-Substituted Barbaralanes

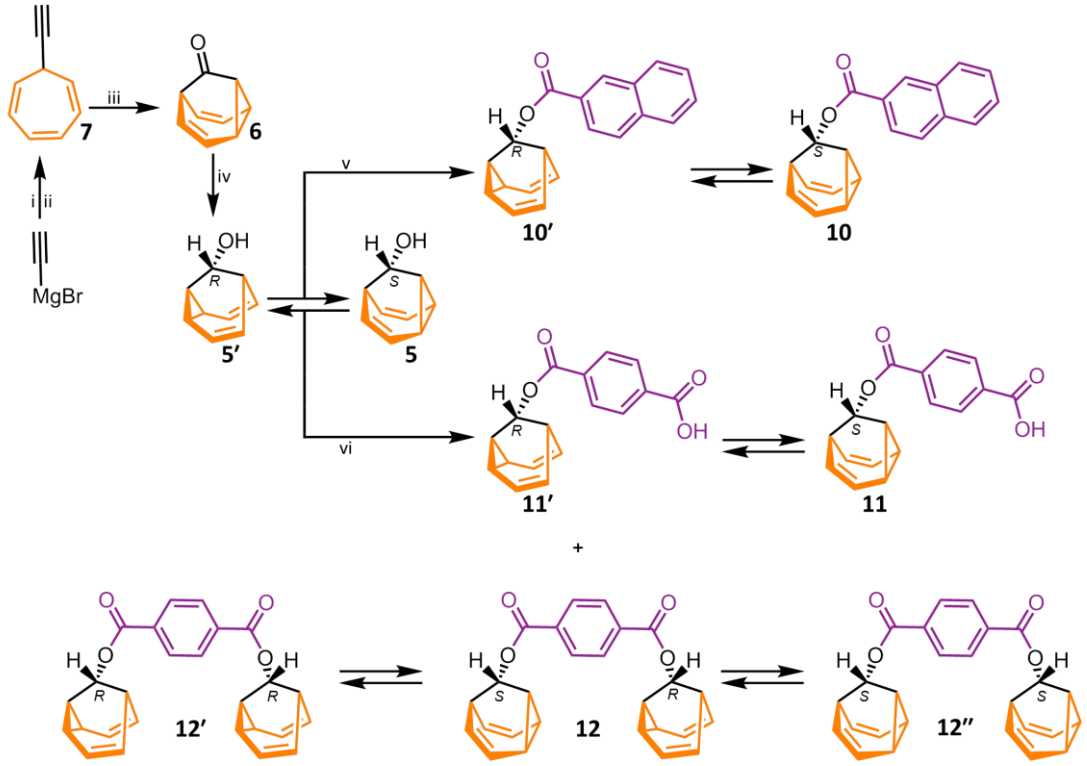

Scheme 3.6. Synthesis of compounds **7**, barbaralone (**6**), barbaralol (**5**/**5′**), naphthyl barbaralane (**10**/**10′**), carboxylic acid barbaralane (**11**/**11′**) and dimeric carboxylic acid barbaralane (**12**/**12′**/**12″**). Reagents and conditions: (i) LiCl, / THF / –78 °C, (ii) tropylium tetrafluoroborate / rt, (iii) IPrAu(MeCN)BF_4 (5 mol%) / Ph_2SO (2 equiv.) / CH_2Cl_2 / rt / 16 h, (iv) $LiAlH_4$ / Et_2O / 0 °C / 3 h / 78%, (v) 2-naphthoyl chloride / $CHCl_3$ / barbaralol / DMAP / Et_3N, (vi) terephthaloyl chloride / $CHCl_3$ / barbaralol / DMAP / Et_3N. IPr = 1,3-bis(2,6-diisopropylphenyl)imidazol-2-ylidene.

In room temperature solutions, each of the barbaralanes **10**/**10′** and **11**/**11′** exist as a mixture of two rapidly interconverting stereoisomers, whereas barbaralane **12**/**12′**/**12″** exist as a mixture of three interconverting stereoisomers. For clarity, we have only labelled one of the stereoisomers, but all stereoisomers are in fast exchange on account of rapid strain-assisted Cope rearrangement. The chemical shifts of each nucleus are representative of the time-averaged chemical environments they experience as part of the two (or three) stereoisomers.

2-Naphthoyl Chloride

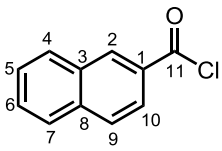

To a round-bottomed flask was added 2-naphthoic acid (250 mg, 1.45 mmol) and SO_2Cl (1.87 mL, 0.02 mol). The mixture was heated to 75 °C and left for 4 h. The reaction was then cooled down to rt before the solution was concentrated under vaccum to yield the title compound as a cream-coloured solid (275 mg, 1.45 mmol, >99%). **M.P.** 52 – 54 °C. **^{1}H NMR** (700 MHz, $CDCl_3$) δ 8.75 (dd, *J* = 1.9, 0.8 Hz, 1H, H_2), 8.06 (dd, *J* = 8.7, 1.9 Hz, 1H, H_{10}), 8.02 (dq, *J* = 8.2, 0.7 Hz, 1H, H_4), 7.92 (dd, *J* = 4.9, 0.7 Hz, 1H, H_9), 7.91 (dd, *J* = 4.6, 0.9 Hz, 1H, H_7), 7.69 (ddd, *J* = 8.2, 6.8, 1.3 Hz, 1H, H_6), 7.62 (ddd, *J* = 8.1, 6.9, 1.2 Hz, 1H, H_5). **^{13}C NMR** (176 MHz, $CDCl_3$) δ 168.5 (C_{11}), 136.6 (C_8), 134.9 (C_2), 132.43 (C_3), 130.5 (C_1), 130.2 (C_4), 130.0 (C_6), 129.0 (C_9), 128.0 (C_7), 127.6 (C_5), 125.5 (C_{10}). **HRMS-ASAP** *m/z* = 155.0502 $[M\text{-}Cl]^+$ (calculated for $C_{11}H_7O^+$ = 155.0497).

(±)-Tricyclo[3.3.1.0^{2,8}]nona-3,6-dien-9-yl-naphthalene-2-carboxylate (10/10′)

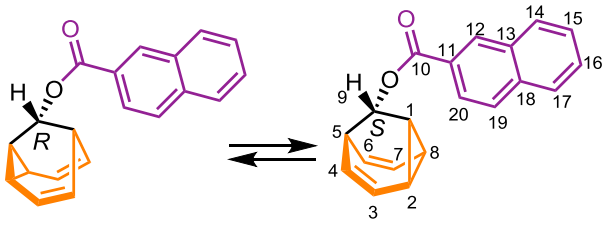

To an oven-dried round-bottomed flask, under a N_2 atmosphere was added 2-naphthoyl chloride (85 mg, 0.44 mmol) in anhydrous $CHCl_3$ (4.2 mL). Tricyclo[3.3.1.0^{2,8}]nona-3,6-dien-9-ol (50 mg, 0.37 mmol), DMAP (37 mg, 0.30 mmol) and Et_3N (0.15 mL, 1.09 mmol) were then added to the mixture. The reaction was left to stir at rt for 5 d. The reaction was quenched with an aqueous solution of NH_4Cl (25 mL, saturated) then extracted with $CHCl_3$ (3 × 20 mL). The combined organic extracts were dried over $MgSO_4$ and the solvent was removed under reduced pressure. The crude residue was purified by column chromatography (Teledyne Isco CombiFlash Rf+ system, 12 g SiO_2, hexanes−CH_2Cl_2, gradient elution) to give the title compound as a white solid (90 mg, 0.31 mmol, 84%). **M.P.** 114 – 115 °C. **^{1}H NMR** (600 MHz, $CDCl_3$) δ 8.53 (dd, *J* = 1.6, 0.8 Hz, 1H, H_{12}), 8.00 (dd, *J* = 8.6, 1.7 Hz, 1H, H_{20}), 7.94 (ddd, *J* = 8.8, 1.3, 0.6 Hz, 1H, H_{14}),

7.89 – 7.85 (m, 1H, H_{19}), 7.86 – 7.82 (m, 1H, H_{17}), 7.57 (ddd, *J* = 8.2, 6.8, 1.4 Hz, 1H, H_{16}), 7.52 (ddd, *J* = 8.1, 6.9, 1.3 Hz, 1H, H_{15}), 5.90 (t, *J* = 7.9 Hz, 1H, H_7), 5.61 (t, *J* = 7.7 Hz, 1H, H_3), 5.01 (t, *J* = 3.3 Hz, 1H, H_9), 4.21 – 4.12 (m, 2H, H_2 and H_4), 4.12 – 4.07 (m, 2H, H_8 and H_6), 2.85 – 2.67 (m, 2H, H_5 and H_1). **^{13}C NMR** (151 MHz, $CDCl_3$) δ 166.6 (C_{10}), 135.5 (C_{18}), 132.4 (C_{13}), 130.9 (C_{12}), 129.3 (C_{14}), 128.1 (C_{16}), 128.0 (C_{19} or C_{17}), 127.9 (C_{11}), 127.7 (C_{19} or C_{17}), 126.5 (C_{15}), 125.3 (C_{20}), 121.8 (C_7), 121.1 (C_3), 75.0 (C_2 and C_4), 72.8 (C_8 and C_6) 67.1 (C_9), 28.4 (C_5 and C_1). **HRMS-ASAP** *m/z* = 289.1236 $[M-H]^+$ (calculated for $C_{20}H_{17}O_2^+$ = 289.1229).

(±)-4-({Tricyclo[3.3.1.0^{2,8}]nona-3,6-dien-9-yloxy}carbonyl)benzoic acid (11/11′)

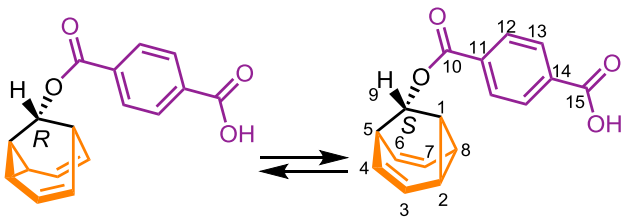

To an oven-dried round-bottomed flask, under a N_2 atmosphere was added terephthaloyl chloride (90 mg, 0.44 mmol) in anhydrous $CHCl_3$ (4.2 mL). Tricyclo-[3.3.1.0^{2,8}]nona-3,6-dien-9-ol (50 mg, 0.37 mmol), DMAP (37 mg, 0.30 mmol) and Et_3N (0.15 mL, 1.09 mmol) were then added to the mixture. The reaction was left to stir at rt for 3 d. The reaction was quenched with an aqueous solution of NH_4Cl (25 mL, saturated) then extracted with $CHCl_3$ (3 × 20 mL). The combined organic extracts were dried over $MgSO_4$ and the solvent was removed under reduced pressure. The crude residue was purified by column chromatography (Teledyne Isco CombiFlash Rf+ system, 12 g SiO_2, hexanes−EtOAc, gradient elution including 0.1% Et_3N in the elution) to give the title compound as a white solid (26 mg, 0.1 mmol, 25%). **M.P.** 224 – 226 °C. **^{1}H NMR** (600 MHz, $CDCl_3$) δ 8.14 (d, *J* = 8.6 Hz, 2H, H_{12} or H_{13}), 8.07 (d, *J* = 8.6 Hz, 2H, H_{12} or H_{13}), 5.87 (t, *J* = 7.9 Hz, 1H, H_7), 5.60 (t, *J* = 7.7 Hz, 1H, H_3), 4.98 (t, *J* = 3.3 Hz, 1H, H_9), 4.36 – 4.11 (m, 2H, H_2 and H_4), 4.11 – 4.03 (m, 2H, H_8 and H_6), 2.72 (td, *J* = 6.1, 3.2 Hz, 1H, H_5 and H_1). **^{13}C NMR** (151 MHz, $CDCl_3$) δ 170.5 (C_{10} or C_{15}), 165.6 (C_{10} or C_{15}), 135.4 (C_{14} or C_{11}), 132.9 (C_{11} or C_{14}), 130.2 (C_{12} or C_{13}), 129.8 (C_{12} or C_{13}), 122.0 (C_7), 121.3 (C_3), 75.1 (C_2 and C_4), 72.7 (C_8 and C_6) 67.9 (C_9), 28.5 (C_5 and C_1). **HRMS-ASAP** *m/z* = 283.0971 $[M+H]^+$ (calculated for $C_{17}H_{15}O_4^+$ = 283.0970).

(±)-Tricyclo[3.3.1.$0^{2,8}$]nona-3,6-dien-9-yl 4-{tricyclo[3.3.1.$0^{2,8}$]nona-3,6-dien-9-carbonyl} benzoate (12/12′/12″)

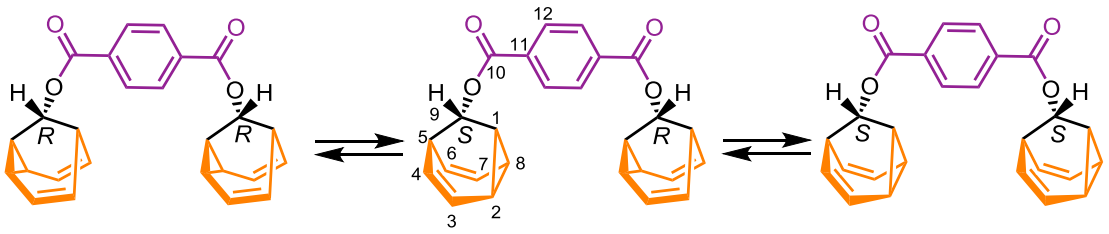

During the above procedure, the title compound was also isolated as a white solid (40 mg, 0.1 mmol, 27%). **M. P.** 215 – 217 °C. **^{1}H NMR** (600 MHz, $CDCl_3$) δ 8.01 (s, 4H, H_{12}), 5.86 (t, *J* = 7.9 Hz, 2H, H_7), 5.61 (t, *J* = 7.6 Hz, 2H, H_7), 4.96 (t, *J* = 3.3 Hz, 2H, H_9), 4.20 – 4.10 (m, 4H, H_2 and H_4), 4.08 – 4.01 (m, 4H, H_8 and H_6), 2.81 – 2.64 (m, 4H, H_5 and H_1). **^{13}C NMR** (151 MHz, $CDCl_3$) δ 165.8 (C_{10}), 134.5 (C_{11}), 129.6 (C_{12}), 122.0 (C_7), 121.3 (C_3), 75.2 (C_2 and C_4), 72.8 (C_8 and C_6), 67.7 (C_9), 28.5 (C_5 and C_1). **HRMS-ASAP** *m/z* = 299.1608 $[M+H]^+$ (calculated for $C_{26}H_{23}O_4^+$ = 299.2048).

3.6 Appendix of Supplementary Data and Discussion

3.6.1 Appendix for Covalent Control

3.6.1.1 Structural Assignment by 2D NMR

In order to distinguish the ‘front’ of the molecule from the ‘back’ of the molecule, we used 2D NMR spectroscopy. Briefly, we are able to differentiate which peaks are on the same face of the molecule through analysis of COSY correlations (Figure 3.13). For example, the olefin which is either 3/3′ only correlates to one pair of the olefin and cyclopropane positions (2/4′ and 4/2′). Therefore, we can confirm that these positions are on the same face.

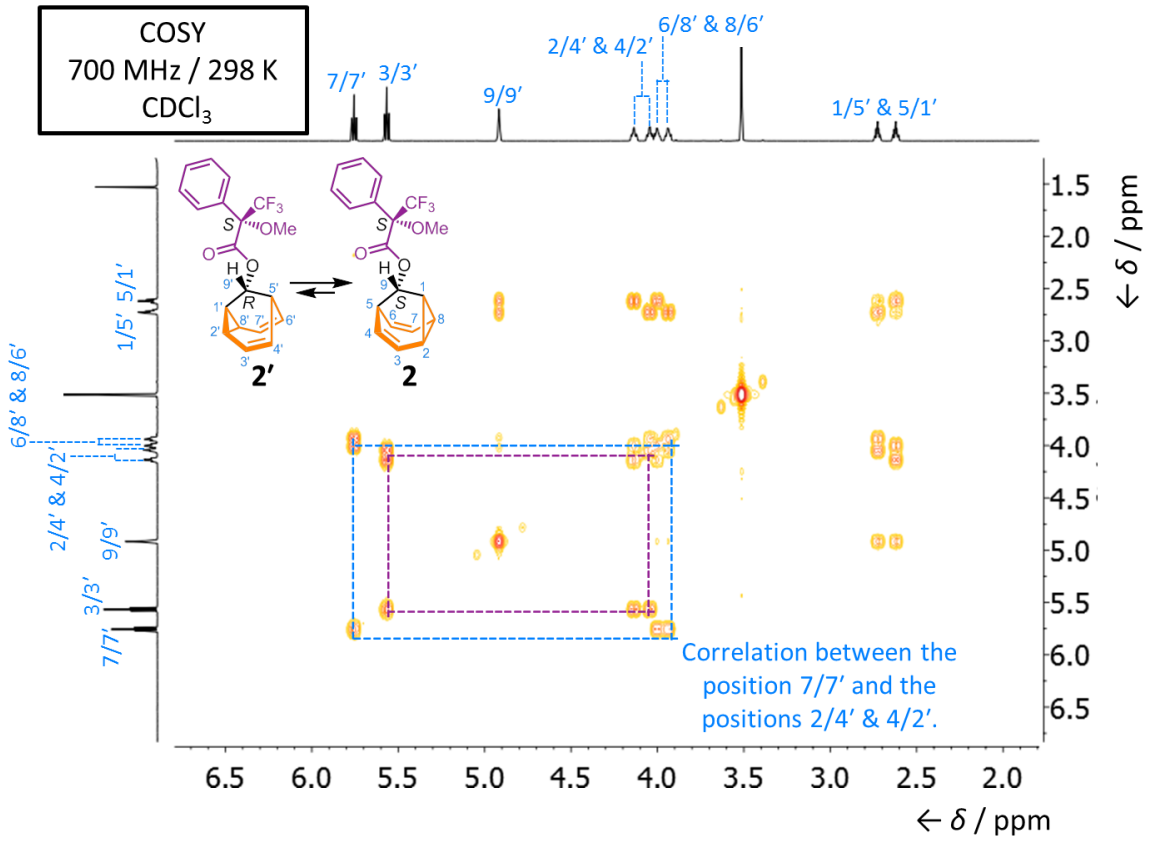

Figure 3.13. Partial COSY spectrum of **2**/**2′**.

A NOESY correlation between the hydrogen at position 9/9′ to a proton environment on one of the faces of the barbaralyl core allows for determination of the relative configuration of the stereogenic centre. A critical NOESY correlation between the proton at position 9/9′ and a pair of olefin and cyclopropane positions (2/4′ and 4/2′) confirms that these environments must be on the same face, therefore the front and back of the barbaralyl core can be distinguished (Figure 3.14). This assignment can be applied to barbaralane **1**/**1′**. Barbaralanes **3**/**3′** and **4**/**4′** do not exhibit a NOESY correlation. However, we observe the same chemical shift peak pattern as barbaralane **2**/**2′** and, therefore, assign the front and back signals by analogy. 2D NMR spectroscopy does not allow us to differentiate between some of the protons on the barbaralyl core. For example, we cannot differentiate between the positions 2/4′ and 4/2′ of compound **2**/**2′**.

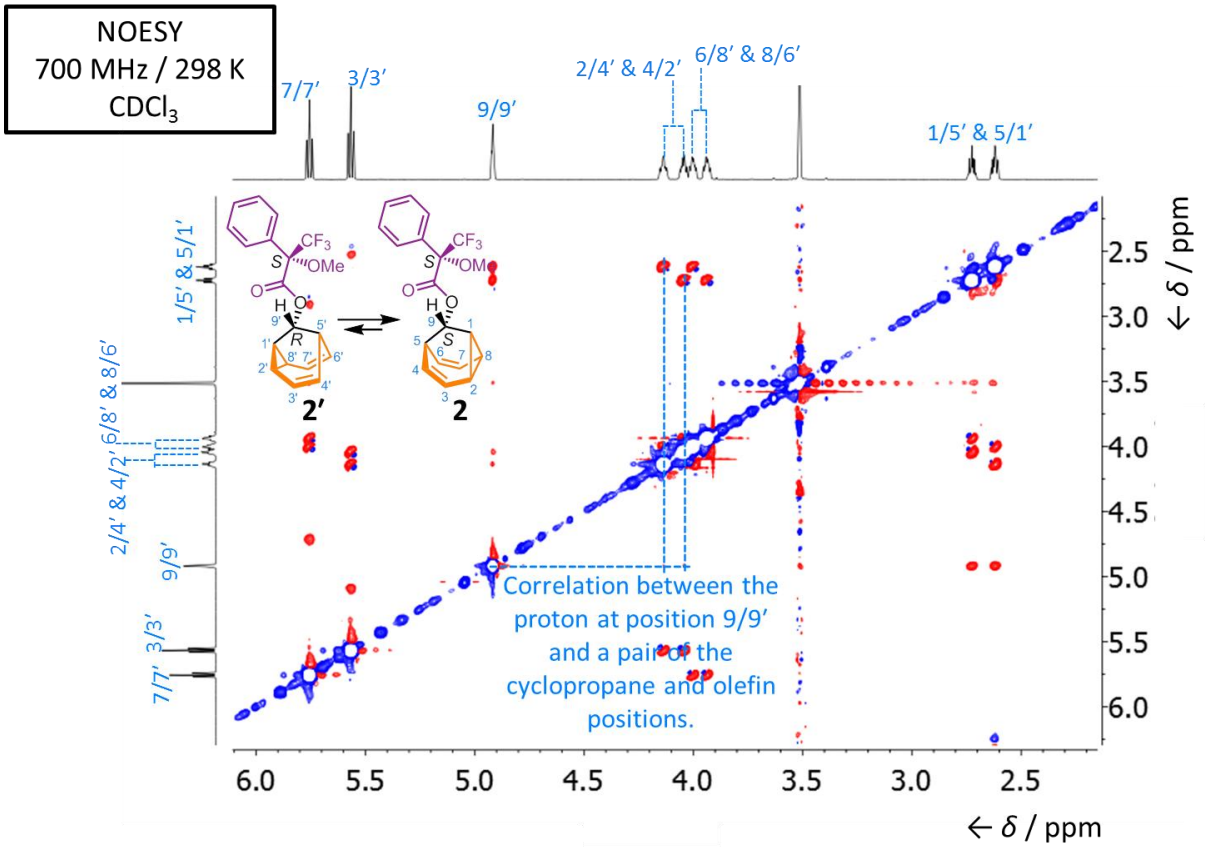

Figure 3.14. Partial NOESY spectrum of **2/2′**.

3.6.1.2 Solution State *In Silico* Modelling

Barbaralanes **1**/**1′**, **2**/**2′**, **3**/**3′** and **4**/**4′** interconvert *via* a [3,3]-sigmatropic Cope rearrangement allowing the switching between two diastereoisomers. These diastereoisomers are nondegenerate and the equilibrium is slightly shifted towards one species at room temperature in the solution state, however at low temperatures in the solution state the equilibrium shifts completely towards one diastereoisomer. To determine the more stable diastereoisomer, *in silico* methods were utilised. First, a set of conformer states for each diastereoisomer of barbaralanes **1**/**1′** and **3**/**3′** were generated through molecular mechanics sampling of the potential energy surface, using Confab.[37] These geometries were then further optimised using density functional theory (DFT) with the M06-2X[38] and ωB97XD[39] functionals using a 6-311G++(d,p) basis set in Gaussian 09, rev A. 02.[40] C-PCM model[41] and integral formalism variant was used to describe carbon disulphide as the solvent. This analysis

generated a set of conformer states for the two diasteremeric isomers of **1**/**1′** and **3**/**3′**, and the associated energy difference between each conformation (Figure 3.15). Such calculations only enable the determination of relative energies and not absolute Gibbs free energies, as the effect of entropy was not taken into account. The ground-state energy difference for diastereisomers **1** and **1′** was calculated to be 6.88 $kJ \cdot mol^{-1}$. The calculations also showed that the lower energy isomer **1′** is thermodynamically favoured. The ground state energy difference for diastereisomers **3** and **3′** was calculated to be 3.11 $kJ \cdot mol^{-1}$. The calculations also showed that the lower energy isomer **3** is thermodynamically favoured

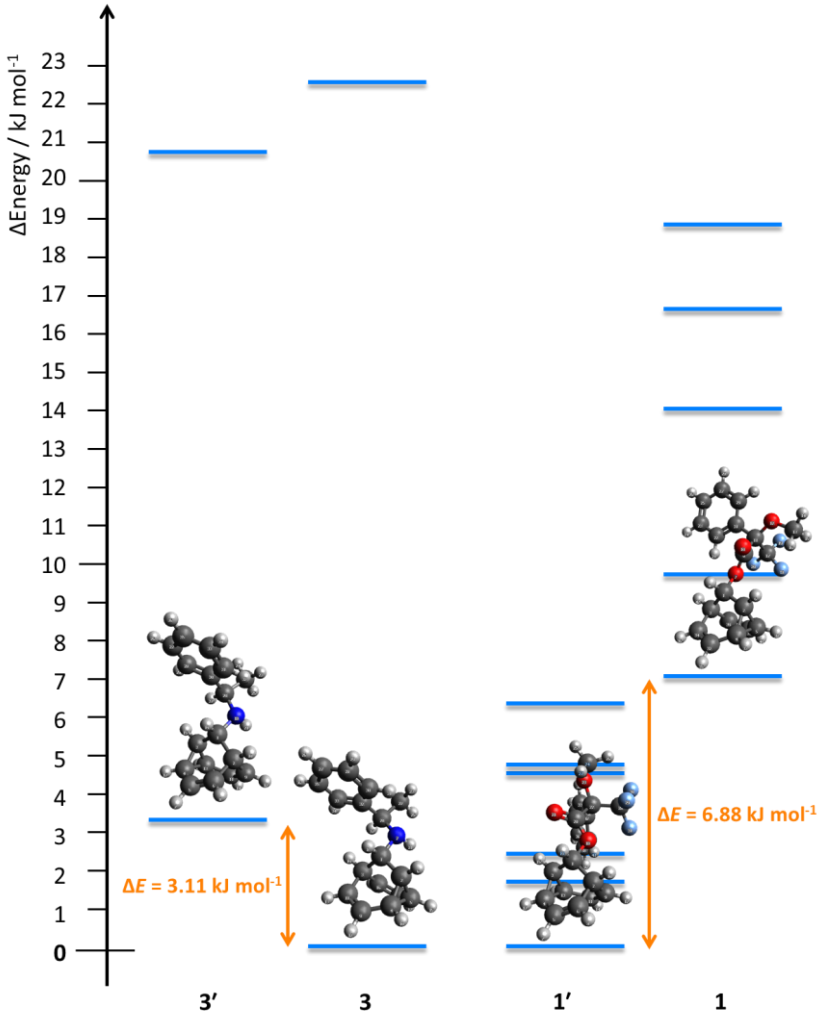

Figure 3.15. Plot of the relative energies of conformer states as determined using the ωB97XD functional and the 6-311++(d,p) basis set for the chiral tether compounds **1**/**1′** and **3**/**3′**. Molecular structures of the minimum energy conformers for each diastereomer are included (represented as blue lines), with the energy difference between them shown in orange.

Having calculated the optimised geometries, the ^{1}H and ^{13}C NMR chemical shifts of **5**/**5′** were predicted using the gauge-independent atomic orbital method with the same basis set and solvent model (Figures 3.16 and 3. 17). The ^{1}H and ^{13}C NMR spectra from each unique geometry were then combined as a weighted average based on the Boltzmann distribution of the structures at equilibrium to predict the chemical shift of peaks in the fast-exchange NMR spectrum. Functionals M06-2X and ωB97XD were used to obtain independent data sets.

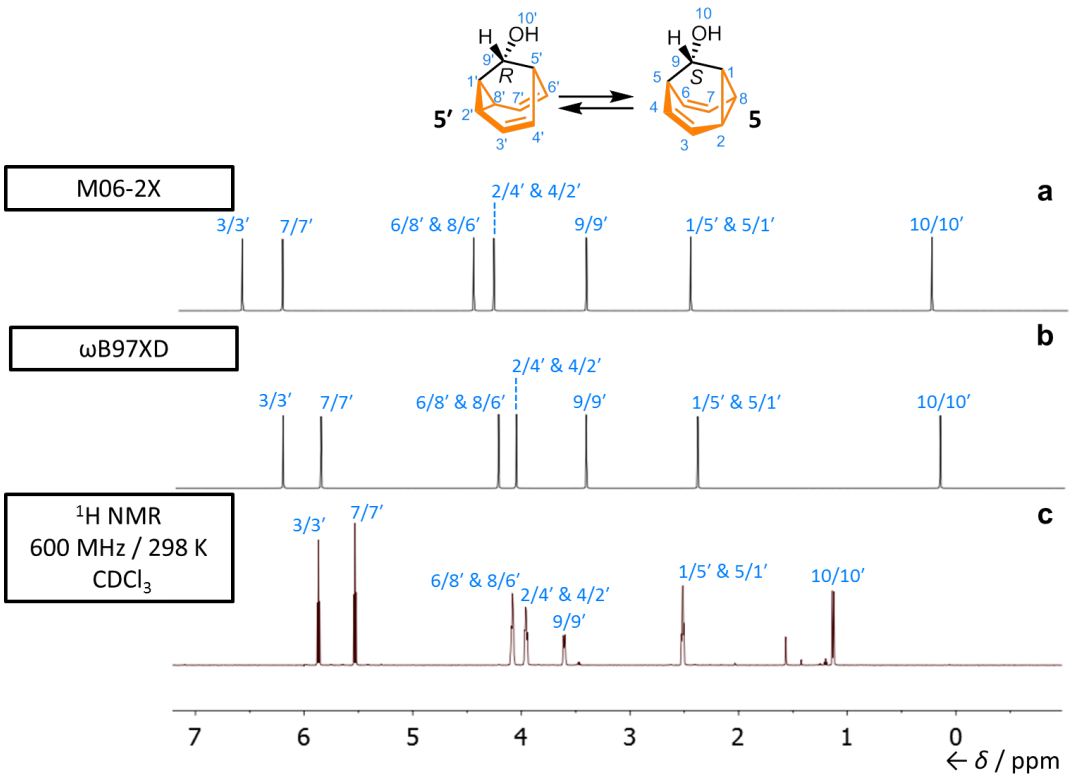

Figure 3.16. Comparison of the partial ^{1}H NMR spectra of barbaralol **5**/**5′**. (a) Computationally predicted spectrum using the DFT functional M06-2X, (b) computationally predicted spectrum using the DFT functional ωB97XD and (c) experimental spectrum.

The computationally predicted fast exchange ^{1}H and ^{13}C NMR spectra for the interconverting enantiomers of **5**/**5′** matched well with the experimental spectrum. The cage-like structure of the barbaralyl core acts to restrict the molecule; therefore, for each enantiomer only one conformation was found to be energetically stable. Calculations, therefore, only required the consideration of two geometries of equivalent ground-state energy, so that predicted chemical shifts resided exactly halfway between the two discrete chemical environments in exchange. The calculated

NMR spectra from both functionals showed the same relative order of peaks with small variations in the chemical shifts themselves (Tables 3.1 and 3. 2). The calculated spectra inaccurately describe the chemical shift of the hydroxyl proton of **5**/**5′**, as the solvent medium used in the calculations was carbon disulphide, and not $CDCl_3$, in which the experimental sample was measured. The assignment of **5**/**5′** was completed based on the predictions of *in silico* calculations.

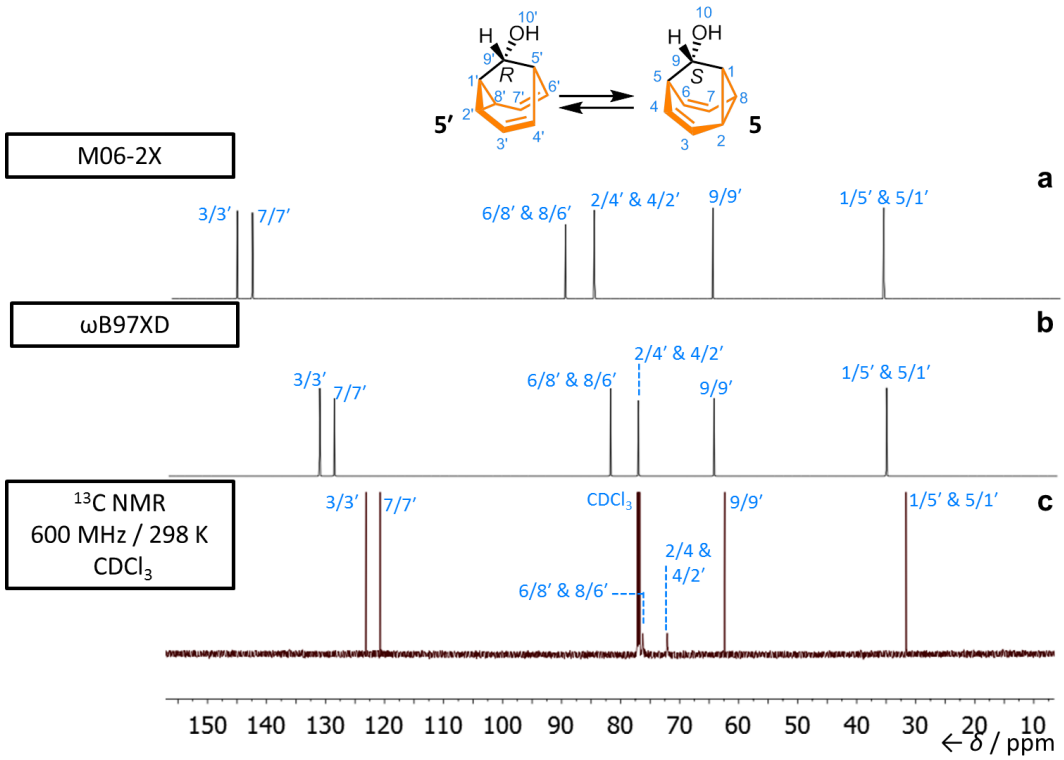

Figure 3.17. Comparison of the partial ^{13}C NMR spectra of barbaralol **5**/**5′**. (a) Computationally predicted spectrum using the DFT functional M06-2X, (b) computationally predicted spectrum using the DFT functional ωB97XD and (c) ^{1}H NMR experimental spectrum.

Table 3.1. Comparison of experimental ^{1}H NMR solution-state chemical shifts against DFT calculated solution-state ^{1}H chemical shifts (ppm) of **5**/**5′**.

Atom	Observed ^{1}H NMR Chemical Shift (δ)	M06-2X Calculated ^{1}H NMR Chemical Shift (δ)	ωB97XD Calculated ^{1}H NMR Chemical Shift (δ)
10/**10′**	1.13	0.28	0.17
1/**5′ and 5**/**1′**	2.52	2.50	2.40
9/**9′**	3.61	3.46	3.43
2/**4′ and 4**/**2′**	3.97	4.32	4.07
6/**8′ and 8**/**6′**	4.09	4.49	4.24
7/**7′**	5.54	6.26	5.87
3/**3′**	5.88	6.63	6.62

Table 3.2. Comparison of experimental ^{13}C NMR solution-state chemical shifts against DFT calculated solution-state ^{1}H chemical shifts (ppm) of **5**/**5′**.

Atom	Observed ^{13}C NMR Chemical Shift (δ)	M06-2X Calculated ^{13}C NMR Chemical Shift (δ)	ωB97XD Calculated ^{13}C NMRChemical Shift (δ)
1/**5′ and 5**/**1′**	31.83	36.44	35.47
9/**9′**	62.51	65.42	64.70
2/**4′ and 4**/**2′**	72.25	85.48	77.50
6/**8′ and 8**/**6′**	76.38	90.37	82.24
7/**7′**	120.94	143.43	129.03
3/**3′**	123.29	146.00	131.51

Having determined the validity of the *in silico* method on the degenerate system of **5**/**5′**, it was applied to the more complex chiral tether systems, which comprise nondegenerate stereoisomers in exchange. While the chiral tether derivatives were expected to be more complex due to the nondegeneracy of the diastereomers, the calculations were further complicated by the existence of multiple low-energy conformers. The flexible chiral tethers were found to adopt multiple orientations, resulting in the possibility of many conformer states. Instead of the predicted NMR spectrum being based on two diastereomers, multiple unique conformers of each diastereoisomer also needed to be considered. The relative energies of these structures determined their respective Boltzmann factors, which affected their contribution to the averaged NMR spectrum. Large disparity between the calculated NMR spectra and the experimental spectra of the chiral tether derivatives was found, likely due to

the failing of the calculations in accurately predicting the relative energy of conformers, leading to the incorrect weighting of discrete states in the averaged chemical shifts. Therefore, *in silico* methods were incapable of accurately predicting the fast-exchange regime NMR spectra of barbaralanes **1**/**1′** and **3**/**3**.

3.6.1.3 Variable-Temperature NMR Spectroscopy

The barbaralanes undergo a rapid and reversible Cope rearrangement in solution. For example, diastereoisomer **2** is in fast exchange with isomer **2′**, giving rise to a single set of resonances in the ^{13}C NMR spectrum recorded (Figure 3.18) at ambient temperature. The chemical shift of each nucleus is indicative of its time-averaged chemical environment. Upon reducing the temperature to 159 K, the equilibrium shifts in favour of diastereoisomer **2′**. This is evidenced as the peaks corresponding to the olefinic and cyclopropane environments broaden into the base and re-emerge. For example, two of the olefinic and cyclopropane environments are ~70 ppm at room temperature but at colder temperatures they have shifted to ~25 ppm (the change in chemical shift is highlighted by two blue boxes). The remaining olefinic and cyclopropane environments shift in the opposite direction. Environments labelled as 1/1′, 5/5′, 3/3′ and 7/7′ also broaden into the baseline at higher temperatures and re-emerge at colder temperatures.

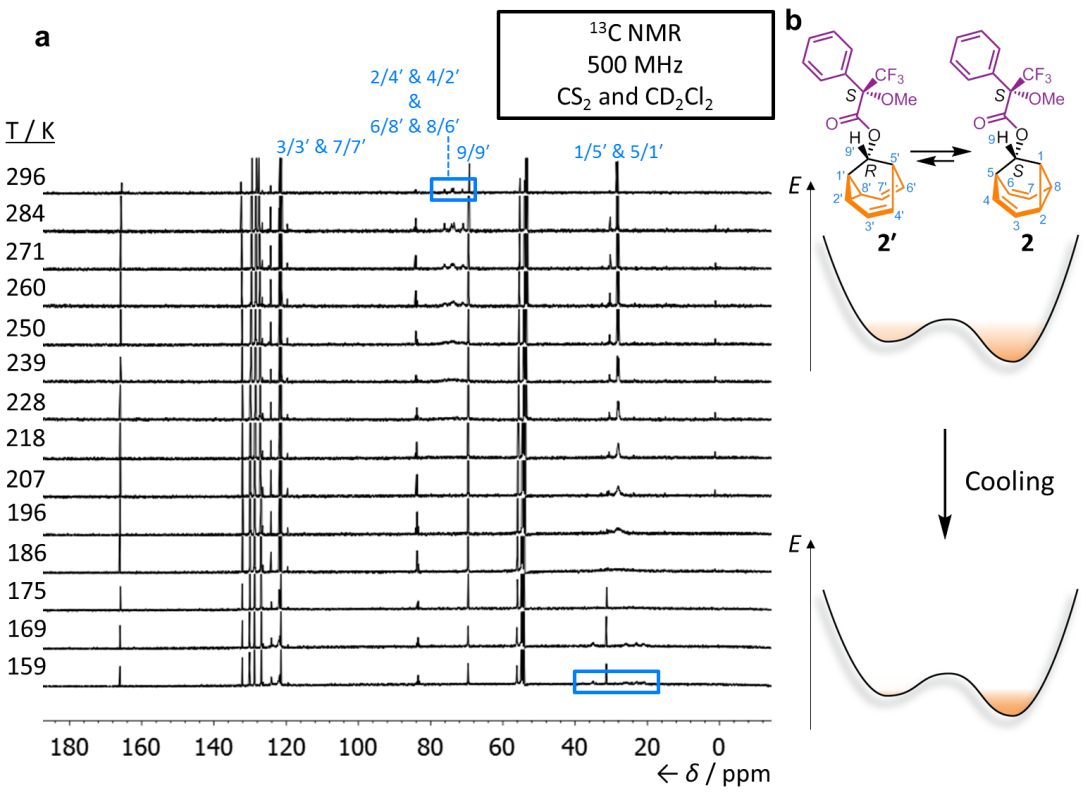

Figure 3.18. (a) Partial ^{13}C NMR spectra of **2**/**2′** and (b) a schematic illustration of the change in equilibrium population on a simplified potential energy surface as temperature decreases.

3.6.1.4 X-ray Crystallographic Analysis

Tricyclo[3.3.1.$0^{2,8}$]nona-3,6-dien-9-yl (*R*)-3,3,3-trifluoro-2-methoxy-2-phenylproponate (1′)

Crystals of **1′** suitable for X-ray diffraction were grown by slow evaporation of a saturated Et_2O solution. See Figure 3.4 in the Results and Discussion.

Crystal System: Orthorhombic

Space group: $P2_12_12_1$

Unit Cell Parameters: a = 7.3559(3) Å, b = 12.5594(5) Å, c = 17.2298(7) Å, α = 90 °, β = 90 °, γ = 90 °, V = 1591.79(11) $Å^3$, Z = 4

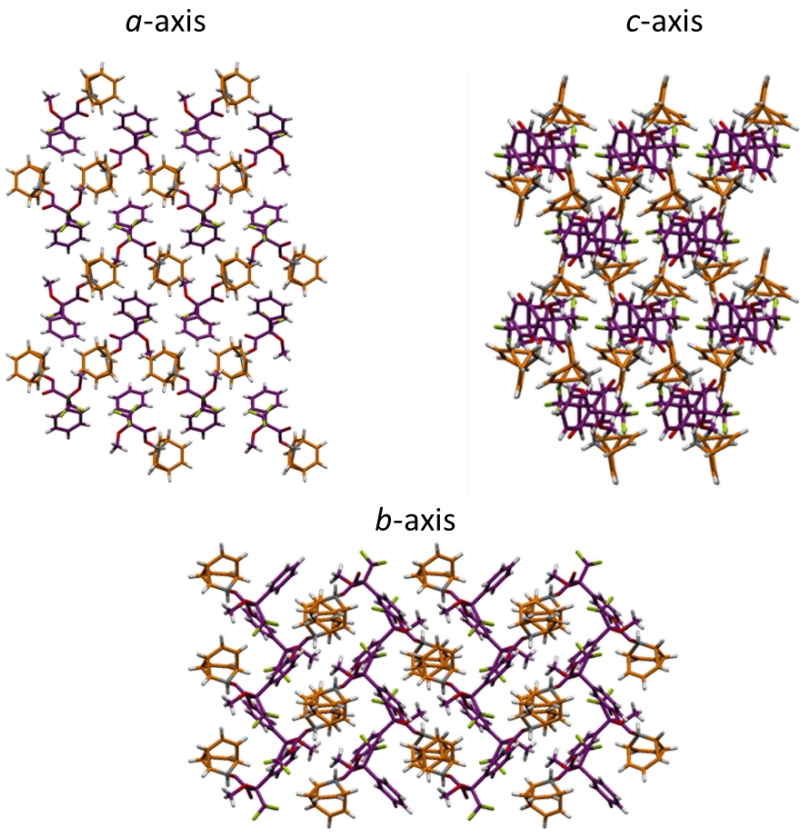

Figure 3.19. Solid-state superstructure of **1′** viewed along the three unit cell axes.

Tricyclo[3.3.1.$0^{2,8}$]nona-3,6-dien-9-yl (*S*)-3,3,3-trifluoro-2-methoxy-2-phenylproponate (2)

Crystals of **2** suitable for X-ray diffraction were grown by slow evaporation of a saturated Et_2O solution. See Figure 3.4 in the Results and Discussion.

Crystal System: Orthorhombic

Space group: $P2_12_12_1$

Unit Cell Parameters: a = 7.36678(15) Å, b = 12.5886(2) Å, c = 17.2671(3) Å, α = 90 °, β = 90 °, γ = 90 °, V = 1601.30(5) $Å^3$, Z = 4

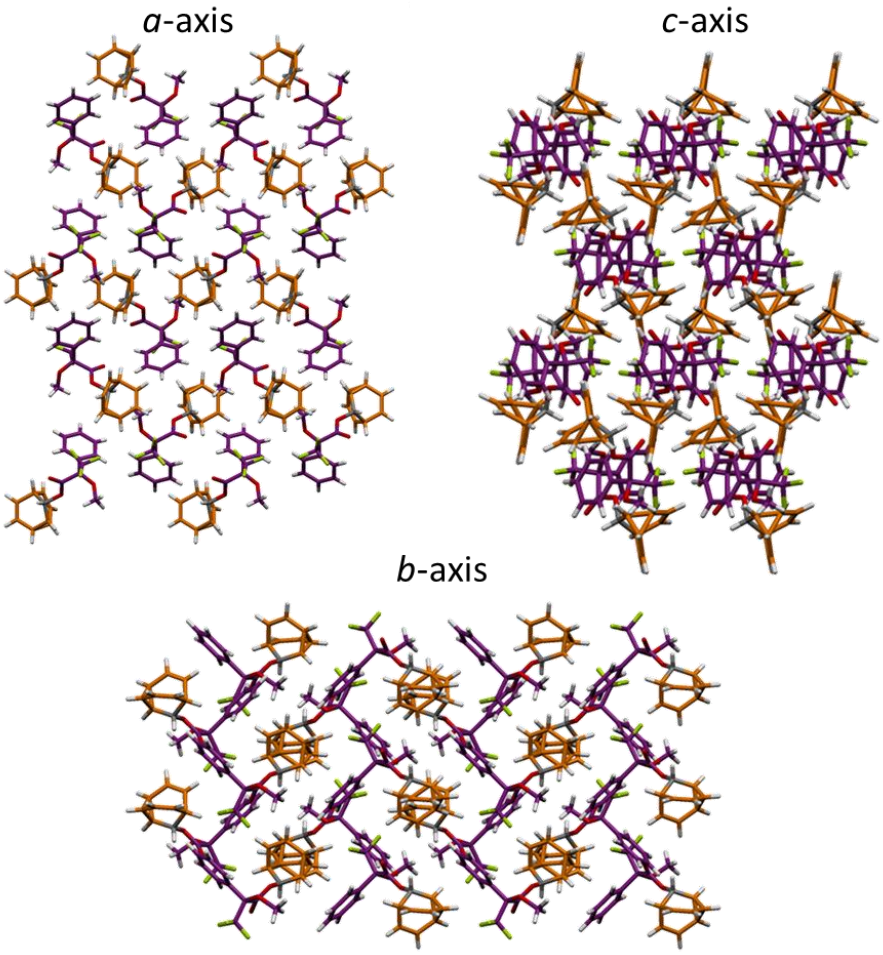

Figure 3.20. Solid-state superstructure of **2** viewed along the three unit cell axes.

N-(*R*)-1-(Phenylethynyl)-tricyclo[3.3.1.$0^{2,8}$]-nona-3,6-dien-9-amine (3)

Crystals of **3** suitable for X-ray diffraction were grown by slow cooling of the sample at a temperature of 5 °C from room temperature and were transferred to the diffractometer by a 'dry ice' technique.

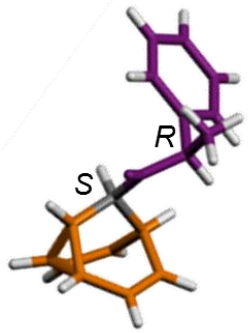

Crystal System: Triclinic

Space group: P1

Unit Cell Parameters: a = 6.1684(9) Å, b = 6.3485(9) Å, c = 28.326(4) Å, α = 84.356(4) °, β = 87.233(4) °, γ = 61.967(4) °, V = 974.4(2) $Å^3$, Z = 3

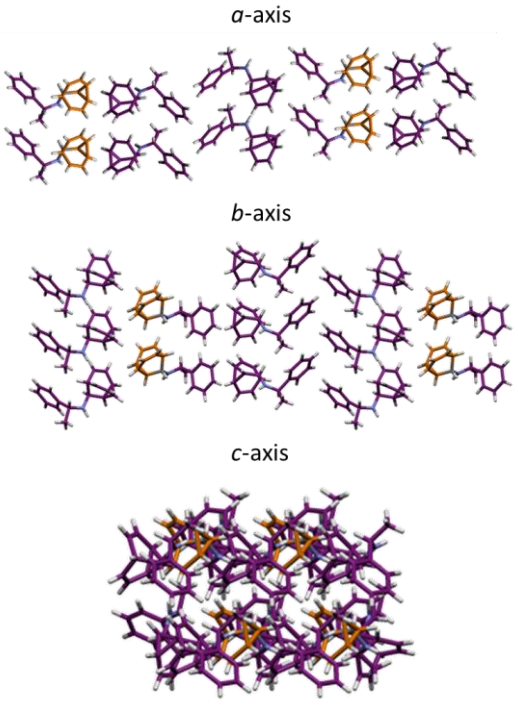

Figure 3.21. Solid-state superstructure of **3** viewed along the three unit cell axes.

3.6.1.5 Calculation of ^{13}C Solid-State NMR Chemical Shifts

First principles calculations of NMR shifts in crystalline forms were carried out using the GIPAW method implemented in CASTEP v17.2.[42] All calculations were performed using the PBE functional[43] and on-the-fly generated ultrasoft pseudopotentials with a cut-off energy of 600 eV. Geometry optimisation of all atomic positions was carried out with the centre of mass and unit cell parameters fixed at the values determined by single-crystal X-ray diffraction. Integrals were taken over the Brillouin zone using a Monkhorst-Pack grid with a maximum *k*-point sample spacing of 0.1 $Å^{-1}$.

Table 3.3. Comparison of solution-state experimental ^{13}C NMR chemical shifts against experimental and calculated ^{13}C NMR chemical shifts.

Atom	Solution-State Experimental ^{13}C NMR Chemical Shift (δ)	Solid-State Calculated ^{13}C NMR Chemical Shift (δ)	Solid-State Experimental ^{13}C NMR Chemical Shift (δ)
1 or 5′	20.52	19.49	20.30
2 or 4′	22.35	21.93	24.21
3 or 3′	[a]	121.75	[a]
4 or 2′	[a]	125.33	[a]
5 or 1′	34.50	34.01	34.79
6 or 8′	[a]	122.01	[a]
7 or 7′	[a]	125.60	[a]
8 or 6′	25.20	27.61	28.63
9 or 9′	69.07	69.92	69.37
10 or 10′	165.43	169.00	166.66
11 or 11′	83.02	87.81	84.90
12 or 12′	[a]	134.55	[a]
13 or 13′	[a]	126. 07 and 127.34	[a]
14 or 14′	[a]	130.83	[a]
15 or 15′	[a]	130.22	[a]
16 or 16′	[a]	136.56	[a]
17 or 17′	55.52	55.60	56.25

[a] unable to assign unambiguously.

Comparing the calculated ^{13}C NMR chemical shifts against the solid state and in solution experimental chemical shifts demonstrates relatively similar values (Table 3.3). The simulated ^{13}C solid-state NMR spectrum matches well with both experimental values, allowing for the reliable assignment of the lower frequency section of the NMR. The downfield portion the ^{13}C solid-state NMR spectrum is

however very poorly separated in the spectrum with many different chemical environments overlapping with similar chemical shifts hampering full assignment.

3.6.2 Appendix for Noncovalent Control

3.6.2.1 Structural Assignment by 2D NMR

In order to distinguish the 'front' of the molecule from the 'back' of the molecule in combination with the structural assignment we used 2D NMR spectroscopy. The same COSY correlation as shown in Figure 3.13 was observed, allowing us to differentiate which peaks are on the same face of the molecule.

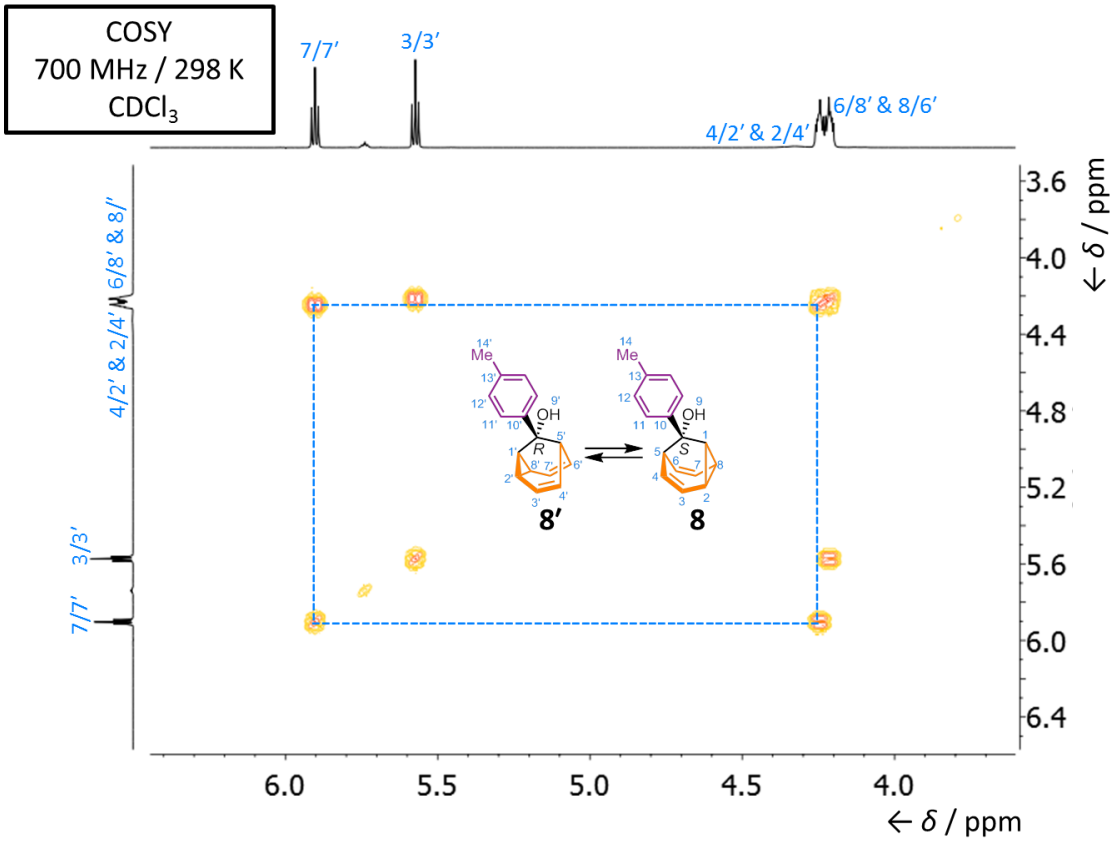

Figure 3.22. Partial COSY spectrum of **8/8′**.

A NOESY correlation between the proton at position 9/9′ and that at 3/3′ confirms that these environments must be on the same face; therefore, the front and back of the barbaralyl core can be distinguished (Figure 3.23). As 11/11′ also correlates only to positions 4/2′ and 2/4′ (11/11′ cannot correlate to 6/8′ and 8/6′) we can confirm the

assignment. The same COSY and NOESY correlations can be seen with barbaralane **9**/**9′**, **11**/**11′** and **12**/**12′**/**12″**. For barbaralane **10**/**10′**, the COSY demonstrates the same pattern, however a NOESY correlation is not observed. Assignment for **10**/**10′** is based on similar structures (*i.e.*, **11**/**11′**).

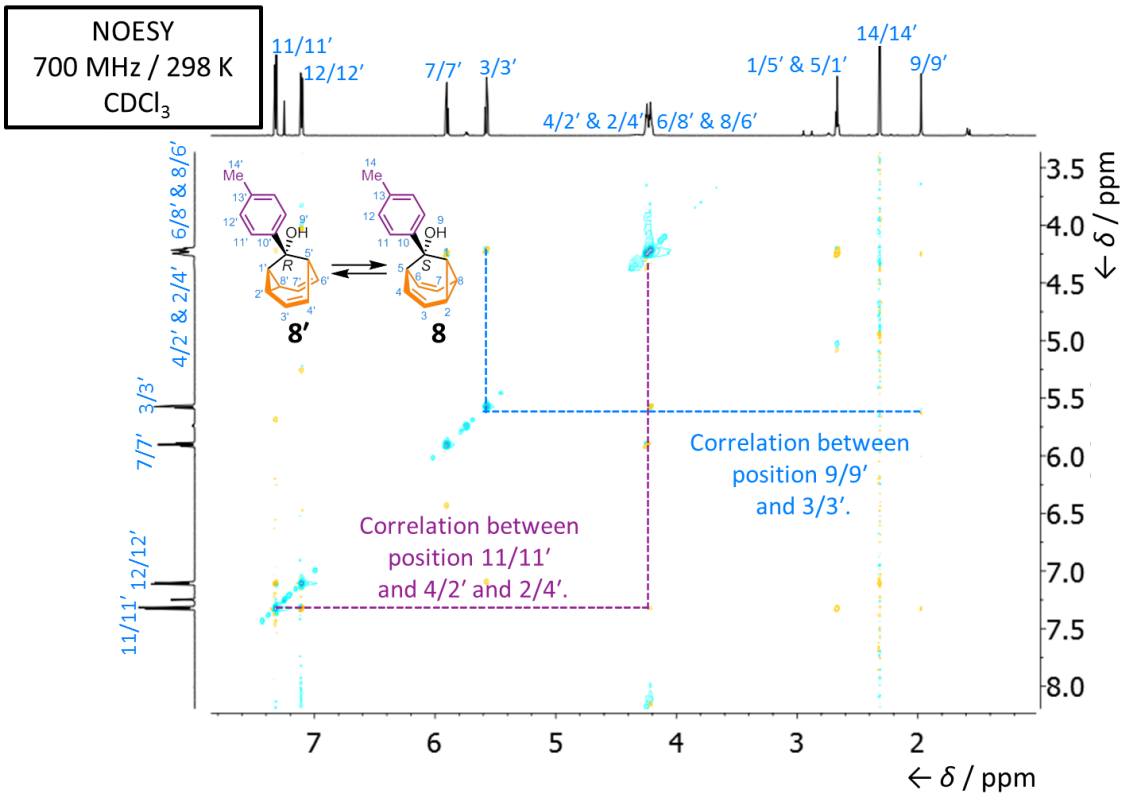

Figure 3.23. Partial NOESY spectrum of **8**/**8′**.

3.6.2.2 Initial Binding Studies

Initial binding studies were conducted on barbaralane **8**/**8′**, barbaralol **5**/**5′** and barbaralone **6**. The general method for preparing samples included making a solution of the guest (1 equiv.) in D_2O (1.0 mL) and the corresponding CD (2 equiv.) in another 1.0 mL of D_2O. 0.5 mL of the guest solution was added to an NMR tube followed by the addition of another 0.5 mL of D_2O. A ^1H NMR spectrum was acquired. 0.5 mL of the CD solution was added to an NMR tube followed by the addition of another 0.5 mL of D_2O. A ^1H NMR spectrum was acquired. The remaining 0.5 mL of the guest solution was combined in an NMR tube with 0.5 mL

of the of CD solution. This method has been completed with α-, β- and γ-CD for barbaralane **8**/**8′**, barbaralol **5**/**5′** and barbaralone **6**.

Solution-phase ^{1}H NMR studies of barbaralol **5**/**5′** with α-, β- or γ-cyclodextrin does not demonstrate any splitting of the peaks because a mirror plane is present within the molecule, however a change in the chemical shift is observed (Figure 3.24). The change in the chemical shift upon the addition of α-, β- or γ-CD is rather small (~0.1 ppm). Investigations with compound **6** only show a slight adjustment in the chemical shift (>0.05 ppm) indicating that the fluxional sp^3–carbon stereocentre in combination with chiral β–CD helps a binding event to take place (Figure 3.25).

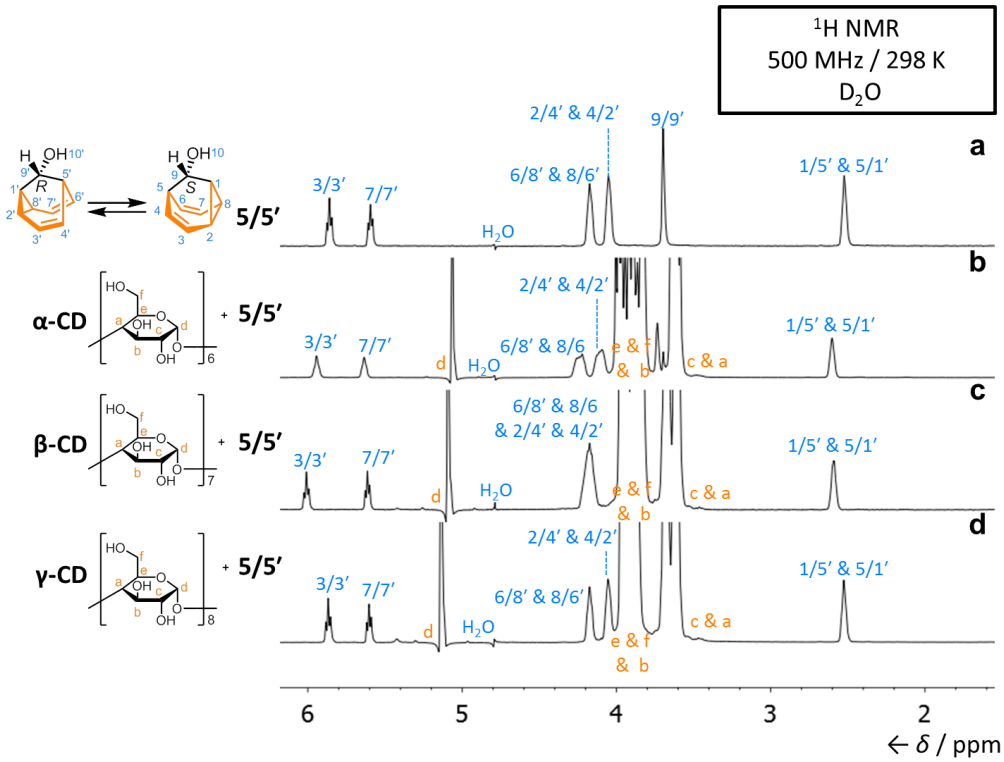

Figure 3.24. Partial ^{1}H NMR of (a) barbaralol (**5**/**5′**) (12.5 mM), (b) barbaralol **5**/**5′** (12.5 mM) and α-CD (25.0 mM), (c) barbaralol **5**/**5′** (6.0 mM) and β-CD (12.0 mM) and (d) barbaralol **5**/**5′** (12.5 mM) and γ-CD (25.0 mM). All spectra have been acquired using presaturation with Robust-5 and PROJECT pulse sequences to suppress the water signal.

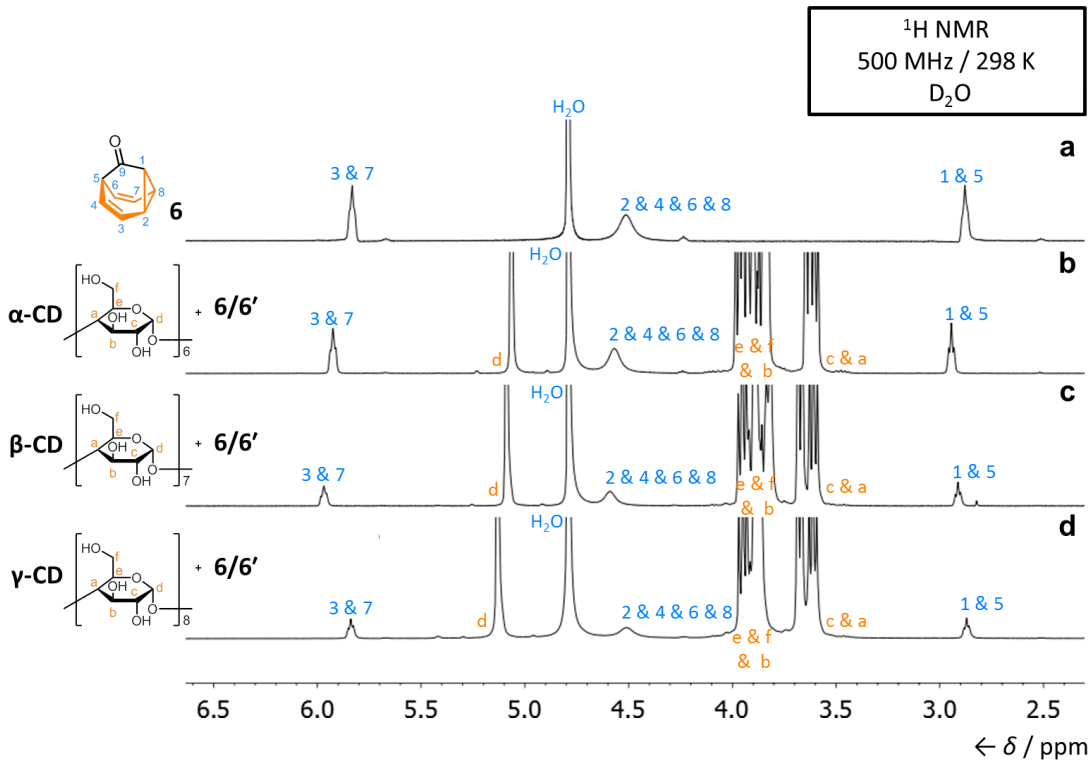

Figure 3.25. Partial ^{1}H NMR of (a) barbaralone (**6**) (13.5 mM), (b) barbaralone **6** (13.5 mM) and α-CD (27.0 mM), (c) barbaralone **6** (6.0 mM) and β-CD (12.0 mM) and (d) barbarlane **6** (13.5 mM) and γ-CD (27.0 mM).

3.6.2.3 ^{1}H NMR Titrations

In order to determine the stoichiometry and the association constant between the guest molecules (**8**/**8′**, **5**/**5′**, **6**) and the host (β-CD), ^{1}H NMR titrations were conducted (Figures 3.26 to 3.35). For each guest molecule, an NMR titration was completed at two different concentrations. The two concentrations for guest–host (β-CD) are 12.33 mM:1.23 mM and 6.16 mM:0.62 mM, respectively. The general method for preparing samples includes making a solution of the guest (1 equiv.) in D_2O (1.0 mL). 0.5 mL of the guest solution was transferred to a clean NMR tube and a ^{1}H NMR spectrum was acquired. To the remaining 0.5 mL of the guest solution, β-CD (5 equiv.) was added (this is the solution to be titrated into the NMR tube). After each addition of the host–guest solution, the NMR tube was inverted several times and a ^{1}H NMR spectrum was acquired.

β-CD (6.16 mM) titrated into barbaralane **8**/**8′** (0.62 mM)

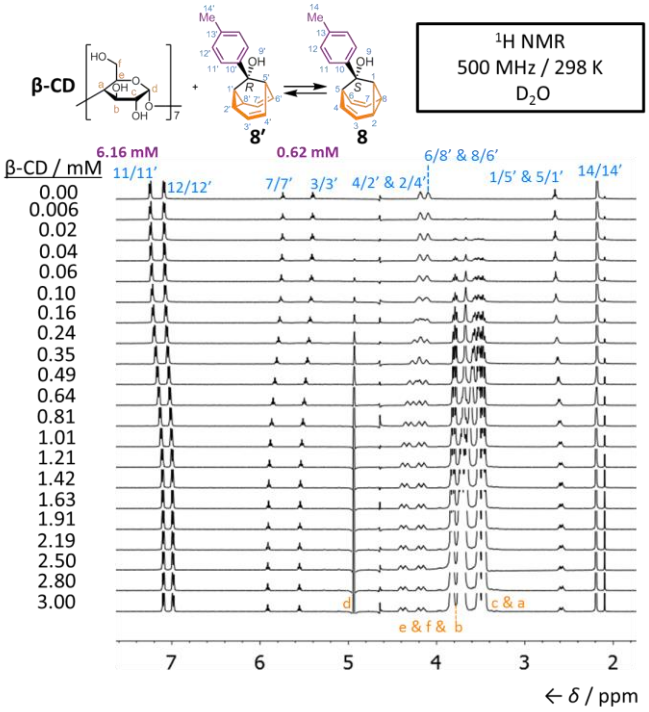

Figure 3.26. Partial ^{1}H NMR spectra of barbaralane **8**/**8′** (0.62 mM) solutions containing different concentrations of β-CD. All spectra have been acquired using presaturation with Robust-5 and PROJECT pulse sequences to suppress the water signal.

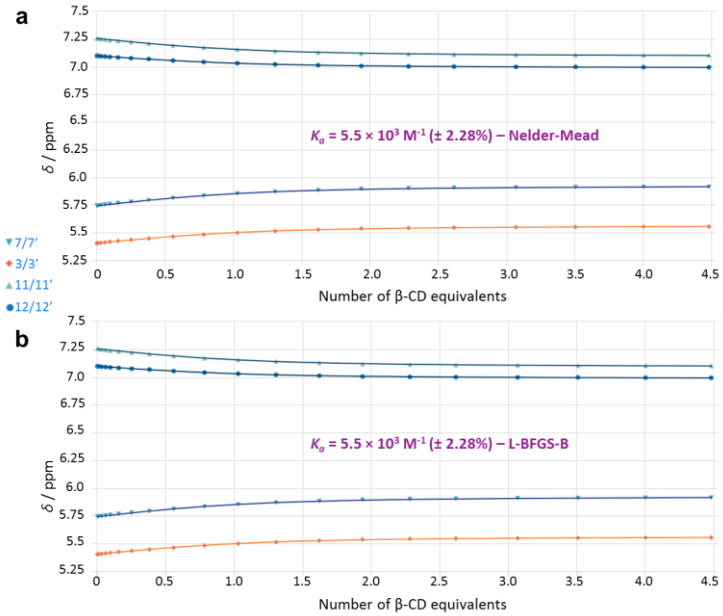

Figure 3.27. Chemical shift (ppm) plotted against number of β-CD equivalents and fit to a one-to-one binding curve using the (a) Nelder-Mead algorithm or the (b) L-BFGS-B algorithm. Association constants are given with their respective errors. Proton labels correspond to those shown in Figure 3.26.

β-CD (12.33 mM) titrated into barbaralol **5**/**5′** (1.23 mM)

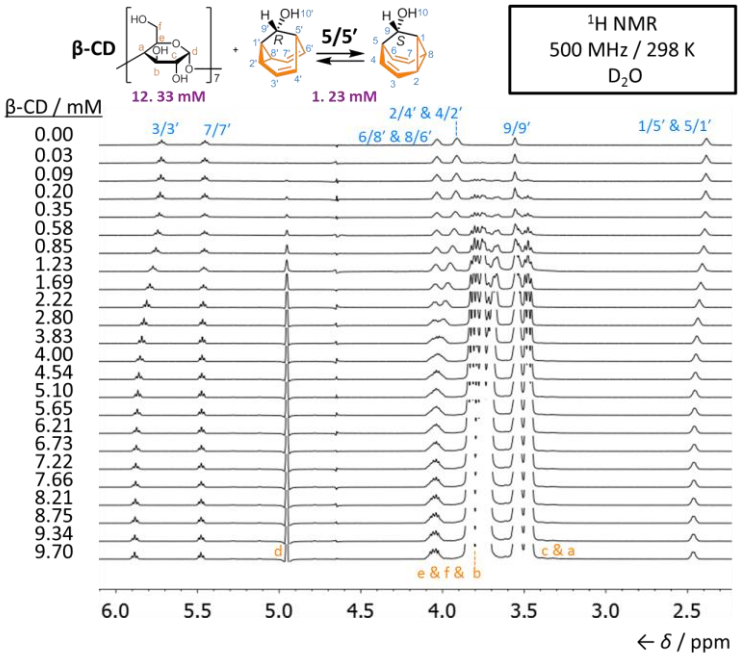

Figure 3.28. Partial ^{1}H NMR spectra of barbaralol **5**/**5′** (12.33 mM) solutions containing different concentrations of β-CD. All spectra have been acquired using presaturation with Robust-5 and PROJECT pulse sequences to suppress the water signal.

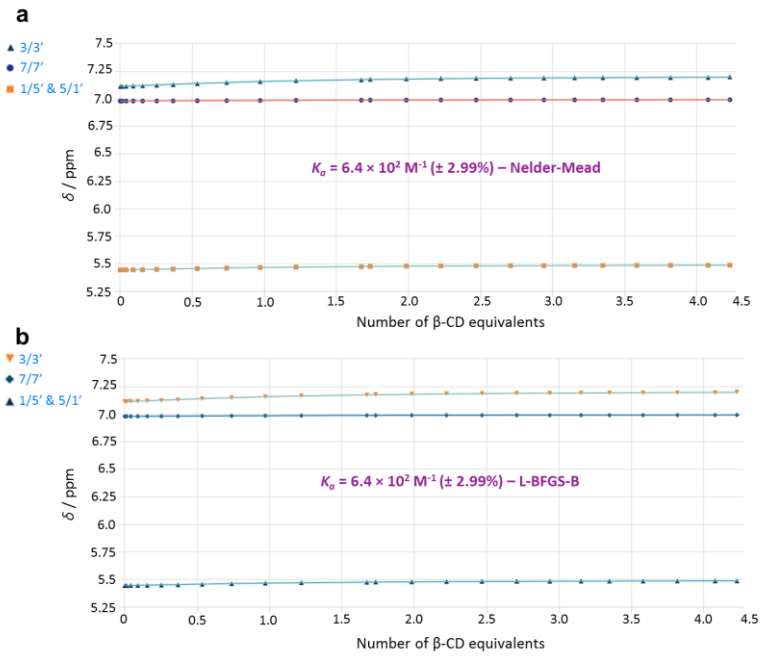

Figure 3.29. Chemical shift (ppm) plotted against number of β-CD equivalents and fit to a one-to-one binding curve using the (a) Nelder-Mead algorithm or the (b) L-BFGS-B algorithm. Association constants are given with their respective errors. Proton labels correspond to those shown in Figure 3.28.

β-CD (6.16 mM) titrated into barbaralol **5**/**5′** (0.62 mM)

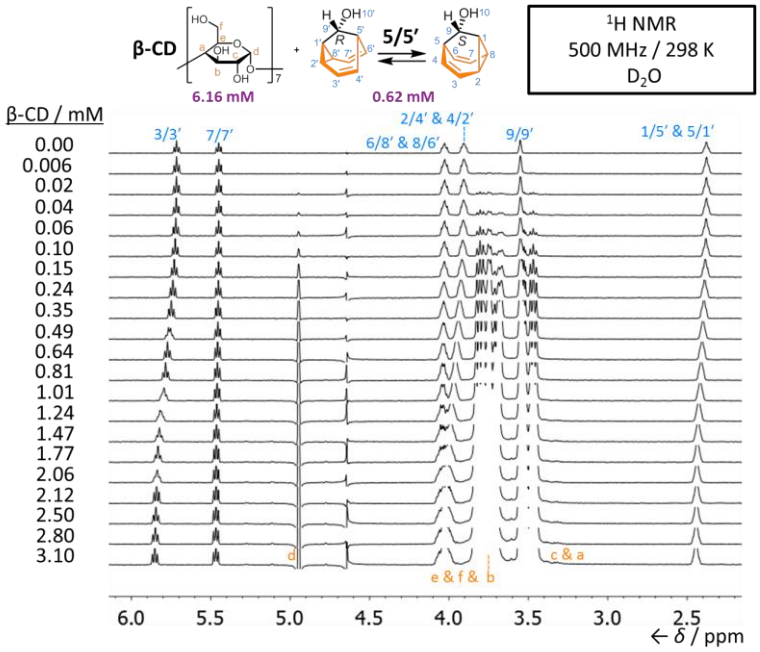

Figure 3.30. Partial ^{1}H NMR spectra of barbaralol **5**/**5′** (6.16 mM) solutions containing different concentrations of β-CD. All spectra have been acquired using presaturation with Robust-5 and PROJECT pulse sequences to suppress the water signal.

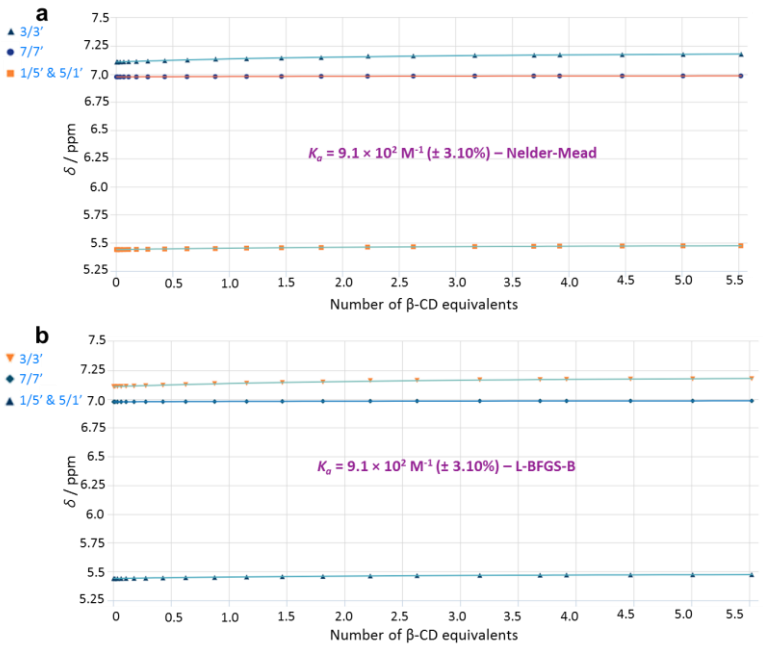

Figure 3.31. Chemical shift (ppm) plotted against number of β-CD equivalents and fit to a one-to-one binding curve using the (a) Nelder-Mead algorithm or the (b) L-BFGS-B algorithm. Association constants are given with their respective errors. Protons labels correspond to those in Figure 3.30.

β-CD (12.33 mM) titrated into barbaralone **6** (1.23 mM)

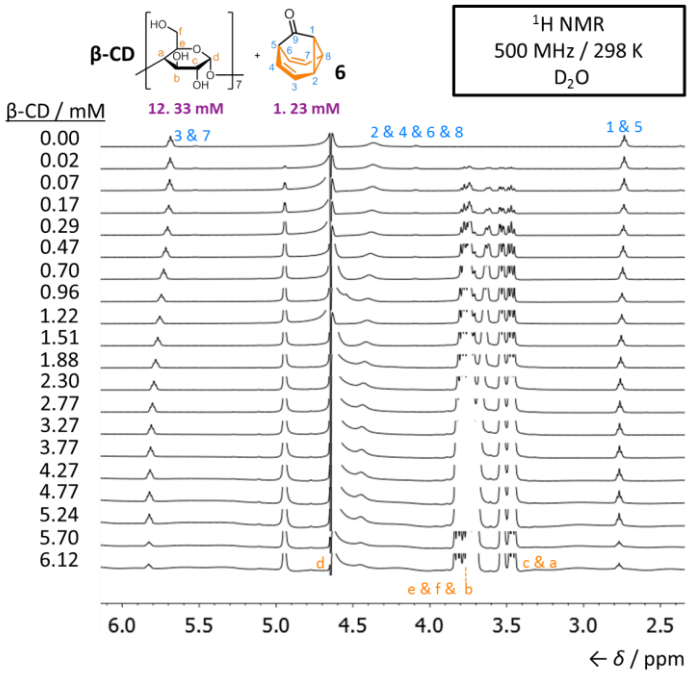

Figure 3.32. Partial ^{1}H NMR spectra of barbaralone **6** (12.33 mM) solutions containing different concentrations of β-CD. All spectra have been acquired using presaturation with Robust-5 and PROJECT pulse sequences to suppress the water signal.

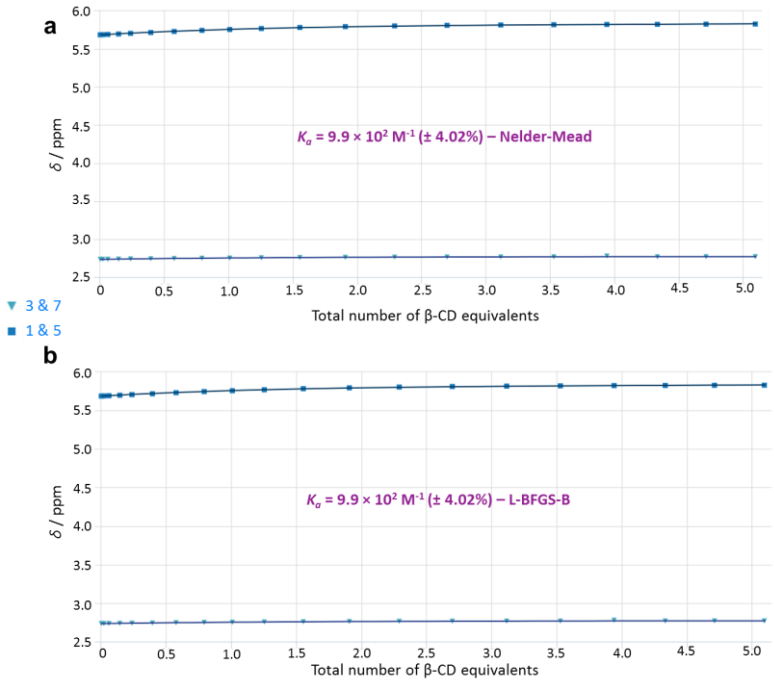

Figure 3.33. Chemical shift (ppm) plotted against number of β-CD equivalents and fit to a one-to-one binding curve using the (a) Nelder-Mead algorithm or the (b) L-BFGS-B algorithm. Association constants are given with their respective errors. Protons labels correspond to those in Figure 3.32.

β-CD (6.16 mM) titrated into barbaralone **6** (0.62 mM)

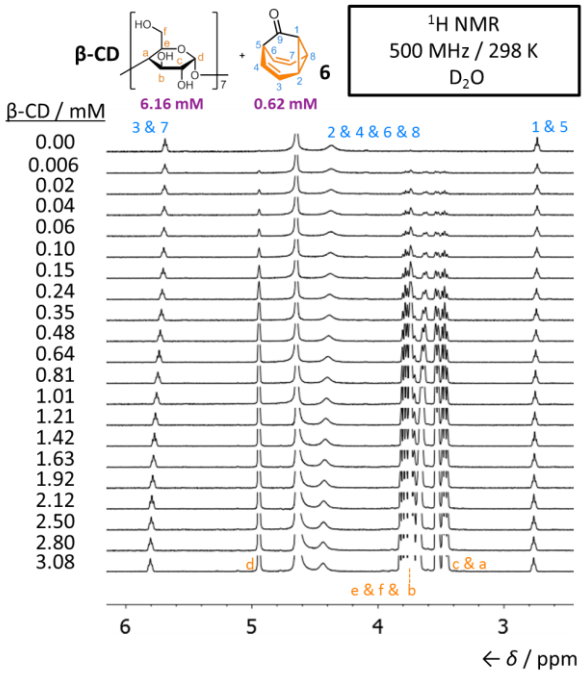

Figure 3.34. Partial ^{1}H NMR spectra of barbaralone **6** (6.16 mM) solutions containing different concentrations of β-CD. All spectra have been acquired using presaturation with Robust-5 and PROJECT pulse sequences to suppress the water signal.

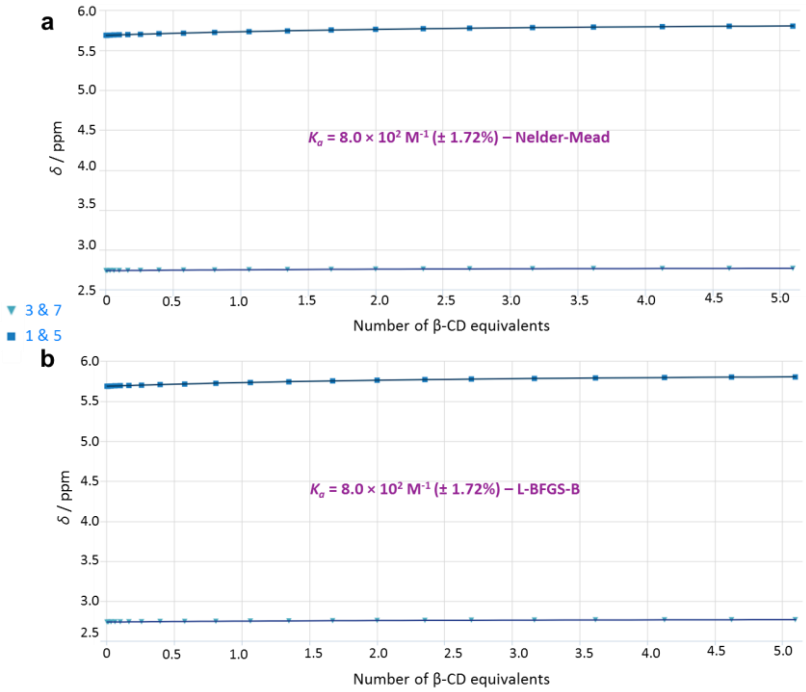

Figure 3.35. Chemical shift (ppm) plotted against number of β-CD equivalents and fit to a one-to-one binding curve using the (a) Nelder-Mead algorithm or the (b) L-BFGS-B algorithm. Association constants are given with their respective errors. Protons labels correspond to those in Figure 3.34.

The ^{1}H NMR titrations completed at two different concentrations with compound **8**/**8′** show that upon the addition of β-CD, the cyclopropane and olefinic environments split into four distinct peaks (Figures 3.26 to 3.27). Positions 1/5′ and 5/1′ also demonstrate a change in multiplicity due to two overlapping inequivalent resonances. Without any β-CD the signal is a clear triplet however, upon the addition of β-CD the signal changes to a multiplet. The chemical shift for positions 11/11′, 12/12′, 3/3′ and 7/7′ are plotted against the number of equivalents of β-CD producing an association constant. All generated association constants for barbaralane **8**/**8′** and β-CD are in good agreement with one another, showing minimal error. The same titrations at the same concentrations were repeated with barbaralol **5**/**5′** (Figures 3.28 to 3.31). The chemical shift for positions 3/3′, 7/7′, 1/5′ and 5/1′ in barbaralol **5**/**5′** are plotted against the number of equivalents of β-CD producing an average association constant of 7.8×10^2 M^{-1} ± 3.10%. The generated association constants for barbaralane **5**/**5′** and β-CD only demonstrate slight variations. ^{1}H NMR titrations completed with compound **6** do not show any splitting – only a change in the chemical shift is observed (Figures 3.32–3.35). The chemical shift for positions 3, 7, 1 and 5 in barbaralol **5**/**5′** are plotted against the number of equivalents of β-CD, producing association constants which are also all in good agreement with one another.

The results for the ^{1}H NMR titrations are summarised in Table 3.4. To determine the overall association constant and accompanying error, an average was calculated for all titrations (including different concentrations and optimisation algorithms) carried out with β-CD (Table 3.5). The results demonstrate that barbaralane **8**/**8′** has the strongest association constant (5.5×10^3 M^{-1} ± 2.81%) with β-CD, showing a six-fold enhancement compared to barbaralol **5**/**5′** and barbaralone **6**. All guest molecules are shown to form one-to-one inclusion complexes.

Table 3.4. Comparison of association constants and their respective errors between β-CD and barbaralane **8**/**8′**, barbaralol **5**/**5′** and barbaralone **6** at two different concentrations.

Host–Guest	Nelder-Mead Association Constant (K_a) / M^{-1}	L-BFGS-B Association Constant (K_a) / M^{-1}
β-CD (12.33 mM)–8/8′ (1.23 mM)	5.5×10^3 (± 3.33%)	5.5×10^3 (± 3.33%)
β-CD (6.16 mM)–8/8′ (0.62 mM)	5.5×10^3 (± 2.28%)	5.5×10^3 (± 2.28%)
β-CD (12.33 mM)–5/5′ (1.23 mM)	6.4×10^2 (± 2.99%)	6.4×10^2 (± 2.99%)
β-CD (6.16 mM)–5/5′ (0.62 mM)	9.1×10^2 (± 3.10%)	9.1×10^2 (± 3.10%)
β-CD (12.33 mM)–6 (1.23 mM)	9.9×10^2 (± 4.02%)	9.9×10^2 (± 4.02%)
β-CD (6.16 mM)–6 (0.62 mM)	8.0×10^2 (± 1.72%)	8.0×10^2 (± 1.72%)

Table 3.5. Averaged association constants and errors between β-CD and barbaralane **8**/**8′**, barbaralol **5**/**5′** and barbaralone **6**.

Host–Guest	Average Association Constant (K_a) / M^{-1} and Error / %
β-CD–8/8′	5.5×10^3 ± 2.81%
β-CD–5/5′	7.8×10^2 ± 3.10%
β-CD–6	9.0×10^2 ± 2.87%

3.6.2.4 X-ray Crystallographic Analysis

(±)-Tricyclo[3.3.1.$0^{2,8}$]nona-3,6-dien-9-ol (5/5′)

Crystals of **5/5′** suitable for X-ray diffraction were grown by slow evaporation of a saturated MeCN solution.

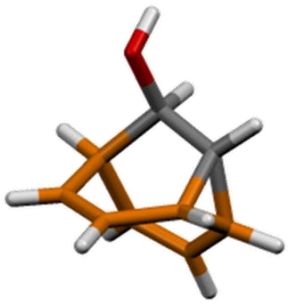

Crystal System: Monoclinic

Space group: C2/c

Unit Cell Parameters: a = 21.0930(5) Å, b = 12.8259(3) Å, c = 20.9409(5) Å, α = 90 °, β = 104.2572(10) °, γ = 90 °, V = 5490.8(2) $Å^3$, Z = 32

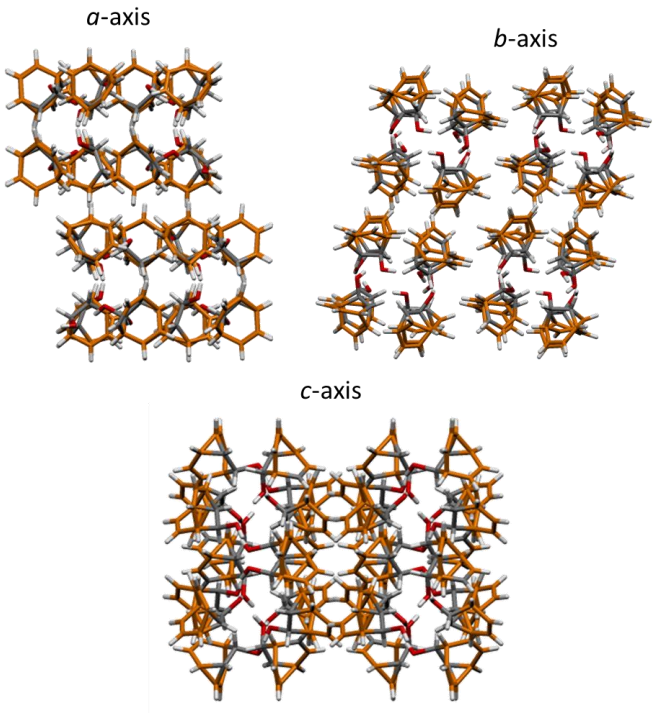

Figure 3.35. Solid-state superstructure of **5/5′** viewed along the three unit cell axes.

(±)-6-(4-Methylphenyl)bicyclo[3.2.2]nona-3,8-dien-6-ol (8/8′)

Crystals of **8/8′** suitable for X-ray diffraction were grown by slow evaporation of a saturated CH_2Cl_2 solution.

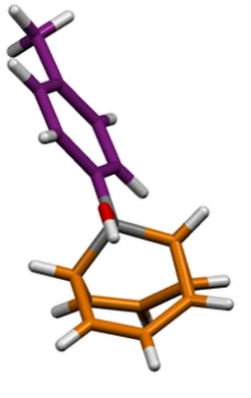

Crystal System: Monoclinic

Space group: $P2_1/n$

Unit Cell Parameters: a = 10.2068(4) Å, b = 11.9926(4) Å, c = 19.6537(7) Å, α = 90 °, β = 103.9617(14) °, γ = 90 °, V = 2334.66(15) $Å^3$, Z = 8

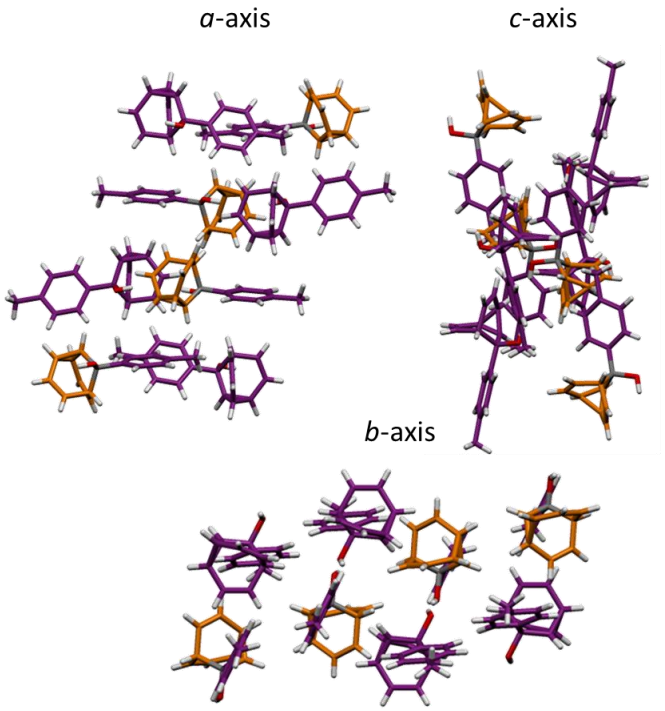

Figure 3.36. Solid-state superstructure of **8/8′** viewed along the three unit cell axes.

(±)-4-({Tricyclo[3.3.1.$0^{2,8}$]nona-3,6-dien-9-yloxy} carbonyl) benzoic acid(11/11′)

Crystals of **11/11′** suitable for X-ray diffraction were grown by slow evaporation of a saturated MeCN solution.

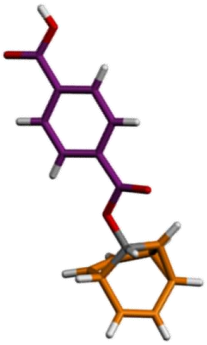

Crystal System: Monoclinic

Space group: C2/c

Unit Cell Parameters: a = 11.439(3) Å, b = 6.3633(15) Å, c = 42.650(10) Å, α = 90 °, β = 95.091(5) °, γ = 90 °, V = 3092.3(13) $Å^3$, Z = 8

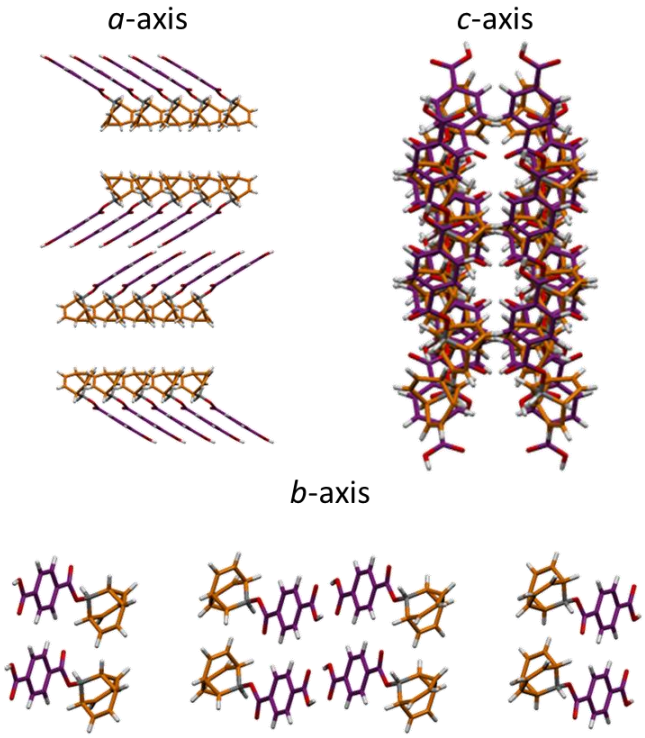

Figure 3.37. Solid-state superstructure of **11/11′** viewed along the three unit cell axes.

(±)-4-({Tricyclo[3.3.1.$0^{2,8}$]nona-3,6-dien-9-yl 4-{tricyclo[3.3.1.$0^{2,8}$]nona-3,6-dien-9-carbonyl} benzoate (12)

Crystals of **12** suitable for X-ray diffraction were grown by slow evaporation of a saturated MeCN solution.

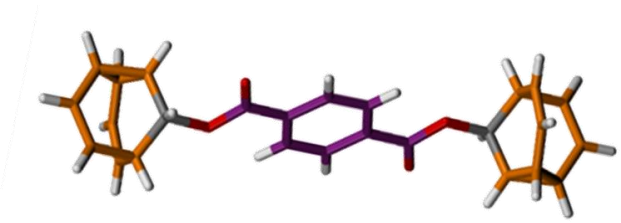

Crystal System: Triclinic

Space group: P-1

Unit Cell Parameters: a = 6.4905(12) Å, b = 10.678(2) Å, c = 13.900(3) Å, α = 90.748(5) °, β = 96.640(5) °, γ = 956.2(3) °, V = 3092.3(13) $Å^3$, Z = 2

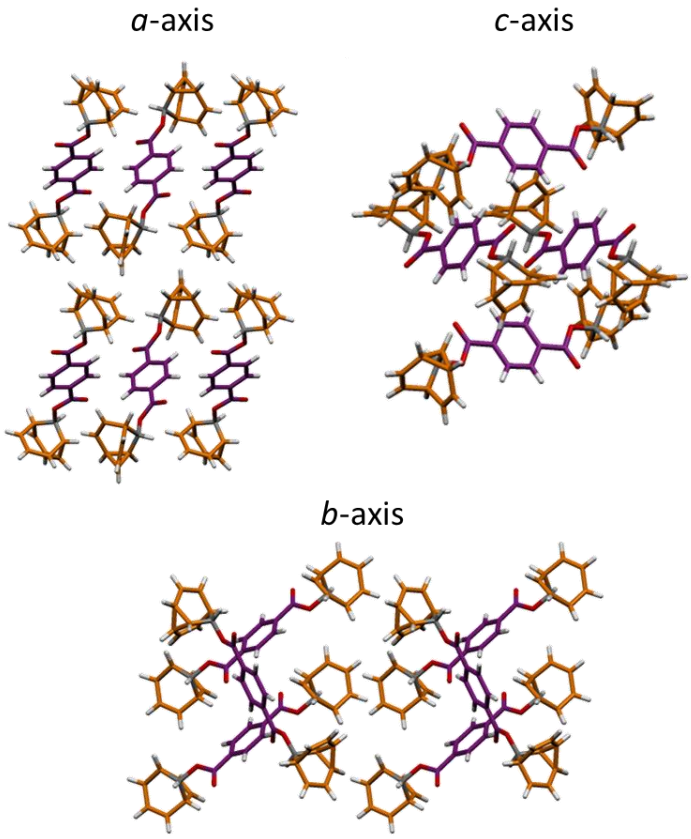

Figure 3.38. Solid-state superstructure of **12** viewed along the three unit cell axes.

Host–Guest Complex: β-CD–Tricyclo[3.3.1.$0^{2,8}$]nona-3,6-dien-9-ol (5)

Crystals of the host–guest complex suitable for X-ray diffraction were grown by the slow cooling of an aqueous H_2O solution of the two compounds in a one-to-one ratio from 100 °C to room temperature over the course of two weeks which was followed by slow evapouration of the solution. See Figure 3.12 in the Results and Discussion.

Crystal System: Monoclinic

Space group: $P2_1$

Unit Cell Parameters: a = 15.0368(9) Å, b = 10.3400(6) Å, c = 20.0143(12) Å, α = 90 °, β = 102.729(2) °, γ = 90 °, V = 3035.4(3) $Å^3$, Z = 2

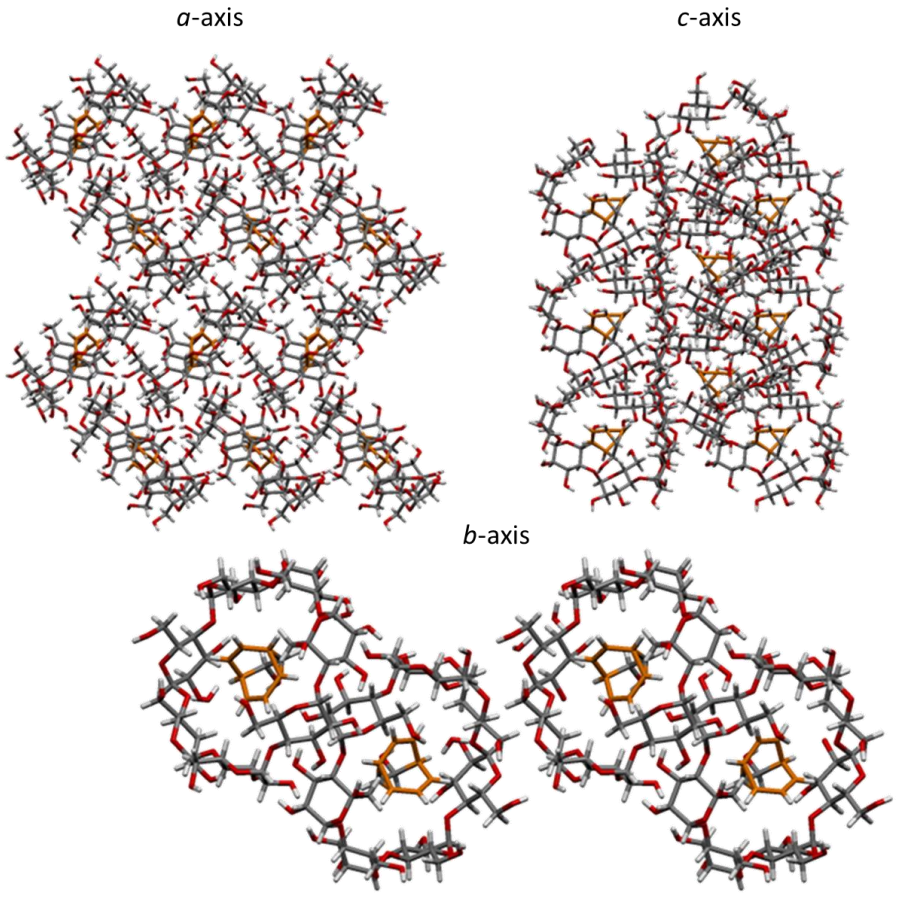

Figure 3.39. Solid-state superstructure of the host–guest complex viewed along the three unit cell axes.

3.7 References

1. (a) E. L. Eliel and S. H. Wilen, *Stereochemistry of Organic Compounds*, John Wiley & Sons, Inc., New York, 1st edition, 1994; (b) D. G. Morris, *Stereochemistry*, Royal Society of Chemistry, Cambridge, 1st edition, 2001.

2. J. R. Brandt, F. Salerno and M. J. Fuchter, *Nat. Rev. Chem.* 2017, **1**, 1.

3. (a) L. Pasteur, *C. R. Séances Acad. Sci.* 1848, **26**, 535; (b) L. Pasteur, *C. R. Séances Acad. Sci.* 1858, **46**, 615.

4. J. Gal, *Chirality*. 2008, **20**, 1.

5. (a) C. Brown, *Chirality in Drug Design and Synthesis*, Academic Press, Harcourt BraceJovanovich Publishers, 1st edition, 1990; (b) I. K. Reddy and R. Mehvar, *J. Med. Chem.* 2005, **48**, 3935; (c) W. H. Brooks, W. C. Guida and K. G. Daniel, *Curr. Top. Med. Chem.* 2011, **11**, 760.

6. (a) N. H. Evans, *Chem. Eur. J*. 2018, **24**, 3101; J. –C. Chambrom, C. Dietrich-Buchecker and J. –P. Sauvage, *Top. Curr. Chem.* 1993, **165**, 131; (c) C. Wolf, Dynamic *Stereochemisty of Chiral Compounds: Principles and Applications*, Royal Society of Chemistry, Cambridge, 1st edition, 2007

7. S. M. Marrow, A. J. Bissette and S. P. Fletcher, *Nat. Nanotechnology*. 2017, **12**, 410.

8. A. Forni, I. Moretti and G. Torre, *J. Chem. Soc. Chem. Commun.* 1977, 731.

9. (a) A. Raku, L. C. Allen and K. Mislow, Curr. *Angew. Chem. Int. Ed*. 1970, **9**, 400; (b) M. W. Gillick-Healy, E. V. Jennings, H. Meller-Bunz, Y. Ortin, K. Nikitin and D. G. Gilheany, *Chem. Eur. J.* 2017, **23**, 2332.

10. (a) S. Sugiyama, S. Wantabe, T. Inoue, R. Kurihara, T. Itou and K. Ishiii, *Tetrahedron.* 2003, **59**, 3417; (b) M. Alvarez-Pérez, S. M. Goldup, D. A. Leigh and A. M. Z. Slawin, *J. Am. Chem. Soc.* 2008, **130**, 1836.

11. B. Kim, G. Storch, G. Banerjee, B. Q. Mercado, J. Castillo-Lora, G. W. Brudvig, J. M. Mayer and S. J. Miller, *J. Am. Chem. Soc*. 2017, **139**, 15329.

12. (a) D. Barasch, O. Zipori, I. Ringel, I. Ginsburg, A. Samuni and J. Katzhendler, *Eur. J. Med. Chem.* 1999, **7**, 569; (b) T. P. A. Devasagayam, J. C. Tilak, K. K. Boloor, K. S. Sane, S, S, Ghaskadbi and R. D. Lele, *J. Assoc. Physicians. India.* 2004, **52**, 794.

13. (a) W. von E. Doering and W. R. Roth, *Tetrahedron* 1963, **19**, 715; (b) G. Schröder, *Angew. Chem.* 1963, **75**, 722; (c) A. Ault, *J. Chem. Educ.* 2001, **78**, 924; (d) O. Yahiaoui, L. F. Pašteka, B. Judeel and T. Fallon, *Angew. Chem. Int. Ed.* 2018, **57**, 2570.

14. (a) P. Ahlberg, D. L. Harris and S. Winstein, *J. Am. Chem. Soc*. 1970, **92**, 4454; (b) D. Cremer, P. Svensson, E. Kraka and P. Ahlberg, *J. Am. Chem. Soc.* 1993, **115**, 7445.

15. (a) A. R. Lippert, A. Naganawa, V. L. Keleshian and J. W. Bode, *J. Am. Chem. Soc.* 2010, **132**, 15790; (b) K. K. Larson, M. He, J. F. Teichert, A. Naganawa and J. W. Bode, *Chem. Sci.* 2012, **3**, 1825; (c) J. F. Teichert, D. Mazunin and J. W. Bode, *J. Am. Chem. Soc.* 2013, **135**, 11314.

16. (a) J. G. Henkel and J. T. Hane, *J. Org. Chem.* 1983, **48**, 3858; (b) C. Engdahl and P. Ahlberg, *J. Am. Chem. Soc.* 1979, **101**, 3940; (c) L. G. Greifenstein, J. B. Lambert, M. J. Broadhurst, L. A. Paquette, *J. Org. Chem.* 1973, **38**, 1210; (d) G. G. Cristoph, S. Hardwick, U. Jacobsson Y.-B. Koh, R. Moerck and L. A. Paquette, *Tetrahedron. Lett.* 1977, **14**, 1249.

17. (a) J. A. Dale and D. L. Dull and H. S. Mosher, *J. Org. Chem.* 1969, **34**, 2543; (b) D. E. Ward and C. K. Rhee, *Tetrahedron Lett.* 1991, **32**, 7165.

18. R. F. Borch and A. I. Hassid, *J. Org. Chem.* 1972, **37**, 1673.

19. (a) P. R. McGonigal, C. de León, Y. H. Wang, A. Homs, C. R. Solorio-Alvarado and A. M. Echavarren, *Angew. Chem. Int. Ed.* 2012, **51**, 13093; (b) S. Ferrer, A. M. Echavarren, *Angew. Chem. Int. Ed*. 2016, **55**, 11178.

20. R. E. Moore, J. A. Pettus and J. Mistysyn, *J. Org. Chem.* 1974, **39**, 2201.

21. E. Pretsch, P. Bühlmann and M. Badertscher, *Structure Determination of Organic Compounds*, Springer-Verlag, Berlin Heidelberg, 4th edition, 2009.

22. L. M. Harwood and T. D. W. Claridge, *Introduction into Organic Spectroscopy*, Oxford University Press, Oxford, 1st edition, 1996.

23. A CH_2Cl_2-CS_2 solvent mixture gave the best compromise of solubility and low freezing point, but freezes below 149 K.

24. (a) R. O. Gould, C. L. Jones, T. A. Stephenson and D. A. Tocher, *J. Organomet. Chem.* 1984, **264**, 365; (b) J. L. Davidson, W. F. Wilson, L. Manojlović-Muir and K. W. Muir, *J. Organomet. Chem.* 1983, **254**, C6–C10; (c) K. M. J. Brands and A. J. Davies, *Chem. Rev.* 2006, **106**, 2711; (d) Y. Kitamoto, K. Suzuki, N. Morohashi, K. Sakai and T. Hattori. *J. Org. Chem.* 2013, **78**, 597; (e) M. Sakamoto and T. Mino *Advances in Organic Crystal Chemistry: Comprehensive Reviews*, ed. R. Tamura and M. Miyata, Springer, Tokyo, 1st edition, 2015.

25. Some monosubstituted bullvalenes resolve to single isomers upon crystallisation. (a) K. Müller, H. Zimmermann, C. Krieger, R. Poupko and Z. Luz, *J. Am. Chem. Soc.* 1996, **118**, 8006; (b) R. Poupko, K. Müller, C. Krieger, H. Zimmermann and Z. Luz, *J. Am. Chem. Soc.* 1996, **118**, 8015; (c) Z. Luz, L. Olivier, R. Poupko, K. Müller, C. Krieger and H. Zimmermann, *J. Am. Chem. Soc.* 1998, **120**, 5526.

26. H. D. Flack, *Helv. Chim. Acta.* 2003, **86**, 905.

27. (a) P. Thordarson, *Chem. Soc. Rev.* 2011, **40**, 1305; (b) D. Brynn Hibbert and P. Thordarson, *Chem. Commun.* 2016, **52**, 12792.

28. http://app.supramolecular.org/bindfit/ (accessed 1st June 2019)

29. (a) J. A. Nelder and R. Mead, *The Computer Journal.* 1965, **7**, 308; (b) W. Spendley, G. R. Hext and F. R. Himsworth, *Technometrics.* 1962, **4**, 441.

30. (a) R. H Byrd, P. Lu, J. Nocedal and C. Zhu, *SIAM J. Sci. Comput.* 1995, **16**, 1190; (b) C. Zhu, R. H. Byrd, P. Lu, and J. Nocedal, *ACM Transitions on Mathematical Software.* 1997, **23**, 550.

31. D. Grandero, J. Bordello, M. J. Pérez-Alvite, M. Novo and W. Al-Soufi, *Int. J. Mol. Sci.* 2010, **11**, 173.

32. (a) K. Sadrerafi, E. E. Moore and M. W. Lee Jr, *J. Inc. Phenom.Macrocycl. Chem.* 2015**, 83**, 159; (b) M. R. Eftink, M. L. Andy, K. Bystrom, H. D. Perlmutter and D. S. J. Kristol, *J. Am. Chem. Soc.*1989, **111**, 6765; (c) W. C. Cromwell, K. Bystrom and M. R. Eftink, *J. Phys. Chem.* 1985, **89**, 326.

33. (a) C. Senac, S. Desgranges, C. Contino-Pépin, W. Urbach, P. F. J. Fuchs and N. Taulier, *ACS Omega.* 2018, **3**, 1014; (b) B. Seigal and R. Breslow, *J. Am. Chem. Soc.* 1975, **97**, 6896; (c) R. Zhao, T. Tan and C. Sandstrom, *J. Phys. Chem.* 2011, **37**, 146.

34. (a) J. A. Aguilar and A. M. Kenwright, *Analyst.* 2016, **141**, 236; (b) J. A. Aguilar, M. Nilsson, G. Bodenhausen and G. A. Morris, *Chem. Commun.* 2012, **48**, 811.

35. O. V. Dolomanov, L. J. Bourhis, R. J. Gildea, J. A. K. Howard, H. J. Puschmann, *Appl. Crystallogr.* 2009, **42**, 339.

36. G. M. Sheldrick. *Acta. Crystallogr. Sect. A Found. Crystallogr.* 2008, **64**, 112.

37. N. M. O'Boyle, T. Vandermeersch, C. J. Flynn, A. R. Maguire and G. R. Hutchinson, *J. Cheminf.* 2011, **3**, 8.

38. Y. Zhao, D. Truhlar, *Theor. Chem. Acc.* 2008, **120**, 215.

39. J.-D Chai, M. Head-Gordon, *Phys. Chem. Chem. Phys.* 2008, **10**, 6615.

40. Guassian 09, Revision A.02, M. J. Frisch, G. W. Trucks, H. B. Schlegel, G. E. Scuseria, M. A. Robb, J. R. Cheeseman, G. Scalmani, V. Barone, G. A. Petersson, H. Nakatsuji, X. Li, M. Caricato, A. V. Marenich, J. Bloino, B. G. Janesko, R. Gomperts, B. Mennucci, H. P. Hratchian, J. V. Ortiz, A. F. Izmaylov, J. L. Sonnenberg, D. Williams-Young, F. Ding, F. Lipparini, F. Egidi, J. Goings, B. Peng, A. Petrone, T. Henderson, D. Ranasinghe, V. G. Zakrzewski, J. Gao, N. Rega, G. Zheng, W. Liang, M. Hada, M. Ehara, K. Toyota, R. Fukuda, J. Hasegawa, M. Ishida, T. Nakajima, Y. Honda, O. Kitao, H. Nakai, T. Vreven, K. Throssell, J. A. Jr. Montgomery, J. E. Peralta, F. Ogliaro, M. J. Bearpark, J. J. Heyd, E. N. Brothers, K. N. Kudin, V. N. Staroverov, T. A. Keith, R. Kobayashi, J. Normand, K. Raghavachari, A. P. Rendell, J. C. Burant, S. S. Iyengar, J. Tomasi, M. Cossi, J. M. Millam, M. Klene, C. Adamo, R. Cammi, J. W. Ochterski, R. L. Martin, K. Morokuma, O. Farkas, J. B. Foresman, D. J. Fox, Gaussian, Inc., Wallingford CT, 2016.

41. M. Cossi, N. Rega. G. Scalmani, V. J. Barone, *Comput. Chem.* 2003, **24**, 669.

42. S. J. Clark, M. D. Segall, C. J. Pickard, P. J. Hasnip, M. J. Probert, K. Refson and M. C. Z. Payne, *Kristallogr.* 2005, **220**, 567.

43. J. P. Perdew, K. Burke and M. Ernzerhof, *Phys. Rev. Lett.* 1996, **77**, 3865.

CHAPTER 4

STABILISING CATIONIC FLUXIONAL CARBON CAGES

Synopsis

This Chapter discusses three unique synthetic methodologies, which utilise gold catalysis, towards creating several series of novel hydroxy barbaralanes. These hydroxy barbaralanes are subjected to superacidic conditions to generate their corresponding barbaralyl cation species. Through dynamic NMR we show that these barbaralyl cations are 'frozen' molecules (on the NMR timescale that we observe) with a higher activation energy barrier to exchange and a higher energy barrier to the irreversible rearrangement we observe in comparison to other barbaralyl cations present in the literature. We show that adding substituents (preferably electron-donating) to the barbaralyl cation in turn permit for the stability to be tuned by substituent effects, allowing for in-depth studies into isomerisations and dynamics which have previously proven to be challenging.

Acknowledgements

The following people are gratefully acknowledged for their contribution to this chapter: MChem student Gemma L. Parker helped with the synthesis of compound **4a**. Andrew Turley helped synthesise tropylium **14**. Dr Jiri Sturala carried out the *in silico* modelling and also helped to synthesise compounds **15a**–**d**. The experimental procedure to generate barbaralyl cations was developed in collaboration with Professor G. K. Surya Prakash and Archith Nirmalchander at the University of Southern California. Dr Dimitry S. Yufit solved all of the X-ray crystal structures. We thank Dr Alain Goeppert for useful discussions and the Royal Society of Chemistry for a research mobility grant. We are grateful to Allan Kershaw and Dr Juan A. Aguilar for assistance with NMR measurements.

4.1 Introduction

Fluxional carbon cages such as bullvalene[1] and the barbaralyl cation[2] are notable for their unique bonding composition, which favour multiple sequential, strain-assisted Cope rearrangements.[3] As a result, these Cope rearrangements allow for every carbon atom to exchange with every other carbon atom giving rise to 1 209 600 and 181 400 degenerate valence isomers, respectively. Bode *et al.* have elegantly demonstrated[4] how constitutionally dynamic bullvalene derivatives can be exploited as single-molecule sensing arrays. They have revealed that when a shapeshifting sensor interacts with an analyte through noncovalent or dynamic covalent bonding, the distribution of the oligo-substituted bullvalene isomers is shifted to a population which is unique to that analyte consequently showing a distinctive spectroscopic fingerprint (Figure 4.1a). For example, the reversible condensation of the two boronic acid groups of tetra-substituted bullvalene with diol groups present in a variety of polyols (exemplified using ten structurally diverse carbohydrates, sialic acids and flavanols) gives rise to characteristic and distinguishable ^{13}C NMR spectra which can be translated into a readout technique.[4] However, the development of shapeshifting sensors based on bullvalene have been severely restricted by the linear, low-yielding syntheses of typically fifteen steps or more required to make them.

Fluxional barbaralyl cations were first postulated as fleeting intermediates[5] during solvolysis,[6] but it was not until the seminal studies conducted by Winsein and Ahlberg that they were prepared as long-lived species (albeit, through multistep syntheses and under harsh conditions). Barbaralyl cations have been synthesised by dehydration of the corresponding barbaralol precursors in superacid, whereupon their methine groups interchange rapidly and reversibly at temperatures between –150 °C and –135 °C with an activation energy to rearrangement ($\Delta G^{\neq}$) of 21.5 kJ·mol^{-1}.[6] At higher temperatures, an irreversible allylic rearrangement to a bishomotropylium cation occurs ($\Delta G^{\neq}$ = 43.5 kJ·mol^{-1}),[7] and has prevented barbaralyl cations and other simple derivatives from being further studied and exploited (Figure 4.1b). Notably, however, one report has revealed that an electron-rich ferrocenyl substituent increases the cation's stability (in trifluoroacetic acid at 33 °C) demonstrating that substitution also drastically raises the stability.[8] Through the recently reported gold-catalysed

isomerisation of alkynyl cycloheptatrienes[9] (Figure 4.1c) passing through a fleeting barbaralyl cation and forming barbaralyl cation precursors, we can now easily access barbaralanes bearing electron rich substituents. We hypothesise that synthesising barbaralanes which bear several electron-rich substituents (in order to increase the stability of the cation), and subjecting them to superacidic conditions will allow for a new series of stable cationic fluxional carbon cages, which may have the potential to be used as a new class of shapeshifting sensors.

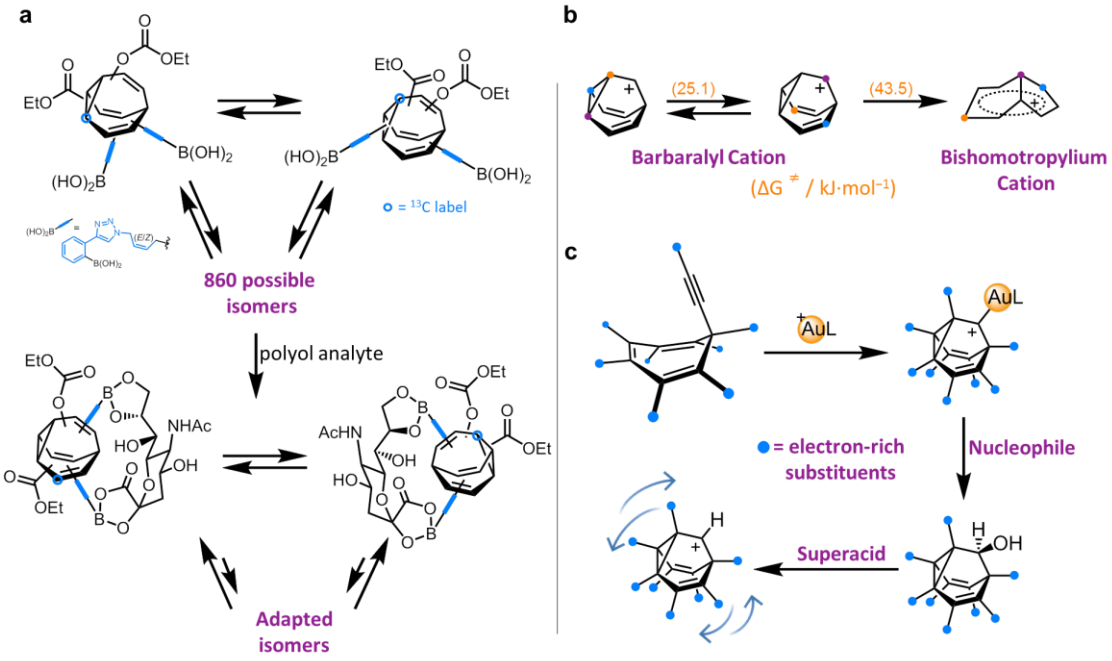

Figure 4.1. (a) A tetra-substituted bullvalene showing a shift in equilibrium and isomer distribution upon binding with a polyol analyte and (b) the barbaralyl cation with its activation energy to rearrangement ($\Delta G^{\neq}$) and activation energy for its irreversible rearrangement ($\Delta G^{\neq}$) to the bishomotropylium cation. (c) A scheme showing a potential synthetic route towards stable cationic carbon cages bearing electron-rich substituents.

Here we report on three novel synthetic methodologies which have all been utilised in generating several series of unique hydroxy barbaralanes. Subsequently, these hydroxy barbaralanes have been subjected to superacidic conditions, which has allowed for the generation of a new series of cationic fluxional carbon cages. By completing several NMR experiments and calculating either the rate of exchange or the rate of the irreversible reaction, we observe that (i) the generated barbaralyl cations appear to show that the presence of an electron-deficient group reduces the stability of the cation, and (ii) introducing more substituents to the barbaralyl core

increases the activation energy barrier to exchange also increasing the energy barrier to the irreversible rearrangement that we observe. Overall, we are able to tune the ability the stability of the barbaralyl core *via* the addition of substituent effects.

4.2 Results and Discussion

In order to confirm our hypothesis that electron-rich groups increases cation stability, we first performed preliminary DFT calculations in Gaussian 16 rev A.03[10] using the MN12-L functional[11] and def2-SVP basis set,[12] with W06 density fitting functions. The *in silico* investigations determined the effect of systematically replacing the hydrogen atoms in the barbaralyl cation with either methyl or phenyl groups (Figure 4.2).

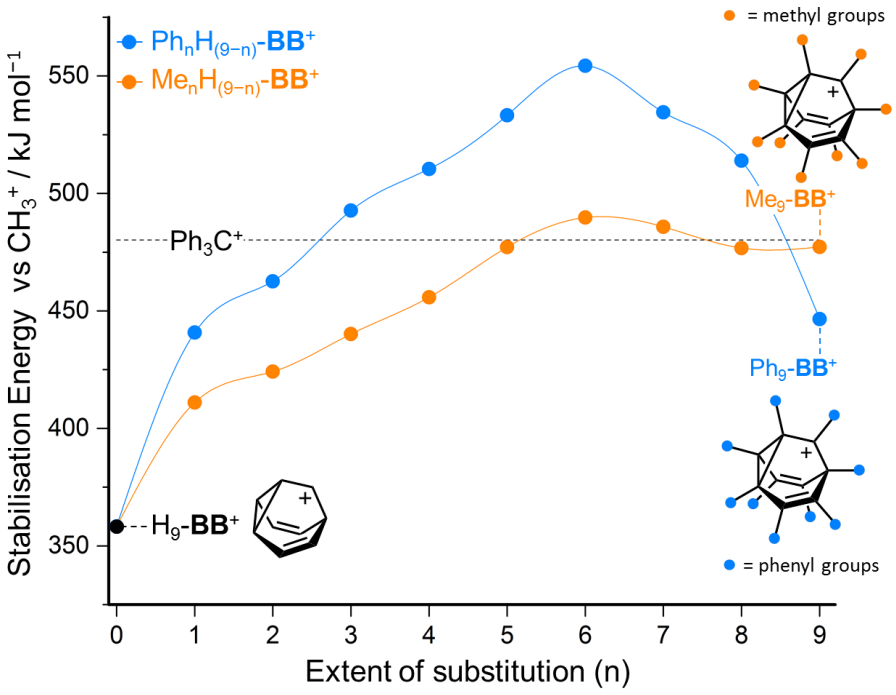

Figure 4.2. Preliminary DFT calculations showing the predicted stability of substituted barbaralyl cations based on stabilisation energies relative to CH_3^+.

To provide a frame of reference, a stabilisation energy of 480 kJ·mol^{-1} has been calculated for a cationic triphenylmethyl (Ph_3C^+) species, which is a long-lived species under ambient conditions, exhibits indefinite stability in non-nucleophilic solvents and even persists on the on the microsecond timescale (half-life of four microseconds)[13] when dissolved in a two-to-one mixture of water and acetonitrile.

The calculations validate the hypothesis that appropriate substituents, such as phenyl groups, will generate barbaralyl cations which are stable under ambient laboratory conditions. Importantly, the calculations also predict that similar or even larger stabilisation energies (up to 555 $kJ \cdot mol^{-1}$) would be obtained for some oligomethyl and oligophenyl barbaralyl cations. Six substituents provide the highest stabilisation energies for both phenyl and methyl substituents, however, the calculations show that only three phenyl groups are required to bypass the stabilisation energy of the cationic triphenylmethyl species.

With the calculations in hand we set out to produce several families of barbaralane precursors (with varying degrees of substitution, different functionalities and different placement around the barbaralyl core) which, when subjected to superacidic conditions, would produce stable cationic fluxional carbon cages by way of subsequent dehydraton. Utilising the gold-catalysed isomerisation of alkynyl cycloheptatrienes[9a] as demonstrated by Echavarren and co-workers in 2012, we first synthesised a series of barbaralanes bearing a methoxy functional group (**1a**–**1d**) (Scheme 4.1).

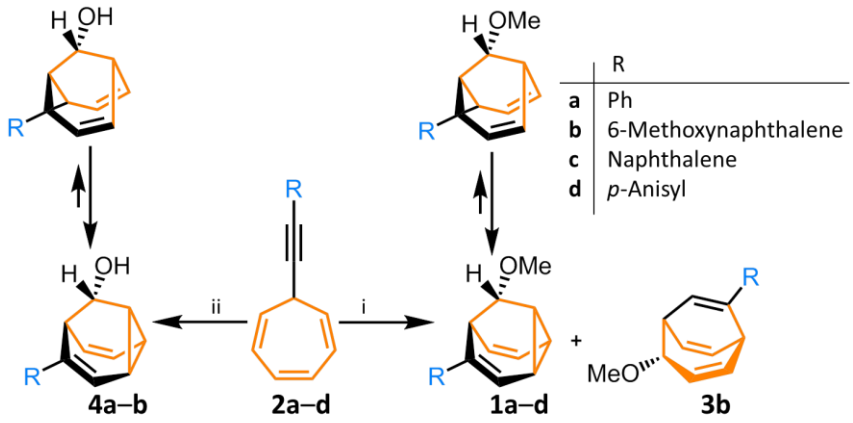

Scheme 4.1. Synthesis of barbaralanes bearing either a methoxy (**1a**–**d**) or hydroxy functional group (**4a**–**b**) as well as a bicyclononatriene (**3b**). Methoxy and hydroxy barbaralanes are formed as a mixture of regioisomers. Reagents and conditions: (i) MeOH:CH_2Cl_2 (2:1 or 1:1), 0 °C to rt, JohnPhos Au(MeCN)SbF_6 (2 mol%), 16 h, 34–49% (**1a**–**d**) and 13% (**3b**); (ii) H_2O:MeCN or H_2O: $(CH_3)_2CO$ (1:4), 0 °C to rt, JohnPhos Au(MeCN)SbF_6 (2 mol%), 16 h, 30% (**4a**) and 34% (**4b**). JohnPhos = (2-biphenyl)di-*tert*-butylphosphine.

The synthesis of methoxy barbaralanes utilises the gold catalyst JohnPhos Au(MeCN)SbF_6 which effectively promotes a cyclisation reaction through first

coordinating to the alkyne triple bond of the cycloheptatriene (**2**), before mediating the formation of a fluxional barbaralyl cation intermediate. The intermediate is readily intercepted with methanol, forming the desired methoxy barbaralanes (in 34–49% yields) as a mixture of regioisomers. In every case, the methoxy barbaralanes (**1a**–**1d**) formed one major regioisomer with minor regioisomers usually obtained as mixtures which cannot be fully separated into individual components. In one instance, an unexpected bicyclononatriene (**3b**) product bearing a 6-methoxynaphthalene functional group was formed (13% yield) and confirmed by X-ray crystallographic analysis (Appendix, Section 4.6.5). Compound **3b** is proposed to have formed as a result of nucleophilic attack on the fluxional barbaralyl cation intermediate at the strained cyclopropyl ring system rather than attack at the position of the cationic gold complex.

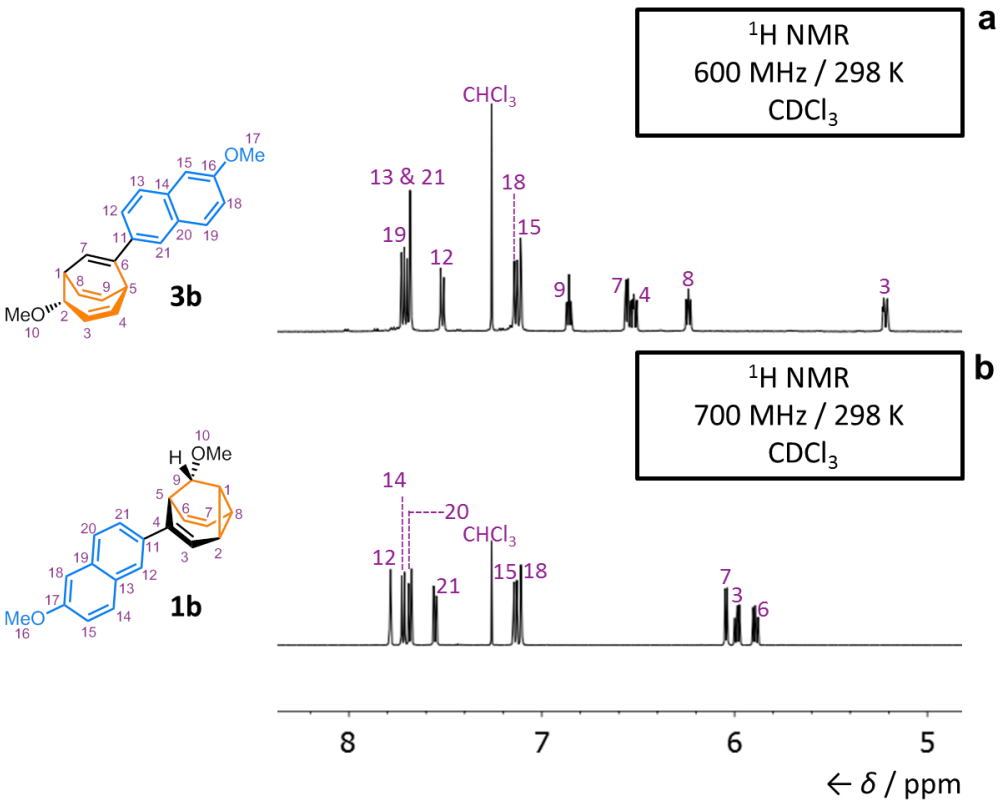

Figure 4.3. Partial ^{1}H NMR spectra for (a) bicyclononatriene (**3b**) and (b) methoxy barbaralane (**1b**). The spectra show the difference in the alkene region between the two structures.

The structure of bicyclononatriene **3b** was corroborated by 2D NMR spectroscopy (Appendix, Section 4.6.1) and the ^{1}H NMR spectrum was compared to the methoxy

barbaralane bearing the same functional group (Figure 4.3). The main difference in the ^{1}H NMR spectra is found in the alkene region. Bicyclononatriene **3b** demonstrates five alkene peaks corresponding to five alkene protons, whereas the methoxy barbaralane structure (**1b**) only possesses three alkene peaks. The identification of the bicyclononatriene product (**3b**) not only confirms the presence of the fluxional barbaralyl intermediate, but demonstrates that the intermediate can be intercepted by different pathways, forming unanticipated products.

The synthesis of barbaralyl cation precursors bearing a hydroxy functional group is of paramount importance with literature precedent[14-16] showing that their dehydration under acidic conditions directly affords barbaralyl cations. The same nucleophilic methodology as reported for methoxy barbaralanes (**1**) was exploited to form two hydroxy barbaralanes **4a** and **4b** in yields of 30% and 34%, respectively, using water as the co-solvent instead of methanol (Scheme 4.1). Acetonitrile and acetone are less nucleophilic than water, and were therefore used as the main co-solvents in the reaction in order to prevent a competing nucleophilic addition reaction. Hydroxy barbaralanes (**4**) are also formed as a mixture of regioisomers with the major isomer successfully being isolated and characterised by NMR spectroscopy.

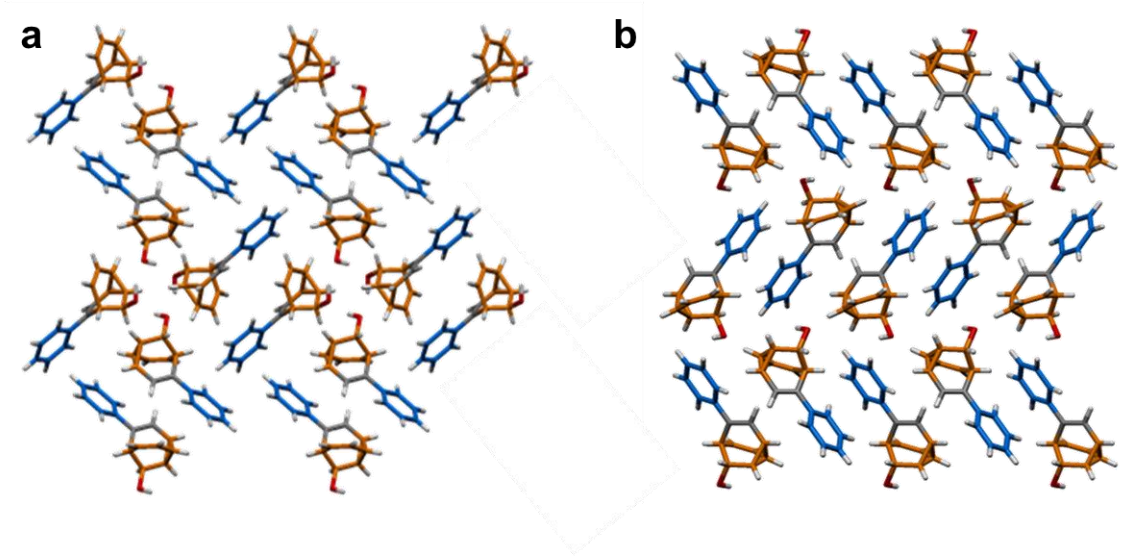

Figure 4.4. Solid-state superstructure of hydroxy barbaralane (**4a**) viewed along the *a*-axis in two different polymorphs (a) and (b).

Crystals of **4a** suitable for X-ray diffraction were grown using two different methods which resulted in two distinct polymorphs (Figure 4.4) (Appendix, Section 4.6.5). The first method used slow evapouration of an acetone and water solution, whereas the second method used slow evapouration of a saturated solution in water. The first polymorph (Figure 4.4a) contains two molecules in a triclinic system connected by strong hydrogen bonding (1.79 Å). The hydroxy barbaralane molecules have arranged themselves in a windmill-like motif on account of hydrogen-bonding interactions in the solid state. The second polymorph (Figure 4.4b) only contains one molecule in an orthorhombic system which demonstrates relatively weak hydrogen bonding (2.9 Å). The packing in the second polymorph is not dictated by hydrogen bonding, so the molecules have arranged themselves in a manner in which the aromatic stacking arrangement is parallel and face-centered.[17] Although the variation in the polymorphs can be clearly seen, the arrangement of the barbaralane molecules is similar in the manner in which steric repulsion between the bulky tricyclic frameworks is minimised.

As alcohol precursors are key intermediates when producing barbaralyl cations,[14-16] and since intercepting a fluxional barbaralyl cation with water only produced two hydroxy barbaralane isomers (**4**) with moderate yields (other alkynyl cycloheptatrienes presented solubility issues), we then set out to use Echavarren's synthesis of barbaralones to form hydroxy barbaralanes where the substitution of the aryl ring is in a different position (either on the 1 or 9 position of the barbaralyl core).[9b] The syntheses of barbaralones (which can bear different aryl functional groups) allow a large family of mono- and di-substituted hydroxy barbaralanes to be synthesised *via* the classic Grignard reaction,[18] which allows for the carbonyl present on barbaralone to form a tertiary alcohol.

The syntheses of mono-substituted (**5**/**5′**) and di-substituted (**6**/**6′**) barbaralanes follows the same synthetic methodology, only differing by the presence an aryl substituent on the starting alkynyl cycloheptatriene (**2**) (also present on the barbaralone intermediate (**7**)) for the synthesis of di-substituted barbaralanes (**6**/**6′**) (Scheme 4.2). The mono- and di-substituted hydroxy barbaralanes are synthesised from alkynyl cycloheptatrienes (**2**) which undergo gold-catalysed cycloisomerisation

to form a fluxional barbaralyl cation. This intermediate fluxional cation is then oxidised *in situ* by diphenyl sulphoxide yielding the intermediate barbaralones (**7**). The barbaralones (**7**) are then subjected to addition of an arylmagnesium bromide reagent (also generated *in situ*) which gives either hydroxy barbaralanes **5**/**5′** which bear a tertiary alcohol and one aromatic ring, or hydroxy barbaralanes **6**/**6′** which have an additional aromatic ring. In solution at room temperature these hydroxy barbaralanes (**5**/**5′** and **6**/**6′**) each exist as a mixture of two rapidly interconverting valence isomers and enantiomers; therefore, the fluxional nature of the molecules in solution leads to an averaged set of resonances being observed by NMR spectroscopy.

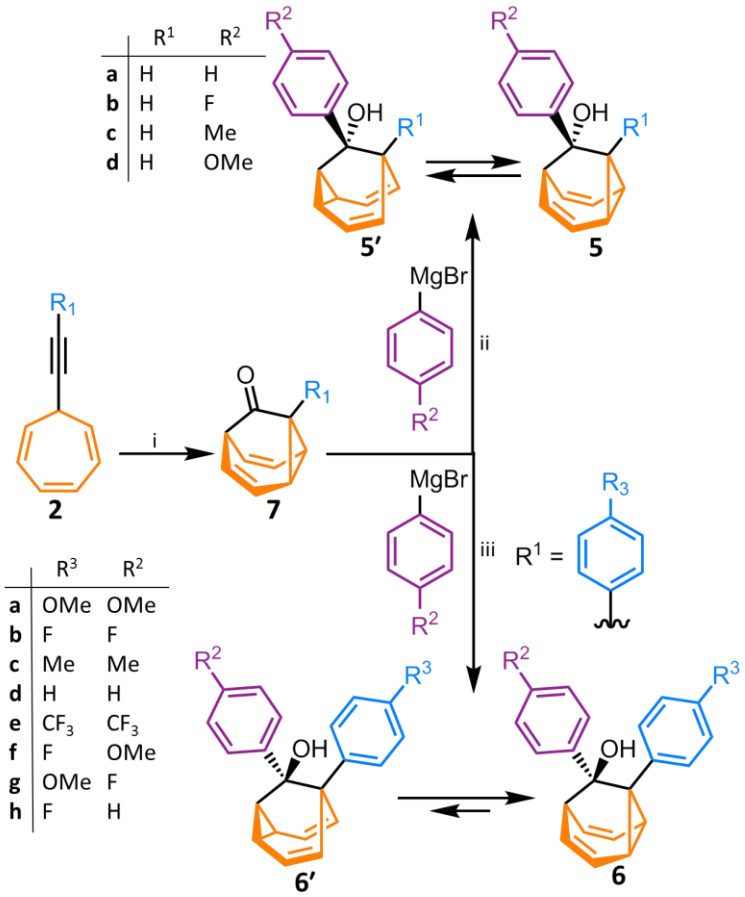

Scheme 4.2. General synthesis of mono-substituted hydroxy barbaralanes (**5**/**5′**) and di-substituted hydroxy barbaralanes (**6**/**6′**) through intermediates barbaralones (**7**) and alkynyl cycloheptatrienes (**2**). Reagents and conditions: (i) IPrAu(MeCN)BF_4 (5 mol%), rt, 16 h, 58–75%; (ii) THF, reflux to rt, then 0 °C to rt, 67–82%; (iii) THF, reflux to rt, then 0 °C to rt, 34–98%. IPrAu(MeCN)BF_4 (5 mol%), rt, 16 h. IPr = 1,3-bis(2,6-diisopropylphenyl)imidazol-2-ylidene.

As the DFT calculations (Figure 4.2.) predict that three phenyl groups are required to bypass the stabilisation energy of the cationic triphenylcyclopropenylium species, and our current synthetic methods only demonstrate barbarlyl cation precursors which bear two non-hydrogen groups, we then focused our efforts towards synthesising hydroxy barbaralanes which contain three or more aryl substituents. The synthetic methodology we follow by Echavarren and co-workers[9] utilises a tropylium salt (tropylium tetrafluoroborate)[19] to form the desired alkynyl cycloheptatrienes. The synthesis of the alkynyl cycloheptatrienes involves treatment of the starting terminal alkyne substrate with *n*-butyllithium, which generates a lithium acetylide. The organolithium species is then treated with the tropylium salt and the desired alkynyl cycloheptatriene is formed as a result of nucleophilic addition. We reasoned that creating tropylium salts bearing aryl substituents could replace tropylium tetrafluoroborate in the alkynyl cycloheptatriene synthesis, generating barbaralone precursors which could undergo subsequent addition of arylmagnsium bromides to generate hydroxy barbaralanes bearing more than two non-hydrogen groups.

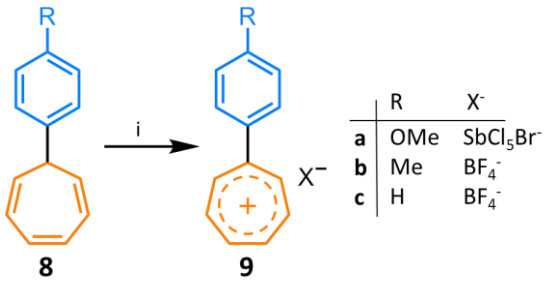

Scheme 4.3. Synthesis of substituted tropylium salts (**9**) through cycloheptatrienes (**8**). Reagents and conditions: (i) either (a) bromodiethylsulfonium bromopentachloroantimonate(V), $CHCl_3$, rt, 16 h, 13% (**9a**) or (b) MeCN, tritylium tetrafluoroborate, 50 °C, 10 min then Et_2O, 44% (**9b**) and 51% (**9c**).

We first synthesised cycloheptatrienes bearing an aryl substituent (**8**) in a similar manner to that of alkynyl cycloheptatrienes. To generate the corresponding tropylium salt (Scheme 4.3) we first utilised the oxidant bromodiethylsulphonium bromopentachloride(V) (BDSB) as Treitler *et al.* reported successful effects of bromonium-induced π-cyclisations with a diverse set of compounds.[20] BDSB successfully induced hydride abstraction with compound **8a**, however cycloheptatrienes **8b** and **8c** did not produce any of the corresponding cation. It is possible that the reaction only proceeds with cycloheptatriene **8a** as its ability to

donate electrons is much stronger in comparison to cycloheptatrienes **8b** and **8c**. In order to develop a general synthetic procedure towards substituted tropylium salts, we next utilised the oxidant tritylium tetrafluoroborate[19a] which effectively mediated hydride abstraction from cycloheptatrienes **8b** and **8c**. The corresponding tropylium salts **9b** and **9c** were synthesised in moderate yields of 44% and 51%, respectively. This reaction was not attempted with compound **8a**. Tritylium tetrafluoroborate was deemed as a better oxidant than BDSB, owing to higher yields and a more simplified procedure that could be applied to two cycloheptatrienes bearing an aryl substituent.

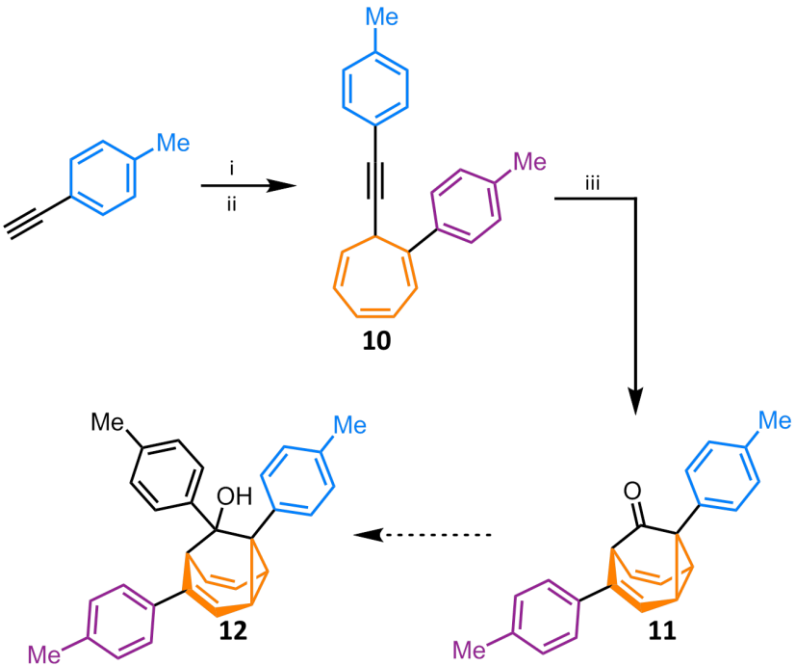

Scheme 4.4. Synthesis of substituted alkynyl cycloheptatriene (**10**) and di-substituted barbaralone (**11**). Reagents and conditions: (i) THF, *n*-BuLi, –78 °C, 1 h; (ii) **9b**, rt, 16 h, 44%; (iii) 3,5-dichloropyridine *N*-oxide, CH_2Cl_2, IPrAu(MeCN)BF_4 (5 mol%), rt, 16 h, 33%. IPr = 1,3-bis(2,6-diisopropylphenyl)imidazol-2-ylidene.

In order to synthesise a barbaralone bearing two aryl substituents (Scheme 4.4), we treated 4-ethynyltoluene with *n*-butyllithium, forming an organolithium species, which was subsequently treated with tropylium **9b** to form the desired alkynyl cycloheptatriene (**10**). The alkynyl cycloheptatriene (**10**) is initially formed as a mixture of positional isomers. Purification *via* column chromatography allows for one of the products to be isolated with the others remaining as an inseparable mixture. The gold(I) catalyst, IPrAu(MeCN)BF_4, is then employed in promoting a cyclisation reaction to form a fluxional barbaralyl intermediate which is oxidised by 3,5-

dichloropyridine *N*-oxide to furnish the desired barbaralone (**11**) in 33% yield. Due to the synthesis of **11** being completed on a small scale (~8 mg), subsequent addition of the arylmagneisum bromide was not attempted. However, the nucleophilic addition is known to proceed with similar barbaralone molecules, therefore we envision that hydroxy barbaralane **12** can be synthesised and utilised to form stable barbaralyl cation species.

In parallel to the synthesis of barbaralane **11**, we also synthesised heptaphenylcycloheptatriene **13** (using adapted synthetic procedures from Breslow[21] and Battise[22]) in order to synthesise a barbaralane core bearing seven or eight phenyl groups (Scheme 4.5).

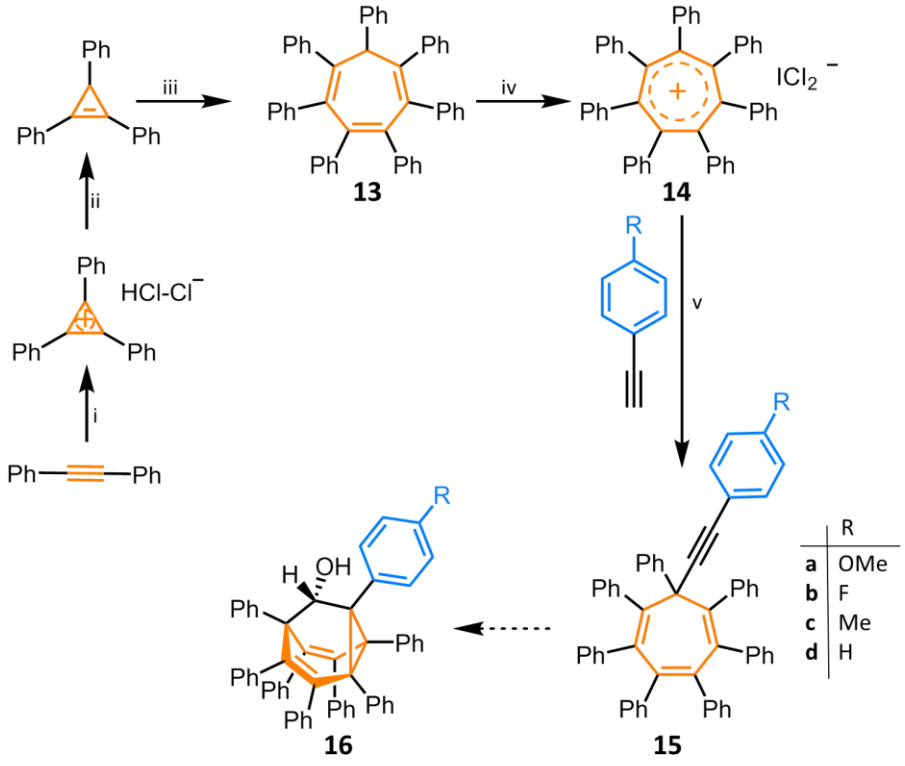

Scheme 4.5. Synthesis of heptaphenyltropylium (**14**) and heptaphenyl alkynyl cycloheptatrienes (**15**). Reagents and conditions: i) α,α-dichlorotoluene, $(CH_3)_3COK$, benzene, 3 h, 80 °C, (ii) $NaBH_4$, EtOH, rt, (iii) tetraphenylcyclopentadienone, *p*-xylene, 140 °C, 36 h (iv) ICl, CH_2Cl_2, rt, 24 h, (v) THF, *n*-BuLi, rt, 16 h.

Heptaphenylcycloheptatriene **13** was treated with a solution of iodine monochloride which successfully induced hydride abstraction, generating the desired heptaphenyltropylium (**14**). As heptaphenyltropylium **14** cannot be purified by

column chromatography owing to its interactions with silica and moderate susceptibility to nucleophilic attack, precipitation with a mixture of acetonitrile and diethyl ether was utilised to isolate the desired compound. X-ray crystallographic analysis confirmed the identity of the compound as well as the counterion (Appendix, Section 4.6.5).

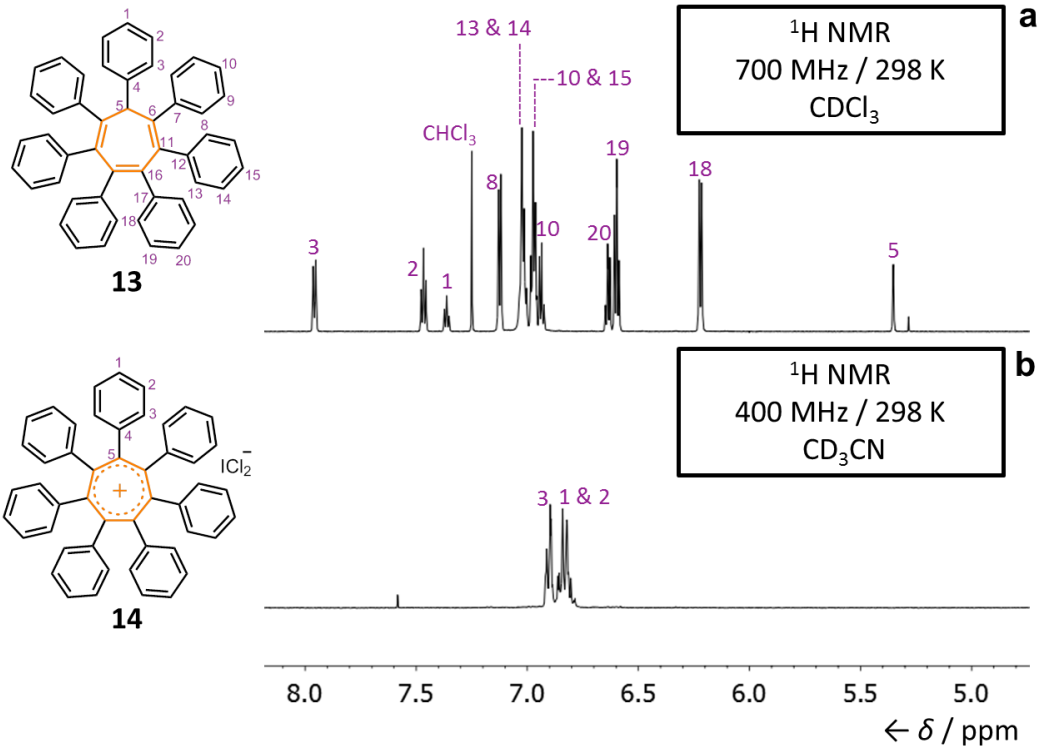

Figure 4.5. Partial ^{1}H NMR spectra for (a) heptaphenylcycloheptatriene (**13**) and (b) heptaphenyltropylium (**14**). The spectra show the significant change in symmetry between the two molecules.

The structure of compound **14** was corroborated by 2D NMR spectroscopy (Appendix, Section 4.6.1) and the ^{1}H NMR spectrum was compared to that of heptaphenylcycloheptatriene **13** (Figure 4.5). Heptaphenyl cycloheptatriene (**13**) possess one plane of symmetry within the molecule; therefore the ^{1}H NMR displays several inequivalent proton environments (Figure 4.5a). Removal of the sp^3 hybridised proton changes the ^{1}H NMR significantly by creating an element of seven-fold symmetry, reducing the number of unique proton environments from thirteen to three (Figure 4.5b).

The desired alkynyl cycloheptatrienes (**15**) were formed in a similar manner to the synthesis of compound **10**. The terminal alkyne was treated with *n*-butyllithium followed by the addition of heptaphenyltropylium **14**. The heptaphenyl alkynyl cycloheptatrienes (**15**) were formed as single isomers and purification was easily accomplished *via* column chromatography. Four substrates synthesised in yields ranging from 55% to 94%. Crystals of **15a** and **15d** suitable for X-ray diffraction were both grown by the slow cooling of a saturated acetonitrile solution (Figure 4.6) (Appendix, Section 4.6.5). The solid-state structure of cycloheptatrienes **15a** and **15d** both contain two molecules in a triclinic unit cell. The packing of cycloheptatriene **15a** shows that the molecules have arranged themselves in a head-to-tail manner so that steric repulsions are minimised between the many phenyl rings. The anisyl functional groups have organised themselves in an alternative manner with the phenyl rings slightly overlapping, demonstrating a face-to-face offset aromatic interaction. The packing of cycloheptatriene **15d** demonstrates that the molecules have aligned themselves in a 'slanted staircase' manner. The molecules are situated in pairs such that the alkynyl linked phenyl groups from each molecule face one another, allowing all the aromatic rings to pack together in the most efficient fashion.

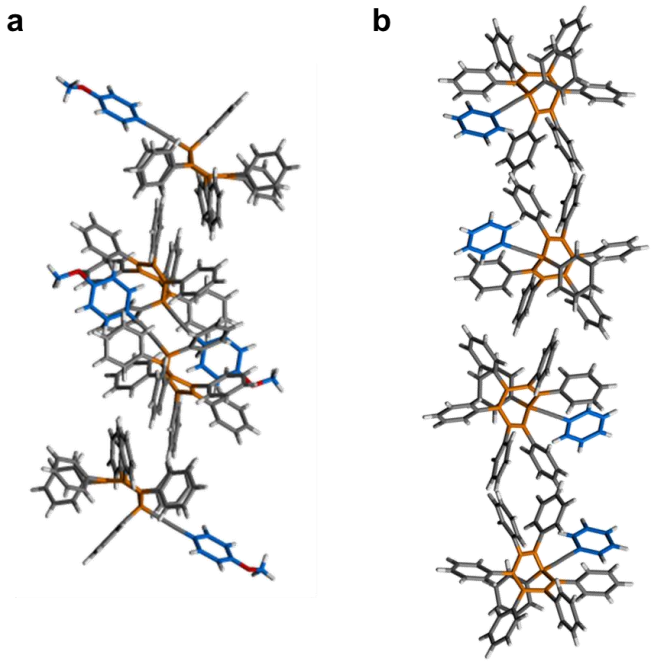

Figure 4.6. Solid-state superstructure of (a) heptaphenyl alkynyl cycloheptatriene **15a** viewed along the *a*-axis and (b) heptaphenyl alkynyl cycloheptatriene **15d** viewed along the *b*-axis.

The alkynyl cycloheptatrienes (**15**) were utilised in the attempted synthesis of barbaralanes which would bear seven phenyl rings directly attached to the barbaralane core (**16**). Preliminary investigations were completed with cycloheptatriene **15d**. The alkynyl cycloheptatriene (**15d**) was subjected to NMR-scale experiments in deuterated chloroform for two hours at 25 °C with a series of gold(I) catalysts (Table 4.1) to determine whether the gold catalyst could effectively promote a cyclisation reaction and form the barbaralyl cation intermediate. Analysis *via* ^{1}H NMR spectroscopy consistently demonstrated only the starting material. In an attempt to drive the reaction forwards and obtain the desired barbaralane core, the same reactions were attempted with the temperature increased to 50 °C (Table 4.1). The reactions with the increased temperatures also resulted in observing only the starting material. It is possible that the reaction does not proceed due to the several phenyl groups creating steric hindrance, which doesn't allow the cyclisation reaction to occur.

Table 4.1. Gold catalysts and temperatures utilised for the attempted synthesis of barbaralane molecules. Starting material = SM.[a]

Gold Catalyst (2 mol%)	Temperature / °C	Result[c]
JohnPhos[b] Au(MeCN)SbF_6	25	SM
JohnPhos[b] AuCl	25	SM
Chloro(tricyclohexylphosphine)gold	25	SM
Dichloro(2-pyridinecarboxylato)gold	25	SM
Chloro[tris(2,4-di-*tert*-butylphenyl)phosphite]gold	25	SM
JohnPhos[b] Au(MeCN)SbF_6	50	SM
JohnPhos[b] AuCl	50	SM
Chloro(tricyclohexylphosphine)gold	50	SM
Dichloro(2-pyridinecarboxylato)gold	50	SM
Chloro[tris(2,4-di-*tert*-butylphenyl)phosphite]gold	50	SM

[a]Conditions: Gold catalyst, temperature, $CDCl_3$, 2 h; [b]JohnPhos = (2-biphenyl)di-*tert*-butylphosphine; [c]Analysed by ^{1}H NMR spectroscopy of the reaction mixture.

With several hydroxy barbaralanes in hand, **4a** was first investigated for the generation of a barbaralyl cation. The hydroxy group in comparison to a methoxy group is a better leaving group, and the literature clearly shows that alcohol precursors under acidic conditions are directly dehydrated to form barbaralyl cations – hence we chose barbaralane **4a**.[23] We also chose hydroxy barbaralane **4a** as the barbaralane core only contains one phenyl group, so the barbaralyl cation generated would be easier to analyse by NMR spectroscopy in comparison to a cation with

several aryl substituents. Following the literature and experimental techniques[23] demonstrated by Ahlberg and Winstein,[14-16] we first carried out an experimental procedure utilising either trifluoromethanesulphonic or magic acid (HSO_3F:SbF_5, 1:1) under inert conditions and at low temperatures. Hydroxy barbaralane **4a** was subjected to both conditions during several experiments; however, the ^{1}H NMR spectra at –100 °C consistently did failed to show the desired cation, with the spectra acquired at higher temperatures showing inconclusive results. It is most likely that the failed results were due to significant difficulties in handling the superacids and rigorously maintaining low temperatures during the cation formation.

Following the unsuccessful generation of a fluxional barbaralyl cation, a new experimental procedure was developed (in collaboration with the Prakash research group at the University of Southern California) using a mixture of SO_2ClF:HSO_3F (10:1) at temperatures as low as –131 °C. Hydroxy barbaralanes **5**/**5′** were utilised to generate barbaralyl cations (Scheme 4.6) rather than hydroxy barbaralane **1a**, as the former would produce tertiary carbocations (*e.g.*, **17**), while the latter would produce less stable secondary carbocations.[24,25] Hydroxy barbaralanes **5**/**5′** were subjected to the new experimental procedure and the successful generation of the corresponding barbaralyl cations (**17**) was observed through ^{1}H NMR spectroscopy (Figure 4.7).

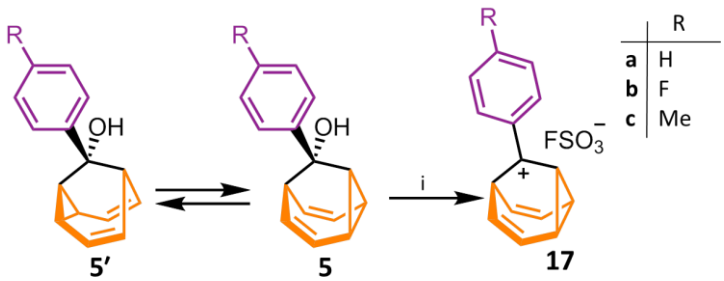

Scheme 4.6. Generation of barbaralyl cations (**17**). Reagents and conditions: (i) SO_2ClF precooled to –78 °C, HSO_3F precooled to –78 °C, liquid N_2 and *n*-pentane cooling bath at –131 °C.

The barbaralyl cations (**17**) generated appear to be ‘frozen’ molecules (*i.e.*, no interconversion is taking place) on time timescale of the NMR measurements between 165 K and 195 K. Comparing barbaralane **5c**/**5c′** to its corresponding cation (**17c**), we see that all the proton environments have shifted to a higher frequency (by ~0.5 ppm) due to deshielding from the cationic carbon centre. We also see that the

one peak labelled as positions 1 and 5 (~2.65 ppm) in Figure 4.7a has split into two inequivalent chemical environments (~5.0 and ~6.0 ppm) (Figure 4.7b) upon the formation of the cation, presumably due to the molecule entering the slow-exchange regime. On the other hand, the two inequivalent chemical environments in Figure 4.7a labelled as positions 7 and 3 (~5.6 and ~5.8 ppm) merge and form one peak around 6.2 ppm due to the hydride abstraction inducing a mirror plane (Figure 4.7b). The same splitting and merging of the chemical environments is observed for all the barbaralyl cations generated. The spectra also show that the barbaralyl cation **17b**, which bears an electron-withdrawing group, is less stable in comparison to barbaralyl cation **17c**, which bears an electron-donating group. The stability is observed as the ^{1}H NMR spectra are recorded at different temperatures for the different barbaralyl cations, and although the spectrum for **17b** is acquired at the lowest temperature (165 K), peaks corresponding to another product (which barbaralyl cation **17b** may be rearranging into) are already appearing showing that a transformation is taking place; albeit it potentially occurring slowly. The ^{1}H NMR spectrum for cation **17a** has been acquired at a higher temperature of 185 K; however, small peaks between 7 and 8 ppm already show that a rearrangement is taking place. The spectra acquired at different temperatures confirm that an electron-rich substituent increases the barbaralyl cation's stability.

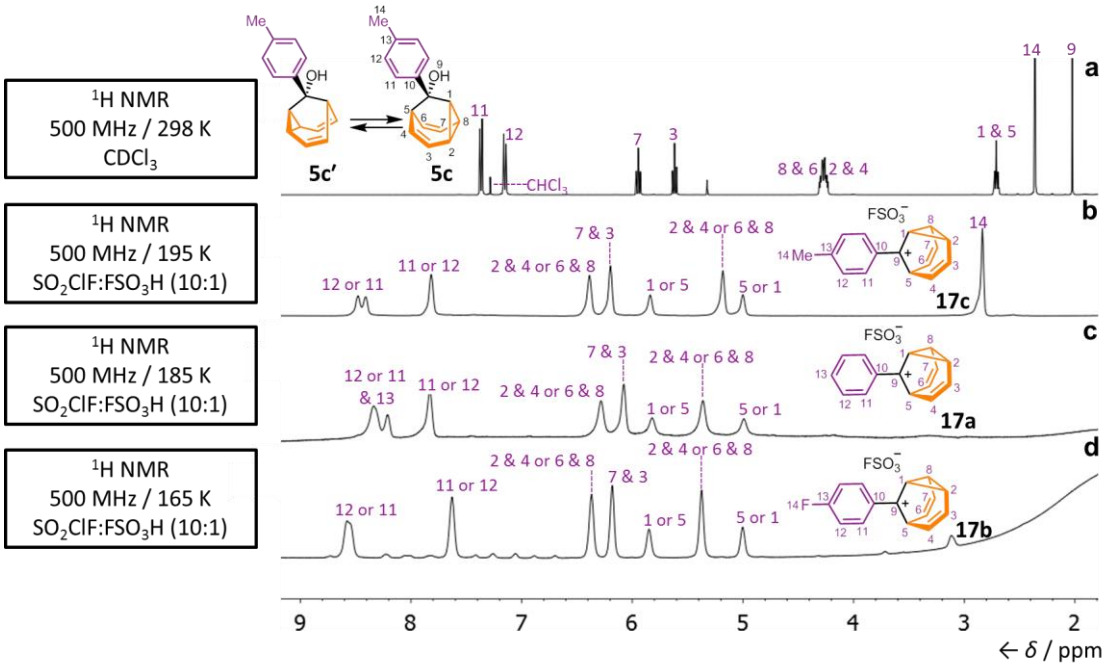

Figure 4.7. Partial ^{1}H NMR spectra of (a) hydroxy barbaralane **5c**/**5c′** (for clarity only one enantiomer has been labelled in the ^{1}H NMR spectrum; however both valence isomers are in fast exchange) at room temperature, (b) barbaralyl cation **17c**, (c) barbaralyl cation **17a** and (d) barbaralyl cation **17b**.

We next sought to determine the activation energy barrier to exchange ($\Delta G^{\neq}$) by utilising NMR spectroscopy (Appendix, Sections 4.6.2 and 4.6.3); with the reasoning that calculating the rate of exchange through exchange spectroscopy (EXSY) experiments. First, a nuclear overhauser effect spectroscopy (NOESY) experiment was run however, we were unable to distinguish between NOESY and EXSY peaks (all cross peaks were within the same phase), so a rotating frame nuclear overhauser effect spectroscopy (ROESY) experiment was acquired. The ROESY spectrum (Figure 4.8) allowed for differentiation between NOESY and EXSY peaks, as the EXSY peaks were the same phase as the diagonal (revealing chemical exchange), whereas NOESY peaks were of a different phase. The EXSY peaks (in combination with integration and the chemical shift of the peaks) also allowed for partial assignment of the ^{1}H NMR spectrum, as only certain proton environments within the barbaralyl cation can exchange, elucidating the identity of each environment. The exchange peaks also show that we are only observing dvcpc–dvcpc pathway and that the structure we observe is only partially degenerate as the peaks labelled as positions 5 or 1 and 2, 4, 6 and 8 are not observed to be in exchange.

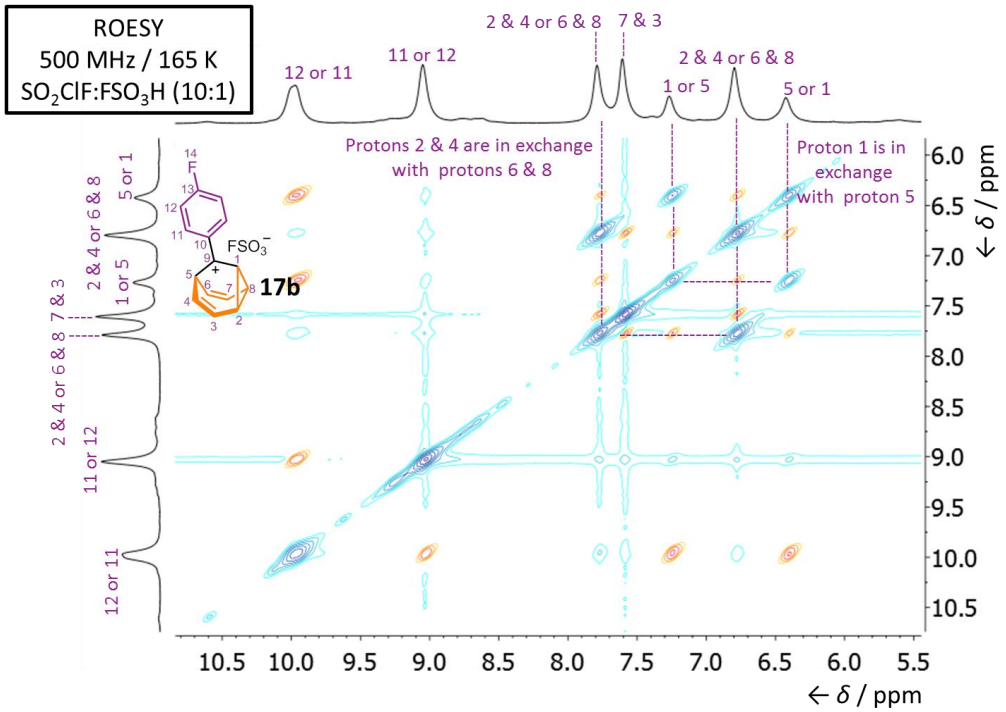

Figure 4.8. Partial ROESY NMR spectrum of barbaralyl cation **17b**. The spectrum demonstrates which peaks are in exchange (purple dashed lines) and which are NOESY correlations.

Upon determining which cross-peaks identified exchange, exchange spectroscopy calculations were performed[26] with barbaralyl cation **17c** using intensity data obtained from four EXSY spectra. The spectra have mixing times ranging from 90 ms to 200 ms (Appendix, Section 4.6.2). In each EXSY spectrum, the amplitudes of the diagonal resonances are compared against the cross-peaks, generating a peak intensity ratio which allows for the rate constant for chemical exchange to be calculated (Figure 4.9).[26] At the experimental temperature of 165 K, the average rate of exchange between the positions labelled as 2, 4, 6 and 8 was calculated to be 2.09 s^{-1}, whereas the average rate of exchange between the positions labelled as 1 and 5 was calculated to be 1.84 s^{-1}. Substituting the calculated rates of exchange into a variation of the Eyring equation allows for the average activation energy barrier to exchange ($\Delta G^{\neq}$) to be calculated as 36.0 kJ·mol^{-1} (Appendix, Section 4.6.3). Given that the literature shows that the parent barbaralyl cation[2,6,23] (without any substitution) experiences a barrier to rearrangements of 16 kJ·mol^{-1}, our average activation energy barrier to exchange is significantly higher. Our results demonstrate that an addition of a phenyl group can increase the activation energy barrier by ~20.0 kJ·mol^{-1}.

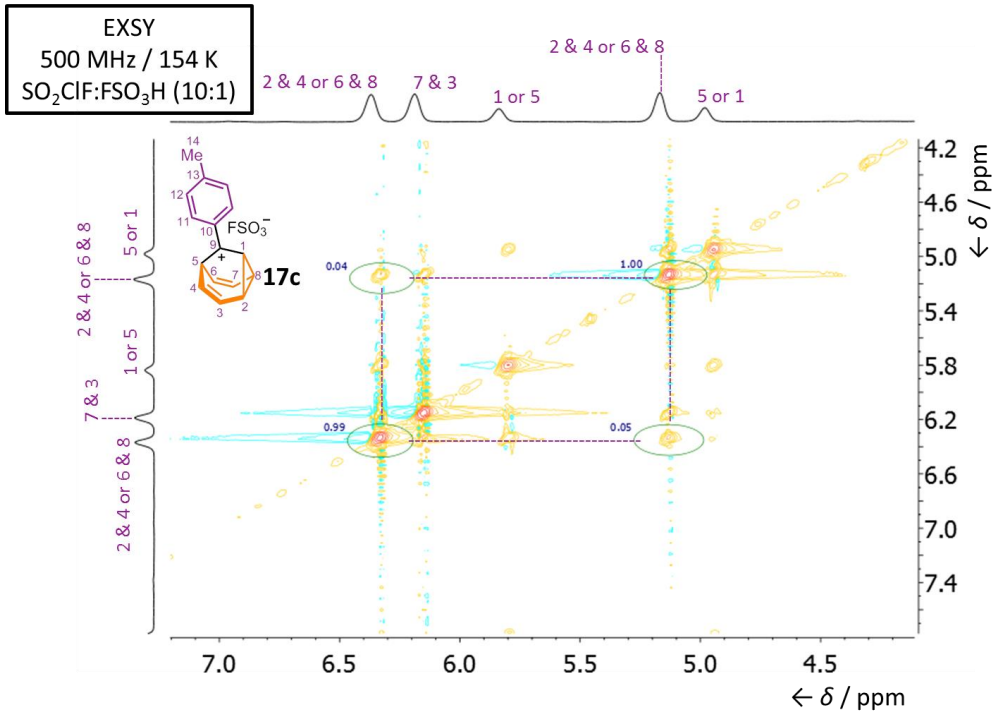

Figure 4.9. Partial EXSY NMR spectrum of barbaralyl cation **17c** at a mixing time of 90 ms. The spectrum compares the integration of the diagonal resonances against the cross-peaks for the positions labelled as1 or 5 and 5 or 1. (purple dashed lines). Absolute integral values were used in calculations.

As the barbaralyl cations (**17**) undergo an irrerversible rearrangement when raising the temperature, we next looked at determining whether we could decipher the identity of the product(s) formed from the irreversible rearrangement that **17c** undergoes above 193 K. However, on raising the temperature, the peaks in the NMR spectra corresponding to cation **17c** broadened into the baseline and re-emerged as several indistinguishable peaks in both the aromatic and aliphatic region. Due to the complicated NMR spectra and low boiling point of suphuryl chloride fluoride (280 K), we were unable to umambiguously identify the rearrangement product(s). Next, efforts were made to determine an energy barrier for the irreversible rearrangement that we observe.

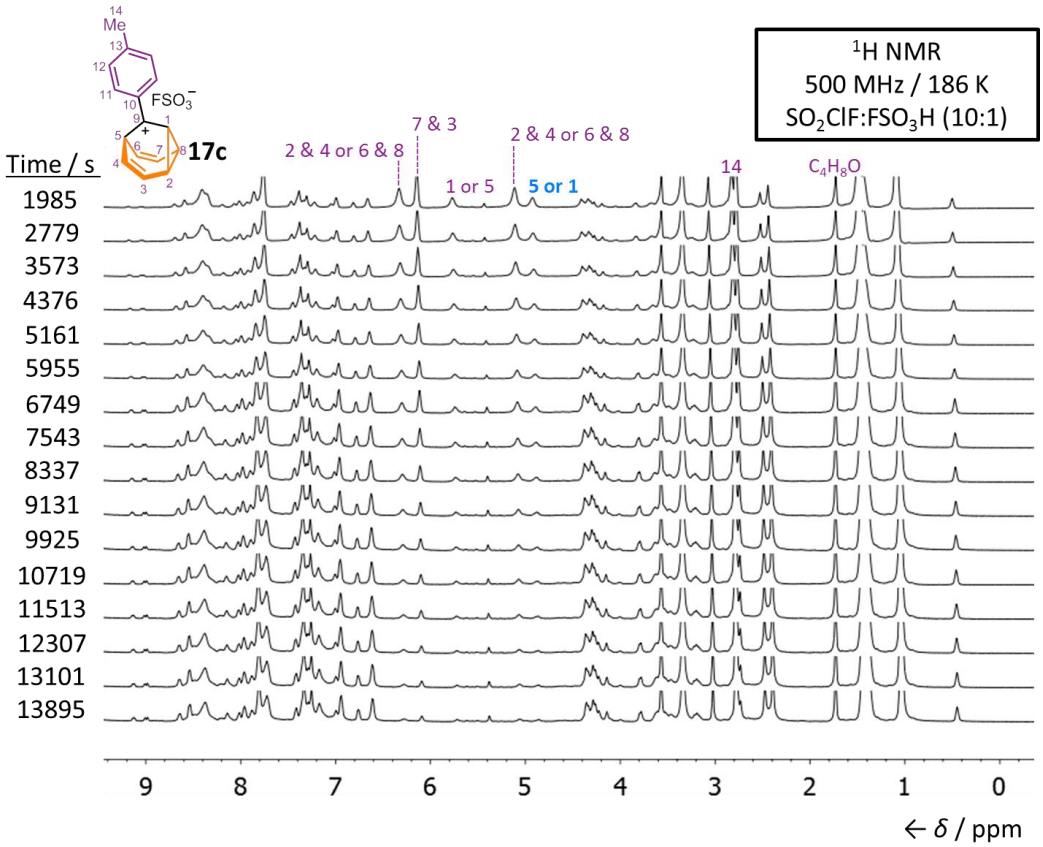

Figure 4.10. Selected partial ^{1}H NMR spectra of barbaralyl cation **17c** with a C_4D_8O capillary insert. ln(mole fraction) has been calculated according to the conversion of the proton environment labelled as 5 or 1 (bold blue text).

To determine an energy barrier for the irreversible rearrangement that we observe, a series of ^{1}H NMR spectra was recorded at a constant temperature of 186 K (such that the exact time between each acquired spectra is known), during which the cation was observed to undergo the irreversible rearrangement (Figure 4.10) (Appendix, Section 4.6.4). A capillary insert containing deuterated THF was inserted into the NMR tube at the beginning of the experimental procedure to provide an internal integration standard, so that the conversion of cation **17c** to the rearranged product could be calculated. The spectra demonstrate that over time (and at a constant temperature of 186 K) the proton environment labelled as 5 or 1 (Figure 4.10, bold blue text) slowly diminshes while aromatic and aliphatic peaks form. Using the rate of conversion measured in the ^{1}H NMR spectra, the ln(mole fraction) has been calculated and plotted against time which confirms a first-order reaction with a slope of -2.3×10^{-4} s^{-1} (Figure 4.11). Therefore, the rate constant is 2.3×10^{-4} s^{-1}.

Substituting the calculated rate constant into a variation of the Eyring equation allows for an energy barrier for the irreversible rearrangement ($\Delta G^{\neq}$) to be calculated as 58.0 kJ·mol^{-1} (Appendix, Section 4.6.4). This higher energy barrier proves our hypothesis of substituting electron-donating groups allowing for a more stable cation with a higher activation energy barrier.

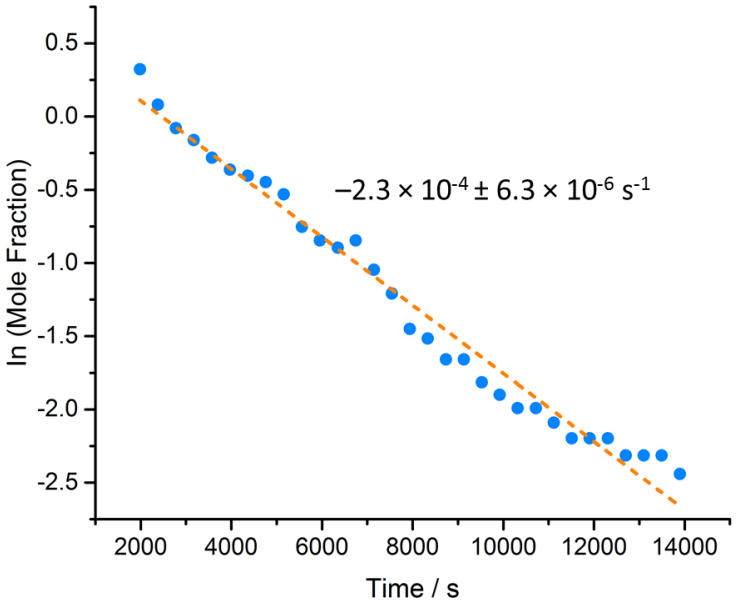

Figure 4.11. Plot of ln(mole fraction) against time. The rate constant of a first-order reaction is determined from the slope. The reported error is the statistical error of the fit.

Although we cannot determine that the irreversible rearrangement we see forms a bishomotropylium cation (possibly as a mixture of regioisomers), the literature precedent[2,6,23] shows that a bishomotropylium cation is the most likely product. The barrier to the irreversible rearrangement to the bishomotropylium cation for the parent barbaralyl cation has been measured as 43.5 kJ·mol^{-1}, whereas the same barrier for a methyl barbaralyl cation has been observed as 46.0 kJ·mol^{-1}. Our energy barrier is significantly higher, demonstrating that the addition of a phenyl group increases the energy barrier by ~12.0 kJ·mol^{-1}, validating our hypothesis that electron rich substituents allow for a more stable cation overall.

4.3 Conclusions

In summary, by synthesising novel hydroxy barbaralanes and subjecting them to superacidic conditions to form barbaralyl cation species, we have found that electron-rich substituents added to the barbaralyl core allow for higher activation energy barriers to exchange. At the same time we observe higher activation energy barriers to the irreversible rearrangement that we observe. These activation energy barriers are higher than any barbaralyl cation reported in the literature. The several routes created towards novel hydroxy barbaralanes show that varying degrees of substitution to the tricyclic framework are possible and that gold catalysis is a powerful tool for the construction of molecular complexity from simple substrates. Unique cationic tropylium species have also proven to be imperative intermediates for the synthesis of substituted alkynyl cycloheptatrienes. The three barbaralyl cations generated show that the presence of an electron-deficient group lowers the stability of the cation (*i.e.*, the temperature at which an irreversible rearrangement takes place is much lower in comparison to an electron-donating group). Our measured activation energy barrier ($\Delta G^{\neq}$) is 36.0 kJ·mol^{-1} and proves to be higher by ~20.0 kJ·mol^{-1} in comparison to other barbaralyl cations, showing that an aromatic group increases the activation energy barrier slightly. Although we are currently unable to determine the product(s) of the irreversible rearrangement, our measured energy barrier for the irreversible rearrangement (58.0 kJ·mol^{-1}) is approximately 12.0 kJ·mol^{-}1 higher than the barrier to the irreversible rearrangement to the bishomotropylium cation for the parent and methyl-substituted barbaralyl cations. This comparison shows that the energy barrier for the irreversible rearrangement is increased significantly by the addition of just an aromatic group. Although more in-depth studies are still required, these results show that stable cationic fluxional carbon cages may in principle be generated and that they have the ability to form long-lived species under ambient temperatures.

4.4 Future Work

Future experiments will continue investigate and determine the activation energy barriers and the energy barriers for the irreversible rearrangement for the remaining barbaralyl cations generated. The data acquired will help to validate that addition of

electron-donating groups to the barbaralyl core raises the stability. Next, we will focus on determining the product(s) formed upon the irreversible rearrangement through quenching experiments. Elucidating the product formed from the irreversible rearrangement will either confirm the presence of a bishomotropyliuum cation or show that different rearrangement pathways can take place, which may also be of interest. In addition, di-substituted hydroxy barbaralanes will be subjected to the same superacidic conditions to determine their activation energy barriers and irreversible rearrangement barriers which we hope will also corroborate our hypothesis of adding electron-donating groups to the barbaralyl core raises the stability. Finally, the synthesis of tri- and hepta- or octa-substituted hydroxy barbaralanes should be pursued, as *in silico* calculations predict that only three phenyl groups are required to bypass the stabilisation energy of the cationic triphenylmethyl species. Once generated, these stable multi-substituted barbaralyl cations should have the ability to form long-lived species under ambient temperatures.

4.5 Experimental Details

4.5.1 Specific Experimental Methods

For general experimental details see page *xix*. The X-ray single-crystal diffraction data were collected at 120.0(2) K using λMoKα radiation (λ = 0.71073 Å) on either a Bruker D8Venture (Photon100 CMOS detector, IμS-microsource, focusing mirrors) diffractometer for compounds **3b**, **6c**/**6c′**, **14**, **15c**, **15d** and triphenylcyclopropenium hydrogen dichloride or an Agilent XCalibur (Sapphire-3 CCD detector, fine-focus sealed tube, graphite monochromator) diffractometer for both polymorphs of compound **4a**. Both diffractometers are equipped with a Cryostream (Oxford Cryosystems) open-flow nitrogen cryostat. All structures were solved by direct method and refined by full-matrix least squares on F2 for all data using Olex2[27] and SHELXT[28] software. All non-hydrogen atoms were refined anisotropically and hydrogen atoms were placed in the calculated positions and refined in riding mode.

Several compounds have previously been studied and are reported in either Chapters 2 or 3. Synthetic methodology and experimental details for these compounds are outlined in Chapter 2, Section 2.4.2 or Chapter 3, Sections 3.5.2 or 3.5.3. During this Chapter, some compounds have been utilised in multiple synthetic routes so their experimental details have not been repeated beyond their first mention.

4.5.2 Synthesis of Methoxy and Hydroxy Barbaralanes

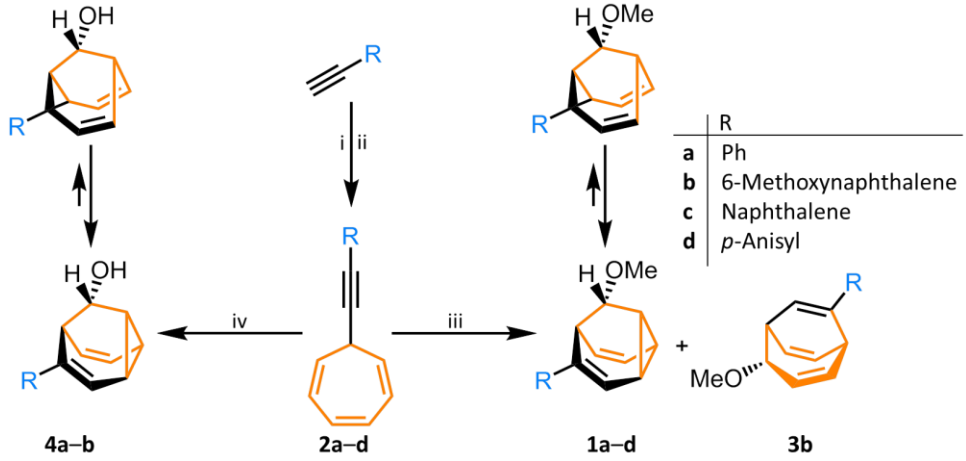

Scheme 4.7. Synthesis of alkynyl cycloheptatrienes (**2a**–**d**), methoxy barbaralanes (**1a**–**d**), methoxy bicyclononatrienes (**3b**) and hydroxy barbaralanes (**4a**–**b**) according to modified literature procedures.[9] Reagents and conditions: (i) *n*-Buli / THF / –78 °C / 40 min, (ii) tropylium tetrafluoroborate / rt / 16 h, (iii) MeOH:CH_2Cl_2 (2:1 or 1:1) / 0 °C to rt / JohnPhos Au(MeCN)SbF_6 (2 mol%), (iv) H_2O:MeCN (1:4) / 0 °C to rt / JohnPhos Au(MeCN)SbF_6 (2 mol%). JohnPhos = (2-biphenyl)di-*tert*-butylphosphine.

1-[2-(Cyclohepta-2,4,6-trien-1-yl)ethynyl]naphthalene (2c-relative to Scheme 4.7)

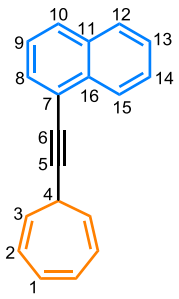

1-Ethynylnaphthalene (380 mg, 2.5 mmol) was placed into an oven-dried round-bottomed flask fitted with a septum under a N_2 atmosphere. Anhydrous THF (15 mL) was added and the resulting solution was cooled to –78 °C before adding *n*-BuLi (1.0 mL, 2.56 mmol, 2.5 M in hexanes) and stirring for 40 min at this temperature. Tropylium tetrafluoroborate (455 mg, 2.5 mmol) was added, and the mixture was allowed to reach rt and stirred for 16 h. The reaction was quenched with a saturated aqueous solution of NH_4Cl (30 mL), then extracted with EtOAc (3 × 20 mL). The combined organic extracts were dried over $MgSO_4$, filtered and the solvent

removed under reduced pressure. The crude residue was purified by column chromatography (Teledyne Isco CombiFlash Rf+ system, 24 g SiO_2, hexanes−EtOAc, gradient elution) to yield the title compound as a yellow oil that solidified upon standing (538 mg, 2.22 mmol, 88%). **M.P.** 68 – 70 °C (lit.[9a] 62 – 64 °C). **^{1}H NMR** (600 MHz, $CDCl_3$) δ 8.39 (d, *J* = 8.3 Hz, 1H, H_{15}), 7.86 – 7.84 (m, 1H, H_{12}), 7.82 (d, *J* = 8.2 Hz, 1H, H_{10}), 7.74 – 7.66 (m, 1H, H_8), 7.64 – 7.55 (m, 1H, H_{14}), 7.56 – 7.48 (m, 1H, H_{13}), 7.49 – 7.38 (m, 1H, H_9), 6.89 – 6.60 (m, 2H, H_1), 6.41 – 6.16 (m, 2H, H_2), 5.56 (dd, *J* = 9.0, 5.6 Hz, 2H, H_3), 2.91 (tt, *J* = 5.6, 2.8 Hz, 1H, H_4). **^{13}C NMR** (151 MHz, $CDCl_3$) δ 133.8 (C_{16}), 133.5 (C_{11}), 131.5 (C_1), 130.7 (C_8), 128.7 (C_{10}), 128.6 (C_{12}), 127.0 (C_{14}), 126.7 (C_{13}), 126.6 (C_{15}), 125.6 (C_9), 125.3 (C_2), 123.6 (C_3), 121.5 (C_7), 96.4 (C_5), 82.3 (C_6), 32.9 (C_4). **HRMS-ASAP** *m/z* = 243.1178 $[M+H]^+$, calculated for $C_{19}H_{15}$: 243.1174.

Spectroscopic data were consistent with those published previously.[9a]

2-[2-(Cyclohepta-2,4,6-trien-1-yl)ethynyl]-6-methoxynaphthalene (2b-relative to Scheme 4.7)

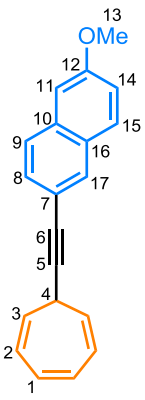

2-Ethynyl-6-methoxynaphthalene (455 mg, 2.5 mmol) was placed into an oven-dried round-bottomed flask fitted with a septum under a N_2 atmosphere. Anhydrous THF (15 mL) was added and the resulting solution was cooled to –78 °C before adding *n*-BuLi (1.0 mL, 2.56 mmol, 2.5 M in hexanes) and stirring for 40 min at this temperature. Tropylium tetrafluoroborate (455 mg, 2.5 mmol) was added, and the mixture was allowed to reach rt and stirred for 16 h. The reaction was quenched with a saturated aqueous solution of NH_4Cl (30 mL), then extracted with EtOAc (3 × 20 mL). The combined organic extracts were dried over $MgSO_4$, filtered and the solvent removed under reduced pressure. The crude residue was purified by column chromatography (Teledyne Isco CombiFlash Rf+ system, 24 g SiO_2, hexanes−EtOAc, gradient elution) to yield the title compound as a white solid (466 mg, 2.62 mmol, 69%). **M.P.** 110 – 112 °C. **^{1}H NMR** (400 MHz, $CDCl_3$) δ 7.91 (s, 1H, H_{17}), 7.68 (d, *J* = 8.5 Hz, 2H, H_9 and H_{14}), 7.48 (dd, *J* = 8.5, 1.7 Hz, 1H, H_8), 7.15 (dd, *J* = 8.9, 2.5 Hz, 1H, H_{15}), 7.11 (d, *J* = 2.6 Hz, 1H, H_{11}), 6.71 (dd, *J* = 3.7, 2.7 Hz, 2H, H_1), 6.29 –

6.17 (m, 2H, H_2), 5.47 (dd, *J* = 8.6, 5.5 Hz, 2H, H_3), 3.93 (s, 3H, H_{13}), 2.75 (tt, *J* = 5.6, 1.5 Hz, 1H, H_4). **^{13}C NMR** (101 MHz, $CDCl_3$) δ 158.6 (C_{12}), 134.4 (C_7), 131.7 (C_{17}), 131.5 (C_1), 129.7 (C_{14}), 129.7 (C_8), 129.0 (C_{10}), 127.2 (C_9), 125.2 (C_2), 123.8 (C_3), 119.8 (C_{15}), 118.8 (C_{16}), 106.3 (C_{11}), 91.1 (C_5), 81.5 (C_6), 55.8 (C_{13}), 32.8 (C_4). **HRMS-ASAP** *m/z* = 273.1264 $[M+H]^+$, calculated for $C_{20}H_{17}O$: 273.1269.

Methoxy and hydroxy barbaralanes are formed as a mixture of regioisomers. Only the major regioisomer in each case has been fully characterised. The minor regioisomers were usually obtained as mixtures that could not be fully separated into individual components through column chromatography. The mixtures of minor regioisomers were only observed through NMR spectroscopy. In room-temperature solutions the methoxy and hydroxy barbaralanes below exist as mixtures of two rapidly interconverting isomers. The NMR spectroscopic assignments below, which have been made with the aid of two-dimensional NMR techniques, are labelled according to numbering of the major species which is most likely favoured due to the functional group being present on one olefin.

(±)-(1*R*,5*S*,8*R*,9*S*)-9-Methoxy-4-(naphthalen-1-yl)tricyclo[3.3.1.0^{2,8}]nona-3,6-diene (1c)

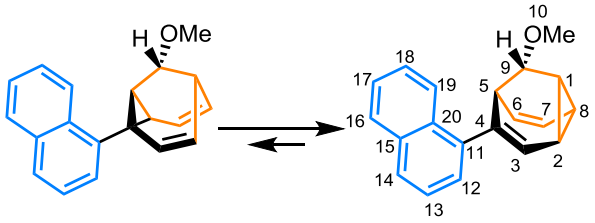

A solution of 1-[2-(cyclohepta-2,4,6-trien-1-yl)ethynyl]naphthalene (395 mg, 1.63 mmol) in a MeOH:CH_2Cl_2 (2.6 mL:1.3 mL) was sealed in a round-bottomed flask and cooled to 0 °C, with no special precautions taken to exclude air or moisture. (Acetonitrile)[(2-biphenyl)di-*tert*-butylphosphine]-gold(I) hexafluoroantimonate (25 mg, 0.03 mmol, 2 mol%) was then added. The mixture was left for 16 h, and the temperature was raised from 0 °C to rt, following removal of the ice bath. The solvent was removed under reduced pressure and the crude residue was purified by column chromatography (Teledyne Isco CombiFlash Rf+ system, 24 g SiO_2, hexanes−EtOAc, gradient elution) to yield the title compound as a yellow oil (219 mg, 0.79 mmol, 49%). **^{1}H NMR** (700 MHz, $CDCl_3$) δ 7.97 – 7.92 (m, 1H, H_{19}), 7.90 – 7.85 (m, 1H,

H_{16}), 7.77 (d, *J* = 8.0 Hz, 1H, H_{14}), 7.53 – 7.47 (m, 2H, H_{17} and H_{18}), 7.45 – 7.39 (m, 1H, H_{13}), 7.35 (d, *J* = 7.1 Hz, 1H, H_{12}), 6.06 – 5.97 (m, 1H, H_7), 5.73 (dd, *J* = 6.8, 1.3 Hz, 1H, H_3), 5.55 – 5.48 (m, 1H, H_6), 3.74 (br s, 1H, H_9), 3.39 (s, 3H, H_{10}), 3.35 – 3.29 (m, 1H, H_5), 2.74 (q, *J* = 7.1 Hz, 1H, H_2), 2.64 (q, *J* = 6.9 Hz, 1H, H_8), 2.53 – 2.44 (m, 1H, H_1). **^{13}C NMR** (176 MHz, $CDCl_3$) δ 140.0 (C_{11}), 133.7 (C_{15}), 131.4 (C_{20}), 129.9 (C_4), 128.4 (C_{16}), 127.3 (C_{14}), 126.1 (C_{12}), 125.8 (C_{17}), 125.7 (C_{18} or C_{19}), 125.6 (C_{18} or C_{19}), 125.3 (C_{13}), 122.7 (C_7), 121.3 (C_3), 115.7 (C_6), 72.7 (C_9), 56.4 (C_{10}), 39.7 (C_5), 32.1 (C_2), 30.4 (C_8), 22.5 (C_1). **HRMS-ASAP** *m/z* = 244.1247 $[M-OCH_3]^+$, calculated for $C_{20}H_{19}O$: 244.1252.

Spectroscopic data were consistent with those published previously.[9a]

(±)-(1*R*,5*S*,8*R*,9*S*)-9-Methoxy-4-(6-methoxynaphthalen-2-yl)tricyclo[3.3.1.0^{2,8}]-nona-3,6-diene (1b)

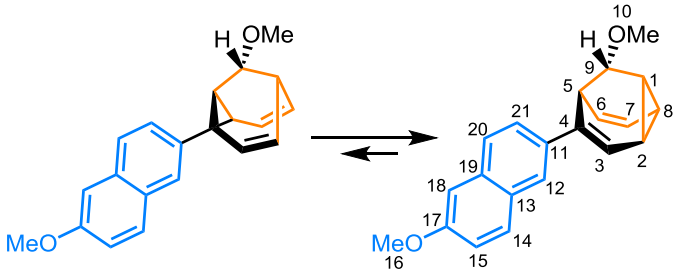

A solution of 2-[2-(cyclohepta-2,4,6-trien-1-yl)-ethynyl]-6-methoxynaphthal-ene (409 mg, 1.50 mmol) in a MeOH:CH_2Cl_2 (2.7 mL:2.7 mL) was sealed in a round-bottomed flask and cooled to 0 °C, with no special precautions taken to exclude air or moisture. (Acetonitrile)[(2-biphenyl)di-*tert*-butylphosphine]-gold(I) hexafluoro-antimonate (23 mg, 0.03 mmol, 2 mol%) was then added. The mixture was left for 16 h, and the temperature was raised from 0 °C to rt, following removal of the ice bath. The solvent was removed under reduced pressure and the crude residue was purified by column chromatography (Teledyne Isco CombiFlash Rf+ system, 24 g SiO_2, hexanes−EtOAc, gradient elution) to yield the title compound as a yellow oil (155 mg, 0.51 mmol, 34%). **M.P.** 116 – 118 °C. **^{1}H NMR** (600 MHz, $CDCl_3$) δ 7.79 – 7.75 (m, 1H, H_{12}), 7.71 (d, *J* = 8.8 Hz, 1H, H_{14}), 7.67 (d, *J* = 9.0 Hz, 1H, H_{20}), 7.54 (dd, *J* = 8.6, 1.9 Hz, 1H, H_{21}), 7.12 (dd, *J* = 8.9, 2.5 Hz, 1H, H_{15}), 7.10 – 7.09 (m, 1H, H_{18}), 6.04 – 6.02 (m, 1H, H_7), 6.00 – 5.95 (m, 1H, H_3), 5.90 – 5.86 (m, 1H, H_6), 3.91 (s, 3H, H_{16}), 3.67 – 3.64 (m, 1H, H_5), 3..47 (s, 1H, H_9), 3.40 (s, 3H, H_{10}), 2.48 (q, *J* =

7.5, 6.7 Hz, 1H, H_2), 2.38 – 2.27 (m, 2H, H_1 and H_8). **^{13}C NMR** (151 MHz, $CDCl_3$) δ 157.9 (C_{17}), 137.9 (C_4), 135.3 (C_{11}), 133.9 (C_{19}), 129.8 (C_{14}), 129.3 (C_{13}), 127.3 (C_{20}), 124.7 (C_{21}), 123.7 (C_3), 123.6 (C_{12}), 123.4 (C_6), 119.3 (C_{15}), 118.1 (C_7), 106.0 (C_{18}), 73.3 (C_9), 57.0 (C_{10}), 55.7 (C_{16}), 38.2 (C_5), 25.7 (C_2), 22.98 (C_1), 21.7 (C_8). **HRMS-ASAP** *m/z* = 305.1538 $[M+H]^+$, calculated for $C_{21}H_{21}O_2$: 305.1542.

(±)-(2*S*,1*R*,9*R*)-2-Methoxy-6-{2-methoxybicyclo[3.2.2]nona-2,6,8-trien-6-yl}-naphthalene (3b)

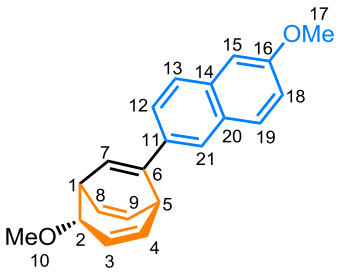

During the above procedure the title compound as a yellow oil (59 mg, 0.19 mmol, 13%). **M.P.** 136 – 138 °C. **^{1}H NMR** (600 MHz, $CDCl_3$) δ 7.72 (d, *J* = 8.9 Hz, 1H, H_{19}), 7.70 (br s, 1H, H_{13}), 7.68 (br s, 1H, H_{21}), 7.52 (dd, *J* = 8.5, 1.9 Hz, 1H, H_{12}), 7.14 (dd, *J* = 8.9, 2.5 Hz, 1H, H_{18}), 7.11 (d, *J* = 2.5 Hz, 1H, H_{15}), 6.91 – 6.83 (m, 1H, H_9), 6.56 (dd, *J* = 6.7, 2.0 Hz, 1H, H_7), 6.54 – 6.50 (m, 1H, H_4), 6.30 – 6.20 (m, 1H, H_8), 5.29 – 5.17 (m, 1H, H_3), 3.92 (s, 3H, H_{17}), 3.84 – 3.81 (m, 1H, H_5), 3.81 – 3.78 (m, 1H, H_1), 3.76 – 3.72 (m, 1H, H_2), 3.47 (s, 3H, H_{10}). **^{13}C NMR** (151 MHz, $CDCl_3$) δ 157.6 (C_{16}), 153.6 (C_{11}), 140.2 (C_9), 136.1 (C_4), 133.9 (C_6), 133.8 (C_{14}), 129.5 (C_{19}), 128.8 (C_{20}), 128.4 (C_8), 126.9 (C_{13}), 126.8 (C_3), 124.1 (C_{12}), 123.4 (C_7), 123.0 (C_{21}), 118.9 (C_{18}), 105.6 (C_{15}), 73.4 (C_2), 56.6 (C_{10}), 55.2 (C_{17}), 40.5 (C_1), 39.5 (C_5). **HRMS-ASAP** *m/z* = 273.1274 $[M-OCH_3]^+$, calculated for $C_{21}H_{21}O_2$: 273.1279.

(±)-(1*R*, 5*S*, 8*R*, 9*S*)-9-Methoxy-4-(4-anisyl)tricyclo[3.3.1.0^{2,8}]nona-3,6-diene (1d)

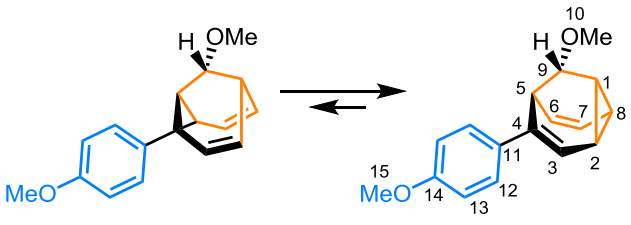

A solution of 7-[2-(4-anisyl)ethynyl]cyclohepta-1,3,5-triene (409 mg, 1.50 mmol) in a MeOH:CH_2Cl_2 (2.4 mL:1.2 mL) was sealed in a round-bottomed flask and cooled to 0 °C, with no special precautions taken to exclude air or moisture. (Acetonitrile)[(2-biphenyl)di-*tert*-butylphosphine-]-gold(I) hexafluoroantimonate (24 mg, 0.03 mmol, 2 mol%) was then added. The mixture was left for 16 h, and the

temperature was raised from 0 °C to rt, following removal of the ice bath. The solvent was removed under reduced pressure and the crude residue was purified by column chromatography (Teledyne Isco CombiFlash Rf+ system, 24 g SiO_2, hexanes−EtOAc, gradient elution) to yield the title compound as a light yellow solid (158 mg, 0.62 mmol, 39%). **M.P.** 83 – 85 °C. **^{1}H NMR** (700 MHz, $CDCl_3$) δ 7.43 – 7.33 (m, 2H, H_{12}), 6.93 – 6.83 (m, 2H, H_{13}), 5.97 – 5.93 (m, 1H, H_7), 5.85 – 5.82 (m, 1H, H_3), 5.82 – 5.79 (m, 1H, H_6), 3.81 (s, 3H, H_{15}), 3.51 – 3.47 (m, 1H, H_5), 3.43 (s, 1H, H_9), 3.38 (s, 3H, H_{10}), 2.42 (ddd, *J* = 7.6, 6.7 Hz, 1H, H_2), 2.34 – 2.22 (m, 2H, H_1 and H_8). **^{13}C NMR** (176 MHz, $CDCl_3$) δ 159.0 (C_{14}), 137.6 (C_4), 132.9 (C_{11}), 126.6 (C_{12}), 123.6 (C_6), 123.2 (C_7), 116.6 (C_3), 114.2 (C_{13}), 73.2 (C_9), 56.9 (C_{10}), 55.7 (C_{15}), 38.3 (C_5), 25.5 (C_2), 22.7 (C_1), 21.5 (C_8). **HRMS-ASAP** *m/z* = 255.1385 $[M+H]^+$, calculated for $C_{17}H_{19}O_2$: 255.1385.

(±)-(1*R*, 5*S*, 8*R*, 9*S*)-9-Methoxy-4-phenyltricyclo[3.3.1.0^{2,8}]nona-3,6-diene (1a)

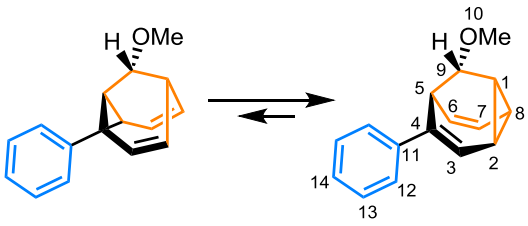

A solution of 7-[2-phenylethynyl)cycloheptа-1,3,5-triene (1.0 g, 5.18 mmol) in a MeOH:CH_2Cl_2 (6.6 mL:3.3 mL) was sealed in a round-bottomed flask and cooled to 0 °C, with no special precautions taken to exclude air or moisture. (Acetonitrile)[(2-biphenyl)di-*tert*-butylphosphine-]-gold(I) hexafluoroantimonate (80 mg, 0.10 mmol, 2 mol%) was then added. The mixture was left for 16 h, and the temperature was raised from 0 °C to rt, following removal of the ice bath. The solvent was removed under reduced pressure and the crude residue was purified by column chromatography (Teledyne Isco CombiFlash Rf+ system, 24 g SiO_2, hexanes−EtOAc, gradient elution) to yield the title compound as a cream-coloured solid (570 mg, 2.54 mmol, 49%). **M.P.** 66 – 67 °C. **^{1}H NMR** (700 MHz, $CDCl_3$) δ 7.47 – 7.40 (m, 2H, H_{12}), 7.33 (t, *J* = 7.6 Hz, 2H, H_{13}), 7.25 – 7.21 (m, 1H, H_{14}), 5.99 – 5.91 (m, 2H, H_7 and H_3), 5.86 – 5.81 (m, 1H, H_6), 3.56 – 3.49 (m, 1H, H_5), 3.43 (br s, 1H, H_9), 3.38 (s, 3H, H_{10}), 2.45 (ddd, *J* = 7.2 Hz, 1H, H_2), 2.34 – 2.28 (m, 2H, H_1 and H_8). **^{13}C NMR** (176 MHz, $CDCl_3$) δ 140.3 (C_4), 138.0 (C_{11}), 128.8 (C_{13}), 127.1 (C_{14}), 125.5 (C_{12}), 123.5 (C_7), 123.1 (C_6),

118.4 (C_3), 73.1 (C_9), 56.9 (C_{10}), 38.2 (C_5), 25.6 (C_2), 23.0 (C_1), 21.6 (C_8). **HRMS-ASAP** *m/z* = 193.1015 $[M-OCH_3]^+$, calculated for $C_{15}H_{13}$: 193.1017.

(±)-(1*R*, 5*S*, 8*R*, 9*S*)-4-Phenyltricyclo[3.3.1.0^{2,8}]nona-3,6-dien-9-ol (4a)

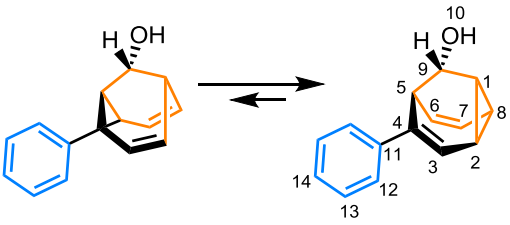

A solution of 7-[2-phenylethynyl)-cyclohepta-1,3,5-triene (460 mg, 2.18 mmol) in a H_2O:MeCN (3.0 mL:12.0 mL) was sealed in a round-bottomed flask and cooled to 0 °C, with no special precautions taken to exclude air or moisture. (Acetonitrile)[(2-biphenyl)di-*tert*-butylphosphine-]-gold(I) hexafluoroantimonate (37.5 mg, 0.05 mmol, 2 mol%) was then added. The mixture was left for 16 h, and the temperature was raised from 0 °C to rt, following removal of the ice bath. The solvent was removed under reduced pressure and the crude residue was purified by column chromatography (Teledyne Isco CombiFlash Rf+ system, 40 g SiO_2, hexanes−EtOAc, gradient elution) to yield the title compound as a yellow oil that solidified upon standing (79 mg, 0.37 mmol, 30%). **M.P.** 93 – 95 °C. **^{1}H NMR** (600 MHz, $CDCl_3$) δ 7.46 – 7.39 (m, 2H, H_{12}), 7.34 – 7.30 (m, 2H, H_{13}), 7.25 – 7.21 (m, 1H, H_{14}), 6.02 – 5.97 (m, 1H, H_7), 5.93 (dd, *J* = 6.6, 1.2 Hz, 1H, H_3), 5.81 – 5.76 (m, 1H, H_6), 3.83 (br s, 1H, H_9), 3.48 – 3.40 (m, 1H, H_5), 2.50 (ddd, *J* = 7.2 Hz, 1H, H_2), 2.30 – 2.25 (m, 2H, H_8 and H_1). **^{13}C NMR** (151 MHz, $CDCl_3$) δ 139.6 (C_4), 138.1 (C_{11}), 128.4 (C_{13}), 126.8 (C_{14}), 125.1 (C_{12}), 124.2 (C_7), 122.3 (C_6), 117.5 (C_3), 63.2 (C_9), 41.7 (C_5), 26.8 (C_2), 24.6 (C_1), 22.4 (C_8). **HRMS-ASAP** *m/z* = 193.1017 $[M-OH]^+$, calculated for $C_{15}H_{13}$: 193.1017.

(±)-(1*R*,5*S*,8*R*,9*S*)-4-(6-Methoxynaphthalen-2-yl)tricyclo[3.3.1.0^{2,8}]nona-3,6-dien-9-ol (4b)

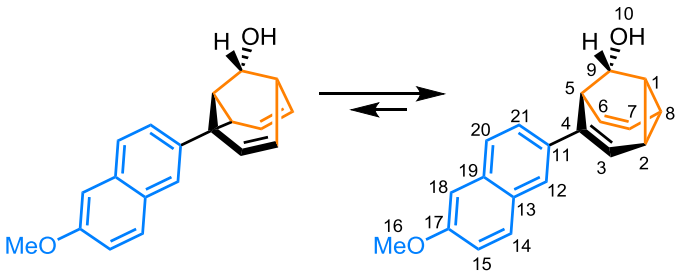

A solution of 2-[2-(cyclohepta-2,4,6-trien-1yl)ethynyl]-6-methoxynaphthalene (100 mg, 0.56 mmol) in a H_2O:$(CH_3)_2CO$ (0.6 mL:2.4 mL) was sealed in a round-bottomed flask and cooled to 0 °C, with no special precautions taken to exclude air or moisture. (Acetonitrile)[(2-biphenyl)di-*tert*-butylphosphine-]-gold(I) hexafluoroantimonate (9.0 mg, 0.01 mmol, 2 mol%) was then added. The mixture was left for 16 h, and the temperature was raised from 0 °C to rt, following removal of the ice bath. The solvent was removed under reduced pressure and the crude residue was purified by column chromatography (Teledyne Isco CombiFlash Rf+ system, 40 g SiO_2, hexanes−EtOAc, gradient elution). The solid was recrystallised by slow evapouration of a CH_2Cl_2:EtOH (2.0 mL:1.0 mL) solution to yield the title compound as a light brown solid (56 mg, 0.19 mmol, 34%). **M.P.** 148 – 150 °C. **^{1}H NMR** (700 MHz, $CDCl_3$) δ 7.78 (br s, 1H, H_{12}), 7.71 (d, J = 8.8 Hz, 1H, H_{14}), 7.67 (d, J = 8.7 Hz, 1H, H_{20}), 7.54 (d, J = 8.6 Hz, 1H, H_{21}), 7.14 – 7.12 (m, 1H, H_{15}), 7.11 – 7.09 (m, 1H, H_{18}), 6.05 – 5.99 (m, 2H, H_3 and H_7), 5.86 – 5.81 (m, 1H, H_6), 3.92 (d, J = 1.5 Hz, 3H, H_{16}), 3.88 (br s, 1H, H_9), 3.62 – 3.55 (m, 1H, H_5), 2.53 (ddd, J = 7.1 Hz, 1H, H_2), 2.34 – 2.27 (m, 2H, H_8 and H_1). **^{13}C NMR** (176 MHz, $CDCl_3$) δ 157.6 (C_{17}), 138.1 (C_4), 134.6 (C_{11}), 133.5 (C_{19}), 129.5 (C_{14}), 128.9 (C_{13}), 126.9 (C_{20}), 124.3 (C_7), 124.2 (C_{21}), 123.3 (C_{12}), 122.5 (C_6), 118.9 (C_{15}), 117.2 (C_3), 105.6 (C_{18}), 63.3 (C_9), 55.3 (C_{16}), 41.7 (C_5), 26.8 (C_2), 24.7 (C_1), 22.4 (C_8). **HRMS-ASAP** *m/z* = 273.1277 $[M-OH]^+$, calculated for $C_{20}H_{17}O$: 273.1279.

4.5.3 Synthesis of Mono-Substituted Hydroxy Barbaralanes

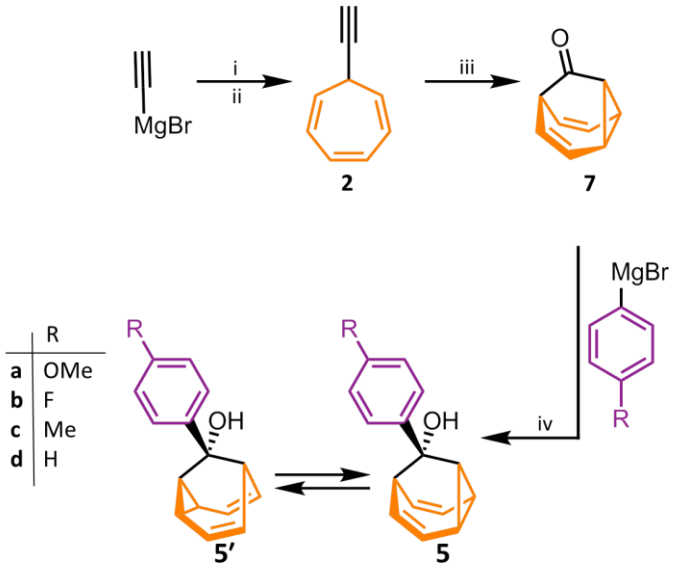

Scheme 4.8. General synthesis of alkynyl cycloheptatriene (**2**), barbaralone (**7**) and mono-substituted hydroxy barbaralanes (**5**/**5′**) according to modified literature procedures.[9b] Reagents and conditions: (i) LiCl / THF / tropylium tetrafluoroborate / –78 °C to rt, (ii) IPrAu(MeCN)BF_4 (5 mol%) / Ph_2SO (2 equiv.) / CH_2Cl_2 / rt / 16 h, (iii) magnesium turnings / THF / reflux to rt then barbaralone / 0 °C to rt. IPr = 1,3-bis(2,6-diisopropylphenyl)imidazol-2-ylidene.

In solutions at room temperature, each of the barbaralanes (**5**/**5′**) exists as mixtures of two rapidly interconverting stereoisomers. For clarity, we have only labelled one of the enantiomers, but all enantiomers are in fast exchange on account of rapid strain-assisted Cope rearrangements. The chemical shifts of each nucleus are representative of the time-averaged chemical environment they experience as part of the two enantiomers.

(±)-6-(4-Ansiyl)bicyclo[3.2.2]nona-3,8-dien-6-ol (5d/5d′)

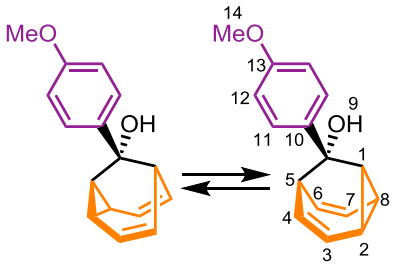

Magnesium turnings (240 mg, 10.0 mmol) and I_2 (124 mg, 0.49 mmol, 5 mol%) were placed in an oven-dried two-necked round-bottomed flask fitted with a condenser and a septum under a N_2 atmosphere. The flask was gently heated with a heat gun until the I_2 started to sublime. The flask was cooled down to rt. A quarter of a solution of 4-bromoanisole (1.68 g, 9.80 mmol) in

anhydrous THF (10 mL) was added to the reaction mixture, which was heated until it reached reflux. Upon gentle reflux, the remaining solution of 4-bromoanisole in anhydrous THF was added dropwise over 30 min. The reaction mixture was heated at reflux for 30 min before cooling to rt. Tricyclo[3.3.1.$0^{2,8}$]nona-3,6-dien-9-one (125 mg, 0.95 mmol) was transferred to an oven-dried round-bottomed flask, and the flask was purged with N_2. Anhydrous THF (10 mL) was added and the solution was cooled to 0 °C. The Grignard solution (prepared above) was added dropwise over 30 min to the barbaralone. The reaction mixture was stirred for 16 h, and the temperature was raised from 0 °C to rt, following removal of the ice bath. The reaction was quenched with a saturated aqueous solution of NH_4Cl (10 mL), then extracted with EtOAc (3 × 20 mL). The combined organic extracts were dried over $MgSO_4$, filtered and the solvent removed under reduced pressure. The crude residue was purified by column chromatography (Teledyne Isco CombiFlash Rf+ system, 24 g SiO_2, hexanes−CH_2Cl_2, gradient elution including 0.5% Et_3N in the elution) to yield the title compound as a yellow oil (176 mg, 0.73 mmol, 73%). **^{1}H NMR** (700 MHz, $CDCl_3$) δ 7.36 (d, *J* = 8.9 Hz, 2H, H_{12}), 6.84 (d, *J* = 8.9 Hz, 2H, H_{11}), 5.91 (t, *J* = 7.7 Hz, 1H, H_7), 5.58 (t, *J* = 7.6 Hz, 1H, H_3), 4.28 – 4.24 (m, 2H, H_8 and H_6), 4.24 – 4.20 (m, 2H, H_4 and H_2), 3.79 (s, 3H, H_{14}), 2.78 – 2.51 (m, 2H, H_5 and H_1), 1.98 (s, 1H, H_9). **^{13}C NMR** (176 MHz, $CDCl_3$) δ 158.7 (C_{10}), 135.6 (C_{13}), 127.6 (C_{12}), 123.2 (C_7), 120.9 (C_3), 113.2 (C_{11}), 77.8 (C_4 and C_2), 75.5 (C_8 and C_6), 68.4 (C_9), 55.3 (C_{14}), 38.2 (C_5 and C_1). **HRMS-ASAP** *m/z* = 223.1123 $[M\text{-}OH]^+$, calculated for $C_{16}H_{15}O$: 223.1123.

(±)-9-Phenyltriyclo[3.3.1.$0^{2,8}$]nona-3,6-dien-9-ol (5a/5a′)

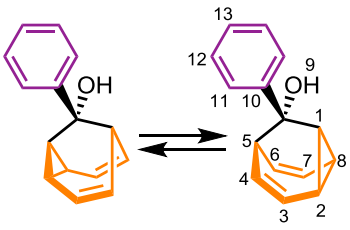

Magnesium turnings (119 mg, 4.95 mmol) and I_2 (62 mg, 0.25 mmol, 5 mol%) were placed in an oven-dried two-necked round-bottomed flask fitted with a condenser and a septum under a N_2 atmosphere. The flask was gently heated with a heat gun until the I_2 started to sublime. The flask was cooled down to rt. A quarter of a solution of bromobenzene (770 mg, 4.90 mmol) in anhydrous THF (10 mL) was added to the reaction mixture, which was heated until it reached reflux. Upon gentle reflux, the

remaining solution of bromobenzene in anhydrous THF was added dropwise over 30 min. The reaction mixture was heated at reflux for 30 min before cooling to rt. Tricyclo[3.3.1.$0^{2,8}$]nona-3,6-dien-9-one (125 mg, 0.95 mmol) was transferred to an oven-dried round-bottomed flask, and the flask was purged with N_2. Anhydrous THF (10 mL) was added and the solution was cooled to 0 °C. The Grignard solution (prepared above) was added dropwise over 30 min to the barbaralone. The reaction mixture was stirred for 16 h, and the temperature was raised from 0 °C to rt, following removal of the ice bath. The reaction was quenched with a saturated aqueous solution of NH_4Cl (10 mL), then extracted with EtOAc (3 × 20 mL). The combined organic extracts were dried over $MgSO_4$, filtered and the solvent removed under reduced pressure. The crude residue was purified by column chromatography (Teledyne Isco CombiFlash Rf+ system, 24 g SiO_2, hexanes−CH_2Cl_2, gradient elution including 0.5% Et_3N in the elution) to yield the title compound as a colourless oil (142 mg, 0.67 mmol, 82%). **^{1}H NMR** (700 MHz, $CDCl_3$) δ 7.46 – 7.43 (m, 2H, H_{11}), 7.30 (dd, *J* = 8.3, 7.0 Hz, 2H, H_{12}), 7.27 – 7.21 (m, 1H, H_{13}), 5.92 (t, *J* = 7.7 Hz, 1H, H_7), 5.59 (t, *J* = 7.7 Hz, 1H, H_3), 4.29 – 4.25 (m, 2H, H_8 and H_6), 4.25 – 4.21 (m, 2H, H_2 and H_4), 2.95 – 2.52 (m, 2H, H_5 and H_1), 2.01 (s, 1H, H_9). **^{13}C NMR** (176 MHz, $CDCl_3$) δ 143.4 (C_{10}), 127.9 (C_{12}), 127.2 (C_{13}), 126.5 (C_{11}), 123.3 (C_7), 121.0 (C_3), 77.9 (C_4 and C_2), 75.5 (C_6 and C_8), 68.8 (C_9), 38.3 (C_5 and C_1). **HRMS-ASAP** *m/z* = 193.0992 $[M\text{-}OH]^+$, calculated for $C_{15}H_{13}$: 193.1017.

4.5.4 Synthesis of Di-Substituted Hydroxy Barbaralanes

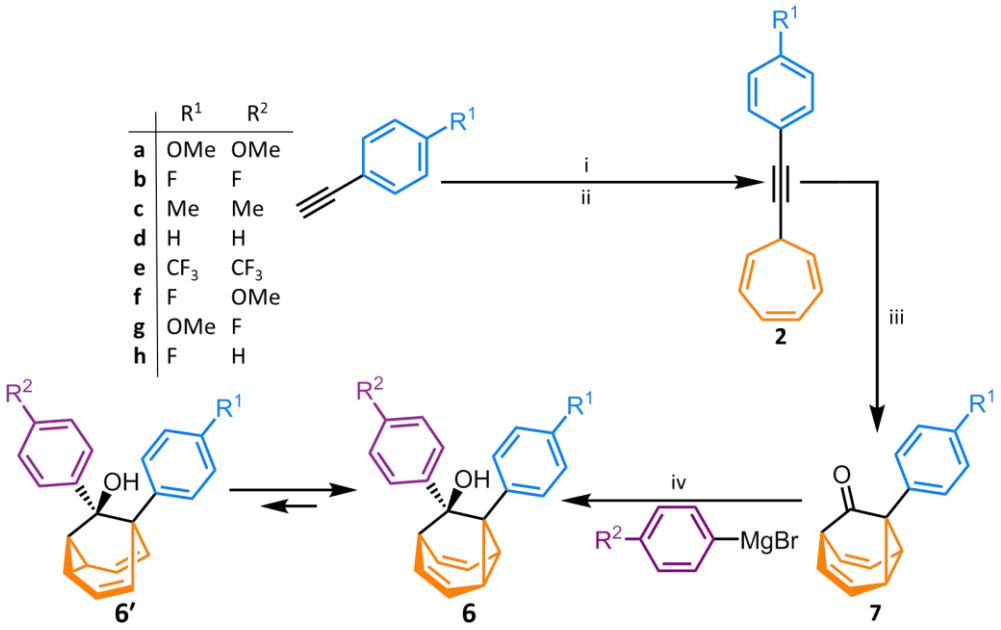

Scheme 4.9. General synthesis of substituted alkynyl cycloheptatrienes (**2**), substituted barbaralanes (**7**) and di-substituted barbaralanes (**6**/**6′**) according to modified literature procedures.[9] Reagents and conditions: (i) *n*-BuLi / THF / –78 °C / 40 min, (ii) tropylium tetrafluoroborate / rt / 16 h, (iii) IPrAu(MeCN)BF_4 (5 mol%) / Ph_2SO (2 equiv.) / CH_2Cl_2 / rt / 16 h, (iv) either (a) THF / 0 °C to rt / 16 h or (b) diglyme / Bu_4NI / THF / 0 °C to rt / 16 h. IPr = 1,3-bis(2,6-diisopropylphenyl)imidazol-2-ylidene.

7-[2-(4-Tolyl)ethynyl]cyclohepta-1,3,5-triene (2c-relative to Scheme 4.9)

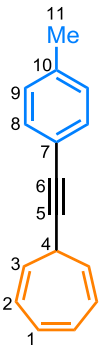

4-Ethynyltoluene (580 mg, 5.0 mmol) was placed into an oven-dried round-bottomed flask fitted with a septum under a N_2 atmosphere. Anhydrous THF (15 mL) was added and the resulting solution was cooled to –78 °C before adding *n*-BuLi (2.0 mL, 5.12 mmol, 2.5 M in hexanes) and stirring for 40 min at this temperature. Tropylium tetrafluoroborate (910 mg, 5.0 mmol) was added, and the mixture was allowed to reach rt and stirred for 16 h. The reaction was quenched with a saturated aqueous solution of NH_4Cl (30 mL), then extracted with EtOAc (3 × 20 mL). The combined organic extracts were dried over $MgSO_4$, filtered and the solvent removed under reduced pressure. The crude residue was purified by column chromatography (Teledyne Isco CombiFlash Rf+ system, 24 g SiO_2, hexanes−EtOAc, gradient

elution) to yield the title compound as a yellow oil (838 mg, 4.06 mmol, 81%). **^{1}H NMR** (600 MHz, $CDCl_3$) δ 7.37 (d, *J* = 8.1 Hz, 2H, H_8), 7.12 (d, *J* = 7.8 Hz, 2H, H_9), 6.77–6.59 (m, 2H, H_1), 6.30 – 6.14 (m, 2H, H_2), 5.44 (dd, *J* = 9.0, 5.5 Hz, 2H, H_3), 2.71 (tt, *J* = 5.1, 1.1 Hz, 1H, H_4), 2.36 (s, 3H, H_{11}). **^{13}C NMR** (151 MHz, $CDCl_3$) δ 137.9 (C_{10}), 131.5 (C_8), 130.9 (C_1), 128.9 (C_9), 124.6 (C_2), 123.3 (C_3), 120.3 (C_7), 90.2 (C_5), 80.6 (C_6), 32.2 (C_4), 21.4 (C_{11}). **HRMS-ASAP** *m/z* = 207.1165 $[M+H]^+$, calculated for $C_{16}H_{15}$: 207.1174.

Spectroscopic data were consistent with those published previously.[9a]

7-{2-[4-(Trifluoromethyl)phenyl]ethynyl}cyclohepta-1,3,5-triene (2e-relative to Scheme 4.9)

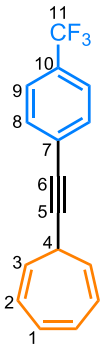

4-Ethynyl-α-α-α-trifluorotoluene (425 mg, 2.5 mmol) was placed into an oven-dried round-bottomed flask fitted with a septum under a N_2 atmosphere. Anhydrous THF (15 mL) was added and the resulting solution was cooled to –78 °C before adding *n*-BuLi (1.0 mL, 2.56 mmol, 2.5 M in hexanes) and stirring for 40 min at this temperature. Tropylium tetrafluoroborate (455 mg, 2.5 mmol) was added, and the mixture was allowed to reach rt and stirred for 16 h. The reaction was quenched with a saturated aqueous solution of NH_4Cl (30 mL), then extracted with EtOAc (3 × 20 mL). The combined organic extracts were dried over $MgSO_4$, filtered and the solvent removed under reduced pressure. The crude residue was purified by column chromatography (Teledyne Isco CombiFlash Rf+ system, 24 g SiO_2, hexanes−EtOAc, gradient elution) to yield the title compound as a yellow solid (483 mg, 1.86 mmol, 74%). **M.P.** 67 – 68 °C (lit.[9a] 65 – 67 °C). **^{1}H NMR** (700 MHz, $CDCl_3$) δ 7.57 (d, *J* = 2.6 Hz, 2H, H_9), 7.56 (d, *J* = 8.8 Hz, 2H, H_8), 6.70 (dddd, *J* = 3.5, 2.7, 0.8, 0.8 Hz, 2H, H_1), 6.26 – 6.21 (m, 2H, H_2), 5.47 – 5.37 (m, 2H, H_3), 2.75 (tt, *J* = 5.6, 1.5 Hz, 1H, H_4). **^{13}C NMR** (176 MHz, $CDCl_3$) δ 132.11 (C_8), 131.23 (C_1), 129.84 (q, J_{CF} = 32.6 Hz, C_{11}), 127.47 (d, J_{CF} = 1.5 Hz, C_7), 125.32 (q, J_{CF} = 3.8 Hz, C_9), 125.18 (C_2), 123.34 (C_{10}), 122.56 (C_3), 93.87 (C_5), 79.63 (C_6), 32.31 (C_4). **^{19}F NMR** (376 MHz, $CDCl_3$) δ –62.9 (s, F_{11}). **HRMS-ASAP** *m/z* = 260.0824 $[M]^+$, calculated for $C_{16}H_{11}F_3$: 260.0813.

Spectroscopic data were consistent with those published previously.[9a]

In solutions at room temperature, each of the barbaralones and barbaralanes[29] below exist as mixtures of two rapidly interconverting valence isomers. Based on our experimental observations, the structures bearing an aryl group at position 1 are the major species present in solution for all of the compounds investigated. The NMR spectroscopic assignments below, which have been made with the aid of two-dimensional NMR techniques, are labelled according to numbering of the major species. However, the species are in fast exchange on account of rapid strain-assisted Cope rearrangement. The chemical shifts of each nucleus are representative of the time-averaged chemical environment they experience as part of the two isomers.

(±)-1-(4-Tolyl)tricyclo[3.3.1.0^{2,8}]nona-3,6-dien-9-one (7c)

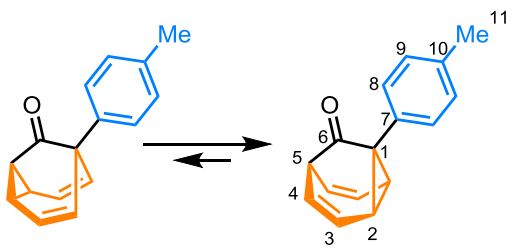

7-[2-(4-Tolyl)ethynyl]cyclohepta-1,3,5-triene (830 mg, 4.02 mmol) and diphenyl sulphoxide (1.62 g, 8.04 mmol) were charged in a flask and dissolved in anhydrous CH_2Cl_2 (15 mL) at rt, with no particular precautions to exclude air. (Acetonitrile)[1,3-bis(2,6-diisopropylphenyl)imidazol-2-ylidene]gold(I) tetrafluoroborate (143 mg, 0.20 mmol, 5 mol%) was added in one portion at the same temperature and the reaction mixture was stirred for 16 h. The reaction was quenched with Et_3N (8 drops) and the solvent was removed under reduced pressure. The crude residue was purified by column chromatography (Teledyne Isco CombiFlash Rf+ system, 24 g SiO_2, hexanes−EtOAc, gradient elution) to yield the title compound as a cream-coloured solid (554 mg, 2.49 mmol, 62%). **M.P.** 121 – 123 °C (lit.[9a] 123 – 125 °C). **^{1}H NMR** (700 MHz, $CDCl_3$) δ 7.19–7.16 (m, 2H, H_8), 7.13 (d, J = 8.1 Hz, 2H, H_9), 5.93 – 5.89 (m, 2H, H_4), 5.88 – 5.84 (m, 2H, H_3), 3.23 (tt, J = 6.5, 0.9 Hz, 1H, H_5), 3.11 – 3.02 (m, 2H, H_2), 2.34 (s, 3H, H_{11}). **^{13}C NMR** (176 MHz, $CDCl_3$) δ 208.5 (C_6), 137.8 (C_{10}), 134.1 (C_7), 129.8 (C_9), 129.6 (C_8), 125.0 (C_4), 121.7 (C_3), 49.3 (C_5), 42.5 (C_2), 31.3 (C_1), 21.5 (C_{11}). **HRMS-ASAP** *m/z* = 223.1112 $[M+H]^+$, calculated for $C_{16}H_{15}O$: 223.1123.

Spectroscopic data were consistent with those published previously.[9a]

(±)-1-[4-(Trifluoromethyl)phenyl]tricyclo[3.3.1.0^{2,8}]nona-3,6-dien-9-one (7e)

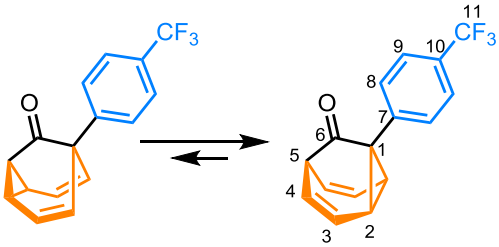

7-{2-[4-(Trifluoromethyl)phenyl]ethynyl}-cyclohepta-1,3,5-triene (542 mg, 1.74 mmol) and diphenyl sulpjoxide (704 mg, 3.48 mmol) were charged in a flask and dissolved in anhydrous CH_2Cl_2 (15 mL) at rt, with no particular precautions to exclude air. (Acetonitrile)[1,3-bis(2,6-diisopropyl-phenyl)imidazol-2-ylidene]gold(I) tetrafluoroborate (61 mg, 0.09 mmol, 5 mol%) was added in one portion at the same temperature and the reaction mixture was stirred for 16 h. The reaction was quenched with Et_3N (6 drops) and the solvent was removed under reduced pressure. The crude residue was purified by column chromatography (Teledyne Isco CombiFlash Rf+ system, 24 g SiO_2, hexanes−EtOAc, gradient elution) to yield the title compound as a yellow solid (279 mg, 1.01 mmol, 58%). **M.P.** 138 – 140 °C (lit.[9a] 137 – 140 °C). **^{1}H NMR** (700 MHz, $CDCl_3$) δ 7.62 (d, J = 8.1 Hz, 2H, H_9), 7.37 (d, J = 8.0 Hz, 2H, H_8), 5.94–5.90 (m, 2H, H_4), 5.89–5.86 (m, 2H, H_3), 3.26 (t, J = 6.4 Hz, 1H, H_5), 3.15–3.11 (m, 2H, H_2). **^{13}C NMR** (176 MHz, $CDCl_3$) δ 207.5 (C_6), 141.0–140.9 (m, C_7), 130.1 (C_8), 129.9 (q, J_{CF} = 32.4 Hz, C_{10}), 125.5 (q, J_{CF} = 3.8 Hz, C_9), 124.4 (C_4), 124.2 (q, J_{CF} = 272.1 Hz, C_{11}), 121.2 (C_3), 48.8 (C_5), 42.6 (C_2), 39.5 (C_1). **^{19}F NMR** (376 MHz, $CDCl_3$) δ -62.6 (s, F_{11}). **HRMS-ASAP** m/z = 277.0833 $[M+H]^+$, calculated for $C_{16}H_{12}OF_3$: 277.0840.

Spectroscopic data were consistent with those published previously.[9a]

(±)-1,9-Bis(4-tolyl)tricyclo[3.3.1.0^{2,8}]nona-3,6-dien-9-ol (6c/6c′)

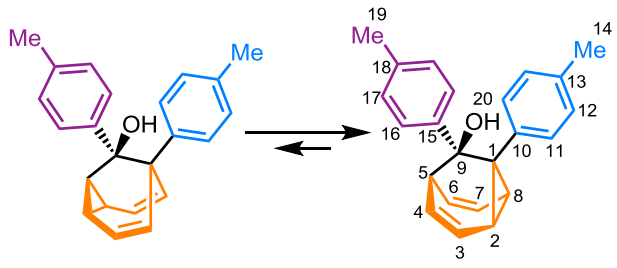

Magnesium turnings (350 mg, 14.40 mmol) and I_2 (183 mg, 0.72 mmol, 5 mol%) were placed in an oven-dried two-necked round-bottomed flask fitted with a condenser and a septum under a N_2 atmosphere. The flask was gently heated with a heat gun until the I_2 started to sublime. The flask was cooled down to rt. A quarter of a solution of 4-bromotoluene

(2.47 g, 14.44 mmol) in anhydrous THF (10 mL) was added to the reaction mixture, which was heated until it reached reflux. Upon gentle reflux, the remaining solution of 1-bromo-4-fluorobenzene in anhydrous THF was added dropwise over 30 min. The reaction mixture was heated at reflux for 30 min before cooling to rt. 1-(4-Tolyl)tricyclo[3.3.1.$0^{2,8}$]nona-3,6-dien-9-one (540 mg, 2.43 mmol) was transferred to an oven-dried round-bottomed flask, and the flask was purged with N_2. Anhydrous THF (10 mL) was added and the solution was cooled to 0 °C. The Grignard solution (prepared above) was added dropwise over 30 min to the barbaralone. The reaction mixture was stirred for 16 h, and the temperature was raised from 0 °C to rt, following removal of the ice bath. The reaction was quenched with a saturated aqueous solution of NH_4Cl (10 mL), then extracted with EtOAc (3 × 20 mL). The combined organic extracts were dried over $MgSO_4$, filtered and the solvent removed under reduced pressure. The crude residue was purified by column chromatography (Teledyne Isco CombiFlash Rf+ system, 24 g SiO_2, hexanes−CH_2Cl_2, gradient elution including 0.5% Et_3N in the elution) to yield the title compound as a white powder (623 mg, 1.98 mmol, 81%). **M.P.** 101 – 103 °C. **^{1}H NMR** (700 MHz, $CDCl_3$) δ 7.21 (d, *J* = 6.6 Hz, 2H, H_{16}), 7.20 (d, *J* = 6.6 Hz, 2H, H_{11}), 6.97 (d, *J* = 7.8 Hz, 2H, H_{12}), 6.95 (d, *J* = 8.0 Hz, 2H, H_{19}), 6.04 (ddd, *J* = 8.8, 6.8, 0.8 Hz, 1H, H_7), 5.83 (ddd, *J* = 8.8, 6.7, 0.6 Hz, 1H, H_3), 5.68 (dddd, *J* = 8.9, 6.6, 1.1, 1.1 Hz, 1H, H_4), 5.55 (dddd, *J* = 8.6, 6.9, 1.6, 0.9 Hz, 1H, H_6), 3.42 (ddd, *J* = 6.9, 6.9, 1.5 Hz, 1H, H_8), 2.98 (ddd, *J* = 6.9, 6.9, 1.5 Hz, 1H, H_2), 2.81 (t, *J* = 6.8 Hz, 1H, H_5), 2.24 (s, 3H, H_{19} or H_{14}), 2.24 (s, 3H, H_{19} or H_{14}), 2.16 (s, 1H, H_{20}). **^{13}C NMR** (176 MHz, $CDCl_3$) δ 139.9 (C_{15}), 137.5 (C_{10}), 136.2 (C_{18} or C_{13}), 136.0 (C_{18} or C_{13}), 130.2 (C_{11}), 128.5 (C_{12}), 128.0 (C_{17}), 127.3 (C_{16}), 124.0 (C_7), 121.9 (C_3), 115.4 (C_6), 114.3 (C_4), 70.0 (C_5), 47.5 (C_8), 46.2 (C_1), 46.1 (C_2), 43.6 (C_9), 21.1 (C_{19} or C_{14}), 21.1 (C_{19} or C_{14}). **HRMS-ASAP** *m/z* = 313.1592 $[M-H]^+$, calculated for $C_{23}H_{21}O$: 313.1593.

(±)-1,9-Bis(4-tolyl) tricyclo[3.3.1.0^{2,8}]nona-3,6-dien-9-ol (6e/6e′)

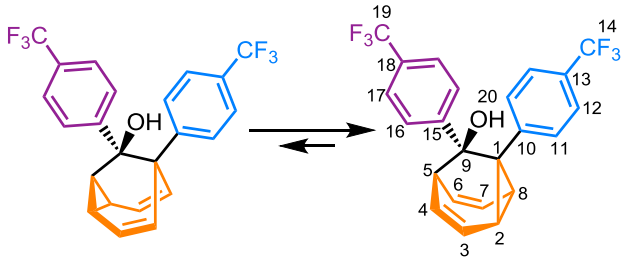

Magnesium turnings (115 mg, 6.36 mmol) and I_2 (81 mg, 0.32 mmol, 5 mol%) were placed in an oven-dried two-necked round-bottomed flask fitted with a condenser and a septum under a N_2 atmosphere. The flask was gently heated with a heat gun until the I_2 started to sublime. The flask was cooled down to rt. A quarter of a solution of 4-bromobenzotrifluoride (1.36 g, 6.06 mmol) in anhydrous THF (10 mL) was added to the reaction mixture, which was heated until it reached reflux. Upon gentle reflux, the remaining solution of 1-bromo-4-fluorobenzene in anhydrous THF was added dropwise over 30 min. The reaction mixture was heated at reflux for 30 min before cooling to rt. 1-[4-(Trifluoromethyl)phenyl]tricyclo[3.3.1.0^{2,8}]nona-3,6-dien-9-one (162 mg, 0.72 mmol) was transferred to an oven-dried round-bottomed flask, and the flask was purged with N_2. Anhydrous THF (10 mL) was added and the solution was cooled to 0 °C. The Grignard solution (prepared above) was added dropwise over 30 min to the barbaralone. The reaction mixture was stirred for 16 h, and the temperature was raised from 0 °C to rt, following removal of the ice bath. The reaction was quenched with a saturated aqueous solution of NH_4Cl (10 mL), then extracted with EtOAc (3 × 20 mL). The combined organic extracts were dried over $MgSO_4$, filtered and the solvent removed under reduced pressure. The crude residue was purified by column chromatography (Teledyne Isco CombiFlash Rf+ system, 24 g SiO_2, hexanes−CH_2Cl_2, gradient elution including 0.5% Et_3N in the elution) to yield the title compound as a sticky yellow gel (416 mg, 0.99 mmol, 98%). **^{1}H NMR** (600 MHz, $CDCl_3$) δ 7.53 (d, *J* = 8.5 Hz, 2H, H_{16}), 7.49–7.45 (m, 6H, H_{11}, H_{12} and H_{17}), 6.13 (dd, *J* = 8.7, 6.9 Hz, 1H, H_3), 5.93 (dd, *J* = 8.6, 7.0 Hz, 1H, H_7), 5.64 (dddd, *J* = 8.3, 6.7, 1.3, 1.3 Hz, 1H, H_4), 5.53 (dddd, *J* = 8.7, 6.9, 1.4, 1.4 Hz, 1H, H_6), 3.66 (ddd, *J* = 6.9, 6.8, 1.5 Hz, 1H, H_8), 3.23 (ddd, *J* = 6.8, 6.8, 1.4 Hz, 1H H_2), 2.89 (t, *J* = 6.8 Hz, 1H, H_5), 2.45 (s, 1H, H_{20}). **^{13}C NMR** (151 MHz, $CDCl_3$) δ 146.5 (C_{15}), 144.4 (s, C_{10}), 130.2 (C_{11}), 128.9 (q, J_{CF} = 32.2 Hz, C_{13}), 128.8 (q, J_{CF} = 32.3 Hz, C_{18}), 127.6 (C_{16}), 124.6 (q, J_{CF} = 3.6 Hz, C_{12}), 124.4 (q, J_{CF} = 271.9 Hz, C_{19}), 124.3 (q, J_{CF} = 272.0 Hz,

C_{14}), 124.3 (q, J_{CF} = 3.8 Hz, C_{17}),124.3 (C_3), 121.9 (C_7), 112.1 (C_6), 110.6 (C_4), 70.0 (C_1), 50.5 (C_8), 49.4 (C_2), 45.4 (C_5), 44.2 (C_9). **^{19}F NMR** (376 MHz, $CDCl_3$) δ -62.4 (s, F_{14} or F_{19}), -62.5 (s, F_{14} or F_{19}). **HRMS-ASAP** *m/z* = 422.1125 $[M]^+$, calculated for $C_{23}H_{16}OF_2$: 422.1105.

(±)-1,9-Diphenyltricyclo[3.3.1.0.^{2,8}]nona-3,6-dien-9-ol (6d/6d′)

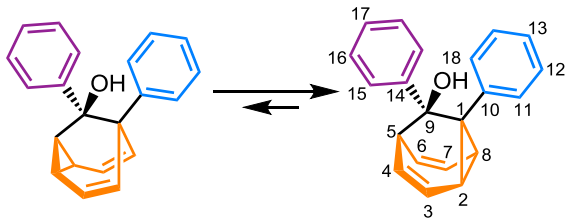

Magnesium turnings (70 mg, 2.78 mmol) and I_2 (33 mg, 0.13 mmol, 5 mol%) were placed in an oven-dried two-necked round-bottomed flask fitted with a condenser and a septum under a N_2 atmosphere. The flask was gently heated with a heat gun until the I_2 started to sublime. The flask was cooled down to rt. A quarter of a solution of bromobenzene (430 mg, 2.60 mmol) in anhydrous THF (10 mL) was added to the reaction mixture, which was heated until it reached reflux. Upon gentle reflux, the remaining solution of 1-bromo-4-fluorobenzene in anhydrous THF was added dropwise over 30 min. The reaction mixture was heated at reflux for 30 min before cooling to rt. 1-Phenyltricyclo[3.3.1.0.^{2,8}]nona-3,6-dien-9-one (96mg, 0.46 mmol) was transferred to an oven-dried round-bottomed flask, and the flask was purged with N_2. Anhydrous THF (10 mL) was added and the solution was cooled to 0 °C. The Grignard solution (prepared above) was added dropwise over 30 min to the barbaralone. The reaction mixture was stirred for 16 h, and the temperature was raised from 0 °C to rt, following removal of the ice bath. The reaction was quenched with a saturated aqueous solution of NH_4Cl (10 mL), then extracted with EtOAc (3 × 20 mL). The combined organic extracts were dried over $MgSO_4$, filtered and the solvent removed under reduced pressure. The crude residue was purified by column chromatography (Teledyne Isco CombiFlash Rf+ system, 24 g SiO_2, hexanes−CH_2Cl_2, gradient elution including 0.5% Et_3N in the elution) to yield the title compound as a white solid (45 mg, 0.16 mmol, 34%). **M.P.** 88 – 90 °C. **^{1}H NMR** (700 MHz, $CDCl_3$) δ 7.32 – 7.29 (m, 2H, H_{15}), 7.28 – 7.26 (m, 2H, H_{11}), 7.18 – 7.13 (m, 3H, H_{12} and H_{13}), 7.13 – 7.08 (m, 3H, H_{16} and H_{17}), 6.07 (ddd, *J* = 8.7, 6.9, 0.8 Hz, 1H, H_3), 5.88 – 5.82 (m, 1H, H_7), 5.62 – 5.56 (m, 1H, H_4), 5.51 – 5.47 (m, 1H,

H_6), 3.59 – 3.52 (m, 1H, H_8), 3.24 – 3.13 (m, 1H, H_2), 2.85 (t, J = 6.8 Hz, 1H, H_5), 2.22 (s, 1H, H_{18}). **^{13}C NMR** (176 MHz, $CDCl_3$) δ 142.7 (C_{14}), 140.5 (C_{10}), 130.3 (C_{11}), 127.7 (C_{12}), 127.4 (C_{15}), 127.2 (C_{16}), 126.6 (C_{17}), 126.6 (C_{13}), 124.0 (C_3), 121.8 (C_7), 112.1 (C_6), 110.8 (C_4), 70.0 (C_1), 50.9 (C_8), 49.5 (C_2), 45.4 (C_5), 44.6 (C_9). **HRMS-ASAP** *m/z* = 269.1324 $[M+H]^+$, calculated for $C_{21}H_{17}$: 269.1330.

4.5.5 Synthesis of Substituted Tropyliums

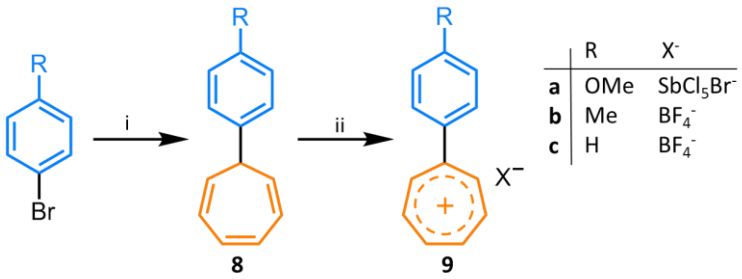

Scheme 4.10. General synthesis of cycloheptatrienes (**8**) and substituted tropyliums (**9**). Reagents and conditions: (i) THF / *n*-BuLi / tropylium tetrafluoroborate / –78 °C to rt, (ii) either (a) bromodiethylsulphonium bromopentachloroantimonate(V) / $CHCl_3$ / rt / 16 h or (b) MeCN / tritylium tetrafluoroborate / 50 °C / 10 min then Et_2O.

7-(4-Ansiyl)cyclohepta-1,3,5-triene (8a)

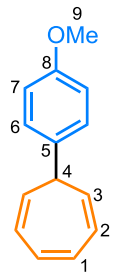

4-Bromoanisole (1.26 g, 6.74 mmol) was placed into an oven-dried round-bottomed flask fitted with a septum under a N_2 atmosphere. Anhydrous THF (15 mL) was added and the resulting solution was cooled to –78 °C before adding *n*-BuLi (5.0 mL, 8.08 mmol 1.6 M in hexanes) and stirring for 1 h at this temperature. Tropylium tetrafluoroborate (1.19 g, 6.74 mmol) was added, and the mixture was allowed to reach rt and stirred for 16 h. The reaction was quenched with an aqueous solution of NH_4Cl (30 mL, saturated) then extracted with EtOAc (3 × 20 mL). The combined organic extracts were dried over $MgSO_4$ and the solvent was removed under reduced pressure. The crude residue was purified by column chromatography (Teledyne Isco CombiFlash Rf+ system, 24 g SiO_2, hexanes−EtOAc, gradient elution) to give the title compound as a pale yellow oil. (600 mg, 3.0 mmol, 45%). **^{1}H NMR** (700 MHz, $CDCl_3$) δ 7.28 (d, J = 8.6 Hz, 2H, H_6), 6.91 (d, J = 8.5 Hz, 2H, H_7), 6.82 – 6.60 (m, 2H, H_1), 6.33 – 6.15 (m, 2H, H_2), 5.52 – 5.21 (m, 2H, H_3), 3.82 (s, 3H, H_9), 2.67 (t, J = 5.7 Hz, 1H, H_4). **^{13}C NMR** (176 MHz, $CDCl_3$) δ 158.6 (C_8), 136.4 (C_5), 131.3 (C_1), 128.8 (C_6),

127.0 (C_3), 124.6 (C_2), 114.4 (C_7), 55.6 (C_9), 44.8 (C_4). **HRMS-ASAP** *m/z* = 197.0976 $[M-H]^+$, calculated for $C_{14}H_{13}O$: 197.0976.

7-(4-Tolyl)cyclohepta-1,3,5-triene (8b)

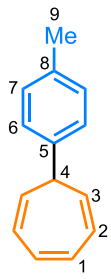

4-Bromotoluene (1.00 g, 5.85 mmol) was placed into an oven-dried round-bottomed flask fitted with a septum under a N_2 atmosphere. Anhydrous THF (15 mL) was added and the resulting solution was cooled to –78 °C before adding *n*-BuLi (2.6 mL, 6.43 mmol 2.5 M in hexanes) and stirring for 1 h at this temperature. Tropylium tetrafluoroborate (1.04 g, 5.85 mmol) was added, and the mixture was allowed to reach rt and stirred for 16 h. The reaction was quenched with an aqueous solution of NH_4Cl (30 mL, saturated) then extracted with EtOAc (3 × 20 mL). The combined organic extracts were dried over $MgSO_4$ and the solvent was removed under reduced pressure. The crude residue was purified by column chromatography (Teledyne Isco CombiFlash Rf+ system, 24 g SiO_2, hexanes−EtOAc, gradient elution) to give the title compound as a pale yellow oil. (585 mg, 3.21 mmol, 55%). **^{1}H NMR** (700 MHz, $CDCl_3$) δ 7.31 – 7.25 (m, 2H, H_6), 7.24 – 7.19 (m, 2H, H_7), 6.85 – 6.64 (m, 2H, H_1), 6.40 – 6.15 (m, 2H, H_2), 5.57 – 5.32 (m, 2H, H_3), 2.72 (tt, *J* = 5.6, 2.8 Hz, 1H, H_4), 2.39 (s, 3H, H_9). **^{13}C NMR (**176 MHz, $CDCl_3$) δ 141.1 (C_5), 136.3 (C_8), 131.1 (C_1), 129.5 (C_7), 127.6 (C_6), 126.7 (C_3), 124.5 (C_2), 45.1 (C_4), 21.2 (C_9). **HRMS-ASAP** *m/z* = 181.1025 $[M-H]^+$, calculated for $C_{14}H_{13}$: 181.1017.

7-Phenylcyclohepta-1,3,5-triene (8c)

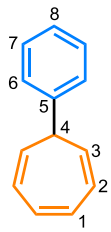

Bromobenzene (329 g, 2.5 mmol) was placed into an oven-dried round-bottomed flask fitted with a septum under a N_2 atmosphere. Anhydrous THF (15 mL) was added and the resulting solution was cooled to –78 °C before adding *n*-BuLi (1.1 mL, 2.75 mmol 2.5 M in hexanes) and stirring for 1 h at this temperature. Tropylium tetrafluoroborate (455 mg, 2.5 mmol) was added, and the mixture was allowed to reach rt and stirred for 16 h. The reaction was quenched with an aqueous solution of NH_4Cl (30 mL, saturated) then extracted with EtOAc (3 × 20 mL). The combined organic extracts were dried over $MgSO_4$ and the solvent was removed under reduced pressure. The crude residue was

purified by column chromatography (Teledyne Isco CombiFlash Rf+ system, 24 g SiO_2, hexanes−EtOAc, gradient elution) to give the title compound as a colourless oil. (253 mg, 1.50 mmol, 60%). **^{1}H NMR** (400 MHz, $CDCl_3$) δ 7.42 (d, *J* = 4.4 Hz, 4H, H_7 and H_8), 7.40 – 7.26 (m, 1H, H_8), 6.84 – 6.76 (m, 2H, H_1), 6.39 – 6.23 (m, 2H, H_2), 5.48 (dd, *J* = 9.4, 5.7, 0.7 Hz, 2H, H_3), 2.78 (tt, *J* = 5.6, 1.5 Hz, 1H, H_4). **^{13}C NMR** (176 MHz, $CDCl_3$) δ 144.0 (C_5), 131.0 (C_1), 128.8 (C_6), 127.7 (C_7), 126.8 (C_8), 126.4 (C_3), 124.6 (C_2), 45.5 (C_4). **HRMS-ASAP** m/z = 167.0867 [M-H], calculated for $C_{13}H_{11}$: 167.0861.

1-(4-Ansiyl)cyclohepta-1,3,5-triene-1-ylium Bromopentachloroantimonate (V) (9a)

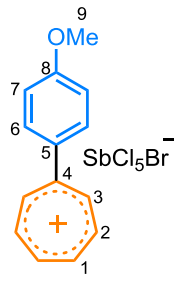

A solution of bromodiethylsulphonium bromopentachloroantimonate(V) (227 mg, 0.41 mmol) in $CHCl_3$ (1.5 mL) was added to a solution of 7-(4-anisyl)cyclohepta-1,3,5-triene (82 mg, 0.41 mmol) in $CHCl_3$ (0.75 mL), with no particular precautions to exclude air. The reaction was left to stir at rt for 16 h. Fine solids were formed and these were centrifuged, the liquid decanted and the remaining solid dried under vacuum to yield the title compound as a red solid (30 mg, 0.05 mmol, 13%). **M.P.** 156 – 158 °C. **^{1}H NMR** (600 MHz, CD_3CN) δ 9.00 (d, *J* = 10.3 Hz, 2H, H_3), 8.73 – 8.66 (m, 2H, H_2), 8.62 – 8.59 (m, 2H, H_1), 7.76 (d, *J* = 9.0 Hz, 2H, H_6), 7.01 (d, *J* = 9.0 Hz, 2H, H_7), 3.71 (s, 3H, H_9). **^{13}C NMR** (151 MHz, CD_3CN) δ 168.7 (C_4), 165.5 (C_8), 153.1 (C_2), 152.6 (C_1), 152.3 (C_3), 133.8 (C_6), 131.7 (C_5), 117.0 (C_7), 56.8 (C_9). **HRMS-ASAP** *m/z* = 197.0970 $[M]^+$, calculated for $C_{14}H_{13}O^+$: 197.0966.

1-(4-Tolyl)cyclohepta-1,3,5-triene-1-ylium Tetrafluoroboranuide (9b)

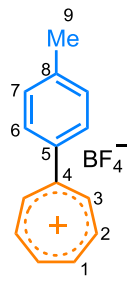

7-(4-Tolyl)cyclohepta-1,3,5-triene (200 mg, 1.1 mmol) was dissolved in anhydrous MeCN (5 mL) followed by the addition of tritylium tetrafluoroborate (360 mg, 1.1 mmol), with no particular precautions to exclude air. The mixture was heated for 10 min at 50 °C before cooling to rt. Anhydrous Et_2O (40 mL) was added to precipitate a solid which was isolated by filtration, washed with anhydrous Et_2O (3 × 20 mL) and dried under vacuum to give the title compound as a golden solid (128 mg, 0.48 mmol, 44%). **M.P.** 146 – 148 °C. **^{1}H NMR** (600 MHz, CD_3CN) δ 9.44 – 9.21 (m, 2H, H_1), 9.08 – 9.03 (m, 2H, H_2), 9.01 – 8.96 (m, 1H, H_3), 7.88 (d, *J* = 8.3 Hz, 2H, H_6), 7.62 – 7.42 (m, 2H, H_7), 2.50 (s, 3H, H_9). **^{13}C NMR** (151 MHz, CD_3CN) δ 169.3 (C_4), 153.8 (C_2), 153.7 (C_3), 153.6 (C_1), 145.6 (C_8), 137.0 (C_5), 131.9 (C_7), 131.4 (C_6), 21.5 (C_9). **HRMS-ESI** *m/z* = 181.1034 $[M]^+$, calculated for $C_{14}H_{13}^+$: 181.1012.

1-Phenylcyclohepta-1,3,5-triene-1-ylium Tetrafluoroboranuide (9c)

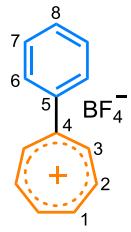

7-Phenylcyclohepta-1,3,5-triene (185 mg, 1.1 mmol) was dissolved in anhydrous MeCN (2 mL) followed by the addition of tritylium tetrafluoroborate (360 mg, 1.1 mmol), with no particular precautions to exclude air. The mixture was heated for 10 min at 50 °C before cooling to rt. Anhydrous Et_2O (40 mL) was added to precipitate a solid which was isolated by filtration, washed with anhydrous Et_2O (5 × 20 mL) and dried under vacuum to give the title compound as an orange solid (145 mg, 0.55 mmol, 51%). **M.P.** 141 – 143 °C. **^{1}H NMR** (700 MHz, $(CD_3)_2CO$) δ 9.55 – 9.41 (m, 2H, H_3), 9.28 – 9.21 (m, 2H, H_2), 9.20 – 9.14 (m, 2H, H_1), 8.11 – 8.02 (m, 2H, H_7), 7.89 – 7.85 (m, 1H, H_8), 7.85 – 7.81 (m, 2H, H_6). **^{13}C NMR** (176 MHz, $(CD_3)_2CO$) δ 169.2 (C_8), 154.5 (C_3), 154.2 (C_2), 154.1 (C_1), 139.9 (C_4), 133.6 (C_5), 131.3 (C_6), 131.1 (C_7). **HRMS-ESI** *m/z* = 167.0857 [M], calculated for $C_{13}H_{11}^+$: 167.0855.

4.5.6 Synthesis of Di-Substituted Barbaralones

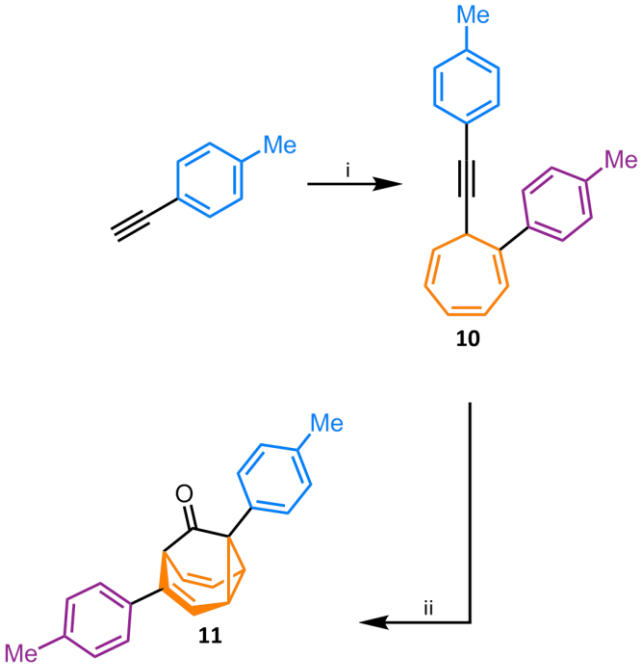

Scheme 4.11. General synthesis of substituted alkynyl cycloheptatriene (**10**) and di-substituted barbaralone (**11**) according to modified literature procedures.[9] (i) THF / *n*-BuLi / **9b** / –78 °C to rt, (ii) 3,5-dichloropyridine *N*-oxide / CH_2Cl_2 / IPrAu(MeCN)BF_4 (5 mol%), / rt / 16 h. IPr = 1,3-bis(2,6-diisopropylphenyl)imidazol-2-ylidene.

Substituted alkynyl cycloheptatrienes are formed as a mixture of products with varying degrees of substitution to the cycloheptatriene ring. The main product only has one tolyl group attached to the cycloheptatriene ring (shown in Scheme 4.11), whereas other products have either one or two tolyl groups substituted to the cycloheptatriene ring at different positions.

1-(4-Tolyl)-7-[2-(4-tolyl)ethynyl]cyclohepta-1,3,5-triene (10)

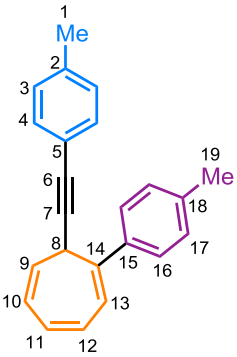

4-Ethynyltoluene (120 mg, 1.1 mmol) was placed into an oven-dried round-bottomed flask fitted with a septum under a N_2 atmosphere. Anhydrous THF (10 mL) was added and the resulting solution was cooled to –78 °C before adding *n*-BuLi (0.16 mL, 0.41 mmol, 2.5 M in hexanes) and stirring for 40 min at this temperature. 1-(4-Tolyl)cyclohepta-1,3,5-triene-1-ylium tetrafluoroboranuide (300 mg, 1.1 mmol) was added, and the

mixture was allowed to reach rt and stirred for 16 h. The reaction was quenched with a saturated aqueous solution of NH_4Cl (30 mL), then extracted with EtOAc (3 × 20 mL). The combined organic extracts were dried over $MgSO_4$, filtered and the solvent removed under reduced pressure. The crude residue was purified by column chromatography (Teledyne Isco CombiFlash Rf+ system, 12 g SiO_2, hexanes−EtOAc, gradient elution) to yield the title compound as a yellow oil (144 mg, 0.05 mmol, 44%). **^{1}H NMR (**400 MHz, $CDCl_3$) δ 7.48 – 7.40 (m, 2H, H_{16}), 7.18 – 7.15 (m, 4H, H_4 and H_{17}), 7.04 (dd, *J* = 8.5, 0.8 Hz, 2H, H_3), 6.81 – 6.75 (m, 1H, H_{12}), 6.75 – 6.67 (m, 1H, H_{11}), 6.48 – 6.40 (m, 1H, H_{13}), 6.36 – 6.27 (m, 1H, H_{10}), 5.71 – 5.56 (m, 1H, H_9), 3.87 (d, *J* = 7.4 Hz, 1H, H_8), 2.37 (s, 3H, H_{19}), 2.31 (s, 3H, H_1). **^{13}C NMR** (176 MHz, $CDCl_3$) δ 137.8 (C_2), 137.6 (C_{15}), 137.3 (C_{18}), 135.0 (C_{14}), 131.6 (C_4), 130.7 (C_{12}), 129.9 (C_{11}), 129.0 (C_3), 128.8 (C_{16}), 128.8 (C_{17}), 126.1 (C_{10}), 123.4 (C_{13}), 122.8 (C_9), 120.8 (C_5), 88.3 (C_7), 82.6 (C_6), 35.3 (C_8), 21.6 (C_1), 21.3 (C_{19}). **HRMS-ASAP** *m/z* = 297.1651 $[M+H]^+$, calculated for $C_{23}H_{21}$: 297.1643.

1,4-Bis-(4-tolyl) tricyclo[3.3.1.0.^{2,8}]nona-3,6-dien-9-one (11)

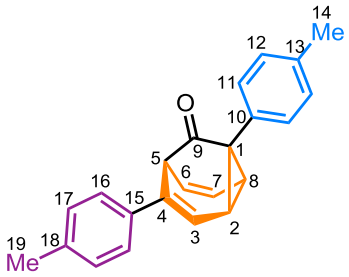

1-(4-Tolyl)-7-[2-(4-tolyl)ethynyl]cyclohepta-1,3,5-triene (8 mg, 0.03 mmol) and 3,5-dichloropyridine *N*-oxide (10 mg, 0.06 mmol) were charged in a flask and dissolved in anhydrous CH_2Cl_2 (15 mL) at rt, with no particular precautions to exclude air. (Acetonitrile)[1,3-bis(2,6-diisopropylphenyl)imidazol-2-ylidene]gold(I) tetrafluoroborate (1 mg, 0.001 mmol, 5 mol%) was added in one portion at the same temperature and the reaction mixture was stirred for 16 h. The reaction was quenched with Et_3N (1 drop) and the solvent was removed under reduced pressure. The crude residue was purified by column chromatography (Teledyne Isco CombiFlash Rf+ system, 24 g SiO_2, hexanes−EtOAc, gradient elution) to yield the title compound as a yellow solid (3 mg, 9.3 mmol, 33%). **M.P.** 132 – 134 °C. **^{1}H NMR** (700 MHz, $CDCl_3$) δ 7.34 – 7.29 (m, 2H, H_{16}), 7.21 – 7.17 (m, 4H, H_{11} and H_{12}), 7.15 (d, *J* = 8.0 Hz, 2H, H_{17}), 6.19 – 6.12 (m, 1H, H_3), 6.11 – 6.01 (m, 1H, H_6), 5.99 – 5.92 (m, 1H, H_7), 3.90 – 3.83 (m, 1H, H_5), 3.09 – 3.02 (m, 1H, H_2), 3.01 – 2.95 (m, 1H, H_8), 2.35 (d, *J* = 1.9 Hz, 6H, H_{14} and H_{19}). **^{13}C NMR** (176 MHz, $CDCl_3$) δ 208.5 (C_9), 141.6

(C_4), 137.7 (C_{10} or C_{18}), 137.7 (C_{10} or C_{18}), 135.2 (C_{15}), 133.6 (C_{13}), 129.7 (C_{11}), 129.5 (C_{12} or C_{17}), 129.4 (C_{12} or C_{17}), 129.0 (C_6), 125.4 (C_{16}), 122.6 (C_7), 116.1 (C_3), 53.1 (C_5), 38.7 (C_1), 38.6 (C_8), 38.0 (C_2), 21.4 (C_{14} or C_{19}), 21.3 (C_{14} or C_{19})**. HRMS-ASAP** *m/z* = 313.1592 $[M+H]^+$, calculated for $C_{23}H_{21}O$: 313.1592.

4.5.7 Synthesis of Heptaphenyl Alkynyl Cycloheptatrienes

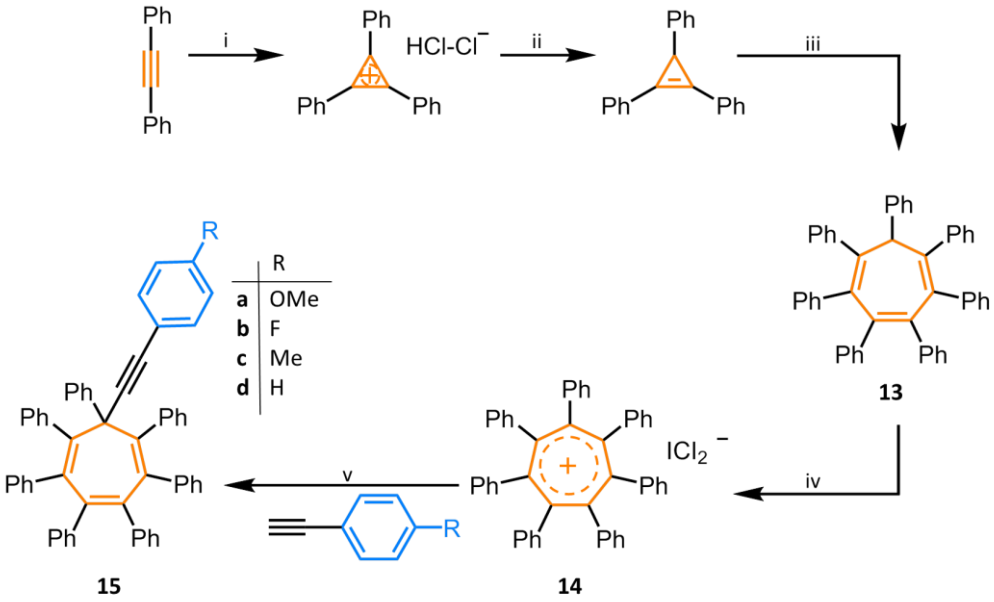

Scheme 4.12. Synthesis of heptaphenylcycloheptatriene (**13**), heptaphenyltropylium (**14**) and heptaphenyl alkynyl cycloheptatriene (**15**) according to modified literature procedures.[21,22] Reagents and conditions: (i) α,α-dichlorotoluene / $(CH_3)_3COK$ / benzene / 3 h / 80 °C, (ii) $NaBH_4$ / EtOH / rt, (iii) tetraphenylcyclopentadienone / *p*-xylene / 140 °C / 36 h (iv) ICl / CH_2Cl_2 / rt / 24 h, (v) THF / *n*-BuLi / rt / 16 h.

Triphenylcyclopropenium Hydrogen Dichloride

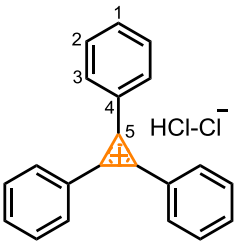

Diphenylacetylene (18.5 g, 104 mmol) and potassium *tert*-butoxide (35.0 g, 312 mmol) were placed in a two-necked oven-dried round-bottomed flask fitted with a septum, under a N_2 atmosphere. Anhydrous benzene (200 mL) was added and the mixture was stirred. α,α-Dichlorotoluene (25.0 g, 155 mmol) was added to the reaction mixture uniformly over a period of 30 min using a syringe pump. The reaction mixture was then heated to reflux for 3 h at 80 °C. After cooling, H_2O (200 mL) was added to dissolve the inorganic salts. The layers

were separated and the aqueous layer was extracted with Et_2O (2 × 200 mL). The ether extracts were combined with the benzene layer and dried over $MgSO_4$, before the solvent was removed under reduced pressure to give a solid, orange residue. This crude mixture was dissolved in a mixture of 2:1 Et_2O–CH_2Cl_2 (200 mL) and then sparged with gaseous HCl, leading to the formation of a colorless precipitate. Sparging was continued until no more precipitation was observed, then the mixture was filtered through a sintered glass funnel and the solid washed with Et_2O. The solid was dried under vacuum to yield the title as cream powder (18.6 g, 61.4 mmol, 43%). **M.P.** 186 – 188 °C. **^{1}H NMR** (600 MHz, CD_3CN) δ 8.83 – 8.39 (m, 6H, H_3), 8.20 – 8.00 (m, 3H, H_1), 7.97 – 7.86 (m, 6H, H_2). **^{13}C NMR** (151 MHz, CD_3CN) δ 154.1 (C_5), 139.1 (C_1), 136.6 (C_2), 131.4 (C_3), 121.6 (C_4). **HRMS-ESI** *m/z* = 267.1169 $[M]^+$ (calculated for $C_{21}H_{15}^+$ = 267.1168).

Triphenylcyclopropene

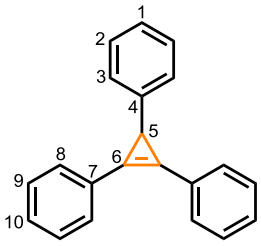

Sodium borohydride (9.3 g, 246 mmol) was added to a solution of triphenylcyclopropenium hydrogen dichloride (18.6 g, 61.4 mmol) in EtOH (460 mL). The mixture was allowed to stir overnight at rt. The reaction was quenched with H_2O (500 mL) then extracted with Et_2O (3 × 200 mL). The organic layers were combined and washed with H_2O (500 mL) and brine (500 mL). The combined organic extracts were then dried over $MgSO_4$ and the solvent was removed under reduced pressure to give the title compound as a colorless solid (14.2 g, 53.1 mmol, 97%).. **M.P.** 113 – 115 °C (lit.[21] 114 – 115.5 °C). **^{1}H NMR** (400 MHz, $CDCl_3$) δ 7.71 – 7.66 (m, 4H, H_8), 7.47 – 7.40 (m, 4H, H_9), 7.38 – 7.32 (m, 2H, H_{10}), 7.24 (br s, 2H, H_2), 7.23 – 7.22 (m, 2H, H_3), 7.17 – 7.10 (m, 1H, H_1), 3.27 (s, 1H, H_5). **^{13}C NMR** (101 MHz, $CDCl_3$) δ 144.6 (C_4), 130.0 (C_8), 128.9 (C_9), 128.8 (C_{10}), 128.7 (C_7), 128.3 (C_3), 126.0 (C_2), 125.6 (C_1), 112.7 (C_6), 24.5 (C_5). **HRMS-ESI** *m/z* = 267.1172 $[M-H]^+$ (calculated for $C_{21}H_{15}$ = 267.1174).

Spectroscopic data were consistent with those published previously.[21]

Heptaphenylcyclohepta-1,3,5-triene (13)

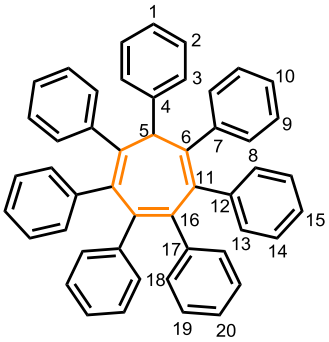

To a 20 mL microwave vial was added triphenylcyclopropene (1.2 g, 4.47 mmol), tetraphenylcyclopentadienone (1.79 g, 4.47 mmol) and anhydrous *p*-xylene (13.5 mL). The reaction vessel was sealed and the mixture deoxygenated (3 × freeze–pump–thaw cycles under N_2) then stirred for 36 h at 140 °C in a microwave reactor. Upon cooling to rt, a crystalline solid formed, which was isolated by filtration through a sintered glass funnel, washing with Et_2O (3 × 10 mL). The solid was dried under vacuum to yield the title compound as a pale pink solid (2.3 g, 3.68 mmol, 82%). **M.P.** 291 – 292 °C (lit.[22] 285 – 287.5 °C). **^{1}H NMR** (700 MHz, $(CD_3)_2CO$) δ 8.17 – 7.99 (m, 2H, H_3), 7.62 – 7.48 (m, 2H, H_2), 7.44 – 7.34 (m, 1H, H_1), 7.26 – 7.18 (m, 4H, H_8), 7.15 (br s, 4H, H_{13}), 7.05 – 7.02 (m, 4H, H_{14}), 7.02 – 6.98 (m, 4H, H_9), 6.98 – 6.96 (m, 2H, H_{15}), 6.96 – 6.93 (m, 2H, H_{10}), 6.63 – 6.59 (m, 2H, H_{20}), 6.60 – 6.55 (m, 4H, H_{19}), 6.36 – 6.32 (m, 4H, H_{18}), 5.35 (s, 1H, H_5). **^{13}C NMR** (176 MHz, $(CD_3)_2CO$) δ 144.8 (C_{16}), 144.4 (C_7), 144.1 (C_4), 141.9 (C_{12}), 141.6 (C_{17}), 140.2 (C_6), 138.0 (C_{11}), 132.7 (C_{13}), 132.3 (C_{18}), 130.7 (C_8), 129.4 (C_2), 128.5 (C_9), 128.1 (C_{14}), 127.9 (C_3), 127.7 (C_1), 127.3 (C_{10}), 126.93 (C_{15}), 126.87 (C_{19}), 126.0 (C_{20}), 59.0 (C_5). **HRMS-ESI** *m/z* = 625.2892 $[M+H]^+$ (calculated for $C_{47}H_{37}$ = 625.2895).

Spectroscopic data were consistent with those published previously.[22]

Heptaphenylcyclohepta-1,3,5-trien-1-ylium Chloro-Iodanyl Chloranide (14)

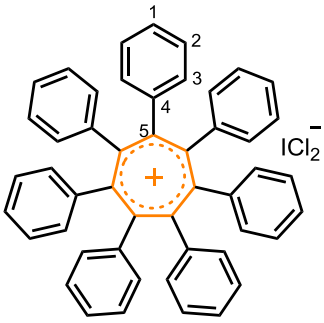

To a round-bottomed flask was added heptaphenylcyclohepta-1,3,5-triene (100 mg, 0.16 mmol) dissolved in anhydrous CH_2Cl_2 (10 mL). A solution of iodine monochloride (1.0 mL, 1.0 mmol, 1.0 M in CH_2Cl_2) was added to the mixture which was stirred at rt for 24 h. The solvent was then removed under reduced pressure, before adding anhydrous MeCN (15 mL) followed by anhydrous Et_2O (25 mL) to precipitate a solid which was collected, washed with anhydrous Et_2O

(3 × 15 mL) and dried under vacuum to yield the title compound as a red solid (97 mg, 0.01 mmol, 60%). **M.P.** 293 – 294 °C. **^{1}H NMR** (600 MHz, $CDCl_3$) δ 7.01 (d, *J* = 7.6 Hz, 14H, H_3), 6.82 (t, *J* = 7.5 Hz, 14H, H_2), 6.76 (t, *J* = 7.4 Hz, 7H, H_1). **^{13}C NMR** (151 MHz, $CDCl_3$) δ 167.5 (C_5), 141.0 (C_4), 130.0 (C_3), 127.3 (C_1), 127.1 (C_2). **HRMS-ASAP** *m/z* = 624.2729 $[M+H]^+$, calculated for $C_{49}H_{36}^+$: 624.2811.

For heptaphenyl substituted alkynyl cycloheptatrienes (**15**), where possible the individual ^{1}H and ^{13}C resonances have been assigned using bidimensional NMR techniques. However, some resonances could not be assigned on account of overlap between peaks and the similarity of some nuclear environments. The number of distinct ^{1}H and ^{13}C resonances demonstrates that rotation of some of the phenyl rings may be slow on the timescale of the 2D NMR experiments.

7-[2-(4-Anisyl)ethynyl)heptaphenylcycloheptatriene (15a)

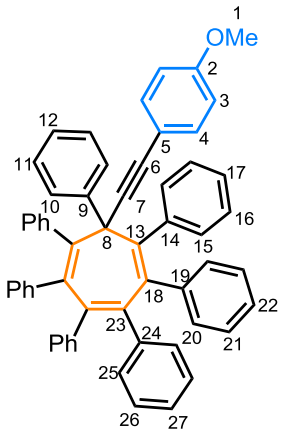

4-Ethynylanisole (160 mg, 1.21 mmol) was placed into an oven-dried round-bottomed flask fitted with a septum under a N_2 atmosphere. Anhydrous THF (5 mL) was added and the resulting solution was cooled to –78 °C before adding *n*-BuLi (0.5 mL, 1.24 mmol, 2.5 M in hexanes) and stirring for 40 min at this temperature. *sym*-Heptaphenylcyclohepta-1,3,5-trien-1-ylium chloro-iodanyl chloranide (580 mg, 0.58 mmol) was added, and the mixture was allowed to reach rt and stirred for 16 h. The reaction was quenched with a saturated aqueous solution of NH_4Cl (20 mL), then extracted with CH_2Cl_2 (3 × 20 mL). The combined organic extracts were then washed with H_2O (20 mL) and brine (20 mL) before drying over $MgSO_4$, filtering and removing the solvent under reduced pressure. The crude residue was purified by column chromatography (Teledyne Isco CombiFlash Rf+ system, 24 g SiO_2, hexanes−EtOAc, gradient elution) to yield the title compound as a yellow solid (240 mg, 0.32 mmol, 55%). **M.P.** 247 – 249 °C. **^{1}H NMR** (600 MHz, $CDCl_3$) δ 8.14 – 8.07 (m, 2H, H_{10}), 7.76 (d, *J* = 7.8 Hz, 2H), 7.54 – 7.41 (m, 2H, H_{11}), 7.38 – 7.32 (m, 1H, H_{12}), 7.22 – 7.10 (m, 3H), 7.08 – 6.88 (m, 14H), 6.87 – 6.81 (m, 3H), 6.68 – 6.64 (m, 2H, H_{27}), 6.63 – 6.59 (m, 4H, H_{26}), 6.50

(br s, 4H, H_4 and H_3), 6.24 – 6.11 (m, 4H, H_{25}), 3.66 (s, 3H, H_1). **^{13}C NMR** (151 MHz, $CDCl_3$) δ 158.8 (C_2), 146.2 (C_9), 143.2 (C_{23}), 143.0, 141.3, 140.9, 140.1 (C_{24}), 137.6, 132.2, 132.0 (C_3 or C_4), 131.2 (C_{25}), 131.3, 128.8 (C_{11}), 127.2 (C_{10}), 127.1 (C_{12}), 127.1, 126.9, 126.20, 126.1 (C_{26}), 126.0, 125.9, 125.3 (C_{27}), 116.2 (C_5), 113.3 (C_3 or C_4), 94.1 (C_6), 93.3 (C_7), 56.2 (C_8), 55.2 (C_1). **HRMS-ASAP** *m/z* = 755.3302 $[M+H]^+$, calculated for $C_{58}H_{43}O$: 755.3314.

7-[2-(4-Fluorophenyl)ethynyl)heptaphenylcycloheptatriene (15b)

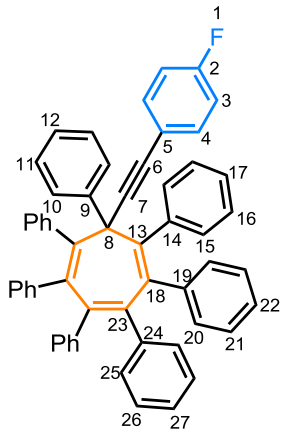

1-Ethynylfluorobenzene (98 mg, 0.82 mmol) was placed into an oven-dried round-bottomed flask fitted with a septum under a N_2 atmosphere. Anhydrous THF (5 mL) was added and the resulting solution was cooled to –78 °C before adding *n*-BuLi (0.35 mL, 0.84 mmol, 2.5 M in hexanes) and stirring for 40 min at this temperature. *sym*-Heptaphenylcyclohepta-1,3,5-trien-1-ylium chloro-iodanyl chloranide (400 mg, 0.39 mmol) was added, and the mixture was allowed to reach rt and stirred for 16 h. The reaction was quenched with a saturated aqueous solution of NH_4Cl (20 mL), then extracted with EtOAc (3 × 20 mL). The combined organic extracts were then washed with H_2O (20 mL) and brine (20 mL) before drying over $MgSO_4$, filtering and removing the solvent under reduced pressure. The crude residue was purified by column chromatography (Teledyne Isco CombiFlash Rf+ system, 24 g SiO_2, hexanes−EtOAc, gradient elution) to yield the title compound as a white solid (235 mg, 0.32 mmol, 79%). **M.P.** 266 – 268 °C. **^{1}H NMR** (700 MHz, $CDCl_3$) δ 8.14 – 8.06 (m, 2H, H_{10}), 7.75 (d, *J* = 7.8 Hz, 2H), 7.53 – 7.46 (m, 2H, H_{11}), 7.40 – 7.34 (m, 1H, H_{12}), 7.15 (m, 2H), 7.04 – 6.90 (m, 14H), 6.88–6.82 (m, 4H), 6.68–6.66 (m, 2H, H_3), 6.66 – 6.64 (m, 2H, H_{27}), 6.61 (dd, *J* = 8.2, 6.8 Hz, 4H, H_{26}), 6.55 – 6.47 (m, 2H, H_4), 6.20 – 6.11 (m, 4H, H_{25}). **^{13}C NMR** (176 MHz, $CDCl_3$) δ 162.6 (C_5 or C_2), 161.2 (C_5 or C_2), 145.9 (C_9), 143.2 (C_{23}), 142.8, 141.2, 140.9, 140.0 (C_{24}), 137.8, 132.5 (d, J_{CF} = 8.2 Hz, C_4), 132.1, 131.6, 131.4, 131.4 (C_{25}), 131.2, 128.8 (C_{11}), 127.3 (C_{12}), 127.2 (C_{10}), 127.1, 127.0, 126.7, 126.3, 126.2 (C_{26}), 126.1, 126.0, 125.4 (C_{27}), 125.3, 119.8, 119.8, 114.8 (d, J_{CF} = 21.9 Hz, C_3), 94.4 (C_6), 93.2 (C_7), 56.2 (C_8). **^{19}F NMR** (376 MHz, $CDCl_3$) δ -112.8 (tt, *J* =

8.8, 5.5 Hz, F_1). **HRMS-ASAP** *m/z* = 743.3123 $[M+H]^+$, calculated for $C_{58}H_{39}F$: 743.3114.

7-[2-(4-Tolyl)ethynyl)heptaphenylcycloheptatriene (15c)

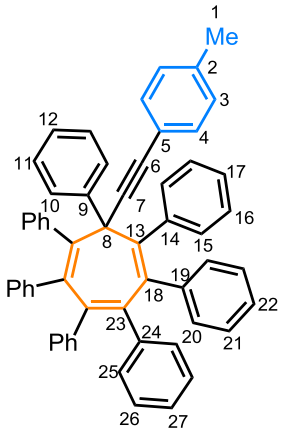

1-Ethynyl-4-fluorobenzene (95 mg, 0.82 mmol) was placed into an oven-dried round-bottomed flask fitted with a septum under a N_2 atmosphere. Anhydrous THF (5 mL) was added and the resulting solution was cooled to –78 °C before adding *n*-BuLi (0.35 mL, 0.84 mmol, 2.5 M in hexanes) and stirring for 40 min at this temperature. *sym*-Heptaphenylcyclohepta-1,3,5-trien-1-ylium chloro-iodanyl chloranide (400 mg, 0.39 mmol) was added, and the mixture was allowed to reach rt and stirred for 16 h. The reaction was quenched with a saturated aqueous solution of NH_4Cl (20 mL), then extracted with EtOAc (3 × 20 mL). The combined organic extracts were then washed with H_2O (20 mL) and brine (20 mL) before drying over $MgSO_4$, filtering and removing the solvent under reduced pressure. The crude residue was purified by column chromatography (Teledyne Isco CombiFlash Rf+ system, 24 g SiO_2, hexanes−EtOAc, gradient elution) to yield the title compound as a white solid (240 mg, 0.32 mmol, 82%). **M.P.** 245 – 247 °C. **^{1}H NMR** (700 MHz, $CDCl_3$) δ 8.12 (dd, *J* = 8.3, 1.3 Hz, 2H, H_{10}), 7.80 – 7.71 (m, 2H), 7.47 (dd, *J* = 8.2, 7.3 Hz, 2H, H_{11}), 7.39 – 7.33 (m, 1H, H_{12}), 7.18 – 7.14 (m, 2H), 7.04 – 6.90 (m, 14H), 6.87 – 6.83 (m, 5H), 6.78 (d, *J* = 8.5 Hz, 2H, H_3), 6.69 – 6.65 (m, 2H, H_{27}), 6.63 – 6.60 (m, 4H, H_{26}), 6.48 (d, *J* = 8.2 Hz, 2H, H_4), 6.25 – 6.11 (m, 4H, H_{25}), 2.17 (s, 3H, H_1). **^{13}C NMR** (176 MHz, $CDCl_3$) δ 146.1 (C_9), 143.2 (C_{23}), 142.9 (C), 141.3, 140.9, 140.8, 140.4, 140.1 (C_{24}), 137.6, 137.1 (C_2), 132.2, 131.6, 131.4, 131.3, 130.6 (C_4), 128.7 (C_{11}), 128.4 (C_3), 127.2 (C_{10}), 127.2 (C_{12}), 127.1, 126.9, 126.7, 126.2, 126.1, 126.1, 125.9, 125.3 (C_{27}), 125.3, 120.8 (C_5), 94.4 (C_6), 94.0 (C_7), 77.3, 56.2 (C_8), 21.4 (C_1), 21.2**. HRMS-ASAP** *m/z* = 739.3382 $[M+H]^+$, calculated for $C_{58}H_{43}$: 739.3365.

Heptaphenyl-7-(2-phenylethynyl)cycloheptatriene (15d)

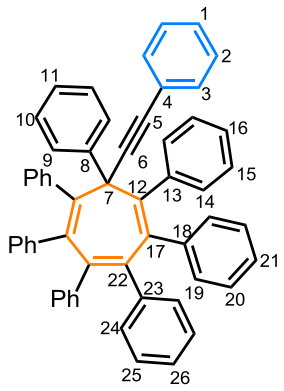

Phenylacetylene (47 mg, 0.46 mmol) was placed into an oven-dried round-bottomed flask fitted with a septum under a N_2 atmosphere. Anhydrous THF (5 mL) was added and the resulting solution was cooled to –78 °C before adding *n*-BuLi (0.2 mL, 0.48 mmol, 2.5 M in hexanes) and stirring for 40 min at this temperature. *sym*-Heptaphenylcyclohepta-1,3,5-trien-1-ylium chloro-iodanyl chloranide (200 mg, 0.20 mmol) was added, and the mixture was allowed to reach rt and stirred for 16 h. The reaction was quenched with a saturated aqueous solution of NH_4Cl (20 mL), then extracted with CH_2Cl_2 (3 × 20 mL). The combined organic extracts were then washed with H_2O (20 mL) and brine (20 mL) before drying over $MgSO_4$, filtering and removing the solvent under reduced pressure. The crude residue was purified by column chromatography (Teledyne Isco CombiFlash Rf+ system, 24 g SiO_2, hexanes−EtOAc, gradient elution) to yield the title compound as a yellow solid (136 mg, 0.19 mmol, 94%). **M.P.** 256 – 258 °C. **^{1}H NMR** (600 MHz, $CDCl_3$) δ 8.16 – 8.07 (m, 2H, H_8), 7.82 – 7.73 (m, 2H), 7.51 – 7.44 (m, 2H, H_9), 7.36 (ddd, *J* = 8.5, 5.2, 3.2 Hz, 1H, H_{10}), 7.21 – 7.12 (m, 2H), 7.05 – 6.88 (m, 16H), 6.88 – 6.81 (m, 3H, H_1), 6.68 – 6.64 (m, 2H, H_{25}), 6.62 – 6.61 (m, 2H, H_2), 6.61 – 6.56 (m, 4H, H_{24}), 6.21 – 6.10 (m, 4H, H_{23}). **^{13}C NMR** (151 MHz, $CDCl_3$) δ 146.0 (C_7), 143.2 (C_{21}), 142.8 (C_3), 141.2, 140.8, 140.0 (C_{22}), 137.7, 132.2, 131.6, 131.4 (C_{23}), 131.3, 130.7 (C_{24}), 128.8 (C_9), 127.6, 127.2 (C_{10}), 127.2 (C_8), 127.1, 126.9 (C_1), 126.7, 126.3, 126.2, 126.1 (C_4), 126.1, 126.0, 125.9, 125.3 (C_{25}), 123.8, 94.7 (C_4), 94.3 (C_5), 56.2 (C_6). **HRMS-ASAP** *m/z* = 725.3113 $[M+H]^+$, calculated for $C_{58}H_{40}$: 725.3208.

4.5.8 Synthesis of SO_2ClF

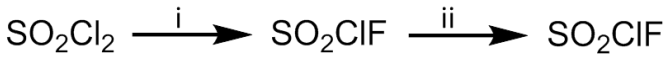

Scheme 4.13. Synthesis of SO_2ClF according to modified literature procedures.[30] Reagents and conditions: (i) NH_4F / CF_3COOH / 30 min / rt then 10 min / 50 °C / dewars at –78 °C, (ii) rt / 1 h / dewars at –78 °C.

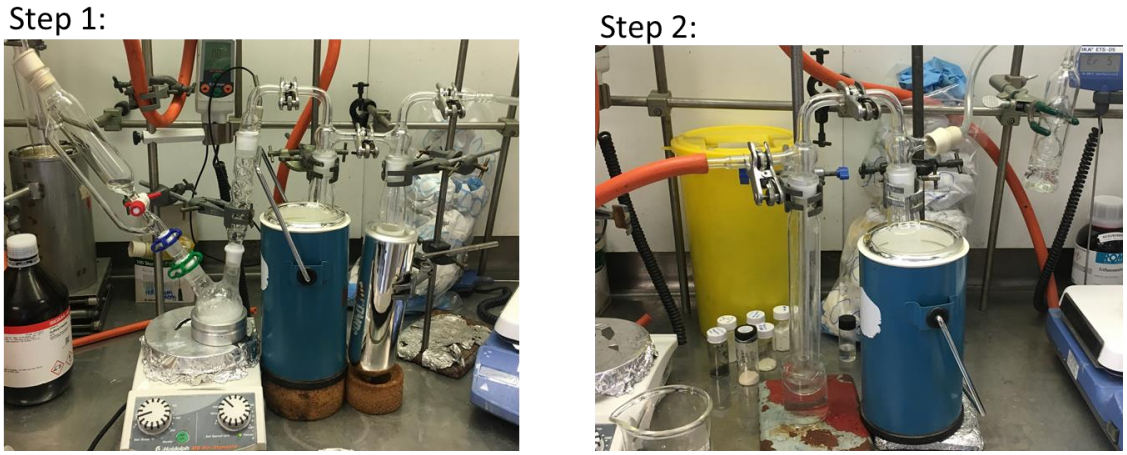

Figure 4.12. Images demonstrating the apparatus set-up used to generate SO_2ClF.

Step 1:

All glassware was oven-dried and a constant flow of N_2 (from left to right was passed through the apparatus) as shown in Figure 4.12. The apparatus was set us as shown above. A 100 mL two-necked round-bottomed flask has one neck attached to a reflux condenser and the other fitted with a dropping funnel and was placed into a 100 mL heating block. The condenser was attached to an adaptor which connects to the in-line trap. The first in-line trap is connected in an air-tight manner to the second in-line trap. Both in-line traps are placed into dewars which are at –78 °C. All glassware connections use a metal clip. Teflon tape is used to ensure all seals are air-tight.

To an oven-dried round-bottomed flask was added NH_4F (8.2 g, 0.22 mmol) and SO_2Cl_2 (30 mL, 0.37 mmol). CF_3COOH (11.2 mL, 0.15 mol) was added to the dropping funnel and over a period of 10 min the CF_3COOH was added to the contents of the round-bottomed flask. The mixture was left to stir for 30 min before heating the mixture to 50 °C for 10 min. The reaction flask was then cooled down to rt. The first in-line trap contains SO_2ClF with SO_2. To remove the unwanted SO_2, disconnect the

in-line trap and treat the mixture with 1 mL of anhydrous SbF_5 before directly placing in the freezer.

Step 2:

All glassware was oven-dried and maintained a constant flow of N_2 (from left to right). The apparatus was set us as shown above. The first in-line trap contains the SO_2ClF generated from the step 1 of the procedure (ensure that this in-line trap is added to the set-up at the end) and is connected to the second in-line trap which is placed into a dewar which is at –78 °C. All glassware connections use a metal clip. Teflon tape is used to ensure all seals are air-tight.

The first in-line trap was taken out of the freezer and directly added to the set-up. The mixture was distilled, as the temperature was allowed to increase from –7 °C to rt over a period of 30 min. Hot H_2O was then added to a beaker and placed around the first in-line trap for 30 min to ensure distaillation of SO_2ClF was complete. The second in-line trap will contain the desired SO_2ClF, whereas the first in-line trap will contain any remaining impurities. Disconnect the second in-line trap and directly place in the freezer.

This two-step procedure yields SO_2ClF as a colourless liquid (7.0 mL, 0.10 mol, 63%). **^{19}F NMR** (500 MHz, 271 K) δ 100.7.

4.5.9 Barbaralyl Cation Generation

The NMR spectrometer was precooled to the desired temperature. To a clean NMR tube was added finely ground hydroxy barbaralane (~ 5 mg). A ceramic NMR spinner was placed around the NMR tube containing the hydroxy barbaralane. Cold SO_2ClF was placed into a precooled clean test tube which was placed in a dry ice–acetone bath (–78 °C). An *n*-pentane and liquid N_2 cooling bath (– 131 °C) was made (a slush-like mixture confirmed the formation) and the NMR tube with the spinner was placed into this cooling bath. Precooled (–78 °C) SO_2ClF (0.6 mL) was added to the NMR tube using a clean pasteur pipette. Draw the precooled SO_2ClF several times (to cool the pasteur pipette) before adding to the NMR tube. Ensure the hydroxy

barbaralane is fully dissolved in the SO_2ClF before proceeding to the next step. If the hydroxy barbaralane doesn't dissolve, vortex the sample repeatedly (ensuring the sample is kept at –78 °C) until the solid disappears. FSO_3H (0.1 mL) was placed into a precooled clean test tube which was placed in a dry ice–acetone bath (–78 °C). Draw the precooled FSO_3H several times (to cool the pasteur pipette) before adding to the NMR tube. Precooled (–78 °C) FSO_3H (1 drop) was added to the mixture in the NMR tube and the corresponding cation was formed and the NMR tube was placed into the precooled NMR spectrometer. If the sample requires a C_4D_8O capillary insert, cool the insert in the *n*-pentane and liquid N_2 cooling bath and clean quickly (with a tissue) before inserting into the sample – the C_4D_8O should be a solid when inserting into the sample.

4.6 Appendix of Supplementary Data and Discussion

4.6.1. Structural Assignment by 2D NMR

Assignment of ^{1}H and ^{13}C NMR signals for all compounds were accomplished by 2D NMR spectroscopy (COSY, NOESY, HSQC and HMBC). In order to distinguish the 'front' and 'back' faces of barbaralane molecules COSY and NOESY experiments were employed as discussed in Chapter 2, Section 2.5.1 and Chapter 3, Sections 3.6.1.1 and 3.6.2.1.

4.6.2. Rate of Exchange Calculations

To calculate the rate of exchange (K_r), we first determined which cross-peaks were in exchange utilising ROESY NMR of compound **17b** (Figure 4.8) and this assignment was applied to all generated barbaralyl cations. The ROESY spectrum revealed that two sites were exchanging. For both pairs of exchanging environments an average rate of exchange was calculated using intensity data obtained from four EXSY spectra with different mixing times. In each EXSY spectrum, the amplitudes of the diagonal resonances are compared against the cross-peaks, generating a peak intensity ratio which allows for the rate of chemical exchange to be calculated[26] (with a known mixing time) using the equation:

$$K_r = \frac{2}{t_m} \ln\frac{r+1}{r-1}$$

where:

$$r = \frac{I_{AA} + I_{BB}}{I_{AB} + I_{BA}}$$

Equation 4.1. A variation of the rate of exchange equation.

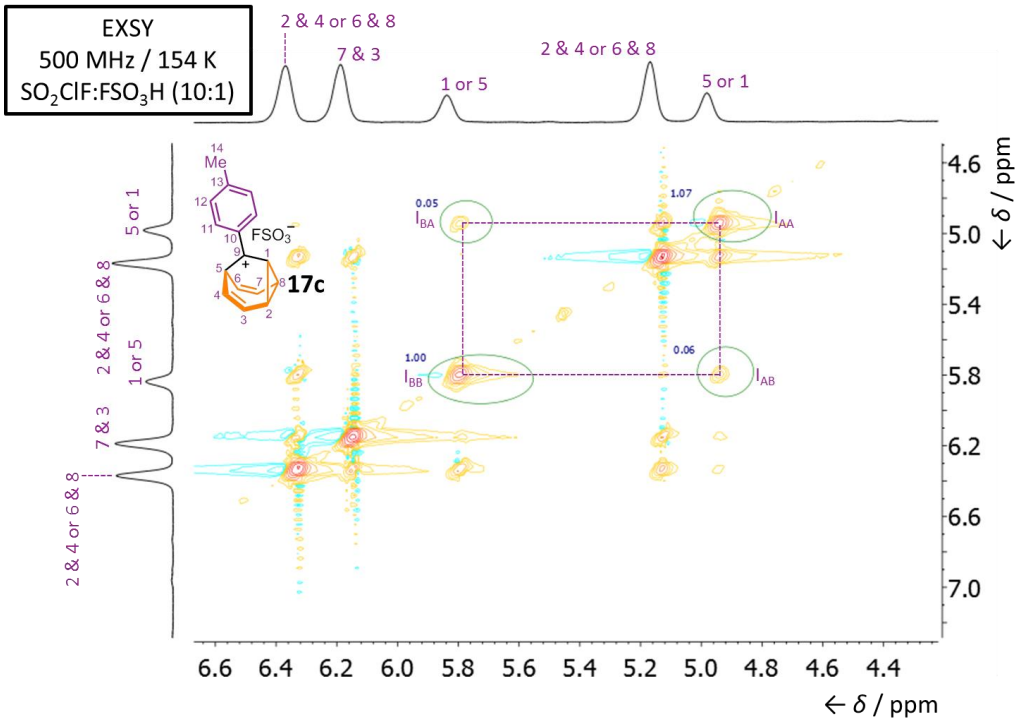

Figure 4.13. Partial EXSY NMR spectrum of barbaralyl cation **17c** at a mixing time of 120 ms. The spectrum compares the integration of the diagonal resonances against the cross-peaks for the positions labelled as1 or 5 and 5 or 1. (purple dashed lines). Absolute integral values were used in calculations.

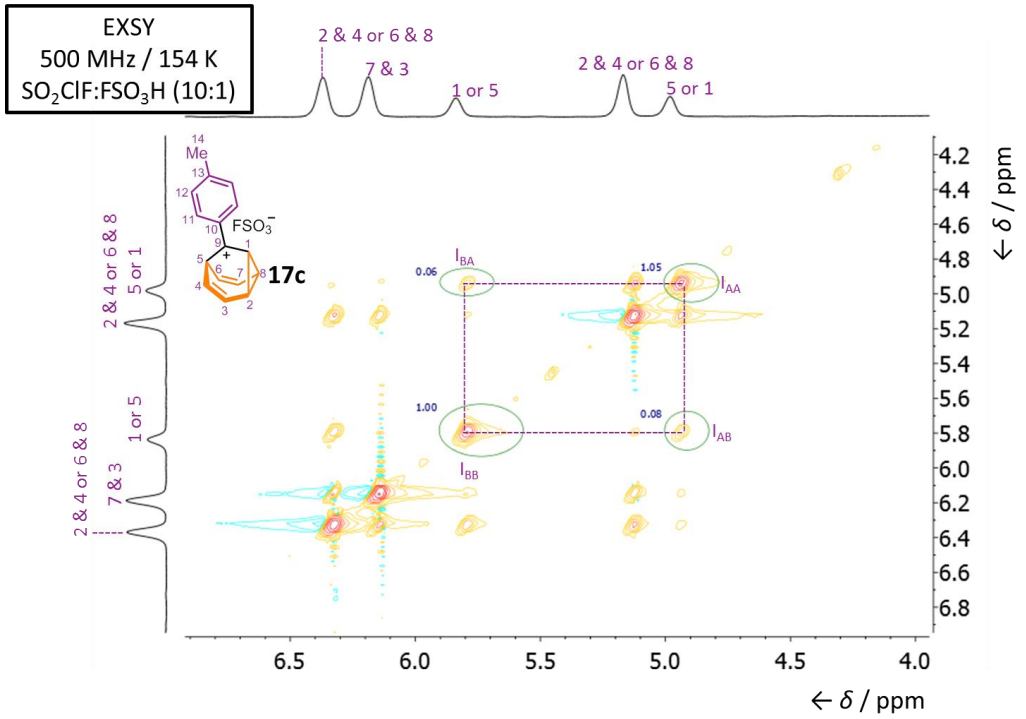

Figure 4.14. Partial EXSY NMR spectrum of barbaralyl cation **17c** at a mixing time of 150 ms. The spectrum compares the integration of the diagonal resonances against the cross-peaks for the positions labelled as1 or 5 and 5 or 1. (purple dashed lines). Absolute integral values were used in calculations.

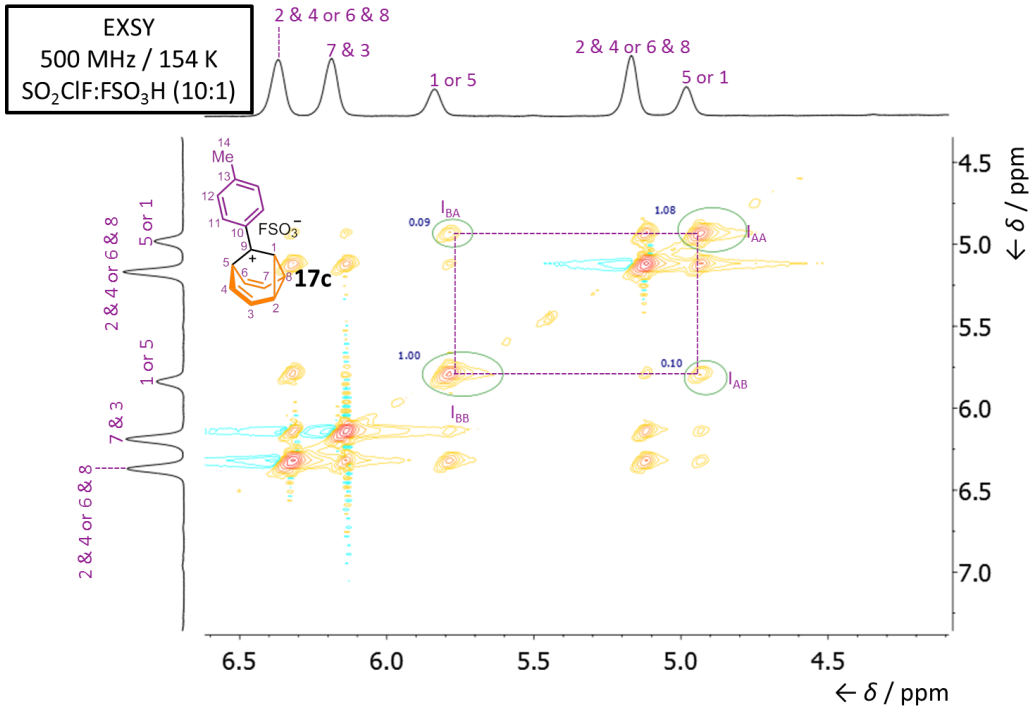

Figure 4.15. Partial EXSY NMR spectrum of barbaralyl cation **17c** at a mixing time of 200 ms. The spectrum compares the integration of the diagonal resonances against the cross-peaks for the positions labelled as1 or 5 and 5 or 1. (purple dashed lines). Absolute integral values were used in calculations.

Table 4.1. Calculated rates of chemical exchange for the positions labelled as 1 or 5 and 5 or 1 at different mixing times.

Exchange Peaks	I_{AA}	I_{BB}	I_{AB}	I_{BA}	t_m / ms	K_r / s^{-1}
1 or 5 and 5 or 1	20.16	20.06	0.65	0.99	90	1.81
1 or 5 and 5 or 1	17.63	16.54	0.79	1.07	120	1.81
1 or 5 and 5 or 1	14.64	14.00	0.81	1.15	150	1.83
1 or 5 and 5 or 1	11.72	10.89	0.92	1.12	200	1.90

The average rate of exchange between the positions labelled as 1 and 5 was calculated to be 1.84 s^{-1}.

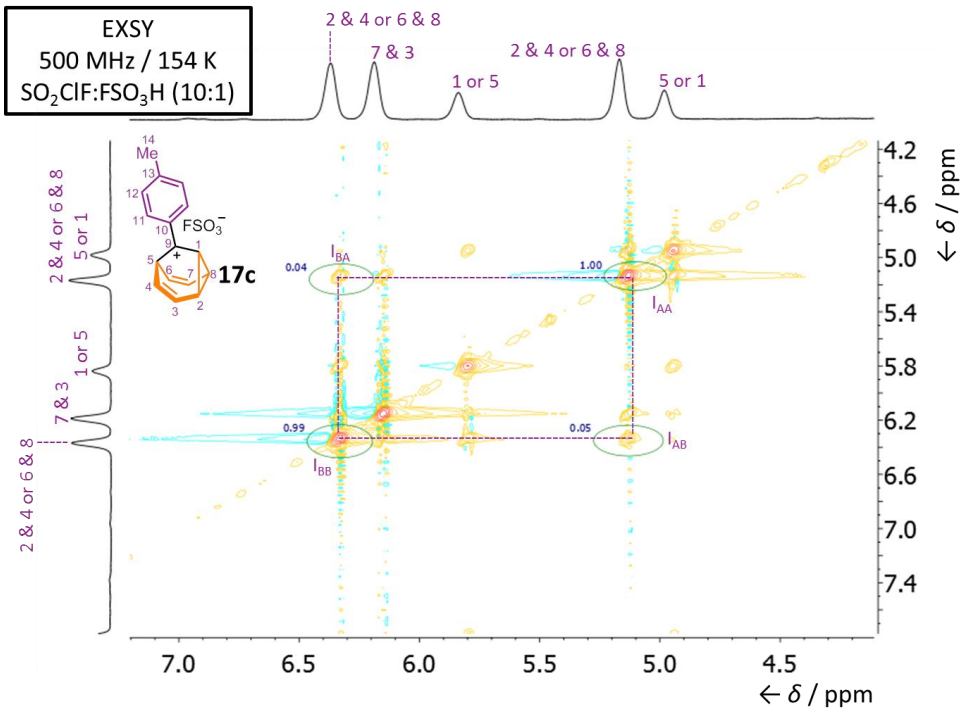

Figure 4.16. Partial EXSY NMR spectrum of barbaralyl cation **17c** at a mixing time of 90 ms. The spectrum compares the integration of the diagonal resonances against the cross-peaks for the positions labelled as 2 and 4 and 6 and 8. (purple dashed lines). Absolute integral values were used in calculations.

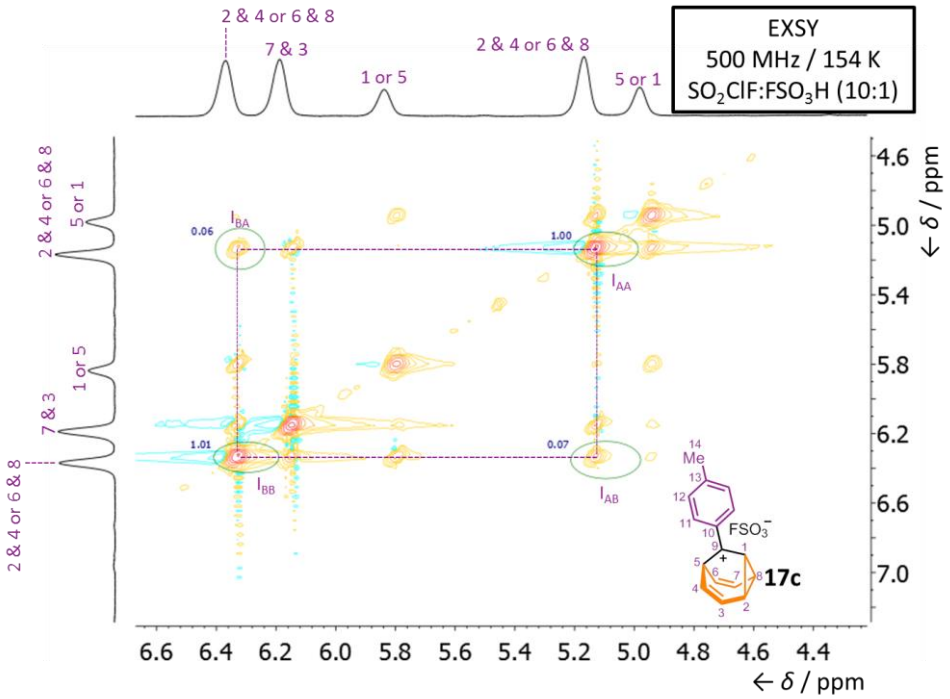

Figure 4.17. Partial EXSY NMR spectrum of barbaralyl cation **17c** at a mixing time of 120 ms. The spectrum compares the integration of the diagonal resonances against the cross-peaks for the positions labelled as 2 and 4 and 6 and 8. (purple dashed lines). Absolute integral values were used in calculations.

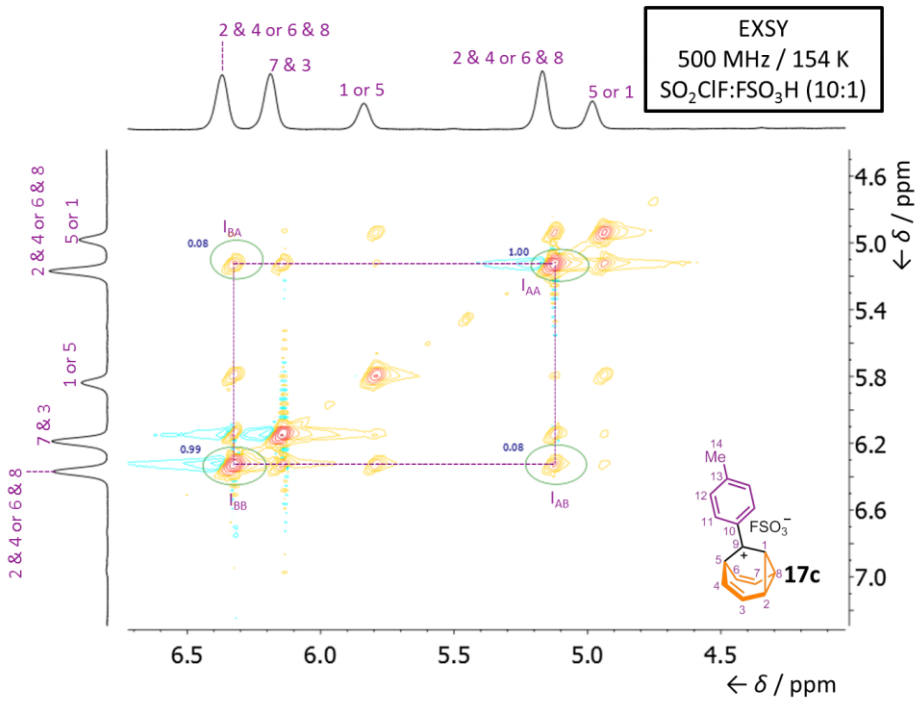

Figure 4.18. Partial EXSY NMR spectrum of barbaralyl cation **17c** at a mixing time of 150 ms. The spectrum compares the integration of the diagonal resonances against the cross-peaks for the positions labelled as 2 and 4 and 6 and 8. (purple dashed lines). Absolute integral values were used in calculations.

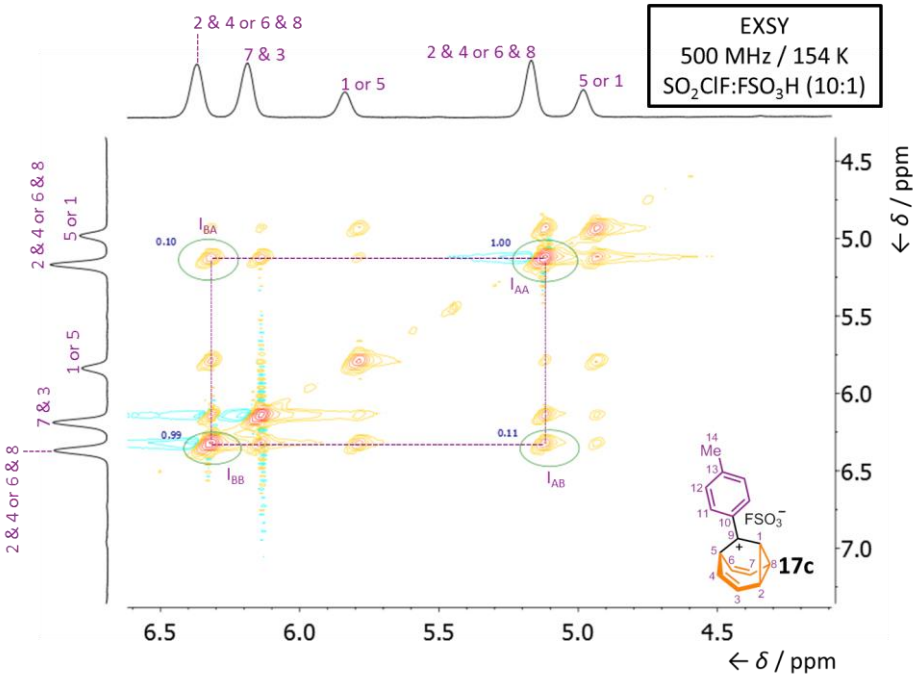

Figure 4.18. Partial EXSY NMR spectrum of barbaralyl cation **17c** at a mixing time of 200 ms. The spectrum compares the integration of the diagonal resonances against the cross-peaks for the positions labelled as 2 and 4 and 6 and 8. (purple dashed lines). Absolute integral values were used in calculations.

Table 4.2. Calculated rates of chemical exchange for the positions labelled as 2 or 4 and 6 or 8 at different mixing times.

Exchange Peaks	I_{AA}	I_{BB}	I_{AB}	I_{BA}	t_m / ms	K_r / s^{-1}
2 and 4 and 6 and 8	47.83	48.19	1.85	2.48	90	2.01
2 and 4 and 6 and 8	43.36	43.87	2.39	3.02	120	2.07
2 and 4 and 6 and 8	38.10	38.32	2.90	3.25	150	2.15
2 and 4 and 6 and 8	31.67	32.05	3.21	3.62	200	2.15

The average rate of exchange between the positions labelled as 2 and 4 and 6 and 8 was calculated to be 2.09 s^{-1}.

4.6.3. Activation Energy Barrier to Exchange Calculations

Activation energy barriers ($\Delta G^{\neq}$) to the rate of exchange were calculated by substituting in the measured rate constant (K_r) to a variation of the Eyring equation:

$$\Delta G^{\ddagger} = -RT \ln \frac{k_r h}{k_B T}$$

Equation 4.2. A variation of the Eyring Equation.

Table 4.2. Calculated activation energy barriers to exchange.

Exchange Peaks	K_r / s^{-1}	$\Delta G^{\neq}$ / kJ·mol^{-1}
1 or 5 and 5 or 1	1.81	36.07
1 or 5 and 5 or 1	1.81	36.07
1 or 5 and 5 or 1	1.83	36.07
1 or 5 and 5 or 1	1.90	36.03
2 and 4 and 6 and 8	2.01	35.95
2 and 4 and 6 and 8	2.07	35.90
2 and 4 and 6 and 8	2.15	35.86
2 and 4 and 6 and 8	2.15	35.86

The average activation energy barrier to exchange ($\Delta G^{\neq}$) was calculated as 36.0 kJ·mol^{-1}. The value we have calculated is ~20.0 kJ·mol^{-1} higher than the average activation energy barrier to total degenerate rearrangements for the barbaralyl cation (16 kJ·mol^{-1}), proving that the addition of a phenyl group raises the activation energy barrier.

4.6.4. Irreversible Rearrangement Calculations

In order to determine an energy barrier for the irreversible rearrangement that we observe, a series ^{1}H NMR spectra were acquired at a constant temperature 186 K (the time between each acquired spectra is known), where the cation was observed to undergo the irreversible rearrangement (Figure 4.10). The conversion of cation **17c** to the rearranged product(s) was monitored over time by integrating the deuterated THF against a peak corresponding to the cation (Figure 4.19).

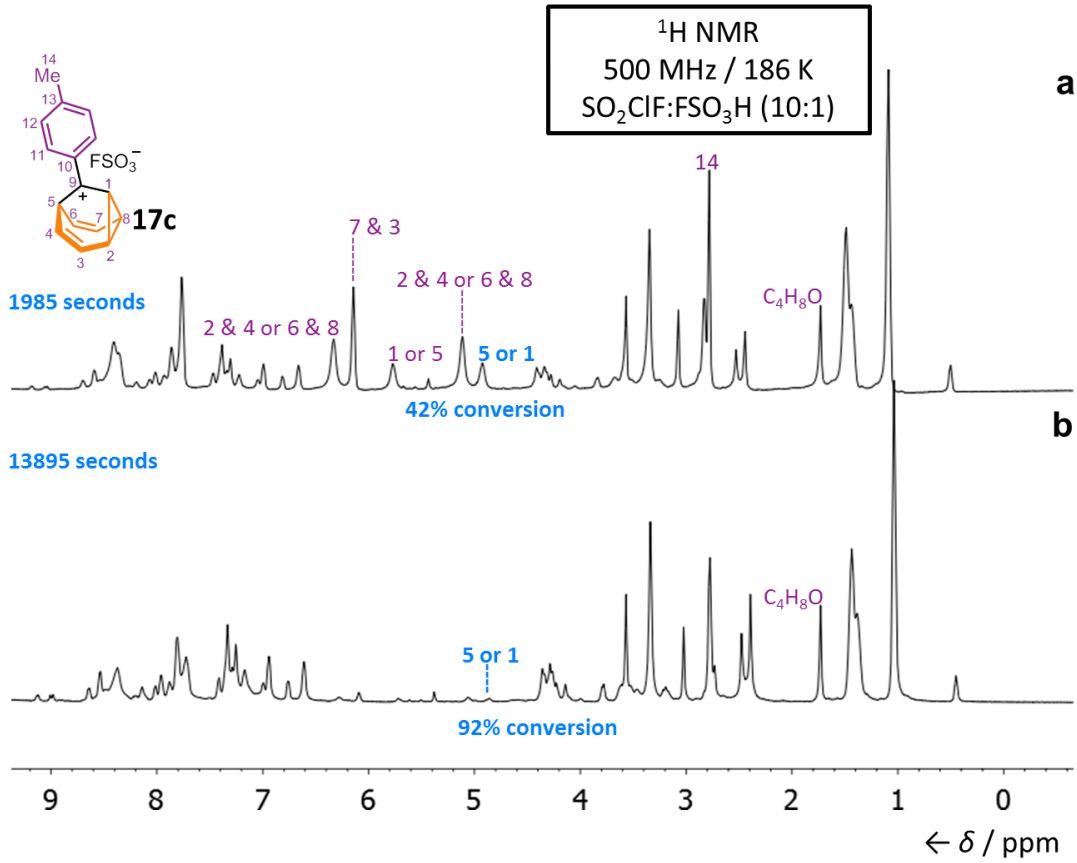

Figure 4.19. Partial ^{1}H NMR spectra of barbaralyl cation **17c** at (a) 1985 seconds showing a 42% conversion to the irreversible rearrangement product(s) and at (b) 13895 seconds showing a 92% conversion to the irreversible rearrangement product(s), determined by integration of the 5 or 1 (bold blue text) peak relative to the THF standard.

The spectra demonstrate that over time (and at a constant temperature of 186 K) the proton environment labelled as 5 or 1 slowly broadens into the baseline proving the conversion to the rearranged product(s) as aromatic and aliphatic peaks form. The observed conversion was then calculated as ln(mole fraction) (integral/initial integral) and a plot against time confirmed a first-order reaction (Figure 4.11) with a slope of -2.3×10^{-4} s^{-1}, providing the rate constant (K_r) as 2.3×10^{-4} s^{-1}. The activation energy barrier ($\Delta G^{\neq}$) to the irreversible rearrangement was calculated by substituting in the measured rate constant (K_r) to Equation 2.

The activation energy barrier to the irreversible rearrangement ($\Delta G^{\neq}$) was calculated to be 58.0 kJ·mol^{-1}. At present, we cannot state whether the irreversible rearrangement we see forms a bishomotropylium cation, but comparing our activation

energy barrier to those for the parent barbaralyl cation (43.5 $kJ \cdot mol^{-1}$) and a methyl barbaralyl cation (46.0 $kJ \cdot mol^{-1}$) shows again, that the addition of a phenyl ring to the barbaralyl core increases the energy barrier by ~12.0 $kJ \cdot mol^{-1}$.

4.6.5. X-ray Crystallographic Analysis

Several compounds have previously been studied and are reported in either Chapters 2 or 3. X-ray crystallographic analyses for these compounds are outlined in either Chapter 2, Section 2.5.5. or Chapter 3 Sections 3.6.1.4. or 3.6.2.4.

(±)(2*S*,1*R*,9*R*)-2-Methoxy-6-{2-methoxybicyclo[3.2.2]nona-2,6,8-trien-6-yl} naphthalene (3b)

Crystals of **3b** suitable for X-ray diffraction were grown by the slow cooling of a saturated MeCN solution.

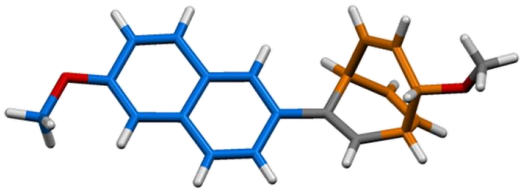

Crystal System: Monoclinic

Space group: $P2_1$

Unit Cell Parameters: a = 6.3966(4) Å, b = 7.6116(5) Å, c = 16.0508(9) Å, α = 90 °, β = 98.276(2) °, γ = 90 °, V = 773.35(8) $Å^3$, Z = 2

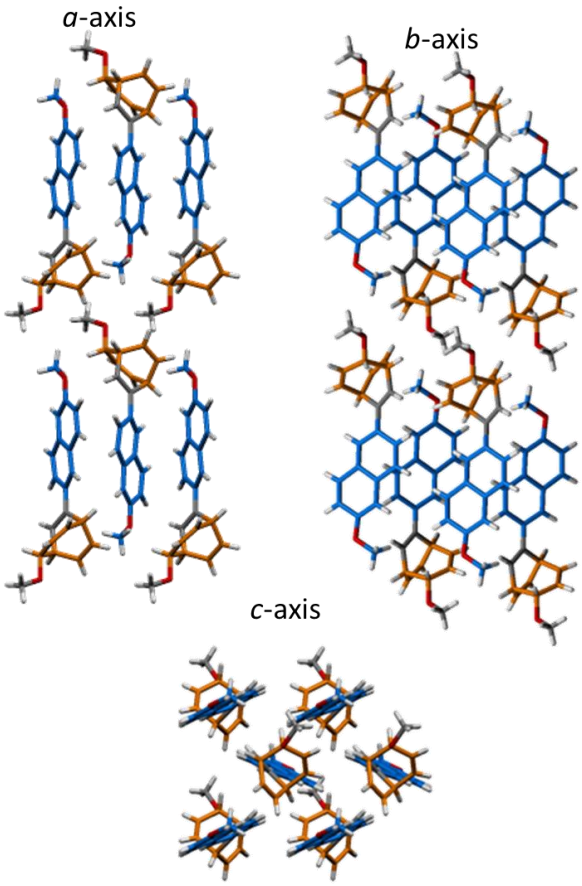

Figure 4.20. Solid-state superstructure of **3b** viewed along the three unit cell axes.

(±)(1*R*, 5*S*, 8*R*, 9*S*)-4-Phenyltricyclo[3.3.1.0^{2,8}]nona-3,6-dien-9-ol (4a)

Crystals of **4a** (polymorph 1) suitable for X-ray diffraction were grown by the slow evapouration of a $(CH_3)_2CO$ and H_2O solution.

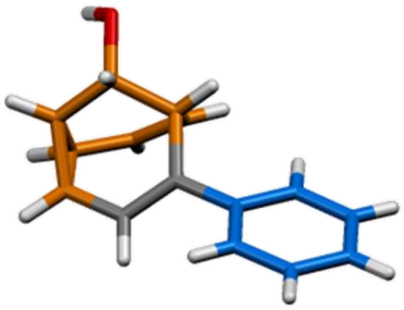

Crystal System: Triclinic

Space group: P-1

Unit Cell Parameters: a = 6.1794(3) Å, b = 12.4841(6) Å, c = 14.0776(7) Å, α = 91.098(2) °, β = 93.340(2) °, γ = 90.588(2) °, V = 1083.89(9) Å^3, Z = 4

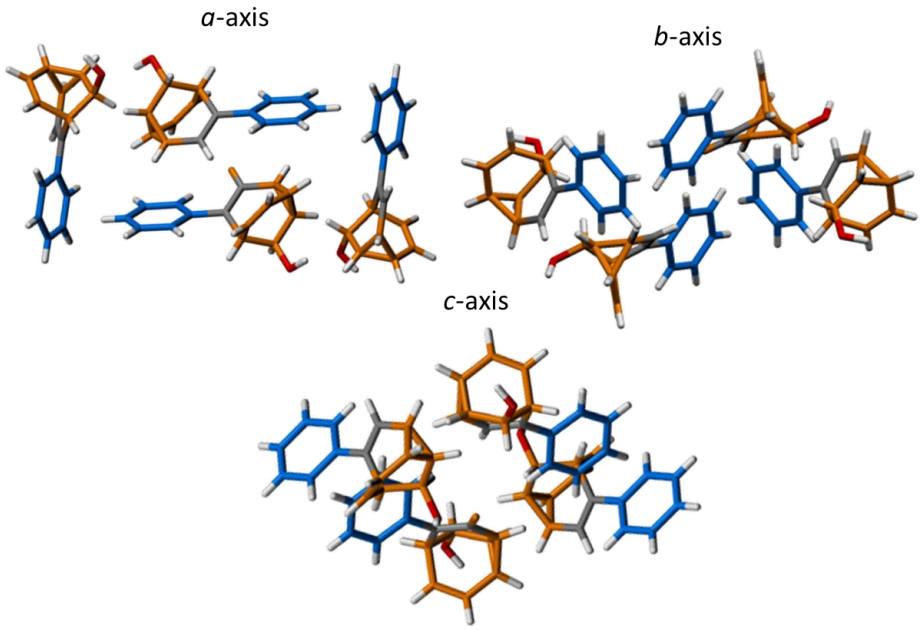

Figure 4.21. Solid-state superstructure of **4a** (polymorph 1) viewed along the three unit cell axes.

(±)(1*R*, 5*S*, 8*R*, 9*S*)-4-Phenyltricyclo[3.3.1.0^{2,8}]nona-3,6-dien-9-ol (4a)

Crystals of **4a** (polymorph 2) suitable for X-ray diffraction were grown by the slow evapouration of a H_2O solution.

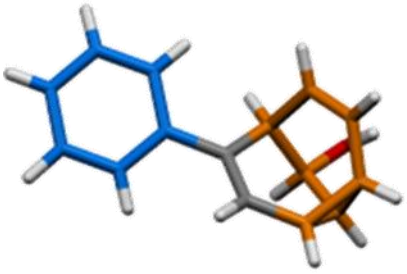

Crystal System: Orthorhombic

Space group: $P2_12_12_1$

Unit Cell Parameters: a = 5.996(2) Å, b = 9.991(4) Å, c = 17.775(7) Å, α = 90 °, β = 90 °, γ = 90 °, V = 1064.8(8) Å^3, Z = 4

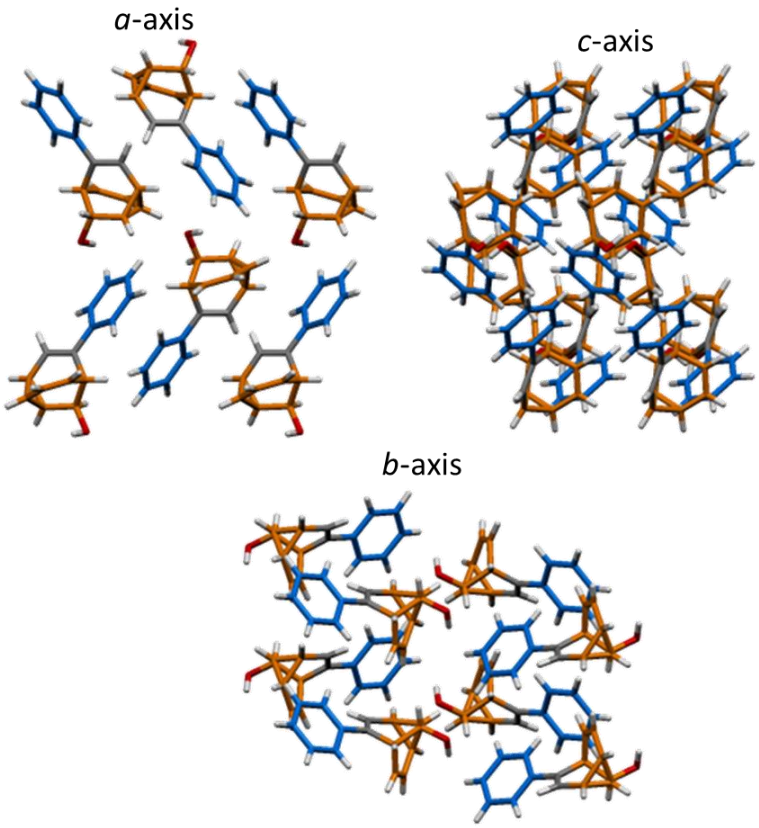

Figure 4.22. Solid-state superstructure of **4a** (polymorph 2) viewed along the three unit cell axes.

(±)-1,9-Bis(4-tolyl) tricyclo[3.3.1.0^{2,8}]nona-3,6-dien-9-ol (6c/6c′)

Crystals of **6c/6c′** suitable for X-ray diffraction were grown by the slow cooling of a saturated MeCN solution.

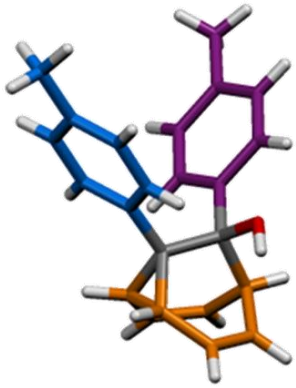

Crystal System: Monoclinic

Space group: $P2_1/n$

Unit Cell Parameters: a = 6.5497(8) Å, b = 39.005(4) Å, c = 13.0805(15) Å, α = 90 °, β = 90.998(4) °, γ = 90 °, V = 3341.2(7) Å^3, Z = 8

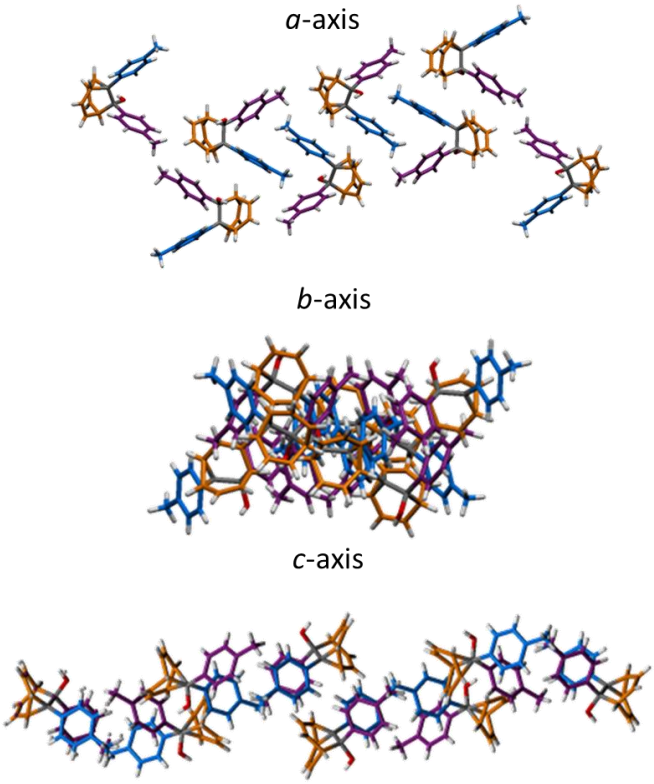

Figure 4.23. Solid-state superstructure of **6c/6c′** viewed along the three unit cell axes.

Triphenylcyclopropenium Hydrogen Dichloride

Crystals of triphenylcyclopropenium hydrogen dichloride suitable for X-ray diffraction were grown by the slow cooling of a saturated MeCN solution.

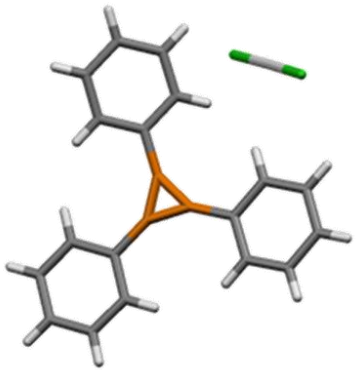

Crystal System: Triclinic

Space group: P-1

Unit Cell Parameters: a = 8.1608(7) Å, b = 9.0459(8) Å, c = 12.2953(10) Å, α = 95.447(3) °, β = 100.331(3) °, γ = 103.571(3) °, V = 859.06(13) Å^3, Z = 2

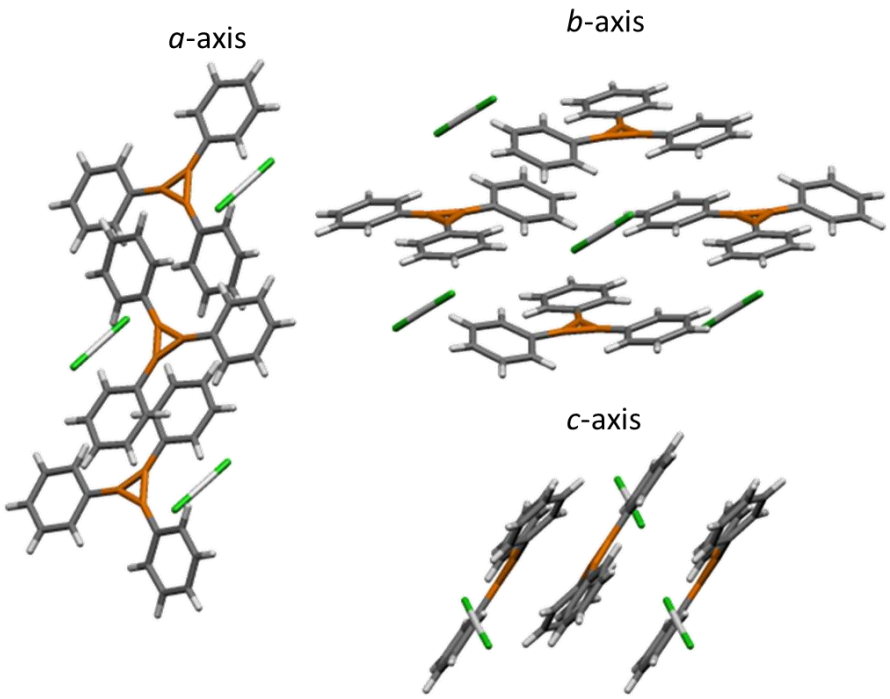

Figure 4.24. Solid-state superstructure of triphenylcyclopropenium hydrogen dichloride viewed along the three unit cell axes.

Heptaphenylcyclohepta-1,3,5-trien-1-ylium Chloro-Iodanyl Chloranide (14)

Crystals of **14** suitable for X-ray diffraction were grown by layer diffusion of a hexanes and CH_2Cl_2 solution.

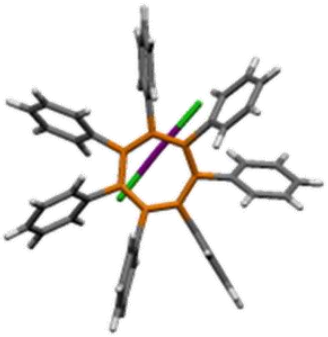

Crystal System: Monclinic

Space group: $P2_1/c$

Unit Cell Parameters: a = 26.964(2) Å, b = 27.059(2) Å, c = 22.8873(17) Å, α = 90 °, β = 94.601(3) °, γ = 90 °, V = 16645(2) $Å^3$, Z = 16

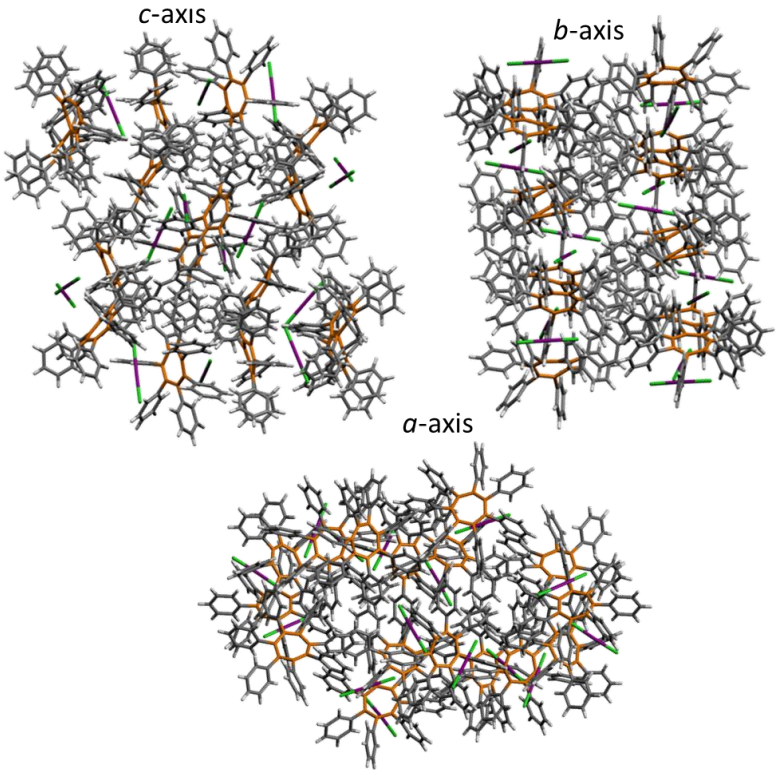

Figure 4.25. Solid-state superstructure of **14** viewed along the three unit cell axes.

7-[2-(4-Tolyl)ethynyl)heptaphenylcycloheptatriene (15a)

Crystals of **15a** suitable for X-ray diffraction were grown by the slow cooling of a saturated MeCN solution.

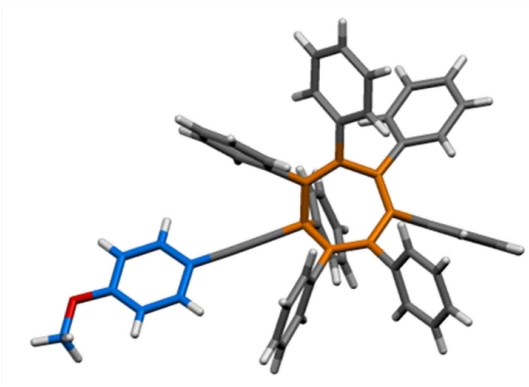

Crystal System: Triclinic

Space group: P-1

Unit Cell Parameters: a = 11.6636 (7) Å, b = 13.2612 (8) Å, c = 28.1143(18) Å, α = 79.163(2) °, β = 82.289(2) °, γ = 77.863(2) °, V = 4155.2(4) Å^3, Z = 4

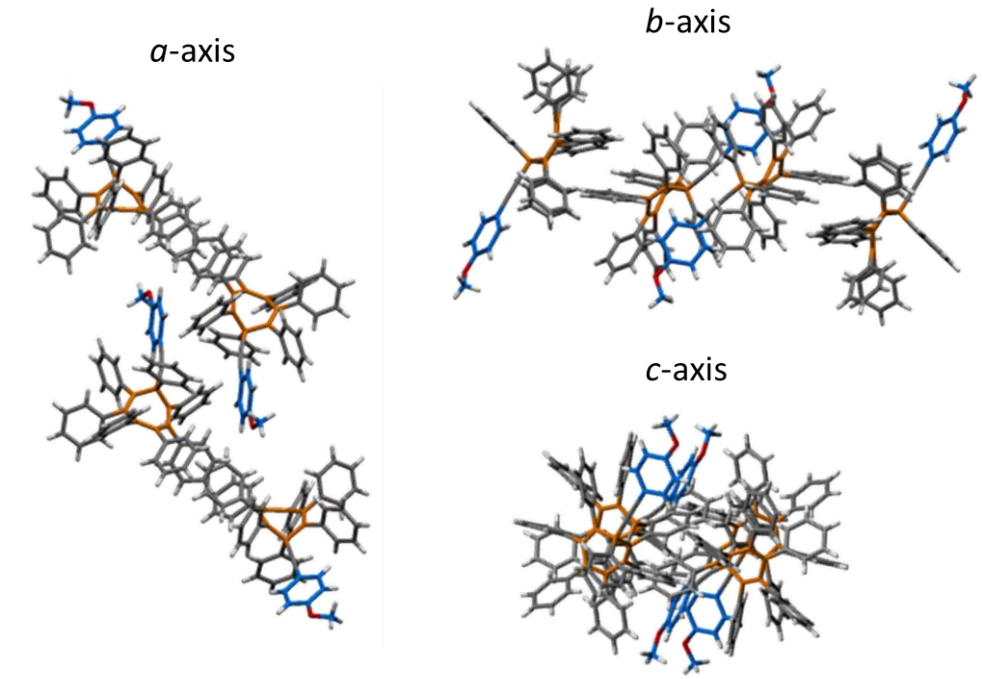

Figure 4.26. Solid-state superstructure of **15a** viewed along the three unit cell axes.

Heptaphenyl-7-(2-phenylethynyl)cycloheptatriene (15d)

Crystals of **15d** suitable for X-ray diffraction were grown by the slow cooling of a saturated MeCN solution.

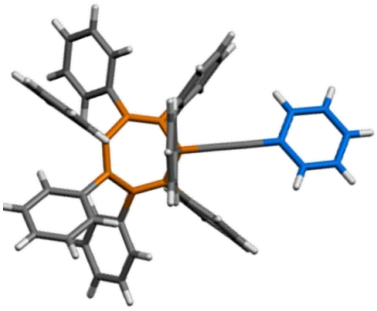

Crystal System: Triclinic

Space group: P-1

Unit Cell Parameters: a = 9.1652(3) Å, b = 12.6841(4) Å, c = 40.1211(14) Å, α = 86.019(2) °, β = 88.512(2) °, γ = 87.859(2) °, V = 4648.4(3) $Å^3$, Z = 4

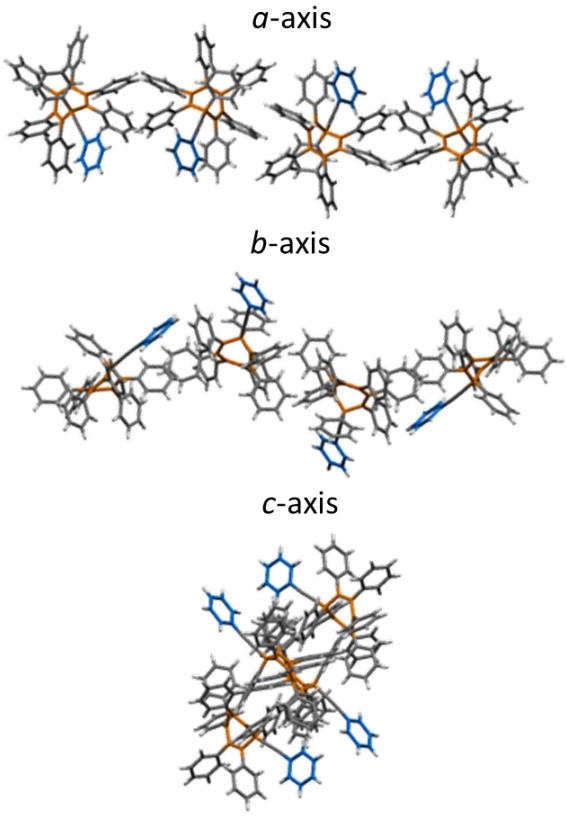

Figure 4.27. Solid-state superstructure of **15d** viewed along the three unit cell axes.

4.7 References

1. (a) W. von E. Doering and W. R. Roth, *Tetrahedron* 1963, **19**, 715; (b) G. Schröder, *Angew. Chem.* 1963, **75**, 722; (c) A. Ault, *J. Chem. Educ.* 2001, **78**, 924; (d) O. Yahiaoui, L. F. Pašteka, B. Judeel and T. Fallon, *Angew. Chem. Int. Ed.* 2018, **57**, 2570.

2. (a) P. Ahlberg, D. L. Harris and S. Winstein, *J. Am. Chem. Soc.* 1970, **92**, 4454; (b) D. Cremer, P. Svensson, E. Kraka and P. Ahlberg, *J. Am. Chem. Soc.* 1993, **115**, 7445.

3. R. Hoffmann and W. –D. Stohrer, *J. Am. Chem. Soc.* 1971, **93**, 6941.

4. (a) A. R. Lippert, J. Kaeobamrung and J. W. Bode, *J. Am. Chem. Soc.* 2006, **128**, 14738; (b) M. He and J. W. Bode, *PNAS.* 2011, **108**, 14752; (c) K. K. Larson, M. He, J. F. Teichart, A. Naganawa and J. W. Bode, *Chem. Sci.* 2012, **3**, 1825; (d) J. F. Teichart, D. Mazunin and J. W. Bode, *J. Am. Chem. Soc.* 2013, **135**, 11314.

5. J. C. Barborak, J. Daub and P. v. R. Schleyer, *J. Am. Chem. Soc.* 1969, **91**, 7760.

6. (a) P. Ahlberg, J. B Grutzner, D. L. Harris and S. Winstein, *J. Am. Chem. Soc.* 1970, **92**, 3478; (b) J. B Grutzner and S. Winstein, *J. Am. Chem. Soc.* 1970, **92**, 3186.

7. D. Cremer, P. Svensson, E. Krakra and P. Ahlberg, *J. Am. Chem. Soc.* 1993, **115**, 7445.

8. T. S. Abram and W. E. Watts, *J. Organomet. Chem.* 1976, **105**, C16.

9. (a) P. R. McGonigal, C. de León, Y. H. Wang, A. Homs, C. R. Solorio-Alvarado and A. M. Echavarren, *Angew. Chem. Int. Ed.* 2012, **51**, 13093; (b) S. Ferrer, A. M. Echavarren, *Angew. Chem. Int. Ed*. 2016, **55**, 11178; (c) S. Ferrer and A. M. Echavarren, *Synthesis.* 2019, **51**, 1037.

10. Guassian 16, Revision A.03, M. J. Frisch, G. W. Trucks, H. B. Schlegel, G. E. Scuseria, M. A. Robb, J. R. Cheeseman, G. Scalmani, V. Barone, G. A. Petersson, H. Nakatsuji, X. Li, M. Caricato, A. V. Marenich, J. Bloino, B. G. Janesko, R. Gomperts, B. Mennucci, H. P. Hratchian, J. V. Ortiz, A. F. Izmaylov, J. L. Sonnenberg, D. Williams-Young, F. Ding, F. Lipparini, F. Egidi, J. Goings, B. Peng, A. Petrone, T. Henderson, D. Ranasinghe, V. G. Zakrzewski, J. Gao, N. Rega, G. Zheng, W. Liang, M. Hada, M. Ehara, K. Toyota, R. Fukuda, J. Hasegawa, M. Ishida, T. Nakajima, Y. Honda, O. Kitao, H. Nakai, T. Vreven, K. Throssell, J. A. Jr. Montgomery, J. E. Peralta, F. Ogliaro, M. J. Bearpark, J. J. Heyd, E. N. Brothers, K. N. Kudin, V. N. Staroverov, T. A. Keith, R. Kobayashi, J. Normand, K. Raghavachari, A. P. Rendell, J. C. Burant, S. S. Iyengar, J. Tomasi, M. Cossi, J. M. Millam, M. Klene, C. Adamo, R. Cammi, J. W. Ochterski, R. L. Martin, K. Morokuma, O. Farkas, J. B. Foresman, D. J. Fox, Gaussian, Inc., Wallingford CT, 2016

11. R. Peverati and D. G. Truhlar, *Phys. Chem. Chem. Phys.* 2012, **14**, 13171.

12. (a) F. Weigend and R. Ahlrichs, *Phys. Chem. Chem. Phys.* 2005, **7**, 3297; (b) S. Grimme, J. Antony, S. Ehrlich and H. J. Krieg, *J. Chem. Phys.* 2010, **131**, 154104.

13. R. A. McClelland, N. Banait and S. Steeken, *J. Am. Chem. Soc.* 1986, **108**, 7023.

14. G. Olah and G. K. Surya Prakash, *Carbocation Chemistry*, A John Wiley and Sons, 1st edition, 2004.

15. G. Olah. G. K. Surya Prakash, Árpád Molnár and Jean Sommer, *Superacid Chemistry*, A John Wiley and Sons, 2nd edition, 2009.

16. P. Ahlberg, G. Jonsäll and C. Engdahl *Advances in Physical Organic Chemistry*, Elsevier, 1st edition, 2008.

17. C. R. Martinez and B. L. Iverson, *Chem. Sci.* 2012, **3**, 2191.

18. V. Grignard, *Compt. Rend.* 1900, **130**, 1322.

19. (a) K. Conrow, *Org. Synth.* 1963, **43**, 101; (b) W. von E. Doering and L. H. Knox, *J. Am. Che. Soc.* 1954, **76**, 3023.

20. S. N. Synder and D. S. Trietler, *Angew. Chem. Int. Ed.* 2009, **121**, 8039.

21. R. Breslow and H. W. Chang, *J. Am. Chem. Soc.* 1961, **83**, 2367.

22. M. A. Battise, *Chem. Ind.* 1961, 550.

23. (a) P. Ahlberg, D. L. Harris and S. Winstein, *J. Am. Chem. Soc.* 1970, **92**, 2146; (b) J. B. Gruntzer and S. Winsten, *J. Am. Chem. Soc.* 1968, **90**, 6562; (c) C. Engdalh and P. Ahlberg, *J. Am. Chem. Soc.* 1979, **101**, 3940.

24. Eric V. Anslyn and Dennis A. Dougherty, *Modern Physical Organic Chemistry* University Science Books,1st edition, 2006.

25. Felix A. Carroll, *Perspectives on Structure and Mechanisms in Organic Chemistry*, John Wiley & Sons, Inc., 2nd edition, 2010.

26. C. L Perrin and T. J. Dwyer, *Chem. Rev.* 1990, **90**, 935.

27. O. V. Dolomanov, L. J. Bourhis, R. J. Gildea, J. A. K. Howard, H. J. Puschmann, *Appl. Crystallogr.* 2009, **42**, 339.

28. G. M. Sheldrick. *Acta. Crystallogr. Sect. A Found. Crystallogr.* 2008, **64**, 112.

29. E. R. Johnston, S. J. Barber, M. Jacormet and J. C. Barboark, *J. Am. Chem. Soc.* 1998, **120**, 1489.

30. V. P. Reddy, D. R. Bellew and G. K. Surya Prakash, *Journal of Flourine Chemistry*, 1992, **56**, 195.

CHAPTER 5

SUMMARY AND OUTLOOK

This Thesis has highlighted recent advances in the synthesis of fluxional barbaralane cages and understanding their equilibria, dynamics and rearrangements within different environments – all of which has been achieved in the period of October 2015 to June 2019. Research into fluxional carbon cages dates back to the 1960's with development into new synthetic strategies continuing to this day. At the outset of the research discussed in this Thesis, only tetra-substituted bullvalenes had been exploited in applications prompting minor investigations into their isomeric composition and equilibria which were unable to allow for the precise determination of structures due to complex fluxional mixtures. The most pertinent synthetic advance in regards to this Thesis – the formation of fluxional carbon cages through gold(I)-catalysed cycloisomerisations of alkynyl cycloheptatrienes – was established in 2012 with advances continuing at the same time of this Thesis. The efficient preparation of these fluxional carbon cages through gold(I) catalysis served as a springboard for much of the work discussed herein and in turn allowed for in-depth and unprecedented insights into barbaralane molecules – in particular their rearrangements and equilibria .

Chapter 2 of this Thesis described the novel synthesis of a series of barbaralane molecules which equilibrate between two sets of non-equivalent valence isomers, but resolve to a single valence isomer in the solid state. Out of the five cases, we saw three barbaralane molecules crystallise as the major solution-phase isomer and unexpectedly, in two cases we saw the minor solution-phase isomer resolve. We show that the isomer observed in the solid state is 'frozen' and that the small differences between the substituents direct which valence isomer crystallises out. Therefore, we are able to show that the isomer that we observe in the solid state is not a direct result of the equilibrium distribution in solution or any specific noncovalent interactions. Instead, the size and shape of the molecules are able to match their surroundings (*i.e.*, the solution or solid state) and offset their energetic preference (between very closely relates structures) of the equilibrium present in the solution state. Although this finding was entirely unplanned, rearrangements within a series of fluxional carbon cages have been fully explored and understood for the first time by providing a comparative analysis between solution-phase and solid-state dynamic systems. It is possible that understanding the relationship between the size- and shape-matching of

these fluxional carbon cages as well as the energetics will pave the way for the precise determination of complex isomeric mixtures which have previously proven to be challenging.

Chiral molecules remain a major scientific focus because of their importance in biology and emerging application in materials science. Although one of the key difficulties in the synthesis of chiral molecules is the production of pure samples of one mirror-image form (enantiomer) of the product; another outstanding challenge is the complete control over dynamically chiral molecules which have the potential to allow for tuning towards the desired enantiomer. Chapter 3 of this Thesis described one of the first steps taken towards controlling a fluxional sp^3–carbon stereocentre by way of covalent modifications and noncovalent bonding interactions. We demonstrate that covalently affixing a chiral tether to a barbaralane core allows biases the solution-state equilibrium (which can be dominated at low temperatures) towards the thermodynamically favoured diastereoisomer. The dynamic chirality of the fluxional sp^3–carbon stereocentre is arrested in the solid state, also forming the thermodynamically favoured diastereoisomer and revealing that the dynamic chirality is reliant upon the barbaralanes environment. Noncovalent bonding interactions with chiral β-CD macrocycles not only cause the formation of a one-to-one host–guest complex, but also bias the stereochemistry of the fluxional sp^3–carbon stereocentre in the solid state, and presumably in the solution state, too. The stereochemistry of the cyclodextrin dictates the dynamic chirality through noncovalent bonding interactions. Considering the central role of chirality in chemistry, and the fact that dynamic sp^3-carbon-centered chirality is a rare phenomenon, our research shows a new and unique pathway for favouring a desired enantiomer or diastereoisomer, which has the potential to open new avenues for the development of biologically-active chiral molecules or molecular devices.

Chapter 4 of this Thesis describes novel synthetic methodologies we have developed to make several series of hydroxy barbaralane molecules. The barbaralanes have been subjected to superacidic conditions, generating their corresponding barbaralyl cations. Through dynamic NMR experiments we have measured activation energy barriers, demonstrating that the stability of these cations can be tuned by substituent effects

(*i.e.*, electron-donating groups allow for a more stable cation in comparison to electron-withdrawing groups). The routes we devised to make the barbaralane cores with varying degrees of substitution should allow for the formation of long-lived species under ambient temperatures. Generating stable fluxional cationic cages may provide fundamental insight into important concepts such as valence isomerisation and unveil innovative applications within the area of systems chemistry, such as a new class of stable shapeshifting sensors.

In 2019 there is certainly still room to broaden the scope of synthetic methodologies towards fluxional carbon cages (also forming different mechanistic pathways towards unprecedented molecular architectures), while continuing to explore and understand the equilibria, dynamics and rearrangements with differing functionalities, varying degrees of substitution to the barbaralyl core and within new environments such as biological systems. Although we have successfully shown that the fluxionality of barbaralane core allows for the molecule to alter its size, shape and stereochemistry to the environment it is placed within while also demonstrating that our molecules are also able to form highly fluxional cations where the stability can be tuned by substituent effects – we have just scratched the surface and are yet to tap into the fields full potential.

PUBLISHED PAPERS

'Shape-Selective Crystallisation of Fluxional Carbon Cages' – A. N. Bismillah, J. Sturala, B. M. Chapin, D. S. Yufit, P. Hodgkinson and P. R. McGonigal, *Chem. Sci.* 2018, **9**, 8631.

'Excited-State Aromatic Interactions in the Aggregation-Induced Emission of Molecular Rotors' – J. Sturala, M. K. Etherington, A. N. Bismillah, H. F. Higginbotham, W. J. Trewby, J. A. Aguilar, E. H. C. Bromley, A.-J. Avestro, A. P. Monkam and P. R. McGonigal, *J. Am. Chem. Soc.* 2017, **139**, 17882.

'Persistent Dimer Emission in Thermally Activated Delayed Fluorescence Materials' – M. K. Etherington, N. A. Kukhta, H. F. Higginbotham, A. Danos, A. N. Bismillah, D. R. Graves, P. R. McGonigal, N. Haase, A. Morherr, A. S. Bastanov, C. Pflumm, V. Bhalla, M. R. Bryce and A. P. Monkman, *J. Phys. Chem. C.* 2019, **123**, 11109.

'Revealing Resonance Effects and Intramolecular Dipole Interactions in the Positional Isomers of Benzonitrile-Core Thermally Activated Delayed Fluorescence Materials' – N. A. Kukhta, H. F. Higginbotham, T. Matulaitis, A. Danos, A. N. Bismillah, N. Haase, M. K. Etherington, D. S. Yufit, P. R. McGonigal, J. V. Grazulevicius and A. P. Monkman, *J. Mat. Chem. C.* 2019, DOI: 10.1039/c9tc02742d.

Volume 9 | Number 46 | 14 December 2018 | Pages 8623–8766

Chemical Science

rsc.li/chemical-science

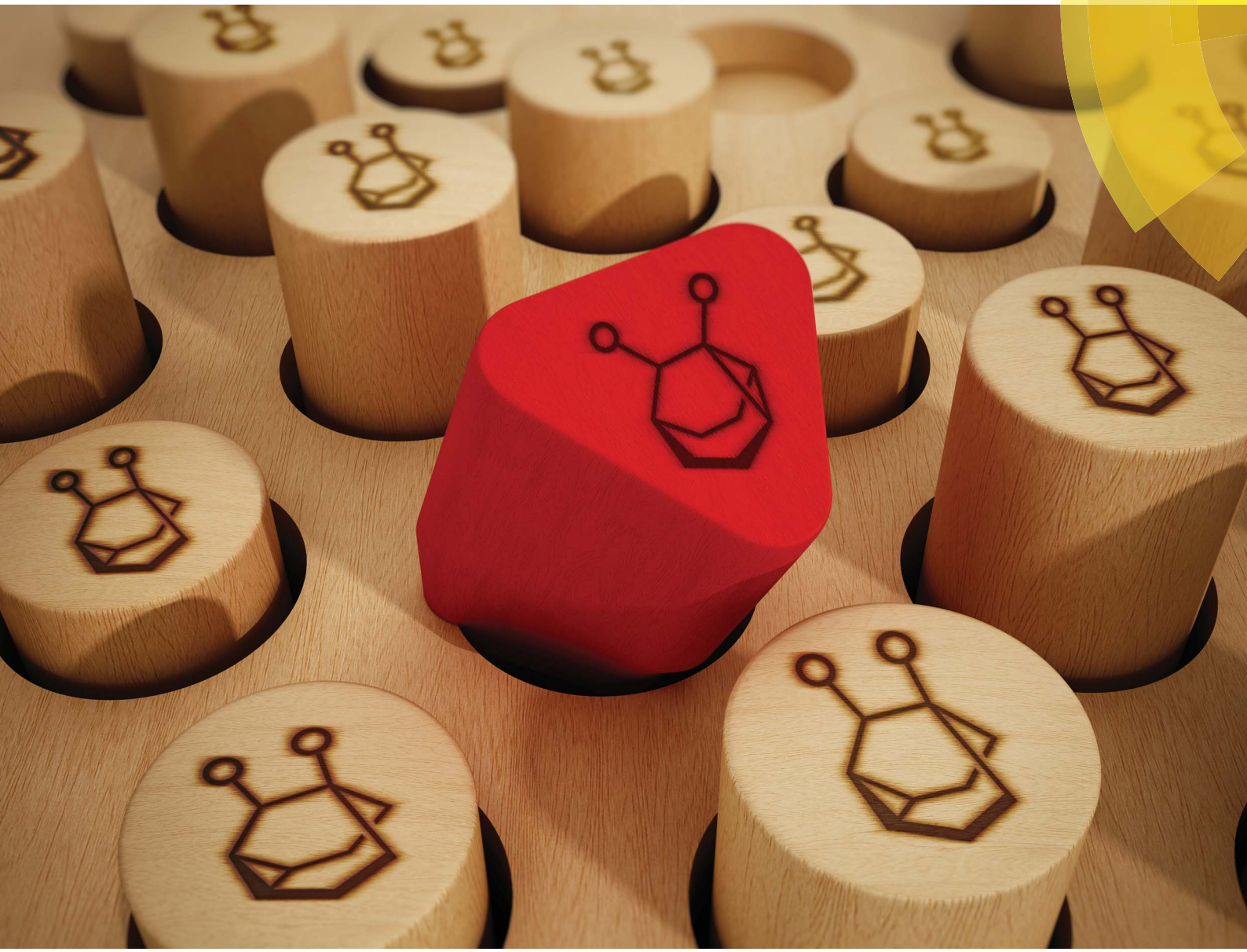

ISSN 2041-6539

ROYAL SOCIETY OF CHEMISTRY

EDGE ARTICLE
Paul R. McGonigal *et al.*
Shape-selective crystallisation of fluxional carbon cages

Chemical Science

EDGE ARTICLE

View Article Online
View Journal | View Issue

Cite this: *Chem. Sci.*, 2018, **9**, 8631

All publication charges for this article have been paid for by the Royal Society of Chemistry

Received 27th September 2018
Accepted 19th October 2018

DOI: 10.1039/c8sc04303e

rsc.li/chemical-science

Shape-selective crystallisation of fluxional carbon cages†

Aisha N. Bismillah, Jiri Sturala, ‡ Brette M. Chapin, Dmitry S. Yufit, Paul Hodgkinson and Paul R. McGonigal *

Dynamic covalent rearrangements of fluxional carbon cages, such as bullvalenes and barbaralanes, impart 'shapeshifting' molecular properties. Here, a series of five barbaralanes each interconvert dynamically between two constitutional isomers in solution, but resolve to single isomers upon crystallisation. Unexpectedly, the minor solution-phase isomers are resolved in two instances. Through dynamic NMR, crystallographic and DFT analyses, we show that the isomer observed in the solid state is not a direct consequence of the equilibrium distribution in solution or any specific noncovalent interactions. Rather, the dynamic preferential crystallisation is dictated by differences in molecular size and shape.

Introduction

Fluxional carbon cages, such as bullvalene[1] and the barbaralyl cation[2] (Fig. 1a), undergo reversible pericyclic rearrangements on a grand scale.[3] Sequential, low-energy steps interconvert large numbers of degenerate isomers. For example, bullvalene passes back and forth between 1.2 million degenerate valence isomers[1] by strain-assisted Cope rearrangements. Functionalised derivatives, on the other hand, give rise (Fig. 1b) to nondegenerate valence isomers with distinct constitutions.[4] When their C–C bonds trade places with one another, the positions and relative orientations of their substituents are altered, endowing them with dynamic shapes (Fig. 1c) and making them ideal building blocks for adaptive chemistry.[5] Bode *et al.*[6] have taken advantage of these phenomena to design shapeshifting bullvalene sensors—the equilibrium distribution of tetrasubstituted bullvalene isomers is shifted in a characteristic manner when interacting with different guests, either by specific noncovalent interactions[6b] or dynamic covalent bonds.[6c]

Here, we report on the influence of shape over the crystallisation of fluxional carbon cages. Neutral barbaralane derivatives, which equilibrate (Fig. 1b) between sets of two non-equivalent valence isomers[7] in solution, are resolved to single valence isomers upon crystallisation. By analysing NMR spectra of solutions and powdered samples, X-ray crystal structures and DFT models, we observe that (i) the dynamic isomerism is 'frozen' in the solid state and (ii) relatively small differences in the substituents dictate which constitutional isomer is found upon crystallisation. Three of the compounds crystallise as the major solution-phase valence isomers, *i.e.*, their molecular structures in the solid state match those of the thermodynamically favoured species in solution. However, two compounds crystallise (Fig. 1c) as the minor solution-phase valence isomers, achieving more densely packed crystals by adopting molecular structures that fit together more effectively. Size- and shape-matching of these fluxional molecules to their surroundings outweigh the inherent energetic preference of the shapeshifting equilibrium.

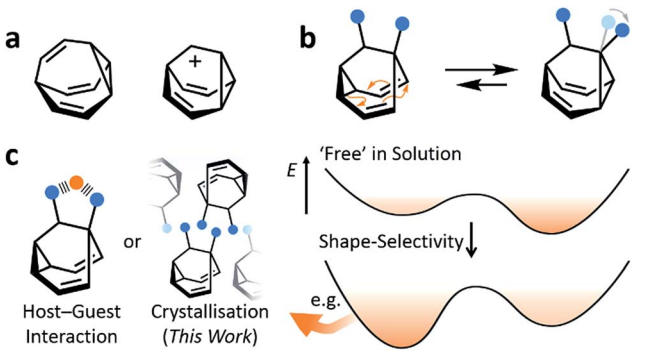

Fig. 1 Structural formulas of (a) bullvalene, the barbaralyl cation and (b) a disubstituted barbaralane, showing its isomerisation. The relative orientations of the substituents, which are represented by blue circles, are altered by the isomerisation. (c) A schematic representation illustrates changes in relative energies of isomers in panel b as a result of a shape-selective intermolecular contact, *e.g.*, through noncovalent bonding with a guest, represented as an orange circle, or by crystal packing.

Department of Chemistry, Durham University, Lower Mountjoy, Stockton Road, Durham, DH13LE, UK. E-mail: paul.mcgonigal@durham.ac.uk

† Electronic supplementary information (ESI) available. CCDC 1857573–1857583, 1857874. For ESI and crystallographic data in CIF or other electronic format see DOI: 10.1039/c8sc04303e

‡ Present address: Department of Inorganic Chemistry, University of Chemistry and Technology Prague, Technická 5, Prague 6 16628, Czech Republic.

Results and discussion

We synthesised (Scheme 1) fluxional mixtures of nondegenerate barbaralanes **1**/**1′** in two steps from alkynyl cycloheptatriene precursors **2** (for experimental details see the ESI†). Gold-catalysed cycloisomerisation of **2** proceeds[2c] through barbaralyl cation intermediates, which are oxidised[2d] *in situ* by Ph_2SO to afford barbaralones **3** in 58–75% yields. Subsequent addition of arylmagnesium bromides to **3** gives barbaralanes **1**/**1′**, each bearing a tertiary alcohol§ and two aromatic rings. The aromatic ring at the 1/5′-position of each barbaralane breaks the symmetry of the Cope rearrangements, giving rise to the pairs of valence isomers **1** and **1′**. We reasoned that these pairs of nondegenerate valence isomers would be useful compounds for probing the shapeshifting properties of fluxional carbon cages. Compared to the huge numbers of valence isomers accessible to other systems, analysis of the double-well-type potential energy surface (Scheme 1) of **1**/**1′** is more tractable. At the same time, the rearrangement still modulates the molecular shape to some extent—the strain present in the tricyclic cores of **1** and **1′** is slightly different, regulating the relative orientations of the two aromatic rings. Five sets of barbaralanes (**1a–e**/**1a′–e′**) were prepared in which the groups at the *p*-positions of the aromatic rings (R^1 and R^2) are varied between OMe, F, and H.

Isomers **1** and **1′** are in fast exchange (Fig. S15–S48†) when observed by solution-phase NMR spectroscopy. Consequently, each pair of exchangeable sites gives rise to one peak. The chemical shift of each peak represents an average of the two discrete chemical environments, weighted by the position of the equilibrium, which enables us to identify the major isomer. For example, the ^{13}C peak associated with position 2 of **1a** and position 4′ of **1a′** appears (Fig. S16†) at 49.6 ppm in $CDCl_3$ at 298 K, which is closer to the resonance of a divinyl cyclopropane group[8] (~25 ppm) than that of a *cis*-dialkylolefin group[9] (~135 ppm). This observation allows us to assign **1a** as the major isomer[10] and to estimate an equilibrium constant, *K*, of ~3.5, as well as a Gibbs free energy difference, Δ*G*, of ~3 kJ mol^{-1}. These conclusions are supported by DFT modelling, which predicts (Table S5†) that **1a** is lower in energy than **1a′** by a margin of ~5 kJ mol^{-1} (for calculation details see the ESI†). Further NMR and DFT analyses reveal (Fig. S17–S48 and Table S5†) that *K* is only minimally affected by varying the R^1 and R^2 groups at the *p*-positions of the aromatic rings. The substituents are sufficiently remote from the barbaralane core that their electronic and steric differences have little impact – structure **1** remains the thermodynamically favoured solution-phase valence isomer for all derivatives (**1a–e**). In order to probe the equilibria further, we also recorded solution-phase ^1H NMR spectra of bis(4-anisyl)barbaralane **1a**/**1a′** (Fig. S29†) and bis(4-fluorophenyl)barbaralane **1b**/**1b′** (Fig. 2) at low temperatures. The temperature-dependent spectroscopic changes are consistent with the behaviour of two nondegenerate valence isomers interconverting rapidly through a low-lying transition state. For example, the signal for the 8/6′ positions of **1b**/**1b′** shifts (Fig. 2) from 3.55 ppm at 292 K to 3.31 ppm at 165 K, moving further towards the chemical shift expected for a cyclopropyl resonance, while the signal associated with 6/8′ moves towards the olefinic region, shifting from 5.50 ppm at 292 K to 5.60 ppm at 149 K. Therefore, the equilibrium shifts further in favour of the thermodynamically favoured isomer **1b** at lower temperatures, which would be expected for a Boltzmann distribution of nondegenerate isomers.

All five **1**/**1′** derivatives form crystalline solids, allowing us to analyse (Fig. 3) their solid-state structures by single-crystal X-ray diffraction.† The fluxional mixtures of **1**/**1′** undergo dynamic preferential crystallisation,[11] *i.e.*, just one valence isomer from each pair of fluxional carbon cages crystallises from the mixture.[12,13] The bis(4-anisyl)barbaralane crystallises (Fig. 3a) as the major solution-phase valence isomer **1a**. Similarly, the barbaralanes bearing one 4-fluorophenyl group and one 4-anisyl group each adopt the major solution-phase structures **1c** and **1d** upon crystallisation. Surprisingly, however, we observed the more strained molecular structures in crystals of the bis(4-fluorophenyl)barbaralane **1b′** and its phenyl analogue **1c′**.

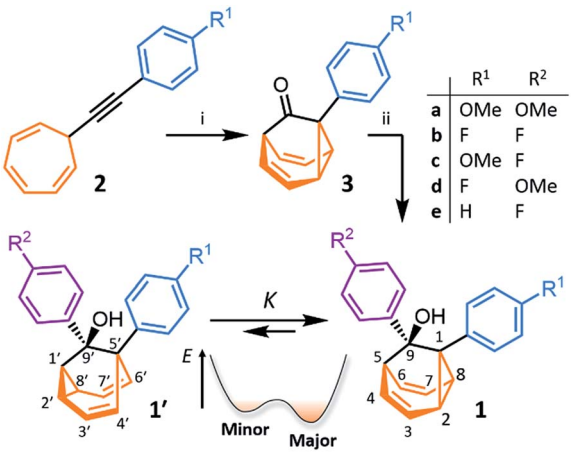

Scheme 1 Synthesis of fluxional carbon cages **1**/**1′**. Reagents and conditions: (i) IPrAu(MeCN)BF_4 (5 mol%), Ph_2SO (2 equiv.), CH_2Cl_2, rt, 16 h, 58–75%; (ii) *p*-$R^2C_6H_4MgBr$, THF, 0 °C to rt, 16 h, 43–96%. A schematic potential energy diagram illustrates the equilibrium, *K*, between **1′** and **1**. IPr = 1,3-bis(2,6-diisopropylphenyl)imidazol-2-ylidene.

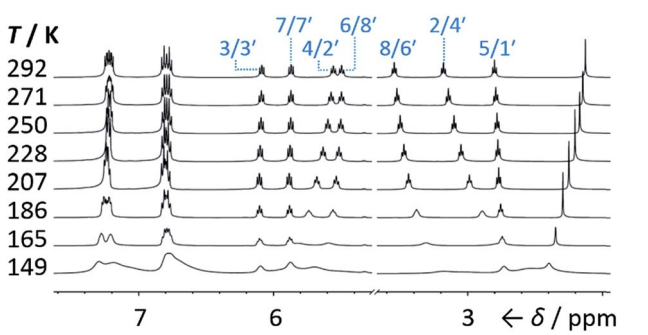

Fig. 2 Partial ^1H NMR spectra (500 MHz, CS_2–CD_2Cl_2) of **1b**/**1b′**. As the temperature is decreased, the equilibrium shifts towards the lower-energy isomer **1b**. At temperatures below 186 K, the broadening of peaks indicates the reversible Cope rearrangement is entering the slow-exchange regime. Selected resonances are labelled according to the numbering in Scheme 1.

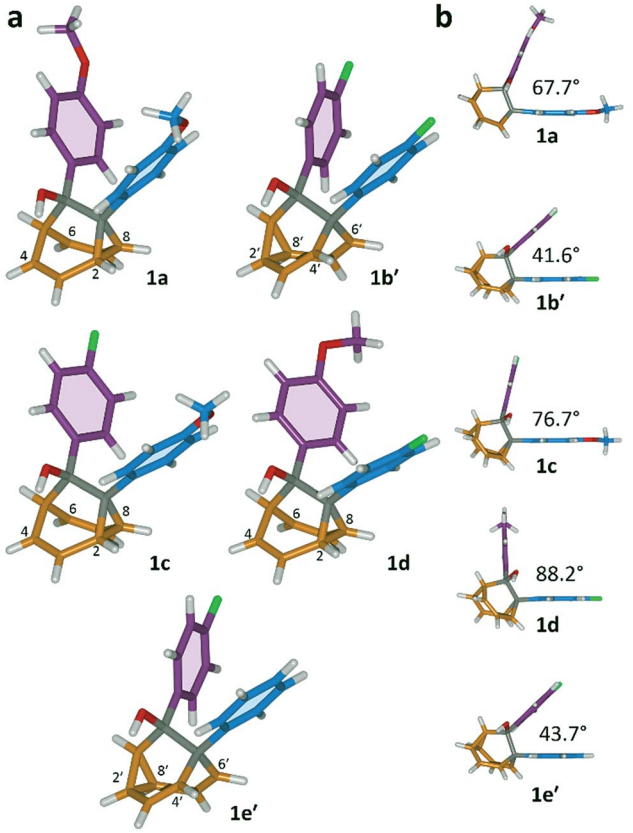

Fig. 3 X-ray crystal structures of **1**/**1**′ shown in stick representations.† (a) Whereas the major solution-phase valence isomers are obtained in some cases (**1a**, **1c** and **1d**), the minor solution-phase isomers crystallise preferentially in others (**1b**′ and **1e**′). (b) Side-on views show the variation in dihedral angles between the planes of the aromatic rings. Selected interatomic distances at 120 K (Å): **1a**, C2–C8 1.592(2), C4···C6 2.359(2); **1b**′, C2′–C8′ 1.592(3), C4′···C6′ 2.353(2); **1c**, C2–C8 1.582(2), C4···C6 2.364(2); **1d**, C2–C8 1.586(2), C4···C6 2.367(2); **1e**′, C2′–C8′ 1.591(2), C4′···C6′ 2.345(2). Oxygen atoms are shown in red, fluorine atoms are green, hydrogen atoms are white, and carbon atoms are blue, purple, orange or grey.

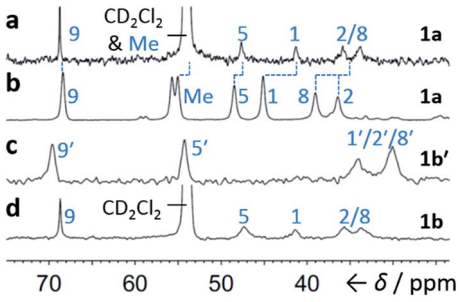

Fig. 4 Comparison of partial ^{13}C NMR spectra of **1a**/**1a**′ and **1b**/**1b**′ acquired (a and d) as CS_2–CD_2Cl_2 solutions at low temperature (126 MHz, 149 K), and (b and c) as powders at ambient temperature (105 MHz). Peaks are labelled according to the numbering in Scheme 1.

While the *p*-substituents have little influence over the solution-state valence isomerism of the five **1**/**1**′ derivatives, it appears that a subtle change at a position distant from the barbaralane core, such as switching out the OMe group of **1c**/**1c**′ for a F atom (*i.e.*, giving **1b**/**1b**′), is sufficient to bias crystallisation in favour of another valence isomer.¶

Although some fluxional carbon cages[14] are known to become 'fixed' structures upon crystallisation, others[15] remain fluxional. Variable-temperature X-ray diffraction (VT-XRD) measurements performed on single crystals of **1a** and **1b**′ show (Fig. S42 and S43†) negligible changes in C–C distances of bonds involved in Cope rearrangement. For example, the C2–C8 bond length of **1a** only changes from 1.592 Å at 120 K to 1.604 Å at 370 K. The identities of **1** and **1**′ isomers in the solid state can also be distinguished by comparing (Fig. 4) their low-temperature solution and ambient-temperature solid-state ^{13}C NMR spectra. At 149 K, the solution-phase equilibria are biased heavily towards **1a** and **1b**, so both solution-phase spectra show (Fig. 4a,d) similar patterns of peaks in their alkyl regions. Unlike the solid-state NMR (ssNMR) spectrum of the bis(4-anisyl) barbaralane (Fig. 4b), which matches closely with its solution spectra (in keeping with its assignment by X-ray diffraction as structure **1a**), the ssNMR spectrum (Fig. 4c) of the bis(4-fluorophenyl)barbaralane is markedly different. The ssNMR spectrum indicates structure **1b**′ is favoured over **1b**. Hence, the ssNMR and VT-XRD data are both consistent with the barbaralanes **1**/**1**′ having fixed constitutions in the solid state.

The barbaralane cage acts as a hinge between its two aromatic substituents, giving (Fig. 3b) the molecules V-shaped structures. Notably, the dihedral angles between the planes of these aromatic rings in the solid state vary substantially between the different derivatives. Compounds **1a**, **1c**, and **1d** have relatively wide dihedral angles > 67°, whereas the dihedral angles of **1b**′ and **1e**′ are both <44°.‖ Inspection (Fig. 5 and S57–S61†) of the solid-state superstructures reveals that these changes in dihedral angles are linked to differences in the crystal packing. Indeed, the packing is dominated by the way in which the V-shaped units fit together, rather than any specific noncovalent interactions. Compounds **1a**, **1c**, and **1d** pack with a preference to arrange their V-shaped structures head-to-tail, while **1b**′ and **1e**′ are arranged head-to-head, allowing their aromatic groups to interdigitate. We

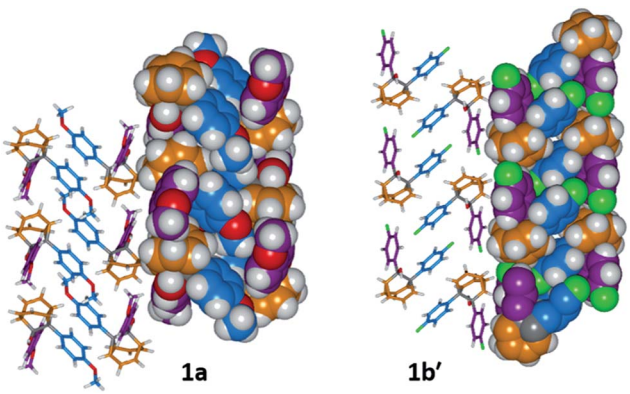

Fig. 5 Solid-state superstructures of **1a** and **1b**′ shown in partial stick and space-filling representations and viewed along the crystallographic *b*-axes. The superstructures of **1c** and **1d** (Fig. S59 and S60†) are similar to **1a**, whereas the superstructure of **1e**′ (Fig. S61†) is isostructural with **1b**′. Calculated densities (g cm^{-3}): **1a**, 1.33; **1b**′, 1.44; **1c**, 1.35; **1d**, 1.35; **1e**′, 1.39.

attribute changes between these two modes of packing primarily to differences in the sizes of the R^1 and R^2 groups. A 4-anisyl group is too large to allow efficient interdigitation, so the head-to-tail arrangement is favoured in which the aromatic rings are splayed around a neighbouring barbaralane. This geometry is most easily accommodated by the **1**-isomer form. Conversely, **1b′** and **1e′** lack 4-anisyl groups, so they are able to achieve more densely packed lattices than the other derivatives (1.39–1.44 *vs.* 1.33–1.35 g cm^{-3}) by adopting head-to-head arrangements. The 4-fluorophenyl and phenyl groups are small enough for the aromatic rings to pack together efficiently, favouring smaller dihedral angles that are more accessible when the barbaralane adapts to the slightly higher energy **1′**-isomer. Although there is more strain in the molecular structure, the relatively small (~5 kJ mol^{-1}) energy penalty to adopt the structure of the minor solution-state isomer must be overridden by a more favourable lattice energy, making the **1′**-isomer favoured in the solid state.[16]

The alcohol function (which might normally be expected to dictate[17] the packing) is overcrowded and electrostatic potential maps show (Fig. S66†) that the aromatic rings are only mildly polarised. In order to search for noncovalent bonding interactions, we calculated the Hirshfeld surfaces[18] of each crystal structure. The Hirshfeld surfaces show (Fig. S67–S72†) that no interatomic distances are significantly closer than the sum of the respective van der Waals radii. For example, the most prominent close contacts present (Fig. 6) in **1d** and **1e′** are weak O–H···C and C–H···C interactions, which each remain within ~0.2 Å of the sum of the van der Waals radii.[19] We confirmed this lack of significant, specific noncovalent bonding interactions by performing DFT modelling (CE-B3LYP**) of all the intermolecular interactions in the solid state. These calculations allow us to elucidate the total interaction energies (E_{tot}) between neighbouring molecules based on the individual energetic components of electrostatics (E_{ele}), polarisation (E_{pol}), dispersion forces (E_{dis}) and repulsion (E_{rep}).[20] For example, we examined (Fig. 7) a cluster of 14 neighbouring molecules surrounding a central molecule in the structure of **1e′**. The 14 neighbours account for all of the molecules that come within 3.8 Å of the central molecule. As would be expected, the pairs of **1e′** molecules that are closest, having the smallest centroid-to-centroid distances (R), generally interact most strongly with one another. Molecules in position D and F are separated (Table 1) from the central molecule by R < 7 Å and have interaction energies of E_{tot} = −31.1 and −43.5 kJ mol^{-1}, respectively, which are the strongest pairings present in the structure. Dispersion forces account for the majority of their attractive intermolecular interactions, contributing energies of E_{dis} = −46.8 kJ mol^{-1} for D and E_{dis} = −51.4 kJ mol^{-1} for F. Overall, the modelling for the full series of five **1**/**1′** derivatives shows (Tables S10–S14†) that dispersion forces[21] (which are influenced by the shape of the molecules and their packing) make up the major component of the interactions between molecules in all

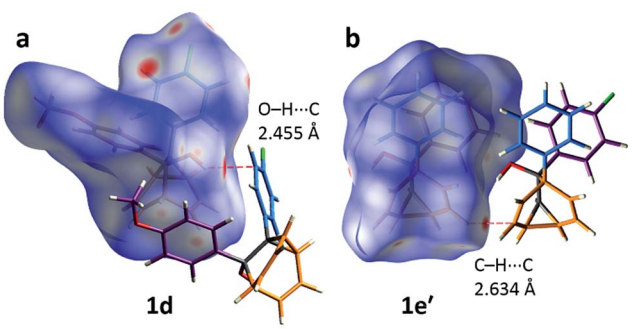

Fig. 6 Calculated Hirshfeld surfaces for the X-ray crystal structures of (a) **1d** and (b) **1e′**, showing the most significant close contacts with neighbouring molecules, which do not correspond to appreciable noncovalent bonding interactions.

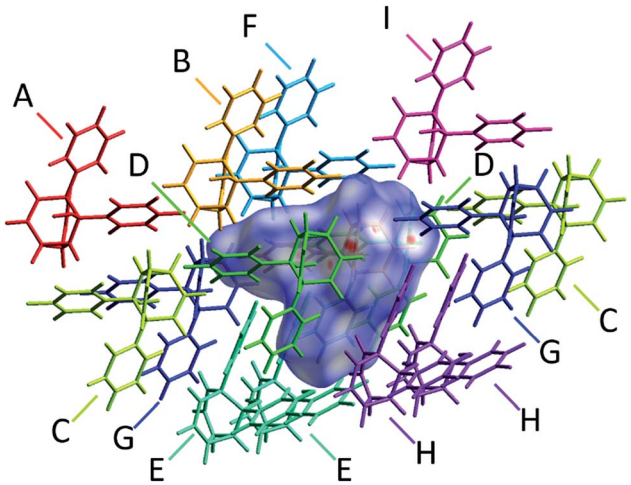

Fig. 7 A section of the solid-state superstructure of **1e′** in which a central molecule (overlaid with its modelled Hirshfeld surface) is surrounded by its 14 nearest neighbours (labelled A–I). Molecules A–I are shown in stick representation. Labels are duplicated for molecules that reside at symmetry-related coordinates relative to the central molecule.

Table 1 Calculated intermolecular interaction energies (kJ mol^{-1}) for pair of molecules in the solid-state structure of **1e′**

		Interaction energies/kJ mol^{-1}				
Neighbouring molecule[a]	R/Å[b]	E_{ele}	E_{pol}	E_{dis}	E_{rep}	E_{tot}[c]
A	13.29	2.1	−0.2	−1.3	0.0	1.0
B	7.94	−10.1	−1.4	−31.2	20.3	−26.3
C	11.59	−2.3	−0.4	−3.8	0.6	−5.6
D	6.20	−8.4	−2.4	−46.8	32.8	−31.1
E	8.26	−5.0	−0.9	−30.3	18.7	−20.8
F	6.63	−14.8	−2.8	−51.4	30.9	−43.5
G	9.79	−5.0	−0.8	−16.1	11.7	−12.7
H	7.90	−6.3	−1.1	−31.5	17.9	−23.8
I	11.04	1.1	−0.4	−8.1	1.8	−5.1

[a] The labels A–I correspond to those shown in Fig. 7 and refer to the nearby molecules in the solid state. [b] R is the centroid-to-centroid distance between the labelled molecule and the central molecule. Centroids are based on the coordinates of all atoms in each molecule and are not weighted by mass. [c] E_{tot} is the scaled sum of the individual interaction energy components E_{ele}, E_{pol}, E_{dis} and E_{rep}.

of the packing motifs, dominating the overall lattice energies in each case. This observation is consistent with our description of these molecules packing in the solid state in a manner that is influenced more by molecular shape than by any specific non-covalent bonding interactions.

Conclusions

In summary, by investigating the dynamic isomerisation of nondegenerate barbaralanes, we have found that their crystallisation is directed by the shapes of their fluxional isomers. Either the major or the minor solution-phase isomer may be resolved as a result of their assembly in crystal lattices, becoming trapped in the solid state. At present, it has not been possible to discern precisely the shapes available to the most advanced shapeshifting sensors,[6] which encompass hundreds of constitutional isomers and conformationally flexible substituents. Our observations, based on a bistable fluxional carbon cage with rigid substituents, illustrate that shape-selective interactions can override the inherent thermodynamic differences between even closely related valence isomers. Understanding the relationship between shape-selectivity and the energetics of fluxional carbon cages will aid the development of shapeshifting sensors and other applications of adaptive molecules.

Conflicts of interest

There are no conflicts to declare.

Acknowledgements

A. N. B. acknowledges an EPSRC DTG. J. S. acknowledges an Experientia Foundation Fellowship, Advanced Functional Nanorobots (CZ.02.1.01/0.0/0.0/15_003/0000444 financed by the EFRR), and computational resources from the MSMT under the CESNET (LM2015042) and CERIT-Scientific Cloud (LM2015085) projects. B. M. C. and P. R. M. thank the EPSRC for funding (EP/N029992/1). We thank Dr Mark Miller and Prof. Jon Steed for useful discussions. We are grateful to Dr David Apperley and Dr Raquel Belda-Vidal for assistance with NMR measurements.

Notes and references

§ Barbaralanes **1**/**1′** were prepared and isolated as racemic mixtures. For simplicity, only one enantiomer of each compound is shown.

¶ During our experiments, we did not observe any crystals of solvates or conformational polymorphs. The limited conformational freedom of **1**/**1′** and limited potential for hydrogen bonding suggest they are unlikely to be highly polymorphic.

‖ The differences in dihedral angles coincide with changes to the C1–C9/C5′–C9′ distances in the barbaralane core. The averaged C1–C9 distance for **1a**, **1c**, and **1d** is 1.534 Å, whereas the averaged C5′–C9′ distance for **1b′** and **1e′** is 1.586 Å, showing that the movement of the divinylcyclopropane motif influences the geometries near the aromatic rings.

** The CE-B3LYP functional was used instead of other DFT functionals, *e.g.*, CAM-B3LYP or MN15-L, because its implementation in CrystalExplorer allows calculation of the individual interaction energy terms in addition to the total energy. It should be noted that CE-B3LYP is different to the original B3LYP functional, which is not suitable for calculation of weak interactions. It reproduces counterpoise-corrected B3LYP-D2/6-31G(d,p) energies with a mean absolute deviation of about 1 kJ mol^{-1} and gives a mean absolute deviation of just 2.5 kJ mol^{-1} compared to CCSD(T)/CBS while using much less computational time. See ref. 20.

1 (*a*) W. von E. Doering and W. R. Roth, *Tetrahedron*, 1963, **19**, 715; (*b*) G. Schröder, *Angew. Chem.*, 1963, **75**, 722; (*c*) A. Ault, *J. Chem. Educ.*, 2001, **78**, 924; (*d*) O. Yahiaoui, L. F. Pašteka, B. Judeel and T. Fallon, *Angew. Chem., Int. Ed.*, 2018, **57**, 2570.
2 (*a*) P. Ahlberg, D. L. Harris and S. Winstein, *J. Am. Chem. Soc.*, 1970, **92**, 4454; (*b*) D. Cremer, P. Svensson, E. Kraka and P. Ahlberg, *J. Am. Chem. Soc.*, 1993, **115**, 7445; (*c*) P. R. McGonigal, C. de León, Y. H. Wang, A. Homs, C. R. Solorio-Alvarado and A. M. Echavarren, *Angew. Chem., Int. Ed.*, 2012, **51**, 13093; (*d*) S. Ferrer and A. M. Echavarren, *Angew. Chem., Int. Ed.*, 2016, **55**, 11178.
3 S. Jalife, J. I.-C. Wu, G. Martínez-Guajardo, P. von Ragué Schleyer, M. A. Fernández-Herrera and G. Merino, *Chem. Commun.*, 2015, **51**, 5391.
4 (*a*) D. J. Tantillo and R. Hoffmann, *Acc. Chem. Res.*, 2006, **39**, 477; (*b*) J.-M. Lehn, *Top. Curr. Chem.*, 2012, **322**, 1.
5 J.-M. Lehn, *Angew. Chem., Int. Ed.*, 2015, **54**, 3276.
6 (*a*) A. R. Lippert, A. Naganawa, V. L. Keleshian and J. W. Bode, *J. Am. Chem. Soc.*, 2010, **132**, 15790; (*b*) K. K. Larson, M. He, J. F. Teichert, A. Naganawa and J. W. Bode, *Chem. Sci.*, 2012, **3**, 1825; (*c*) J. F. Teichert, D. Mazunin and J. W. Bode, *J. Am. Chem. Soc.*, 2013, **135**, 11314.
7 C. W. Jefford, J. C. Rossier and J. A. Zuber, *Angew. Chem., Int. Ed. Engl.*, 1982, **21**, 549.
8 R. E. Moore, J. A. Pettus and J. Mistysyn, *J. Org. Chem.*, 1974, **39**, 2201.
9 E. Pretsch, P. Bühlmann and M. Badertscher, *Structure Determination of Organic Compounds*, Springer-Verlag, Berlin Heidelberg, 4th edn, 2009, p. 91.
10 Previous investigations have shown the preference of alkyl and aryl substituents to occupy a barbaralane 1-position over a 5-position. J. C. Barborak, S. Chari and P. von Ragué Schleyer, *J. Am. Chem. Soc.*, 1971, **93**, 5275. See also ref. 2*d*.
11 (*a*) R. O. Gould, C. L. Jones, T. A. Stephenson and D. A. Tocher, *J. Organomet. Chem.*, 1984, **264**, 365; (*b*) J. L. Davidson, W. F. Wilson, L. Manojlović-Muir and K. W. Muir, *J. Organomet. Chem.*, 1983, **254**, C6–C10; (*c*) K. M. J. Brands and A. J. Davies, *Chem. Rev.*, 2006, **106**, 2711; (*d*) Y. Kitamoto, K. Suzuki, N. Morohashi, K. Sakai and T. Hattori, *J. Org. Chem.*, 2013, **78**, 597; (*e*) M. Sakamoto and T. Mino, in *Advances in Organic Crystal Chemistry: Comprehensive Reviews*, ed. R. Tamura and M. Miyata, Springer, Tokyo, 1st edn, 2015, vol. 1, p. 445.
12 Some monosubstituted bullvalenes resolve to single isomers upon crystallisation (*a*) K. Müller, H. Zimmermann, C. Krieger, R. Poupko and Z. Luz, *J. Am. Chem. Soc.*, 1996, **118**, 8006; (*b*) R. Poupko, K. Müller, C. Krieger, H. Zimmermann and Z. Luz, *J. Am. Chem. Soc.*, 1996, **118**, 8015; (*c*) Z. Luz, L. Olivier, R. Poupko, K. Müller, C. Krieger and H. Zimmermann, *J. Am. Chem. Soc.*, 1998, **120**, 5526.

13 There has been one report of a minor valence isomer crystallising from a solution of a bullvalene derivative. However, the assignment of the major species in the solution-phase equilibrium is somewhat ambiguous and it has not been possible to discern what forces control the crystallisation. P. Luger and K. Roth, *J. Chem. Soc., Perkin Trans. 2*, 1989, 649.

14 (*a*) R. D. Miller and C. S. Yannoni, *J. Am. Chem. Soc.*, 1980, **102**, 7396; (*b*) W. W. Win, K. G. Grohmann and L. Todaro, *J. Org. Chem.*, 1994, **59**, 2803; (*c*) J. Siegwarth, J. Bornhöft, C. Näther and R. Herges, *Org. Lett.*, 2009, **11**, 3450. See also articles cited in ref. 2*d*, 12 and 13.

15 (*a*) V. Macho, R. D. Miller and C. S. Yannoni, *J. Am. Chem. Soc.*, 1983, **105**, 3735; (*b*) I. Sellner, H. Schuster, H. Sichert, J. Sauer and H. Nöth, *Chem. Ber.*, 1983, **116**, 3751; (*c*) L. M. Jackman, A. Benesi, A. Mayer, H. Quast, E. M. Peters, K. Peters and H. G. von Schnering, *J. Am. Chem. Soc.*, 1989, **111**, 1512; (*d*) S. Schlick, Z. Luz, R. Poupko and H. Zimmermann, *J. Am. Chem. Soc.*, 1992, **114**, 4315; (*e*) R. V. Williams, V. R. Gadgil, P. Luger, T. Koritsanszky and M. Weber, *J. Org. Chem.*, 1999, **64**, 1180; (*f*) A. Benesi, R. Bertermann, H. Förster, M. Heubes, L. M. Jackman, T. Koritsanszky, P. Luger, A. Mayer, H. Quast, M. Seefelder and D. Zobel, *J. Am. Chem. Soc.*, 2000, **122**, 4455.

16 Differences in lattice energies of $\sim$5 kJ mol^{-1} between conformational polymorphs are relatively common. See(*a*) P. G. Thompson and G. M. Day, *Chem. Sci.*, 2014, **5**, 3173; (*b*) J. Nyman and G. M. Day, *CrystEngComm*, 2015, **17**, 5154. Even though the isomerisation of the barbaralanes described here causes changes in constitution, rather than just conformation, the energetic differences are of similar magnitude to some conformational changes. It is reasonable, therefore, that the small energetic preference of the fluxional Cope rearrangements can be outweighed upon crystallisation.

17 E. N. Baker and R. E. Hubbard, *Prog. Biophys. Mol. Biol.*, 1984, **44**, 97.

18 M. A. Spackman and D. Jayatilaka, *CrystEngComm*, 2009, **11**, 19.

19 R. S. Rowland and R. Taylor, *J. Phys. Chem.*, 1996, **100**, 7384.

20 M. J. Turner, S. Grabowsky, D. Jayatilaka and M. A. Spackman, *J. Phys. Chem. Lett.*, 2014, **5**, 4249.

21 J. P. Wagner and P. R. Schreiner, *Angew. Chem., Int. Ed.*, 2015, **54**, 12274.

JACS JOURNAL OF THE AMERICAN CHEMICAL SOCIETY

Article

Cite This: J. Am. Chem. Soc. 2017, 139, 17882–17889

pubs.acs.org/JACS

Excited-State Aromatic Interactions in the Aggregation-Induced Emission of Molecular Rotors

Jiri Sturala,[†,§] Marc K. Etherington,[‡] Aisha N. Bismillah,[†] Heather F. Higginbotham,[‡] William Trewby,[‡] Juan A. Aguilar,[†] Elizabeth H. C. Bromley,[‡] Alyssa-Jennifer Avestro,*[,†] Andrew P. Monkman,*[,‡] and Paul R. McGonigal*[,†]

[†]Department of Chemistry and [‡]Department of Physics, Durham University, Lower Mountjoy, Stockton Road, Durham DH1 3LE, United Kingdom

Supporting Information

ABSTRACT: Small, apolar aromatic groups, such as phenyl rings, are commonly included in the structures of fluorophores to impart hindered intramolecular rotations, leading to desirable solid-state luminescence properties. However, they are not normally considered to take part in through-space interactions that influence the fluorescent output. Here, we report on the photoluminescence properties of a series of phenyl-ring molecular rotors bearing three, five, six, and seven phenyl groups. The fluorescent emissions from two of the rotors are found to originate, not from the localized excited state as one might expect, but from unanticipated through-space aromatic-dimer states. We demonstrate that these relaxed dimer states can form as a result of intra- or intermolecular interactions across a range of environments in solution and solid samples, including conditions that promote aggregation-induced emission. Computational modeling also suggests that the formation of aromatic-dimer excited states may account for the photophysical properties of a previously reported luminogen. These results imply, therefore, that this is a general phenomenon that should be taken into account when designing and interpreting the fluorescent outputs of luminescent probes and optoelectronic devices based on fluorescent molecular rotors.

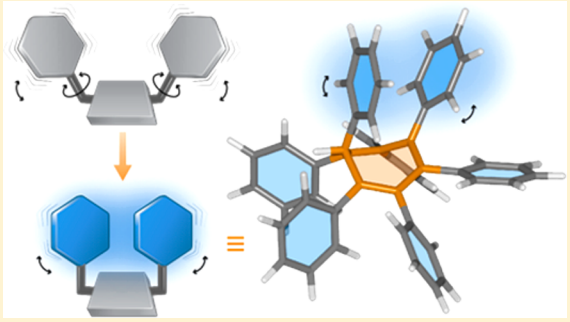

INTRODUCTION

The development of advanced organic luminogens underpins progress in areas as diverse[1] as fluorescent microscopy,[2] mechanoluminescent materials,[3] and organic light-emitting diodes.[4] In recent years, traditional planar luminogens have been modified[5] to introduce hindered rotation around sterically overcrowded single bonds, juxtaposing "bright" and "dark" excited states as a function of rotational and vibrational freedom. The resulting fluorescent molecular rotors have been exploited, among other applications, as materials for photovoltaic devices[6] or as probes to measure viscosities[7] in microheterogeneous environments, such as biological cells.[8]

Some of these molecular rotors exhibit aggregation-induced emission[9] (AIE). That is, they fluoresce weakly, or not at all, when dissolved, but become significantly more emissive in the solid state. In the most extreme cases, photoluminescence quantum yields have been shown[10] to increase from below detection limits in solution to near unity upon aggregation—behavior that is not only desirable for applications in solid-state devices, but is also contrary to the aggregation-caused quenching (ACQ) commonly observed for traditional, planar luminogens.[11] A general tactic[9b] used to convert traditional luminogens into fluorescent molecular rotors is to introduce simple aromatic groups, such as phenyl rings,[5a,c−e] positioned in close proximity to one another. Steric overcrowding favors nonplanar conformations and introduces hindered single-bond rotations. Tetraarylethylenes,[12] for example, which are archetypal AIE luminogens, can be viewed as stilbenes modified by the addition of two aromatic groups to impart propeller-like arrangements of the rings. Many of the other common AIE motifs[1,13] are similarly comprised of phenyl rings projecting out from a central core.

The AIE phenomenon, in general, has been attributed[9] to the suppression of nonradiative decay pathways. Confinement in the rigid environment of amorphous aggregates or crystalline solids attenuates vibrations, which leads to enhanced levels of photoluminescence from conformationally restricted excited states. However, an in-depth understanding of these excited states and of why AIE luminogens behave differently from ACQ systems is yet to be fully developed.[7e,9c] To date, the accepted roles of commonly used, monocyclic aromatic rings have generally been limited to creating sterically overcrowded bonds.

Here, we report the unusual fluorescent properties of a series of phenyl-ring molecular rotors, which give us insights into their aggregated states. Not only do the emission intensities of the rotors change under different conditions, but, unexpectedly, the emission energies are also variable. Two of the rotors emit

Received: August 11, 2017
Published: November 18, 2017

DOI: 10.1021/jacs.7b08570
J. Am. Chem. Soc. 2017, 139, 17882–17889

light from two distinct excited states depending on their environments. We have investigated the luminescent properties of these rotors (i) in solution across a range of temperatures and viscosities, as well as in the solid state, as part of (ii) thin films, (iii) crystals, and (iv) amorphous aggregates. By analysis of the steady-state and time-resolved emission spectra, solid-state superstructures, and density functional theory (DFT) models, we distinguish (Figure 1) locally excited (LE) state

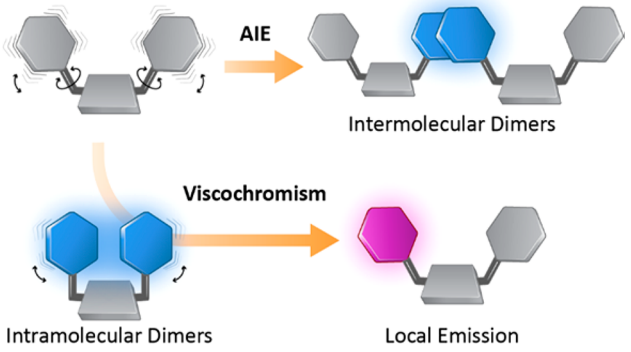

Figure 1. Schematic representation of the two processes that lead to face-to-face aromatic dimer formation, observed in the luminescence of the phenyl-ring molecular rotors. In the crystalline or aggregated states, enforced proximity of phenyl rings leads to emission from intermolecular aromatic dimers (shown in blue). A pair of interacting molecules is depicted, representing the local structure in an extended solid-state structure. In solution, (i) the excitation may be lost through nonradiative decay, (ii) emission may arise from a relaxed state, brought about by intramolecular pairing (blue) of aromatic rings, or (iii) if dimer formation is prevented, a locally excited state decays by higher energy emission (purple).

emission from lower energy emission of excited face-to-face aromatic dimers.[14] The flexibility of the rotors and the relative orientations of their peripheral rings influence the likelihood of aromatic dimer formation, which can occur (Figure 1) in an intra- or intermolecular fashion, despite a lack of complementary donor–acceptor interactions. This analysis allows insight into the excited states responsible for emission in aggregates. Moreover, with the aid of DFT calculations, we demonstrate that the formation of face-to-face aromatic dimer states accounts for the behavior of a previously reported multichromic luminogen, suggesting this is a general phenomenon that should be considered when designing and exploiting fluorescent molecular rotors.

RESULTS AND DISCUSSION

Chemical Structures of the Molecular Rotors. *sym*-Triphenylcyclopropene (**Ph_3C_3H**), *sym*-pentaphenylcyclopentadiene (**Ph_5C_5H**), hexaphenylbenzene (**Ph_6C_6**), and *sym*-heptaphenylcycloheptatriene (**Ph_7C_7H**) make up (Figure 2) a homologous series of molecular rotors in which a central, unsaturated carbocycle of increasing size is functionalized with a phenyl ring at each vertex. The absence of heteroatoms in these compounds simplifies the analysis of their photophysical properties, while the radial substitution pattern of phenyl rings projecting out from the central carbocycles establishes a sterically encumbered environment. Analysis of X-ray crystal structures reveals (Figure 2) that, for the most part, the close proximities of the phenyl rings prevent coplanar conformations. The only exception is **Ph_3C_3H**, in which the central

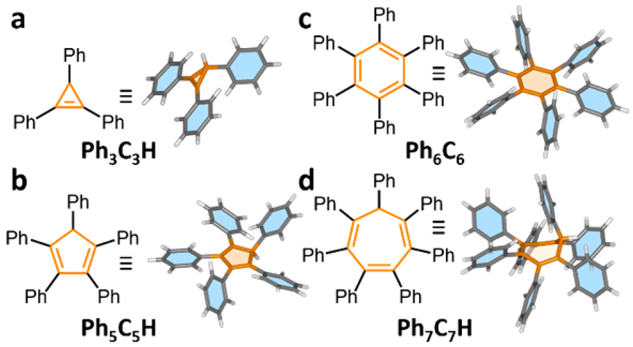

Figure 2. Structural formulas and X-ray crystal structures of (a) **Ph_3C_3H**, (b) **Ph_5C_5H**, (c) **Ph_6C_6**, and (d) **Ph_7C_7H**, showing the radial orientations of the peripheral phenyl rings around the central carbocycles (orange).

cyclopropene ring lies (Figure 2a) coplanar with two of its relatively unhindered phenyl rings, allowing for favorable orbital overlap and conjugation without unfavorable steric interactions. The propeller-like conformations of phenyl rings that predominate in these compounds would be expected[9b] to impart AIE-type properties. Indeed, **Ph_5C_5H**[1b] and **Ph_6C_6**[13r] are known to be emissive in the solid state. Although all of the rotors are relatively rigid on account of their cyclic, conjugated cores, **Ph_5C_5H** and **Ph_7C_7H** possess moderate flexibilities around the single sp^3 center present in their five- or seven-membered ring, respectively. As a result, the cycloheptatriene of **Ph_7C_7H** adopts (Figure 2d) a shallow, boat-like conformation in the solid state, in which the phenyl ring bonded to the sp^3 center is oriented above the central carbocycle.

Two-State Luminescence of Dissolved Rotors. To probe the photoluminescence of the molecular rotors, we acquired steady-state emission spectra[15] of dilute 2-methyltetrahydrofuran (2-MeTHF) solutions. All four of the rotors are only weakly luminescent in solution at room temperature. Upon cooling, however, their emission intensities (Figures S27–S30) increase significantly. Cooling **Ph_7C_7H** solutions below 200 K brings about a gradual hypsochromic shift (Figure 3) as the temperature decreases, with concurrent increases in viscosity.[16] The emission maximum (E_{em}) shifts from 2.84 eV at 200 K to 3.32 eV at 90 K, undergoing a change in peak shape. These observations lead us to conclude that **Ph_7C_7H** emits from two different excited states under these conditions.

An excitation energy (E_{ex}) of 3.94 eV is used (Table 1) to excite **Ph_7C_7H**. Therefore, the observed peaks correspond to Stokes shifts of 1.04 and 0.62 eV, respectively. While the lower energy emission is broad and featureless, there is some vibronic structure apparent for the 3.32 eV peak, indicating[11] that this higher energy emission arises from the LE state, that is, $S_1 \rightarrow S_0$ transitions. No solvatochromism was observed in a series of fluorescence spectra acquired (Figure S31) using solvents of differing polarities, so the shifts in emission do not arise as a result of solvent relaxation. The emission at 2.84 eV must, therefore, correspond to an electronic transition from a relaxed state that resides below the S_1 energy level. A similar, but less pronounced, phenomenon is also observed (Figure 3, inset) for solutions of **Ph_5C_5H**, whereby lowering the temperature enhances photoluminescence at E_{em} = 2.73 eV, which gradually shifts to E_{em} = 2.91 eV at 80 K. The emission profiles of **Ph_3C_3H** and **Ph_6C_6**, on the other hand, do not exhibit changes in peak shapes or significant shifts of the emission maxima in low temperature solutions. Their luminescence is enhanced at

DOI: 10.1021/jacs.7b08570
J. Am. Chem. Soc. 2017, 139, 17882–17889

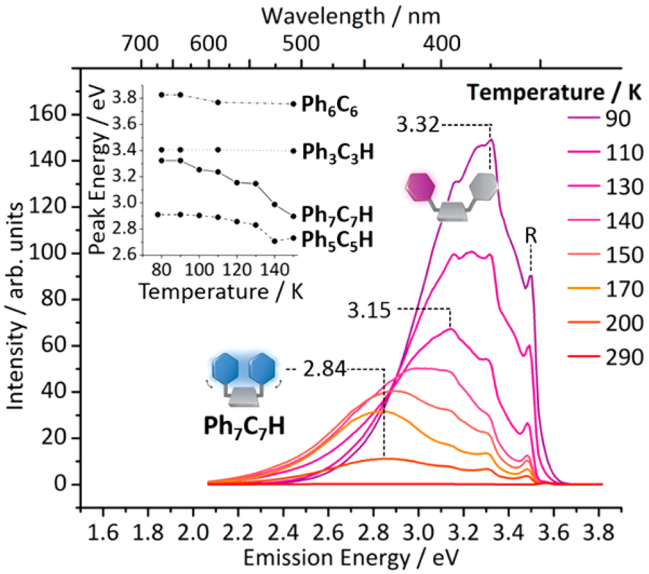

Figure 3. Steady-state photoluminescence spectroscopy of **Ph_7C_7H** (10 μM solution in 2-MeTHF, E_{ex} = 3.94 eV, l = 10 mm) at a range of temperatures reveals luminescence from two different states. Inset: In contrast to **Ph_7C_7H**, the emission maxima of **Ph_3C_3H** and **Ph_6C_6** change very little as temperature is varied, whereas the emission from **Ph_5C_5H** undergoes a small hypsochromic shift at low temperature. The peak labeled "R" is a result of Raman scattering from the solvent.[17]

lower temperatures, but the observed peaks are consistent with LE state emissions.

We also acquired photoluminescence spectra of 1:5 v/v methylcyclohexane−isopentane (MCH−*i*-pentane) solutions at low temperatures. Unlike the 2-MeTHF solutions (T_g = 91 K), MCH−*i*-pentane solutions (T_g = 77 K) do not freeze under the experimental conditions.[18,19] No significant differences were observed (Figures S27−30) between the spectra acquired in the two solvent systems, indicating that the photoluminescence is not influenced by the solvent phase change. Given the low concentrations[20] (1−10 μM) of the solutions analyzed by variable temperature and viscosity experiments, we hypothesized that an intramolecular phenomenon was responsible for the emergence of two-state luminescence, prompting us to investigate the available modes of intramolecular motion present in the rotors.

Role of Conformational Freedom. The fluorescence lifetimes, τ, of **Ph_7C_7H** and **Ph_5C_5H** increase (Table 1) at lower temperatures, consistent with the decrease in rates of nonradiative decay reported for other molecular rotors.[21] To gain insight into the relative rates of phenyl ring rotations, which presumably contribute to the nonradiative decay, we used DFT methods to calculate (Table S2) the associated energy barriers. Variable-temperature NMR spectroscopy measurements revealed (Figure S9) an energy barrier of 39.3 kJ mol^{-1} for the 180° rotation of the most hindered phenyl rings present in **Ph_7C_7H**. This measured energy barrier is slightly lower than the calculated energy barrier of 42.5 kJ mol^{-1}, but demonstrates reasonably good agreement between calculation and experiment. The DFT calculations indicate (Table 1) that the phenyl rings of **Ph_6C_6** are the most hindered, followed by **Ph_7C_7H**, **Ph_5C_5H**, and then **Ph_3C_3H**. This trend is reflected in temperature-dependent behavior; while the luminescence of **Ph_3C_3H** solutions (Figure S27) increases sharply only below about 100 K, for example, **Ph_6C_6** solutions begin to emit (Figure S29) brightly from just under 250 K.

The ground-state geometries (Figure 4, purple) predicted for the four rotors resemble closely the single-crystal X-ray

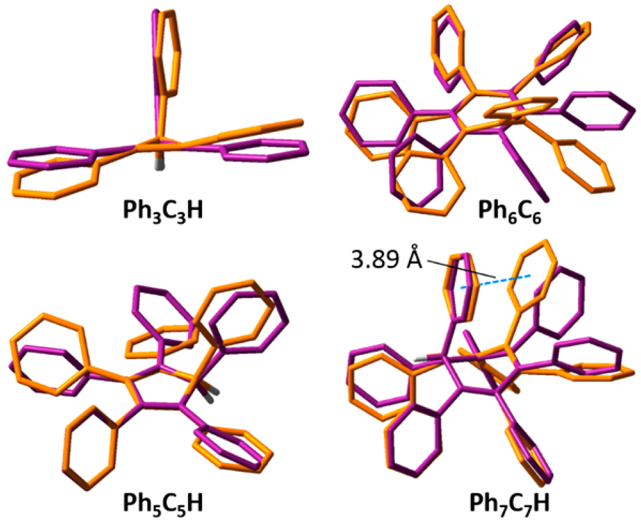

Figure 4. DFT minimum energy geometries calculated for the S_0 (purple) and S_1 (orange) electronic states of (a) **Ph_3C_3H**, (b) **Ph_5C_5H**, (c) **Ph_6C_6**, and (d) **Ph_7C_7H**, using the CAM-B3LYP[22] functional, Def2-SVP basis set, and a C-PCM model to approximate PhMe as solvent. The dotted blue line illustrates a face-to-face interaction between distal phenyl rings of **Ph_7C_7H** in the S_1 state, characterized by a centroid−centroid distance of 3.89 Å and torsion angle of 22°. All H atoms at sp^2-carbon centers are omitted for clarity.

structures (Figure 2). However, there are significant differences in the calculated minimum energy geometries for the S_1 excited states (Figure 4, orange). Calculations were performed using the CAM-B3LYP[22] functional, Def2-SVP basis set, and a

Table 1. Physical Properties of the Molecular Rotors

		E_{em} (eV)					QY (%)			τ (ns)[c]	
rotor	E_{ex}[a] (eV)	2-MeTHF, 150 K	2-MeTHF, 80 K	crystal	film	DMF−H_2O (2:8)	MeCN	MeCN−H_2O (2:8)	E_{rot}[b] (kJ mol^{-1})	2-MeTHF, 290 K	2-MeTHF, 80 K
Ph_3C_3H	3.76	3.40	3.41	3.10	3.17	3.34	–[d]	–[d]	20.61	2.07	2.05
Ph_5C_5H	3.65	2.73	2.91	2.70	2.73	2.76	0.3	14[e]	30.06	0.61	2.90
Ph_6C_6	4.43	3.76	3.83	3.67	3.78	3.83	0.4	4	79.22	0.46	1.63
Ph_7C_7H	3.94	2.90	3.32	3.04	2.77	2.89	0.1	6	42.47	0.91	1.31

[a]Excitation wavelengths were chosen to match peaks in absorption spectra (Figure S26). [b]Calculated for the most hindered phenyl ring (BMK, Table S2). [c]Values including errors can be found in Tables S7−S9. [d]QYs of **Ph_3C_3H** could not be measured accurately on account of ACQ (Figure S46). [e]QY of 3:7 MeCN−H_2O suspension.

DOI: 10.1021/jacs.7b08570
J. Am. Chem. Soc. 2017, 139, 17882−17889

C-PCM model to approximate PhMe as solvent. Most noticeably, the minimum energy excited-state geometry of **Ph_7C_7H** reveals close face-to-face contact between phenyl rings at the 3- and 7-positions of the central cycloheptatriene. This unexpected intramolecular interaction is characterized by a centroid-to-centroid distance of 3.89 Å, aligning the two phenyl rings close together in space and allowing their π-systems to interact.[23] We attribute our observation of two-state luminescence to this interaction; excitation to a LE state can be followed by the formation of a face-to-face aromatic dimer by transannular interaction of the phenyl rings, leading to a relaxed exciton and a red-shifted emission.[24,25] Indeed, more than one distinct minimum was found (Figure S38) for **Ph_7C_7H** by sampling the potential energy surface of the first excited state. The temperature- and viscosity-dependent changes in E_{em} can be rationalized, therefore, by considering that the formation of a relaxed dimer is only possible under conditions that allow for larger amplitude conformational reorganization, that is, at higher temperatures and lower viscosities. At lower temperatures and higher viscosities, on the other hand, the conformational reorganization is slow on the time scale of the fluorescent emission,[16] and higher energy emission from the initial LE state is observed.

Rotor **Ph_7C_7H**, in particular, is predisposed to undergoing conformational reorganization to form an intramolecular aromatic dimer on account of its sp^3 center, which allows the central cycloheptatriene ring to deviate from planarity. There are no such transannular interactions evident in the excited-state geometries of **Ph_3C_3H** or **Ph_6C_6**, which is consistent with their more conventional photophysical properties. By drawing analogy to **Ph_7C_7H**, the small changes in E_{em} observed for solutions of **Ph_5C_5H** are attributed to weak through-space interactions that develop between the π-systems by conformational reorganization in the excited state, which has (Figure S38) a rather flat potential energy surface. The minimum energy torsional angle between the phenyl rings at the 2- and 3-positions decreases from 72° in the ground state to 55° in the excited state, favoring a weak through-space interaction of the π-electrons.[26]

Aromatic Interactions in the Solid State. To gain further insight into the excited face-to-face aromatic dimers, we analyzed the photophysical properties of the molecular rotors in the solid state. We measured the fluorescence spectra of crystalline solids, neat films, and 1 wt% dispersions in optically clear poly(methyl methacrylate) (PMMA) and cyclic olefin polymer (ZEONEX) matrixes, which were prepared by either drop-casting or spin-coating polymer–rotor solution mixtures onto quartz substrates. In the rigid environments of the closely packed crystalline solids, the large-amplitude geometric reorganizations required to form the intramolecular face-to-face aromatic dimers are suppressed.[27] Despite this restricted motion, crystalline samples of **Ph_7C_7H** emit (Figure 5a) at lower energy as compared to the LE state observed in 2-MeTHF at 80 K, indicative of a relaxed excited state. Similarly, crystalline samples of **Ph_5C_5H** also fluoresce from partially relaxed excited states; the onset[28] of emission occurs (Figure 5b) about 0.3 eV below that of the LE state observed in 2-MeTHF at 80 K.

Analysis of the solid-state superstructures of **Ph_7C_7H** (Figure 5c) and **Ph_5C_5H** (Figure 5d) reveals coplanar, face-to-face interactions between the phenyl rings of neighboring molecules in the crystals. Thus, similar to the relaxation of dilute solutions, the initial excitons evolve to form excited aromatic dimers, but

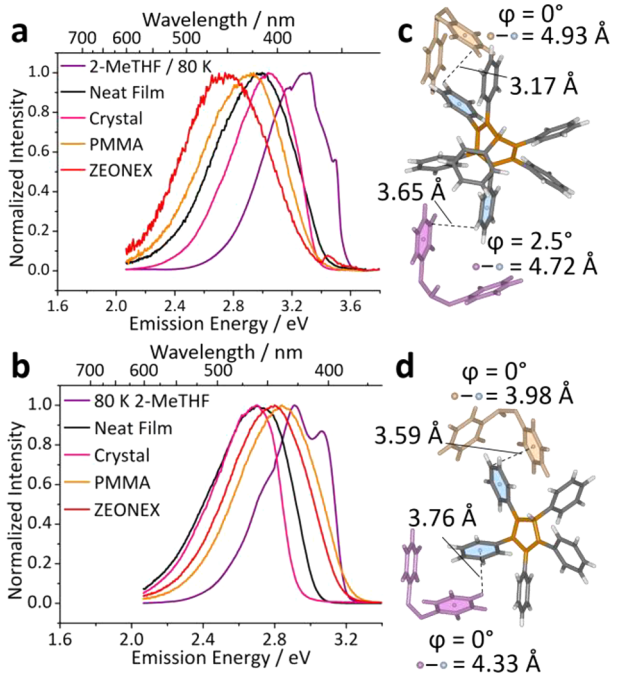

Figure 5. Emission profiles of (a) **Ph_7C_7H** and (b) **Ph_5C_5H** in crystalline and amorphous condensed phases are contrasted with the emission from frozen 2-MeTHF solutions. Solid-state packing interactions are shown for the carbocycles in (c) and (d), respectively. Colored spheres denote centroids, and φ denotes the torsion angles between the planes defined by the atoms of the benzene rings.

they do so as a result of intermolecular contacts, rather than by intramolecular phenyl-ring dimer formation. Notably, the phenyl rings involved in these interactions in the solid state are different from those in solution; for example, the phenyl group at the sp^3-carbon center of **Ph_7C_7H**, which takes part in the face-to-face aromatic dimer in solution, is only in close contact with the edges of neighboring aromatic rings in the crystal (Figure S22). Nevertheless, the spectroscopic data show that the photophysical outcome is similar. The exciton relaxes from the S_1 energy level by sharing the excitation energy across two phenyl rings, reaching an excited state that resides at an energy similar to that observed in solution. Neither **Ph_3C_3H** nor **Ph_6C_6** displays any evidence of relaxed emission in the solid state, which is consistent with the lack (Figures S12 and S18) of significant face-to-face contacts of their conjugated phenyl rings.

The neat films also emit from aromatic dimer states. Emission onsets of both **Ph_7C_7H** and **Ph_5C_5H** films are close (Figure 5) to those observed for crystalline samples, although the peaks are broader on account of the greater inhomogeneity in the amorphous samples. Slightly higher energy emissions are observed from the films, which are presumably a result of the less efficient packing in the amorphous films, reducing the likelihood of close face-to-face contacts between phenyl rings.

By preparing polymer blends of the rotors, we dilute their concentrations in the films, which would be expected to diminish the presence of intermolecular dimers and favor fluorescence from LE states. The emission onsets of the 1 wt% **Ph_5C_5H** films do indeed coincide with the LE state emission observed from the frozen 2-MeTHF solution, showing that the rotor is well-dispersed in the PMMA or ZEONEX and is, therefore, prevented from forming intermolecular aromatic interactions. Atomic force microscopy (AFM) images (Figure

DOI: 10.1021/jacs.7b08570
J. Am. Chem. Soc. 2017, 139, 17882–17889

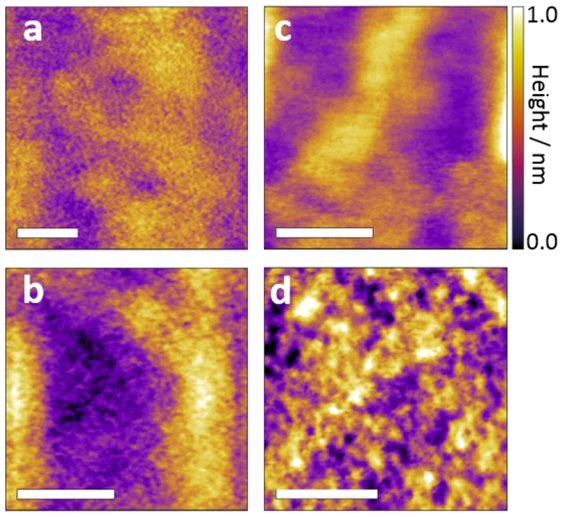

Figure 6. AFM images of spin-coated films of (a) Ph_5C_5H in PMMA, (b) Ph_5C_5H in ZEONEX, (c) Ph_7C_7H in PMMA, and (d) Ph_7C_7H in ZEONEX. Scale bars = 200 nm.

6) reveal that both of the spin-coated Ph_5C_5H–polymer films have smooth topographies, supporting the notion that the films are homogeneous and the Ph_5C_5H is evenly distributed.

In contrast to Ph_5C_5H, the fluorescence of the 1 wt% films of Ph_7C_7H appears to be dominated (Figure 5a) by relaxed dimer emission. The emission maxima move (Figure S25) in response to changes in temperature, similar to the behavior observed (Figure 3) for 2-MeTHF solutions, which is indicative of similar intramolecular phenyl-ring dimers. Notably, however, the higher viscosity environment of the polymer matrixes causes these changes to occur at higher temperatures. AFM topographical images of the Ph_7C_7H–ZEONEX film show (Figure 6d) a surface that is significantly rougher than the other films. There are visible protrusions of ~20 nm, suggesting that the Ph_7C_7H is not well dispersed, but has formed some small aggregates.[29] The values for surface roughness, R_q, were measured to be 153.6 pm for the PMMA film and 212.5 pm for ZEONEX. Moreover, the emission from the Ph_7C_7H–ZEONEX film is slightly red-shifted (Figure 5a) relative to the PMMA film. In addition to the intramolecular iterations, therefore, there is also some contribution from intermolecular interactions present in the Ph_7C_7H–ZEONEX film.

Effects of Aggregation. Distinguishing the interactions between molecules during the aggregation process is crucial to developing a robust understanding of AIE processes.[30] Having established the luminescence pathways for the phenyl-ring molecular rotors in solution and bulk solid phases, we investigated the emissive properties (Figures 7 and S34–S37) of nanoaggregates prepared by adding a poor solvent (water) to dimethylformamide (DMF) and MeCN solutions of the rotors.

On the basis of emission intensities alone, it is clear that Ph_3C_3H undergoes ACQ, whereas the other three rotors are AIE active. Apart from Ph_3C_3H, the photoluminescence quantum yields (QYs) of the rotors increase upon precipitation from MeCN (Table 1) or DMF (Table S10) solutions. The differing behaviors of the rotors are dictated by the preferred orientations of their phenyl rings and the geometrical restraints placed on their interactions. The least hindered rotor, Ph_3C_3H, preferentially takes up (Figure 2a) a coplanar, stilbene-like conformation, which leads to static quenching[11] of fluorescence upon aggregation. Aggregates of Ph_6C_6, on the other hand,

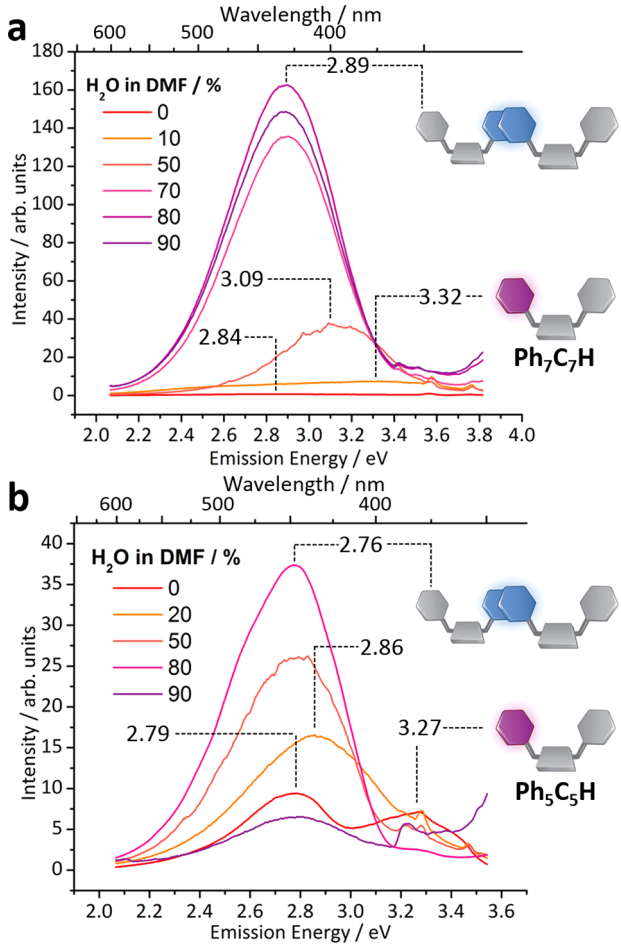

Figure 7. Steady-state photoluminescence spectra of (a) Ph_7C_7H and (b) Ph_5C_5H suspensions in H_2O–DMF (E_{ex} = 3.94 eV [Ph_7C_7H]/ 3.65 eV [Ph_5C_5H], l = 10 mm, T = 298 K). As increasing proportions of water are added to the DMF solutions, emissive aggregates are formed. At high water contents, the emission energies are similar to the relaxed phenyl-dimer states observed in crystalline samples, which we ascribe to intermolecular interactions in the aggregates. Low intensity, higher energy emissions are observed from suspensions with lower water content (e.g., 10–50% for Ph_7C_7H), consistent with some localized emission. Small, sharp peaks above 3.20 eV in (b) correspond to Raman scattering from the solvent.

display conventional AIE characteristics, emitting with increasing brightness as the concentration of water is increased, but without undergoing variation in E_{em}. Recalling that Ph_6C_6 is the most hindered (Table 1) of the four luminogens, (i) the peripheral phenyl groups are held out of the plane of the central benzene, but (ii) they are also unable to undergo either intra- or intermolecular pairing in the nanoaggregates.

Unlike Ph_3C_3H and Ph_6C_6, the AIE spectroscopic characteristics of Ph_7C_7H (Figure 7a) and Ph_5C_5H (Figure 7b) are dominated by excited face-to-face aromatic dimers. Dynamic light scattering (DLS) measurements show an increase in scattering (Figure S23), consistent with the formation of nanoaggregates under these conditions. Intermolecular interactions, similar to those observed (Figure 6) in the crystals, are responsible for the relaxed emission. Comparison of the UV–vis spectra of solutions and aggregated mixtures shows (Figure S26) red-shifts in the absorption peaks, arising from the intermolecular aromatic interactions. In DMF solution, Ph_5C_5H displays two distinct fluorescence peaks, one at

DOI: 10.1021/jacs.7b08570
J. Am. Chem. Soc. 2017, 139, 17882–17889

E_{em} = 3.27 eV that is assigned to the LE state, and the other at E_{em} = 2.76 eV that is characteristic of relaxed phenyl-ring dimers. Similarly, there is some contribution from the LE state to emissions from **Ph_7C_7H** suspensions at low water contents, for example, 10% water in DMF, as evidenced by a low intensity peak at E_{em} = 3.32 eV. However, the strongly emissive aggregates that form at higher water contents (i.e., above 50%) display E_{em} values and onset energies that match the relaxed excited states discussed above.

Discussion. Shifts in the emission wavelengths of fluorophores under different experimental conditions are not uncommon. Depending on the structure of the fluorophore, they may be attributed to phenomena such as (i) solvent relaxation, (ii) internal charge transfer, or (iii) changes in the Coulombic coupling of aggregates (i.e., J- or H-aggregation).[11,22] Yet these effects are normally only prominent for fluorophores that (i) are polar, (ii) contain donor and acceptor groups, or (iii) are comprised of a large, planar π-surface. The molecular rotors described here are nonplanar, apolar hydrocarbons; they lack any of the features that would normally be associated with variable E_{em} in different environments, so the significant shifts between the LE and relaxed emissions of **Ph_7C_7H** and **Ph_5C_5H** are surprising.[24] Observation of the aromatic-dimer excited states for these rotors, therefore, raises the questions "is this a general phenomenon?" and "which factors favor formation of the aromatic dimers?".

In answer to the first question, a survey of previously reported data for phenyl-ring luminogens shows that, in some cases,[9c,13g,k,n,p] there are spectroscopic shifts upon formation of nanoaggregates that are comparable to our observations (Figure 7). So, it appears that the excited-state aromatic dimer formation may be a general phenomenon that is not limited to the carbocyclic rotors reported here. For example, 2,2′-biindene **1** (Figure 8), which was described by Tian et al. in

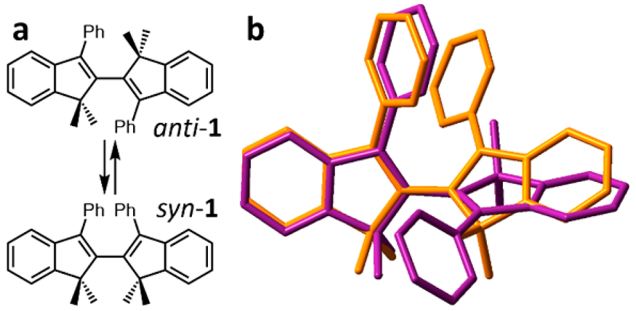

Figure 8. (a) Previously reported 2,2′-biindene **1** undergoes hypsochromic shift in its fluorescence upon aggregation. (b) Our DFT modeling of the S_0 (purple) and S_1 (orange) electronic states suggests this effect results from a through-space aromatic dimer in solution, which cannot form in the aggregated state. All H atoms are omitted for clarity.

2011, shows distinct peaks at E_{em} = 2.58 eV and E_{em} = 3.00 eV in its photoluminescence spectra in the solution and aggregated states, respectively.[13g] Rotation around the central single bond of **1** interconverts (Figure 8a) the *anti*- and *syn*-isomers. Our calculations indicate (Figure 8b) that *anti*-**1** is preferred in the ground state, but a *syn*-conformation becomes favorable in the excited state, which is accompanied by a face-to-face interaction between the phenyl rings. Therefore, the hypsochromic shift[13g] brought about by aggregation can be attributed to intramolecular aromatic dimer formation in solution. The dimer formation is prevented by the restricted environment of the aggregates, leading to higher energy emission from the LE state.

On the other hand, there are, of course, many examples of molecular rotors that do not form aromatic dimer excited states. There do not seem to be any reported data that suggest the widely used tetraarylethylenes[12] are subject to this phenomenon, for example, and nor are **Ph_3C_3H** and **Ph_6C_6**, according to the data described here.

At this stage, it is difficult to delineate the structural characteristics that favor aromatic dimers over LE in the excited states. In the solid state, weak noncovalent interactions dictate the packing and ultimately determine whether or not the aromatic groups of neighboring molecules are held together, promoting intermolecular aromatic dimer states. However, analysis of the series of rotors reported here does hint that the degree of conformational flexibility is an important factor for intramolecular dimer formation;[31] there must be sufficient flexibility to allow the faces of the aromatic rings to come into contact, while also maintaining a sterically crowded environment to minimize nonradiative decay. Moreover, an intramolecular aromatic dimer may form in the excited state, even when the relevant conformation is not favored in the ground state. It is well-established that weak ground-state interactions[32] between phenyl rings stabilize[33] the secondary structures of proteins, and that the interaction potential energy surface of two aromatic rings is relatively flat. So, the stabilizing effect of a shared exciton could provide the driving force to alter minimum energy conformations in this way.

Overall, our results indicate that simple aromatic rings present in molecular rotors can do more than merely introduce steric hindrance. Their interactions can lead to emission from previously unexpected excited-state dimers. This phenomenon should be considered, therefore, when designing and interpreting the behavior of fluorescent molecular rotors, even those based on unfunctionalized hydrocarbon backbones. Shifts in emission energy need not always be attributed simply to "solvent effects". At a time when molecular rotors are being used more frequently as probes for quantitative measurements, it is important to have a full understanding of how their photophysical output can respond to changes in their environments.

CONCLUSION

In summary, by investigating the properties of a series of phenyl-ring molecular rotors, we have identified photoluminescence from through-space aromatic dimers. The dimers form in either an intra- or an intermolecular fashion between small, unfunctionalized aromatic rings, leading to relaxed excited states. Previously, fluorophores lacking large, flat π-systems or polarized functional groups have generally not been expected to undergo such significant relaxation.[24] The least hindered rotor, **Ph_3C_3H**, shows the characteristics of a traditional fluorophore, undergoing quenching in the solid state, while the most hindered, **Ph_6C_6**, undergoes AIE. Both fluoresce from the LE state under all conditions. Rotors **Ph_7C_7H** and **Ph_5C_5H**, on the other hand, emit from the LE state at very low temperatures or high viscosities, but otherwise luminesce from through-space aromatic dimer states. Intramolecular dimer formation appears to be influenced by the degree of conformational flexibility present in the rotors in solution, while the intermolecular excited states are governed by the interdigitation of the rotors in the solid state. Our results illustrate that, given the right spatial orientations, interactions

DOI: 10.1021/jacs.7b08570
J. Am. Chem. Soc. 2017, 139, 17882−17889

between simple aromatic rings are sufficient to cause significant shifts in photoluminescence energies. DFT modeling and analysis of previously published spectroscopic data suggest that this is a general phenomenon. Care should be taken, therefore, when designing and interpreting the results of sensing systems or optoelectronic devices based around similar molecular rotors.

■ ASSOCIATED CONTENT

Supporting Information

The Supporting Information is available free of charge on the ACS Publications website at DOI: 10.1021/jacs.7b08570.

Synthetic procedures, characterization data, X-ray crystallographic data, experimental methods, additional optical data, theoretical calculations, and time-resolved fluorescence (PDF)

■ AUTHOR INFORMATION

Corresponding Authors

*alyssa.j.avestro@durham.ac.uk
*a.p.monkman@durham.ac.uk
*paul.mcgonigal@durham.ac.uk

ORCID

Marc K. Etherington: 0000-0003-2101-5757
Heather F. Higginbotham: 0000-0003-0245-5327
Elizabeth H. C. Bromley: 0000-0002-7678-1187
Andrew P. Monkman: 0000-0002-0784-8640
Paul R. McGonigal: 0000-0002-8538-7579

Present Address

§Department of Inorganic Chemistry, University of Chemistry and Technology Prague, Technická 5, Prague 6 16628, Czech Republic.

Notes

The authors declare no competing financial interest.

■ ACKNOWLEDGMENTS

J.S. gratefully acknowledges the support of an Experientia Foundation Fellowship and an EPSRC Impact Acceleration Account, as well as access to computational resources provided by the CESNET LM2015042 and the CERIT Scientific Cloud LM2015085, provided under the programme "Projects of Large Research, Development, and Innovations Infrastructures". M.K.E. and H.F.H. acknowledge the EU's Horizon 2020 for funding the PHEBE project under grant no. 641725. A.-J.A. thanks the Royal Commission for the Exhibition of 1851 for the award of a Science and Engineering Research Fellowship. A.P.M. acknowledges the EPSRC for funding under grant number EP/L02621X/1. P.R.M. acknowledges the support of an EPSRC First Grant (EP/N029992/1) and a Royal Society Research Grant (RG150558). We thank Dr. Lars-Olof Pålsson, Dr. Qing He, Prof. David Parker, and Prof. Andy Beeby for access to instruments and useful discussions. We thank Dr. Dmitry Yufit for performing X-ray crystallographic analysis of Ph_3C_3H.

■ REFERENCES

(1) (a) Zhao, Y. S.; Fu, H.; Hu, F.; Peng, A. D.; Yao, J. *Adv. Mater.* **2007**, *19*, 3554. (b) Xiao, Y.; Peng, H. D.; Wang, J. Y.; Wu, H. D.; Liu, Z. H.; Pan, G. B. *Phys. Chem. Chem. Phys.* **2016**, *18*, 7019.

(2) (a) Shin, W. S.; Lee, M.-G.; Verwilst, P.; Lee, J. H.; Chi, S.-G.; Kim, J. S. *Chem. Sci.* **2016**, *7*, 6050. (b) Nicol, A.; Qin, W.; Kwok, R. T. K.; Burkhartsmeyer, J. M.; Zhu, Z.; Su, H.; Luo, W.; Lam, J. W. Y.; Qian, J.; Wong, K. S.; Tang, B. Z. *Chem. Sci.* **2017**, *8*, 4634. (c) Cheng, Y.; Sun, C.; Ou, X.; Liu, B.; Lou, X.; Xia, F. *Chem. Sci.* **2017**, *8*, 4571.

(3) (a) Yu, T.; Ou, D.; Yang, Z.; Huang, Q.; Mao, Z.; Chen, J.; Zhang, Y.; Liu, S.; Xu, J.; Bryce, M. R.; Chi, Z. *Chem. Sci.* **2017**, *8*, 1163. (b) Okazaki, M.; Takeda, Y.; Data, P.; Pander, P.; Higginbotham, H.; Monkman, A. P.; Minakata, S. *Chem. Sci.* **2017**, *8*, 2677. (c) Qi, Q. K.; Liu, Y. F.; Fang, X. F.; Zhang, Y. M.; Chen, P.; Wang, Y.; Yang, B.; Xu, B.; Tian, W. J.; Zhang, S. X. A. *RSC Adv.* **2013**, *3*, 7996. (d) Luo, X. L.; Zhao, W. J.; Shi, J. Q.; Li, C. H.; Liu, Z. P.; Bo, Z. S.; Dong, Y. Q.; Tang, B. Z. *J. Phys. Chem. C* **2012**, *116*, 21967.

(4) (a) Zhao, Z.; Chen, S.; Lam, J. W. Y.; Wang, Z.; Lu, P.; Mahtab, F.; Sung, H. H. Y.; Williams, I. D.; Ma, Y.; Kwok, H. S.; Tang, B. Z. *J. Mater. Chem.* **2011**, *21*, 7210. (b) Tsujimoto, H.; Ha, D. G.; Markopoulos, G.; Chae, H. S.; Baldo, M. A.; Swager, T. M. *J. Am. Chem. Soc.* **2017**, *139*, 4894. (c) Tang, C. W.; Vanslyke, S. A. *Appl. Phys. Lett.* **1987**, *51*, 913.

(5) (a) Xie, Z.; Yang, B.; Li, F.; Cheng, G.; Liu, L.; Yang, G.; Xu, H.; Ye, L.; Hanif, M.; Liu, S.; Ma, D.; Ma, Y. *J. Am. Chem. Soc.* **2005**, *127*, 14152. (b) Lee, K. H.; Kwon, Y. S.; Lee, J. Y.; Kang, S.; Yook, K. S.; Jeon, S. O.; Lee, J. Y.; Yoon, S. S. *Chem. - Eur. J.* **2011**, *17*, 12994. (c) Mazumdar, P.; Das, D.; Sahoo, G. P.; Salgado-Moran, G.; Misra, A. *Phys. Chem. Chem. Phys.* **2014**, *16*, 6283. (d) Sharma, K.; Kaur, S.; Bhalla, V.; Kumar, M.; Gupta, A. *J. Mater. Chem. A* **2014**, *2*, 8369. (e) Li, J.; Li, P.; Wu, J.; Gao, J.; Xiong, W. W.; Zhang, G.; Zhao, Y.; Zhang, Q. *J. Org. Chem.* **2014**, *79*, 4438.

(6) Wang, C.; Liu, Z.; Li, M.; Xie, Y.; Li, B.; Wang, S.; Xue, S.; Peng, Q.; Chen, B.; Zhao, Z.; Li, Q.; Ge, Z.; Li, Z. *Chem. Sci.* **2017**, *8*, 3750.

(7) (a) Kuimova, M. K.; Botchway, S. W.; Parker, A. W.; Balaz, M.; Collins, H. A.; Anderson, H. L.; Suhling, K.; Ogilby, P. R. *Nat. Chem.* **2009**, *1*, 69. (b) Liu, T.; Liu, X.; Spring, D. R.; Qian, X.; Cui, J.; Xu, Z. *Sci. Rep.* **2015**, *4*, 5418. (c) Vyšniauskas, A.; Qurashi, M.; Gallop, N.; Balaz, M.; Anderson, H. L.; Kuimova, M. K. *Chem. Sci.* **2015**, *6*, 5773. (d) Sherin, P. S.; López-Duarte, I.; Dent, M. R.; Kubánková, M.; Vyšniauskas, A.; Bull, J. A.; Reshetnikova, E. S.; Klymchenko, A. S.; Tsentalovich, Y. P.; Kuimova, M. K. *Chem. Sci.* **2017**, *8*, 3523. (e) Qian, H.; Cousins, M. E.; Horak, E. H.; Wakefield, A.; Liptak, M. D.; Aprahamian, I. *Nat. Chem.* **2017**, *9*, 83. (f) Vyšniauskas, A.; Ding, D.; Qurashi, M.; Boczarow, I.; Balaz, M.; Anderson, H. L.; Kuimova, M. K. *Chem. - Eur. J.* **2017**, *23*, 11001.

(8) Qian, J.; Tang, B. Z. *Chem* **2017**, *3*, 56.

(9) (a) Mei, J.; Hong, Y.; Lam, J. W.; Qin, A.; Tang, Y.; Tang, B. Z. *Adv. Mater.* **2014**, *26*, 5429. (b) Mei, J.; Leung, N. L.; Kwok, R. T.; Lam, J. W.; Tang, B. Z. *Chem. Rev.* **2015**, *115*, 11718. (c) Xiong, J. B.; Feng, H. T.; Sun, J. P.; Xie, W. Z.; Yang, D.; Liu, M.; Zheng, Y. S. *J. Am. Chem. Soc.* **2016**, *138*, 11469.

(10) Ng, J. C. Y.; Liu, J.; Su, H.; Hong, Y.; Li, H.; Lam, J. W. Y.; Wong, K. S.; Tang, B. Z. *J. Mater. Chem. C* **2014**, *2*, 78.

(11) Lakowicz, J. R. *Principles of Fluorescence Spectroscopy*, 3rd ed.; Springer: New York, 2006.

(12) (a) Dong, Y.; Lam, J. W. Y.; Qin, A.; Liu, J.; Li, Z.; Tang, B. Z.; Sun, J.; Kwok, H. S. *Appl. Phys. Lett.* **2007**, *91*, 011111. (b) Zhao, Z.; Lam, J. W. Y.; Tang, B. Z. *Curr. Org. Chem.* **2010**, *14*, 2109. (c) Zhao, Z.; Lam, J. W. Y.; Tang, B. Z. *J. Mater. Chem.* **2012**, *22*, 23726. (d) Qi, Q.; Qian, J.; Ma, S.; Xu, B.; Zhang, S. X.; Tian, W. *Chem. - Eur. J.* **2015**, *21*, 1149. (e) Li, Y.; Liu, Y.; Zhou, H.; Chen, W.; Mei, J.; Su, J. *Chem. - Eur. J.* **2017**, *23*, 9280.

(13) (a) Kido, J.; Shionoya, H.; Nagai, K. *Appl. Phys. Lett.* **1995**, *67*, 2281. (b) Luo, J.; Xie, Z.; Lam, J. W. Y.; Cheng, L.; Chen, H.; Qiu, C.; Kwok, H. S.; Zhan, X.; Liu, Y.; Zhuc, D.; Tang, B. Z. *Chem. Commun.* **2001**, 1740. (c) Gao, X.-C.; Cao, H.; Huang, L.; Huang, Y.-Y.; Zhang, B.-W.; Huang, C.-H. *Appl. Surf. Sci.* **2003**, *210*, 183. (d) Chen, J.; Xu, B.; Ouyang, X.; Tang, B. Z.; Cao, Y. *J. Phys. Chem. A* **2004**, *108*, 7522. (e) Zhao, Y. S.; Peng, A.; Fu, H.; Ma, Y.; Yao, J. *Adv. Mater.* **2008**, *20*, 1661. (f) Shimizu, M.; Tatsumi, H.; Mochida, K.; Shimono, K.; Hiyama, T. *Chem. - Asian J.* **2009**, *4*, 1289. (g) Zhang, Z. Y.; Xu, B.; Su, J. H.; Shen, L. P.; Xie, Y. S.; Tian, H. *Angew. Chem., Int. Ed.* **2011**, *50*, 11654. (h) Feng, J.; Chen, X.; Han, Q.; Wang, H.; Lu, P.; Wang, Y. *J. Lumin.* **2011**, *131*, 2775. (i) Yang, L.; Ye, J.; Xu, L.; Yang, X.; Gong,

DOI: 10.1021/jacs.7b08570
J. Am. Chem. Soc. 2017, 139, 17882−17889

W.; Lin, Y.; Ning, G. *RSC Adv.* **2012**, *2*, 11529. (j) Zhang, X.; Ye, J.; Xu, L.; Yang, L.; Deng, D.; Ning, G. *J. Lumin.* **2013**, *139*, 28. (k) Zhao, Z.; He, B.; Nie, H.; Chen, B.; Lu, P.; Qin, A.; Tang, B. Z. *Chem. Commun.* **2014**, *50*, 1131. (l) Kojima, T.; Hiraoka, S. *Org. Lett.* **2014**, *16*, 1024. (m) Wunderlich, K.; Larsen, A.; Marakis, J.; Fytas, G.; Klapper, M.; Müllen, K. *Small* **2014**, *10*, 1914. (n) Zhang, J.; Xu, B.; Chen, J.; Ma, S.; Dong, Y.; Wang, L.; Li, B.; Ye, L.; Tian, W. *Adv. Mater.* **2014**, *26*, 739. (o) Chang, Z. F.; Jing, L. M.; Wei, C.; Dong, Y. P.; Ye, Y. C.; Zhao, Y. S.; Wang, J. L. *Chem. - Eur. J.* **2015**, *21*, 8504. (p) Zhu, Q.; Zhang, Y.; Nie, H.; Zhao, Z.; Liu, S.; Wong, K. S.; Tang, B. Z. *Chem. Sci.* **2015**, *6*, 4690. (q) Lungerich, D.; Reger, D.; Hçlzel, H.; Riedel, R.; Martin, M. M. J. C.; Hampel, F.; Jux, N. *Angew. Chem., Int. Ed.* **2016**, *55*, 5602. (r) Vij, V.; Bhalla, V.; Kumar, M. *Chem. Rev.* **2016**, *116*, 9565. (s) Zhang, Y.; He, B.; Luo, W.; Peng, H.; Chen, S.; Hu, R.; Qin, A.; Zhao, Z.; Tang, B. Z. *J. Mater. Chem. C* **2016**, *4*, 9316. (t) Yang, J.; Ren, Z.; Xie, Z.; Liu, Y.; Wang, C.; Xie, Y.; Peng, Q.; Xu, B.; Tian, W.; Zhang, F.; Chi, Z.; Li, Q.; Li, Z. *Angew. Chem., Int. Ed.* **2017**, *56*, 880.

(14) We use the term "dimer" to describe the pairs of similar (but not chemically equivalent) phenyl rings that exhibit close, face-to-face aromatic interactions through either intra- or intermolecular contacts. To avoid confusion, we have chosen not to use terms such as "excimer", which normally describes an intermolecular dimer formed in the excited state, and other more specific terminology.

(15) Emission spectra are reported in eV and are Jacobian corrected to allow meaningful comparisons of Stokes shifts between compounds, see: Mooney, J.; Kambhampati, P. *J. Phys. Chem. Lett.* **2013**, *4*, 3316.

(16) Previous reports have shown that the increasing viscosities of cold 2-MeTHF solutions can lead to restriction of molecular rotation, see: Lewis, F. D.; Liu, W. Z. *J. Phys. Chem. A* **2002**, *106*, 1976.

(17) Durig, J. R.; Kizer, K. L.; Karriker, J. M. *J. Raman Spectrosc.* **1973**, *1*, 17.

(18) Glass transition temperatures (T_g) have been determined previously for 2-MeTHF and 1:5 *v*/*v* MCH−*i*-pentane, see: (a) Kliger, D. S. *Ultrasensitive Laser Spectroscopy*, 1st ed.; Academic Press: New York, 1983. (b) Mizukami, M.; Fujimori, H.; Oguni, M. *Prog. Theor. Phys. Suppl.* **1997**, *126*, 79.

(19) (a) Mendelovici, E.; Frost, R. L.; Kloprogge, T. *J. Raman Spectrosc.* **2000**, *31*, 1121. (b) Matsuura, H.; Miyazawa, T.; Hiraishi, M. *Spectrochim. Acta Part A Mol. Spectrosc.* **1972**, *A 28*, 2299.

(20) The average expected intermolecular distance at these concentrations is approximately 100 nm. Variable concentration studies show a lack of concentration-dependent shifts in emission that would be expected for an intermolecular phenomenon. See Figure S32.

(21) Kuimova, M. K.; Yahioglu, G.; Levitt, J. A.; Suhling, K. *J. Am. Chem. Soc.* **2008**, *130*, 6672.

(22) Wiggins, P.; Williams, J. A.; Tozer, D. J. *J. Chem. Phys.* **2009**, *131*, 091101.

(23) It is well known that the wavelengths of light emitted from traditional, planar organic chromophores are dependent on the overlap and orientation of π-surfaces. Although this analysis is usually applied to large, polycyclic π-systems, such as perylene, it may also be applied to simple phenyl rings, see: Hestand, N. J.; Spano, F. C. *Acc. Chem. Res.* **2017**, *50*, 341.

(24) For precedent supporting the assignment of excimer-like states in phenyl-ring pairs, see: (a) Hirayama, F. *J. Chem. Phys.* **1965**, *42*, 3163. (b) Nishihara, T.; Kaneko, M. *Makromol. Chem.* **1969**, *124*, 84. (c) Avouris, P.; Ashraf El-Bayoumi, M. *Chem. Phys. Lett.* **1973**, *20*, 59. (d) Tsai, F. J.; Torkelson, J. M. *Polymer* **1988**, *29*, 1004.

(25) While this Article was under review, a manuscript was submitted detailing the interactions between aromatic rings in tetraarylethanes: Zhang, H.; Zheng, X.; Xie, N.; He, Z.; Liu, J.; Leung, N. L. C; Niu, Y.; Huang, X.; Wong, K. S.; Kwok, R. T. K.; Sung, H. H. Y.; Williams, I. D.; Qin, A.; Lam, J. W. Y.; Tang, B. Z. *J. Am. Chem. Soc.* **2017**, *139*, 16264.

(26) Through-space electronic interactions have been observed for macrocycles that constrain aromatic systems at torsional angles of ~60°, see: Schneebeli, S. T.; Frasconi, M.; Liu, Z.; Wu, Y.; Gardner, D. M.; Strutt, N. L.; Cheng, C.; Carmieli, R.; Wasielewski, M. R.; Stoddart, J. F. *Angew. Chem., Int. Ed.* **2013**, *52*, 13100.

(27) Rapid, large-amplitude motions are uncommon in crystals, but they can be engineered by designing crystalline solids with large cavities, see: (a) Jiang, X.; O'Brien, Z. J.; Yang, S.; Lai, L. H.; Buenaflor, J.; Tan, C.; Khan, S.; Houk, K. N.; Garcia-Garibay, M. A. *J. Am. Chem. Soc.* **2016**, *138*, 4650. (b) Catalano, L.; Perez-Estrada, S.; Wang, H. H.; Ayitou, A. J. L.; Khan, S. I.; Terraneo, G.; Metrangolo, P.; Brown, S.; Garcia-Garibay, M. A. *J. Am. Chem. Soc.* **2017**, *139*, 843.

(28) Onset values are used as they better represent the highest energy transition of species that have a broadband emission, for example, charge-transfer states, see: (a) Etherington, M. K.; Gibson, J.; Higginbotham, H. F.; Penfold, T. J.; Monkman, A. P. *Nat. Commun.* **2016**, *7*, 13680. (b) Turro, N. J.; Ramamurthy, V.; Scaiano, J. C. *Principles of Molecular Photochemistry: An Introduction*, 1st ed.; University Science Books: South Orange, NJ, 2009.

(29) See Section 16 of the Supporting Information.

(30) Through-space interactions of π-systems have previously been shown to influence the emission of AIE-active luminogens, based upon the conventional interactions of donor−acceptor pairs or large polycyclic systems: (a) Dai, Q.; Liu, W.; Zeng, L.; Lee, C.-S.; Wu, J.; Wang, P. *CrystEngComm* **2011**, *13*, 4617. (b) Liu, Y.; Zhang, Y.; Wu, X.; Lan, Q.; Chen, C.; Liu, S.; Chi, Z.; Jiang, L.; Chen, X.; Xu, J. *J. Mater. Chem. C* **2014**, *2*, 1068. See also ref 4a.

(31) The size of polystyrene macrocycles has been found to dictate the relative amount of excimer-like fluorescence. This effect has been ascribed to changes in the relative orientations of phenyl rings, see: Gan, Y. D.; Dong, D. H.; Carlotti, S.; Hogen-Esch, T. E. *J. Am. Chem. Soc.* **2000**, *122*, 2130.

(32) Martinez, C. R.; Iverson, B. L. *Chem. Sci.* **2012**, *3*, 2191.

(33) (a) Burley, S. K.; Petsko, G. A. *Science* **1985**, *229*, 23. (b) Sun, S.; Bernstein, E. R. *J. Phys. Chem.* **1996**, *100*, 13348. (c) Aravinda, S.; Shamala, N.; Das, C.; Sriranjini, A.; Karle, I. L.; Balaram, P. *J. Am. Chem. Soc.* **2003**, *125*, 5308.

DOI: 10.1021/jacs.7b08570
J. Am. Chem. Soc. 2017, 139, 17882−17889

THE JOURNAL OF PHYSICAL CHEMISTRY C

Article

Cite This: J. Phys. Chem. C 2019, 123, 11109−11117

pubs.acs.org/JPCC

Persistent Dimer Emission in Thermally Activated Delayed Fluorescence Materials

Marc K. Etherington,*[,†] Nadzeya A. Kukhta,[‡] Heather F. Higginbotham,[†] Andrew Danos,[†] Aisha N. Bismillah,[‡] David R. Graves,[†] Paul R. McGonigal,[‡] Nils Haase,[§,∥] Antonia Morherr,[§] Andrei S. Batsanov,[‡] Christof Pflumm,[§] Vandana Bhalla,[‡,⊥] Martin R. Bryce,[‡] and Andrew P. Monkman[†]

[†]Department of Physics and [‡]Department of Chemistry, Durham University, South Road, Durham DH1 3LE, U.K.

[§]Merck KGaA, Performance Materials—Display Solutions, Frankfurter Straße 250, 64293 Darmstadt, Germany

[∥]Institute of Physics, Experimental Physics IV, University of Augsburg, Universitätsstr. 1, 86135 Augsburg, Germany

[⊥]Department of Chemistry, Guru Nanak Dev University, Grand Trunk Road, Off NH 1, Amritsar, Punjab 143005, India

Supporting Information

ABSTRACT: We expose significant changes in the emission color of carbazole-based thermally activated delayed fluorescence (TADF) emitters that arise from the presence of persistent dimer states in thin films and organic light-emitting diodes (OLEDs). Direct photoexcitation of this dimer state in 1,2,3,5-tetrakis(carbazol-9-yl)-4,6-dicyanobenzene (**4CzIPN**) reveals the significant influence of dimer species on the color purity of its photoluminescence and electroluminescence. The dimer species is sensitive to the sample preparation method, and its enduring presence contributes to the widely reported concentration-mediated red shift in the photoluminescence and electroluminescence of evaporated thin films. This discovery has implications on the usability of these, and similar, molecules for OLEDs and explains disparate electroluminescence spectra presented in the literature for these compounds. The dimerization-controlled changes observed in the TADF process and photoluminescence efficiency mean that careful consideration of dimer states is imperative in the design of future TADF emitters and the interpretation of previously reported studies of carbazole-based TADF materials.

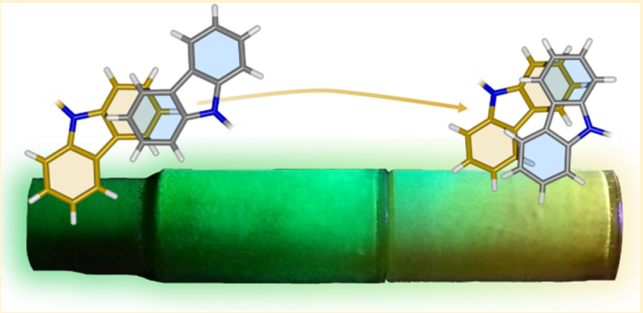

INTRODUCTION

Thermally activated delayed fluorescence (TADF) has become a topic of intense interest to improve the performance of organic light-emitting diodes (OLEDs) through the utilization of the nonemissive triplet manifold.[1−3] The triplet states formed in the emitter molecules during device operation are converted back into emissive singlet states through the reverse intersystem crossing (rISC) mechanism. Recent experimental and theoretical evidence has shown that rISC in these organic emitters is not simply reliant on a small singlet−triplet gap between two states, but that spin-vibronic coupling plays a significant role.[4,5]

A typical molecular scheme to achieve TADF is a donor−acceptor (D−A) system that can form intramolecular charge-transfer (CT) states with a very small singlet−triplet energy gap. However, there is significant evidence to suggest that a close-in-energy locally excited triplet state (^{3}LE) is required to mediate rISC between the charge-transfer triplet (^{3}CT) and charge-transfer singlet (^{1}CT) states.[4,5] This mediation of rISC by ^{3}LE is the basis of the spin-vibronic coupling mechanism. Due to the sensitivity of these CT states to their local environment (i.e., solvent or solid-state host), the spin-vibronic model explains the ability to tune the rISC and TADF by changing the polarity of the host, and thus minimizing the energy gap between the CT manifold and ^{3}LE.[6−8] As a result, the choice of emitter host has become a crucial factor during OLED fabrication.

Going beyond the polarity of the host, concentration-induced shifts of the photoluminescence[9−11] and electroluminescence[12−17] maxima in samples that employ 1,2,3,5-tetrakis(carbazol-9-yl)-4,6-dicyanobenzene (**4CzIPN**) as an emitter are commonly reported in the literature. A study by Kim et al.[9] showed that increasing the concentration of **4CzIPN** in a nonpolar host caused a significant shift in the CT state emission of **4CzIPN**. They attributed this shift to the polarity of the dopant **4CzIPN** molecules (ground-state dipole moment, 3.95 D[18]) influencing other **4CzIPN** molecules indirectly, just as solvent molecules would do in solution. Due to its similarity to the polarity effect of solvents on CT state emission, the shift of CT emission in films is known as the solid-state solvation effect (SSSE). It implies that consideration

Received: February 14, 2019
Published: April 3, 2019

of the concentration of the emitter is also an important variable for fabrication of TADF OLEDs.

However, recent work by Northey et al.[19] has shown that SSSE is not as effective as the analogous phenomenon in liquid solvents in changing the emission of CT states when comparing solvents and hosts of similar polarity. The difference arises due to the inability of the solid-state host to reorganize around the emitter molecule, which is the manifold that gives rise to the solvatochromism in solution. In this work, we use **4CzIPN** (Figure 1a) to demonstrate that, rather than

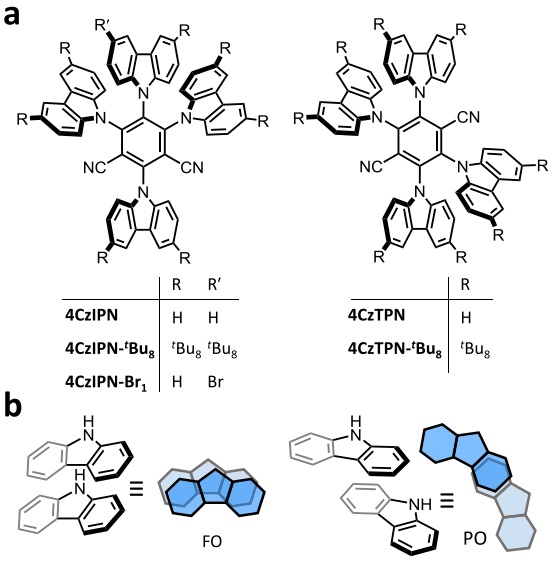

Figure 1. (a) Structural formulas of TADF-active compounds. (b) Fully overlapped (FO) and partially overlapped (PO) dimers formed by two carbazole units.

SSSE, the formation of aggregated/dimer states is instead the predominant reason for the significant emission shifts observed with concentration for multi-carbazole TADF emitters. This explanation is based on the wealth of literature relating to carbazole-based compounds, e.g., poly(*N*-vinylcarbazole) (PVK) and 4,4′-bis(*N*-carbazolyl)-1,1′-biphenyl (CBP) as well as carbazole's known propensity for intermolecular interactions through either fully overlapped (FO) or partially overlapped (PO) co-facial dimers (Figure 1b).[20−24] This aggregate/dimer interpretation is built on recent work performed on several multifunctional materials that exhibit aggregation-induced emission, TADF, and mechanochromic luminescence (MCL)[25−30] while enabling further discussion on how to tackle the problem of color purity for TADF molecules. On this basis, we expect that future studies of TADF-active emitters will benefit from the use of a broader range of analytical techniques to fully interpret novel molecules' properties.

RESULTS AND DISCUSSION

In this study, **4CzIPN** is used as the model system. However, to provide supporting evidence for the conclusions and to expand the generality of our findings, four other similar molecules were also investigated (Figure 1a). Synthetic procedures and NMR spectroscopic characterization can be found in Schemes S1−S3 and Figures S1−S8 in the Supporting Information.

Photoluminescence of Dilute Solutions and Crystals.

Differences in the emission energy between dilute solutions and crystals are not conclusive evidence for aggregation/dimerization and could be explained by SSSE. However, the significant emission shifts we observed for all molecules (Figures 2a,b and S9) would be difficult to explain by SSSE

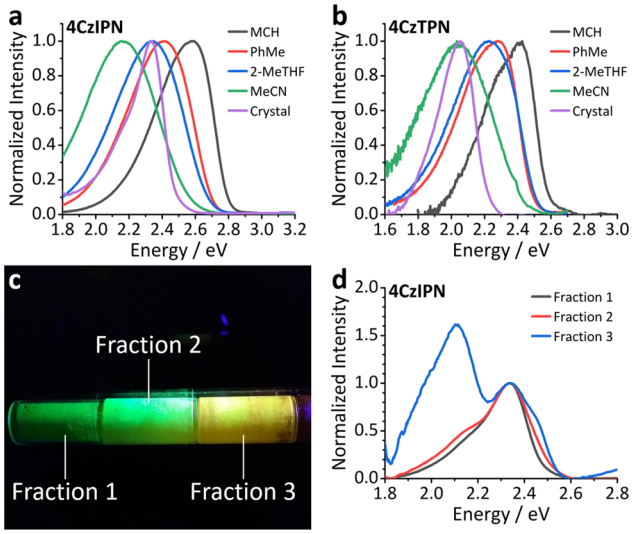

Figure 2. (a) Steady-state photoluminescence of **4CzIPN** in a series of solvents (20 μm) and in crystal form (Fraction 1 from sublimation). (b) Solvent series for **4CzTPN** (10 μm, due to low solubility) and as a crystal (Fraction 1 from sublimation). (c) Photograph of **4CzIPN** after sublimation. The sublimation tube is illuminated by an ultraviolet torch and the observed colors are indicative of crystal polymorphs with different emission properties. The regions referred to as Fractions 1, 2, and 3 are labelled. (d) The steady-state fluorescence spectra of Fractions 1, 2, and 3 of **4CzIPN**.

alone. The energies of the peaks and onsets of the emission spectra of the molecules in solution and crystal states are shown in Table 1.

The crystals of both **4CzIPN** and **4CzTPN** have an emission onset lower in energy than equivalent solutions in acetonitrile. If the shifts in emission energies were solely a result of SSSE, considering the findings reported by Northey et al., it would imply that these small molecules have the same solvation effect as acetonitrile (dielectric constant (ε) = 37.5), even though they lack the ability to reorganize. Furthermore, while the full-width at half-maximum (FWHM) of a molecule's CT emission profile typically increases with increasing solvent polarity,[31−33] the emission spectra of the crystals feature relatively sharp peaks. Therefore, their narrower FWHM contradicts the hypothesis that the solid-state emission energies are influenced significantly by SSSE. We suggest that the red shift in emission is instead a result of direct intermolecular interactions.

The need to go beyond SSSE as an explanation for these emission shifts is further emphasized in Figure S10 which shows the difference between polycrystalline **4CzTPN** and **4CzTPN** in dimethylsulfoxide (DMSO). Upon allowing the crystals to take up DMSO solvent, we observe that the fluorescence of the polycrystalline sample changes from orange to yellow (emission blue shift). This would suggest that **4CzTPN** in the crystal has a polarity effect greater than DMSO (ε = 47.2)! Based on the findings by Northey et al.,[19] we consider it implausible that such a solid-state shift arises from SSSE, thus we must consider that the breakup of the

DOI: 10.1021/acs.jpcc.9b01458
J. Phys. Chem. C 2019, 123, 11109−11117

Table 1. Onset and Peak Emission Energies of the Compounds in Solution and Crystal States[a]

compound	MCH	PhMe	2-MeTHF	MeCN	crystal
4CzIPN	2.80 (2.58)	2.71 (2.41)	2.68 (2.34)	2.57 (2.16)	2.47 (2.33)
4CzTPN	2.58 (2.42)	2.49 (2.28)	2.52 (2.22)	2.44 (2.04)	2.23 (2.06)
4CzIPN-^{t}Bu$_8$	2.68 (2.47)	2.60 (2.33)	2.58 (2.25)	2.44 (2.05)	2.52 (2.35)
4CzTPN-^{t}Bu$_8$	2.48 (2.34)	2.41 (2.21)	2.41 (2.16)		2.21 (2.04)
4CzIPN-Br$_1$	2.80 (2.60)	2.72 (2.43)	2.71 (2.35)	2.57 (2.16)	2.50 (2.27)

[a]Peak energies are in parentheses. All values are in eV.

intermolecular interactions (dimerization/aggregation) is the cause for such a large perturbation of the emission. Figure S9 also reveals that the bulky *tert*-butyl groups of **4CzIPN-^{t}Bu$_8$** and **4CzTPN-^{t}Bu$_8$** do very little to stop dimer formation in these molecules, as they behave like their non-tert-butylated analogues.

The spectra attributed to the crystal form for these compounds relate to the first fraction obtained by sublimation, "Fraction 1", which is identified in the photograph (Figure 2c) using **4CzIPN** as an example. It is also apparent from this photograph and Figure 2d that the emission color of **4CzIPN** changes as a function of recrystallization temperature along the sublimation tube. These differences in the emission spectra of the sublimation "Fractions" of **4CzIPN** will be explained in more detail later.

Photoluminescence of Doped Zeonex Thin Films. These intermolecular interactions not only dominate in the crystalline form but are also present in doped thin films. Figure 3 shows that the emission spectra of **4CzIPN**-doped zeonex

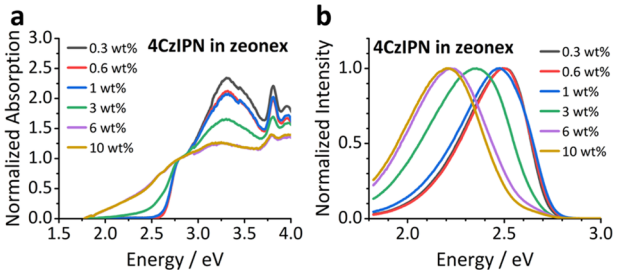

Figure 3. (a) Normalized absorption of **4CzIPN** in a zeonex host at different doping concentrations. The band edge begins to red-shift at 1 wt %, with the shift saturating between 6 and 10 wt %. (b) The photoluminescence of the same films showing the same red shift in emission with increasing concentration. The shift occurs at the same concentrations as for the absorption and again saturates between 6 and 10 wt %. The high-energy tail in the high concentration films (3 wt % and above) is attributed to inhomogeneous dimer/aggregate formation, leaving regions of relatively isolated **4CzIPN**.

films red-shift as a function of increasing concentration of the emitter. At 10 weight percent (wt %), the emission profile resembles that observed by Kim et al.[9] in neat film. Due to the high viscosity of zeonex, we ruled out large rotational movement of the carbazole donor moieties in the excited state as the cause of this emission shifts—an assumption supported by studying the variable-temperature NMR (VT NMR) spectra of **4CzIPN-Br$_1$** (Figure S11). The ground-state barrier to 180° rotation around the carbazole N−C bond was found to be >87 kJ/mol in solution (see the VT NMR Spectroscopy section of the Supporting Information). Furthermore, there is a red shift in the absorption band of the films with increasing **4CzIPN** concentration, which cannot be explained by SSSE and instead we attribute to the presence of ground-state dimers. This new absorption band allows for direct excitation of a charge-transfer dimer state (^{1}CT$_D$).

The time-resolved photoluminescence of ^{1}CT$_D$ in **4CzIPN** (Figure 4) was measured by exciting the 10 wt % film at

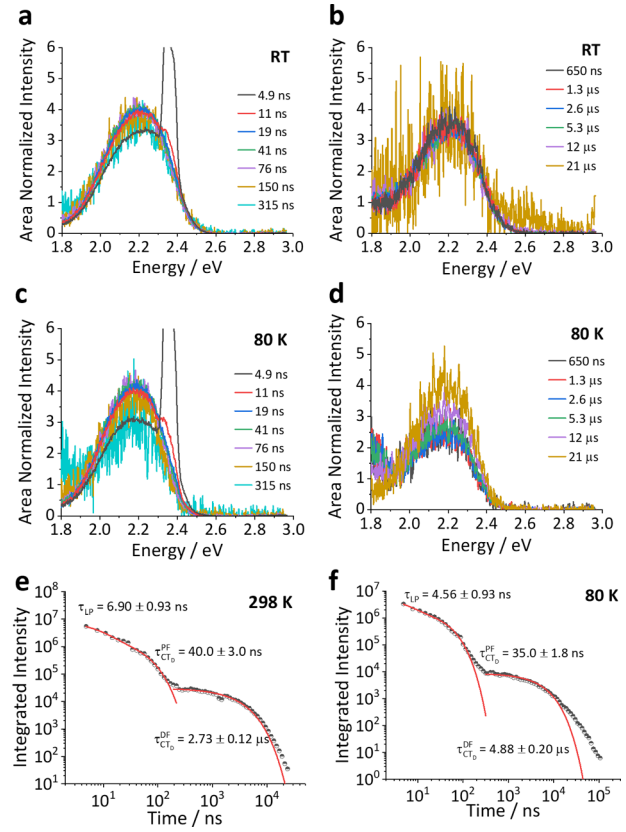

Figure 4. Time-resolved emission spectra and decays of 10 wt % doped **4CzIPN**:zeonex film excited at 532 nm. (a, b) The room temperature spectra of the film, showing the consistent line shape maintained throughout the prompt and delayed time regions. (c, d) The spectra also remain unchanged at 80 K, and TADF is still observed, suggesting a very small singlet−triplet gap. (e) Time-resolved emission decay at RT and (f) at 80 K.

2.33 eV [532 nm], which is significantly below the **4CzIPN** monomer charge-transfer (^{1}CT$_M$) absorption (2.5 eV). The emission spectrum of ^{1}CT$_D$ remains constant as a function of time and is identical to that observed in both the high concentration films in Figure 3 and the emission spectra of the neat films reported in the literature.[9,11] ^{1}CT$_D$ is also found to be TADF active, meaning that it is not just the monomer species of **4CzIPN** that undergoes rISC in this material. The delayed fluorescence (DF) lifetime of ^{1}CT$_D$ is 2.7 μs at room temperature (RT), which increases to 4.8 μs at 80 K. The presence of delayed emission at 80 K suggests an efficient rISC process and a small singlet−triplet energy gap for ^{1}CT$_D$. The

DOI: 10.1021/acs.jpcc.9b01458
J. Phys. Chem. C 2019, 123, 11109−11117

full kinetic fittings for the room temperature and 80 K data are shown in Table S1. All of the data include a short lifetime (4–6 ns) contribution, arising from the tail of the high-energy laser pulse (>200 μJ) required to achieve reasonable signal-to-noise using direct ^1CT_D excitation.

Overlaying the prompt emission spectra of ^1CT_D with the time-resolved photoluminescence spectra of the 0.3, 1, and 10 wt % films (excited at 355 nm i.e., into the monomer absorption band) allows the significant influence of this dimer state to be fully uncovered (Figure 5).

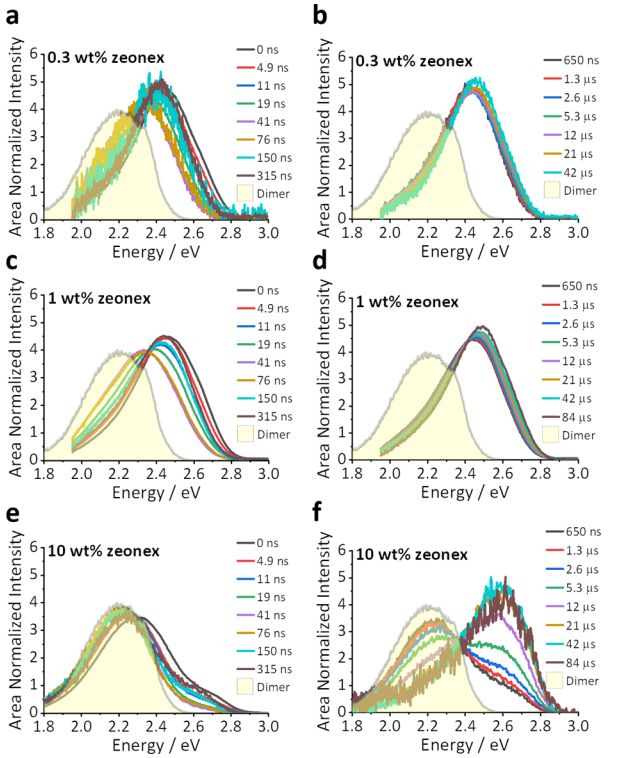

Figure 5. Time-resolved emission spectra of the doped **4CzIPN**:zeonex films at room temperature. (a, b) The prompt and delayed emission of the 0.3 wt % doped film, which is dominated by monomer emission in a nonpolar environment (onset 2.78 eV [446 nm]). (c, d) The 1 wt % film has a small red shift at intermediate times of 50–100 ns because of the dimeric species and returns to full monomer TADF at longer times. (e, f) The 10 wt % film is dominated by the dimer emission but has contributions from the monomer species at prompt and long times, a result of the slower rISC rate for the CT_M in a nonpolar environment. The filled yellow peak overlaid in each panel is the dimer emission observed after a 11 ns delay time from a 10 wt % zeonex film of **4CzIPN** at RT using 532 nm excitation (as shown in Figure 4a).

While the 10 wt % film emission is predominantly from ^1CT_D (shaded area), even in the 1 wt % film there is also a small red shift at intermediate times as a result of the dimer. The observation of dimer contribution in such a dilute film is very surprising and conflicts with the assumption (often tacit) in previous studies of **4CzIPN** that emission from "low" concentration films (<10%) comes exclusively from the monomer. In the 10 wt % films, a small contribution from ^1CT_M is present, which accounts for the high-energy onset of 2.78 eV [446 nm] in the prompt spectra. This high-energy component is absent with 532 nm excitation, giving further support to the assertion that the 532 nm laser excites ^1CT_D directly, rather than through donor ^1LE excitation. The formation of ^1CT_M by 355 nm excitation accounts for the emergence of monomer TADF line shape in the 10 wt % film at longer times. The full shifts of the emission peaks of these doped films as a function of concentration and temperature are shown in Figure S12.

The prompt lifetimes of ^1CT_M in these films is approximately 5–7 ns, which is shorter than the 8 ns lifetime observed for ^1CT_M in methylcyclohexane (MCH) solution (Figure S13 and Table S2). This small reduction in lifetime is attributed to quenching of ^1CT_M to form ^1CT_D states (lifetime 20–30 ns) in the solid state. The 10 wt % film at room temperature has a shorter DF lifetime (2.05 μs) than the MCH solution and 0.3 and 1 wt % films, which is attributed to the faster rISC in ^1CT_D. The full decay profiles and fittings are shown in Figure S14 and Tables S3–S5.

The photoluminescence quantum yields (PLQYs) of the 10 and 1 wt % films were measured to identify if quenching processes shorten the measured DF lifetimes. The natural lifetimes for the DF are shown in Table S6. Even considering the significant reduction in PLQY with increasing concentration, the natural lifetime of ^1CT_D is still shorter than ^1CT_M, consistent with the smaller ^1CT_D–^3LE_D energy gap (ΔE_{ST} for the dimer).

Spectra and decays obtained at 80 K (Figure S15) show that the ^1CT_M TADF in the 0.3 and 1 wt % films is significantly reduced, although delayed emission from ^1CT_D remains. This smaller temperature dependence in the ^1CT_D delayed emission intensity is further evidence that ^1CT_D has a much smaller singlet–triplet energy gap—with its associated dimeric locally excited triplet (^3LE_D)—than the monomer. This phenomenon is also seen in the 10 wt % film, where the ^1CT_D exhibits significant TADF even at 80 K. For all films at long times, the phosphorescence of the monomer species (^3LE_M) is observed (onset 2.69 eV [460 nm]), which is a direct result of the excitation wavelength (355 nm) exciting the ^1LE_M state of the molecule.

Excitation fluence dependence measurements of the delayed emission (Figures S16 and S17) confirm that emission arises from TADF and not any bimolecular process occurring in the aggregate regions, even at low temperature where rISC is inhibited.

Evaporated Films and Device Physics. The photophysical analysis of the doped zeonex films demonstrates that dimer formation for **4CzIPN** and related molecules is critically dependent on the conditions of sample preparation. In Figure 6, the photoluminescence spectra of evaporated films of **4CzIPN** in 3,3′-bis(*N*-carbazolyl)-1,1′-biphenyl (mCBP) show the same trend as that observed in zeonex films. This surprising presence of dimer species even in evaporated films also explains the observed behavior of **4CzIPN** and related materials in OLED devices.

This red shift in emission is also replicated in the electroluminescence spectra from model devices with an emissive layer of **4CzIPN** co-doped in mCBP at different concentrations. A full series of concentration measurements is shown in Figure S18, and the device structure is detailed in the caption of Figure 6. The changes in the electroluminescence spectra are consistent with the photoluminescence emission[9−11] and are thus independent of the device structure and transport layers. The phenomena are related to the emissive layer only and are consistent with the emission red shifts reported in solution-processed and evaporated films by

DOI: 10.1021/acs.jpcc.9b01458
J. Phys. Chem. C 2019, 123, 11109−11117

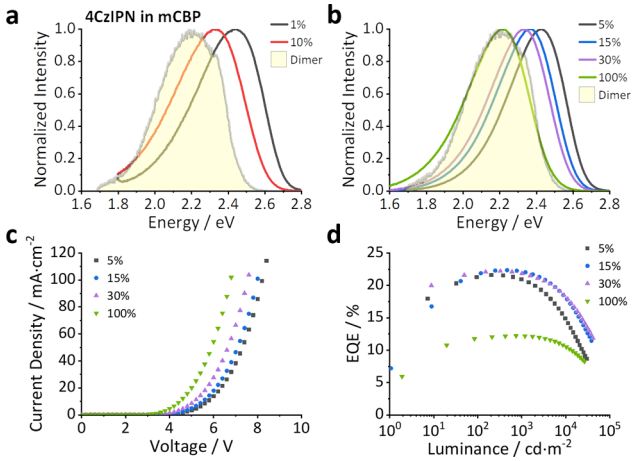

Figure 6. Photoluminescence from evaporated films and device data from a **4CzIPN** OLED. (a) Emission from 100 nm evaporated films of **4CzIPN** doped into mCBP. (b) The electroluminescence from a device with a **4CzIPN**-doped mCBP emissive layer of different concentrations (X = 5, 15, 30, 100). (c) The current density voltage curves and (d) the external quantum efficiency (EQE) versus luminance curves of the same series of devices. The device structure used for these measurements was indium tin oxide (ITO) (20 nm)/buffer (20 nm)/hole injection layer (20 nm)/hole transport layer (30 nm)/electron blocking layer (10 nm)/mCBP:**4CzIPN** (X%, 15 nm)/hole blocking layer (10 nm)/electron transport layer (40 nm)/aluminum (100 nm).

others.[9,10,12−16] Device data shown in Figure 6c,d demonstrate that the monomer and dimer concentrations within the emissive layer play a dominant role in all aspects of the device performance, both electrical and optical. The current−voltage (J−V) and EQE curves for the full device series are shown in Figure S18. The data demonstrate that dimer formation in **4CzIPN** and related compounds is present and influences the emission color at typical concentrations used in device fabrication.

Pristine and Annealed Neat Films. The dimer state in **4CzIPN** can be controlled through thermal annealing. This was demonstrated by measuring the emission of a neat dropcast film before and after heating to 250 °C. Upon heating, the emission onset of the film blue-shifted from 2.55 eV [486 nm] to 2.66 eV [466 nm] (Figure S19). This was attributed to the breakup of dimer species in the pristine film and is a property shared by **4CzIPN** and **4CzIPN-^{t}Bu$_8$** as shown in Videos S1 and S2. This further implies that the addition of *tert*-butyl groups to the compounds is insufficient to prevent these intermolecular interactions. The process is also completely reversible by dissolving the annealed film in solvent.

Interestingly, the emission onset of the annealed film is lower in energy than that of the dilute (0.3 and 1 wt %) films even though it is most likely the monomer state of **4CzIPN**. The comparison of the onset and peak energies of the emission for the pristine, annealed, and 1 wt % films is shown in Table 2, alongside the singlet−triplet gap and empirical rISC rate. The difference between the annealed and 1 wt % emission is attributed to SSSE and the mechanism proposed by Kim et al.;[9] however, the further shift between the annealed and pristine films arises from the intermolecular interactions.

Emission from ^1CT_D still dominates the time-resolved spectra of the pristine neat film at room temperature and 80 K, whereas the annealed film retains the higher energy contribution from ^1CT_M (Figures S20 and S21). At longer times in the 80 K spectra, both films tend toward the dimer phosphorescence (^3LE_D), which is almost isoenergetic to the ^1CT_D emission. The lifetime fits are shown in Figure S22 and Tables S7, S8.

By comparing the natural lifetimes (see Table S6) of the films, ^1CT_M in a neat film is found to have a shorter DF lifetime than ^1CT_D, even though they have very similar energy gaps. The rISC rate of ^1CT_M is slow in zeonex and fast in the annealed film due to the change in the ^1CT_M−^3LE_M energy gap from 0.09 eV to approximately 0.03 eV due to SSSE. The experimentally calculated rISC rate of ^1CT_D is quite low considering its small singlet−triplet energy gap. However, this is attributed to the low PLQY of the dimer state.

Sublimed Crystals. To deconvolute the steady-state spectra of the **4CzIPN** crystals obtained after sublimation, the time-resolved photoluminescence of these samples was analyzed (see Figures S23 and S24). While the spectra are dominated by ^1CT_D emission, all fractions have a small contribution from ^1CT_M, resulting in the high-energy onset above 2.6 eV [477 nm]. This monomer contribution is more prominent in Fractions 2 and 3, where there is also a blue shift in the TADF. The prompt and DF emission lifetimes of ^1CT_M and ^1CT_D are consistent with those observed in the neat films (Figure S25 and Tables S9−S11).

The structure observed in the time-resolved spectra of the sublimed crystals is attributed to the nature of the dimer state. We consider the dimers to be intermolecular species, and there will be a fixed distance between the carbazoles in a single crystal. Consequently, certain modes and geometries will be prevalent. This phenomenon is the origin of the vibronic structure in the spectra of the sublimed crystals.

Upon analyzing the powder X-ray diffraction (PXRD) data obtained from these samples (Figure S26a), it appears that the contribution from ^1CT_M in Fractions 2 and 3 is due to a reduction in the long-range intermolecular order. The diffraction patterns from the powdered samples are in good agreement with the simulated PXRD pattern based on the single crystal X-ray structure of material obtained from Fraction 1 (Figure S26b).

Solvent-Grown Crystals. Crystals formed as solvates were grown from solvent mixtures of acetone/hexanes, tetrahydrofuran (THF)/hexanes, and chloroform/hexanes. The 532 nm-excited ^1CT_D spectrum matches perfectly with the time-resolved emission of these solvent-grown crystals (Figures S27

Table 2. Measured Energies of ^{1}CT and ^{3}LE, Respective $\Delta E_{S\text{-}T}$, and Reverse Intersystem Crossing Rates of 4CzIPN Samples[a]

sample	^{1}CT/eV	^{3}LE/eV	$\Delta E_{S\text{-}T}$/eV	k_{rISC} ($\times 10^5$ s^{-1})
1 wt % zeonex film	2.78 (2.48)	2.69 (2.43)	0.09	3.8
pristine	2.48 (2.26)	2.50 (2.28)	0.02	1.2
annealed	2.66 (2.43)	2.69 (2.43)[b], 2.50 (2.23)[c]	0.03[b], 0.16[c]	28

[a]Peak energies are in parentheses. [b]Monomer ^{3}LE. [c]Dimer ^{3}LE.

DOI: 10.1021/acs.jpcc.9b01458
J. Phys. Chem. C 2019, 123, 11109−11117

and S28), as do the decay lifetimes (Figure S29 and Tables S12−S14).

Crystal Structures and Polymorphism. Single crystal X-ray diffraction data of the Fraction 1 sublimed crystals of **4CzIPN** and **4CzTPN** (Figure 7) reveal face-to-face contacts

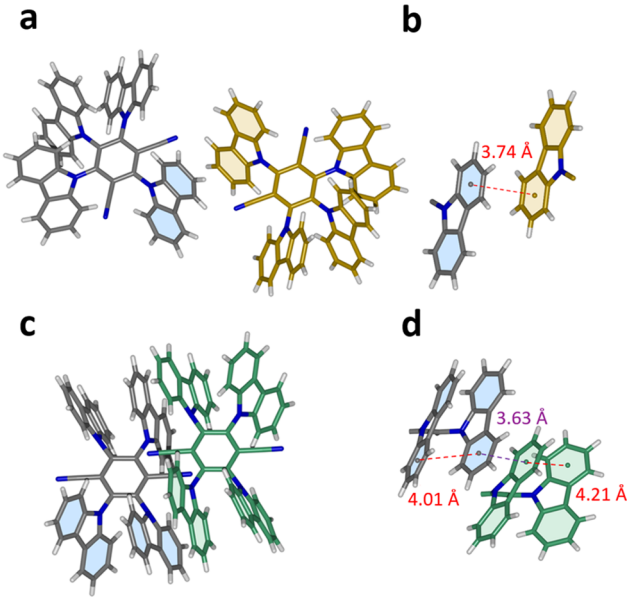

Figure 7. Packing in the crystal structures of **4CzIPN** and **4CzTPN** obtained by sublimation. (a) Two neighboring molecules of **4CzIPN** with the carbazoles involved in the interaction are highlighted. (b) The measured distance between the two interacting molecules. (c) Two neighboring molecules of **4CzTPN** with the carbazoles involved are highlighted. (d) The intermolecular and intramolecular distances between the involved carbazoles.

between the aromatic groups of the molecules, particularly in the structure of **4CzTPN**. **4CzIPN** also has some neighboring-molecule interactions reminiscent of PO carbazole dimers (Figure 1b), which account for the red shift compared to MCH solution in Figure 2a. The same is true for the remaining compounds in the series (Figures S30 and S31). The dimer emission in the solvent-grown crystals is also explained by these interactions (Figures S32 and S33).

Although **4CzIPN** was isolated as a crystalline solid after synthesis, the sublimation of the sample gave several visually different fractions (Figure 2c). Nonetheless, all fractions gave NMR spectra identical to the original material showing that these changes in appearance, like the color change of the annealed neat film, are not a result of decomposition. Fractions 1 and 2 were characterized by differential scanning calorimetry (DSC) (Figure S34) and thermogravimetric analysis (TGA) (Figure S35). For both fractions, the DSC data show two endothermic peaks: a sharp one at 651.0 K and a shoulder at 650.7 K that is more pronounced in Fraction 2. These observations are consistent with the presence of polymorphs of **4CzIPN** in the sublimed fractions. Different temperatures of initial decomposition (676 and 685 K for Fractions 1 and 2, respectively) were observed by TGA, which also supports the presence of polymorphs.

The DSC data of the solvent-grown crystals show several possible melting peaks ranging from 650.1 to 651.0 K (Figure S34), whose prevalence depends on the preparation conditions. Upon grinding the crystals obtained from chloroform/hexanes, only one sharp melting peak at 650.1 K appears in the DSC. This observation provides evidence that mechanical force can modulate the dimer formation in solid-state samples of this compound (to be discussed in detail later).

On the other hand, **4CzTPN** and **4CzTPN-^{t}Bu$_8$** do not show polymorphism. After sublimation, both **4CzTPN** and **4CzTPN-^{t}Bu$_8$** retain their orange color both in reflectance and fluorescence, characteristics that are attributed to the dimer species of these molecules. The emission profiles also do not change during the excited-state lifetime of **4CzTPN** at room temperature and 80 K (Figure S36), which is attributed to the intermolecular interactions/dimers that are seen in its crystal structure (Figure 7). The DF lifetime of the dimer state in **4CzTPN** at room temperature is 1.89 μs as shown in Figure S36 and Table S15. The lifetime fit at 80 K is shown in Figure S37.

Mechanochromic Luminescence (MCL). The MCL of **4CzIPN** (Figure S38) is also related to these dimeric interactions. When crystals of sublimed **4CzIPN** were ground by hand in a pestle and mortar, a significant red shift and broadening of the emission occurred. This red shift was attributed to an increase of the dimer states and the resultant emission is consistent with that of ^{1}CT$_D$. However, when a host molecule was included in the grinding, weaker MCL and a reduced red shift in emission were observed. Even the introduction of a polar host bis[2-(diphenylphosphino)phenyl] ether oxide (DPEPO), which has a ground-state dipole moment of 8.06 D,[19,34] did not lead to the significant shifts in emission observed upon grinding of the neat crystals. The reduction in the red shift of the emission by introducing a more polar molecule than **4CzIPN** once again confirms that SSSE cannot explain the reported emission shifts in **4CzIPN** and related molecules.

CONCLUSIONS

We have discovered that **4CzIPN** and related molecules form intermolecular ground-state dimers, which impact on their emission energy and TADF performance, even in evaporated films previously assumed to emit only from **4CzIPN** monomers. The influence of these aggregate/dimer states on the TADF mechanism has been characterized through analysis of their fluorescence (in crystal, film, and solution), crystal structures, and MCL behavior. The crystal analysis shows that the molecules pack closely leading to this aggregate/dimer formation, which explains previously reported phenomena, including a significant emission red shift observed by Kim et al.[9] Interestingly, the dimer state (^{1}CT$_D$) undergoes TADF with its own characteristic kinetics.

Our observations also contribute to understanding the photoinduced absorption measurements of Hosokai et al.,[35] who reported TADF from "local" and "delocalized" CT triplet states. Their observations of the photoinduced absorption of these states in toluene solution of **4CzIPN** would be consistent with excited-state-induced absorption from monomer and dimer states, respectively. Moreover, we find that the ^{1}CT$_D$−^{3}LE$_D$ gap is very small, giving efficient TADF in nonpolar hosts, consistent with the observations of Hosokai et al.[35] that the best design of a TADF emitter comes from the delocalized component (or in our interpretation, the dimer). However, the low PLQY of the dimer state means that it is more likely to act as a triplet-trap state in applications.

This work highlights the ubiquity and importance of dimerization in carbazole-based materials and the effects this

DOI: 10.1021/acs.jpcc.9b01458
J. Phys. Chem. C 2019, 123, 11109−11117

can have on TADF behavior and color purity. Without this knowledge, specious interpretations may be made. We suggest that the unpredictable behavior of many well-known carbazole-based TADF emitters may arise from similar dimer formation in films. As a result, observations in the literature should be reinterpreted within this model and future molecular design should be directed to the choice of bulkier sterically hindered units, which will minimize intermolecular interactions and ensure the predictable properties of the emitters in OLEDs.

EXPERIMENTAL SECTION

Sample Preparation. Zeonex films were prepared via drop-casting using a mixture of dopant and host (zeonex) at the weight percentage specified. The initial solution concentrations were 1 mg/mL for the dopant and 100 mg/mL for zeonex. The films were dropcast onto a quartz substrate at room temperature to avoid any thermal annealing. The crystal samples were prepared using either the sublimed or solvent-grown crystals fixed with vacuum grease on a quartz substrate. The **4CzIPN**-doped mCBP films were evaporated at 100 nm thickness onto a sapphire substrate using a Kurt J. Lesker deposition chamber at a vacuum below 10^{-6} mbar.

Sublimation. The materials were sublimed using a Creaphys DSU05 organic sublimation system.

Optical Characterization. Optical measurements in solution used concentrations in the 10^{-5}–10^{-2} M range. Degassed solutions were prepared via the freeze–thaw method (5 repeats). Absorption and emission spectra were collected using a UV-3600 double beam spectrophotometer (Shimadzu) and a Fluoromax fluorimeter (Jobin Yvon). The MCL measurements were performed using an Ocean Optics spectrometer and a 395 nm UV torch. The PLQY measurements were performed using 365 nm excitation from an Ocean Optics LLS-LED and an integrating sphere connected to an Ocean Optics QePro Spectrometer.

Time-Resolved Photoluminescence. Time-resolved photoluminescence spectra and decays were recorded using a nanosecond gated spectrograph-coupled iCCD (Stanford) using either an Nd:YAG laser emitting at 355 nm (EKSPLA) or an N_2 laser (Lasertechnik Berlin) emitting at 337 nm.[36] Values of k_{rISC} were calculated according to "approach b" reported by dos Santos et al.[37] using the natural lifetime and the integrals of the prompt and delayed fluorescence.

Device Fabrication. OLED devices were fabricated using precleaned indium tin oxide (ITO)-coated glass substrates with an ITO thickness of 50 nm. A 20 nm thick PEDOT:PSS layer was spin-coated to the precleaned ITO substrates and the substrates were heated afterward for 10 min at 180 °C. The small-molecule and cathode layers were thermally evaporated using a Kurt J. Lesker deposition chamber below 10^{-6} mbar.

Single Crystal X-ray Diffraction. Experimental details and a detailed description of the **4CzIPN** crystal dihedral angles can be found in Figures S39–S42 and Tables S16–S18.

ASSOCIATED CONTENT

Supporting Information

The Supporting Information is available free of charge on the ACS Publications website at DOI: 10.1021/acs.jpcc.9b01458.

General methods; synthetic methods; Photographs of **4CzTPN** in powder form and DMSO solution under room light and UV light conditions; Photoluminescence (PL) spectroscopy of zeonex films and methylcyclohexane solution of **4CzIPN**; PL spectroscopy of sublimed crystals of **4CzIPN**; molecular packing and interactions in the solids; mechanochromic luminescence; X-ray crystallography (PDF)

Breakup of dimer species in pristine films of **4CzIPN** and **4CzIPN-^{t}Bu$_8$** (AVI) (AVI)

CCDC 1873416–1873427 contains the supplementary crystallographic data for this paper (ZIP)

AUTHOR INFORMATION

Corresponding Author

*E-mail: marc.k.etherington@durham.ac.uk.

ORCID

Marc K. Etherington: 0000-0003-2101-5757
Heather F. Higginbotham: 0000-0003-0245-5327
Andrew Danos: 0000-0002-1752-8675
Paul R. McGonigal: 0000-0002-8538-7579
Andrei S. Batsanov: 0000-0002-4912-0981
Vandana Bhalla: 0000-0002-8740-1928
Martin R. Bryce: 0000-0003-2097-7823
Andrew P. Monkman: 0000-0002-0784-8640

Notes

The authors declare no competing financial interest.

ACKNOWLEDGMENTS

We thank W. D. Carswell for obtaining DSC and TGA data, Gary Oswald for collecting the powder X-ray diffraction patterns, and Dr D. S. Yufit for help with the single crystal X-ray study. The Diamond Light Source (RAL) is thanked for the award of instrument time on Station I19 (MT 11145) and the instrument scientists for their kind support. Funding: M.K.E., H.F.H., and A.P.M. acknowledge the EU's Horizon 2020 research and innovation programme for funding the PHEBE project under Grant No. 641725. M.K.E., A.D., N.H., C.P., A.M., M.R.B., and A.P.M. also acknowledge the EU's Horizon 2020 research and innovation programme for funding the HyperOLED project under grant agreement No. 732013. A.P.M. and M.R.B. also acknowledge the EPSRC for funding under grant number EP/L02621X/1. A.N.B. is supported by an EPSRC doctoral training grant. P.R.M. and A.P.M. thank BEIS and UUKi for support through a Rutherford Strategic Partner Grant. D.R.G. thanks Merck KGaA for funding his PhD studies.

REFERENCES

(1) Nakagawa, T.; Ku, S.-Y.; Wong, K.-T.; Adachi, C. Electroluminescence Based on Thermally Activated Delayed Fluorescence Generated by a Spirobifluorene Donor–Acceptor Structure. *Chem. Commun.* **2012**, *48*, 9580.

(2) Uoyama, H.; Goushi, K.; Shizu, K.; Nomura, H.; Adachi, C. Highly Efficient Organic Light-Emitting Diodes from Delayed Fluorescence. *Nature* **2012**, *492*, 234–238.

(3) Dias, F. B.; Bourdakos, K. N.; Jankus, V.; Moss, K. C.; Kamtekar, K. T.; Bhalla, V.; Santos, J.; Bryce, M. R.; Monkman, A. P. Triplet Harvesting with 100% Efficiency by Way of Thermally Activated Delayed Fluorescence in Charge Transfer OLED Emitters. *Adv. Mater.* **2013**, *25*, 3707–3714.

(4) Etherington, M. K.; Gibson, J.; Higginbotham, H. F.; Penfold, T. J.; Monkman, A. P. Revealing the Spin–Vibronic Coupling Mechanism of Thermally Activated Delayed Fluorescence. *Nat. Commun.* **2016**, *7*, No. 13680.

(5) Gibson, J.; Monkman, A. P.; Penfold, T. J. The Importance of Vibronic Coupling for Efficient Reverse Intersystem Crossing in

DOI: 10.1021/acs.jpcc.9b01458
J. Phys. Chem. C 2019, 123, 11109–11117

Thermally Activated Delayed Fluorescence Molecules. *ChemPhysChem* **2016**, *17*, 2956−2961.
(6) dos Santos, P. L.; Ward, J. S.; Bryce, M. R.; Monkman, A. P. Using Guest−Host Interactions To Optimize the Efficiency of TADF OLEDs. *J. Phys. Chem. Lett.* **2016**, *7*, 3341−3346.
(7) Santos, P. L.; Ward, J. S.; Data, P.; Batsanov, A. S.; Bryce, M. R.; Dias, F. B.; Monkman, A. P. Engineering the Singlet−Triplet Energy Splitting in a TADF Molecule. *J. Mater. Chem. C* **2016**, *4*, 3815−3824.
(8) Dos Santos, P. L.; Etherington, M. K.; Monkman, A. P. Chemical and Conformational Control of the Energy Gaps Involved in the Thermally Activated Delayed Fluorescence Mechanism. *J. Mater. Chem. C* **2018**, *6*, 4842−4853.
(9) Kim, H. S.; Park, S.-R.; Suh, M. C. Concentration Quenching Behavior of Thermally Activated Delayed Fluorescence in a Solid Film. *J. Phys. Chem. C* **2017**, *121*, 13986−13997.
(10) Niwa, A.; Haseyama, S.; Kobayashi, T.; Nagase, T.; Goushi, K.; Adachi, C.; Naito, H. Triplet-Triplet Annihilation in a Thermally Activated Delayed Fluorescence Emitter Lightly Doped in a Host. *Appl. Phys. Lett.* **2018**, *113*, No. 083301.
(11) Kim, B. S.; Lee, J. Y. Phosphine Oxide Type Bipolar Host Material for High Quantum Efficiency in Thermally Activated Delayed Fluorescent Device. *ACS Appl. Mater. Interfaces* **2014**, *6*, 8396−8400.
(12) Wang, P.; Zhao, S.; Xu, Z.; Qiao, B.; Long, Z.; Huang, Q. The Electroluminescence Mechanism of Solution-Processed TADF Emitter 4CzIPN Doped OLEDs Investigated by Transient Measurements. *Molecules* **2016**, *21*, No. 1365.
(13) Zhu, F.; Zhou, C.; Zhou, D.; Yu, J. Improving Electroluminescent Efficiency and Ultraviolet Detectivity of Optoelectronic Integrated Devices by Doping a Thermally Activated Delayed Fluorescent Material in an Aggregation-Induced Emission Material as an Active Layer. *Opt. Mater. Express* **2017**, *7*, 3538.
(14) Nakanotani, H.; Masui, K.; Nishide, J.; Shibata, T.; Adachi, C. Promising Operational Stability of High-Efficiency Organic Light-Emitting Diodes Based on Thermally Activated Delayed Fluorescence. *Sci. Rep.* **2013**, *3*, No. 2127.
(15) Komatsu, R.; Sasabe, H.; Inomata, S.; Pu, Y.-J.; Kido, J. High Efficiency Solution Processed OLEDs Using a Thermally Activated Delayed Fluorescence Emitter. *Synth. Met.* **2015**, *202*, 165−168.
(16) Li, N.; Fang, Y.; Li, L.; Zhao, H.; Quan, Y.; Ye, S.; Fan, Q.; Huang, W. A Universal Solution-Processable Bipolar Host Based on Triphenylamine and Pyridine for Efficient Phosphorescent and Thermally Activated Delayed Fluorescence OLEDs. *J. Lumin.* **2018**, *199*, 465−474.
(17) Liu, Z.; Lei, Y.; Fan, C.; Peng, X.; Ji, X.; Jabbour, G. E.; Yang, X. Simple-Structure Organic Light Emitting Diodes: Exploring the Use of Thermally Activated Delayed Fluorescence Host and Guest Materials. *Org. Electron.* **2017**, *41*, 237−244.
(18) Noguchi, Y.; Kim, H.-J.; Ishino, R.; Goushi, K.; Adachi, C.; Nakayama, Y.; Ishii, H. Charge Carrier Dynamics and Degradation Phenomena in Organic Light-Emitting Diodes Doped by a Thermally Activated Delayed Fluorescence Emitter. *Org. Electron.* **2015**, *17*, 184−191.
(19) Northey, T.; Stacey, J. E.; Penfold, T. J. The Role of Solid State Solvation on the Charge Transfer State of a Thermally Activated Delayed Fluorescence Emitter. *J. Mater. Chem. C* **2017**, *5*, 11001−11009.
(20) Jankus, V.; Monkman, A. P. Is Poly(Vinylcarbazole) a Good Host for Blue Phosphorescent Dopants in PLEDs? Dimer Formation and Their Effects on the Triplet Energy Level of Poly(N-Vinylcarbazole) and Poly(N-Ethyl-2-Vinylcarbazole). *Adv. Funct. Mater.* **2011**, *21*, 3350−3356.
(21) Tani, K.; Tohda, Y.; Takemura, H.; Ohkita, H.; Ito, S.; Yamamoto, M. Synthesis and Photophysical Properties of [3.3](3,9)-Carbazolophanes. *Chem. Commun.* **2001**, 1914−1915.
(22) de Sainte Claire, P. Molecular Simulation of Excimer Fluorescence in Polystyrene and Poly(Vinylcarbazole). *J. Phys. Chem. B* **2006**, *110*, 7334−7343.
(23) Saiful, I. S. M.; Heinze, P.; Ohba, Y.; Yamauchi, S.; Yamamoto, M.; Tohda, Y.; Tani, K. Interplanar Interactions in the Excited Triplet States of Carbazole Dimers by Means of Time-Resolved EPR Spectroscopy. *Mol. Phys.* **2006**, *104*, 1535−1542.
(24) Wex, B.; Kaafarani, B. R. Perspective on Carbazole-Based Organic Compounds as Emitters and Hosts in TADF Applications. *J. Mater. Chem. C* **2017**, *5*, 8622−8653.
(25) Pashazadeh, R.; Pander, P.; Lazauskas, A.; Dias, F. B.; Grazulevicius, J. V. Multicolor Luminescence Switching and Controllable Thermally Activated Delayed Fluorescence Turn on/Turn off in Carbazole−Quinoxaline−Carbazole Triads. *J. Phys. Chem. Lett.* **2018**, *9*, 1172−1177.
(26) Skuodis, E.; Bezvikonnyi, O.; Tomkeviciene, A.; Volyniuk, D.; Mimaite, V.; Lazauskas, A.; Bucinskas, A.; Keruckiene, R.; Sini, G.; Grazulevicius, J. V. Aggregation, Thermal Annealing, and Hosting Effects on Performances of an Acridan-Based TADF Emitter. *Org. Electron.* **2018**, *63*, 29−40.
(27) Huang, B.; Chen, W.-C.; Li, Z.; Zhang, J.; Zhao, W.; Feng, Y.; Tang, B. Z.; Lee, C.-S. Manipulation of Molecular Aggregation States to Realize Polymorphism, AIE, MCL, and TADF in a Single Molecule. *Angew. Chem., Int. Ed.* **2018**, *57*, 12473−12477.
(28) Hladka, I.; Volyniuk, D. Y.; Bezvikonnyi, O.; Kinzhybalo, V.; Bednarchuk, T.; Danyliv, Y.; Lytvyn, R.; Lazauskas, A.; Grazulevicius, J. V. Polymorphism of Derivatives of *tert*-Butyl Substituted Acridan and Perfluorobiphenyl as Sky-Blue OLED Emitters Exhibiting Aggregation Induced-Active Thermally Activated Delayed Fluorescence. *J. Mater. Chem. C* **2018**, 13179−13189.
(29) Zeng, X.; Zhou, T.; Liu, J.; Wu, K.; Li, S.; Xiao, X.; Zhang, Y.; Gong, S.; Xie, G.; Yang, C. Incorporating Thermally Activated Delayed Fluorescence into Mechanochromic Luminescent Emitters: High-Performance Solution-Processed Yellow Organic Light Emitting Diodes. *Adv. Opt. Mater.* **2018**, No. 1801071.
(30) Sturala, J.; Etherington, M. K.; Bismillah, A. N.; Higginbotham, H. F.; Trewby, W.; Aguilar, J. A.; Bromley, E. H. C.; Avestro, A.-J.; Monkman, A. P.; McGonigal, P. R. Excited-State Aromatic Interactions in the Aggregation-Induced Emission of Molecular Rotors. *J. Am. Chem. Soc.* **2017**, *139*, 17882−17889.
(31) Verbeek, G.; Depaemelaere, S.; Van der Auweraer, M.; De Schryver, F. C.; Vaes, A.; Terrell, D.; De Meutter, S. Amino Derivatives of Symmetric 1,3,5-Triphenylbenzene. Nature of the Polar Singlet Excited State. *Chem. Phys.* **1993**, *176*, 195−213.
(32) Laguitton-Pasquier, H.; Pansu, R.; Chauvet, J.-P.; Collet, A.; Faure, J.; Lapouyade, R. The Charge Transfer State of Excited Bianthryl and a Derivative: Solvatochromism, Emission CT Spectra Broadening in Homogeneous Solvents. *Chem. Phys.* **1996**, *212*, 437−455.
(33) Brunschwig, B. S.; Ehrenson, S.; Sutin, N. Solvent Reorganization in Optical and Thermal Electron-Transfer Processes: Solvatochromism and Intramolecular Electron-Transfer Barriers in Spheroidal Molecules. *J. Phys. Chem.* **1987**, *91*, 4714−4723.
(34) Méhes, G.; Goushi, K.; Potscavage, W. J.; Adachi, C. Influence of Host Matrix on Thermally-Activated Delayed Fluorescence: Effects on Emission Lifetime, Photoluminescence Quantum Yield, and Device Performance. *Org. Electron.* **2014**, *15*, 2027−2037.
(35) Hosokai, T.; Matsuzaki, H.; Nakanotani, H.; Tokumaru, K.; Tsutsui, T.; Furube, A.; Nasu, K.; Nomura, H.; Yahiro, M.; Adachi, C. Evidence and Mechanism of Efficient Thermally Activated Delayed Fluorescence Promoted by Delocalized Excited States. *Sci. Adv.* **2017**, *3*, No. e1603282.
(36) Jankus, V.; Data, P.; Graves, D.; McGuinness, C.; Santos, J.; Bryce, M. R.; Dias, F. B.; Monkman, A. P. Highly Efficient TADF OLEDs: How the Emitter-Host Interaction Controls Both the Excited State Species and Electrical Properties of the Devices to Achieve Near 100% Triplet Harvesting and High Efficiency. *Adv. Funct. Mater.* **2014**, *24*, 6178−6186.
(37) dos Santos, P. L.; Ward, J. S.; Congrave, D. G.; Batsanov, A. S.; Eng, J.; Stacey, J. E.; Penfold, T. J.; Monkman, A. P.; Bryce, M. R. Triazatruxene: A Rigid Central Donor Unit for a D-A 3 Thermally Activated Delayed Fluorescence Material Exhibiting Sub-Microsecond

DOI: 10.1021/acs.jpcc.9b01458
J. Phys. Chem. C 2019, 123, 11109−11117

Reverse Intersystem Crossing and Unity Quantum Yield via Multiple Singlet-Triplet State Pairs. *Adv. Sci.* **2018**, *5*, No. 1700989.

NOTE ADDED AFTER ASAP PUBLICATION

This paper was published ASAP on April 18, 2019, with incorrect Supporting Information due to a production error. The corrected version was reposted on April 18, 2019.

DOI: 10.1021/acs.jpcc.9b01458
J. Phys. Chem. C 2019, 123, 11109−11117

Journal of Materials Chemistry C

PAPER

View Article Online
View Journal

Cite this: DOI: 10.1039/c9tc02742d

Revealing resonance effects and intramolecular dipole interactions in the positional isomers of benzonitrile-core thermally activated delayed fluorescence materials†

Nadzeya A. Kukhta, ‡[ab] Heather F. Higginbotham,‡[c] Tomas Matulaitis, [bd] Andrew Danos, *[c] Aisha N. Bismillah, [a] Nils Haase,[ef] Marc K. Etherington, [c] Dmitry S. Yufit, [a] Paul R. McGonigal, [a] Juozas Vidas Gražulevičius [b] and Andrew P. Monkman *[c]

Received 22nd May 2019,
Accepted 28th June 2019

DOI: 10.1039/c9tc02742d

rsc.li/materials-c

We report on the properties of the three positional isomers of (2,7-di-*tert*-butyl-9,9-dimethylacridin-10(9*H*)-yl)benzonitrile, which are found to have comparable donor steric environments and donor–acceptor dihedral angles. An unexpected intramolecular dipole interaction imparts a unique molecular geometry to the *ortho*-linked isomer, while comparison of the *meta*- and *para*-isomers uncovers how positional differences in acceptor strengths (a consequence of differences in aromatic π-system electron density) lead to very different triplet harvesting and emission properties. These positional-isomer effects on TADF follow the well-known aromatic directing rules from organic synthesis, in keeping with their common origin arising from contributions of multiple electronic resonance structures. Understanding these positional effects and methods of dihedral control is critical to the future design of efficient TADF emitters.

Introduction

Recent commercial applications of organic light-emitting diodes (OLEDs) can largely be attributed to the development of triplet harvesting materials with internal quantum efficiencies up to 100%—a marked increase from the upper limit of 25% achievable through conventional fluorescence. In contrast to iridium- or platinum-based triplet harvesting phosphors, purely organic OLEDs based on thermally activated delayed fluorescence (TADF)[1] hold the potential to yield high-efficiency and reduced-cost devices for lighting and displays, using materials that are readily available and of low toxicity.[2–8]

Designing efficient TADF materials often requires delicate tuning of charge-transfer (CT) character in the molecular excited-state. Non-overlapping highest occupied molecular orbitals (HOMOs) and lowest unoccupied molecular orbitals (LUMOs) in donor–acceptor (D–A) or donor–acceptor–donor (D–A–D) structures reliably yield such CT states with low electron exchange energy, and thus minimal singlet–triplet energy gaps (ΔE_{ST}). More recently, through-space D–A interactions and non-overlapping single molecule resonance structures have also been shown to deliver outstanding TADF performance.[9–12] Reducing this gap leads to exponentially faster reverse intersystem crossing (rISC), which enables triplets to be harvested for emission. The rISC is mediated by second order spin–vibronic coupling between the CT triplet (^{3}CT) and a local triplet state (^{3}LE) of either the donor or acceptor.[13] While increasing CT character often reduces ΔE_{ST}, it also redshifts the emission colour and reduces the fluorescence rate constant through a lower oscillator strength (reduced HOMO/LUMO overlap). Therefore, in designing high-efficiency blue TADF materials the trade-off between emissive and triplet-harvesting properties must be carefully considered, as each puts competing constraints on the molecular design.

The maximum achievable CT character of D–A(–D) TADF materials is controlled by the choice of donor and acceptor, while the actual contribution to excited-state properties is modulated by the D–A dihedral angle. Perpendicular structures hinder π-system conjugation across the molecule, spatially

[a] Department of Chemistry, Durham University, South Road, Durham, DH1 3LE, UK
[b] Department of Polymer Chemistry and Technology, Kaunas University of Technology, Radvilenu pl. 19, LT-254 Kaunas, Lithuania
[c] Department of Physics, Durham University, South Road, Durham, DH1 3LE, UK. E-mail: andrew.danos@durham.ac.uk, a.p.monkman@durham.ac.uk
[d] Organic Semiconductor Centre, EaStCHEM School of Chemistry, University of St Andrews, St Andrews, Fife, KY16 9ST, UK
[e] Merck KGaA, Performance Materials—Display Solutions, Frankfurter Straße 250, 64293 Darmstadt, Germany
[f] Institute of Physics, Experimental Physics IV, University of Augsburg, Universitätsstr. 1, 86135 Augsburg, Germany

† Electronic supplementary information (ESI) available. CCDC 1917139–1917141. For ESI and crystallographic data in CIF or other electronic format see DOI: 10.1039/c9tc02742d

‡ These authors contributed equally.

separating the HOMO and LUMO to yield strong CT character in the lowest-energy excited-state from which emission originates (although this CT state sometimes requires stabilisation by a polar environment to actually be the lowest energy excited-state – see discussion of emission solvatochromism below and Fig. S9.2, ESI†). Coplanar structures instead stabilise whole-molecule π-system excited-states with locally excited (LE) character (and large ΔE_{ST}), as these permit the greatest electron delocalisation. Therefore, control of D–A angles has been identified as critical for effective TADF material design. This control is most commonly achieved by repulsive contact forces (*i.e.* steric effects) between the donor and acceptor units or between multiple donor units around the same acceptor. Indeed, well-designed studies of differently substituted or connected donor units – or of donor units in different conformations – demonstrate how both TADF and room temperature phosphorescence can be selectively activated by control of the D–A angle and CT character.[14–18]

While the behaviour of smaller donor units such as carbazole have been shown to be dominated by inter-donor and D–A steric interactions,[19,20] this understanding cannot be *a priori* generalised to larger donor units or those with interrupted conjugation. Similarly, the conformational effects seen in phenothiazine and other flexible donors are not necessarily shared by more rigid donors.[21] 9,9-Dimethyl-9,10-dihydroacridine (DMAC) is an example of a large and rigid donor that has become popular for designing blue TADF materials[22–25] due to its intermediate donor strength (higher than carbazole and diphenylamine, but lower than phenoxazine and phenothiazine according to HOMO energies[26]). It is therefore desirable to understand how this donor responds to different steric (and electronic) environments, so that it can be effectively incorporated into the design of advanced TADF emitters.

Initially with the aim of understanding these steric effects for DMAC, we here present synthesis and photophysical characterisation of the three positional isomers of DMAC coupled to benzonitrile (BZN) as acceptor (***ortho*-1**, ***meta*-2**, and ***para*-3**, Scheme 1 and collectively DMAC–BZN). Time-resolved emission spectra show that these positional isomers display very different rISC rates and TADF performance, which has been loosely attributed to steric or conjugation differences for similar materials in the past.[27–31] However, our detailed density functional theory analysis of these materials reveal that the *meta*- and *para*-isomers experience extremely similar steric environments relevant to the D–A dihedral angle, while the *ortho*-isomer shows an unexpected intramolecular dipole interaction that restricts its own D–A angle. We are therefore able to reattribute the differences in TADF performance to the differences in BZN electron withdrawing strength at the *meta*- and *para*-positions, consistent with the different resonance and inductive effects around the acceptor unit aromatic π-system. Previously examined in terms of "linear" and "angular" isomers,[15,32–34] this newly understood feature of TADF design mirrors the directing rules from organic chemistry, making it a timely and highly appropriate inclusion in this themed collection celebrating the career achievements of Martin Bryce.

Results and discussion

Design, synthesis and chemical characterization

Scheme 1 presents the synthetic pathways used to isolate the target materials. DMAC and BZN were chosen as donor and acceptor due to their increasing popularity in the design of blue TADF emitters, again in the hope of understanding the different steric effects at different positions around the ring. The popularity of these units for blue TADF materials is due to their well-matched relative electron donating/accepting strengths, as well as their high triplet energies.[26,35] Intermediate iodobenzonitriles were prepared by diazotization–iodination reactions from appropriate starting aminobenzonitriles. The target D–A compounds were then produced using a Buchwald–Hartwig palladium cross-coupling protocol. Full synthetic procedures are included in the ESI† (Section S2). All compounds were purified by column chromatography followed by recrystallisation. The identities and high purities of the target compounds were confirmed by ^{1}H and ^{13}C NMR spectroscopy, mass spectrometry and elemental analysis (ESI,† Sections S2 and S3). Additional characterisation of thermal (TGA and DSC) and electrochemical properties (CV) are included in ESI† Section S7.

NMR analysis

As well as confirming the identities of the isolated target materials, analysis of the NMR chemical shifts reveals subtle

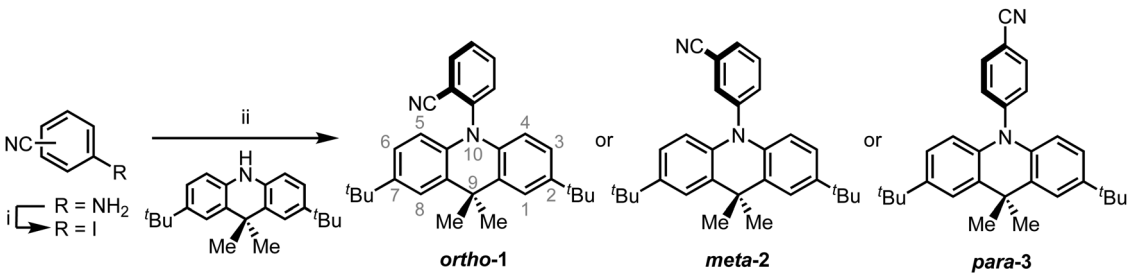

Scheme 1 Synthesis of DMAC–BZN isomers, ***ortho*-1**, ***meta*-2** and ***para*-3**. Reagents and conditions: (i) $NaNO_2$, KI, HCl, Me_2CO, 0 °C to rt, 2 h; (ii) $Pd(PPh_3)_4$, 1,1′-bis(diphenylphosphino)ferrocene, ^{t}BuONa, PhMe, 115 °C, 24 h, ***ortho*-1** 66%, ***meta*-2** 81%, ***para*-3** 75%. The numbering used to label positions of the DMAC ring system are shown for ***ortho*-1**.

differences in ground-state conjugation across the donor and acceptor units in the DMAC–BZN isomers (ESI,† Section S3). We select for comparison the H atoms and associated C atoms closest to the nitrogen of the DMAC units (equivalent pairs at the 4- and 5-positions, Scheme 1), as these positions are closest to the withdrawing BZN ring without directly participating in the acceptor unit π-system. The chemical shifts observed for ***ortho*-1**, ***meta*-2**, and ***para*-3** are 5.98, 6.08, and 6.35 ppm for the ^{1}H nuclei and 113.4, 114.4, and 115.8 ppm for the ^{13}C nuclei, respectively. The nuclear environments at these positions are therefore shielded relative to benzene (7.36 ppm, 128.4 ppm), which we attribute to increased local electron density arising from the nearby DMAC nitrogen lone pair.

The order of these chemical shifts then suggests that the nitrogen atom electron density is increasingly depleted in the order of ***ortho*-1**, ***meta*-2**, and ***para*-3**, presumably due to increased D–A conjugation in the same order. The overall level of conjugation depends on the D–A angle as well as acceptor strength, and so in many TADF systems it is difficult to attribute such differences to a unique cause. Nonetheless based on complementary X-ray and computational studies of these materials we later illustrate that the differences between ***meta*-2** and (more conjugated) ***para*-3** are due to different effective acceptor strengths only. For ***ortho*-1** the D–A angle is restricted closer to perpendicular, preventing stronger D–A conjugation.

Variable temperature NMR was also performed to assess the heights of the barriers to donor unit rotation around the bridging DMAC–BZN C–N bond in these materials (ESI,† Section S4). The C–N bond rotation of ***ortho*-1**, which is hindered by the neighbouring CN group, reaches the slow exchange regime in an accessible temperature range, allowing us to measure a free energy barrier to rotation of approximately 45 kJ mol^{-1}. The less hindered ***meta*-2** isomer, on the other hand, does not reach slow exchange down to temperatures as low as −98 °C. We estimate (ESI,† Section S4), therefore, that its rotational barrier is $<$33 kJ mol^{-1}. The additional plane of symmetry present in ***para*-3** prevents measurement of its rotational barrier, but the steric environment around the DMAC–BZN bond is expected to be similar to ***meta*-2**, with a similarly low barrier to rotation.

X-ray crystallography analysis

X-ray crystallographic analysis of the three materials (ESI,† Section S5, CCDC 1917139–1917141†) reveals near-perpendicular D–A dihedral angles for each in the solid-state. This was unexpected, as with larger conjugation (as inferred from NMR and following optical results) ***para*-3** was anticipated to possess a more coplanar geometry.

Interestingly, we also note a folding of the DMAC unit unique to ***ortho*-1**. Hirshfeld surfaces were calculated for the crystal structures (ESI,† Section S6) to determine whether this folding is the result of packing effects brought about by the orientation of the nitrile group. However, no notable differences in the locations or sizes of close contact areas (where nearest neighbour molecular spacing is smaller than the sum of van der Waals radii) were observed between the three isomers. We note however that this analysis cannot discount the possibility that DMAC folding occurs to minimise molecular volume and eliminate strain that would be present in crystals of ***ortho*-1** with otherwise planar DMAC units. We therefore cannot make definitive claims about the geometry of the DMAC unit of ***ortho*-1** from these X-ray results alone, although DFT calculations presented further below support the observation of DMAC folding.

Photophysical properties

In cyclohexane (CH), chloroform, and dichloromethane (DCM) solutions, ***ortho*-1** and ***meta*-2** show strong absorption peaks at ∼280 nm extending out to 340 nm (Fig. 1 and Fig. S9.1, ESI†). Solutions of ***para*-3** also possess additional absorption bands at 320 and 378 nm, redshifted due to increased conjugation in this material.[36,37] The presence of such low intensity and low energy bands – presumably of n–π* or n–π*/π–π* origin, and none of which are shared with the individual donor or acceptor units – is widely observed in D–A systems.[38–40] Similar absorption bands were attributed to direct CT transitions by Noda *et al.* for similar materials.[27]

Photoluminescence (PL) spectra were recorded in solvents of increasing polarities, experimentally establishing the CT character of the emissive excited-state through the Gaussian line shape and increasing redshift (Fig. S9.2, ESI†). In non-polar CH, vibronically structured emission is observed for all three materials and attributed to an LE singlet state. In other solvents and in non-polar polymer host zeonex all materials exhibit only Gaussian emission from CT excited-states. The size of the solvatochromic shift is different in each molecule, a combined effect of the excited-state dipole moment and CT character. The emission in degassed toluene is also greatly enhanced for each DMAC–BZN isomer (Fig. S10, ESI†), confirming that they are all effective triplet harvesting materials.

The materials were further analysed using time-resolved spectroscopy in both zeonex and polar small molecule host bis[2-(diphenylphosphino)phenyl]ether oxide (DPEPO), and at temperatures between 80 and 300 K. DPEPO is a widely-used high triplet energy host for blue TADF OLEDs and was employed to emulate conditions relevant to device applications.[41,42] The individual spectra (that make up the decay curves presented further below, Fig. 3) reveal information about the excited-state dynamics in the DMAC–BZN isomers. Fig. 2 shows the slight apparent redshift observed for ***ortho*-1** in the early prompt fluorescence (PF) time region, as well as the surprising blueshifts observed for ***meta*-2** and ***para*-3** across similar time intervals. In contrast, Fig. S13 (ESI†) shows similar time-resolved spectra in DPEPO, where only apparent redshifts are observed. After these spectral shifts in the early PF time region the time-resolved spectra remain unchanged throughout the later delayed fluorescence (DF).

All materials were found to emit across two distinct time regimes, with PF occurring over nanoseconds as optically excited ^{1}CT states emit, while DF extends over microseconds as triplet states undergo slower rISC and emit at later times. At low temperatures a third phosphorescence regime can be identified, from which the spectra in Fig. 1 are taken. The emission decay curves of the three DMAC–BZN isomers are presented in Fig. 3 (300 K), and in Fig. S11 (ESI†) for other temperatures.

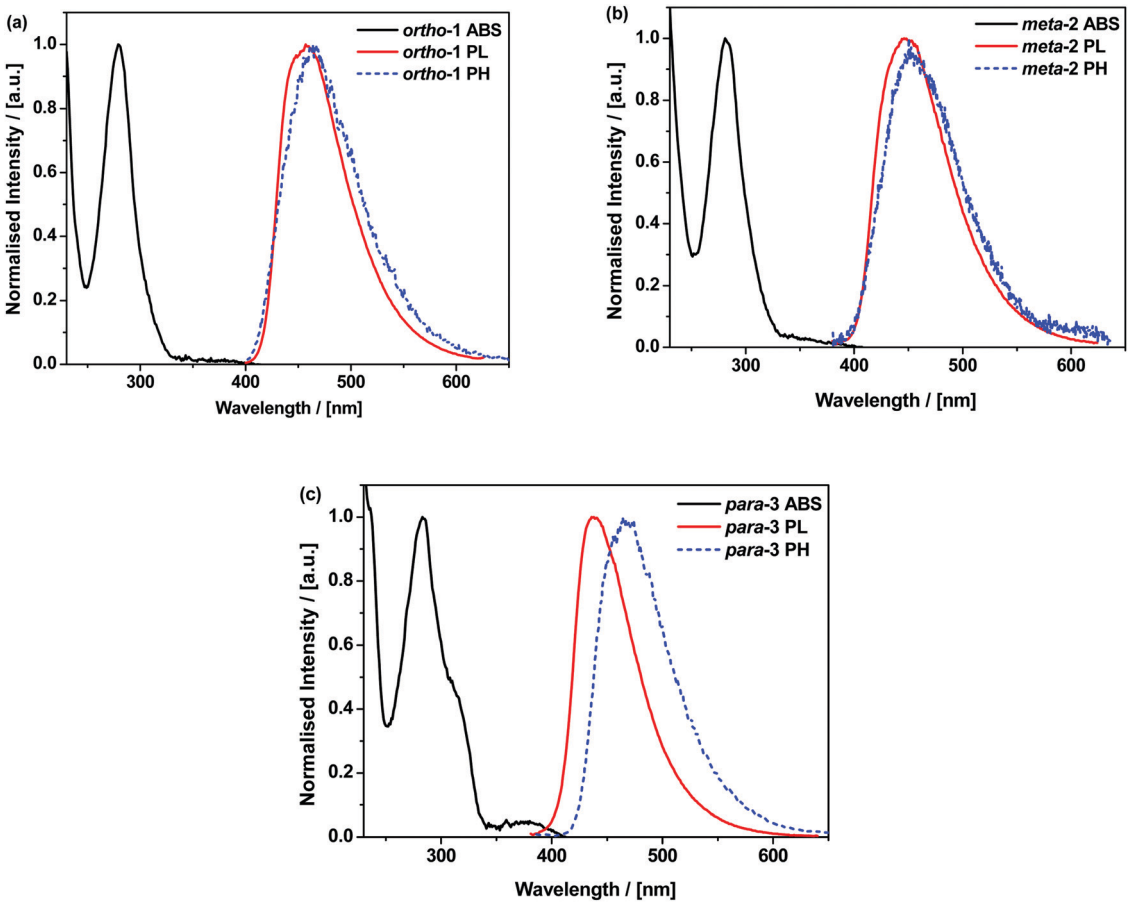

Fig. 1 Normalised absorption in CH (black), emission in zeonex (red), and PH in zeonex (blue dotted) of ***ortho*-1** (a), ***meta*-2** (b) and ***para*-2** (c). PL spectra were recorded using 320, 325, and 330 nm excitation respectively, while PH spectra were recorded 40 ms following 337 nm pulsed excitation at 80 K and in the absence of oxygen.

The emission decay curves can be reasonably well fit with single exponentials in regions representing the PF and DF for ***ortho*-1** and ***para*-3**, with lifetimes at 300 K included in Table 1. Similar fitting is more challenging for ***meta*-2**, especially in the intermediate time region spanning 100–1000 ns where signal to noise ratios were the lowest. Values of the rISC rate constant (k_{rISC}) were also determined by kinetic fitting of the decays as described elsewhere, with decay fits for kinetic and exponential fitting shown in ESI,† Section S15.[43] Measurements of the power dependence of DF emission with excitation dose rule out bimolecular TTA as the DF mechanism (Fig. S12, ESI†). Photoluminescence quantum yields (PLQYs, 380 nm excitation) of the zeonex films were also measured in air (PF component) and after purging with nitrogen (PF + DF components) and are also included in Table 1; DPEPO films of suitable uniformity could not be obtained for PLQY measurements.

Discussion and DFT calculations

The significant differences in the optical properties of these materials are difficult to reconcile with their similar structures. The results raise several questions:

- Despite similar PF decay lifetimes, why are the PF components of the PLQYs for ***meta*-2** and ***para*-3** so different?
- Similarly, with comparable ΔE_{ST}, why are the DF PLQY components of ***ortho*-1** and ***meta*-2** (37% and 12% respectively) so different? How does ***para*-3** have higher PLQY than ***meta*-2** despite a larger ΔE_{ST}?
- Why do the early PF spectra blueshift in zeonex, when redshifts due to D–A angle relaxation or lifetime dispersion are more commonly observed?[40,44] Why is this blueshift seen for ***meta*-2** and ***para*-3** to different extents, but not ***ortho*-1**?
- Despite showing stronger D–A conjugation from NMR, direct CT absorption, and lower triplet energy, how does ***para*-3** still manage to possess a similarly orthogonal D–A angle to the other isomers as revealed by X-ray diffraction?

In order to better understand the behaviour of these materials and answer the questions above, we performed DFT calculations on both ground (S_0) and excited (S_1) state surfaces for the DMAC–BZN isomers.

Due to the proximity of the cyano-group to the DMAC in ***ortho*-1**, we expected this material to exhibit the greatest steric hindrance and a D–A angle most tightly restricted around 90°. This would then result in significantly higher CT character for ***ortho*-1**, in contrast to ***meta*-2** and ***para*-3** which were expected to more freely rotate.[40] Similar differences in rotational freedom have been used to explain differences in

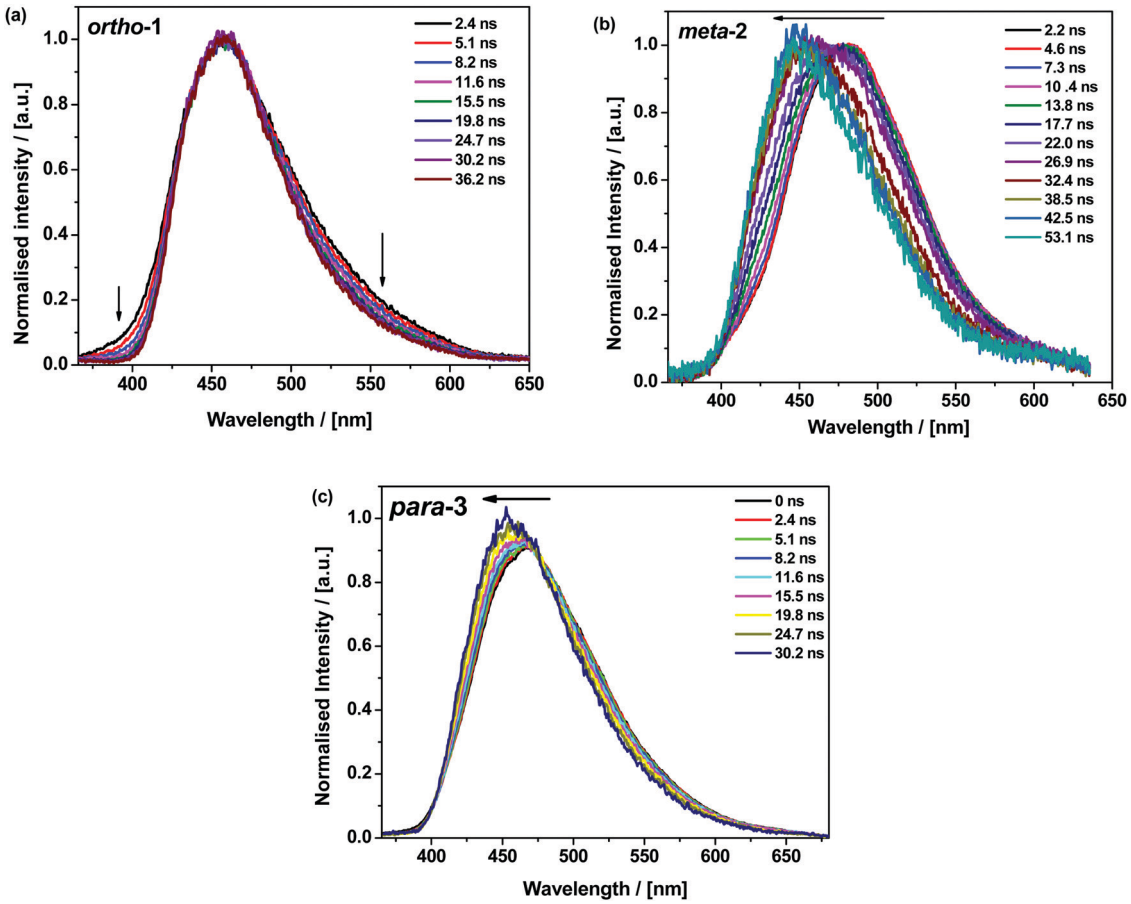

Fig. 2 Early PF time-resolved emission spectra of 1% w/w zeonex films of ***ortho*-1** (a) ***meta*-2** (b) and ***para*-3** (c) at 300 K.

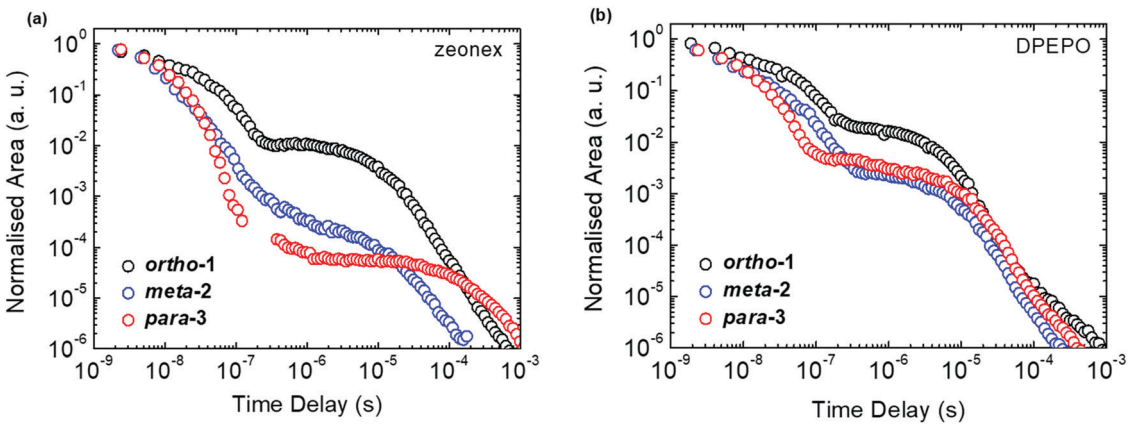

Fig. 3 Emission decays of DMAC–BZN isomers at 300 K in zeonex (a) and DPEPO (b) hosts.

photophysical properties for similar molecules featuring carbazole donors.[17,20,26,42]

Instead – and in agreement with X-ray crystal structures – DFT calculations of the DMAC–BZN isomers (rBMK/6-31G(d) level of theory) reveal similar chromophore arrangements in the optimised ground-state geometry regardless of the substitution pattern. To examine the effects of structural reorganisation in the excited state, the S_1 geometries were initially accessed using TD-DFT (Fig. S8.1, ESI†).[45] Surprisingly, no dramatic change in the D–A torsional angle was observed upon excitation for any of the isomers. The BZN acceptor is attached perpendicularly to the DMAC donor in all cases, which we suggest is due to the innermost DMAC hydrogens (those at the 4- and 5-positions in Scheme 1) capturing the plane of the BZN ring from above and below and locking rotation of the D–A bond. A similar form of dihedral control using inwardly pointing

Table 1 Spectral and kinetic parameters of DMAC–BZN isomers as 1% w/w films in zeonex at 300 K

Material	τ_{PF} (ns)	τ_{DF} (μs)	ΔE_{ST}[a] (meV)	k_{rISC}[b] ($\times 10^5$ s^{-1})	PLQY[c] (N_2)	PLQY[c] (air)	k_F[d] ($\times 10^6$ s^{-1})
***ortho*-1**	47	10	<10	5.7	78	41	8.7
***meta*-2**	20	15	<10	2.3	21	9	4.5
***para*-3**	11	181	110	0.13	47	20	18

[a] ΔE_{ST} from difference in high energy onsets of steady state PL and phosphorescence spectra. [b] k_{rISC} from combined kinetic fitting of PF and DF decay data.[43] [c] PLQYs measured on drop cast films on sapphire substrates using 380 nm excitation. [d] Calculated using $k_F = (PLQY_{AIR})/\tau_{PF}$ following Dias *et al.* eqn (8).[39]

methyl substituents was able to greatly improve the performance of TADF materials with carbazole donors, which are otherwise much freer to rotate.[46] For DMAC the dihedral angle control afforded by the inner C–H bonds relies on the rigid and large 6-member central ring of the DMAC, and so is intrinsic to all three isomers and explains their shared D–A angles. This is in contrast to more common steric control strategies engineered using repulsive contact forces between neighbouring donors or acceptor substituents, as employed in other TADF materials.[14,16–18,34,42,47] In any case, observation of uniformly orthogonal chromophore arrangements means that the differences in photophysical properties between the DMAC–BZN isomers cannot be attributed to different D–A angles.

For further and more detailed structural comparisons the experimentally obtained X-ray crystal structures were taken to represent the ground-state geometries. Additionally, the Tamm–Dancoff (TDA) approximation was employed for further excited-state calculations, using the X-ray structure as input geometries (Fig. 4). The TDA approach was previously shown to describe CT states more accurately than conventional TD-DFT, therefore giving more reliable excited-state geometry information for the DMAC–BZN isomer excited-states.[48,49]

While the converged geometries using this second computational approach are qualitatively similar to those of the first, there are some notable differences. Firstly, the D–A torsion angles in the ground- and excited-states no longer reach precisely 90° (Fig. 4 and 5). These geometrical differences then influence the electron wavefunction distribution: the increased HOMO/LUMO overlap in ***para*-3** (Fig. 4c) is immediately visible compared to ***meta*-2**, consistent with the largest conjugation

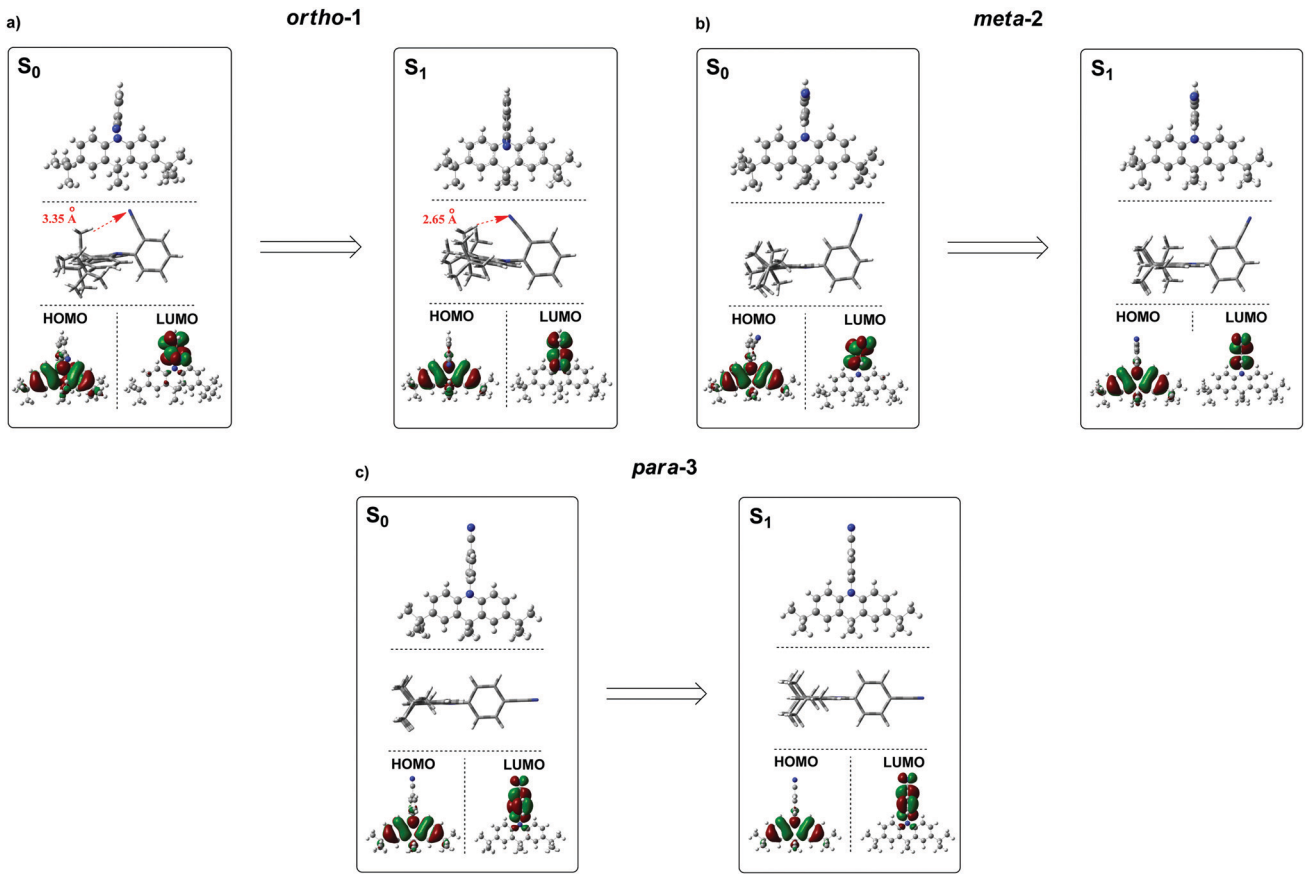

Fig. 4 Ground-state (S_0) and excited-state (S_1) optimised structures of ***ortho*-1**, ***meta*-2** and ***para*-3** along with corresponding HOMO/LUMO isosurfaces (rBMK/6-31G(d) for S_0 and TDA-DFT BMK/6-31G(d) the S_1).

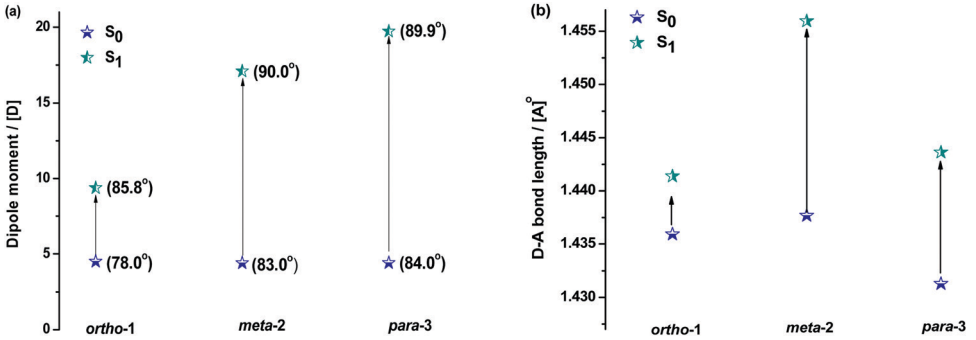

Fig. 5 Changes in the dipole moment and (bracketed) D–A bond angles (a) and D–A bond lengths (b) of DMAC–BZN isomers in ground and excited states (rBMK/6-31G(d) on X-ray geometries for S_0 and TDA-DFT BMK/6-31G(d) for S_1).

(giving rise to strongest LE character) inferred from NMR, lowest triplet energy, shortest ground-state D–A bond length (from the X-ray structures, Fig. 5b), and strongest direct CT absorption bands in this material (both experimental, Fig. 1, and simulated, Fig. S8.2, ESI†). These differences in calculated geometries clearly indicate that simpler TD-DFT approaches cannot fully describe the excited-state characteristics of D–A compounds with strong CT character. The degree of D–A conjugation was also assessed quantitatively for the excited-state geometries by calculating the charge separation index (q) in Multiwfn.[50,51] The values obtained again confirm that ***para*-3** (q = 0.900) is the most conjugated (least charge separation), with ***ortho*-1** (0.916) and ***meta*-2** (0.924) more similar to each other, although in reverse order to the ranking inferred from NMR chemical shifts.

Fig. 5 shows how the D–A bond angles, D–A bond lengths, and (calculated) dipole moments change from the ground to excited-state. We note that these calculations reveal the gas phase properties of the DMAC–BZN isomers, and so are comparable only to measurements recorded in the fluid and non-polar zeonex host. Despite this limitation the structural insight provided by these calculations is what allows us to fully understand the puzzling photophysics arising from positional effects in the DMAC–BZN isomers.

It is immediately noteworthy that the changes in the D–A bond angles upon excitation are not extreme, making direct CT excitation in these materials a near-vertical transition as it concerns the D–A dihedral nuclear coordinate. The excited-state dipole moments increase in line with the charge separation distances, as would be expected for a classical electric dipole. That is, the larger the distance between the electron accepting cyano-group and electron donating DMAC nitrogen (with ***ortho*-1** shortest and ***para*-3** longest), the larger the dipole moment.

The changes in D–A bond lengths also explain the blueshift of the early time-resolved spectra in zeonex, in a manner that similarly appeals to classical intuition. As recently demonstrated in exciplex systems, increasing the CT state electron–hole separation reduces the magnitude of the coulombic binding energy, resulting in blue-shifted emission.[52,53] We propose that the same mechanism causes the ***meta*-2** isomer to blueshift significantly as its D–A bond relaxes by dynamic elongation. From the spectra in Fig. 2 we note this relaxation takes up to 50 ns, which is much longer than typical vibrational mode oscillation periods for this kind of D–A bond stretch. However, we note that any D–A bond stretching mode will be frustrated by the surrounding host. While zeonex provides a relatively fluid environment (compared to compact small molecule OLED hosts like DPEPO), ***meta*-2** must still perform mechanical work to expand its molecular volume against the pressure of the surrounding host. As the polymer host reorganisation required to clear space for the expanding molecule takes time, both the bond length relaxation and associated spectral shift take longer than would be expected for an unhindered vibration. For ***para*-3** the bond elongation and blueshift are both smaller and more rapid, while they are both negligible for ***ortho*-1**.

In contrast to zeonex, the time-resolved spectra do not blueshift in DPEPO. We suggest that the compact small molecule host cannot be so easily pushed aside as the D–A bond attempts to relax, preventing its elongation. As a result only an apparent redshift due to lifetime dispersion is observed, with the particularly long duration of this dispersion in ***meta*-2** (~250 ns, Fig. S13, ESI†) indicative of an extremely broad distribution of excited-state geometries.[40]

While bond lengthening explains the spectral evolution of these materials in zeonex, the differences in bond lengthening in turn demand some explanation. We first consider ***ortho*-1**; why does its D–A bond change so little compared to the others? The answer to this question can be found in the X-ray and TDA excited-state geometries of this material. Fig. 4 shows how the plane of the DMAC unit is tilted with respect to the BZN in the ground state of ***ortho*-1** (X-ray geometry, with the vector normal to the plane of the DMAC unit non-perpendicular to the vector along the D–A bond). For ***meta*-2** and ***para*-3** there is no such tilting (DMAC normal vector completely perpendicular to the D–A bond vector). In the excited state this tilting increases as highlighted in Fig. 6a, with the H···N interatomic distance closing from 3.35 Å to 2.63 Å.

The presence of this tilting in both the X-ray ground state (with crystal packing) and DFT excited-state (gas phase) leads us to conclude that it is indeed a real effect and not an artefact of either approach. We suggest that this tilting is a result of

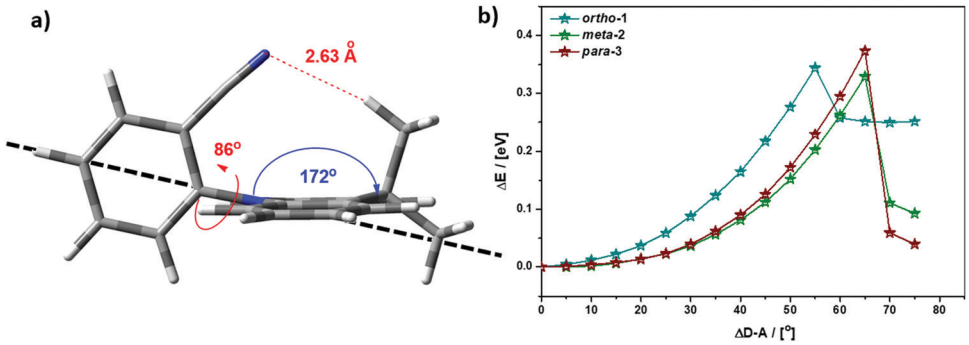

Fig. 6 (a) Profile view of ***ortho*-1** S_1 optimised structure (TDA-DFT BMK/6-31G(d)) showing tilting of DMAC plane, with dashed line to guide the eye to the expected DMAC position. This tilting and the reduced H···N interatomic distance arise from an intramolecular dipole interaction. (b) Conformational analysis of DMAC–BZN isomers in the excited-state (rBMK/6-31G(d)): change in total energy plotted against displacement of D–A dihedral angle (away from optimised values given in Fig. 5a, upper value).

intramolecular dipole interactions between the slightly positive DMAC methyl hydrogen and the partially negative nitrogen of the cyano-group. While D–A bond weakening in the excited state causes it to simply lengthen for ***meta*-2** and ***para*-3**, in ***ortho*-1** this weakening instead allows the dipole interaction to draw the two moieties closer together through space, with little effect on the D–A covalent bond length.

This explanation of bond lengthening in ***ortho*-1** immediately raises another important question: Does this intramolecular dipole interaction impact the D–A dihedral angle? To answer this question, we performed DFT calculations to map out the excited-state energy surfaces of the DMAC–BZN isomers along the nuclear coordinate of D–A bond rotation. The results are shown in Fig. 6b, extending out to angles at which the restricted geometry optimisation begins to seek alternative local minima (55° for ***ortho*-1**, and 65° for ***meta*-2** and ***para*-3**). For angle displacements up to 50° these results demonstrate that while ***meta*-2** and ***para*-3** have identical rotational energy well shapes (controlled in both only by the DMAC hydrogens capturing the plane of the BZN ring), ***ortho*-1** is more tightly constricted. This we believe is due to the intramolecular dipole interaction, which holds the D–A bond angle more closely around its equilibrium value. The use of attractive potentials to control bond dihedral angles is currently rare,[54,55] but holds significant promise as a new tool for TADF molecular design, potentially allowing much finer control over torsion angles than the use of repulsive potentials. In the context of ***ortho*-1** this additional dihedral control would be expected to increase the CT character of the material.

While the smaller bond elongation in ***ortho*-1** is thus understood, there are no structural differences that can easily explain the differences in optical properties of ***meta*-2** and ***para*-3**. As the excited-state D–A bond in ***meta*-2** is significantly longer than in ***para*-3**, for otherwise equal donors and acceptors this greater decoupling of donor and acceptor would be expected to lead to greater CT character and larger rISC rates. We indeed observe this in optical measurements, but stress again that this difference in CT character cannot be attributed to different D–A angles, and that the donor strength of the DMAC should be the same for all three materials. We note however that the assumption of equal acceptor strengths at the different BZN positions is not yet justified.

Indeed, the results above suggest that this assumption cannot actually be justified. Instead, we infer that different accepting strengths exist in the different acceptor positions for BZN, which explains the differences between ***meta*-2** and ***para*-3**. In ***ortho*-1** the additional intramolecular dipole interaction affects the D–A rotational freedom, so we only compare it to ***para*-3**—which we expect to have a similar acceptor strength for reasons detailed immediately below.

To justify the conclusion of different acceptor strengths for the DMAC–BZN isomers (and qualitatively predict their relative acceptor strengths), we recall the general substituent orientation rules from organic chemistry. As nitrile is a relatively strong *meta*-orienting and deactivating group for electrophilic substitution, the opposite rules (*ortho*- and *para*-activating) apply for nucleophilic substitution. Indeed, while a different synthetic strategy was used here (Scheme 1 and ESI,† Section S2), the D–A bonds in the DMAC–BZN materials could potentially be formed by nucleophilic attack of the BZN ring by the deprotonated DMAC unit (with an appropriate leaving group on the BZN). The activating effect towards *ortho*- and *para*-positions is due to reduced π-system electron density at these positions, due to the resonance and inductive effects of the cyano-group, as shown in Fig. 7.

Crucially, there is no reason to expect that these resonance and inductive effects should cease once the D–A bond has formed. The electron withdrawing effects of the cyano-group again result in depleted π-system electron density at *ortho*- and *para*-positions, leading to larger effective acceptor strengths. This leads to different levels of electronic communication between the donor and acceptor, with significant subsequent effects on conjugation and CT character for the isomers. Comparing only ***meta*-2** and ***para*-3**, the weaker acceptor is the reason for ***meta*-2** having reduced D–A conjugation, a weaker (longer) bond, and consequently a greater degree of CT character with low ΔE_{ST}. Thus, at the early times shown in Fig. 2b it has by far the most red-shifted CT emission peak. Indeed, excessive CT character greatly reduces the emission oscillator strength in this material, leading to its low PLQY. This is true even after the D–A bond length has relaxed and ***meta*-2** gains a more LE excitonic character as evidenced by its blue-shifted emission.[52,53] Despite this change, the LE character

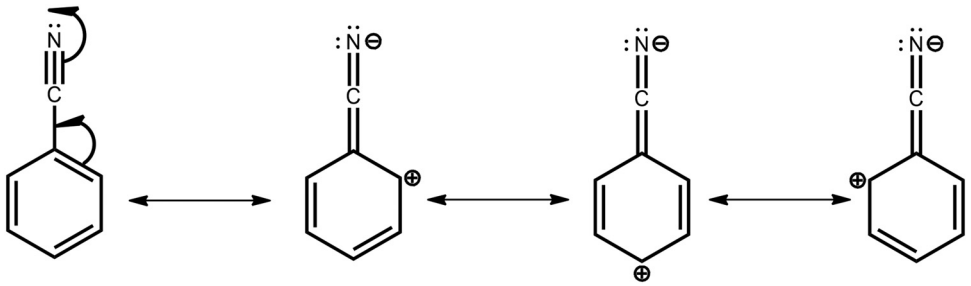

Fig. 7 Resonance structures of BZN unit. The depleted π-system electron densities at the *ortho*- and *para*-positions (2rd, 3rd, and 4th structures) make these positions stronger electron acceptors for both organic synthesis and determining CT character in the DMAC–BZN isomers.

is still too low to promote efficient emission, and this relaxation also comes at a cost of slower rISC in the DF (compared to the early PF ISC occurring at the unrelaxed bond length, bestowing a temporarily increased CT character).

The relatively fast PF lifetime in ***meta*-2** we suggest may be due to faster ISC, itself also a result of the larger CT character compared to the other isomers. Alternatively or additionally, there may be quenching modes associated with the D–A bond stretch, which are enhanced in ***meta*-2** as its weaker bond (with smaller spring constant) makes these modes easier to populate. In contrast, restrictions of quenching vibrational modes have been used to explain the superior performance of TADF materials exhibiting intramolecular hydrogen bonding.[55,56] In the delayed emission the electronic decoupling of donor and (weakest) acceptor in ***meta*-2** results in a material with a low ΔE_{ST} and fast rISC, but one without the ability to effectively undergo radiative decay from the singlet state and thus inferior PLQYs. These changes in CT and LE character during the ***meta*-2** emission decay (and associated ISC and rISC rates) also then explain the difficulty in fitting the decay to a single exponential, while similar fitting is straightforward for the other two isomers.

In contrast, ***para*-3** has a larger ΔE_{ST} and longer (*i.e.*, worse) DF lifetime, but conversely possesses much enhanced emission properties. Radiative rates for all materials in zeonex were calculated from the PF decay lifetime and the air PLQY, according to Dias *et al.*[39] The radiative rate is fastest for ***para*-3**, followed by ***ortho*-1** and then ***meta*-2**. This again reflects the differences in CT character between these materials, with ***para*-3** possessing the most LE character and ***meta*-2** the most CT character. Due to its increased LE character the radiative rate constant is large and PF lifetime is therefore fast for ***para*-3**, a similar outcome to ***meta*-2** but for very different reasons. This interpretation is supported by the larger fraction of PF decays being emissive for ***para*-3** (compare 20% *vs.* 9% PLQYs in air). This compound is not able to harvest triplets as quickly as ***meta*-2**, but the triplets that it does harvest to the singlet state are able to emit more readily, giving ***para*-3** a larger DF PLQY component as well. The emission is also the most blue-shifted, indicating that this material possesses the most LE character, again in agreement with its fast PF rate.[52,53]

We expect similar resonance and inductive effects for ***ortho*-1** compared to ***para*-3**, but the additional dipole interaction further restricts the D–A dihedral angle (and D–A bond elongation) in ***ortho*-1** only. In this way ***ortho*-1** enjoys better conjugation than ***meta*-2** due to increased acceptor strength, while still retaining a higher CT character (and smaller ΔE_{ST}) than ***para*-3**. As a result, ***ortho*-1** has a longer PF lifetime than ***para*-3** but a shorter DF lifetime and overall the best PLQYs. In DPEPO the ΔE_{ST} gaps remain small for ***ortho*-1** and ***meta*-2** and is reduced for ***para*-3** (88 meV, Fig. S15, ESI†), while any excited-state D–A bond lengthening is likely to be severely restricted by host packing. Hence, we observe much more similar kinetic behaviour for all three materials, as shown by the tighter clustering of decay curves in Fig. 3b (compared to the rapid divergence of emission decays in zeonex, Fig. 3a).

Similar arguments appear to explain the differences observed between "angular" and "linear" D–A–D isomers with DMAC donors and similar ΔE_{ST} values.[34] We identify that the "angular" isomers are *para*-substituted with respect to the electron withdrawing moiety of the acceptor unit, while "linear" isomers are *meta*-substituted. As demonstrated in the DMAC–BZN isomers, resonance effects associated with *para*-connectivity result in increased effective acceptor strength which is needed to balance emissive and triplet harvesting properties. The trend seen here and elsewhere of *para*-substituted materials outperforming *meta*-substituted ones may be reversed with more exotic choices of acceptor. Electron accepting groups that are inductively withdrawing towards the *meta*-position (such as CH_2NO_2, NO, and $CHCl_2$) might achieve this, although we are not aware of any reported examples. Similar performance trends comparing *meta*- and *para*-substituted TADF materials are also seen for other donors, although in those cases differences in D–A angles and donor conformation (and ΔE_{ST} values) appear to dominate.[15,21,33]

Finally, the use of physically attractive rather than repulsive potentials to engineer dihedral control is also simultaneously attractive for molecular design. As exhibited by the C–H···N–C– dipole interaction in ***ortho*-1**, this can be used to 'nudge' molecular structural parameters towards the desired values, and then keep them trapped there. This is in contrast to the use of repulsive potentials, where multiple substituents must be used to 'bookend' the target structural parameter at the edges of the desired range. The inner DMAC hydrogens unexpectedly trapping the BZN ring is revealed to be a fortuitous example of this second kind of dihedral control. Alternatively, complete locking of the D–A angle in a perpendicular conformation has

been shown to reduce the dynamic rocking of chromophores necessary for rISC, hence resulting in room temperature phosphorescence.[57]

Conclusions

Detailed DFT calculations have been used to unravel the initially perplexing photophysics of three DMAC–BZN positional isomers. The D–A bond dihedral angles – often the critical factor in similar studies – are found to be much more alike than expected due to the inward pointing DMAC C–H bonds capturing the plane of the BZN acceptor ring. TD-DFT was f-state properties of the structural isomers beyond qualitative comparisons, while use of the Tamm–Dancoff approximation led to much more accurate results.

With identical D–A dihedral environments, the large differences between *meta*- and *para*-isomers are instead attributed to different bond lengths and acceptor strengths associated with resonance and inductive effects in the BZN π-system. The *para*- and *ortho*-isomers are likely similar in acceptor strength, but an additional intramolecular dipole interaction further restricts *ortho*-D–A dihedral angle rotation, and results in improved performance. We also identify D–A bond length relaxation as an important factor in TADF performance, alongside D–A dihedral motion.

Finally, we identify an interesting and useful example of an attractive intramolecular dipole interaction that can be used to control dihedral angles by trapping at favourable angles instead of repelling from unfavourable ones. These kinds of dihedral control open new horizons in TADF rational design.

Conflicts of interest

There are no conflicts to declare.

Acknowledgements

NAK, HFH, MKE, and APM acknowledge the EU's Horizon 2020 for funding the PHEBE project under grant no. 641725. NAK, MKE, AD, NH and APM acknowledge the EU's Horizon 2020 for funding the HyperOLED project under grant no. 641725. APM thanks EPSRC grant EP/L02621X/1 for funding. ANB acknowledges an EPSRC Doctoral Training Grant. TOC image elements adapted from ref. 58, under Creative Commons BY 3.0 license.[58]

References

1 H. Uoyama, K. Goushi, K. Shizu, H. Nomura and C. Adachi, *Nature*, 2012, **492**, 234–238.
2 Z. Yang, Z. Mao, Z. Xie, Y. Zhang, S. Liu, J. Zhao, J. Xu, Z. Chi and M. P. Aldred, *Chem. Soc. Rev.*, 2017, **46**, 915–1016.
3 W. Hu, *Organic optoelectronics*, Wiley-VCH, 2013.
4 D. Volz, M. Wallesch, C. Flechon, M. Danz, A. Verma, J. M. Navarro, D. M. Zink, S. Brase and T. Baumann, *Green Chem.*, 2015, **17**, 1988–2011.
5 C. Adachi, *Jpn. J. Appl. Phys.*, 2014, **53**, 60101.
6 Y. Tao, K. Yuan, T. Chen, P. Xu, H. Li, R. Chen, C. Zheng, L. Zhang and W. Huang, *Adv. Mater.*, 2014, **26**, 7931–7958.
7 M. Y. Wong and E. Zysman-Colman, *Adv. Mater.*, 2017, **29**, 1605444.
8 Q. Zhang, B. Li, S. Huang, H. Nomura, H. Tanaka and C. Adachi, *Nat. Photonics*, 2014, **8**, 326–332.
9 E. Spuling, N. Sharma, I. D. W. Samuel, E. Zysman-Colman and S. Bräse, *Chem. Commun.*, 2018, **54**, 9278–9281.
10 Y. Gao, Q.-Q. Pan, L. Zhao, Y. Geng, T. Su, T. Gao and Z.-M. Su, *Chem. Phys. Lett.*, 2018, **701**, 98–102.
11 K.-L. Woon, C.-L. Yi, K.-C. Pan, M. K. Etherington, C.-C. Wu, K.-T. Wong and A. P. Monkman, *J. Phys. Chem. C*, 2019, **123**, 12400–12410.
12 X. Wang, S. Wang, J. Lv, S. Shao, L. Wang, X. Jing and F. Wang, *Chem. Sci.*, 2019, **10**, 2915–2923.
13 J. Gibson, A. P. Monkman and T. J. Penfold, *ChemPhysChem*, 2016, **17**, 2956–2961.
14 C. Chen, R. Huang, A. S. Batsanov, P. Pander, Y.-T. Hsu, Z. Chi, F. B. Dias and M. R. Bryce, *Angew. Chem.*, 2018, **130**, 16645–16649.
15 M. K. Etherington, F. Franchello, J. Gibson, T. Northey, J. Santos, J. S. Ward, H. F. Higginbotham, P. Data, A. Kurowska, P. Lays, D. Santos, D. R. Graves, A. S. Batsanov, F. B. Dias, M. R. Bryce, T. J. Penfold and A. P. Monkman, *Nat. Commun.*, 2017, **8**, 14987.
16 R. Huang, J. S. Ward, N. A. Kukhta, J. Avó, J. Gibson, T. Penfold, J. C. Lima, A. S. Batsanov, M. N. Berberan-Santos, M. R. Bryce and F. B. Dias, *J. Mater. Chem. C*, 2018, **6**, 9238–9247.
17 C. S. Oh, D. de, S. Pereira, S. H. Han, H.-J. Park, H. F. Higginbotham, A. P. Monkman and J. Y. Lee, *ACS Appl. Mater. Interfaces*, 2018, **10**, 35420–35429.
18 H. F. Higginbotham, C.-L. Yi, A. P. Monkman and K.-T. Wong, *J. Phys. Chem. C*, 2018, **122**, 7627–7634.
19 M. K. Etherington, N. A. Kukhta, H. F. Higginbotham, A. Danos, A. N. Bismillah, D. R. Graves, P. R. McGonigal, N. Haase, A. Morherr, A. S. Batsanov, C. Pflumm, V. Bhalla, M. R. Bryce and A. P. Monkman, *J. Phys. Chem. C*, 2019, **123**, 11109–11117.
20 C. S. Oh, H. L. Lee, S. H. Han and J. Y. Lee, *Chem. – Eur. J.*, 2019, **25**, 642–648.
21 N. A. Kukhta, A. S. Batsanov, M. R. Bryce and A. P. Monkman, *J. Phys. Chem. C*, 2018, **122**, 28564–28575.
22 P. L. dos Santos, J. S. Ward, M. R. Bryce and A. P. Monkman, *J. Phys. Chem. Lett.*, 2016, **7**, 3341–3346.
23 G. Meng, X. Chen, X. Wang, N. Wang, T. Peng and S. Wang, *Adv. Opt. Mater.*, 2019, **7**, 1900130.
24 W. Song and J. Y. Lee, *J. Phys. D: Appl. Phys.*, 2015, **48**, 365106.
25 M. Godumala, S. Choi, M. J. Cho and D. H. Choi, *J. Mater. Chem. C*, 2019, **7**, 2172–2198.
26 Y. Im, M. Kim, Y. J. Cho, J.-A. Seo, K. S. Yook and J. Y. Lee, *Chem. Mater.*, 2017, **29**, 1946–1963.
27 H. Noda, R. Kabe and C. Adachi, *Chem. Lett.*, 2016, **45**, 1463–1466.

28 Y. Zhang, D. Zhang, M. Cai, Y. Li, D. Zhang, Y. Qiu and L. Duan, *Nanotechnology*, 2016, **27**, 94001.
29 K.-C. Pan, S.-W. Li, Y.-Y. Ho, Y.-J. Shiu, W.-L. Tsai, M. Jiao, W.-K. Lee, C.-C. Wu, C.-L. Chung, T. Chatterjee, Y.-S. Li, K.-T. Wong, H.-C. Hu, C.-C. Chen and M.-T. Lee, *Adv. Funct. Mater.*, 2016, **26**, 7560–7571.
30 Y. Geng, L.-S. Cui, J. U. Kim, H. Nakanotani and C. Adachi, *Chem. Lett.*, 2017, **46**, 1490–1492.
31 M. Kim, S.-J. Yoon, S. H. Han, R. Ansari, J. Kieffer, J. Y. Lee and J. Kim, *Chem. – Eur. J.*, 2019, **25**, 1829–1834.
32 F. B. Dias, K. N. Bourdakos, V. Jankus, K. C. Moss, K. T. Kamtekar, V. Bhalla, J. Santos, M. R. Bryce and A. P. Monkman, *Adv. Mater.*, 2013, **25**, 3707–3714.
33 R. Huang, J. Avó, T. Northey, E. Chaning-Pearce, P. L. dos Santos, J. S. Ward, P. Data, M. K. Etherington, M. A. Fox, T. J. Penfold, M. N. Berberan-Santos, J. C. Lima, M. R. Bryce and F. B. Dias, *J. Mater. Chem. C*, 2017, **5**, 6269–6280.
34 P. Stachelek, J. S. Ward, P. L. dos Santos, A. Danos, M. Colella, N. Haase, S. J. Raynes, A. S. Batsanov, M. R. Bryce and A. P. Monkman, *ACS Appl. Mater. Interfaces*, DOI: 10.1021/acsami.9b06364.
35 T.-A. Lin, T. Chatterjee, W.-L. Tsai, W.-K. Lee, M.-J. Wu, M. Jiao, K.-C. Pan, C.-L. Yi, C.-L. Chung, K.-T. Wong and C.-C. Wu, *Adv. Mater.*, 2016, **28**, 6976–6983.
36 C. M. Marian, *Wiley Interdiscip. Rev.: Comput. Mol. Sci.*, 2012, **2**, 187–203.
37 C. M. Marian, *J. Phys. Chem. C*, 2016, **120**, 3715–3721.
38 P. L. dos Santos, J. S. Ward, P. Data, A. S. Batsanov, M. R. Bryce, F. B. Dias and A. P. Monkman, *J. Mater. Chem. C*, 2016, **4**, 3815–3824.
39 F. B. Dias, T. J. Penfold and A. P. Monkman, *Methods Appl. Fluoresc.*, 2017, **5**, 12001.
40 F. B. Dias, J. Santos, D. R. Graves, P. Data, R. S. Nobuyasu, M. A. Fox, A. S. Batsanov, T. Palmeira, M. N. Berberan-Santos, M. R. Bryce and A. P. Monkman, *Adv. Sci.*, 2016, **3**, 1600080.
41 P. L. Dos Santos, J. S. Ward, M. R. Bryce and A. P. Monkman, *J. Phys. Chem. Lett.*, 2016, **7**, 3341–3346.
42 D. R. Lee, M. Kim, S. K. Jeon, S.-H. Hwang, C. W. Lee and J. Y. Lee, *Adv. Mater.*, 2015, **27**, 5861–5867.
43 N. Haase, A. Danos, C. Pflumm, A. Morherr, P. Stachelek, A. Mekic, W. Brütting and A. P. Monkman, *J. Phys. Chem. C*, 2018, **122**, 29173–29179.
44 T. Northey, J. Stacey and T. J. Penfold, *J. Mater. Chem. C*, 2017, **5**, 11001–11009.
45 J.-M. Ku, D.-K. Kim, T.-H. Ryu, E.-H. Jung, Y. Lansac and Y.-H. Jang, *Bull. Korean Chem. Soc.*, 2012, **33**, 1029–1036.
46 L.-S. Cui, H. Nomura, Y. Geng, J. U. Kim, H. Nakanotani and C. Adachi, *Angew. Chem., Int. Ed.*, 2017, **56**, 1571–1575.
47 S.-J. Woo, Y. Kim, S.-K. Kwon, Y.-H. Kim and J.-J. Kim, *ACS Appl. Mater. Interfaces*, 2019, **11**, 7199–7207.
48 S. Hirata and M. Head-Gordon, *Chem. Phys. Lett.*, 1999, **314**, 291–299.
49 A. Chantzis, A. D. Laurent, C. Adamo and D. Jacquemin, *J. Chem. Theory Comput.*, 2013, **9**, 4517–4525.
50 T. Lu and F. Chen, *J. Comput. Chem.*, 2012, **33**, 580–592.
51 S. Huang, Q. Zhang, Y. Shiota, T. Nakagawa, K. Kuwabara, K. Yoshizawa and C. Adachi, *J. Chem. Theory Comput.*, 2013, **9**, 3872–3877.
52 M. Colella, A. Danos and A. P. Monkman, *J. Phys. Chem. Lett.*, 2019, **10**, 793–798.
53 M. Colella, A. Danos and A. P. Monkman, *J. Phys. Chem. C*, DOI: 10.1021/acs.jpcc.9b03538.
54 X.-K. Chen, Y. Tsuchiya, Y. Ishikawa, C. Zhong, C. Adachi and J.-L. Brédas, *Adv. Mater.*, 2017, **29**, 1702767.
55 X. Qiu, Y. Xu, C. Wang, M. Hanif, J. Zhou, C. Zeng, Y. Li, Q. Jiang, R. Zhao, D. Hu and Y. Ma, *J. Mater. Chem. C*, 2019, **7**, 5461–5467.
56 V. Thangaraji, P. Rajamalli, J. Jayakumar, M.-J. Huang, Y.-W. Chen and C.-H. Cheng, *ACS Appl. Mater. Interfaces*, 2019, **11**, 17128–17133.
57 J. S. Ward, R. S. Nobuyasu, A. S. Batsanov, P. Data, A. P. Monkman, F. B. Dias and M. R. Bryce, *Chem. Commun.*, 2016, **52**, 2612–2615.
58 R. Mohapatra and S. Panda, *Int. J. Zool.*, 2014, **2014**, 1–7.